



**HAL**  
open science

# Multi-scale modelling of highly-diluted gasoline premixed flames

Boyang Xu

► **To cite this version:**

Boyang Xu. Multi-scale modelling of highly-diluted gasoline premixed flames. Theoretical and/or physical chemistry. Institut Polytechnique de Paris, 2019. English. NNT: 2019IPPAE003. tel-03544420

**HAL Id: tel-03544420**

**<https://theses.hal.science/tel-03544420>**

Submitted on 26 Jan 2022

**HAL** is a multi-disciplinary open access archive for the deposit and dissemination of scientific research documents, whether they are published or not. The documents may come from teaching and research institutions in France or abroad, or from public or private research centers.

L'archive ouverte pluridisciplinaire **HAL**, est destinée au dépôt et à la diffusion de documents scientifiques de niveau recherche, publiés ou non, émanant des établissements d'enseignement et de recherche français ou étrangers, des laboratoires publics ou privés.

# Compréhension et Modélisation de Flammes d'Essence à Fortes Charges et Fortes Dilutions

Thèse de doctorat de l'Institut Polytechnique de Paris  
préparée à l'ENSTA Paris

École doctorale n°626 Ecole Doctorale de  
l'Institut Polytechnique de Paris (ED IP Paris)  
Spécialité de doctorat: Génie des procédés et énergétique

Thèse présentée et soutenue à Palaiseau, 18 Décembre 2019, par

**Boyang XU**

Composition du Jury :

Nabiha CHAUMEIX Directrice de Recherche, CNRS-INSIS (ICARE)	Présidente et Rapporteuse
Richard WEST Professeur Associé, Northeastern University (College of Engineering)	Rapporteur
René FOURNET Professeur, Université de Lorraine (CNRS-LRGP)	Examineur
Dong HAN Professeur Associé, Shanghai Jiao Tong University (Department of Mechanical Engineering)	Examineur
André NICOLLE Senior Scientist, Aramco Overseas Company (Fuel Research Center)	Examineur
Mickaël MATRAT Project Leader, IFP Energies nouvelles	Examineur
Julian GARREC Enseignant Chercheur, ENSTA Paris (UCP)	Examineur
Laurent CATOIRE Professeur, ENSTA Paris (UCP)	Directeur de thèse



# Contents

<b>1</b>	<b>Introduction</b>	<b>1</b>
1.1	Background . . . . .	1
1.2	Exhaust Gas Recirculation in Gasoline Engines . . . . .	3
1.2.1	Classification of EGR technology . . . . .	4
1.2.2	Effect on Fuel Economy . . . . .	4
1.2.3	Effect on NOx emission . . . . .	4
1.2.4	Effect on Engine Knock . . . . .	5
1.2.5	Difficulty of Reaching High EGR Ratio . . . . .	5
1.3	Experimental and Correlation Studies on the Laminar Flame Speed of Gasoline and Surrogate Fuels at Diluted Conditions . . . . .	5
1.3.1	Surrogate Fuels Development Based on Laminar Flame Speed	6
1.3.2	Laminar Flame Speed Measurements of Gasoline and Surrogate Fuels at Diluted Conditions . . . . .	7
1.3.3	Correlation Studies of the Dilution Effect on Laminar Flame Speed . . . . .	10
1.4	Kinetic Modeling Studies of Gasoline Surrogate Flames . . . . .	12
1.4.1	General Features of Kinetic Modeling and Kinetic Mechanisms	12
1.4.2	The Core (C <sub>0</sub> –C <sub>4</sub> ) Sub-mechanisms . . . . .	14
1.4.3	The Fuel Decomposition Sub-mechanisms . . . . .	16
1.5	The MACDIL Project . . . . .	21
1.6	Objectives and Significance . . . . .	22
1.7	Thesis Structure . . . . .	23
<b>2</b>	<b>Multi-Scale Theories and Computational Details</b>	<b>25</b>
2.1	Methodology . . . . .	25
2.2	Micro-scale: <i>ab initio</i> Electronic Structure . . . . .	27
2.2.1	Basic Principles and Approximations . . . . .	27
2.2.2	Hartree-Fock Method . . . . .	33
2.2.3	Electron Correlation: Wave Function Methods . . . . .	35
2.2.4	Electron Correlation: Density Functional Theory . . . . .	39
2.2.5	Composite Methods for Energy Calculations . . . . .	42
2.3	Micro-scale: Theoretical Rate Coefficient . . . . .	42
2.3.1	Potential Energy Surface . . . . .	42
2.3.2	Transition State Theory . . . . .	44
2.3.3	RRKM/ME . . . . .	45
2.4	Macro-scale: Laminar Flame Speed . . . . .	51
2.4.1	Theoretical and Numerical Presentation . . . . .	51
2.4.2	Experimental Measurements . . . . .	53



2.5	Macro-scale: Dilution Effects . . . . .	56
2.5.1	Categorization of Dilution Effects . . . . .	56
2.5.2	Quantification of Dilution Effects . . . . .	60
2.6	Macro-scale: Kinetic Mechanism Development . . . . .	62
2.6.1	Validation of Calculation Results . . . . .	62
2.6.2	Sensitivity Analysis on Composite Functions . . . . .	63
2.6.3	Improvement of Kinetic Mechanisms . . . . .	65
2.7	Numerical Tools . . . . .	65
2.7.1	Gaussian . . . . .	65
2.7.2	ORCA . . . . .	65
2.7.3	Avogadro . . . . .	65
2.7.4	MESS . . . . .	66
2.7.5	Chemkin Pro . . . . .	66
<b>3</b>	<b>Theoretical Study on the Temperature and Pressure Dependent Rate Coefficients for the Reaction of Ketene with Hydroxyl Radical</b>	<b>67</b>
3.1	Introduction . . . . .	67
3.2	Computational Methods . . . . .	69
3.2.1	Electronic Structure . . . . .	69
3.2.2	Temperature and Pressure Dependent Rate Coefficients . . .	70
3.3	Results . . . . .	71
3.3.1	Potential Energy Surface . . . . .	71
3.3.2	Rate Coefficients . . . . .	72
3.3.3	Branching Ratios . . . . .	75
3.4	Discussion . . . . .	75
3.4.1	Pathway 1: H Abstraction . . . . .	77
3.4.2	Pathway 2: OH Addition on the Olefinic Carbon Atom . . .	78
3.4.3	Pathway 3: OH Addition on the Carbonyl Carbon Atom . .	80
3.4.4	Overall Rate Constant . . . . .	81
3.4.5	Branching Ratios . . . . .	83
3.4.6	Product Formation . . . . .	83
3.4.7	Sensitivity Analysis for TS1, TS2 and TS10 . . . . .	84
3.5	Conclusions . . . . .	87
<b>4</b>	<b>Identification of Key Thermokinetic Parameters for Mechanism Development</b>	<b>89</b>
4.1	Introduction . . . . .	89
4.2	Setup of the Initial Model . . . . .	89
4.2.1	Surrogate Composition . . . . .	89
4.2.2	Mixture Composition . . . . .	91
4.2.3	Investigated Conditions . . . . .	92
4.2.4	Starting Mechanism . . . . .	93
4.3	Important Reactions . . . . .	95
4.3.1	Conventional Sensitivity Analysis Based on $S_L$ . . . . .	96
4.3.2	Sensitivity Analysis Based on Composite Functions of $S_L$ . .	101
4.3.3	Important In-mechanism Reactions . . . . .	104
4.3.4	Radical + Diluent Molecule Reactions . . . . .	105

4.3.5	Reactions of Interests for Further Theoretical Studies . . . . .	106
4.4	Important Thermodynamic Parameters . . . . .	108
4.5	Conclusions . . . . .	110
<b>5</b>	<b>Kinetic Study on the Chemical Effects of H<sub>2</sub>O and CO<sub>2</sub> Dilution on Laminar Flame Speeds</b>	<b>111</b>
5.1	Introduction . . . . .	111
5.2	Diluted Flames of Hydrogen (H <sub>2</sub> ) . . . . .	111
5.2.1	Laminar Flame Speeds . . . . .	111
5.2.2	Effects of H <sub>2</sub> O Dilution on H <sub>2</sub> /air flames . . . . .	114
5.3	Diluted Flames of Syngas (H <sub>2</sub> /CO) . . . . .	122
5.3.1	Laminar Flame Speeds . . . . .	122
5.3.2	Effect of CO <sub>2</sub> Dilution on H <sub>2</sub> /CO/air flames . . . . .	126
5.4	Diluted Flames of Methane (CH <sub>4</sub> ) . . . . .	128
5.4.1	Laminar Flame Speeds . . . . .	128
5.4.2	Effect of CO <sub>2</sub> Dilution . . . . .	130
5.5	Conclusions . . . . .	138
<b>6</b>	<b>Detailed and Semi-Detailed Mechanisms for One Gasoline Surrogate (TRFE): Mechanisms, Validation on <math>S_L</math> and Insights to Correlations of <math>S_L</math></b>	<b>141</b>
6.1	Detailed Mechanism: MACDIL-DTL . . . . .	141
6.1.1	Formulation of the Mechanism . . . . .	142
6.1.2	Preferred Rate Coefficients for Some Key Reactions . . . . .	145
6.2	Semi-Detailed Mechanism: MACDIL-RDC . . . . .	152
6.3	Validation of MACDIL-RDC on the Laminar Flame Speeds of TR- FE/air/EGR Mixtures . . . . .	154
6.3.1	Introduction . . . . .	154
6.3.2	Laminar Flame Speed of TRFE/air/EGR Mixtures . . . . .	154
6.3.3	Effect of EGR on Laminar Flame Speed . . . . .	159
6.3.4	Summary . . . . .	162
6.4	Insights to the Development of Correlations for Laminar Flame speed at Diluted Conditions . . . . .	163
6.5	Conclusions . . . . .	167
<b>7</b>	<b>Conclusions and Future Works</b>	<b>169</b>
7.1	Conclusions . . . . .	169
7.2	Future Works . . . . .	171

## Appendix

<b>A</b>	<b>Supporting Information for Chapter 3</b>	<b>173</b>
A.1	Electronic Structure . . . . .	173
A.1.1	Potential Energy Surface . . . . .	173
A.1.2	Optimized Geometries . . . . .	175
A.1.3	Electronic Energies and T1 diagnostics . . . . .	179
A.1.4	Vibrational Frequencies . . . . .	179
A.1.5	Hindered Rotor Potentials . . . . .	181

A.1.6	ROHF Treatment . . . . .	181
A.2	RRKM/ME . . . . .	182
A.2.1	Long-range TST Treatments . . . . .	182
A.2.2	Entrance Channels . . . . .	184
A.2.3	Quantum Tunneling Treatment . . . . .	184
A.2.4	Rate Coefficients for R3-4a and R3-4b . . . . .	186
A.2.5	Simplified Scheme . . . . .	186
A.2.6	Fitted Arrhenius Expressions . . . . .	186
A.2.7	Effect of the Updated Rate Coefficients on the Laminar Flame Speed of Acetone . . . . .	188
<b>B</b>	<b>Supporting Information for Chapter 4, 5 and 6</b>	<b>191</b>
B.1	Supporting Information for Chapter 4 . . . . .	191
B.2	Supporting Information for Chapter 5 . . . . .	192
B.2.1	Diluted Flames of Syngas ( $\text{H}_2/\text{CO}$ ) . . . . .	192
B.2.2	Diluted Flames of Methane ( $\text{CH}_4$ ) . . . . .	192
B.3	Supporting Information for Chapter 6 . . . . .	192
B.3.1	The Detailed and Semi-Detailed Mechanisms . . . . .	192
B.3.2	Validation of MACDIL-RDC on Laminar Flame Speeds of TRFE/air/EGR Mixtures . . . . .	192

# List of Figures

1-1	Historical and estimated world total primary energy demand (TPED), with breakdown in energy sources. Estimation is based on the New Policies Scenario (NPS), which counts for all existing policies and announced policy intentions. Graphic taken from Ref [1]. . . . .	2
1-2	MACDIL strategy for the development and validation of combustion models for high dilution, temperature and pressure conditions.	22
2-1	General methodology of the present study. . . . .	26
2-2	Macro-scale methodology for the study of dilution effects (a) and the development of kinetic mechanisms (b & c). . . . .	27
2-3	Micro-scale methodology for the theoretical calculation of rate coefficients. . . . .	28
2-4	The harmonic oscillator model. Figures are taken from Ref. [2]. (a) the schematic diagram of two mass connected by a string, to describe the vibrational motion of a diatomic molecule. (b) Comparison of the harmonic oscillator potential (dashed line) with the complete internuclear potential (solid line) of a diatomic molecule. .	30
2-5	Schematic of a rigid rotor, i.e., two masses rotating about their center of mass. Figure taken from Ref. [2]. . . . .	31
2-6	Basic configuration of a one-dimensional freely propagating flame. Figure taken from [3]. . . . .	52
2-7	Schematic diagram showing three experimental methods to measure laminar flame speed. (a) Spherical flame method, graphic taken from Ref. [4]. (b) Heat flux burner, graphic taken from Ref. [5]. (c) Stagnation/counterflow flame method, graphic taken from Ref. [4]. .	54
2-8	Demonstration of the quantification of dilution effects using the false-species method. Use the laminar flame speeds of H <sub>2</sub> /air/H <sub>2</sub> O mixtures as examples. . . . .	62
3-1	Main features of the CH <sub>2</sub> CO + OH potential energy surface. (a) Dominant pathways of the reaction, showing the relative electronic energy (corrected by ZPE) of the most relevant stationary points. (b) Structures of the reactive complex (RC) and transition states TS1, TS2 and TS10. Critical distances and angles are displayed in angstroms and in degrees, respectively. C <sub>α</sub> and C <sub>β</sub> are the olefinic and carbonyl carbon atoms in ketene respectively. . . . .	72

3-2	Rate constant for the overall reaction $\text{CH}_2\text{CO} + \text{OH} \longrightarrow \text{Products}$ . Points are experimentally measured values by Brown <i>et al.</i> [6], Faubel <i>et al.</i> [7] (lower limit), Hatakeyama <i>et al.</i> [8] and Oehlers <i>et al.</i> [9]; the dashed line with gray error area is the recommendation by Baulch <i>et al.</i> [10]; The other lines are calculated values at different pressures (this work). . . . .	73
3-3	Temperature- and pressure-dependent rate coefficients of reaction channels R3-1–R3-3b. $k_1$ and $k_2$ are pressure independent whereas $k_{3a}$ and $k_{3b}$ are pressure dependent. In Figures 3-3a–3-3c, the present rate constants are compared with the rate parameters listed in Table 3.2 which are widely used in kinetic mechanisms. In Figure 3-3a, $k_1$ is compared with the rate coefficients for the analogous reaction propene + OH $\longrightarrow$ propen-1-yl + H <sub>2</sub> O calculated by Zádor <i>et al.</i> [11]. . . . .	74
3-4	Branching ratios of primary product channels at different temperatures and pressures. lines: calculated values for the 4 major product channels by this work; points: RRKM calculations by Hou <i>et al.</i> [12].	76
3-5	Overall rate coefficients for Pathway 3 (OH addition on the carbonyl carbon atom) at different temperatures. . . . .	82
3-6	Effect of the uncertainty in TS1, TS2 and TS10 energies on the rate coefficients of their corresponding pathways at 1 atm. Effects at other pressures are qualitatively the same. . . . .	85
3-7	Effect of the uncertainty in TS1, TS2 and TS10 energies on $k_{\text{overall}}$ at 1 atm. Effects at other pressures are qualitatively the same. If not specified, lines above the nominal case are for reduced energies whereas lines below are for increased energies. (a) Individual effects of TS1, TS2 and TS10 energies. Tweaking TS1 energy results in minor changes, as their curves mostly overlap with the nominal one. (b) Cumulative effects of tweaking TS2 and TS10 energy simultaneously in the same or opposite direction. . . . .	86
4-1	Schematic diagram of the approach used in Chapter 4. . . . .	89
4-2	Comparison of the $S_L$ calculated with the candidate mechanisms. Experimental data are from Endouard <i>et al.</i> [13], for the isooctane/air/CO <sub>2</sub> mixture, $\phi = 1.1$ , $T_u = 423$ K, P = 10 atm. . . . .	94
4-3	Comparison on the calculated $S_L$ by MACDIL 2016 and E-Reitz with experiments. (a) TRFE/air/EGR flames, experimental data from Manna <i>et al.</i> [14]. fuel composition (vol.%): 18% n-heptane, 77% isooctane, 5% toluene; EGR composition: 14% H <sub>2</sub> O, 10% CO <sub>2</sub> , 76% N <sub>2</sub> ; $\phi = 1.1$ , $T_u = 358$ K, P = 6 bar. (b) ERF/air flames with different ethanol concentration, experimental data from Liao <i>et al.</i> [15]. ERF-1 composition (vol.%): 10% n-heptane, 75% isooctane, 15% ethanol; ERF-2 composition: 10% n-heptane, 85% isooctane, 5% ethanol; $T_u = 298.15$ K, P = 1 atm. . . . .	95
4-4	Sensitive reactions at practical conditions (C1 and C2) at different equivalence ratios. (a) $\phi = 1.1$ . (b) $\phi = 0.8$ . (c) $\phi = 1.4$ . . . . .	97
4-5	Sensitive reactions for practical and target conditions (C1–C4) at $\phi = 1.1$ . . . . .	99

4-6	Evolution of sensitivity with EGR ratio, for the common reactions at conditions C1–C4. The relative sensitivity of a reaction at a certain condition is calculated as $s_i^{rel}(Cj) = \frac{s_i(Cj) - s_i(C1)}{s_i(C1)}$ , where $s_i(Cj)$ is the normalized sensitivity of the $i$ th reaction at the $j$ th condition. . . . .	100
4-7	Sensitive reactions for dedicated conditions (C5–C6) at $\phi = 1.1$ . . . . .	100
4-8	Reactions sensitive to the (a) absolute and (b) relative changes in $S_L$ caused by the local variation of EGR ratio. Reference case is condition C2 at $\phi = 1.1$ , based on which EGR ratio in the new calculation is varied locally from 20% to 25%. Methods to derive normalized sensitivity on composite functions, such as the absolute and relative change in $S_L$ , are described in Section 2.6.2. . . . .	102
4-9	Reactions sensitive to the (a) absolute and (b) relative changes in $S_L$ caused by the local variation of initial temperature. Reference case is condition C2 at $\phi = 1.1$ , based on which the $T_u$ in the new calculation is varied locally from 473 to 523 K. Methods to derive normalized sensitivity on composite functions, such as the absolute and relative change in $S_L$ , are described in Section 2.6.2. . . . .	103
4-10	Sensitive reactions for the changes in $S_L$ caused by varying pressure. Reference case is condition C2 at $\phi = 1.1$ , and then change is made on pressure from 5 to 6 bar. . . . .	103
4-11	Reactions sensitive to the (a) absolute and (b) relative changes in $S_L$ caused by the local variation of pressure. Reference case is condition C2 at $\phi = 1.1$ , based on which the pressure in the new calculation is varied locally from 5 to 6 bar. Methods to derive normalized sensitivity on composite functions, such as the absolute and relative change in $S_L$ , are described in Section 2.6.2. . . . .	103
4-12	Resonance structures of the phenoxy radical. Graphic taken from Ref. [16]. . . . .	107
4-13	$\Delta_f^{298}H$ sensitivity of $S_L$ at condition C5 with various equivalence ratios ( $\phi = 1.0, 1.1, 1.2$ ). Results are obtained using the MACDIL 2016 mechanism. . . . .	109
4-14	$\Delta_f^{298}H$ sensitivity of $S_L$ at condition C6 with various equivalence ratios ( $\phi = 1.0, 1.1, 1.2$ ). Results are obtained using the MACDIL 2016 mechanism. . . . .	109
4-15	Comparison of $\Delta_f^{298}H$ sensitivity of $S_L$ at various dilution ratios (30%, 50% and 70%). The rest condition, i.e., initial temperature, pressure, equivalence ratio, are the same as condition C5: 1200 K, 10 bar, $\phi = 1.1$ . Results are obtained using the MACDIL 2016 mechanism. . . . .	110
5-1	Fundamental $S_L$ of $H_2$ /air mixture at 298 K and 1 atm. . . . .	112
5-2	Laminar flame speed of $H_2$ /air/ $H_2O$ mixture with different $H_2O$ dilution ratios. Figures 5-2a–5-2c show evolution of $S_L$ with equivalence ratio, and Figure 5-2d shows evolution with pressure. . . . .	113

5-3	Quantification of H <sub>2</sub> O dilution effects on the $S_L$ of stoichiometric H <sub>2</sub> /air mixtures at initial temperature of 440 K and pressure of 5 atm. Simulations are done using the K�eromn�es 2013 mechanism [17]. The original negative values in Figure 5-3b–5-3d are adjusted to positive for visual convenience. . . . .	115
5-4	Effects of H <sub>2</sub> O dilution on the flame temperature. . . . .	117
5-5	Evolution of maximum mole fraction of H, OH, O, HO <sub>2</sub> , and H <sub>2</sub> O <sub>2</sub> radicals with dilution ratio. . . . .	117
5-6	Dilution effects of iH <sub>2</sub> O, cH <sub>2</sub> O and H <sub>2</sub> O on the maximum mole fraction of the H, OH, O, HO <sub>2</sub> , and H <sub>2</sub> O <sub>2</sub> radicals. (a) Evolution of maximum mole fraction with dilution ratio. (b) Quantification of various dilution effects. The quantification, for example, of the direct reaction effect is calculated as the relative difference of the maximum mole fraction (e.g., [H] <sub>max</sub> ) at a certain dilution ratio of H <sub>2</sub> O with respect to the reference case, i.e., the maximum mole fraction at the same dilution ratio of cH <sub>2</sub> O. . . . .	118
5-7	Evolution of $S_L$ normalized sensitivity with H <sub>2</sub> O dilution ratio. Investigated conditions: H <sub>2</sub> /air/H <sub>2</sub> O flame, $\phi = 1$ , $T_u = 440$ K, $P = 5$ atm. . . . .	120
5-8	Sensitivity of $S_L$ changes caused by chemical effects of H <sub>2</sub> O dilution. Investigated conditions: H <sub>2</sub> /air/H <sub>2</sub> O flame, $\phi = 1$ , $X_d = 0.4$ , $T_u = 440$ K, $P = 5$ atm. . . . .	121
5-9	Evolution, with H <sub>2</sub> O dilution ratio, of the sensitivity of $S_L$ relative changes caused by chemical effects. Investigated conditions: H <sub>2</sub> /air/H <sub>2</sub> O flame, $\phi = 1$ , $T_u = 440$ K, $P = 5$ atm. . . . .	122
5-10	Comparison between mechanism predictions and measurements on the $S_L$ of H <sub>2</sub> /CO/air mixture at standard conditions (298 K, 1 atm). . . . .	123
5-11	Effect of temperature on the $S_L$ of H <sub>2</sub> /CO/air mixture (H <sub>2</sub> /CO = 0.05/0.95) at 1 atm. Experimental data are from Ref. [18]. . . . .	124
5-12	Effect of pressure on the $S_L$ of H <sub>2</sub> /CO/air mixture (H <sub>2</sub> /CO = 0.05/0.95) at 298 K. Experimental data are from Ref. [19, 20]. . . . .	125
5-13	Effect of CO <sub>2</sub> dilution in fuel on the laminar flame speed of equimolar syngas (H <sub>2</sub> /CO = 1/1) at standard conditions (298 K, 1 atm). Experimental data are from Natarajan <i>et al.</i> [18], Prathap <i>et al.</i> [21], and Han <i>et al.</i> [22]. . . . .	125
5-14	Effect of CO <sub>2</sub> dilution in fuel on $S_L$ , with variation of (a) H <sub>2</sub> /CO ratio and (b) initial temperature. Experimental data are Ref [18, 21, 22] and Wang <i>et al.</i> [23]. . . . .	126
5-15	False-species analysis on the different effects of CO <sub>2</sub> on the $S_L$ of syngas/air flames. . . . .	126
5-16	Sensitivity of important reactions in the CO <sub>2</sub> diluted H <sub>2</sub> /CO/air flame, performed based on its (a) $S_L$ , (b) absolute and (c) relative changes in $S_L$ caused by direct reaction effect (difference between CO <sub>2</sub> and cCO <sub>2</sub> dilution). The reference condition is: stoichiometric equimolar H <sub>2</sub> /CO mixture with 40% CO <sub>2</sub> dilution in fuel at standard conditions (298 K, 1 atm). . . . .	127
5-17	Laminar flame speed of CH <sub>4</sub> /air mixtures at standard conditions (298 K, 1 atm). . . . .	129

5-18	Laminar flame speed of CH <sub>4</sub> /air flames at higher temperature and pressure. . . . .	130
5-19	Effect of CO <sub>2</sub> dilution on the $S_L$ of CH <sub>4</sub> /air flames. (a) comparison of $S_L$ with respect to CO <sub>2</sub> dilution ratio at various equivalence ratios. (b) comparison of $S_L$ with respect to equivalence ratio, with false-species analysis to locate the composite effects of CO <sub>2</sub> . . . . .	131
5-20	False-species analysis on the different effects of CO <sub>2</sub> on the $S_L$ of CH <sub>4</sub> /air flames. . . . .	132
5-21	Evolution of the chemical effects of CO <sub>2</sub> dilution with(a) dilution ratio and (b) equivalence ratio. . . . .	132
5-22	Temperature profile of methane/air flames at non-diluted condition and diluted conditions by CO <sub>2</sub> , iCO <sub>2</sub> , and cCO <sub>2</sub> . . . . .	133
5-23	Direct reaction effect of CO <sub>2</sub> dilution on the speciation profiles of the important radicals (H, OH, O, and CH <sub>3</sub> ) and intermediate species (CH <sub>2</sub> O and C <sub>2</sub> H <sub>6</sub> ) in lean CH <sub>4</sub> /air/CO <sub>2</sub> flames ( $\phi = 0.8$ ). . . . .	134
5-24	Direct reaction effect of CO <sub>2</sub> dilution on the speciation profiles of the important radicals (H, OH, O, and CH <sub>3</sub> ) and intermediate species (CH <sub>2</sub> O and C <sub>2</sub> H <sub>6</sub> ) in stoichiometric CH <sub>4</sub> /air/CO <sub>2</sub> flames ( $\phi = 1.0$ ). . . . .	135
5-25	Direct reaction effect of CO <sub>2</sub> dilution on the speciation profiles of the important radicals (H, OH, O, and CH <sub>3</sub> ) and intermediate species (CH <sub>2</sub> O and C <sub>2</sub> H <sub>6</sub> ) in rich CH <sub>4</sub> /air/CO <sub>2</sub> flames ( $\phi = 1.2$ ). . . . .	136
5-26	Composite sensitivity analysis based on absolute changes in $S_L$ caused by the direct reaction effect of CO <sub>2</sub> . $S_L$ absolute changes is calculated based on 10% CO <sub>2</sub> and 10% cCO <sub>2</sub> diluted cases. . . . .	136
5-27	Composite sensitivity analysis based on relative changes in $S_L$ caused by the direct reaction effect of CO <sub>2</sub> . $S_L$ relative changes is calculated based on 10% CO <sub>2</sub> and 10% cCO <sub>2</sub> diluted cases. . . . .	137
6-1	Rate coefficients of the O + H <sub>2</sub> = H + OH reaction. . . . .	147
6-2	Rate coefficients of the H <sub>2</sub> + OH = H + H <sub>2</sub> O reaction. . . . .	148
6-3	Rate coefficients of the OH + OH = H <sub>2</sub> O + O reaction. . . . .	149
6-4	Comparison of the predictive ability of MACDIL-RDC with respect to MACDIL-DTL, based on the ignition delay time of TR-FE/air/mixtures at initial temperature of 600–1000 K and pressure of 10 bar. . . . .	154
6-5	Validation of the MACDIL-RDC mechanism on the $S_L$ of TR-FE/air/EGR flames at 473 K with various pressures and EGR ratio. Experiments are from Ref. [24]. Predictions by the starting mechanism (LLNL 2011 [25]) is also compared. In Figure (a), there is only one curve predicted LLNL 2011 at the 0% EGR condition due to convergence problem using the computational detail described in Section 6.3.1. At the 10% EGR condition, there is one point $\phi \approx 1.1$ converged. At the 10% EGR condition, none of the points converged. For details about the data, please refer to Table B.3 in Appendix B. . . . .	156



6-6	Additional comparison with predictions by correlations at the 473 K, 5 bar condition (Figure 6-5d). The experimental data are the same as in Figure 6-5d. The Gülder <i>et al.</i> [26] correlation is designated for isooctane/ethanol blend diluted by N <sub>2</sub> /CO <sub>2</sub> and the Yahyaoui <i>et al.</i> [27]. . . . .	158
6-7	Evolution of $S_L$ with EGR ratio for TRFE/air/EGR mixtures with $\phi \approx 1.1$ at $T_u = 473$ K at various. The data shown are the same as that in 6-5. The predicted line at P = 1 bar using LLNL 2011 (the purple dashed line) stops at 10% of EGR ratio, as only calculations at 0% and 10% EGR converged. . . . .	159
6-8	Evolution of normalized $S_L$ with EGR ratio for TRFE/air/EGR mixtures with $\phi \approx 1.1$ at $T_u = 473$ K and various pressures. The data shown in these figures are reproduced from those in Figure 6-7 and Figure 6-5. Normalized $S_L$ at a certain EGR ratio is defined as the ratio between its $S_L$ over the $S_L$ at the reference case, i.e., the 0% EGR case. In the P = 1bar figure, the predicted (dashed) line for LLNL 2011 stops at 10% of EGR ratio, as only calculations at 0% and 10% EGR converged. . . . .	160
6-9	Effect of CO <sub>2</sub> , H <sub>2</sub> O, N <sub>2</sub> dilution on the $S_L$ of isooctane/air flames at $T_u = 423$ K, P = 5 bar, and $\phi = 1.1$ . The EGR composition is 12.4% CO <sub>2</sub> , 14% H <sub>2</sub> O, and 73.6% N <sub>2</sub> . Experimental data are from Endouard <i>et al.</i> [13]. . . . .	161
6-10	Equivalence ratio dependence of the EGR effect on the $S_L$ of TRFE/air flames at $T_u = 473$ K and pressure of (a) 1 bar and (b) 5 bar. The data shown in the two figures are reproduced from those in Figure 6-5. Normalized $S_L$ at a certain EGR ratio is defined as the ratio between its $S_L$ over the $S_L$ at the reference case, i.e., the 0% EGR case. In Figure 6-10b predictions from correlations are also compared. For the formulas of the two correlations, please refer to the text. . . . .	162
6-11	Pressure dependence of the EGR effect on the $S_L$ of TRFE/air flames at $T_u = 473$ K and equivalence ratios of (a) $\phi \approx 1$ and (b) $\phi \approx 1.1$ . The data shown in the two figures are reproduced from those in Figure 6-5. Normalized $S_L$ at a certain EGR ratio is defined as the ratio between its $S_L$ over the $S_L$ at the reference case, i.e., the 0% EGR case. . . . .	163
6-12	Effect of EGR on the laminar flame speeds of TRFE/air/EGR mixtures, at 673 K, 5 bar and $\phi = 1.1$ , predicted by the MACDIL-RDC mechanism. . . . .	164
6-13	The dilution term used in the present work and its derivative. . . .	165
6-14	Comparison on the performance of the proposed dilution term (Equation 6.7) and other dilution terms in the literature in fitting the EGR effects on the laminar flame speeds predicted by MACDIL-RDC as shown in Figure 6-12. . . . .	166

7-1	Laminar flame speeds of TRFE/air mixtures at initial conditions the near negative temperature (NTC) region. Elevated $S_L$ of rich mixtures are observed at initial temperature of 873 K and pressure of 10 bar and 5 bar. (a) the $S_L$ at different pressures predicted with MACDIL-RDC. (b) comparison of the predictions between MACDIL-RDC and LLNL 2011 on the $S_L$ of TRFE/air mixtures at $T_u = 873$ K and $P = 10$ bar. . . . .	172
A-1	The $\text{CH}_2\text{CO}+\text{OH}$ potential energy surface (including ZPE). Total relative electronic energy for all and geometry for some stationary points are demonstrated. Black lines: barrierless formation of the reactive complex (RC); Orange lines: Pathway 1; Green lines: Pathway 2; Blue lines: Pathway 3. Solid lines: most probable product channels; Dashed lines: less probable product channels. Geometries were obtained at B2PLYP-D3/cc-pVTZ level and energies were obtained using CCSD(T)-F12/cc-pVTZ-F12 with extrapolation to basis set limit (See Equation 3.1). . . . .	174
A-2	Comparison between restricted open shell (ROHF) and unrestricted (UHF) reference wave functions on the potential energy surface of the channel $\text{CH}_2(\text{O})\text{CHO} \longrightarrow \text{CH}_2\text{O} + \text{CHO}$ and $\text{CH}_2(\text{O})\text{CHO} \longrightarrow \text{H} + (\text{HCO})_2$ . . . . .	183
A-3	Comparison on the overall rate constant of Pathway 2 with and without using the 2TS method. . . . .	185
A-4	Comparison of different 1D tunneling models on the calculated rate coefficients. . . . .	185
A-5	Arrhenius plot for $\text{CH}_2\text{COOH}$ dissociation channel R3-4a and R3-4b.	186
A-6	Simplified Scheme of the $\text{CH}_2\text{CO} + \text{OH}$ reaction. It includes 6 significant reaction channels and 4 major products. . . . .	187
A-7	Effect of the updated rate coefficients on the laminar flame speeds of acetone/air mixture at standard conditions (298 K, 1 atm). Aramco Mech 3.0 is used as the reference mechanism in simulations. . . . .	189
B-1	Effect of $\text{CO}_2$ dilution in fuel on the laminar flame speed of lean equimolar syngas ( $\text{H}_2/\text{CO} = 1/1$ ) at standard conditions (298 K, 1 atm). Experimental data are from Natarajan <i>et al.</i> [18], Prathap <i>et al.</i> [21], and Han <i>et al.</i> [22]. . . . .	192
B-2	Comparison of maximum mole fraction of H radicals predicted by the LLNL 2011 and K�eromn�es 2013 mechanisms. . . . .	193
B-3	Evolution of $S_L$ and the number of grid points with adaptive grid control parameters, for the calculation of laminar flame speeds of $\text{CH}_4/\text{air}/$ flames. . . . .	193
B-4	Evolution of species mole fraction against temperature at standard conditions (298 K, 1 atm). . . . .	194
B-5	Effect of $\text{CO}_2$ dilution on the speciation profiles of the important radicals (H, OH, O, and $\text{CH}_3$ ) and intermediate species ( $\text{CH}_2\text{O}$ and $\text{C}_2\text{H}_6$ ) in lean $\text{CH}_4/\text{air}/\text{CO}_2$ flames ( $\phi = 0.8$ ). . . . .	195
B-6	Effect of $\text{CO}_2$ dilution on the speciation profiles of the important radicals (H, OH, O, and $\text{CH}_3$ ) and intermediate species ( $\text{CH}_2\text{O}$ and $\text{C}_2\text{H}_6$ ) in stoichiometric $\text{CH}_4/\text{air}/\text{CO}_2$ flames ( $\phi = 1.0$ ). . . . .	196

B-7 Effect of CO<sub>2</sub> dilution on the speciation profiles of the important radicals (H, OH, O, and CH<sub>3</sub>) and intermediate species (CH<sub>2</sub>O and C<sub>2</sub>H<sub>6</sub>) in rich CH<sub>4</sub>/air/CO<sub>2</sub> flames ( $\phi = 1.2$ ). . . . . 197

# List of Tables

1.1	Laminar flame speed measurements of gasoline and surrogate fuels at diluted conditions . . . . .	8
1.2	High-temperature and low-temperature reaction classes. Table taken from Ref. [28]. . . . .	18
2.1	Stretch extrapolation methods available in literature. Adapted from Konnov <i>et al.</i> [4] . . . . .	55
2.2	Properties of the false species, compared with the real molecule, introduced in the present work, using H <sub>2</sub> O as an example. . . . .	61
3.1	Summary of the computational methods used in this work (in sequential order). . . . .	69
3.2	Widely used rate parameters (in cm <sup>3</sup> molecule <sup>-1</sup> s <sup>-1</sup> ) in kinetic mechanisms. $N_A = 6.022 \times 10^{23}$ molecules mol <sup>-1</sup> is the Avogadro's number, and $R_u = 1.987$ cal K <sup>-1</sup> mol <sup>-1</sup> is the ideal gas constant. . . . .	73
4.1	List of some surrogates candidates. . . . .	90
4.2	Comparison on the properties and composition of the gasoline and its TRFE surrogate. Reproduced from Ref. [24] . . . . .	91
4.3	Composition and mole fraction of the fuel, air and EGR used in the present work. . . . .	92
4.4	Conditions investigated in the present chapter for the identification of key thermokinetic parameters to laminar flame speed. . . . .	93
4.5	List of candidate mechanisms. . . . .	93
4.6	Important in-mechanism reactions identified in the present work. . .	104
4.7	Known reactions between radicals and diluent molecules (CO <sub>2</sub> , H <sub>2</sub> O, CO). . . . .	106
4.8	Reactions of interests for further theoretical investigations. . . . .	106
6.1	Sources of the sub-mechanisms in the MACDIL-DTL mechanism. .	142
6.2	Rate coefficients for reactions in the hydrogen sub-mechanism of MACDIL-DTL. . . . .	145
6.3	Rate coefficients for reactions in the CO sub-mechanism of MACDIL-DTL. . . . .	151
6.4	Conditions used in the reduction of MACDIL-DTL to generate MACDIL-RDC mechanism. . . . .	153
6.5	Continuations used in 1-D $S_L$ calculations of TRFE/air/EGR flames.	155
6.6	List of conditions in the PRISME experiments [24]. . . . .	155

A.1	Total relative energy of the local minima on the $\text{CH}_2\text{CO} + \text{OH}$ potential energy surface and their composition in energy. + : the two fragments are at infinite separation; $\sim$ : the two fragments form a Van der Waals complex. . . . .	179
A.2	Total relative energy of the transition states on the $\text{CH}_2\text{CO} + \text{OH}$ potential energy surface and their composition in energy. + : the two fragments are at infinite separation; $\sim$ : the two fragments form a Van der Waals complex. . . . .	180
A.3	List of Frequencies for the stationary points. . . . .	180
A.4	1D hindered rotor potential profiles scanned by increments of $30^\circ$ at B2PLYPD3/cc-pVTZ level for the stationary points. . . . .	181
A.5	Energies relative to $\text{CH}_2(\text{O})\text{CHO}$ (INT02) and barrier heights ( $\text{kcal mol}^{-1}$ ) obtained by calculations with restricted open shell (ROHF) reference wave functions for channel $\text{CH}_2(\text{O})\text{CHO} \longrightarrow \text{CH}_2\text{O} + \text{CHO}$ and $\text{CH}_2(\text{O})\text{CHO} \longrightarrow \text{H} + (\text{HCO})_2$ , compared with values obtained with unrestricted (UHF) reference wave functions. (+ : means the two fragments are at infinite separation; $\sim$ : means the two fragments form a Van der Waals complex.) . . . . .	182
A.6	Parameters used in long-range TST calculations. . . . .	183
B.1	List of important species and reactions, with evaluation of investigation interests for the present work. . . . .	191
B.2	Compositions in mole fractions of the mixtures used in the experiments at different equivalence ratios and EGR ratios. The measured equivalence ratios are from Ref. [24]. . . . .	198
B.3	Laminar flame speeds of TRFE/air/EGR mixtures. Experimental measurements from Ref. [24] and predictions using the LLNL 2011 [25] and the MACDIL-RDC mechanisms are compared. . . . .	199

# Chapter 1

## Introduction

### 1.1 Background

The world is currently struggling between environmental conservation and energy utilization (production and consumption). Various environmental problems are strongly related to energy production and consumption, e.g., global warming by the persistently rising CO<sub>2</sub> emission, acid rain by NO<sub>x</sub> and SO<sub>x</sub>, air pollution by particulate matter (PM), shortage of fossil fuel reservoirs by the growing consumption. As the global energy demand is expected to grow by more than a quarter to the year of 2040 [1], current policies, technologies and measures are still insufficient to prevent the rise of energy-related CO<sub>2</sub> emission.

The solution to this conflict should not be unitary, but multi-fold with different approaches conducted simultaneously. The most favorable one is to develop clean and renewable energies, e.g., solar, wind, and biomass energy. But these technologies, at their current states, are yet able to provide neither compatible economics to conventional energy nor full cleanness within the entire life cycle. Thus they are suitable for long-term development, but not sufficient to deliver a short-term effect. An alternative approach is to make conventional energy cleaner. As shown in Figure 1-1, the demand for oil and coal is expected to increase from 8185 Mtoe (millions of tonnes of oil equivalent) in 2017 to 8703 Mtoe in 2040 and maintain its dominant share (58% in 2017 and 49% expected in 2040) in the world total primary energy demand (TPED), despite of all existing measures. [1] Therefore, it is more realistic and effective in the short-term to reduce emission and pollution of conventional energy.

In the foreseeable future, combustion is expected to remain the dominant way how people utilize energy. In other words, primary energy sources, e.g., oil, coal, natural gas, and bioenergy, are mostly consumed or converted through combustion. So it is crucial to reduce pollution and increase fuel economy during combustion processes. Various technologies to achieve this purpose fall into three categories: pre-combustion, in-combustion and post-combustion treatments. Pre-combustion treatments deal with the physical and chemical nature of the fuel, e.g., decarbonation or removal of pollutant sources in fuel through gasification or hydrotreatment. In-combustion treatments reduce pollutant emission by modifying the fluid dynamics through burner designs to achieve in-stages or zoned combustion, by modifying heat transfer and reaction kinetics through the introduction of dilution, alteration of initial temperature and pressure and optimization of mixture

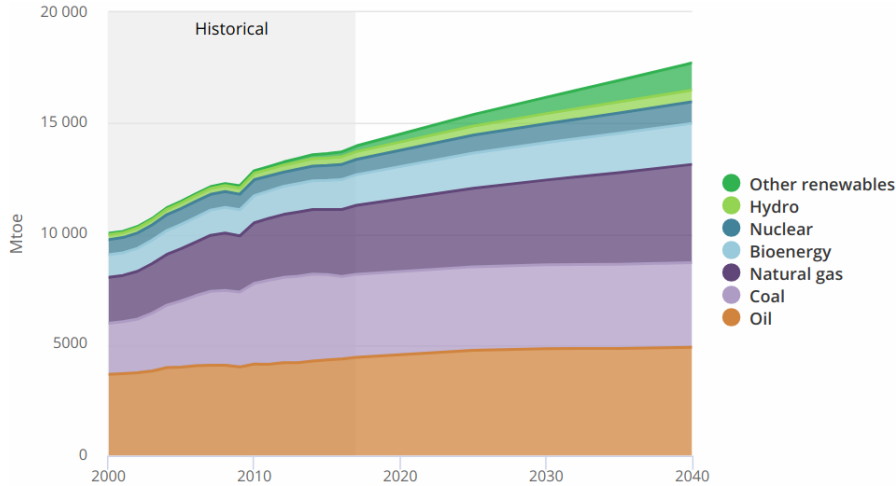


Figure 1-1: Historical and estimated world total primary energy demand (TPED), with breakdown in energy sources. Estimation is based on the New Policies Scenario (NPS), which counts for all existing policies and announced policy intentions. Graphic taken from Ref [1].

compositions. Post-combustion treatments remove the pollutant in the exhaust gases mostly through chemical catalysts.

Among these technologies, diluted combustion is receiving growing interests. As a in-combustion treatment, it intends to increase fuel economy and lower emission by introducing diluents, such as  $N_2$ ,  $CO_2$ ,  $H_2O$ , air or exhaust gas, in the unburned fuel/oxidizer mixture. Strictly speaking, most of the combustion events are naturally diluted, since air, the most common oxidizer, contains 79% of  $N_2$ . Without any dilution, combustion processes are fast and fierce. Whereas the presence of diluent can slow down combustion and make it moderate. Therefore, most applications of diluted combustion require more diluent contents or more enhanced dilution effects with respect to the ones using air. Diluted combustion has various applications, e.g., exhaust gas recirculation (EGR) technology in internal combustion engines (ICE), internal recirculation technology in furnaces which is usually associated with mild combustion [29], and oxyfuel combustion in gas turbines and solid combustion burners. The diluent affects combustion processes physically, thermally and chemically. Physical effects are mainly through heat transfer by convection and radiation, and molecular diffusion. Thermally, the diluent, with higher specific heat capacity, could reduce the temperature elevation in combustion processes (i.e., the temperature difference between burned and unburned mixtures). With the same initial temperature, it results in lower peak temperature which has benefits such as reducing NO production and thermal dissociation of combustion products. Chemically, the diluent slow down the process by (i) shifting the equilibrium of reactions involving the diluent molecules, and (ii) reducing radical pool concentration through direct reactions or collisions. The mechanism according to which dilution affects combustion behaviors is complex and a better understanding is necessary and crucial for applying diluted combustion into practice more efficiently.

In the ground transportation sector, gasoline Spark Ignition (SI) engines power 70% of light-duty vehicles and should still represent more than 50% in 2030, re-

maintaining the major energy source and CO<sub>2</sub> contributor for passenger cars. In response to the global demand in the reduction of CO<sub>2</sub> and pollution emission, as well as the more stringent regulations on vehicle emission and fuel economy developed by various countries [30–32], the technology trend today is downsizing, which consists in reducing the displacement and increasing the specific power by using a turbocharger. The turbocharged SI engines are becoming more popular in the world market due to their compactness and high power density. [33] However, due to the higher temperature and pressure during combustion than in standard engines, they lead to increasing abnormal combustion phenomena (knock and super-knock), which lead to using sub-optimal spark timings, and high temperature of exhaust gas at high loads [34]. The increasing temperature may also cause the increase of NO<sub>x</sub> emission. Accordingly, Exhaust Gas Recirculation (EGR) technology was introduced to SI engines, aiming to prevent these phenomena and to improve efficiency.

The EGR technology, re-introducing the exhaust gas to the combustion chamber, can benefit SI engines in many ways. The extra dilution can (i) reduce knock tendency and improve spark timing because of the longer Ignition Delay Time (IDT) of the mixture, (ii) increase fuel economy because of the reduction in throttling loss and wall heat losses, and (iii) reduce NO<sub>x</sub> emission because of the lower peak in-cylinder temperature. Unfortunately, this process leads to a decrease in the heat release rate and to an increase of cycle to cycle fluctuations of Indicated Mean Effective Pressure (IMEP). It is found that the fluctuations of IMEP remain acceptable for intermediate dilution (lower than 25% of EGR), but grow exponentially and become troublesome at high dilution regimes (above 25% of EGR). At high dilution, engine stability and heat release rate can not be sufficiently improved through increasing turbulence level and advanced spark ignition systems that work for the intermediate dilution regime. This indicates the necessity of a better understanding of gasoline premixed flames at highly diluted conditions, especially in the aspect of combustion chemistry.

## 1.2 Exhaust Gas Recirculation in Gasoline Engines

One widely seen application of diluted combustion is the Exhaust Gas Recirculation (EGR) technology, commonly used in both diesel and gasoline engines. Diluted combustion is implemented, as the name implies, by recirculating a portion of the exhaust gas back into the cylinders. Using EGR in gasoline engines is known to have three types of effects: (i) improvement of fuel economy, (ii) reduction of NO<sub>x</sub> emission, (iii) inhibition of knock tendency. As mentioned in Section 1.1, although downsizing of SI engines using turbochargers reduces the displacement and increases the specific power, it gives rise to other problems such as knock combustion and higher NO<sub>x</sub> emission. Therefore EGR is widely adopted in turbocharged SI engines to meet the market requirement of “doing more with less”. [35]



### 1.2.1 Classification of EGR technology

EGR technology can be categorized into various types according to different aspects. Based on the position where the exhaust gas is introduced, it can be divided into (i) external EGR and (ii) internal EGR. External EGR is achieved by EGR control valves connecting the intake and exhaust tracts, which can adjust the EGR ratio effectively according to different work conditions. [33, 36–39] Internal EGR can be realized through negative valves overlap (NVO), but its application is greatly limited because of the difficulty to obtain variable valve timing though camshaft improvement and the impossibility to control the EGR ratio. Therefore we only discuss External EGR below and all occurrences of “EGR” refer to External EGR unless specified.

EGR can be classified by the temperature of injected exhaust gas, into hot EGR and cooled EGR. Hot EGR recirculates the high temperature exhaust without treatment, which preheats the intake to improve combustion quality. [33, 40] Whereas cooled EGR reduces the temperature of the exhaust gas using heat exchangers before introducing it into the fresh charge. Cooled EGR leads to increased inlet density and thus enables higher volumetric efficiency for engines. In addition, the reduced peak temperature caused by cooled EGR can lower NO<sub>x</sub> emission. Therefore, cooled EGR is more commonly used compared to hot EGR. This thesis focuses mainly on external cooled EGR and all occurrences of EGR refer to it unless specified.

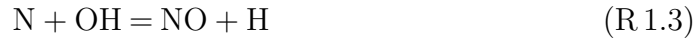
### 1.2.2 Effect on Fuel Economy

As EGR introduces extra gaseous content for a certain torque or power output, larger opening positions of the throttles, than that without EGR, are allowed. This reduces the pumping losses and leads to increased fuel economies, especially at part-load conditions. In addition, the higher specific heat capacity of the diluent lowers the peak in-cylinder combustion temperature. Under such conditions, the respectively smaller temperature difference decreases the heat losses through chamber walls. The chemical dissociation of combustion products (such as CO<sub>2</sub>), which is highly endothermic and faster at higher temperature, is also inhibited so that larger fraction of the fuel is converted to complete combustion products. The above effects all lead to an increase in fuel economy.

### 1.2.3 Effect on NO<sub>x</sub> emission

The generation of NO<sub>x</sub> is highly sensitive to temperature and oxygen concentration. It is reported that the rate of NO formation is very low at a temperature lower than 1800 K, but increase exponentially and becomes very fast at 2000 K. [33] It can be explained by the extended Zeldovich Mechanism [41–43], where NO is generated thermally in high-temperature post-flame region by reaction R 1.1–R 1.3.





Accordingly, EGR reduces NO<sub>x</sub> emission by decreasing temperature and oxygen concentration. It is achieved by the three effects of the exhaust gas: (1) dilution effect, which reduces oxygen concentration directly; (2) thermal effect, which reduces the flame temperature by the higher heat capacity of the exhaust gas; (3) chemical effect, which may affect both the temperature and oxygen concentration since the CO<sub>2</sub> and H<sub>2</sub>O in the exhaust gas could participate in reactions.

#### 1.2.4 Effect on Engine Knock

Although downsized turbocharged engines can achieve higher power density and fuel economy, it brings problems such as knock combustion and high exhaust gas temperature. [44] Knock combustion can be described as the auto-ignition of some portion of the fresh charge, instead of being ignited by the propagating flames. It is affected by the elevated temperature and pressure of the unburnt mixture resulted from the piston movement or the flame expansion. Currently, technologies of knock suppression aim to reduce in-cylinder temperature and fall into three types [45,46]: (1) reduction of effective compression ratio or delayed ignition timing; (2) injection of excessive fuel; and (3) dilution by EGR. The first type may lead to reduced engine power and the second type may lead to incomplete combustion and lower fuel economy. In contrast, EGR reduces flame temperature, allows the use of stoichiometric mixture, and maintains the same power output. Therefore, EGR has great advantages among other knock inhibition techniques. [47]

#### 1.2.5 Difficulty of Reaching High EGR Ratio

Despite many advantages, current EGR technology typically works with only 5% to 15% of EGR ratio. As mentioned in Section 1.1, high dilution is difficult to achieve due to the reduced heat release rate and increased fluctuations of IMEP, which could not be improved by methods that work at normal dilution regimes. In addition, they At high dilution, engine stability and heat release rate can not be sufficiently improved through increasing turbulence level and advanced spark ignition systems that work for the intermediate dilution regime. To tackle this problem, it is necessary to understand better the combustion behaviors of gasoline at highly-diluted conditions, through various aspects, from its combustion chemistry, fundamental flame characteristics, to turbulence flows, etc.

### 1.3 Experimental and Correlation Studies on the Laminar Flame Speed of Gasoline and Surrogate Fuels at Diluted Conditions

Laminar flame speed ( $S_L$ ), or laminar burning velocity, or fundamental flame speed, is an important combustion characteristic of a combustible mixture, which is also a combined result of thermodynamics, diffusion, and reaction kinetics. [4] It is of great significance for not only engine development by providing input values for CFD simulations of turbulent flames, such as the flame surface density

model, but also fundamental combustion chemistry research by being used to validate and improve kinetic mechanisms. Therefore, accurate measurements of the laminar flame speed are necessary and provide building blocks for combustion research. Although laminar flame speeds are unique properties of the fuels, they are influenced by physical and chemical conditions, such as the equivalence ratio, initial temperature, pressure, and dilution. Therefore, despite the fact that most measurements are performed at room conditions (around 298 K and 1 atm), more and more experiments are conducted at unconventional conditions, e.g., low and increased temperature, low and elevated pressure, oxygen-enriched and high dilution conditions, to study new combustion regimes and to assist new engine designs.

Since the topic of this thesis falls into highly diluted combustion regimes, the following of this section will mainly focus on the laminar flame speeds measurements at diluted conditions.

### 1.3.1 Surrogate Fuels Development Based on Laminar Flame Speed

Gasoline fuels are complex mixtures of hundreds of compounds, whose composition and other physical and chemical properties are found to affect the engine performance. Because of this complexity, it is impossible to study real-world gasoline fuels directly through computational models which are essential for engine development. To understand their combustion chemistry so that their combustion characteristics can be modeled accurately, surrogates with simplified composition but similar properties are necessary. [48–50] The surrogate fuels should have close values to real gasoline for many properties, which include not only the physical and chemical properties but also combustion characteristics, such as laminar flame speed and ignition delay time. Since it is essential for predicting flame propagation inside engines, laminar flame speed can be used for the validation and development of surrogates fuels.

Isooctane ( $i\text{-C}_8\text{H}_{18}$ ),  $n$ -heptane ( $n$ -heptane) and their blends are among the most simple and common surrogates for gasoline, which is because of (i) their representative ability for linear and branched alkanes in real gasoline fuels, (ii) their similar laminar flame speeds as gasoline, and (iii) the convenience in emulating the research octane number (RON, defined as  $\text{RON}_{n\text{-heptane}}=0$  and  $\text{RON}_{\text{isooctane}}=100$ ). Their binary mixture is called primary reference fuel (PRF), whose laminar flame speed is measured by several studies. [15, 51–53] Zhao *et al.* [54] determined the  $S_L$  of a CR-87 gasoline (RON=87) using stagnation jet-wall flame method and compared with that of the PRF 90 (RON=90) surrogate. Equivalence ratio (0.6–1.4) and temperature (353 and 500 K) variations were covered and they concluded that PRF 90 is suitable to represent CR-87 gasoline for laminar flame speed emulation. Jerzembeck *et al.* [55] compared experimental values of a standard gasoline and PRF 87 (RON=87) at an unburnt temperature of 373 K and high pressures of 10–25 bar. Results of  $S_L$  shown overall good agreement, although some deviations at fuel-rich conditions are observed. Therefore PRF is found satisfactory to represent some gasoline fuels over most conditions, but improvement is still necessary. Later studies [56, 57] show that PRF is only satisfactory at fuel-lean conditions and introduction of toluene in the surrogate composition is needed to better rep-

resent gasoline containing a high fraction of aromatics. The surrogate is named toluene reference fuel (TRF, ternary isooctane/n-heptane/toluene mixture). Due to the relatively low reactivity of toluene, it slows the consumption of the "end gases" in gasolines which lead to increased octane rating. [28] The laminar flame speeds of TRF are measured and compared with experiments on real gasoline over wide ranges of equivalence ratio, temperature, and pressure, e.g., TAE7000 gasoline by Dirrenberger *et al.* [57], Exxon gasoline by Sileghem *et al.* [56], FACE gasoline (fuels for advanced combustion engines) by Manna *et al.* [14, 58]. Their results show that TRF surrogates agree well over the investigated conditions. As ethanol addition in gasoline becomes more common in dealing with the environmental problems, TRF surrogates with ethanol addition (TRFE, four-component isooctane/n-heptane/toluene/ethanol mixture) are used for emulation and investigation of ethanol addition effects. The degenerated low-temperature reactivity of ethanol makes it a good gasoline additive to increase octane rating and octane sensitivity. [59] Dirrenberger *et al.* [57] and Manna *et al.* [58] tested TRFE in their work, and it is found that introduction of ethanol increases the laminar burning velocity and the enhancement effect is similar for gasoline and TRFE.

As study advances, the composition of surrogates become complex, which exhibits the following trends as Sarathy *et al.* [60] summarized: (1) increasing number of components in the surrogate fuel mixtures, from initially single component (e.g., isooctane), to binary (e.g., isooctane/n-heptane), ternary (e.g., isooctane/n-heptane/toluene), and multi-component mixtures that span the entire carbon range of gasoline fuels ( $C_4$ – $C_{10}$ ); (2) addition of oxygenated fuels (ethanol, butanol, MTBE, etc.); (3) surrogate fuels that can model more and more phenomena, e.g., vaporization, mixture formation, auto-ignition, burning velocity; (4) surrogate fuels for new combustion systems which use fuel properties as additional control parameters.

### 1.3.2 Laminar Flame Speed Measurements of Gasoline and Surrogate Fuels at Diluted Conditions

With the advantages of exhaust gas recirculation (EGR) mentioned in section 1.2, diluted combustion is of great research interest. Therefore, experimental measurements of laminar flame speeds at diluted conditions are helpful to study the mechanism of dilution effects. However, measurements at these conditions are not as abundant as those without dilution. Table 1.1 listed the available experimental studies on the  $S_L$  at diluted conditions for gasoline and surrogate fuels. These studies cover fuels from pure compounds to their blends, PRF, TRF, TRFE, and finally real gasoline. The composition of the diluent gases also become complicated, from pure  $N_2$  to ternary  $N_2/CO_2/H_2O$ , and eventually real EGR.

Most works study on pure compounds as fuels, such as isooctane and n-heptane, which brought simplicity for the investigation of dilution effects. Some early studies by Ryan and Lestz [61], Metghalchi and Keck [62], Gülder [63, 77] measured laminar flame speeds ( $S_L$ ) at various temperature, pressure and dilution, for Retail Motor Fuel Dispenser-303 (RMFD-303), indolene blend fuels and single-component fuels such as methanol, ethanol, propane, n-heptane, and isooctane. The diluent they used is a synthetic blend of  $CO_2/N_2$  (with small variation around 15%/85%), which has heat capacities similar to combustion products. The same

Table 1.1: Laminar flame speed measurements of gasoline and surrogate fuels at diluted conditions

year	author(s)	fuel(s)	experimental method	$\phi$	$T$ (K)	$p$ (bar)	$x_d$	diluent	ref.
1980	Ryan and Lestz	isooctane, n-heptane, methanol, propane, methane	spherical flame	0.7–1.3	470–570	6	0–0.3	N <sub>2</sub> /CO <sub>2</sub>	[61]
1982	Mergalchi and Keck	indolene (RMFD303), isooctane, methanol	spherical flame	0.8–1.5	298–700	0.4–50	0–0.2	N <sub>2</sub> /CO <sub>2</sub>	[62]
1984	Gilder	isooctane, methane, propane, methanol, ethanol	spherical flame	0.7–1.4	300–600	1–20	0–0.2	H <sub>2</sub> O	[63]
1985	Rhodes and Keck	indolene (RMFD303)	spherical flame	0.7–1.6	350–550	0.4–12	0–0.3	N <sub>2</sub> /CO <sub>2</sub>	[64]
2007	Kumar <i>et al.</i>	isooctane, n-heptane	counterflow flame	0.7–1.4	298–470	1	N <sub>2</sub> /air = 0.785–0.805	N <sub>2</sub>	[65]
2009	Halter <i>et al.</i>	isooctane, methane	spherical flame	1	300	1	0–0.16	N <sub>2</sub> , CO <sub>2</sub> , N <sub>2</sub> /CO <sub>2</sub>	[66]
2009	Jerzembeck <i>et al.</i>	standard gasoline, PRF, isooctane, n-heptane	spherical flame	0.7–1.2	373	10–25	O <sub>2</sub> /air = 0.15, 0.17	N <sub>2</sub>	[55]
2009	Smallbone <i>et al.</i>	n-heptane	counterflow flame	0.7–1.4	298–350	0.5–2	N <sub>2</sub> /air = 0.82	N <sub>2</sub>	[67]
2011	Tahtouh <i>et al.</i>	isooctane/hydrogen	spherical flame	1	300	1	0–0.4	N <sub>2</sub>	[68]
2011	Marshall <i>et al.</i>	n-heptane, isooctane, toluene, ethylbenzene, ethanol	spherical flame	0.7–1.4	310–450	0.5–4	0–0.3	real EGR	[69]
2011	Zhou <i>et al.</i>	isooctane	spherical flame	0.8–1.4	373	1	CO <sub>2</sub> /oxidizer = 0–0.28	CO <sub>2</sub>	[70]
2012	Galmiche <i>et al.</i>	isooctane	spherical flame	0.6–1.6	323–473	1–10	0–0.25	N <sub>2</sub>	[71]
2014	Knorsch <i>et al.</i>	n-heptane, n-butanol, isobutanol, ethanol	flat flame	0.7–1.6	373–423	1	0–0.2	N <sub>2</sub>	[72]
2015	Bhattacharya <i>et al.</i>	V-Power gasoline from Shell	flat flame	0.6–1.3	423	1	0–0.25	N <sub>2</sub> /CO <sub>2</sub>	[73]
2015	Manna <i>et al.</i>	FACE-C gasoline, TRF	spherical flame	0.8–1.6	358	1–6	0–0.3	real EGR	[74]
2016	Endouard <i>et al.</i>	isooctane	spherical flame	0.7–1.5	323–473	1–10	0–0.25	CO <sub>2</sub> , H <sub>2</sub> O, N <sub>2</sub> /CO <sub>2</sub> /H <sub>2</sub> O	[13]
2017	Manna <i>et al.</i>	FACE-C gasoline, TRF, TRFE	spherical flame	0.8–1.6	383	1–6	0–0.3	real EGR, N <sub>2</sub> /CO <sub>2</sub> /H <sub>2</sub> O	[75]
2019	Duva <i>et al.</i>	isooctane	spherical flame	0.8–1.6	373–473	1	0–0.15	CO <sub>2</sub>	[76]

trend was observed within their investigation range (up to 30% dilution) that the decrease in  $S_L$  is linear to dilution ratio and independent to unburnt gas temperature. Kumar *et al.* [65] studied  $N_2$  dilution effect for both isooctane/air and n-heptane/air flames at various temperatures using the counterflow flame method. Laminar flame speed is observed to decrease linearly with increasing fractions of  $N_2$  in air. They also found that the  $S_L$  for isooctane/air mixtures can be 5–10  $\text{cm, s}^{-1}$  lower than that of n-heptane/air mixtures under the same equivalence ratio. Calculations of  $S_L$  using the kinetic mechanism by Hasse *et al.* [78] agree well for isooctane/air mixture, but not for n-heptane/air mixture. Sensitivity analysis showed the importance of  $C_2$ – $C_3$  chemistry on flame propagation. In terms of isooctane, recent measurements are mainly performed by the research team from the CNRS PRISME laboratory. Halter *et al.* [66] measured the laminar flame speed of stoichiometric isooctane/air mixture at atmospheric conditions (300 K, 1 bar), diluted by  $N_2$ ,  $CO_2$  and their blend to emulate exhaust gas recirculation. Larger reduction effect was observed for  $CO_2$  than  $N_2$ , which can be attributed mostly to the larger heat capacity of  $CO_2$ . The authors found that some part of the difference is also due to the dissociation of  $CO_2$ , although the thermal effect is predominant. Tahtouh *et al.* [68] from the same team studied the combined effect of hydrogen addition and nitrogen dilution for stoichiometric isooctane/air mixtures. It is reported that laminar flame speed decreases with dilution ratio and increases with hydrogen mass fraction in fuel, both linearly. Galmiche *et al.* [71] extended previous measurements to a wider range of temperature, pressure and equivalence ratio.  $N_2$  dilution up to 25% and oxygen-enrichment environment were both studied. It is found that laminar flame speed increases linearly with oxygen fraction in air. By comparing with computational results, it is found that the two isooctane kinetic mechanisms used ([55] and [78]) both overestimated laminar flame speed and improvement in kinetic modeling of isooctane oxidation is needed. Endouard *et al.* [13] first included  $H_2O$  as diluent in their experiments, which is commonly difficult because of condensation problems. They also considered  $CO_2$  and a ternary synthetic EGR ( $N_2/CO_2/H_2O$ ) as dilution, which further enriched the available experimental data. In contrast to the linear dilution effect of  $N_2$ , the results clearly show non-linear trends for  $CO_2$ ,  $H_2O$  and EGR. The relation in the dilution effect observed between  $CO_2$ ,  $H_2O$ , EGR, and  $N_2$  (from greater to lower), could be explained by the different heat capacities of the diluent. In addition, the authors also found that pressure effect on  $S_L$  may be different for lean and rich mixtures. In a recent measurement by Duva *et al.* [76],  $CO_2$  dilution effect was studied and it is found that 15%  $CO_2$  dilution could result in a 47–51% decrease in  $S_L$ . It is reported that simulations using the mechanism by Chaos *et al.* [79] agree well with measurements for  $\phi = 0.8$ – $1.2$ , but slightly underestimate for  $\phi = 1.3$ – $1.6$ .

Compared with pure compounds, measurements for surrogate mixtures and real gasoline are even less. Jerzembeck *et al.* [55] measured laminar flame speeds of standard gasoline/air mixtures diluted by pure nitrogen, which is achieved by vitiating the oxygen fraction in air (down to 15% and 17%). The results are compared with the calculated values for a primary reference fuel (PRF 87, isooctane/n-heptane = 87%/13%). Good agreement was found for lower dilution or high pressure cases, while a large deviation was found for high dilution and low pressure cases. This suggests that PRF could not sufficiently represent

the dilution effect on gasoline flames. Knorsch *et al.* [72] measured the laminar flame speed of n-butanol, isobutanol, and ethanol, using a flat flame burner, with increased temperature and dilution by nitrogen up to 20%. Small uncertainties below 1.5% were estimated for the measured results by the authors. It is found that N<sub>2</sub> dilution reduces  $S_L$  linearly, to about 50% at 20% dilution ratio, and high dilution could also lead to decreased flammability for both lean and rich mixtures. Bhattacharya *et al.* [73] measured the  $S_L$  of a commercial gasoline (V-Power from Shell) using a heat flux burner and compared with that of the PRF95 surrogate (95%isooctane/5%n-heptane) obtained by kinetic simulation. A mixture of 15%CO<sub>2</sub>/85%N<sub>2</sub> was used as dilution and a flame species fCO<sub>2</sub> was used in simulations to distinguish the thermal and chemical effects of CO<sub>2</sub> dilution. They concluded that the reduction in  $S_L$  by dilution can be recovered by increase initial temperature and the chemical and dilution effects of CO<sub>2</sub> are about equal. Manna *et al.* [74] conducted experiments on the laminar flame speeds of the FACE-C gasoline (Fuels for Advanced Combustion Engine) and its surrogate of toluene reference fuel (TRF) (17.6%n-heptane/77.4%isooctane/5%toluene), with the dilution of real combustion residuals produced by preliminary explosions. It is observed that the recirculation of combustion residuals reduces the laminar flame speed monotonically but enhances flame stability indicated by increased Markstein length especially at fuel-lean conditions. Their later work [75] studied the same fuels and conditions but considered coupled effects of EGR and ethanol addition. They found that the reduction in  $S_L$  by 10% of EGR can be compensated by 60% of ethanol blending.

In summary, available measurements for PRF, TRF, TRFE, and real gasoline at diluted conditions are limited. Most studies use N<sub>2</sub> as the diluent, which only affects  $S_L$  through mixture heat capacity and is not sufficient to emulate real combustion residuals. For dilution containing CO<sub>2</sub> and H<sub>2</sub>O, the chemical effect is expected to be important but the mechanism is still less known. In addition, high dilution ratios (greater than 50%), the objective for future EGR technologies, are still difficult to realize in experiments because of the difficulty to obtain a detectable flame front without increase initial temperature. It is necessary for future experiments to focus more on the dilution effects of CO<sub>2</sub> and H<sub>2</sub>O, and more extreme conditions such as high temperature, high pressure and high dilution ratio.

### 1.3.3 Correlation Studies of the Dilution Effect on Laminar Flame Speed

Mathematical correlations of laminar flame speeds with respect to parameters, such as equivalence ratio, temperature, and pressure, are often useful in CFD simulations of the flame propagation in engine cylinders. Derived from the fitting of existing experimental or kinetic simulation results, they can be used to make predictions of  $S_L$  at conditions where there's no data. They are widely used in CFD simulations, instead of kinetic calculations, because they are less expensive in computational power. A typical laminar flame speed correlation has the form of,

$$S_L = S_{L,0} \left( \frac{T_u}{T_0} \right)^\alpha \left( \frac{p}{p_0} \right)^\beta \quad (1.1)$$

where  $S_{L,0}$  is the laminar flame speed at a defined standard condition ( $T_0, p_0$ ) which is a function of equivalence ratio,  $T_u$  is the unburnt gas temperature,  $p$  is the pressure, and  $\alpha$  and  $\beta$  are fitted coefficients. Correlations considering the dilution effect as a parameter can also be established following the same manner.

In the early experiments by Ryan and Lestz [61], Metghalchi and Keck [62], Gülder [63, 77], linear trends of  $S_L$  with dilution ratio were observed. Based on these findings, correlation expressions considering dilution effects were proposed in the form of,

$$\begin{aligned} S_L &= S_{L,0} \left( \frac{T_u}{T_0} \right)^\alpha \left( \frac{p}{p_0} \right)^\beta (1 - ax_d) \\ &= S_{L,x_d=0} (1 - ax_d) \end{aligned} \quad (1.2)$$

where  $S_{L,0}$ ,  $\alpha$ ,  $\beta$ , and  $a$  are fitted coefficients,  $x_d$  is the dilution ratio. Although different values of the  $a$  coefficient were obtained (2.1, 2.3, and 2.5 for [62], [63], and [61] respectively), the term  $(1 - ax_d)$  suggests a linear correlation. In a similar experimental study later by Rhodes and Keck [64], using a  $\text{CO}_2/\text{N}_2$  (20%/80%) mixture as diluent, a non-linear correlation with respect to dilution ratio was proposed,

$$S_L = S_{L,x_d=0} (1 - ax_d^b) \quad (1.3)$$

where  $a = 2.06$  and  $b = 0.733$  are the fitting coefficients. In the book by Heywood [80], he summarized the above works and suggested recommended values,  $a = 2.06$  and  $b = 0.77$  for Equation 1.3. Syed *et al.* [81] simulated the laminar flame speed of gasoline/ethanol blends at various conditions using the kinetic mechanism by Andrae and Head [82]. Based on these results, they proposed the non-linear correlation term as,

$$S_L = S_{L,x_d=0} (1 - ax_d)^b \quad (1.4)$$

where the coefficients  $a$  and  $b$  vary slightly with ethanol fraction. Larger deviation with respect to the measurements and correlations by the above works was found for higher dilution ratios, which, as the authors claimed, maybe due to the fact that a ternary  $\text{H}_2\text{O}/\text{CO}_2/\text{N}_2$  mixture was used as diluent instead of the binary  $\text{CO}_2/\text{N}_2$  mixture. Marshall *et al.* [69] measured the laminar flame speed of some liquid fuels (e.g., n-heptane, isooctane, toluene, ethylbenzene, and ethanol) diluted by real combustion residual which was produced and retained in the chamber by preliminary explosions. Based on these measurements, they suggested a more complex correlation term for dilution effect,

$$S_L = S_{L,x_d=0} \left( 1 - \mu_1 x_d^{\left( \mu_2 + (\phi - 1) \mu_3 \right)} \right) \quad (1.5)$$

which indicates that dilution effect is dependent of equivalence ratio. Fu *et al.* [83] further sophisticated this term based on kinetic simulations on  $S_L$  of isooctane/n-butanol blends, so that it is applicable over wide ranges of equivalence ratio, dilution ratio and dilution compositions. They concluded that the dilution effect is independent of temperature and pressure and depend only on equivalence ratio, and proposed a more complex expression which include the quadratic dependence on  $\phi$  to fit better over wide range datasets, constants  $\phi_m$  to adjust  $\phi$  positions, and the summation over dilution components to count for different diluent com-



positions,

$$S_L = S_{L,x_d=0} \left( 1 - \sum_{i=1}^n X_i \mu_{1,i} x_d^{\left( \mu_{2,i} + \mu_{3,i}(\phi - \phi_{m,i}) + \mu_{4,i}(\phi - \phi_{m,i})^2 \right)} \right) \quad (1.6)$$

where  $X_i$  is the mole fraction of a component (e.g., CO<sub>2</sub>, N<sub>2</sub>, and H<sub>2</sub>O) in the  $n$ -component diluent mixture, and  $\phi_{m,i}$ ,  $\mu_{1,i}$ – $\mu_{4,i}$  are fitting coefficients.

It can be seen that through the years the correlation term for dilution effect becomes complex, and it is expected to be even more complicated as research advances. The hypothesis that it is independent of temperature and pressure, could be questioned by further studies, especially by new experimental results.

## 1.4 Kinetic Modeling Studies of Gasoline Surrogate Flames

### 1.4.1 General Features of Kinetic Modeling and Kinetic Mechanisms

Kinetic modeling is used to reproduce and predict various fundamental combustion properties of fuels using detailed understandings in combustion chemistry. Such properties include adiabatic flame temperature, auto-ignition delay time, fundamental laminar flame speed, product composition, concentration of detectable intermediate species, and etc. They are described as fundamental because they are obtained under ideal conditions and can be used as inputs when modeling real-life flames which introduces more physical complexity, e.g., flame stretch, turbulence flow, and acoustics. Briefly, a kinetic model is a system of differential equations with boundary conditions and the resulted properties are its steady-state solutions. Accordingly, it consists mainly of four elements: (1) a reactor model and (2) a kinetic mechanism, which defines the differential equations; (3) reactant composition and (4) physical properties of the initial state (such as temperature and pressure), which are the boundary conditions. Among them, a kinetic mechanism is a series of elementary reactions, which describe the transformation from reactants to products at the molecular level, with information about their reaction rates and thermodynamic and transport properties of the involving species. This information is a summary of the accumulated understandings by scientists on the chemical nature of combustion. Since the other three aspects describe the target problems, with the same computational specifications, the accuracy of the combustion properties obtained depends on how close the kinetic mechanism is to reality. Therefore, developing mechanisms which well interpret the fuel combustion chemistry, is fundamental and essential for combustion modeling.

Kinetic Mechanisms can be considered as a compilation of human’s understandings on how combustion proceeds at the molecular level. Their development is also advanced by the new understandings which rely heavily on the previous ones. Based on the chemical detail they contain, kinetic mechanisms could be categorized into various types.

- **Detailed Mechanisms** attempt to include as many chemical species and elementary reactions (instead of global ones) as possible, and to be capable

of predicting combustion phenomena over a wide range of conditions (e.g., temperature, pressure, and fuel/oxidizer ratio).

- **Reduced Mechanisms**, usually obtained by mechanism reduction from detailed ones by removing species that are less important at certain conditions, have fewer species and elementary reactions and are applicable within a designated range of conditions.
- **Skeletal Mechanisms**, which are further reduced in sizes, contain lumped species and global reactions to minimize the computational cost when used in CFD simulations.
- **High-Temperature Mechanisms** contain only reactions that could occur at high temperature (usually above 900 K), which are mostly adequate for flame speed calculations or ignition calculations with high initial temperature.

In this section, we focus mainly on detailed mechanisms, as they contain more chemical detail.

Kinetic mechanisms exhibit some common features, although they vary from each other for different fuels.

- Combustion mechanisms exhibit a hierarchical manner [84, 85] where they have a common core mechanism consists of reactions involving light species, especially for the combustion of hydrocarbon-based fuels. This is because combustion is a process of breaking large fuel molecules into smaller ones (e.g., complete combustion product  $\text{CO}_2$  and  $\text{H}_2\text{O}$  are molecules with only one heavy atom).
- Combustion is radical-driven, because that it is predominated by reactive light radicals with unpaired electrons, which play an important role in the breakage of larger molecules by extracting. The free radicals with unpaired electrons, more reactive than stable molecules, can break bonds in fuel molecules, abstract H atoms from them, and gradually crack them into small molecules and eventually to final combustion products. The chain reactions generating or eliminating radicals, affect the concentration of the radical pool and therefore affect many combustion properties.
- Combustion is also a process of consuming distinct chemical kinetic functionalities of the fuels. [86]
- Combustion kinetics is temperature sensitive, which originated from the fact that chemical reaction are mostly temperature sensitive too. It is commonly accepted that the kinetics at high and low temperature are significantly different.

The hierarchical nature is consistent with the concept of sub-mechanisms, which could be used either independently or as a building block for a larger mechanism. Recent research using sensitivity analysis on ignition delay and laminar flame speed show that important reactions are mostly the ones involving  $\text{C}_0$ – $\text{C}_4$  molecules or the decomposition of the fuel molecules into fuel radicals, while reactions in between are usually not as important. [85] The  $\text{C}_0$ – $\text{C}_4$  sub-mechanism, also called the core mechanism, is fundamental to combustion and applies to all hydrocarbon fuels. The fuel decomposition sub-mechanisms are specific to the fuel molecules and reflect the process of cracking large species into smaller ones which then participate in the core mechanism. Literature is reviewed separately for the two sub-mechanisms in the following sections.

## 1.4.2 The Core (C<sub>0</sub>–C<sub>4</sub>) Sub-mechanisms

The core sub-mechanisms are detailed mechanisms for the oxidation of some small molecules and are also fundamental in developing models for larger fuels.

### Hydrogen (H<sub>2</sub>)

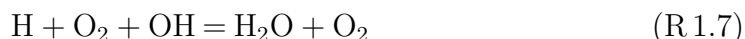
The hydrogen mechanism is the simplest (containing about only 20 reactions) and the most fundamental for hydrocarbon oxidation. It provides the H, OH, and O radicals, which are the most dominant ones in combustion systems and contribute largely to the reactivity of the system. For example, It provides the most common chain branching reaction,  $\text{H} + \text{O}_2 = \text{O} + \text{OH}$ , which is found to be the most sensitive reaction in hydrocarbon combustion events. Although the reactions in the hydrogen mechanism are extensively studied, it is reported recently that critical uncertainty remains, considering the high sensitivity of these reactions to the combustion of all hydrocarbon fuels. [87–89] As a consequence, advancing the hydrogen mechanism seems to be a never-ending task. Especially in recent decades, considerable progress has been made, owing to the assist of more advanced kinetic experiments and the increasing accuracy and involvement of theoretical chemistry.

Following attentions to the main uncertainty identified in previous works [87–89], Hong *et al.* [90] developed an updated H<sub>2</sub>/O<sub>2</sub> model, with improved rate constants obtained from their shock tube measurements. The four improved rate constants for reaction,  $\text{H} + \text{O}_2 = \text{O} + \text{OH}$ ,  $\text{H}_2\text{O}_2 (+ \text{M}) = \text{OH} + \text{OH} (+ \text{M})$ ,  $\text{OH} + \text{H}_2\text{O}_2 = \text{HO}_2 + \text{H}_2\text{O}$ , and  $\text{O}_2 + \text{H}_2\text{O} = \text{OH} + \text{HO}_2$ , are found to improve significantly the prediction on ignition delay time and shock tube speciation. Burke *et al.* [91] revisited the hydrogen mechanism and improved the predictions for laminar flame speeds. They found that the pressure dependence of HO<sub>2</sub> formation and consumption reactions are important at high pressure and low temperature conditions, especially the three body reaction  $\text{H} + \text{O}_2 (+ \text{M}) = \text{HO}_2 (+ \text{M})$ . Kromns *et al.* [17] found that the reaction sequence  $\text{H}_2 + \text{HO}_2\text{H} = \text{H} + \text{H}_2\text{O}_2$  followed by  $\text{H}_2\text{O}_2 (+ \text{M}) = \text{OH} + \text{OH} (+ \text{M})$  plays a key role in hydrogen ignition under such conditions. Olm *et al.* [92] compared the performance of the above hydrogen mechanisms over a large set of experimental data, and concluded that the mechanism by Kromns *et al.* [17] has the best overall performance in predicting ignition delay time and laminar flame speed.

Later, Alekseev and Konnov [93] analyzed existing laminar flame speed measurements of hydrogen flames, and found that experiments using heat flux method from various laboratories are consistent and thus highly valuable for mechanism validations. In this analysis, the Konnov 2015 [94] mechanism, which contains either experimentally measured or theoretically calculated rate coefficients for many reactions, was found to over-predict the laminar flame speed. It indicates that the chemical understanding of hydrogen combustion still needs to be improved.

Recently, Burke and Klippenstein [95–97] suggested that chemically termolecular reactions, where the 3rd-body collider is not inert, may play a significant role in combustion kinetics. For example, the  $\text{H} + \text{O}_2 + \text{X} \longrightarrow \text{products}$  reactions (R 1.4–R 1.7), where X could be H, O, OH or other radicals, are demonstrated to

lower the predicted  $S_L$  when integrated in kinetic mechanisms. [95]

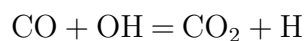
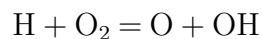


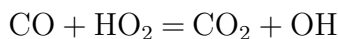
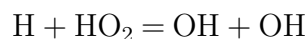
This significant reduction in  $S_L$  evokes problems and implies that some other parts in the mechanism must also be modified to obtain sufficient agreement with experiments. Konnov [98] suggested that use of the theoretically calculated transport properties by Jasper *et al.* [99, 100] increase  $S_L$  and could compensate the reduction caused by R 1.4–R 1.5. However, this approach only affects on the laminar flame speeds results, and could not compensate characteristic obtained from 0-D calculations, e.g., ignition delay times and speciation profiles. Therefore, other compensating approaches in terms of kinetic or thermodynamic parameters are still necessary.

In summary, a more accurate understanding of the chemistry of hydrogen combustion is still necessary to improve model predictions, especially under conditions close to applications, such as high pressure, intermediate temperature, and high dilution.

### Carbon Monoxide (CO)

Similarly, the CO sub-mechanism is also fundamental and important to hydrocarbon combustion because it is nearly the only precursor to the production of  $\text{CO}_2$  and provides the major heat release. Olm *et al.* [92] compared comprehensively the performance of 16 syngas mechanisms based on a large set of experimental data (4970 data points in 408 datasets) in ignition delay times, flame speeds, and species concentration profiles. They concluded that five mechanisms, namely NUIG-NGM-2010 [101], Kromns-2013 [17], Davis-2005 [102], Li-2007 [103] and USC-II-2007 [104], reproduced the experimental data similarly well. Concerning the laminar flame speed reproductions, even for these mechanisms with overall good performance, some common weakness are observed: (i) less accurate at fuel-rich conditions; (ii) larger error function at high initial temperature (i.e., over 500 K); (iii) larger deviation at low pressure (i.e., lower than 1.5 atm); (iv) significantly worse for hydrogen-rich mixtures (i.e.,  $\text{CO}/\text{H}_2$  ratio less than unity). By performing comprehensive sensitivity analysis, it is revealed that the different performance between the mechanisms is tightly related to their choices in rate coefficients of the four most sensitive reactions:





. Among them, the rate coefficients of the  $\text{CO} + \text{OH} = \text{CO}_2 + \text{H}$  reaction is worth noting, because of its high sensitivity and unique role as the major heat release step, in the oxidation of syngas as well as many hydrocarbon fuels. The selection of its rate coefficients should be done carefully, as it is found to proceed via a multi-channel mechanism through the HOCO intermediate. [105] Recent studies have also found that its reaction kinetics are affected by a third  $\text{CO}_2$  [106] or  $\text{H}_2\text{O}$  [107] molecule.

### Comprehensive Core Mechanisms

Besides CO and  $\text{H}_2$ , the combustion of hydrocarbon fuels leads to a multitude of intermediate species, which are usually stable small molecules, such as small alkanes, alkenes, alkynes, aldehydes, alcohol, and ethers. These small hydrocarbons and oxygenated hydrocarbons can also serve as fuel themselves and their oxidation kinetics are also present in the combustion of larger fuels. Therefore, the core mechanism should contain sufficiently the sub-mechanisms for these intermediates. One commonly used core mechanism is GRI Mech 3.0 [108] which is designated for the combustion of natural gas. It is a sufficient core mechanism because the combustion mechanism of methane and ethane, common components in natural gas, could lead to molecules as large as  $\text{C}_4$  species. Unfortunately, it is not updated in the recent decade. Another core mechanism is the Aramco Mech 3.0, which has been constantly updated with sub-mechanism for new molecules. It is comprehensively validated and contains sub-mechanism for many  $\text{C}_0$ – $\text{C}_4$  molecules [109–113] and is currently being extended to  $\text{C}_5$  hydrocarbons [114,115]. Since larger fuels are expected to be cracked into the radicals and smaller intermediates that fall into the core mechanism, the development of core mechanisms is of great significance and facilitates the kinetic investigation of larger fuels.

### 1.4.3 The Fuel Decomposition Sub-mechanisms

The mechanisms of cracking large fuel molecules are different and depend on the structure of the fuel. The hundreds component in gasoline can be categorized into 5 types: linear alkanes (i.e., paraffins), branched alkanes (i.e., isoparaffins), alkene (i.e., olefins), cycloalkanes (i.e., naphthenes) and aromatics.

#### Linear Alkanes

For linear alkanes (n-alkanes), the high temperature oxidation kinetics is well understood [116–118] and found to be remarkably similar regardless of the size (i.e., carbon number) of the fuels [84,119], except for methane and ethane. The alkane molecules are first cracked, through H abstraction (breaking of C–H bonds), into alkyl radicals (with the same carbon number), which then undergo  $\beta$ -scission to give smaller alkyl radicals and alkene. The alkyl radicals are cracked further into smaller sizes through the same process and the alkene molecules undergo

H-abstraction. At very high temperature or pyrolysis environment (absent of oxidizer), *n*-alkanes are decomposed through the breaking of C–C bonds in the carbon chain. As the molecules get sufficiently small in size, they participate in the core mechanism of light species.

During the cracking of alkane fuels, a mixture of different alkyl radicals are generated, some of which decompose to produce H radicals accelerating the combustion process, while some produce methyl (CH<sub>3</sub>) radicals slowing down the process. [28] For the two special alkanes, the cracking of methane (CH<sub>4</sub>) produces only methyl radicals, while ethane (C<sub>2</sub>H<sub>6</sub>) produces only H radicals. Therefore, they mark the lower and upper bounds of alkane fuel reactivity, respectively. As all *n*-alkanes can be considered as an ethane molecule having numbers of CH<sub>2</sub> groups inserted inside, they have only two distinct C–H bonds, primary bonds located at the terminal carbon atoms, and secondary bonds located at the interior carbon atoms. As the carbon chain grows longer, the rate of H abstraction from secondary sites increases because of its increasing number while the rate from primary sites stays the same because there are only 6 sites for all *n*-alkanes. Because secondary C–H bonds are not only easier to break (weaker in bond energy), but also more numerous than primary ones, the H abstraction occurs more preferentially on secondary C–H bonds. With the above features in common, the oxidation mechanisms for *n*-alkanes are similar and have the same reaction classes, which is summarized by Westbrook and Curran [28] and shown in Table 1.2.

One common *n*-alkane in gasoline surrogate fuels is *n*-heptane (*n*-C<sub>7</sub>H<sub>16</sub>), who has an octane rating (RON) of 0 and is usually used to represent normal alkanes. Early efforts in establishing *n*-heptane oxidation mechanism include detailed model developed by Westbrook *et al.* [120], semi-detailed model by Ranzi *et al.* [121], auto-generated models by Chevalier *et al.* [122] and Côme *et al.* [123]. Curran *et al.* [124] studied *n*-heptane oxidation systematically and established a comprehensive mechanism, where important reactions are categorized into 25 different reaction classes for both high- and low-temperature regimes. This mechanism is adopted and further refined by Mehl *et al.* [25] to develop mechanisms for gasoline surrogates. Recent measurements by Herbinet *et al.* [125] using synchrotron vacuum ultraviolet photoionization mass spectrometry (SVUV-PIMS) identifies unstable intermediate species that are not detectable using gas chromatography (GC), such as molecules with hydroperoxy functions. They observed the formation of several intermediates in the low-temperature chemistry, in which attention was drawn to diones, ketohydroperoxides and acetic and propanoic acids, which are rarely reported. By adding reaction classes for these species, Pelucchi *et al.* [126] developed an improved *n*-heptane mechanism, which exhibit good agreement with various experimental data. Later Seidel *et al.* [127] observed more than 80 species generated in premixed *n*-heptane flame at 40 mbar. Zhang *et al.* [128] further improves the mechanism, implementing updated reaction classes and rate rules, updating the thermodynamic database using recently published values from Burke *et al.* [129] for C<sub>1</sub>–C<sub>4</sub> species. The model is validated on various types of experimental data including laminar flame speeds at elevated temperature and pressure, where overall good agreement with measurements is found and good consistency is expected with the oxidation kinetics of other *n*-alkanes. It is worth noting that the *n*-heptane mechanism is being continuously studied and advanced both experimentally and numerically, with attentions especially on new reaction pathways in

Table 1.2: High-temperature and low-temperature reaction classes. Table taken from Ref. [28].

High temperature reaction classes	Low temperature reaction classes
1. Unimolecular fuel decomposition	11. Addition of O <sub>2</sub> to alkyl radicals ( $\dot{R} + O_2 = R\dot{O}_2$ )
2. H-atom abstraction from the fuel	12. $\dot{R} + R\dot{O}_2 = R\dot{O} + R\dot{O}$
3. Alkyl radical decomposition	13. $\dot{R} + H\dot{O}_2 = R\dot{O} + \dot{O}H$
4. Alkyl radical isomerisation	14. $\dot{R} + CH_3\dot{O}_2 = R\dot{O} + CH_3\dot{O}$
5. H-atom abstraction reactions from alkenes	15. Alkyl-peroxyl radical isomerization ( $R\dot{O}_2 = \dot{Q}OOH$ )
6. Addition of radical species $\ddot{O}$ and $\dot{O}H$ to alkenes	16. Concerted eliminations ( $R\dot{O}_2 = \text{alkene} + H\dot{O}_2$ )
7. Reactions of alkenyl radicals with $H\dot{O}_2$ , $CH_3\dot{O}_2$ , and $C_2H_5\dot{O}_2$	17. $R\dot{O}_2 + H\dot{O}_2 = ROOH + O_2$
8. Alkenyl radical decomposition	18. $R\dot{O}_2 + H_2O_2 = ROOH + H\dot{O}_2$
9. Alkene decomposition	19. $R\dot{O}_2 + CH_3\dot{O}_2 = R\dot{O} + CH_3\dot{O} + O_2$
10. Retroene decomposition reactions	20. $R\dot{O}_2 + R\dot{O}_2 = R\dot{O} + R\dot{O} + O_2$
	21. $ROOH = R\dot{O} + \dot{O}H$
	22. $R\dot{O}$ decomposition
	23. $\dot{Q}OOH = \text{cyclic ether} + \dot{O}H$ (cyclic ether formation)
	24. $\dot{Q}OOH = \text{alkene} + H\dot{O}_2$ (radical site beta to OOH group)
	25. $\dot{Q}OOH = \text{alkene} + \text{carbonyl} + \dot{O}H$ (radical site gamma to OOH group)
	26. Addition of O <sub>2</sub> to $\dot{Q}OOH$ ( $\dot{Q}OOH + O_2 = \dot{O}_2\dot{Q}OOH$ )
	27. Isomerization of $\dot{O}_2\dot{Q}OOH$ and formation of carbonylhydroperoxide and $\dot{O}H$
	28. Decomposition of carbonylhydroperoxide to form oxygenated radical species and $\dot{O}H$
	29. Cyclic ether reactions with $\dot{O}H$ and $H\dot{O}_2$
	30. Decomposition of large carbonyl species and carbonyl radicals

low-temperature chemistry and fuel-rich conditions.

### Branched Alkanes

The main difference between branched and linear alkanes are two-fold: (i) the branching of carbon chains introduce tertiary C–H bonds, whose bond strength is the weakest compared to primary and secondary bonds; and (ii) the number of primary bonds is increased due to the presence of more terminal carbon atoms, which, as consequence, reduces the number of secondary bonds. The former increase reactivity as H abstraction on tertiary bonds is easier, while the latter

reduces reactivity due to the increased number of primary C–H bonds that more difficult to break. For high temperature kinetics, it affects mainly on the external H abstraction by radicals, such as H, O, OH, HO<sub>2</sub> and CH<sub>3</sub>, which happen preferentially on tertiary sites for branched alkanes. The following chain-cracking processes through  $\beta$ -scission are similar to that of *n*-alkanes. For low-temperature kinetics, it affects mainly on the internal H abstractions, converting RO<sub>2</sub> to QOOH, whose rate depends on both the type of C–H bond and the size of the transition state ring. It is found that H abstraction from a tertiary site that is 2 carbon atoms away from the C–O–O· moiety is even faster than from a secondary site that is 3 carbon atoms away. [28] It is worth noting that, these differences have moderate influences on high-temperature characteristics, such as laminar flame speed, but affect significantly the low-temperature chemistry, such as ignition delay times at negative temperature coefficient (NTC) conditions.

Isooctane is the representative of branched alkanes in gasoline surrogate fuels. The oxidation kinetics of isooctane was studied by Curran *et al.* [130] comprehensively, and a kinetic model was developed in the analogy of the reaction pathways and rate rules for the oxidation of *n*-heptane [124] but with modifications for better predictive ability. It is improved later by Mehl *et al.* [25], with focus on the low-temperature chemistry. The improved mechanism, LLNL 2011 [25] is comprehensively validated and exhibits good agreement with various types of experimental data. However, it is reported that the mechanism underestimates the reactivity at low and intermediate temperatures and lean conditions, typical in HCCI engines. [131–135] Recently Atef *et al.* [136] developed a comprehensive isooctane oxidation mechanism, with 2768 species and 9220 reactions, based on the LLNL 2011 mechanism. The mechanism includes theoretically calculated thermochemistry and kinetics, such as the heat of formation, entropy and specific heat capacity for isooctane and its radicals [137], thermochemistry and reaction kinetics for the reaction of secondary isooctyl radical with oxygen [138] and tertiary isooctyl radical with oxygen [139]. and pressure-dependent rate coefficients for isooctane unimolecular decomposition and the  $\beta$ -scission and isomerisation of isooctyl radicals [140]. It also includes alternative isomerization pathways for peroxy-alkylhydroperoxide (OOQOOH) and third oxygen addition pathways suggested by Wang *et al.* [141,141]. The mechanism is validated based on the measurements of ignition delay time in the same work [136] in addition to a vast amount of experimental data in the literature on ignition delay, speciation profiles, and laminar flame speeds.

## Alcohols

The main structural difference between alkanes and alcohols is that at least one terminal C–H moiety is replaced by the C–O–H group. The oxidation mechanism of alcohols is similar to that of alkanes, for the most part of both high- and low-temperature chemistry. However, the presence of the OH group changes the preferential order of H abstraction. The H atom in the OH group is difficult to be abstracted, due to the high O–H bond energy. [28] However, the presence of OH group delocalizes electron density sufficiently, which makes the C–H bonds at the  $\alpha$  sites (most adjacent to the OH group) weaker by 2–4 kcal mol<sup>−1</sup> comparing with the primary bonds in analogous alkanes, while C–H bonds on the  $\beta$ -sites



(second adjacent) become stronger by about amount of energy compared with the secondary bonds in alkanes. [59, 142, 143] This makes H abstraction happen preferentially on the C–H bonds adjacent to the OH group. At high temperatures,  $\beta$ -scission occurs following the abstraction of H atoms, similar to that of alkanes, and produce another radical and unsaturated alkenes or alcohols. At low temperature, after the H abstraction at preferential  $\alpha$ -site, the hydroxyalkyl radical undergoes the process of  $R-\dot{C}HOH \longrightarrow R-CH(O\dot{O})OH \longrightarrow R-CH(OOH)\dot{O} \longrightarrow R-CH=O + H\dot{O}_2$ , where  $O_2$  addition on the  $\alpha$ -site is followed promptly by H transfer from OH to  $O\dot{O}$  group, and then dissociation into a stable aldehyde molecule and a less reactive  $HO_2$  radical. [144, 145] As a result, this pathway inhibit further low temperature reactions, different than usual chain branching  $RO_2$  isomerisation pathways for alkanes. The inhibiting effect is especially significant for small alcohol molecules, while the low-temperature chain branching by  $RO_2$  isomerization is enhanced for large alcohol molecules with a longer carbon chain. [146–148]

Ethanol is one of the main additives to gasoline fuels to improve knock resistance. Early kinetic mechanisms developed for ethanol oxidation include the model by Egolfopoulos *et al.* [149] and Marinov and Nick [150], based on which most later mechanism are developed. Later mechanisms [109, 151–155], developed mostly based on these two mechanisms, improve the performance with validation on new experiments on wider conditions such as higher pressures. A recently developed mechanism by Zhang *et al.* [156] improves the low temperature chemistry for ignition delay time, by integrating recent kinetic studies by Mittal *et al.* [157]. Validation of the mechanism shows good agreement with various types of experimental data.

## Aromatics

Different than alkanes, aromatic compounds are difficult to be oxidized. For aromatics with long carbon side chains, the oxidation occurs preferentially on the carbon chain instead of the benzene ring. Then it produces phenyl and benzyl radicals, further reactions of which fall into the toluene/benzene oxidation mechanism. The oxidation of toluene and benzene is complicated and challenging, involving the resonance stabilization of benzyl ( $C_6H_5CH_2$ ) radical, production of Phenyloxidanyl  $C_6H_5\dot{O}$  radical, decomposition of benzyl and phenol radicals, inter-conversions between phenyl ( $C_6H_5$ ) and benzyl radicals, reactions of cyclopentadienyl ( $C_5H_5$ ) radicals, and the difficult cracking of the aromatic ring. [28]

Toluene is the main representative of aromatic compounds in gasoline surrogate fuels. Considerable amount of experiments on toluene oxidation kinetics are available, in terms of ignition delay times [158–164], laminar flame speed [56, 65, 165–169], and speciation profiles in oxidation [158, 170–178], flames [179–183], and pyrolysis [184–195]. Based on the experimental data, several kinetic models have been developed. [172, 174, 175, 178, 196–201] A recently developed toluene oxidation mechanism by Yuan *et al.* [202, 203], consist of 272 species and 1698 reactions, adopts rate coefficients from recent theoretical studies [204–216] for many reactions involving toluene, benzyl radical, fulvenallene and fulvenallenyl radical. The mechanism is validated comprehensively based on the flow reactor and JSR measurements in the same work [202] and a large amount of experimental data from the literature for a wide range of conditions [203]. It is reported that experimental

and kinetic studies on toluene oxidation at high pressure are still lacking. [202]

## Gasoline and Surrogates

Kinetic mechanisms for multi-component fuels can be formulated by compiling the sub-mechanism for the fuel components. A considerable number of kinetic mechanisms [25, 217–219] are available for gasoline and gasoline surrogate fuels, such as PRF, TRF, and TRFE. Mehl *et al.* [25] developed LLNL 2011 mechanism, a detailed kinetic model consisting of 1550 species and 6000 reactions, for gasoline surrogate components under engine conditions. It is comprehensively validated and commonly used as the starting point for the development of other mechanisms. Puduppakkam *et al.* [217] developed a detailed mechanism, consist of 833 species and 8764 reactions, for diesel and gasoline surrogates. Andrane [218] developed a mechanism that could predict the non-linear blending behavior for PRF on MON. Cai and Pitsch [219] developed an optimized mechanism using the optimization methodology based on rate rules [220], with also the integration of ethanol sub-mechanism. The above mechanisms are extensively reviewed by Zhen *et al.* [221], in terms of surrogate types (e.g., isooctane, toluene, PRF, TRF, and multi-components fuels) and mechanism scales (detailed, reduced, and skeletal). They suggested several directions for the future development of gasoline surrogate mechanisms: (1) introduction of more small molecule reactions; (2) consideration of more real components; (3) utilization of new techniques for mechanism validation, e.g., Laser-Induced Breakdown Spectroscopy (LIBS), Laser Excited Atomic Fluorescence (LEAF), and Planar Laser-Induced Fluorescence (PLIF); (4) mechanisms for new combustion regimes, e.g., Moderate and Intense Low Oxygen Dilution (MILD), Premixed Charge Compression Ignition (PCCI), and Reactivity Controlled Compression Ignition (RCCI).

## 1.5 The MACDIL Project

The present work is funded by and is one of the five tasks of the this MACDIL project (ANR-15-CE22-0014), short for “Moteur Allumage Commande forte Dilution” in French, which means “Controlled Ignition Engine with High Dilution” in English. The objectives and strategy of this project are introduced below in this section.

As mentioned in Section 1.1, to ensure engine performance at high EGR rates, increasing the tolerance of SI engines to high dilution remains a major theoretical and technical challenge. The MACDIL project aims to develop novel combustion models that are valid under extreme conditions in terms of dilution rate, but also of pressure and temperature, found in highly downsized SI engines. To fulfill this objective, MACDIL proposes to acquire an unprecedented understanding of combustion under intermediate (15 to 25%) and high (beyond 25%) EGR rates and high pressure and temperature conditions representative of turbocharged SI engines and to capitalize it in the form of CFD codes for both academic and industrial use.

The major scientific challenges to reach its ambitious objectives is the absence of sufficient knowledge of turbulent flames under such extreme conditions, the lack of adapted chemical kinetics, as well as the absence of experimental studies

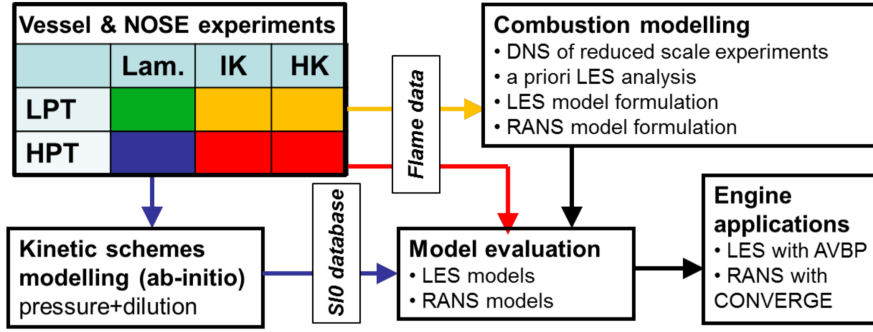


Figure 1-2: MACDIL strategy for the development and validation of combustion models for high dilution, temperature and pressure conditions.

due to the practical difficulty with high pressure and temperature flame measurements. Therefore, MACDIL proposes an integrated research approach combining dedicated experimental studies, ab-initio kinetic modelling (this work), as well as Direct Numerical Simulation (DNS) and Large-Eddy Simulation (LES) model development work, and includes work on transferring the knowledge into the Reynolds Averages Navier Stokes (RANS) CFD context that is largely used in the automotive industry. Since the modeling of highly-diluted combustion is a very challenging task rarely addressed in past studies, MACDIL proposes a step-by-step strategy based on combined usage of dedicated experiments, DNS, LES and RANS, and supported by ab-initio simulations for kinetic rate constants as outlined below and depicted in Figure 1-2.

1. Acquisition of a unique experimental database for Intermediate and high Karlovitz (IK and HK) regimes investigation. (The Karlovitz number is characterized by the ratio of laminar flame thickness  $\delta_l^0$  to Kolmogorov turbulent length scale  $\eta$ ,  $K_a = \left(\frac{\delta_l^0}{\eta}\right)^2$  . )
2. Kinetics modeling of laminar premixed flames at high dilution, temperature and pressure conditions.
3. DNS of the experiment at a reduced scale.
4. LES modeling of IK and HK regimes supported by DNS and experiment.
5. Evaluation of the model developments at engine conditions.

## 1.6 Objectives and Significance

The present work constitutes the second task of the MACDIL project, kinetic modeling of laminar premixed flames at high dilution, temperature and pressure conditions. The objective is (i) to understand the combustion chemistry of fundamental flame speed at highly-diluted conditions and (ii) to establish a detailed kinetic mechanism by multi-scale modeling to predict combustion characteristics of gasoline premixed flames with sufficient accuracy at such extreme conditions.

Therefore, this work is expected to be of significance both scientifically and technically. Scientifically, it explores the chemical detail of diluted combustion

and their effects on the characteristics of laminar premixed flames. Technically, the developed mechanism also provides a database of fundamental flame speeds for the use in computational fluid dynamic (CFD) simulations, and therefore assist engine development.

## 1.7 Thesis Structure

This work is presented in terms of 7 chapters, which are as follows:

**Chapter 1 (This chapter)** gives a general introduction and literature reviews based on the thesis topic.

**Chapter 2** describes the methodology how the work is carried out, and theories, methods, and numerical tools used to obtain the results.

**Chapter 3** studies theoretically the  $\text{CH}_2\text{CO} + \text{OH}$  reaction, which is found important in TRFE flames at highly diluted conditions (Chapter 4), and derives its temperature- and pressure-dependent rate constant using *ab initio* chemical kinetics calculations.

**Chapter 4** identifies key thermokinetic parameters (i.e., rate coefficients of reactions and thermodynamic properties of species) and their corresponding sub-mechanisms, in TRFE flames at highly diluted conditions, using sensitivity analysis based on a starting mechanism.

**Chapter 5** studies the dilution effects of  $\text{CO}_2$  and  $\text{H}_2\text{O}$  on the laminar flame speeds, based on the diluted flames of smaller molecules (corresponding to the sub-mechanisms identified in Chapter 4).

**Chapter 6** introduces two kinetic mechanisms developed for TRFE/air/EGR mixtures, which is formulated and updated based on the important sub-mechanisms and kinetic parameters identified in Chapter 4. The mechanism is validated based on experimental data and a dilution term for correlations of laminar flame speeds at highly diluted conditions is proposed.

**Chapter 7** summaries the work, based on which perspectives are given.

THIS PAGE INTENTIONALLY LEFT BLANK

# Chapter 2

## Multi-Scale Theories and Computational Details

### 2.1 Methodology

The present work utilizes a multi-scale approach to model the laminar flame speed of highly-diluted gasoline premixed flames, as depicted in Figure 2-1. It is consistent with various levels of combustion research (from molecular to device levels) as summarized by Somers *et al.* [85]. Micro-scale methods study theoretically the configuration (electronic structure) and interaction (reaction kinetics) of molecules in a first-principle manner. Macro-scale methods simulate numerically combustion phenomena, such as laminar flame speed ( $S_L$ ), using a theoretical model combined with a kinetic mechanism. The kinetic mechanism is the key component and serves as the bridge between the two scales because it contains kinetic information obtained from the micro-scale methods and provide parameters for the macro-scale simulation. For example, micro-scale methods provide, after suitable upscaling through statistical physics, important thermodynamic and transport properties (e.g., enthalpy  $h$ , entropy  $s$ , specific heat capacity  $c_p$ , thermal conductivity  $\lambda$ , viscosity  $\mu$ , and diffusivity  $D_{ij}$ ) of molecules and rate coefficients (i.e.,  $k(T, p)$ ) of reactions, which are the main components of mechanisms and are used to calculate  $S_L$ .

The macro-scale development aims to (i) study the effect of dilution on laminar flame speed and (ii) establish kinetic mechanisms to predict  $S_L$  at such conditions. The methodology for the first purpose is shown in Figure 2-2a. Dilution effects are categorized and separated using the false-species method (introduced in section 2.5). Their effectiveness is compared and their influencing mechanisms on  $S_L$  are explored using different types of sensitivity analysis (introduced in section 2.6.2). It is worth mentioning that this method can be applied to various targets other than  $S_L$ , for instance, ignition delay time (IDT) and mole fraction of a given species. The methodology for the second purpose is summarized in Figure 2-2b and 2-2c. As shown in Figure 2-2b, based on the first identification using sensitivity analysis, key parameters that fall into several different sub-mechanisms are identified. These parameters, as well as other ones in the corresponding sub-mechanisms, will be studied and updated, using a repeatable routine named “investigation loop”. The investigation loop, as shown in Figure 2-2c, consists of three steps: (i) validation of the mechanism, (ii) identification of key parameters,

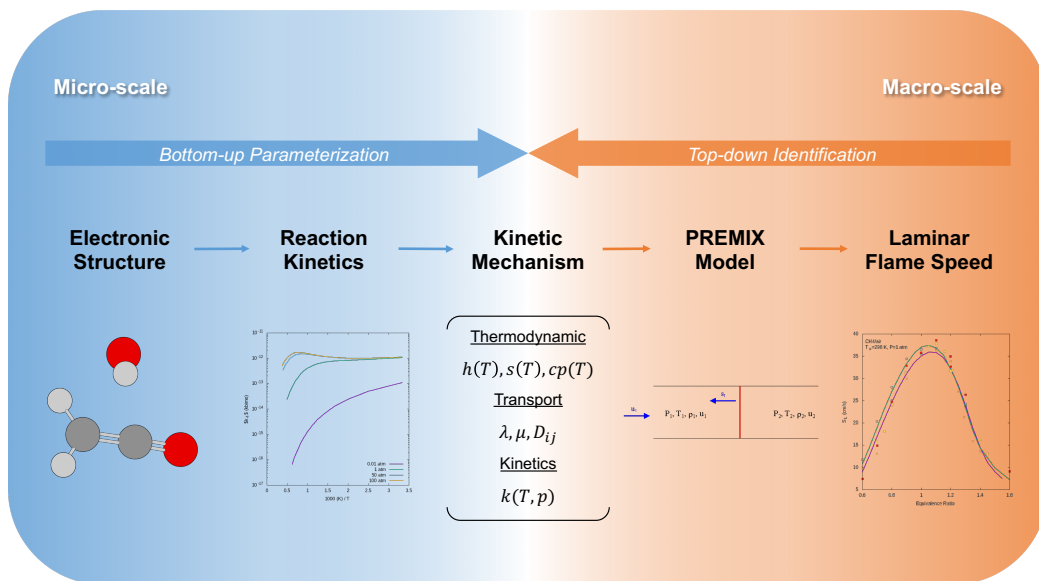
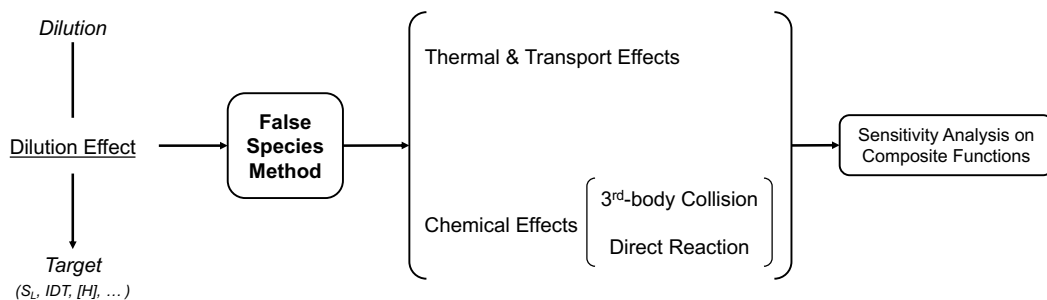


Figure 2-1: General methodology of the present study.

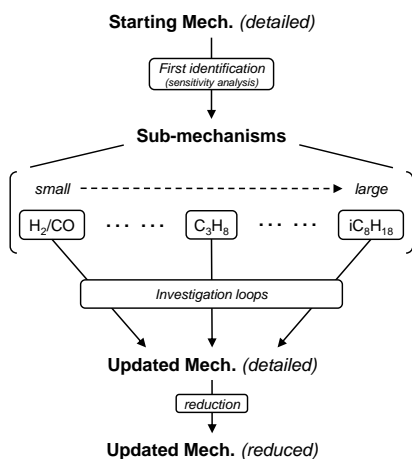
and (iii) modification (or update) using various means. The link of this process to Micro-scale studies is the modification of identified parameters, which can be done by calculations using theoretical chemistry.

Micro-scale developments aim to provide theoretically calculated kinetic parameters for Macro-scale studies, using *ab initio* electronic structures and reaction kinetics. Although all the parameters in mechanisms (as mentioned above) can be calculated theoretically, the present work investigated only in the rate coefficients ( $k(T, p)$ ) of an identified reaction. The methodology to calculate  $k(T, p)$  is shown briefly in Figure 2-3. Density functional theory (DFT) is used to study the given molecular system from scratch, which explores the possible pathways of reaction, and yields the necessary elements of a potential energy surface (PES) (i.e., geometry, energy, frequencies of the stationary points). The energies are then refined to better accuracy, using higher-level wave-function methods and extrapolations to complete basis set limit. On top of the PES obtained by *ab initio* electronic structure, the Rice-Ramsperger-Kassel-Marcus (RRKM) theory, based on transition state theory (TST), is used in couple with master equations (ME) to derive the phenomenological rate coefficients. Different corrections, such tunneling effects, could be considered depending on the complexity of the system.

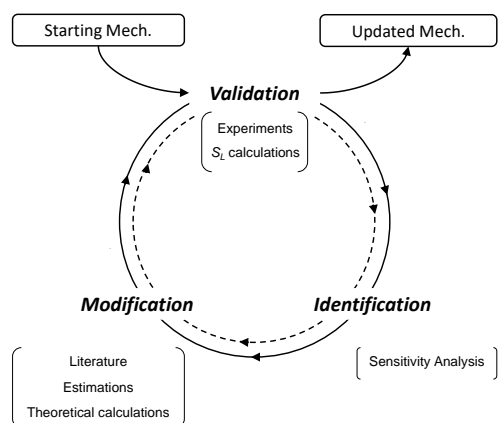
In summary, the methodology adopted by the present work is a multi-scale compilation of various modeling methods. They are explained in detail in the following sections of this chapter.



(a) Study of dilution effects.



(b) Mechanism development



(c) Investigation loop

Figure 2-2: Macro-scale methodology for the study of dilution effects (a) and the development of kinetic mechanisms (b & c).

## 2.2 Micro-scale: *ab initio* Electronic Structure

### 2.2.1 Basic Principles and Approximations

#### Molecular System and Wave Function

A molecule (or an atom) can be described as a certain configuration of a system consisting of nuclei and electrons. In the scope of chemistry (no change inside a nucleus), the interactions within the system (i.e., between nuclei and electrons) is dominated by electromagnetic forces, because other fundamental forces are too small at the distance ranges of interests. The *ab initio* electronic structure studies aim to find a possible stable configuration with the constraint of electromagnetic forces and obtain different properties of the system from it. One way to give a complete description of any system is by using wave functions, which are the solution to the Schrödinger equation in quantum mechanics. In the scope of the present work, only time-independent Schrödinger equation is concerned, which can



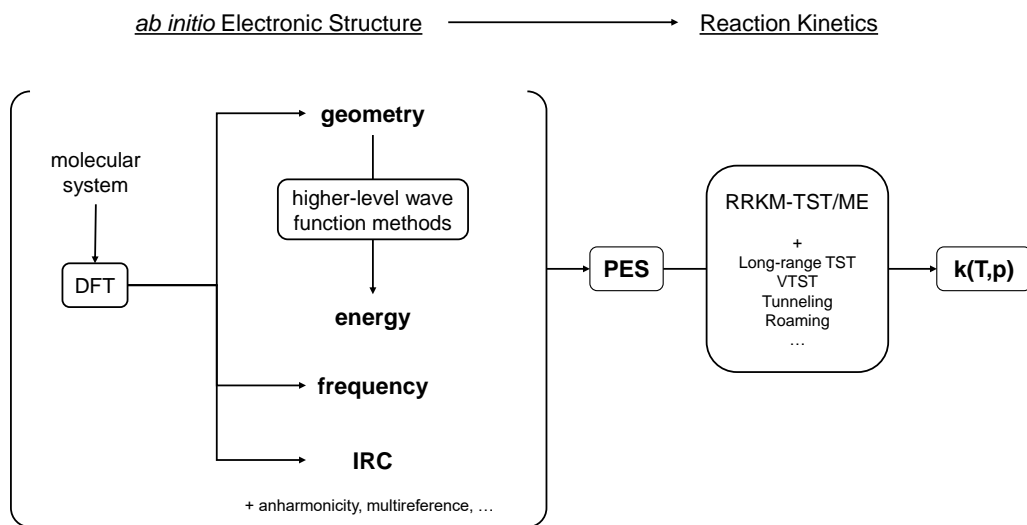


Figure 2-3: Micro-scale methodology for the theoretical calculation of rate coefficients.

be formulated in the form as an eigenvalue problem,

$$\hat{H}|\Psi\rangle = E|\Psi\rangle \quad (2.1)$$

where the wave function  $\Psi$  is the eigenfunction, the Hamiltonian  $\hat{H}$  is the operator, and the energy  $E$  is the eigenvalue. This form suggests a correspondence between operators and properties. For example, the Hamiltonian operator

$$\hat{H} = \underbrace{\frac{-\hbar^2}{2m}\nabla^2}_{\text{kinetic energy}} + \underbrace{V(\mathbf{r})}_{\text{potential energy}} \quad (2.2)$$

is used to derive the total energy of the system, which is the sum of kinetic and potential energy ( $E = \frac{p^2}{2m} + V(\mathbf{r})$ ).

The wave functions and operators in quantum mechanics follow some basic principles or postulates [2]:

- The configuration of a system can be specified completely by a wave function  $\Psi(\mathbf{r})$  that depends upon the coordinate of the particle.
- All possible system information can be derived from  $\Psi(\mathbf{r})$ . For example, the probability of finding the particle in space interval  $d\mathbf{r}$  located at position  $\mathbf{r}$  is expressed as  $\Psi^*(\mathbf{r})\Psi(\mathbf{r})d\mathbf{r}$ .
- The wave function must be normalized, i.e., the probability integrated for all space must equal to unity.

$$\int_{\text{all space}} \Psi^*(\mathbf{r})\Psi(\mathbf{r})d\mathbf{r} = 1 \quad (2.3)$$

- To every observable in classical mechanics there corresponds a linear and

Hermitian operator in quantum mechanics. The observable  $a$  associated with operator  $\hat{A}$  is the eigenvalue of the equation  $\hat{A}\Psi = a\Psi$ . In other words, there are other operators besides the Hamiltonian, e.g., the operator  $\hat{P} = -i\hbar\nabla$  corresponds to momentum ( $p$ ).

- If the wave function  $\Psi$  is normalized, the the average value of the observable is given by  $\langle a \rangle = \int_{\text{all space}} \Psi^* \hat{A} \Psi d\mathbf{r}$ .
- The wave functions (or eigenfunctions) of quantum mechanical operators are orthogonal. For any two different wave functions  $\Psi_m$  and  $\Psi_n$  which correspond to equations  $\hat{A}\Psi_m = a_m\Psi_m$  and  $\hat{A}\Psi_n = a_n\Psi_n$  respectively, must satisfy that

$$\int_{\text{all space}} \Psi_m^* \Psi_n d\mathbf{r} = 0 \quad m \neq n \quad (2.4)$$

## Energy in a Molecule

As Equation 2.2 indicates, a molecular system possesses both potential and kinetic energy. The potential energy depends on the position of the particles in the system and can be expressed as,

$$V = \sum_{i \neq j} \frac{q_i q_j}{4\pi\epsilon_0 r_{ij}} \quad (2.5)$$

where  $\epsilon_0$  is the permittivity of free space,  $q_i$  is the electric charge of the  $i$ th element (e.g.,  $e$  for single-proton nucleus and  $-e$  for electron), and  $r_{ij}$  is the distance between two elements. The kinetic energy is present because the elements in a molecule are constantly moving and it is stored in their movements.

$$K = \frac{\langle \Psi | (\sum_i -\frac{\hbar^2}{2m_i} \nabla^2) | \Psi \rangle}{\langle \Psi | \Psi \rangle} \quad (2.6)$$

Their motion can be categorized into three kinds: vibration, rotation, and translation.

In quantum chemistry, the vibrational motion of a diatomic system is often approximated as a harmonic oscillator. It assumes the two atoms move as if they are connected by a string (Figure 2-4a) and obey the Hook's law,

$$\mu \frac{d^2x}{dt^2} + kx = 0 \quad (2.7)$$

$$\frac{1}{\mu} = \frac{1}{m_1} + \frac{1}{m_2} \quad (2.8)$$

where  $x = l - l_0$  is the stretch (or compress) of the string with respect to its natural position,  $k$  is the force constant, and  $\mu$  is the reduced mass. As the diatomic system vibrates, energy is constantly transferring between kinetic and potential energy. But their total energy remains constant that  $E = K(x)|_{x=0} = V(x)|_{x=A} = \frac{1}{2}kA^2$ , where  $A$  is the vibration amplitude. Equation 2.7 gives an parabolic potential

energy profile,

$$V(x) = \frac{1}{2}kx^2 \quad (2.9)$$

which is an adequate approximation of the internuclear potential around its minimum with small displacements (Figure 2-4b). In addition, the force constant  $k$  is equal to the curvature of  $V(x)$  at the minimum ( $k = \frac{d^2V}{dx^2}|_{x=x_0}$ ). Solving the Schrödinger equation for a harmonic oscillator gives quantized and equally spaced energy levels,

$$E_v = \hbar \left( \frac{k}{\mu} \right)^{1/2} \left( v + \frac{1}{2} \right) = h\nu \left( v + \frac{1}{2} \right) \quad v = 0, 1, 2, \dots \quad (2.10)$$

where  $\nu = \frac{1}{2\pi} \left( \frac{k}{\mu} \right)^{1/2}$  is the frequency of the oscillator. And the energy of the ground state  $E_{v=0} = \frac{1}{2}h\nu$  is the zero-point vibrational energy. The harmonic oscillator model can be extended by addition of higher-order terms,

$$V(x) = \underbrace{\frac{1}{2}kx^2}_{\text{harmonic term}} + \underbrace{\frac{1}{6}\gamma x^3 + \dots}_{\text{anharmonic terms}} \quad (2.11)$$

where  $k$  is equal to the curvature of  $V(x)$  at the minimum ( $k = \frac{d^2V}{dx^2}|_{x=x_0}$ ), and  $\gamma = \frac{d^3V}{dx^3}|_{x=x_0}$ .

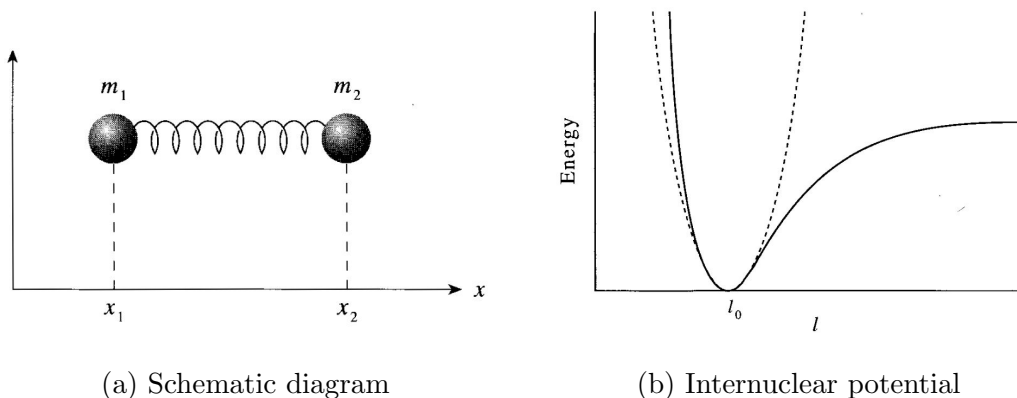


Figure 2-4: The harmonic oscillator model. Figures are taken from Ref. [2]. (a) the schematic diagram of two mass connected by a string, to describe the vibrational motion of a diatomic molecule. (b) Comparison of the harmonic oscillator potential (dashed line) with the complete internuclear potential (solid line) of a diatomic molecule.

The rotational motion of a diatomic system is often approximated as a rigid rotor, where two masses ( $m_1$  and  $m_2$ ) rotate about their center of mass with a fixed distance  $r$  (as shown in Figure 2-5). Although in real cases the molecule vibrates and rotates at the same time, the vibrational amplitude is negligible compared with the bond length  $r$ . Therefore the fixed distance in the rigid rotor approximation

is appropriate. As a consequence, there is no transition from kinetic to potential energy internally and the rotor does not depend on its orientation or position in the external space. Therefore, the total energy is equal to the kinetic energy of the rotation,

$$E = K = \frac{L^2}{2I} \quad (2.12)$$

where  $I = \mu r^2$  is the moment of inertia,  $L = I\omega$  is the angular momentum, and  $\omega$  is the angular velocity. Solving the Schrödinger equation for a rigid rotor also results in quantized energy levels,

$$E_J = \frac{\hbar^2}{2I} J(J+1) \quad J = 0, 1, 2, \dots \quad (2.13)$$

and therefore quantized absorption frequencies,

$$\nu = 2B(J+1) \quad J = 0, 1, 2, \dots \quad (2.14)$$

where  $B = \frac{h}{8\pi^2 I}$  is the rotational constant.

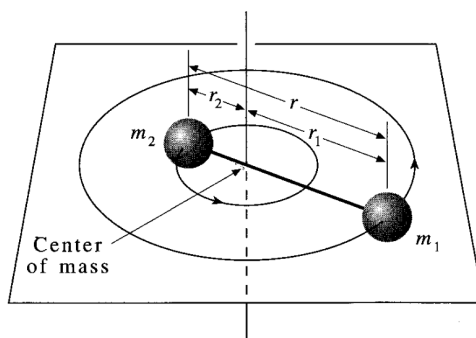


Figure 2-5: Schematic of a rigid rotor, i.e., two masses rotating about their center of mass. Figure taken from Ref. [2].

Besides the external translation motion of the molecule, internal translational motion is often present in transition-states and it leads to the breaking of the system. Therefore, translational motion is useful when studying the kinetics of chemical reactions.

## Hydrogen Atomic Orbitals

The hydrogen atom can be solved exactly by Schrödinger equation, and is useful to study the hydrogen atomic orbitals and their properties. The system consists of a proton fixed at the origin and an electron of mass  $m_e$  interacting with the proton through a Coulombic potential  $V(r) = -\frac{e^2}{4\pi\epsilon_0 r}$ . Therefore, the Hamiltonian operator for a hydrogen atom is

$$\hat{H} = -\frac{\hbar^2}{2m_e} \nabla^2 - \frac{e^2}{4\pi\epsilon_0 r} \quad (2.15)$$

which, using the spherical coordinates and separation of variables that  $\psi(\mathbf{r}) = \psi(r, \theta, \phi) = R(r)Y(\theta, \phi)$ , simplifies the Schrödinger equation into

$$\text{radial equation:} \quad -\frac{1}{R(r)} \left[ \frac{d}{dr} \left( r^2 \frac{dR}{dr} \right) + \frac{2m_e r^2}{\hbar^2} \left( \frac{e^2}{4\pi\epsilon_0 r} + E \right) R(r) \right] = -\beta \quad (2.16)$$

$$\text{angular equation:} \quad -\frac{1}{Y(\theta, \phi)} \left[ \frac{1}{\sin \theta} \frac{\partial}{\partial \theta} \left( \sin \theta \frac{\partial Y}{\partial \theta} \right) + \frac{1}{\sin^2 \theta} \frac{\partial^2 Y}{\partial \phi^2} \right] = \beta \quad (2.17)$$

where  $\beta$  is the separation constant. After several steps of mathematical derivations, the solution gives the radial and angular wave functions,

$$R_{nl}(r) = -\left\{ \frac{(n-l-1)!}{2n[(n+l)!]^3} \right\}^{1/2} \left( \frac{2}{na_0} \right)^{l+3/2} r^l e^{-r/na_0} L_{n+l}^{2l+1} \left( \frac{2r}{na_0} \right) \quad (2.18)$$

$$Y_l^m(\theta, \phi) = \left[ \frac{(2l+1)(l-|m|)!}{4\pi(l+|m|)!} \right]^{1/2} P_l^{|m|}(\cos \theta) e^{im\phi} \quad (2.19)$$

where the quantum numbers are restricted integers,

$$\text{principal:} \quad n = 1, 2, \dots \quad (2.20)$$

$$\text{azimuthal:} \quad l = 0, 1, 2, \dots, n-1 \quad \text{or} \quad 0 \leq l \leq n-1 \quad (2.21)$$

$$\text{magnetic:} \quad m = 0, \pm 1, \pm 2, \dots, \pm l \quad \text{or} \quad |m| \leq l \quad (2.22)$$

$P_l^{|m|}(x)$  are the associated Legendre functions,  $L_{n+l}^{2l+1}(x)$  are the associated Laguerre polynomials, and  $a_0 = \frac{4\pi\epsilon_0\hbar^2}{m_e e^2}$  is the Bohr radius. The above results formulate the shape and other properties of the famous hydrogen atomic orbitals.

For systems larger than the hydrogen atom, Schrödinger equation can not be solved exactly, because they are three-body or many-body problems. Therefore, solid approximations are necessary and critical in theoretical chemistry to get solutions with sufficient accuracy. For example, multi-electron systems, such as the helium atom He (1 nucleus and 2 electrons) requires variational method or perturbation theory, and polyatomic systems, such as the molecular ion  $\text{H}_2^+$  (2 nuclei and 1 electron), need Born-Oppenheimer approximation.

## Born-Oppenheimer Approximation

For a system with  $M$  protons and  $N$  electrons, the Hamiltonian operator has the form,

$$\hat{H} = \underbrace{\hat{K}_n}_{\text{kinetic energy of nuclei}} + \underbrace{\hat{K}_e}_{\text{kinetic energy of electrons}} + \underbrace{\hat{V}_{nn}}_{\text{nucleus-nucleus interactions}} + \underbrace{\hat{V}_{en}}_{\text{electron-nucleus interactions}} + \underbrace{\hat{V}_{ee}}_{\text{electron-electron interactions}} \quad (2.23)$$

which considers all motions and interactions, including the movement of nuclei. However, the nuclei do not move as fast as the electrons because of their significantly larger masses. Therefore, the Born-Oppenheimer approximation considers the nuclei fixed at their positions while electrons move around them. It simplifies the calculation by eliminating the  $\hat{K}_n$  term in Equation 2.23, and making the

$\hat{V}_{nn}$  term constant. Although it can be corrected systematically using perturbation theory, the Born-Oppenheimer approximation is appropriate because these corrections are of the order of the mass ratio ( $\approx 10^{-3}$ ) for most practical cases. [2]

## Variational Method

When Schrödinger equation can not be solved exactly, the exact wave function can be approximated using the variational method, which is based on the principle that

$$\begin{cases} E(\psi_0) = E_0 = \frac{\int \psi_0^* \hat{H} \psi_0 d\tau}{\int \psi_0^* \psi_0 d\tau} \\ E(\psi) \geq E(\psi_0) \end{cases} \quad (2.24)$$

i.e., the energy obtained using any wave function  $\psi$  other than the solution  $\psi_0$  is always greater than the exact value (the ground energy  $E_0$ ). When applying numerically, a trial function  $\psi_{\text{trial}}$  with variational parameters,  $\alpha, \beta, \gamma, \dots$ , are used as the initial guess, and then the approximated value is obtained by minimizing  $E(\alpha, \beta, \gamma, \dots)$ . The accuracy of this method depends greatly on the trial function selected and the number of variational parameters used. In general, more general trial functions with more parameters would obtain more accurate results. However, practical cases are usually trades-off between accuracy and computational cost.

## Perturbation Theory

Another approximation approach is through the perturbation theory, which approximates the solution of the target problem by adding corrections (or perturbations) to the exact solution of a previously-solved problem. For example, the Hamiltonian operator can be expressed as

$$\hat{H} = \hat{H}^{(0)} + \hat{H}^{(1)} + \hat{H}^{(2)} + \dots \quad (2.25)$$

where  $\hat{H}^{(0)}$  is the unperturbed operator and the remaining terms are perturbations. A good way to generate perturbation terms is through Taylor series expansions. In general, higher orders of perturbation would generate more accurate results. It is worth noting that the energy obtained by perturbation theory is not necessarily higher or equal to the exact energy, as the variational method does.

## 2.2.2 Hartree-Fock Method

### Hartree-Fock (HF) approximation

The Hartree-Fock (HF) approach, namely the mean-field approximation, is among the simplest methods towards solving the many-body quantum chemistry problems. It simplifies the problems by assuming that each electron is under the average field created by the other particles in the system. The aim of this assumption is to be able to use the separation of variables approach and express the many-electron wave function as the product of several independent one-electron wave functions, such as

$$\Psi(\mathbf{r}_1, \mathbf{r}_2) = \Psi(\mathbf{r}_1)\Psi(\mathbf{r}_2) \quad (2.26)$$

where the interaction between the two electrons is accounted (only approximately) in  $\Psi(\mathbf{r}_1)$  and  $\Psi(\mathbf{r}_2)$ . The effective (or average) potential energy of electron 1 under the mean field of electron 2 is (in atomic units)

$$V_1^{eff}(r_1) = \int \Psi^*(\mathbf{r}_2) \frac{1}{r_{12}} \Psi(\mathbf{r}_2) d\mathbf{r}_2 \quad (2.27)$$

then the effective one-electron Hamiltonian is,

$$\hat{H}_1^{eff}(\mathbf{r}_1) = -\frac{1}{2}\nabla_1^2 - \frac{2}{r_1} + V_1^{eff}(r_1) \quad (2.28)$$

and eventually the corresponding Schrödinger equation becomes

$$\hat{H}_1^{eff}(\mathbf{r}_1)\Psi(\mathbf{r}_1) = \epsilon_1\Psi(\mathbf{r}_1) \quad (2.29)$$

which is also called the Hartree-Fock equation.

### Self-Consistent Field (SCF) method

Solving the Hartree-Fock equation requires the self-consistent field (SCF) method. It uses a guess form of  $\Psi(\mathbf{r}_2)$  to evaluate  $V_1^{eff}(r_1)$  (Equation 2.27) and  $\hat{H}_1^{eff}(\mathbf{r}_1)$  (Equation 2.28), and then solve Equation 2.29 for  $\Psi(\mathbf{r}_1)$ . As  $\Psi(\mathbf{r}_1)$  and  $\Psi(\mathbf{r}_2)$  in a Helium atom are essentially equivalent, this cycle is repeated until the output and input are sufficiently close, i.e., self-consistent. The resulted wave functions are named Hartree-Fock orbitals.

### Spatial Molecular Orbitals

It is obvious that selecting appropriate trial functions is essential for obtaining accurate results. Since we treat molecules in many cases, we need molecular orbitals (MO) other than the atomic (AO). In practice, molecular orbitals are often established using a linear combination of atomic orbitals (LCAO). For example, the molecular orbital for molecular ion  $\text{H}_2^+$  (nuclei  $A$ ,  $B$  and one electron)

$$\underbrace{\psi(\mathbf{r})}_{\text{MO}} = C_A \underbrace{\phi_A(\mathbf{r} - \mathbf{R}_A)}_{\text{AO}} + C_B \underbrace{\phi_B(\mathbf{r} - \mathbf{R}_B)}_{\text{AO}} \quad (2.30)$$

where  $C_K$  are the variational parameters and the SCF iterations finds the best set of  $C_K$  to minimize the energy. Here we do not need to calculate the atomic orbitals  $\phi_K$  from scratch, but rather choose a set of existing, well-defined functions, which are called basis set.

### Spin Molecular Orbitals

The MOs derived above, i.e., spatial molecular orbitals, do not account for the spin of electrons and therefore may not obey the Pauli exclusion principle. To well assign the electrons to molecular orbitals, the Slater determinant ( $\Psi_{SD}$ ) is used to

establish the spin MOs (H<sub>2</sub> molecule as an example),

$$\Psi(\mathbf{r}_1, \mathbf{r}_2, \sigma_1, \sigma_2) \approx \Psi_{SD} = \frac{1}{\sqrt{2}} \begin{vmatrix} u_1(1) & u_2(1) \\ u_1(2) & u_2(2) \end{vmatrix} = \frac{1}{\sqrt{2}} \begin{vmatrix} \psi(\mathbf{r}_1)\alpha(\sigma_1) & \psi(\mathbf{r}_1)\beta(\sigma_1) \\ \psi(\mathbf{r}_2)\alpha(\sigma_2) & \psi(\mathbf{r}_2)\beta(\sigma_2) \end{vmatrix} \quad (2.31)$$

which is a properly antisymmetrized product of simpler one-electron spin MOs ( $u_i(\mathbf{r})$ ). The spin MOs is the product of the spatial MOs ( $\psi(\mathbf{r}_i)$ ) and the spin function  $\alpha(\sigma_i)$  or  $\beta(\sigma_i)$ , which remedy the deficiency that electron spin could not be aroused naturally from the Schrödinger equation. This also introduces the spin quantum number ( $m_s$ ) of an electron in addition to the three mentioned previously (Equation 2.20–2.22), which has the value in atomic units

$$\text{spin quantum number: } m_s = \pm \frac{1}{2} \quad (2.32)$$

and represents the  $z$  component of the electron spin angular momentum.

### Hartree-Fock Limit

In summary, HF calculations use the self-consistent field method to obtain the solution to the Schrödinger equation, based on a trial function that is well formulated from a chosen basis set. It is worth noting that if we use the variational method with the trial function  $\Psi(\mathbf{r})$  in Equation 2.26 to be completely general, we reach the Hartree-Fock limit which is the best value of the electronic energy that can be obtained using this method. Although more complex methods are needed to obtain more accurate results, the HF calculations provide a good base point to these methods. For example, it provides base elements of the trial function in electron correlation methods where terms containing the electronic distance  $\mathbf{r}_{12}$  are included explicitly,

$$\Psi(\mathbf{r}_1, \mathbf{r}_2, \mathbf{r}_{12}) = \Psi(\mathbf{r}_1)\Psi(\mathbf{r}_2)(1 + c\mathbf{r}_{12}) \quad (2.33)$$

and it can also be used as the unperturbed function in perturbation methods.

### 2.2.3 Electron Correlation: Wave Function Methods

The four sources of error in electronic structure calculations are (1) neglect of or incomplete treatment of electron correlation, (2) the incompleteness of the basis set, (3) relativistic effects, and (4) deviations from the Born-Oppenheimer approximation. [222] Although (3) and (4) can be significant in some regimes, (1) and (2) are still the main source of error in many practical cases. [222] The molecular correlation energy is defined as the difference between the nonrelativistic true molecular energy and the Hartree-Fock limit,

$$E_{corr} \equiv E_{nonrel} - E_{HF} \quad (2.34)$$

which could originate from two types of correlation:

**dynamic correlation** originated from the instantaneous correlations between motions of electrons;



**static correlation** originated from the failure of the single-Slater-determinant HF wave function to well represent the system's state. It is often found when the internuclear distance is large, and corrections to it require multiconfiguration (MC) wave functions.

In order to well account for the  $E_{corr}$ , electron correlation methods are necessary to go beyond the Hartree-Fock approximation.

## Configuration Interaction (CI) Methods

The Configuration Interaction (CI) method uses the occupied and unoccupied MOs obtained from SCF calculations to form configuration state functions (CSFs)  $\Phi_i$ , then formulates the molecular wave function  $\psi$  as a linear combination of the CSFs, and uses variational method to obtain the solution. The CSFs in CI calculations could be singly, doubly, triply excited,  $\dots$ , depending on the number of electrons excited from occupied to unoccupied orbitals. Note that the number of possible CSFs increases radically ( $\propto b^n$ ) with the number of electrons ( $n$ ) and basis functions ( $b$ ).

There are several types of CI methods:

**Full CI (FCI)** The CI calculations that account for all possible CSFs, extremely expansive except for small molecules and small basis sets.

**CI with Frozen-Core approximation (CI(FC))** Consider only the excitation of valence-shell electrons and omit that of core electrons.

**CISD, CISDT, CISDTQ,  $\dots$**  Includes single, double, triple, quadruple excitation, or more.

**Local Correlation (LC)** Use localized SCF MOs instead of canonical SCF MOs as base elements to formulate CSFs.

**Multiconfiguration SCF Method (MCSCF)** Varying the linear combination coefficients before both the CSFs and the MOs. The most commonly used MCSCF is the complete active space SCF (CASSCF) method.

**Multireference CI (MRCI)** A method combining MCSCF and conventional (or single-reference) CI methods to solve problems involving multireference behaviors.

## Coupled-Cluster (CC) Method

The essential idea of the coupled-Cluster (CC) theory is that the exact non-relativistic ground-state wave function  $\Psi_{cc}$  can be expressed by the exponential ansatz,

$$\Psi_{cc} = e^{\hat{T}} \Phi_0 \stackrel{\text{Taylor expansion}}{\left( 1 + \hat{T} + \frac{\hat{T}^2}{2!} + \frac{\hat{T}^3}{2!} + \dots \right)} \Phi_0 \quad (2.35)$$

where  $\hat{T}$  is the cluster operator for a  $n$ -electron molecule.

$$\hat{T} \equiv \hat{T}_1 + \hat{T}_2 + \dots + \hat{T}_n \quad (2.36)$$

The  $\hat{T}_1$  and  $\hat{T}_2$  are the one-particle and two-particle excitation operator, respectively,

$$\hat{T}_1 = \sum_{i,a} t_i^a \Phi_i^a \quad (2.37)$$

$$\hat{T}_2 = \sum_{i>j,a>b} t_{ij}^{ab} \Phi_{ij}^{ab} \quad (2.38)$$

where  $\Phi_i^a$  is a singly excited Slater determinant with the occupied spin-orbital  $u_i$  replaced by the virtual spin-orbital  $u_a$ , and  $t_i^a$  is a numerical coefficient. The operator  $\hat{T}_1$  converts the Slater determinant  $\Phi_0 = |u_1 \cdots u_2|$  into a linear combination of all possible singly excited Slater determinants. The effect of the  $e^{\hat{T}}$  operator is to express  $\Psi_{cc}$  as a linear combination of Slater determinants, which include  $\Phi_0$  and all the possible excitations of electrons from occupied to virtual spin-orbitals. This allows the electrons to keep away from each other and therefore provides for electron correlation.

The CC method solves the wave function  $\Psi_{cc}$ , by finding the coefficients (also called amplitudes)  $t_i^a, t_{ij}^{ab}, t_{ijk}^{abc}, \dots$  for all  $i, j, k, \dots$  and  $a, b, c, \dots$ . However, a Full CC calculation with a complete basis set and no approximations of  $\hat{T}$  can be challenging. Therefore, CC methods apply two approximations: (i) use a finite basis set and (ii) include only some excitation operators in  $\hat{T}$ . The different types of CC method are named following the different combinations of the excitation operators used to approximate  $\hat{T}$ :

**The CCD (coupled-cluster doubles) method** , where

$$\hat{T} \approx \hat{T}_2 \quad (2.39)$$

**The CCSD (CC singles and doubles) method** , where

$$\hat{T} \approx \hat{T}_1 + \hat{T}_2 \quad (2.40)$$

**The CCSDT (CC singles, doubles and triples) method** , where

$$\hat{T} \approx \hat{T}_1 + \hat{T}_2 + \hat{T}_3 \quad (2.41)$$

The CCSDT methods are usually very accurate for correlation energies, but it is very computationally demanding. Therefore, the approximated form, CCSD(T) method, with the inclusion of single and double excitations and perturbative inclusion of triple excitations, is widely used. In the present work, CCSD(T) method is used with explicit inclusion of terms for the interelectronic distance  $r_{12}$  in the CC wave functions to reduce basis-set truncation error through the F12 method, i.e., the CCSD(T)-F12 method.

## Møller-Plesset (MP) Perturbation Theory

The Møller-Plesset (MP) perturbation theory deals with electron correlation problem, using the perturbation theory introduced in Section 2.2.1. Following the same principle as Equation 2.25, the Hamiltonian in Møller-Plesset perturbation theory

is composed of the zero-order electronic Hamiltonian  $\widehat{\mathcal{H}}^{(0)}$  and the perturbation  $\widehat{\mathcal{P}}$ ,

$$\widehat{\mathcal{H}} = \widehat{\mathcal{H}}^{(0)} + \lambda_{\text{MP}} \widehat{\mathcal{P}} \quad \text{where} \quad \lambda_{\text{MP}} = 1 \quad (2.42)$$

where the  $\lambda_{\text{MP}}$  parameter tunes the strength of the perturbation and is set to unity in MP perturbation theory. The zero-order electronic Hamiltonian  $\widehat{\mathcal{H}}^{(0)}$  is chosen to be the sum of Fock operators,

$$\widehat{\mathcal{H}}^{(0)} = \sum_i \widehat{f}(i) \quad (2.43)$$

whose exact ground state eigenfunction and eigenvalue are the HF wave function and the sum of occupied orbitals energies respectively,

$$\Psi_0^{(0)} = \Psi^{\text{HF}} \quad (2.44)$$

$$E_0^{(0)} = \sum_a \epsilon_a \quad (2.45)$$

Furthermore, the perturbation operator becomes the difference between the electronic repulsion operator and the HF effective operator,

$$\widehat{\mathcal{P}} = \sum_{i<j} \frac{1}{r_{ij}} - \sum_i V_{\text{eff}}(i) \quad (2.46)$$

It can be shown that the first order Møller-Plesset ground state energy is simply the HF energy,

$$\begin{aligned} E^{\text{MP1}} &= E_0^{(0)} + E_0^{(1)} \\ &= \langle \Psi^{\text{HF}} | \left( \sum_i \widehat{f}(i) \right) | \Psi^{\text{HF}} \rangle + \langle \Psi^{\text{HF}} | \left( \sum_{i<j} \frac{1}{r_{ij}} - \sum_i V_{\text{eff}}(i) \right) | \Psi^{\text{HF}} \rangle \\ &= E^{\text{HF}} \end{aligned} \quad (2.47)$$

Thus, the first correction to the HF energy occurs at the second order. The corresponding expression is derived as

$$\begin{aligned} E^{\text{MP2}} &= E_0^{(0)} + E_0^{(1)} + E_0^{(2)} \\ &= E^{\text{HF}} + \sum_{a<b}^{\text{occ}} \sum_{r<s}^{\text{vir}} \frac{|[ar|bs] - [as|br]|^2}{\epsilon_a + \epsilon_b - \epsilon_r - \epsilon_s} \end{aligned} \quad (2.48)$$

where  $\sum_{a<b}^{\text{occ}}$  and  $\sum_{r<s}^{\text{vir}}$  stand for sums over occupied and virtual orbitals respectively.

The second-order Møller-Plesset (MP2) approach represents an interesting compromise between accuracy and computational cost. Higher-order calculations (MP3, MP4,...) exhibit computational costs similar to that of other correlated wave function methods introduced above. The main limitation of perturbation methods is that they yield reliable results only if the perturbation is small. In other words, within the framework of MP theory, it is possible to improve an HF calculation only if this zero-order calculation already provides a fairly good

solution to the electronic problem.

## 2.2.4 Electron Correlation: Density Functional Theory

Besides the electron correlation methods based on the wave function, a possible way to account for the correlation energy lies in the density functional theory (DFT), whose central quantity is the electronic density  $\rho_0(\mathbf{r})$ , instead of the multi-electronic wave function. The electronic density depends only on the 3 spatial coordinates and, hence, is a simpler quantity to deal with both conceptually and computationally. Current methods involving modern DFT are based on the two Hohenberg-Kohn theorems and the Kohn-Sham approach.

### The Hohenberg-Kohn Theorem

The Hohenberg-Kohn theorem states that for molecules with a nondegenerate ground state, the ground-state molecular energy, wave function, and all other molecular electronic properties are uniquely determined by and are functionals of the ground-state electron density  $\rho_0(x, y, z)$ . [222] For example, the number of electrons can be obtained from  $n = n[\rho_0] = \int d\mathbf{r} \rho_0(\mathbf{r})$ , and the ground-state energy  $E_0$  is also a functional of  $\rho_0$ .

$$E_0 = E_v[\rho_0] = \bar{T}[\rho_0] + \bar{V}_{ne}[\rho_0] + \bar{V}_{ee}[\rho_0] \quad (2.49)$$

### The Hohenberg-Kohn Variational Theorem

The Hohenberg-Kohn variational theorem states that for every trial density function  $\rho_{\text{trial}}$  that satisfies  $\int \rho_{\text{trial}}(\mathbf{r}) d\mathbf{r} = n$  and  $\rho_{\text{trial}}(\mathbf{r}) \geq 0$  for all  $\mathbf{r}$ ,

$$E_v[\rho_{\text{trial}}] \geq E_0 \quad (2.50)$$

in other words the true ground-state electron density ( $\rho_0(\mathbf{r})$ ) minimizes the functional  $E_v[\rho_{\text{trial}}]$ .

### The Kohn-Sham (KS) Approach

In Equation 2.49, only the functional for external potential can be determined uniquely by  $\rho_0$

$$\bar{V}_{ne}[\rho_0] = \int \rho_0(\mathbf{r}) v(\mathbf{r}) d\mathbf{r} \quad (2.51)$$

where the external potential  $v(\mathbf{r}) = -\sum_A \frac{Z_A}{r_{iA}}$ . Because the other two functionals  $\bar{T}[\rho_0]$  and  $\bar{V}_{ee}[\rho_0]$  are unknown, the above two theorems still could not tell us how to find  $\rho_0$  and calculate  $E_0$  from it. Kohn and Sham (KS) tackled this problem, by introducing a fictitious reference system of non-interacting electrons, each experience the same effective external potential  $v_s(\mathbf{r}_i)$ , such that the electron density of the reference system  $\rho_s(\mathbf{r})$  is equal to the exact ground-state  $\rho_0(\mathbf{r})$ . Therefore, the Hamiltonian of such a system is a sum of one-electron Kohn-Sham

Hamiltonians  $\hat{h}_i^{\text{KS}}$ ,

$$\hat{H}_s = \sum_{i=1}^n \hat{h}_i^{\text{KS}} = \sum_{i=1}^n \left[ -\frac{1}{2} \nabla_i^2 + v_s(\mathbf{r}_i) \right] \quad (2.52)$$

and its exact ground-state solution  $\psi_{s,0}$  is provided by a Slater determinant of the lowest-energy Kohn-Sham spin orbitals  $u_i^{\text{KS}}$ .

$$\psi_{s,0} = |u_1^{\text{KS}} u_2^{\text{KS}} \dots u_i^{\text{KS}}|, \quad u_i^{\text{KS}} = \theta_i^{\text{KS}}(\mathbf{r}_i) \alpha(\sigma_i) \text{ or } \theta_i^{\text{KS}}(\mathbf{r}_i) \beta(\sigma_i) \quad (2.53)$$

$$\hat{h}_i^{\text{KS}} \theta_i^{\text{KS}} = \varepsilon_i^{\text{KS}} \theta_i^{\text{KS}} \quad (2.54)$$

Kohn and Sham defined the exchange-correlation energy functional

$$E_{xc}[\rho] \equiv \Delta \bar{T}[\rho] + E_{ncl} \quad (2.55)$$

which is a sum of two parts: (i)  $\Delta \bar{T}[\rho] \equiv \bar{T}[\rho] - \bar{T}_s[\rho]$ , the difference of kinetic energy obtained by the reference system with respect to the real system, and (ii) the non-classical part of electron-electron interaction potential,  $E_{ncl} = \bar{V}_{ee}[\rho] - V_{cl} = \bar{V}_{ee}[\rho] - \frac{1}{2} \iint \frac{\rho(\mathbf{r}_1)\rho(\mathbf{r}_2)}{r_{12}} d\mathbf{r}_1 d\mathbf{r}_2$ . If  $E_{xc}[\rho]$  would be known, then one could solve Equation 2.54 using the SCF procedure like in the HF schemes to yield the KS orbitals and the total electronic energy. The main difference is that electron correlation is incorporated by the exchange-correlation potential.

Using the above theory into practical use requires an already-known exchange-correlation functional. However, the exact  $E_{xc}[\rho]$  is unknown, which means that further approximations are needed to make this theory of practical use. It is customary to write  $E_{xc}[\rho]$  in terms of the energy per particle, or energy density  $\varepsilon_{xc}[\rho]$ ,

$$E_{xc}[\rho(\mathbf{r})] = \int d\mathbf{r} \rho(\mathbf{r}) \varepsilon_{xc}[\rho(\mathbf{r})] \quad (2.56)$$

$$\text{where } \varepsilon_{xc}[\rho(\mathbf{r})] = \varepsilon_x[\rho(\mathbf{r})] + \varepsilon_c[\rho(\mathbf{r})] \quad (2.57)$$

which is expressed as a sum of an exchange and a correlation term. Many approximations have been proposed for the energy densities  $\varepsilon_x$  and  $\varepsilon_c$  in Equation 2.57.

### Local Density Approximation (LDA)

The local density approximation (LDA) assumes that the electron density locally can be treated as a uniform gas. The exchange energy density of such a system is given by the Dirac formula

$$\varepsilon_x^{\text{LDA}}[\rho(\mathbf{r})] = -\frac{3}{4} \left( \frac{3}{\pi} \right)^{1/3} \rho(\mathbf{r})^{1/3} \quad (2.58)$$

The corresponding correlation energy density  $\varepsilon_c^{\text{LDA}}$  is usually obtained from an interpolation between a series of energy densities that have been computed using accurate Monte Carlo methods for a number of uniform electron gas of different

electron densities. LDA is often found to provide accuracy similar to that of HF theory. In order to improve the approximation of  $E_{xc}[\rho]$ , it is necessary to consider a non-uniform electron gas.

## Generalized Gradient Approximation (GGA)

The generalized gradient approximation (GGA) considers a non-uniform electron gas by making  $E_{xc}[\rho]$  depend on not only the local value of  $\rho(\mathbf{r})$ , but also its gradient  $\nabla\rho(\mathbf{r})$ . A very popular GGA exchange functional is that of Becke (B or B88),

$$\varepsilon_x^{\text{B88}} = \varepsilon_x^{\text{LDA}} - \Delta\varepsilon_x^{\text{B88}} = \varepsilon_x^{\text{LDA}} - \beta\rho(\mathbf{r})^{1/3} \frac{(|\nabla\rho(\mathbf{r})|)^2}{1 + 6\beta \frac{|\nabla\rho(\mathbf{r})|}{\rho(\mathbf{r})^{4/3}} \sinh^{-1} \frac{|\nabla\rho(\mathbf{r})|}{\rho(\mathbf{r})^{4/3}}} \quad (2.59)$$

where the  $\beta$  parameter has been determined from known atomic data. There are also various GGA correlation functionals  $\varepsilon_c^{\text{GGA}}$ . A widely used one is due to Lee, Yang, and Parr (LYP), whose expression is more complicated than Equation 2.59 and involves a few parameters that have been derived by fitting to data for the helium atom (obtained by accurate correlated wave function calculations). Other examples of  $\varepsilon_c^{\text{GGA}}$  are that of Perdew (P86) and Perdew-Wang (PW91). By mixing B88 with either LYP, P86 or PW91, one obtains the exchange-correlation functionals  $\varepsilon_{xc}^{\text{GGA}}$  whose corresponding acronym are BLYP, BP86, and BPW91 respectively. GGA methods provide highly improved results compared to LDA. They often give geometries and vibrational frequencies for stable molecules of the same quality as MP2 or better, at a computational cost similar to that of an HF calculation.

## Hybrid Functionals

Hybrid functional is another class of accurate exchange-correlation functional, whose most popular example is B3LYP,

$$E_{xc}^{\text{B3LYP}} = (1 - a)E_x^{\text{LDA}} + aE_x^{\text{exact}} + b\Delta E_x^{\text{B88}} + (1 - c)E_c^{\text{LDA}} + cE_c^{\text{LYP}} \quad (2.60)$$

where  $a$ ,  $b$  and  $c$  parameters have been determined by fitting to experimental data, and  $E_x^{\text{exact}}$  is the HF exchange energy using KS orbitals. In chapter 3, we used a double hybrid method B2PLYP [223], whose  $E_{xc}[\rho]$  also includes terms from perturbation theory,

$$E_{xc}^{\text{B2PLYP}} = (1 - c_{\text{HF}})E_x^{\text{GGA}} + c_{\text{HF}}E_x^{\text{HF}} + (1 - c_{\text{MP2}})E_c^{\text{GGA}} + c_{\text{MP2}}E_c^{\text{MP2}} \quad (2.61)$$

where  $c_{\text{HF}}$  is the HF exchange mixing parameter and  $c_{\text{MP2}}$  scales the contribution between MP2 and GGA.

## Dispersion Corrections

Despite the accurate geometrical description that they provide for stable molecules, current exchange-correlation functionals have some limitations. They are known to predict relative energies less accurately than correlated wave function methods.

Another disadvantage is that the London dispersion is poorly described. Therefore, dispersion corrections should be applied for DFT calculations. One popular method is the DFT-D methods, which add correction energy onto the calculated DFT energy. The simplest form of the correction term can be expressed as

$$E_{disp} = - \sum_{AB} \frac{C_{AB}}{R_{AB}} f(R_{AB}) \quad (2.62)$$

where  $R_{AB}$  is the distance between the two fragments  $A$  and  $B$ ,  $C_{AB}$  is a coefficient, and  $f(R_{AB})$  is a damping function that makes  $disp$  goes to zero as  $R_{AB} \rightarrow 0$ . The most successful DFT-D method is its third version, DFT-D3, which is used in the present work with the double hybrid functional B2PLYP. Besides DFT-D, other methods to account for dispersion includes the two-parameter VV10 correlation functional, and the M06-2X functional.

## 2.2.5 Composite Methods for Energy Calculations

Composite methods are developed, aiming to compute thermodynamic energy, such as the molecular atomization energy or the enthalpy of formation, with chemical accuracy ( $1 \text{ kcal mol}^{-1}$ ) using less computational power, for molecules containing several non-hydrogen atoms. It is achieved by using a series of *ab initio* calculations, based on which the final result of energy at chemical accuracy is derived. Popular composite methods are the Gaussian composite method, such as the G3 (Gaussian-3) and G4 methods, correlation consistent composite approach (ccCA), Complete Basis Set (CBS) composite methods, such as CBS-Q and CBS-QB3 methods, composite methods developed by the Weizmann Institute, such as the W1, W2, W3 and W4 methods, and the high accuracy extrapolated *ab initio* thermochemistry method (HEAT). In the present work, a composite method to calculate the total relative electronic energy (including ZPE) with chemical accuracy is used, the formula of which is as follows,

$$\begin{aligned} \Delta E_{total} = & \Delta E_{CCSD(T)-F12/cc-pVTZ-F12} \\ & + (\Delta E_{MP2-F12/cc-pVQZ-F12} - \Delta E_{MP2-F12/cc-pVTZ-F12}) \\ & + \Delta ZPE_{B2PLYP-D3/cc-pVTZ} \end{aligned} \quad (2.63)$$

where  $\Delta E_{\text{theory/basis-set}}$  is the relative electronic energy obtained using a certain level of calculation.

## 2.3 Micro-scale: Theoretical Rate Coefficient

### 2.3.1 Potential Energy Surface

As explained in the previous section, we can calculate the ground-state electronic energy of a certain molecular configuration, and it changes when the position of the atoms vary. Therefore, by varying the intermolecular distances, one obtains a surface that describes the energy of a system in terms of its spacial information, which is called the potential energy surface (PES). The PES is usually curvy and described as a system of connected stationary points, which are of kinds: wells

and transition states (TS).

The wells are stable structures of the molecule, and look like “valleys” on the PES. For any degree of freedom (DF), local changes increase energy, and therefore the cross-section has the shape of a positive parabola. The vibrational modes, i.e., motions along its local energy curve of certain DFs, are often approximated as harmonic oscillators. Therefore the ground-state vibrational frequency of the molecules can be obtained through equation

$$\nu = \frac{1}{2\pi} \sqrt{\frac{k}{\mu}} \quad \text{or} \quad \tilde{\nu} = \frac{1}{2\pi c} \sqrt{\frac{k}{\mu}} \quad (2.64)$$

and all have real values due to the positive force constant  $k$ .

Transition states (TS) are special stationary points, who connect two adjacent wells. They look similar to a well in most of the DFs, except the critical one which leads to the transformation from one well to another. Along this critical DF, the cross-section energy curve has the shape of a negative parabola and local change in both directions leads to a decrease in energy. Because of these properties, the PES around a barrier looks like a “saddle” and therefore is also called a saddle point. On the energy curve along the critical DF, the TS is at the top and acts like a barrier between two wells. Therefore, the vibrational frequency along the critical DF is imaginary due to its negative force constant, while the frequencies for other DFs are real.

The above stationary points can be identified and their structure can be calculated, using geometry optimization. A well is identified by searching for a local minima on the PES where the gradient is zero and the curvature is positive for all the DFs. The search for a TS is similar to the wells, except that the curvature along at least one DF must be negative. These procedures can be accelerated by the Newton-Raphson method.

An elementary chemical reaction is a transformation from one well on the PES to another, usually through a TS. In order to find possible reactions, one could use the scan operation assisted by some chemical intuitions. It is a series of geometry optimizations on the points along a user-defined path. For example, if the user forces two atoms to separate from each other, this DF is fixed while all the others are optimized. Combining the results at different separation, one can see how the molecule dissociates and what might be the final products. The scan also generates an energy profile, where TSs are most probably located near the tips and the wells near the minima of the curve. Further optimization based on such points would lead to the optimized structure of the TS and wells.

In order to make sure that the TS actually leads to the desired reactant or product, the intrinsic reaction coordinate (IRC) or minimum energy path (MEP) must be calculated. Similar to the scan, it starts from the TS and moves downhill towards the minima, while at the same time optimizing all the other DFs orthogonal to the path to obtain the minimum energy. The difference is that the path is searched based on the critical motion of the TS. As the critical motion are usually translational, thus it can be performed in either forward or backward direction. As more and more points are calculated along the path, it will eventually reach the minima so that one can check if it is the desired product or reactant. Further optimization is usually needed if the number of calculations is limited by the user.



It is worth noting that the PES marks the potential field in which the molecule could undergo reaction, but it is not the lower bound of the possible energy of the molecule. Therefore it is necessary to consider the zero-point vibrational energy (ZPE) in addition to the electronic energy,

$$E_{\text{ZPE}} = \sum E_{v=0} = \sum \frac{1}{2} h\nu_i \quad (2.65)$$

$$E = E_0 + E_{\text{ZPE}} \quad (2.66)$$

since the molecule is always vibrating even at the ground state.

### 2.3.2 Transition State Theory

Gas-phase reactions are often simplified as unimolecular reactions, which is the isomerisation of an isolated configuration A of the reactant molecule(s), through a transition state  $A^\ddagger$ .



Before the molecules can undergo unimolecular reactions, they must be energized to acquire sufficient energy, which is mostly realized by intermolecular collisions. Therefore collisional energy transfer and unimolecular reactions are the main processes happening in gas-phase reaction systems. Based on these understandings, transition state theory (TST) is established to calculate the rate of the reactions.

Canonical transition state theory (CTST) assumes that (i) the dividing surface (separating reactants and products) is fixed and located at the position of the transition states, (ii) all trajectories crossing the dividing surface with positive velocity is reactive, and (iii) the transition states are effectively in equilibrium with reactant molecules. Therefore, the reaction scheme is



where  $K^\ddagger$  is the equilibrium constant that can be expressed in terms of partition functions, and  $k^\ddagger$  is the rate constant from  $A^\ddagger$  to products. Assuming collisions process is infinitely fast that it is not rate-determining, CTST gives the expression for the high-pressure limiting overall rate constant as

$$k_\infty = \frac{-d[A]/dt}{[A]} = k^\ddagger = \frac{k_B T}{h} \frac{Q^\ddagger}{Q_{\text{reac}}} \exp(-E_0/k_B T) \quad (2.69)$$

where  $k_B T/h$  is the frequency of the TS associated with the critical motion,  $E_0$  is the energy barrier (including ZPE) along this critical degree of freedom,  $Q^\ddagger$  is the partition function for TS except the critical degree of freedom, and  $Q_{\text{reac}}$  is the complete partition function(s) per unit volume for the reactant(s). The total partition function  $Q$  for a molecule is the number of all its possible energy levels and can be separated according to the different types of energy levels,

$$Q = Q_{\text{elec}} Q_{\text{trans}} Q_{\text{vib}} Q_{\text{rot}} \quad (2.70)$$

where the partition functions for electronic, translational, vibrational, and rota-

tional energy levels are expressed as,

$$Q_{elec} = \sum_i g_i \exp(-E_i/k_B T) \stackrel{i=0}{\text{for ground-state molecule}} g_0 \quad (2.71)$$

$$Q_{trans} = \left( \frac{2\pi M k_B T}{h^2} \right)^{3/2} V \quad (2.72)$$

$$Q_{rot} = \frac{\pi^{1/2}}{\sigma} \left( \frac{8\pi^2 I_a k_B T}{h^2} \right)^{1/2} \left( \frac{8\pi^2 I_b k_B T}{h^2} \right)^{1/2} \left( \frac{8\pi^2 I_c k_B T}{h^2} \right)^{1/2} \quad (2.73)$$

$$Q_{vib}^{class} = \prod_{i=1}^n \frac{k_B T}{h\nu_i} \quad \text{or} \quad Q_{vib}^{quan} = \prod_{i=1}^n \frac{\exp(-h\nu_i k_B T)}{1 - \exp(-h\nu_i k_B T)} \quad (2.74)$$

If the geometry of the TS does not deviate too far from the reactants, the various parts other than  $Q_{vib}$  are often approximately canceled out between TS and reactants, thus Equation 2.69 can be approximated as

$$k_\infty = \frac{\nu_1 \nu_2 \cdots \nu_n}{\nu_1^\ddagger \nu_2^\ddagger \cdots \nu_{n-1}^\ddagger} \exp(-E_0/k_B T) \quad (2.75)$$

Therefore, the pre-exponential factor of the rate constants are usually of the order of a vibrational frequency, i.e., about  $10^{13} \text{ s}^{-1}$ .

### 2.3.3 RRKM/ME

The rate constant obtained by TST depends only on temperature, however, in reality, the rate of many reactions also depend on pressure. To obtain pressure-dependent rate constants, energy transfer between molecules by collisions should be considered.

### Hinshelwood-Lindemann Theory

Lindemann theory assumes that the mechanism of unimolecular reactions consist of three steps, (i) collisional energisation, (ii) de-energisation, and (iii) isomerisation or dissociation, as expressed by Equation 2.76 and 2.77



Assuming collisional (de-)energisation is much more rapid than isomerisation, the overall rate of reaction ( $\nu$ ) can be obtained using steady-state approximation.

$$\nu = k_2[A^*] = \frac{(k_1 k_2 / k_{-1})[A]}{1 + \frac{k_2}{k_{-1}}[M]} \quad (2.78)$$

At high pressures, collisional de-energisation dominates so that  $k_{-1}[M] \gg k_2$ , and therefore the high-pressure limiting rate constant  $k_\infty$  can be obtained from

Equation 2.78 that

$$\nu = \left( \frac{k_1 k_2}{k_{-1}} \right) [A] = k_\infty [A] \quad \Rightarrow \quad k_\infty = \frac{k_1 k_2}{k_{-1}} \quad (2.79)$$

A low pressures, isomerisation or dissociation dominates so that  $k_{-1}[M] \ll k_2$ , and therefore the low-pressure limiting rate constant  $k_0$  can be obtained.

$$\nu = k_1[A][M] = k_0[A][M] \quad \Rightarrow \quad k_0 = k_1 \quad (2.80)$$

The overall rate constant of the unimolecular reaction can be expressed as a function of the concentration of collision partners M, which is a parameter associated with pressure.

$$k_{uni} = \frac{\nu}{[A]} = \frac{k_1[M]}{1 + \frac{k_{-1}}{k_2}[M]} \quad (2.81)$$

$$\frac{1}{k_{uni}} = \frac{1}{k_\infty} + \frac{1}{k_0} \frac{1}{[M]} \quad (2.82)$$

Indicated by Equation 2.82,  $k_\infty$  and  $k_0$  can be derived when a plot of  $k_{uni}^{-1}$  vs  $[M]^{-1}$  is at hand.

The Lindemann theory has two problems: (i) the plot of  $k_{uni}^{-1}$  vs  $[M]^{-1}$  is not a straight line as Equation 2.82 suggests, and (ii) measurements find that  $k_1$  exceeds the upper limit according to collision theory. These are due to that the internal energy of a molecule can be stored in the various degrees of freedom, and can be corrected by the Hinshelwood modification. Assuming all modes are vibrational, harmonic and of the same frequency, the probability of a molecule possessing total energy greater than the critical energy  $E_0$  in  $s$  classical degrees of freedom can be corrected,

$$\text{Lindemann:} \quad \exp\left(-\frac{E_0}{k_B T}\right) \quad (2.83)$$

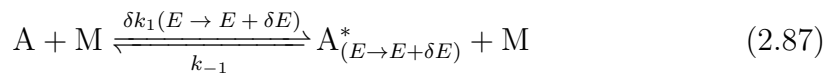
$$\text{Hinshelwood:} \quad \frac{1}{(s-1)!} \left(\frac{E_0}{k_B T}\right)^{s-1} \exp\left(-\frac{E_0}{k_B T}\right) \quad (2.84)$$

and therefore the rate constant  $k_1$ ,

$$\text{Lindemann:} \quad k_1 = Z_1 \exp\left(-\frac{E_0}{k_B T}\right) \quad (2.85)$$

$$\text{Hinshelwood:} \quad k_1 = \frac{Z_1}{(s-1)!} \left(\frac{E_0}{k_B T}\right)^{s-1} \exp\left(-\frac{E_0}{k_B T}\right) \quad (2.86)$$

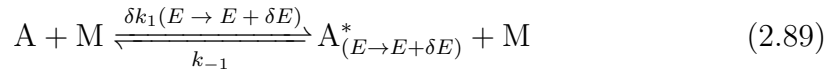
where  $Z_1$  is the pre-exponential factor in collision theory. As consequence, the modified Hinshelwood-Lindemann theory has the mechanism



such that collision energisation rate constant  $k_1$  is a function of energy, while de-energisation  $k_{-1}$  and isomerisation (or dissociation)  $k_2$  is independent of energy. The Hinshelwood modification fits the pressure dependence of the observed rate constant better but deviation still exists at low pressures.

## RRKM theory

Rice-Ramsperger-Kassel (RRK) theory takes a step forward with respect to Hinshelwood-Lindemann theory by taking into account the transition state, and therefore the mechanism becomes



The reason of this consideration is that an energized molecule with sufficient energy does not necessarily have reaction, in addition the energy stored in its vibrations must move to the critical degree of freedom (i.e., the reaction mode) so that it can get to the transition state. This process is known as the intramolecular vibrational relaxation (IVR) and represented by the rate constant of  $k_a(E)$ . Using steady-state approximation for  $[A^\ddagger]$ ,  $k_a(E)$  can be expressed as the product of  $k^\ddagger$  and the probability ( $p^\ddagger$ ) that the energy stored in an energized molecule is in the reactive mode.

$$k_a(E) = k^\ddagger \frac{[A^\ddagger]}{[A_{(E)}^*]} = k^\ddagger p^\ddagger \quad (2.91)$$

Assuming all modes have the same frequency like in the Hinshelwood-Lindemann theory, this probability can be calculated approximately from the degeneracy of energy level  $E$  at the two configurations.

$$p^\ddagger = \frac{G^\ddagger}{G^*} \approx \left( \frac{j-m}{j} \right)^{s-1} = \left( \frac{E-E^\ddagger}{E} \right)^{s-1} \quad (2.92)$$

Therefore,  $k_a(E)$  can be expressed as

$$k_a(E) = k^\ddagger \left( \frac{E-E^\ddagger}{E} \right)^{s-1} \quad (2.93)$$

where  $k^\ddagger$  is often replaced by the frequency  $\nu^\ddagger$  if the reactive mode is considered as vibrational. Further assuming that the processes in Equation 2.89 is in quasi-equilibrium, we get

$$\frac{k_1}{k_{-1}} = \frac{[A^*]}{[A]} = \frac{E^{s-1}}{(s-1)!(k_B T)^s} \exp\left(-\frac{E}{k_B T}\right) \delta E \quad (2.94)$$

which is also the probability that the energized  $A^*$  have energy between  $E$  and  $E + \delta E$ . Substituting 2.94 and  $k_2$  with  $k_a(E)$  using Equation 2.93 into the Lindemann

expression (Equation 2.81), we get the overall rate constant using RRK theory.

$$k_{uni}^{RRK} = \int_{E^\ddagger}^{\infty} \frac{\frac{\nu^\ddagger[M]}{k_B T (s-1)!} \left(\frac{E-E^\ddagger}{k_B T}\right)^{s-1} \exp\left(-\frac{E}{k_B T}\right)}{[M] + \frac{\nu^\ddagger}{k_{-1}} \left(\frac{E-E^\ddagger}{E}\right)^{s-1}} dE \quad (2.95)$$

Although can not be solved analytically, this integral can be evaluated numerically, typically using the strong collision assumption, where every collision of  $[A^*]$  lead to de-energisation so that  $k_{-1}$  is strictly collision limited. It is worth noting that the RRK theory assumes that  $k^\ddagger$  is too fast that it is not rate determining, then steady-state approximation is appropriate and the process of Equation 2.90 is simplified as



Rice-Ramsperger-Kassel-Marcus (RRKM) theory improves RRK theory by removing some arbitrary assumptions or approximations. The mechanism of RRKM is the same as RRK as shown in Equation 2.89 and 2.90 Briefly, RRKM is a microcanonical transition state theory, in which rate constant  $k(E)$  is calculated as a function of energy. The canonical rate constant  $k(T)$ , which is a function of temperature, can be recovered from the microcanonical one by averaging over a Boltzmann distribution. In summary, the basic ideas of RRKM are as follows.

- The pathway of the molecules undergoing reactions is such that collisional energization (Equation 2.89) is followed by internal energy relaxation (IER) which redistributes the energy within its degrees of freedom and lead to the transition state (Equation 2.90).
- RRKM assumes that the redistribution of energy happens on a time scale much faster than reaction.
- Energisation rate  $k_1$  is evaluated as a function of energy by a quantum-statistical-mechanical treatment (instead of classical treatment in RRK theory), while de-energization rate  $k_{-1}$  is treated as pure collisional deactivation and is independent of energy.
- The  $k_a(E)$  in Equation 2.90 is calculated using canonical transition state theory. In addition, the two-step mechanism Equation 2.90 can not be simplified into one step 2.96 like in RRK theory.
- internal degrees of freedom of the energized molecules are divided into two types: adiabatic and active modes. The energy stored in adiabatic modes are fixed and can not be redistributed, while the energy in active modes is free for redistribution.
- RRKM allow using quantum mechanical treatment for vibrational and rotational modes, and removes the assumption in RRK theory that all modes are vibrational, harmonic and of the same frequency.
- RRKM also removes the approximation of partition functions and allows the exact counting of states possible.

Based on these assumptions, RRKM theory gives the result for  $k_a(E)$  and  $k_{uni}$  as

$$k_a(E) = L^\ddagger \frac{Q_1^\ddagger W(E_{vr}^\ddagger)}{Q_1 h\rho(E)} \quad (2.97)$$

$$k_{uni} = \frac{L^\ddagger Q_1^\ddagger}{hQ_1 Q_2} \int_{E=E_0}^{\infty} \frac{W(E_{vr}^\ddagger) \exp(-E/k_B T)}{1 + k_a(E)/k_{-1}[M]} dE \quad (2.98)$$

where  $W(E_{vr}^\ddagger)$  is the total number of all the vibrational-rotational quantum states at all energy levels lower than or equal to  $E^\ddagger$  for the transition state ( $A^\ddagger$ ),  $\rho(E)$  is the local density of states at energy level  $E$  for the energized molecule  $A^*$ ,  $Q_1^\ddagger/Q_1$  is the correction for adiabatic rotation where  $Q_1^\ddagger$  and  $Q_1$  are the partition functions for the adiabatic rotations, and  $L^\ddagger$  is the statistical factor to make corrections on the symmetry of reaction path. It is worth noting that RRKM assumes molecular motions are either adiabatic and active, and energy redistribution is faster than reaction. However, there are cases where some modes are not adiabatic and energy flows slowly from them, such as anharmonic vibrational modes and non-adiabatic rotations. These complications require more complicated treatments.

## Master Equation

A molecular system contains numerous different states, where there is possibility  $P_i$  of finding the molecule in any state  $i$ . The master equation can derive the time evolution  $P_i(t)$  of these probabilities when given information such as transition rates  $w_{ij}$ , concentrations of collision partners, and others. Similar to the formula for concentration, the probability of the molecule being in state  $j$  at time  $t + dt$  can be written as

$$P_j(t + dt) = P_j(t) + \sum_{i \neq j} w_{ij} P_i(t) dt - \sum_{i \neq j} w_{ji} P_j(t) dt \quad (2.99)$$

and then the formula of master equation is expressed as the derivative of  $P_j(t)$ .

$$\frac{dP_j}{dt} = \sum_{i \neq j} (w_{ij} P_i - w_{ji} P_j) \quad (2.100)$$

The transition rate  $w_{ij}$  in Equation 2.100 is defined such that, if the molecule is in state  $i$ , the probability of the molecule to jump to state  $j$  during time interval  $dt$  is equal to  $w_{ij} dt$ . For simplicity, the approximation of homogeneous Markov process is often used, in which the transition rate  $w_{ij}$  does not depend on time.

At equilibrium conditions, the derivative should equal to zero,

$$\frac{dP_j}{dt} = \sum_{i \neq j} (w_{ij} P_i^{(eq)} - w_{ji} P_j^{(eq)}) = 0 \quad \forall j \quad (2.101)$$

one solution to this is called detailed balance, which satisfies that

$$w_{ij} P_i^{(eq)} - w_{ji} P_j^{(eq)} = 0 \quad \forall i, j \quad (2.102)$$

i.e., all the pairs of terms in Equation 2.101 are equal to zero. The detailed balance

condition can be rewritten as

$$\frac{w_{ij}}{w_{ji}} = \frac{P_j^{(eq)}}{P_i^{(eq)}} = \exp\left(-\frac{E_i - E_j}{k_B T}\right) \quad (2.103)$$

because the probabilities obey Boltzmann distributions at equilibrium. Therefore, the ratios between transition rates can be solved, but not their actual values.

Consider a system with only two levels, the master equation is

$$\begin{cases} \frac{dP_1}{dt} = w_{21}P_2 - w_{12}P_1 \\ \frac{dP_2}{dt} = w_{12}P_1 - w_{21}P_2 \end{cases} \quad (2.104)$$

and it satisfy the boundary condition that  $\frac{dP_1}{dt} + \frac{dP_2}{dt} = 0$  or  $P_1 + P_2 = 1$ , so that

$$\frac{dP_1}{dt} = w_{21}(1 - P_1) - w_{12}P_1 \quad (2.105)$$

Then differential equation 2.105 can be solved

$$P_1(t) = \frac{1 - e^{-t(w_{21}+w_{12})}}{1 + w_{21}/w_{12}} + P_1(0)e^{-t(w_{21}+w_{12})} \quad (2.106)$$

and by substituting  $w_{21}/w_{12}$  using Boltzmann detailed balance condition and setting the ground-state energy to zero, i.e.,  $w_{21}/w_{12} = \frac{g_2}{g_1} \exp(-\frac{E_2}{k_B T})$ , we get

$$P_1(t) = \frac{g_1}{Q} \left(1 - e^{-t(w_{21}+w_{12})}\right) + P_1(0)e^{-t(w_{21}+w_{12})} \quad (2.107)$$

From Equation 2.107, we know that  $P_1(t) = P_1(0)$  at  $t = 0$ , and  $P_1(t) \rightarrow \frac{g_1}{Q}$  when  $t \rightarrow \infty$ .

In reality, a molecular is of a large number of states, and the master equation is a set of linear differential equations (each in the form like Equation 2.100). Although difficult, it is in principle always solvable for systems with a finite number of states. It can be expressed as an eigenvalues-eigenfunctions problem,

$$W = \begin{bmatrix} -w_{11} & w_{21} & \cdots & w_{n1} \\ w_{12} & -w_{22} & \cdots & w_{n2} \\ \vdots & \vdots & \ddots & \vdots \\ w_{1n} & w_{2n} & \cdots & -w_{nn} \end{bmatrix} \quad \text{where} \quad w_{ii} = \sum_{j \neq i} w_{ij} \quad (2.108)$$

and its solution can be expressed as a sum of terms involving  $e^{\lambda_i t}$ , where  $\lambda_i < 0 \forall i$  are the eigenvalues. Usually, a large gap in the values (at least one magnitude) separates the obtained eigenvalues into two groups, chemical significant eigenvalues (CSEs) associated with long-term reactions, and internal energy relaxation eigenvalues (IEREs) associated with short-term vibration-rotational relaxations. Therefore we can keep only the CSEs, which are much less in number, to derive rate coefficients. However, for some cases, CSEs and IEREs can not be separated easily or even merge with each other, indicating that some chemical reactions take

place on vibrational-rotational relaxation time scales. In these cases, species reduction is necessary to combine the two rapidly equilibrating species as an effective one.

Microcanonical rate constants can be derived from the master equations. With the given information or assumptions:

- During intramolecular vibrational relaxation (IVR), a molecule jumps randomly among a set of states that are of equal energy, therefore

$$\frac{w_{ij}}{w_{ji}} = \exp\left(-\frac{E_j - E_i}{k_B T}\right) = 1 \quad (2.109)$$

which means that  $w_{ij} = w_{ji} = w$ ,  $\forall i, j$ .

- A molecule reacts as soon as it hits a state with sufficient energy in the reactive mode, which correspond to the transition state  $A^\ddagger$ . And the system can not return from the reactive states.
- The average time required to reach a reactive state is the inverse of the rate constant.

Let  $\mathcal{N}$  and  $\mathcal{R}$  be the set of non-reactive and reactive states respectively, and  $G^\ddagger$ ,  $G_{\mathcal{N}}$ , and  $G^*$  be the degeneracy of a certain energy level for  $\mathcal{R}$ ,  $\mathcal{N}$  and all states ( $\mathcal{N} + \mathcal{R}$ ) respectively. After a series of derivation, the probability that an energized molecule has reacted by time  $t$ , can be expressed as,

$$P_{\mathcal{R}} = 1 - P_{\mathcal{N}} = 1 - e^{-wG^\ddagger t} \quad (2.110)$$

and its probability density is

$$p_{\mathcal{R}}(t) = wG^\ddagger e^{-wG^\ddagger t} \quad (2.111)$$

The average reaction time then can be derive as

$$\langle t \rangle = \int_0^\infty t p_{\mathcal{R}}(t) dt = (wG^\ddagger)^{-1} \quad (2.112)$$

and therefore the rate constant

$$k = \langle t \rangle^{-1} = wG^\ddagger \quad (2.113)$$

is proportional the  $G^\ddagger$  but does not depend on  $G^*$ . It implies that the rate constant depends on how fast IVR takes place, not on how fast the molecule moves through the transition state.

## 2.4 Macro-scale: Laminar Flame Speed

### 2.4.1 Theoretical and Numerical Presentation

Laminar flame speed ( $S_L$ , abbreviated as LFS), also called laminar burning velocity or fundamental flame speed, is defined as the velocity perpendicular to the front of a one-dimensional, freely propagating, adiabatic, laminar, unscratched, planar, steady flame. It is a fundamental property of a combustible mixture, reflecting its exothermicity, diffusivity, and reactivity, and comparable between different mix-



tures at the same “environmental” condition. Studying laminar flame speed is useful in many aspects. Towards the molecular level, it is an important parameter for kinetic model validation. Towards the application level, it is an important element in calculating the turbulent flame speed in CFD simulations using the flame surface density model.

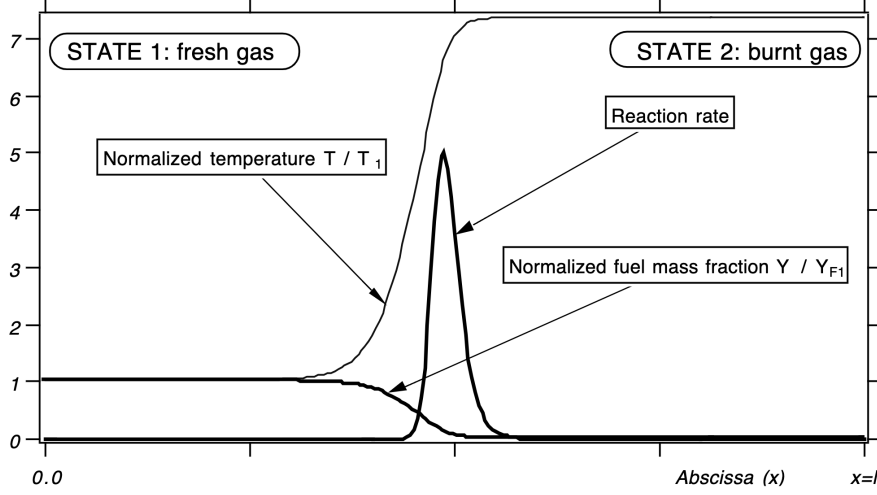


Figure 2-6: Basic configuration of a one-dimensional freely propagating flame. Figure taken from [3].

A typical configuration of such a flame is depicted in Figure 2-6, and by definition,  $S_L$  is equal to the axial velocity of the unburnt gas. To solve  $S_L$  analytically, the following conservation equations must be satisfied for a steady flame (independent of time):

- Mass conservation.

$$\frac{\dot{M}}{A} = \rho u = \text{constant} = \rho_b S_b = \rho_u S_L \quad (2.114)$$

- Species conservation.

$$\dot{M} \frac{dY_k}{dx} + \frac{d}{dx} (\rho A Y_k V_k) - A \dot{\omega}_k W_k = 0 \quad k = 1, 2, \dots, N \quad (2.115)$$

- Energy conservation.

$$\dot{M} \frac{dT}{dx} - \frac{1}{c_p} \frac{d}{dx} \left( \lambda A \frac{dT}{dx} \right) + \frac{A}{c_p} \sum_{k=1}^N \rho Y_k V_k c_{p,k} \frac{dT}{dx} + \frac{A}{c_p} \sum_{k=1}^N \dot{\omega}_k h_k W_k = 0 \quad (2.116)$$

- Equation of state.

$$\rho = \frac{p \bar{W}}{RT} \quad (2.117)$$

where  $\dot{M}$  is the mass flow rate ( $\text{kg s}^{-1}$ ),  $A$  is the cross section area ( $\text{m}^2$ ),  $\bar{W}$ ,  $\lambda$ , and  $c_p$  are the average molecular weight ( $\text{kg mol}^{-1}$ ), thermal conductivity ( $\text{J m}^{-1} \text{s}^{-1} \text{K}^{-1}$ ), and constant pressure heat capacity ( $\text{J kg}^{-1} \text{K}^{-1}$ ) of the mixture. The  $Y_k$ ,  $W_k$ ,  $h_k$ ,  $c_{p,k}$ ,  $V_k$ , and  $\dot{\omega}_k$  of species  $k$  are its mass fraction, molecular

weight, specific enthalpy ( $\text{J kg}^{-1}$ ), constant pressure heat capacity, diffusion velocity ( $\text{m s}^{-1}$ ), and molar rate of production by reactions ( $\text{mols}^{-1}$ ), respectively.

Based on these equations, together with proper approximations, the analytical solution for laminar flame speed can be obtained. The results indicate that  $S_L$  depend on both heat diffusivity and reaction rate,

$$S_L \propto (D_{th}^u R_r)^{1/2} \quad (2.118)$$

and flame thickness is inversely proportional to  $S_L$ .

$$\delta = \frac{\lambda_u}{\rho_u c_p S_L} = \frac{D_{th}^u}{S_L} \quad (2.119)$$

## 2.4.2 Experimental Measurements

Various experimental methods could be used to measure the laminar flame speed of premixed fuel/oxidizer mixtures. Some popular methods are usually categorized into:

- conical flame (Bunsen burner) method
- spherical flame method
- heat flux method
- stagnation/counterflow flame method
- externally heated diverging channel method
- annular step-wise tube method

The first four methods are introduced below.

### Bunsen Burner Method

Bunsen burner, which could create a stable conical flame, is conventionally used by researchers to measure the laminar flame speed, which could be derived from the velocity of fresh gases. Besides laminar flame speed, it is also used to study other flame phenomena, such as the flame tip opening which is related to flame curvature and preferential diffusion. [224] It is reported that Bunsen burner method could measure the flame speed with unity Lewis number ( $Le$ , defined as the ratio of thermal diffusivity to mass diffusivity of a mixture) with sufficient accuracy, but lack of accuracy for non-unity Lewis number mixtures. [225]

### Spherical Flame Method

Spherical flame method can be classified into two types, constant-pressure and constant-volume. In the present work, the constant-pressure spherical flame method is introduced. In the configuration of the spherical flame method (as shown in Figure 2-7), premixed fuel/oxidizer mixture with a certain equivalence ratio, temperature, and pressure, is injected in a confined chamber and ignited at the center. As a result, the flame generated propagates outwardly from the center to the vessel wall and from the burnt gases towards the fresh gases. In the meantime, the motion of the flame is captured using Schlieren photography which can recognize the flame surface by the varying density of the mixture at different positions. Based on the time evolution of the radius of the flame surface ( $r_f(t)$ ), stretched flame

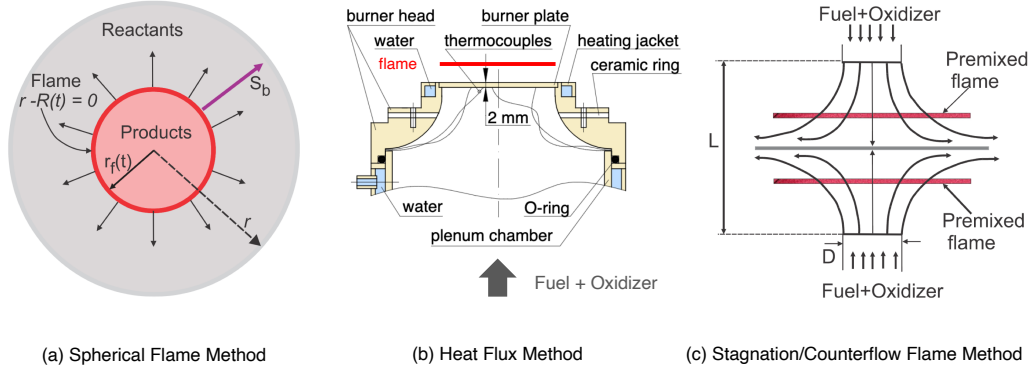


Figure 2-7: Schematic diagram showing three experimental methods to measure laminar flame speed. (a) Spherical flame method, graphic taken from Ref. [4]. (b) Heat flux burner, graphic taken from Ref. [5]. (c) Stagnation/counterflow flame method, graphic taken from Ref. [4].

speed ( $S_b$ ) can be derived.

$$S_b = \frac{dr_f}{dt} \quad (2.120)$$

Oscillations are often observed for the resulted  $S_b$ , which requires smoothing algorithms [226] to remove the oscillations. To obtain the unstretched flame speed ( $S_b^0$ ) and Markstein length ( $L_b$ , defined as the critical wavelength for the stability of the flame front) of the burnt gas, it is necessary to extrapolate  $S_b$  to zero stretch, given the stretch rate ( $K$ ) is defined as

$$K = \frac{1}{A} \cdot \frac{dA}{dt} = \frac{2}{r_f} \cdot \frac{dr_f}{dt} = \frac{2S_b}{r_f} \quad (2.121)$$

for spherical flame, where  $A = 4\pi r_f^2$  is the flame surface. Both linear and non-linear extrapolation methods could be used to obtain  $S_b^0$ . They are summarized by Konnov *et al.* [4] and listed in Table 2.1. Recently integral forms of these methods have been used to fit directly the time history of the flame radius. It is reported that linear models are sufficient for unity Lewis number mixture, while for non-unity Lewis number mixtures non-linear models are more accurate [227], however, it is questioned [4]. In other words, the models in Table 2.1 operate with their optimal accuracy at different ranges of Lewis numbers. The stretch extrapolation process is one of the main sources of experimental uncertainty. Once the unstretched flame speed of burnt gas  $S_b^0$  is obtained, the unstretched laminar flame speed  $S_L^0$  can be derived

$$S_L^0 = S_b^0 \sigma = S_b^0 \cdot \frac{\rho_b^0}{\rho_u} \quad (2.122)$$

where  $\sigma = \rho_b^0/\rho_u$  is the density ratio, and  $\rho_b^0$  is the density of burnt gases assuming its composition and temperature are at equilibrium. Besides stretch extrapolation, another important source of uncertainty is the density ratio ( $\sigma$ ) which is affected

by radiation losses. [228]

Table 2.1: Stretch extrapolation methods available in literature. Adapted from Konnov *et al.* [4]

No.	Type	Expression	Ref.
1	linear	$S_b = S_b^0 - L_b K$	[229–232]
2	linear	$\frac{S_b}{S_b^0} = 1 - 2 \frac{L_b}{r_f}$	[233]
3	non-linear	$\left(\frac{S_b}{S_b^0}\right)^2 \ln \left(\frac{S_b}{S_b^0}\right)^2 = -2 \frac{L_b K}{S_b^0}$	[234]
4	non-linear	$S_b^0 t + c = r_f + 2L_b \ln r_f - 4 \frac{L_b^2}{r_f} - \frac{8}{3} \frac{L_b^2}{r_f^2}$	[235]
5	non-linear	$\frac{S_b}{S_b^0} = 1 - 2 \frac{L_b}{r_f} + \frac{c}{r_f^2}$	[236]
6	non-linear	$\left(\frac{S_b}{S_b^0} + \frac{2\delta^0}{r_f}\right) \ln \left(\frac{S_b}{S_b^0} + \frac{2\delta^0}{r_f}\right) = -\frac{2(L_b - \delta^0)}{r_f}$ $U = 1 - \frac{2L_0}{RU} + \left(\frac{2L_0}{RU}\right)^2 - \left(\frac{2L_0}{RU}\right)^3 + \left(\frac{2L_0}{RU}\right)^2$	[237]
7	non-linear	$U = \frac{S_b}{S_b^0}, \quad L_0 = Le^{-1} - (Z/2)(Le^{-1} - 1)$ $R = \frac{r_f}{\delta^0}, \quad Z = (1 - \sigma)T_a/T_{ad}$	[227]

It is worth noting that the experimental apparatus used by our partner, the PRISME lab, could measure the propagation of both laminar and turbulent flames using the constant-pressure spherical flame method. Details of this experimental setup are described in Ref. [24, 71] They measure the laminar flame speed of TRFE/air/EGR mixtures, which is used in this work to validate the performance of the kinetic mechanisms developed.

## Heat Flux Method

Heat flux method measures the laminar flame speed by producing a planar/flat flame, as shown in Figure 2-7. Premixed fuel/oxidizer mixture flow from the bottom of the burner while the flat flame surface is stabilized above the burner exit. The stabilization of the flat flame can sometimes be difficult [238]. Therefore, the perforated burner plate is heated using hot water circulated in the jacket on the burner head, to compensate for the heat loss from the flame. By altering the unburnt gas velocity, flame stabilization is achieved when the temperature-radius profile, measured using thermocouples placed on the burner plate, becomes flat. [238] At this condition, the laminar flame speed is equal to the unburnt gas velocity. The advantage of heat flux method is that it does not require stretch extrapolation and measurements in literature show good data consistency [93], while the disadvantage is the difficulty to measure large flame speeds (over 80 cm/s) [4], to achieve high initial temperature due to increased radical quenching over the burner plate [239], and to achieve high pressure due to low flame speed and difficult flame stabilization [240].

## Stagnation/Counterflow Flame Method

As shown in Figure 2-7, the stagnation/counterflow method measures the laminar flame speed by producing one (or two symmetrical) stabilized flame(s) in a well-designed stagnation flow field. The stagnation flow field can be achieved through two types of configurations, either stagnating the flow on a solid wall or impinging two identical flows towards each other. The latter configuration does not have conductive heat losses due to the flame symmetry and radiative heat loss is negligible. [241] However, the flame is subject to stretch due to the hydrodynamic strain, which is related to the axial velocity gradient. Using linear or non-linear extrapolation methods, the unstretched laminar flame speed can be derived. The uncertainty associated with this method is mainly from stretch extrapolation, flow rate measurement, mixture preparation of liquid fuels, and particle slip errors. [4]

## 2.5 Macro-scale: Dilution Effects

### 2.5.1 Categorization of Dilution Effects

The dilution effect can be categorized based on the different physical or chemical processes the diluent participates in. Analytically, the laminar flame speed can be expressed using a simplified equation [3],

$$S_L = \left[ \underbrace{\frac{1}{\beta(\beta - 1)}}_{\text{thermal}} \underbrace{D_{th}^u}_{\text{transport}} \underbrace{R_r}_{\text{chemical}} \right]^{\frac{1}{2}} \quad (2.123)$$

where the constant unity Lewis number ( $Le = 1$ ) for all species are assumed,  $D_{th}^u$  is the thermal diffusivity of the unburnt mixture, and  $R_r$  is the global reaction rate. The parameters

$$\alpha = (T_b - T_u)/T_b \quad (2.124)$$

$$\beta = \alpha T_a/T_b \quad (2.125)$$

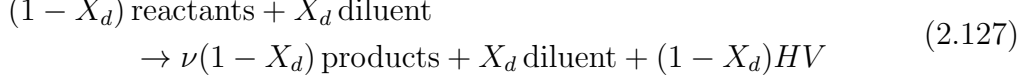
relates to the heat release and activation temperature of the flame respectively, where  $T_u$  and  $T_b$  is the temperature of the unburnt and burnt gases, and  $T_a = E_a/R$  is the activation temperature of the global reaction. Based on Eq. 2.123, it is reasonable that the dilution effect on  $S_L$  could be classified into thermal, transport, and chemical effects respectively.

The thermal effect is usually the most dominant one and affects combustion phenomena, e.g., flame speeds, by altering the flame temperature. The alteration is achieved mainly through (1) reduced heat release of the reactants and (2) changed heat capacity of the product mixture. The former is due to the concentration effect that the fraction of the “useful” or “heat producing” portion (i.e., the stoichiometric part of fuel and oxidizer which will be fully converted into products) is reduced by the introduction of diluent and therefore less heat is produced. Consider the simplified equation of the combustion process when no diluent is in

the system (assuming constant pressure),



, where  $\nu$  is the stoichiometric coefficient and  $HV$  is the heating value of one mole of the reactants. After diluent is introduced, it changes to



, where  $X_d$  is the mole fraction of diluent. Note that the reactant means the entire mixture of fresh gases, and the product means the mixture of burnt gases at normal conditions. Therefore the stoichiometric coefficient is the relative change in moles of the mixture at normal conditions,

$$\nu = \dot{n}_p / \dot{n}_r \quad (2.128)$$

where  $\dot{n}_r$  and  $\dot{n}_p$  are the molar flow rate of the reactants and products respectively. It is necessary to emphasize on the difference between products and burnt mixture, as they are not the same in diluted cases where  $\dot{n}_p / \dot{n}_r = \nu$  remains the same but  $\dot{n}_b / \dot{n}_r = \nu(1 - X_d) + X_d$  changes with dilution ratio. It is clearly shown in Equation 2.126 and 2.127 that the heat release decreases from  $\dot{n}_r HV$  to  $(1 - X_d)\dot{n}_r HV$ , which will lead to lower temperature in the reaction zone and eventually reduced  $S_L$ . The second aspect, changed heat capacity of the product mixture, is due to the fact that the specific heat capacity of diluent is usually not the same as the original product mixture. Letting the molar specific heat capacity of the original product mixture, at a certain temperature (e.g., the average temperature in the reaction zone), to be  $c_{p,m}^p$ , and that of the diluent to be  $c_{p,m}^d$ , one can get the value for diluted burnt gas  $c_{p,m}^b$ , by applying the mixture rule, to be

$$\begin{aligned} c_{p,m}^b &= \frac{\nu(1 - X_d)c_{p,m}^p + X_d c_{p,m}^d}{\nu(1 - X_d) + X_d} \\ &= c_{p,m}^p + \frac{X_d}{\nu(1 - X_d) + X_d} (c_{p,m}^d - c_{p,m}^p) \end{aligned} \quad (2.129)$$

If  $c_{p,m}^d < c_{p,m}^p$ , e.g., when fuel is burnt in pure oxygen (products contain mainly  $\text{CO}_2$  and  $\text{H}_2\text{O}$ ) and diluted with  $\text{N}_2$  ( $c_{p,m}^{\text{N}_2}$  is lower than  $c_{p,m}^{\text{H}_2\text{O}}$ ,  $c_{p,m}^{\text{CO}_2}$ ),  $c_{p,m}^b$  becomes lower than the non-diluted case ( $c_{p,m}^b = c_{p,m}^p$ ), and therefore inhibit or compensate part of the temperature reduction caused by the concentration effect. If  $c_{p,m}^d = c_{p,m}^p$ , i.e., when diluent with the same composition as the original product is introduced, the specific heat of the products mixture is unchanged and thus do not contribute to the temperature reduction. if  $c_{p,m}^d > c_{p,m}^p$ , e.g., when fuel is burnt in air (the most abundant compound in products is  $\text{N}_2$ ) and diluted by  $\text{CO}_2$  or  $\text{H}_2\text{O}$ ,  $c_{p,m}^b$  get larger and then further reduce the flame temperature by acting as heat absorbents.

Although it is not possible to separate the concentration and heat-capacity effects, the overall thermal effect in reducing the flame temperature can be studied analytically. To make the problem simple, we make the approximation that flame temperature ( $T_f$ ), burnt gas temperature ( $T_b$ ) and adiabatic temperature ( $T_{ad}$ ) are all equal. The heat flow rate is then equal to both the heat released by the

reactants (Eq. 2.130) and the sensible heat absorbed by the burnt mixture (Eq. 2.131).

$$\dot{Q} = \dot{n}_r HV \quad (2.130)$$

$$\dot{Q} = \dot{n}_b c_{p,m}^b (T_{ad} - T_u) \quad (2.131)$$

Therefore, by combining Eq. 2.130 and 2.131,  $T_{ad}$  can be derived as

$$T_{ad} = T_u + \frac{\dot{n}_r HV}{\dot{n}_b c_{p,m}^b} \quad (2.132)$$

Taking in Eq. 2.129 and the ratio  $\dot{n}_b/\dot{n}_r = \nu(1 - X_d) + X_d$ , then we get

$$\begin{aligned} T_{ad} &= T_u + \frac{HV}{\nu c_{p,m}^p + (c_{p,m}^d - \nu c_{p,m}^p) X_d} \\ &= T_u + \frac{HV}{\nu c_{p,m}^p} \left[ 1 + \frac{c_{p,m}^d - \nu c_{p,m}^p}{\nu c_{p,m}^p} X_d \right]^{-1} \end{aligned} \quad (2.133)$$

Based on Eq. 2.133, it is found that the temperature rise  $T_{ad} - T_u$  is inversely proportional to  $1 + \frac{c_{p,m}^d - \nu c_{p,m}^p}{\nu c_{p,m}^p} X_d$ . Since  $\frac{c_{p,m}^d - \nu c_{p,m}^p}{\nu c_{p,m}^p} X_d \ll 1$  at most cases, Eq. 2.133 could be further simplified, using the linear approximation  $((1+x)^a \approx 1+ax$  when  $|x| < 1$  and  $|ax| \ll 1$ ).

$$\begin{aligned} T_{ad} &\approx T_u + \frac{HV}{\nu c_{p,m}^p} \left( 1 - \frac{c_{p,m}^d - \nu c_{p,m}^p}{\nu c_{p,m}^p} X_d \right) \\ &= \left( T_u + \frac{HV}{\nu c_{p,m}^p} \right) - \frac{HV(c_{p,m}^d - \nu c_{p,m}^p)}{(\nu c_{p,m}^p)^2} X_d \end{aligned} \quad (2.134)$$

Therefore, the reduction of  $T_{ad}$  with increasing dilution ratio is approximately linear and the slope or effectiveness ( $C_d^{th}$ ) depends on the heat capacity of the diluent, as shown in Eq. 2.135–2.137.

$$T_{ad} \approx T_{ad}^{ref} + C_d^{th} X_d \quad (2.135)$$

$$T_{ad}^{ref} = T_u + \frac{HV}{\nu c_{p,m}^p} \quad (2.136)$$

$$C_d^{th} = -\frac{HV(c_{p,m}^d - \nu c_{p,m}^p)}{(\nu c_{p,m}^p)^2} \quad (2.137)$$

It is worth mentioning that real cases are more complicated, because the heat capacities are not constant and vary with temperature.

The approximation of the overall thermal effect in reducing  $S_L$  can also be estimated analytically. It is realized by studying the influence of the burnt gas temperature ( $T_b$ ), which varies approximately linearly to dilution ratio. Varying  $T_b$  leads to the change in the thermal part of Eq. 2.123, which can be simplified

using approximation shown as follows.

$$\left[ \frac{1}{\beta(\beta-1)} \right]^{-\frac{1}{2}} = \left[ \beta^2 \left(1 - \frac{1}{\beta}\right) \right]^{-\frac{1}{2}} = \frac{1}{\beta} \left(1 - \frac{1}{\beta}\right)^{-\frac{1}{2}} \quad (2.138)$$

$$\approx \frac{1}{\beta} \left(1 + \frac{1}{2\beta}\right)$$

$$\frac{1}{\beta} \left(1 + \frac{1}{2\beta}\right) = \frac{1}{2} \left(1 + \frac{1}{\beta}\right)^2 - \frac{1}{2} \quad (2.139)$$

$$\approx \frac{1}{2} \left(1 + \frac{2}{\beta}\right) - \frac{1}{2} = \frac{1}{\beta}$$

$$\frac{1}{\beta} = \frac{T_b}{\alpha T_a} = \frac{T_b}{\left(1 - \frac{T_u}{T_b}\right) T_a} = \frac{T_b}{T_a} \left(1 - \frac{T_u}{T_b}\right)^{-1} \quad (2.140)$$

$$\approx \frac{T_b}{T_a} \left(1 + \frac{T_u}{T_b}\right) = \frac{T_u}{T_a} + \frac{1}{T_a} T_b$$

Here we must emphasize that the above derivations are only simplified problems and rough estimates. For example, constant  $T_a$  is assumed whereas in real cases it varies with mixture compositions. In addition, Eq. 2.138–2.140 use three approximation steps, which are only valid when  $\frac{1}{2\beta} \ll 1$ ,  $\frac{2}{\beta} \ll 1$ , and  $\frac{T_u}{T_b} \ll 1$ , respectively. The first two conditions, requiring  $\beta = \alpha T_a / T_b \gg 2$ , are usually satisfied, because that (i)  $T_a$  is much greater than  $T_b$  at most cases, and (ii)  $T_a$  increases with increasing  $X_d$  while  $T_b$  decreases. The third requirement,  $T_b \gg T_u$ , is valid when  $X_d$  is low or moderate, but weakened or broken at highly diluted conditions where  $T_b$  is reduced. Therefore, if all requirements are met, it is estimated that change in  $S_L$  is approximately proportional to the change in  $T_b$  and therefore  $S_L$  also reduces approximately linearly with increasing  $X_d$ .

$$\Delta S_L \propto \Delta T_b \propto -\Delta X_d \quad (2.141)$$

The chemical effect is caused by the fact that some diluent is not inert and participate in reactions. Although not as dominant, it affects the flame speed considerably. The diluent contribute to the chemical effect either (1) directly as reactants or products



or (2) indirectly as collision partners in three-body collisions



. Either way, the influence is achieved by the increased concentration of the diluent molecules, which affects the rate of progress of the reactions it involves. For direct reactions like R 2.1,

$$-\frac{d[A]}{dt} = -\frac{d[\text{dilution}]}{dt} = \frac{d[C]}{dt} = \frac{d[D]}{dt} = k_{bi}[A][\text{diluent}] \quad (2.142)$$



and for three-body reactions like R.2.2

$$-\frac{d[A]}{dt} = -\frac{d[B]}{dt} = \frac{d[C]}{dt} = \frac{d[D]}{dt} = k_{ter}[A][B] \cdot \varepsilon_{diluent}[\text{diluent}] \quad (2.143)$$

, where  $[A]$  is the concentration of molecule A,  $k_{bi}$  and  $k_{ter}$  are the bimolecular and termolecular rate constants respectively, and  $\varepsilon_{diluent}$  is the 3rd-body collisional efficiency for the diluent. The  $\varepsilon_{diluent}$  for CO<sub>2</sub> and H<sub>2</sub>O is usually greater than unity, which indicates they are more efficient in changing the rate of three-body reactions than the bath gas molecule (usually N<sub>2</sub>). This influence in rate of progress also changes the concentration of the molecules participating in these reactions (e.g., A, B, C, D in R.2.1 and R.2.2), which propagates further to other molecules in the mixture through the reaction mechanism. Among these changes, the most important is on the concentration of radicals (such as H, O, and OH), to which the system reactivity is very sensitive. These alterations may result in the changes of main reaction pathways, i.e., how the fuel is converted to the final products, which is the main focus of the present work.

Other minor effects could be originated from the transport properties of the diluent molecules, such as the dynamic viscosity ( $\mu_d$ ), thermal conductivity  $\lambda_d$ , and binary diffusion coefficient  $D_{d,j}$ . For example, the binary diffusion coefficient is related to the mass ( $m_d$ ) and collision diameter ( $\sigma$ ) of the diluent molecule, which can be expressed as follows.

$$D_{d,j} = \frac{2}{3} \left( \frac{k_B^3 T}{\pi^2 m_d} \right)^{\frac{1}{2}} \frac{T}{\sigma^2 p} \quad (2.144)$$

$$\propto m_d^{-\frac{1}{2}} \sigma^{-2}$$

The diluent molecule, such as N<sub>2</sub>, H<sub>2</sub>O and CO<sub>2</sub>, have larger  $m_d$  and  $\sigma$  with respect to the small molecules (e.g. H, O, OH radicals), and therefore are less diffusive if in the same environment. As a consequence, the transport effect of dilution is usually not significant.

## 2.5.2 Quantification of Dilution Effects

Experimentally it is not possible to separate the thermal and chemical effects. However, this is possible in simulations by using the false-species method, i.e., using false species with only part of the properties of the real molecule. For each diluent molecule, e.g., H<sub>2</sub>O, the present work introduced three types of false species, namely inert H<sub>2</sub>O (iH<sub>2</sub>O), bath gas H<sub>2</sub>O (bH<sub>2</sub>O), and collider H<sub>2</sub>O (cH<sub>2</sub>O). Table 2.2 lists the properties they possess and Figure 2-8a depicts the different types of dilution effect on laminar flame speeds that they could quantify.

The different effects are quantified as the change in values between the target case (obtained using one false species) and the reference case. It can be calculated as either absolute or relative changes. Consider the property  $f$ , which has the value of  $f_{target}$  and  $f_{ref}$  at the two conditions, then the absolute change ( $g^{abs}$ ) is

Table 2.2: Properties of the false species, compared with the real molecule, introduced in the present work, using H<sub>2</sub>O as an example.

Species	Description	Participate in Reactions	3rd-body efficiency	Thermodynamic Properties	Transport Properties
–	<i>no dilution</i>	–	–	–	–
iH <sub>2</sub> O	inert H <sub>2</sub> O	no	= 0	= H <sub>2</sub> O	= H <sub>2</sub> O
bH <sub>2</sub> O	bath gas H <sub>2</sub> O	no	= 1	= H <sub>2</sub> O	= H <sub>2</sub> O
cH <sub>2</sub> O	collider H <sub>2</sub> O	no	= H <sub>2</sub> O	= H <sub>2</sub> O	= H <sub>2</sub> O
H <sub>2</sub> O	real H <sub>2</sub> O	yes	= H <sub>2</sub> O	= H <sub>2</sub> O	= H <sub>2</sub> O

expressed by Eq. 2.145, and the relative change ( $g^{rel}$ ) by 2.146

$$g^{abs} = f_{target} - f_{ref} \quad (2.145)$$

$$g^{rel} = \frac{f_{target} - f_{ref}}{f_{ref}} \quad (2.146)$$

Take the laminar flame speeds for example, dilution effects on the two types of changes are shown in 2-8b and 2-8c respectively. The numbers are adjusted to positive for convenience since dilution results in reduced  $S_L$ . For thermal and transport effects, the target case is iH<sub>2</sub>O and the reference case is the no dilution case. Unfortunately, it is difficult to further separate thermal from transport effect and the best one can do is the relative thermal (or transport) effect with respect to another diluent molecule. However, this difference could reflect the magnitude of the thermal effect, because the transport effect is usually negligible. It is worth noting that the 3rd-body collision efficiency of iH<sub>2</sub>O must be manually declared to be 0, otherwise they are considered to be unity, which is the same as other undeclared bath gas. It is critical and must be done carefully, in order to accurately separate the thermal and transport effects from others. The chemical effects are situated between the values of iH<sub>2</sub>O and the real H<sub>2</sub>O. The direct reaction effect and 3rd-body collision effect are then separated using cH<sub>2</sub>O, which has the same collision efficiency as H<sub>2</sub>O. The 3rd-body efficiency of bH<sub>2</sub>O is not declared and therefore have the default value of unity. It can be used to study the relative 3rd-body collision effect with respect to that of the bath gas. It is worth mentioning that the above methods can also be applied to properties other than  $S_L$ , such as the ignition delay time, concentration profile of important species (such as the H radicals.).

In order to study the evolution of these dilution effects with respect to the dilution ratio, the effectiveness of these effects could be reflected by the derivative of the relative changes ( $g^{rel}$ ) against dilution ratio ( $X_d$ ). Here we name it ‘‘Dilution Effectiveness’’ with symbol  $\eta_{dil}$ , and it is expressed as Eq. 2.147.

$$\eta_{dil} = \frac{dg^{rel}}{dX_d} = \frac{d}{dX_d} \left( \frac{f_{target} - f_{ref}}{f_{ref}} \right) \quad (2.147)$$

$\eta_{dil}$  is useful when investigating how efficient of a diluent is than others and also whether dilution effects become stronger or weaker as  $X_d$  increases (as shown in Fig. 2-8d).

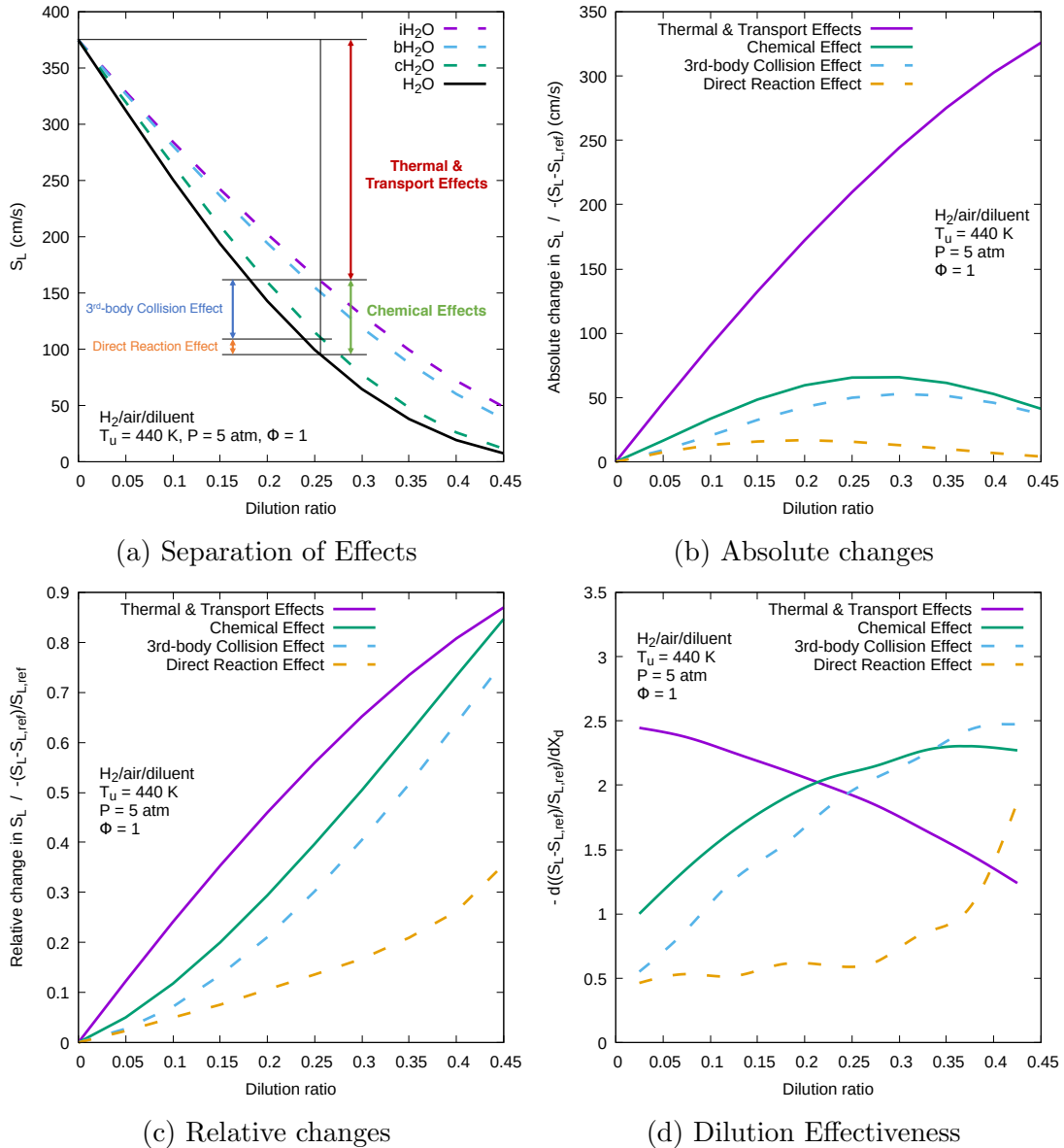


Figure 2-8: Demonstration of the quantification of dilution effects using the false-species method. Use the laminar flame speeds of  $\text{H}_2/\text{air}/\text{H}_2\text{O}$  mixtures as examples.

## 2.6 Macro-scale: Kinetic Mechanism Development

### 2.6.1 Validation of Calculation Results

Kinetic mechanisms should be validated before application, and the only way is by comparing their predictions with experimentally measured properties, such as ignition delay times, laminar flame speeds, speciation profiles. In the present work, validation is mostly done based on laminar flame speeds, which is our main focus. To quantify the difference between predictions and measurements, we use either

mean absolute error (MAE),

$$\text{MAE} = \frac{1}{N} \sum_{i=1}^N |P_i - M_i| \quad (2.148)$$

or mean absolute percentage error (MAPE),

$$\text{MAPE} = \frac{1}{N} \sum_{i=1}^N \frac{|P_i - M_i|}{M_i} \quad (2.149)$$

where  $P_i$  and  $M_i$  are the predicted and measured values respectively for the  $i$ th data point, and  $N$  is the total number of data points. Usually, a set of mechanism predictions with  $\text{MAPE} \leq 20\%$  can be considered satisfactory.

## 2.6.2 Sensitivity Analysis on Composite Functions

Sensitivity analysis is a very useful method in kinetic modeling. It can help us identify key parameters that are sensitive to a certain phenomenological property. Consider the property  $f$  which is a function of  $N$  variables:

$$f = f(\alpha_1, \alpha_2, \dots, \alpha_i, \dots, \alpha_N), \quad i = 1, 2, \dots, N \quad (2.150)$$

The sensitivity of  $\alpha_i$  to the property  $f$  is defined as:

$$s_{\alpha_i}^f = \frac{\partial \log f}{\partial \log \alpha_i} = \frac{\alpha_i}{f} \frac{\partial f}{\partial \alpha_i} \quad (2.151)$$

Some times in kinetics modeling, we are interested in the difference between two properties. For instance, the difference in the laminar flame speed between a normal case and a diluted case can help with the investigation of dilution effects. Thus it would be very helpful to obtain sensitivity directly to this difference. Here we introduce two methods based on partial derivations of composite functions, which derive the sensitivity to the absolute and relative difference respectively.

### Sensitivity to Absolute Differences

Consider the absolute difference  $g^{abs}$  between two functions with the same variables,  $f_1$  and  $f_2$ :

$$g^{abs} = f_1 - f_2 \quad (2.152)$$

The sensitivity to the composite function  $g^{abs}$  can be calculated according to the definition given by Eq. 2.151:

$$s_{\alpha_i}^{g^{abs}} = \frac{\partial \log g^{abs}}{\partial \log \alpha_i} = \frac{\alpha_i}{g^{abs}} \frac{\partial g^{abs}}{\partial \alpha_i} = \frac{\alpha_i}{f_1 - f_2} \left( \frac{\partial f_1}{\partial \alpha_i} - \frac{\partial f_2}{\partial \alpha_i} \right) \quad (2.153)$$

The we transform Eq. 2.151 into  $\frac{\partial f}{\partial \alpha_i} = \frac{f s_{\alpha_i}^f}{\alpha_i}$  and apply it in Eq. 2.153,

$$s_{\alpha_i}^{g^{abs}} = \frac{\alpha_i}{f_1 - f_2} \left( \frac{\partial f_1}{\partial \alpha_i} - \frac{\partial f_2}{\partial \alpha_i} \right) = \frac{\alpha_i}{f_1 - f_2} \left( \frac{f_1 s_{\alpha_i}^{f_1}}{\alpha_i} - \frac{f_2 s_{\alpha_i}^{f_2}}{\alpha_i} \right) = \frac{f_1 s_{\alpha_i}^{f_1} - f_2 s_{\alpha_i}^{f_2}}{f_1 - f_2} \quad (2.154)$$

It indicates that we can derive  $s_{\alpha_i}^{g^{abs}}$  once sensitivity to the two property  $s_{\alpha_i}^{f_1}$  and  $s_{\alpha_i}^{f_2}$  are given. In order to use this result to help investigations, we need to think about what it can tell us. Now let's breakdown Eq. 2.154 to have a closer look.

$$\begin{aligned} s_{\alpha_i}^{g^{abs}} &= \frac{f_1 s_{\alpha_i}^{f_1} - f_2 s_{\alpha_i}^{f_2}}{f_1 - f_2} = \frac{f_1 s_{\alpha_i}^{f_1} - f_1 s_{\alpha_i}^{f_2} + f_1 s_{\alpha_i}^{f_2} - f_2 s_{\alpha_i}^{f_2}}{f_1 - f_2} \\ &= \underbrace{\frac{f_1}{f_1 - f_2} (s_{\alpha_i}^{f_1} - s_{\alpha_i}^{f_2})}_{\text{magnified changes}} + \underbrace{s_{\alpha_i}^{f_2}}_{\text{original value}} \end{aligned} \quad (2.155)$$

Eq. 2.155 shows that  $s_{\alpha_i}^{g^{abs}}$  can be interpreted by the addition of two parts: (i) the original value of  $s_{\alpha_i}^{f_2}$  which considered as a base, and (ii) the difference in sensitivity  $s_{\alpha_i}^{f_1} - s_{\alpha_i}^{f_2}$  magnified by dividing the relative difference  $\frac{f_1 - f_2}{f_1}$ . Therefore, the main feature of this method is that it magnifies the changes in sensitivity while keeping the same values for those unchanged. It is useful when we want to have a first overall look about all the important variables (i.e., both the ones that are sensitive at all conditions and the ones that are sensitive to the condition change).

## Sensitivity to Relative Differences

Besides the absolute ones, relative differences usually are even more useful. If we consider the relative difference of  $f_1$  with respect to  $f_2$ , which can be interpreted as function:

$$g^{rel} = \frac{f_1 - f_2}{f_2} \quad (2.156)$$

So the sensitivity to  $g^{rel}$  can be derived as:

$$\begin{aligned} s_{\alpha_i}^{g^{rel}} &= \frac{\alpha_i}{g^{rel}} \frac{\partial g^{rel}}{\partial \alpha_i} = \frac{f_2 \alpha_i}{f_1 - f_2} \left( \frac{f_2 \frac{\partial (f_1 - f_2)}{\partial \alpha_i}}{f_2^2} - (f_1 - f_2) \frac{\partial f_2}{\partial \alpha_i} \right) \\ &= \frac{\cancel{f_2} \alpha_i}{f_1 - f_2} \left( \frac{f_2 \frac{\partial f_1}{\partial \alpha_i} - \cancel{f_2} \frac{\partial f_2}{\partial \alpha_i}}{f_2 \cdot \cancel{f_2}} - f_1 \frac{\partial f_2}{\partial \alpha_i} + \cancel{f_2} \frac{\partial f_2}{\partial \alpha_i} \right) = \frac{\alpha_i (f_2 \frac{\partial f_1}{\partial \alpha_i} - f_1 \frac{\partial f_2}{\partial \alpha_i})}{f_2 (f_1 - f_2)} \quad (2.157) \\ &= \frac{\frac{\partial f}{\partial \alpha_i} = \frac{f s_{\alpha_i}^f}{\alpha_i}}{\cancel{f_2} (f_1 - f_2)} \frac{\alpha_i (\cancel{f_2} f_1 s_{\alpha_i}^{f_1} - f_1 \cancel{f_2} s_{\alpha_i}^{f_2})}{\cancel{\alpha_i}} = \underbrace{\frac{f_1 (s_{\alpha_i}^{f_1} - s_{\alpha_i}^{f_2})}{f_1 - f_2}}_{\text{magnified changes}} \end{aligned}$$

The expression implies that this method eliminates the original value and keeps only the magnified changes. In other words, the variables, whose sensitivities are unchanged, are ignored. It is useful when we want to look only for the variables that the condition change is sensitive to.

### 2.6.3 Improvement of Kinetic Mechanisms

As a kinetic mechanism is composed of the rate coefficients of reactions, thermodynamic and transport parameters, improvement can be achieved by either the update or addition of these parameters. The sources of the update typically come from mostly three ways:

**Fitting from experimental measurements** For most of the existing and fundamental reactions, various measurements on the rate constants are available in the literature. Kinetic parameters to be used in mechanisms are reviewed and fitted from these measurements. The same measure can be done for thermodynamic and transport properties.

**Fitting from theoretical calculations** As the involvement of theoretical chemistry in combustion kinetics is becoming more intense, rate coefficients of reactions, thermal analysis and collisional characteristics of molecules are calculated with higher accuracy. Although arguments still exist about their uncertainty comparing with measurements, they are considered important and reliable sources of kinetics data.

**Optimization within Uncertainty Band** As the uncertainty (either experimental or numerical) of kinetic parameters, e.g., rate coefficients, are quite large, better performance of the mechanisms can be obtained by optimizing these parameters within their band of uncertainty. Although full parameter optimizations are possible, mechanism optimization is typically done for the pre-exponential factors (A factors).

The present work utilizes the first two measures and updates the mechanism by manually reviewing the parameters.

## 2.7 Numerical Tools

### 2.7.1 Gaussian

Gaussian [242] is a general purpose computational chemistry software package. In the present work, it is used for electronic structure calculations using density functional theory.

### 2.7.2 ORCA

ORCA [243] is an open-source general purpose software for computational chemistry. It has been constantly developed and updated with implementations of state-of-the-art theories and methods. It provides flexible channels to visualize its output files using various visualization software, such as Avogadro [244]. In the present work, it is used for electronic structure calculations using electron-correlation wave function methods, such as CCSD(T)-F12 and MP2-F12.

### 2.7.3 Avogadro

Avogadro [244] is a chemical structure visualization software, which can also perform some theoretical calculation, such as some molecular dynamic force field

methods. In the present work, it is used to visualize the output file generated by ORCA software and for force field calculations.

#### 2.7.4 MESS

In the present work, the numerical tools used to derive phenomenological rate coefficients is the MESS (Master Equation System Solver) code in the PAPR (Predictive Automated Phenomenological Rates) suite of chemical kinetic codes developed by Georgievskii and Klippenstein [245, 246]. The MESS code couples the RRKM theory and microcanonical (i.e., E-resolved or one-dimensional) master equations, and specialized in calculating temperature- and pressure-dependent rate coefficients for complex-forming reactions. It has various models or expressions implemented to describe chemical transformations, number or density of states, and collisional energy transfer.

One important feature of MESS is the automated merging of species. As mentioned in 2.3.3, in some cases chemical reactions take place on vibrational-rotational relaxation time scales leading to the difficulty of separating CSEs and IEREs, are therefore species merging is necessary. In addition, it is important to know if some of the bound species are equilibrating with bimolecular products, and if so, with which ones. The MESS code takes advantage of the kappa-matrix, which provides the coupling coefficients between the bound species and bimolecular products. Its elements should be close to unity for the pairs of bound species and bimolecular products that are in equilibrium with each other and close to zero otherwise. This feature is the main reason why we choose MESS out of other master equation codes.

#### 2.7.5 Chemkin Pro

In the present work, the simulation of laminar flame speed is conducted using the PREMIX code [247] implemented in the Chemkin Pro [248] software. Chemkin Pro software is a software package to facilitate the formation, solution, and interpretation of problems involving elementary gas-phase chemical kinetics. PREMIX is a code to solve the configuration and other properties of 1-D freely-propagating premixed flames, whose numerical detail is consistent with the description in Section 2.4.1. During the calculation of laminar flame speed, adequate values of controlling parameters, such as the domain size, grid adaptive control on gradient (**GRAD**) and curvature (**CURV**), are chosen depending on the investigated mixtures, to ensure a freely-propagating grid-insensitive result. Mixture average transport and the thermal diffusion (Soret) effect are considered in all the calculations. In addition, other operations, such as 0-D homogeneous calculations of ignition delay times, surrogate blend optimization, reduction and merging of kinetic mechanisms, are also conducted using the modules provided in the Chemkin Pro software package in the present work.

## Chapter 3

# Theoretical Study on the Temperature and Pressure Dependent Rate Coefficients for the Reaction of Ketene with Hydroxyl Radical

In this chapter, the rate coefficients of the  $\text{CH}_2\text{CO} + \text{OH}$  reaction is studied theoretically, because this reaction is identified in Chapter 4 to be important to the laminar flame speed of a gasoline surrogate fuel at highly-diluted conditions. Note that the work is published in Ref. [249] and its contents are reproduced here in this chapter.

### 3.1 Introduction

Ketene ( $\text{CH}_2\text{CO}$ ), usually generated in flames by the oxidation of alkynes and alkenes, is an important intermediate in the combustion chemistry of hydrocarbons and oxygenated hydrocarbons, which are major components in transportation fuels (e.g., gasoline, diesel, jet fuel and biofuel). As ketene is highly unstable and reactive towards free radicals [250], numerous studies have been carried out on reactions of  $\text{CH}_2\text{CO}$  with atoms and radicals such as H, O, CH,  $\text{CH}_2$ ,  $\text{CH}_3$ , F, Cl, CN and NCO. [251–265] But studies on reactions with hydroxyl radicals (OH) are not as numerous. The  $\text{CH}_2\text{CO} + \text{OH}$  reaction was first proposed in 1977 by Vandooren and Van Tiggelen [266] who studied acetylene/oxygen flames. The reaction  $\text{CH}_2\text{CO} + \text{OH} \longrightarrow \text{CH}_2\text{O} + \text{HCO}$  was believed to be an important intermediate step, especially under fuel lean conditions where the major acetylene removal channel switches to the one producing ketene ( $\text{C}_2\text{H}_2 + \text{OH} \longrightarrow \text{CH}_2\text{CO} + \text{H}$ ). Ketene is also a key intermediate in acetone oxidation. By reacting with  $\text{O}_2$  [267, 268], H [269–272] or OH [269, 272] radicals, the most dominant initiation steps of acetone consumption form acetyl radical ( $\text{CH}_3\text{COCH}_2$ ).  $\text{CH}_3\text{COCH}_2$  then decomposes into ketene and methyl radical ( $\text{CH}_3\text{COCH}_2 \longrightarrow \text{CH}_2\text{CO} + \text{CH}_3$ ) [269]. The ketene generated is mainly consumed by reactions with H and OH radicals, giving mostly ketenyl (HCCO) and hydroxymethyl ( $\text{CH}_2\text{OH}$ ) radi-



cals. [269,271,273,274] Their successive reactions produce formaldehyde, which is believed to result in an increase in overall reactivity. Faravelli *et al.* [275] studied the oxidation of propyne and allene and found the  $\text{CH}_2\text{CO} + \text{OH}$  reactions to be important intermediate steps, especially at high pressures and fuel-lean conditions. Under such conditions, ketene is formed by propargyl oxidation  $\text{C}_3\text{H}_3 + \text{O}_2 \longrightarrow \text{CH}_2\text{CO} + \text{CHO}$ , and consumed mainly by reactions with hydroxyl radical  $\text{CH}_2\text{CO} + \text{OH} \longrightarrow \text{CO}_2 + \text{CH}_3$  and  $\text{CH}_2\text{CO} + \text{OH} \longrightarrow \text{CH}_2\text{O} + \text{CHO}$ . When studying the laminar burning velocity of diacetyl/air flames, Christensen and Konnov [276] concluded that a more accurate prediction of their mechanism could be achieved by revisiting the  $\text{CH}_2\text{CO} + \text{OH}$  reaction. Sarathy *et al.* [277] measured ketene concentration for the first time in the combustion of methyl decanoate (a type of fatty acid methyl esters (FAME), present in biodiesel fuels). During the combustion of FAME, ketene is generated by the  $\beta$ -scission of methyl ester radicals. Increasing sensitivity of  $\text{CH}_2\text{CO} + \text{OH}$  reactions was spotted in Chapter 4 during our studies on the laminar flame speeds of toluene reference fuels with ethanol addition (TRFE) under highly-diluted conditions. Therefore, rate coefficients of the  $\text{CH}_2\text{CO} + \text{OH}$  reaction over a wide range of temperatures and pressures are required for a better understanding of combustion mechanisms and for more accurate predictions of combustion phenomena.

A few experimental studies on the  $\text{CH}_2\text{CO} + \text{OH}$  reaction were mostly performed at room temperature using discharge flow method. [7–9,261] In the measurements performed by Faubel *et al.* [7] and Hatakeyama *et al.* [8], the major products are  $\text{CO}$ ,  $\text{CO}_2$  and formaldehyde ( $\text{CH}_2\text{O}$ ). Later measurements [9,261] found more products such as  $\text{CH}_2\text{O} + \text{HCO}$ ,  $\text{CH}_2\text{O} + \text{H} + \text{CO}$ ,  $\text{HCCO} + \text{H}_2\text{O}$ ,  $\text{CH}_3\text{O} + \text{CO}$ ,  $\text{CH}_2\text{OH} + \text{CO}$  and  $\text{CH}_3 + \text{CO}_2$ . Based on these observations, the reaction is believed to proceed via  $\text{OH}$  addition on carbon atoms [8,9,261] or by  $\text{H}$  atom abstraction [6,9,261]. Grussdorf *et al.* [261] measured the branching ratio of each product channels at room temperature and pressure and found  $\text{OH}$  addition leading to  $\text{CH}_2\text{OH} + \text{CO}$  is the primary channel ( $k_{\text{CH}_2\text{OH}+\text{CO}}/k_{\text{overall}} = 0.60 \pm 0.10$ ), whereas the branching ratio for  $\text{CH}_2\text{O} + \text{HCO}$  and  $\text{HCCO} + \text{H}_2\text{O}$  are lower than 0.02 and 0.01 respectively. The rate constant of the overall reaction,  $k_{\text{overall}}$ , was also measured at room temperature. The reported  $k_{\text{overall}}$  values in  $\text{cm}^3\text{molecule}^{-1}\text{s}^{-1}$  are  $1.7 \times 10^{-12}$  (lower limit) [7],  $1.8 \times 10^{-11}$  [8],  $3.3 \times 10^{-11}$  [6] and  $1.2 \times 10^{-11}$ . [9] A negative temperature dependency was found at low temperatures (193–423K) by Brown *et al.* [6] with the Arrhenius expression  $k_{\text{overall}} = 6.2 \times 10^{-12} \exp(510/T) \text{ cm}^3\text{molecule}^{-1}\text{s}^{-1}$ , which suggests an apparent activation energy of  $-1.0 \text{ kcal mol}^{-1}$ . No pressure dependence was found in their measurements at 1.76–3.55 Torr. At high temperatures during combustion processes, the only reported value is an indirect measurement by Vandooren and Van Tiggelen [266] for product channel  $\text{CH}_2\text{CO} + \text{OH} \longrightarrow \text{CH}_2\text{O} + \text{HCO}$ :  $k_{\text{CH}_2\text{O}+\text{HCO}} = 4.7 \times 10^{-11} \text{ cm}^3\text{molecule}^{-1}\text{s}^{-1}$ , 480–1000 K. The above works were reviewed by Baulch *et al.* [10] who suggest the expression  $k_{\text{overall}} = 2.8 \times 10^{-12} \exp(510/T) \text{ cm}^3\text{molecule}^{-1}\text{s}^{-1}$  over 296–1000 K for combustion modeling.

A few theoretical studies were conducted. [12,262,278] Sung and Tidwell [262] calculated the structures and energies for  $\text{OH}$  addition on  $\text{CH}_2\text{CO}$  using Density Functional Theory (DFT) B3LYP calculations. They concluded that the attack only occurs perpendicular to the ketene plane and the addition on olefinic carbon atom is barrierless whereas a small barrier was obtained for the addition on

the carbonyl carbon atom. Hou *et al.* [12] obtained a detailed Potential Energy Surface (PES) of the  $\text{CH}_2\text{CO} + \text{OH}$  reaction using *ab initio* G3(MP2) method. H abstraction reaction pathway was included in their calculations, which has a much higher barrier ( $8.7 \text{ kcal mol}^{-1}$ ) than the OH addition pathways. The branching ratios were calculated using the RRKM-TST method, which show that  $\text{CH}_2\text{COOH}$  is the main product at low temperatures while H abstraction product  $\text{HCCO} + \text{H}_2\text{O}$  becomes the primary product at high temperatures. Although they derived the branching ratios, they did not publish any results on the rate coefficients. No other theoretical study was found after the year 2000, despite a review article by Tidwell [278] in 2006. Therefore, so far no theoretically calculated rate coefficient has been published.

In summary,  $\text{CH}_2\text{CO} + \text{OH}$  reaction is shown to have significant impacts on hydrocarbon combustion chemistry, but rate coefficients at high temperatures and pressures are still missing. This paper refines its PES using *ab initio* Electronic Structure calculations, based on which its first theoretically-calculated temperature-and-pressure-dependent rate coefficients are obtained.

## 3.2 Computational Methods

We provide a brief summary of the computational methods used in this work in Table 3.1. They are explained in this section in detail.

Table 3.1: Summary of the computational methods used in this work (in sequential order).

Purpose	Method	Software
Search for Van der Waals complex	Force Field	Avogadro [244]
Search for stationary points Intrinsic reaction coordinate (IRC)	B3LYP/6-31G(d,p)	Gaussian 09 [242]
Geometry optimization Normal mode analysis (Frequency, ZPE) Hindered rotor potential scan	B2PLYP-D3/cc-pVTZ	
Electronic energy	CCSD(T)-F12/cc-pVTZ-F12 MP2-F12/cc-pVQZ-F12 MP2-F12/cc-pVTZ-F12 Composite method (Equation 3.1)	ORCA [243]
Rate coefficients	RRKM-TST/ME	MESS [245, 246]

### 3.2.1 Electronic Structure

Hou *et al.* [12] obtained a potential energy surface of  $\text{CH}_2\text{CO} + \text{OH}$  reaction using the second-order Mller-Plesset perturbation theory (MP2)with Pople basis set 6-31G(d,p)for geometry optimization, and G3(MP2) theoryfor energy which is believed to have an accuracy about  $\pm 2 \text{ kcal mol}^{-1}$  [12]. Based on their work, we

refine the PES using a set of more recent electronic structure methods, in order to derive reasonable rate coefficients.

Initial guesses of the Van der Waals complexes of CH<sub>2</sub>CO and OH were scanned using the force field theory implemented in the Avogadro software [244]. Stationary point search and intrinsic reaction coordinate (IRC) analysis were performed using hybrid functional B3LYP with Pople basis set 6-31G(d,p). Geometry optimizations and normal-mode analysis for each of the stationary points were performed using double hybrid functional B2PLYP with D3 dispersion correction [279] and triple-zeta Dunning basis set cc-pVTZ (B2PLYP-D3/cc-pVTZ). Hindered rotor potentials scans and zero-point vibrational energy (ZPE) calculations were performed using the same method. Energies were computed based on the optimized geometries using a composite post-Hartree-Fock method, which includes coupled cluster theory CCSD(T) with explicitly correlated F12 corrections. The total electronic energy (including ZPE), relative to the bimolecular reactants (CH<sub>2</sub>CO + OH), was calculated using Equation 3.1,

$$\begin{aligned} \Delta E_{total} = & \Delta E_{CCSD(T)-F12/cc-pVTZ-F12} \\ & + (\Delta E_{MP2-F12/cc-pVQZ-F12} - \Delta E_{MP2-F12/cc-pVTZ-F12}) \\ & + \Delta ZPE_{B2PLYP-D3/cc-pVTZ} \end{aligned} \quad (3.1)$$

where  $\Delta E_{\text{theory/basis-set}}$  is the relative electronic energy obtained using a certain level of calculation and  $\Delta ZPE$  is the relative zero-point energy obtained by normal mode analysis using B2PLYP-D3/cc-pVTZ. The differences between MP2-F12/cc-pVQZ-F12 and MP2-F12/cc-pVTZ-F12 calculations were used to add correction on the CCSD(T)-F12 energy towards the complete basis-set limit. This approach is originated from the composite method for extrapolation to the basis-set limit by Helgaker *et al.* [280] and is expected to predict energies with less than 1 kcal mol<sup>-1</sup> error [281]. Spin contamination for all calculations was examined and Restricted open-shell HartreeFock (ROHF) method was adopted to eliminate spin contamination of some troublesome calculations. Multireference behavior was examined by T1 diagnostics for CCSD(T)-F12 calculations. The only possible multireference behavior (with T1 > 0.04 for radicals) was neglected since its position on the PES is unlikely to impact the overall kinetics. DFT calculations were performed using the Gaussian 09 [242] software, whereas post-Hartree-Fock calculations were made with ORCA 4.0.1 [243]. Detailed information about optimized geometries, electronic energies, T1 diagnostics, vibrational frequencies, hindered rotor potentials, and ROHF treatments can be found in Appendix A.

### 3.2.2 Temperature and Pressure Dependent Rate Coefficients

We derived the phenomenological rate coefficients based on the entire PES, in the temperature range of 200–3000 K and pressure range of 0.01–100 atm. It was done by using the MESS [245, 246] code, which utilizes the RiceRamspergerKasselMarcus theory combined with Master Equation (RRKM/ME). The reactions having distinct barriers were treated according to transition state theory (TST) whereas barrierless steps (i.e., the capture of the bimolecular reactants and the dissociation into bimolecular products in this system) were treated according to long-range

transition state theory [282]. The pre-factor  $C_n$  and exponent  $n$  of their interaction potential  $V = -C_n/R^n$  were chosen based on Ref. 282 as input for number of states calculations by phase space theory provided by the MESS code. These parameters are provided in the *SI* along with detailed explanations. For the entrance channels, the number of states for the outer and inner transition states was evaluated independently. Approximations such as the Two Transition State (2TS) method were not applied, however, they were tested and comparisons on the results are provided in the *SI*. For the sum and density of states of the stationary points, non-torsional vibrational modes were treated as independent rigid-rotor harmonic oscillators. Torsional modes were represented as 1D hindered rotors, whose potential profiles were scanned with increments of 30 using B2PLYP-D3/cc-pVTZ. Collisional energy transfer was represented by a single exponential down model  $200(T/300)^{0.85} \text{ cm}^{-1}$ , which is typical for the reactive system considered [283]. Collision frequency was calculated using the Lennard Jones (LJ) model. For the bath gas  $\text{N}_2$ , the LJ parameters,  $\sigma_{\text{N}_2} = 3.681 \text{ \AA}$ ,  $\varepsilon_{\text{N}_2} = 67.89 \text{ cm}^{-1}$ , were taken from Ref. 284. The LJ parameters for the  $\text{C}_2\text{H}_3\text{O}_2$  wells,  $\sigma_{\text{C}_2\text{H}_3\text{O}_2} = 5.182 \text{ \AA}$ ,  $\varepsilon_{\text{C}_2\text{H}_3\text{O}_2} = 285.2 \text{ cm}^{-1}$ , were taken from Ref. 285. Quantum tunneling corrections were associated with all distinct barriers using the one-dimensional (1D) Eckart model.

The overall rate constant  $k_{\text{overall}}$  for  $\text{CH}_2\text{CO} + \text{OH} \longrightarrow \text{products}$  was obtained directly from the RRKM/ME results, which is equal to the sum of the rate constants  $k_i$  for all the channels starting from the reactants. The overall rate constant  $k_{\text{pathway}i}$  for an individual pathway was obtained by performing RRKM/ME calculations on the PES of that specific pathway. This approach is valid since there is no interconnection between pathways in this reaction system. The branching ratio (*BR*) of each reaction channel is calculated as  $BR_i = k_i/k_{\text{overall}}$ . In order to be integrated into kinetic mechanisms, the rate coefficients were fitted into modified Arrhenius expressions and formatted into inputs of kinetic modeling software CHEMKIN [286]. PLOG formalism [287] was used to parameterize pressure-dependent rate constants.

## 3.3 Results

### 3.3.1 Potential Energy Surface

We obtained a PES with 35 stationary points and its dominant pathways are depicted in Figure 3-1a. The reaction proceeds via a common Van der Waals complex (RC) and branches through 3 distinct pathways, namely:

- (**Pathway 1**) starts with a H atom abstraction by the OH radical (TS1), which gives product  $\text{HCCO} + \text{H}_2\text{O}$  (P1);
- (**Pathway 2**) starts with OH radical addition on the olefinic carbon atom ( $C_\alpha$ ) of ketene (TS2), which produces  $\text{CH}_2\text{OH} + \text{CO}$  (P2) and other products;
- (**Pathway 3**) starts with OH radical addition on the carbonyl carbon atom ( $C_\beta$ ) of ketene (TS10), which generates  $\text{CH}_3 + \text{CO}_2$  (P8) or  $\text{CH}_2\text{COOH}$  (INT3).

On these pathways, the structures of the reactive complex (RC) and three important transition states (TS1, TS2 and TS10) are shown in Figure 3-1b. The

entire PES (including insignificant channels) is provided in Appendix A. A detailed description of the PES and comparison with that from Hou *et al.* [12] are presented in the discussion section. Then the rate coefficients are obtained using RRKM/ME calculations based on the entire PES.

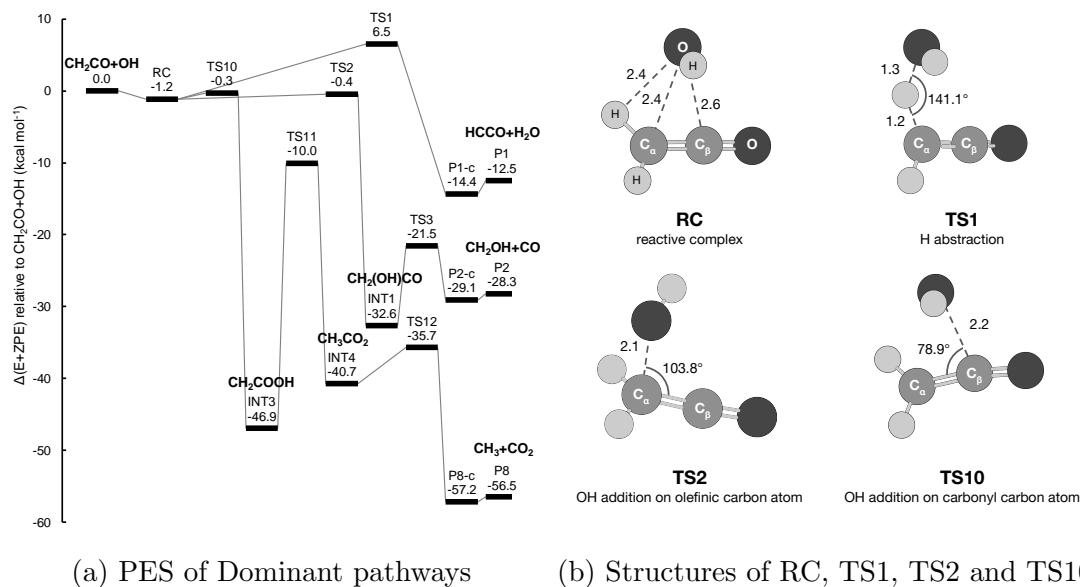
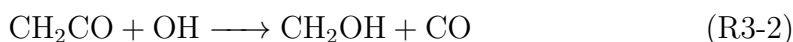
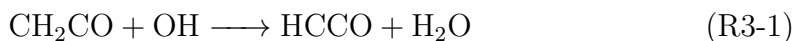


Figure 3-1: Main features of the CH<sub>2</sub>CO + OH potential energy surface. (a) Dominant pathways of the reaction, showing the relative electronic energy (corrected by ZPE) of the most relevant stationary points. (b) Structures of the reactive complex (RC) and transition states TS1, TS2 and TS10. Critical distances and angles are displayed in angstroms and in degrees, respectively. C<sub>α</sub> and C<sub>β</sub> are the olefinic and carbonyl carbon atoms in ketene respectively.

### 3.3.2 Rate Coefficients

The rate constants ( $k_{\text{overall}}$ ) at different pressures for the overall reaction CH<sub>2</sub>CO + OH → products are presented in Figure 3-2. Experimental values measured by Brown *et al.* [6], Hatakeyama *et al.* [8], Oehlers *et al.* [9] and the lower limit measured by Faubel *et al.* [7] are compared with our calculations. The rate expression recommended by Baulch *et al.* [10] are also plotted in Figure 3-2 with a surrounding gray area marking the uncertainty.

Concerning the rate coefficients for individual channels, it is found that the reaction is dominated by 4 significant product channels, as other channels are negligible over the entire temperature and pressure range of the investigation.



R3-1 and R3-2 are pressure independent and they dominate Pathway 1 and Pathway 2 respectively. R3-3a and R3-3b are highly pressure dependent and they

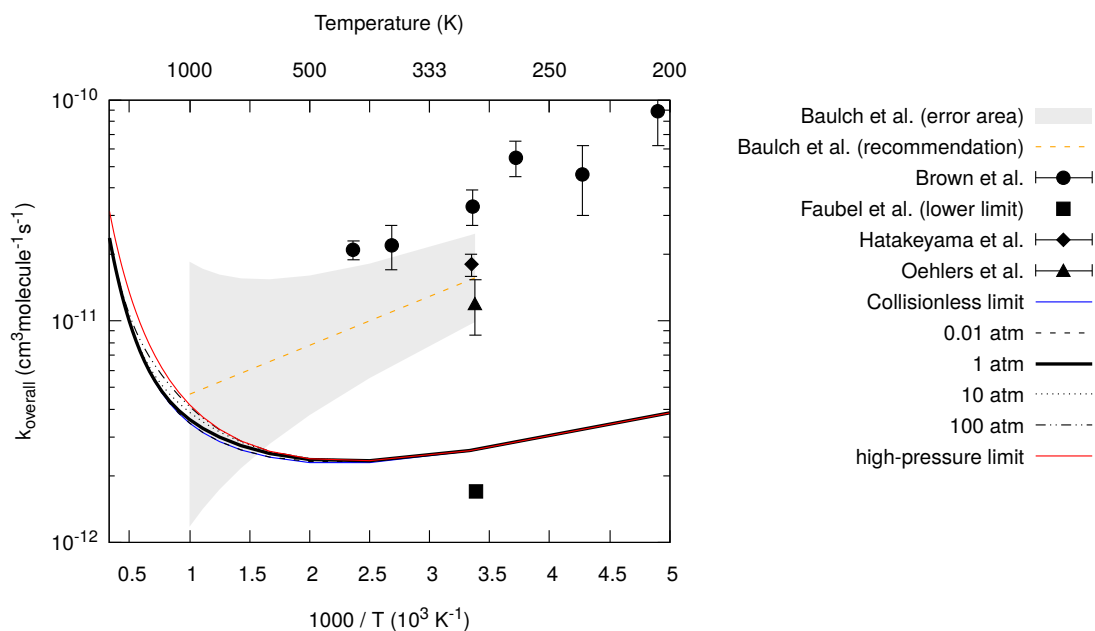


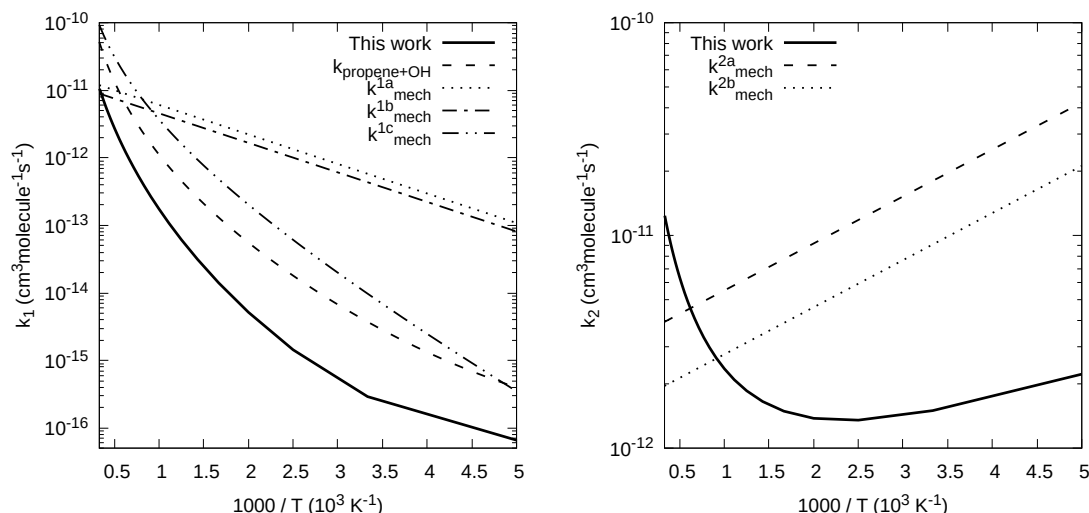
Figure 3-2: Rate constant for the overall reaction  $\text{CH}_2\text{CO} + \text{OH} \longrightarrow \text{Products}$ . Points are experimentally measured values by Brown *et al.* [6], Faubel *et al.* [7] (lower limit), Hatakeyama *et al.* [8] and Oehlers *et al.* [9]; the dashed line with gray error area is the recommendation by Baulch *et al.* [10]; The other lines are calculated values at different pressures (this work).

dominate Pathway 3 together. Their rate coefficients are presented in Figure 3-3, in comparison with some widely used rate parameters in kinetic mechanisms whose values are listed in Table 3.2 and rate coefficients of some analogous reactions.

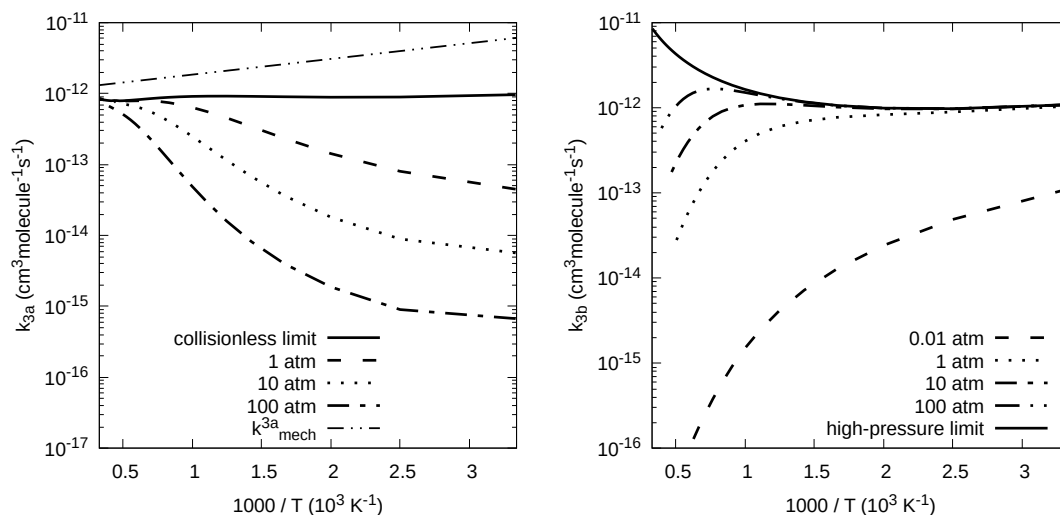
Table 3.2: Widely used rate parameters (in  $\text{cm}^3\text{molecule}^{-1}\text{s}^{-1}$ ) in kinetic mechanisms.  $N_A = 6.022 \times 10^{23}$  molecules  $\text{mol}^{-1}$  is the Avogadro's number, and  $R_u = 1.987$  cal  $\text{K}^{-1}\text{mol}^{-1}$  is the ideal gas constant.

reaction and rate parameters		source mechanism
R3-1	$\text{CH}_2\text{CO} + \text{OH} \longrightarrow \text{HCCO} + \text{H}_2\text{O}$ $k_{\text{mech}}^{1a} = \frac{1 \times 10^{13}}{N_A} \exp\left(-\frac{2000}{R_u T}\right)$ $k_{\text{mech}}^{1b} = 0.75 k_{\text{mech}}^{1a}$ $k_{\text{mech}}^{1c} = \frac{1 \times 10^7}{N_A} T^2 \exp\left(-\frac{3000}{R_u T}\right)$	LLNL [25, 288], Aramco Mech 3.0 [289, 290] GRI Mech 3.0 [291], USC Mech II [104], JetSurf 2.0 [292] Gimenez-Lopez <i>et al.</i> [293]
R3-2	$\text{CH}_2\text{CO} + \text{OH} \longrightarrow \text{CH}_2\text{OH} + \text{CO}$ $k_{\text{mech}}^{2a} = \frac{2 \times 10^{12}}{N_A} \exp\left(\frac{1010}{R_u T}\right)$ $k_{\text{mech}}^{2b} = \frac{1 \times 10^{12}}{N_A} \exp\left(\frac{1013}{R_u T}\right)$	LLNL [25, 288], Aramco Mech 3.0 [289, 290], San Diego Mech [294, 295] Gimenez-Lopez <i>et al.</i> [293]
R3-3a	$\text{CH}_2\text{CO} + \text{OH} \longrightarrow \text{CH}_3 + \text{CO}_2$ $k_{\text{mech}}^{3a} = \frac{6.7 \times 10^{11}}{N_A} \exp\left(\frac{1013}{R_u T}\right)$	Gimenez-Lopez <i>et al.</i> [293]

The faster rate coefficients of R3-3b at low temperature or high pressure, with



(a)  $\text{CH}_2\text{CO} + \text{OH} \longrightarrow \text{HCCO} + \text{H}_2\text{O}$  (R3-1) (b)  $\text{CH}_2\text{CO} + \text{OH} \longrightarrow \text{CH}_2\text{OH} + \text{CO}$  (R3-2)

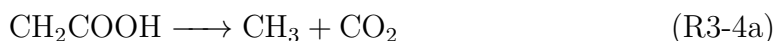


(c)  $\text{CH}_2\text{CO} + \text{OH} \longrightarrow \text{CH}_3 + \text{CO}_2$  (R3-3a) (d)  $\text{CH}_2\text{CO} + \text{OH} \longrightarrow \text{CH}_2\text{COOH}$  (R3-3b)

Figure 3-3: Temperature- and pressure-dependent rate coefficients of reaction channels R3-1–R3-3b.  $k_1$  and  $k_2$  are pressure independent whereas  $k_{3a}$  and  $k_{3b}$  are pressure dependent. In Figures 3-3a–3-3c, the present rate constants are compared with the rate parameters listed in Table 3.2 which are widely used in kinetic mechanisms. In Figure 3-3a,  $k_1$  is compared with the rate coefficients for the analogous reaction propene + OH  $\longrightarrow$  propen-1-yl + H<sub>2</sub>O calculated by Zádor *et al.* [11].

respect to R3-3a, indicate that CH<sub>2</sub>COOH could be collisionally stabilized at these conditions. Thus it is necessary to consider the secondary channels starting from CH<sub>2</sub>COOH to end products. Results show two significant secondary channels: (i) dissociation to bimolecular products CH<sub>3</sub> + CO<sub>2</sub> (R3-4a) and (ii) back dissociation

to the reactants (R3-4b).



Their rate coefficients are provided in Appendix A. In addition, by keeping only the significant channels (R3-1–R3-3b) and the significant secondary channels (R3-4a and R3-4b), the multi-channel reaction is simplified into a reduced system which is provided in Appendix A.

### 3.3.3 Branching Ratios

From the rate coefficients for the individual channels and the overall reaction, branching ratios are obtained as  $BR_i = k_i/k_{\text{overall}}$ . Figure 3-4 presents the calculated branching ratios for the significant product channels (R3-1–R3-3b). For the branching ratios at 1 atm shown in Figure 3-4a, they are compared with the values calculated by Hou *et al.* [12]. Results show that the  $\text{CH}_2\text{OH} + \text{CO}$  product channel (R3-2) is the most dominant one over the entire range of conditions investigated.  $\text{HCCO} + \text{H}_2\text{O}$  product channel (R3-1) becomes dominant at high temperature.  $\text{CH}_3 + \text{CO}_2$  (R3-3a) and  $\text{CH}_2\text{COOH}$  (R3-3b) product channels are highly pressure dependent and they compete with each other within Pathway 3.

## 3.4 Discussion

In order to obtain the rate coefficients, it is necessary to refine the previous PES obtained by Hou *et al.* [12] in terms of (i) the accuracy of molecular properties such as energy, vibrational and rotational modes and (ii) the number of stationary points which enriches the detail of the PES. Using the method explained in Section 3.2.1, the total relative energies calculated in this work are expected to have better accuracy and are found mostly lower than that of MP2/6-31G(d,p) [12], by 2.3 kcal mol<sup>-1</sup> on average for transition states, 3.1 kcal mol<sup>-1</sup> on average for unimolecular wells and 0.8 kcal mol<sup>-1</sup> on average for bimolecular products. The main difference is the relative height in energy between the reactants and OH addition barriers (TS2 and TS10). In the work by Hou *et al.* [12] TS2 and TS10 are slightly higher than the reactants (by 1.0 and 1.1 kcal mol<sup>-1</sup> respectively), whereas in this work they are submerged under the reactants by 0.4 and 0.3 kcal mol<sup>-1</sup> respectively. Because of the low barrier heights, their relative position with respect to the reactants can have significant impacts on overall reaction kinetics. In addition, the calculated imaginary frequencies of transition states in this work are lower than that of Hou *et al.* [12] by 640 cm<sup>-1</sup> on average.

The elementary reaction channels in our PES are mostly in agreement with the previous work [12], except for the channel from  $\text{CH}_2(\text{OH})\text{CO}$  (INT1) to  $\text{HCCO} + \text{CO}$  (P1) [12]. This specific point is discussed later in section 3.4.2. It is worth noting that OH addition might also happen on the O atom of ketene forming  $\text{CH}_2\text{CHOO}$ , which might further lead to  $\text{C}_2\text{H}_3 + \text{O}_2$  and  $\text{C}_2\text{H}_2 + \text{HO}_2$ . However, we did not include this pathway because: (i) we did not find the reaction possible in this direction according to our calculation; (ii) if assuming the same barrier as the reverse direction  $\text{CH}_2\text{CHOO} \longrightarrow \text{CH}_2\text{CO} + \text{OH}$  which is calculated by Goldsmith



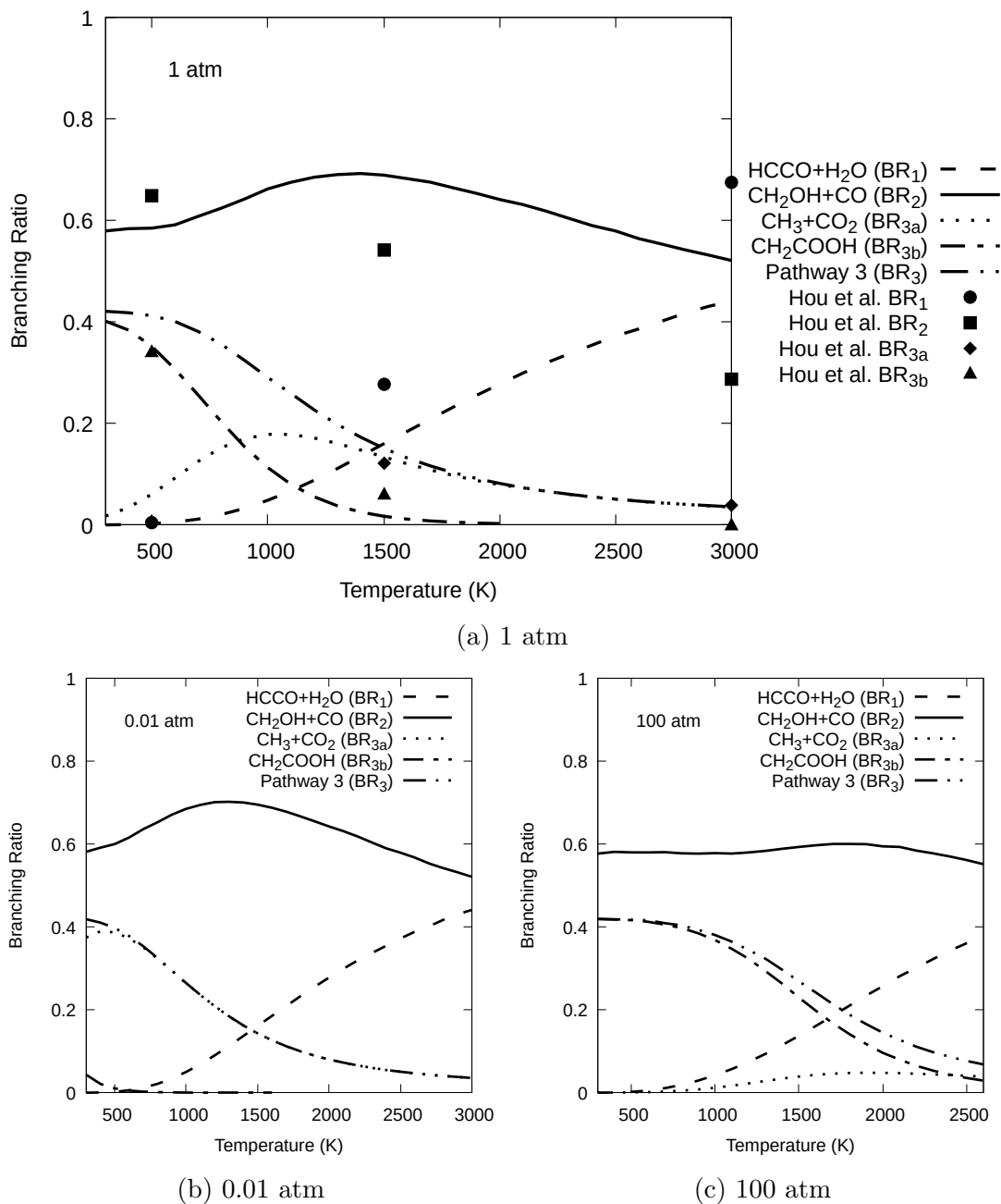


Figure 3-4: Branching ratios of primary product channels at different temperatures and pressures. lines: calculated values for the 4 major product channels by this work; points: RRKM calculations by Hou *et al.* [12].

*et al.* [283], it is too high ( $\sim 80 \text{ kcal mol}^{-1}$ ) to affect the overall kinetics even at high temperatures; (iii) if assuming the same barrier as the reverse direction, these channels and their rate coefficients are already provided [283, 296]. We examined bimolecular Van der Waals interactions and included one reactive complex (RC) and 5 product complexes (P1-c, P2-c, P5-c, P7-c, P8-c). We found that the  $\text{CH}_2\text{CO}$  and OH molecules dock with each other through a barrierless process to form a reactive complex (RC) before undergoing any reactions. Although we did locate several other complexes (local minimas), they were all discarded because that IRC analysis shows all the possible reaction pathways start from RC. In the

optimized structure of RC shown in Figure 3-1a, the hydroxyl radical is located above the ketene plane with its O atom having similar distance to the H atom (2.4 Å), olefinic carbon atom (2.4 Å) and carbonyl carbon atom (2.6 Å) of the ketene molecule, indicating the possibility of RC to further go through the three distinct reaction pathways. It is similar to the reactive complexes for ethylene + OH [297] and propene + OH [11] reactions, in terms of the orientation of OH towards the C=C double bond plane (approximately perpendicular in the three systems) and the well depth (1.2, 1.9 and 2.2 kcal mol<sup>-1</sup> respectively). In addition, the shallow well of RC makes the low barriers of OH addition (i.e., TS2 and TS10) submerged under the reactants, which affect the overall kinetics especially at low temperatures. We also identified product complexes for 5 channels, preceding their barrierless dissociation to bimolecular products. The dissociation energies from the complexes are small, varying from 0.6 to 1.9 kcal mol<sup>-1</sup>. Although these energies can be easily achieved by the excess energy possessed by the molecules after crossing the transition states, we still include them for high-pressure regimes.

### 3.4.1 Pathway 1: H Abstraction

Starting from RC, the O atom in the hydroxyl radical can abstract one H atom from ketene, which goes through a transition state (TS1) of 7.7 kcal mol<sup>-1</sup> higher than RC. The barrier is higher than that for OH addition channels. The transition state is tight with an imaginary frequency of 1561 cm<sup>-1</sup>, which is within the typical range for H abstraction. As shown in the structure of RC (Figure 3-1a), the hydroxyl radical approaches towards the surface, not the side as one might expect, of the ketene plate with the  $O \cdots H - C$  angle of 77.1°. This is consistent with the fact that the transition state for H abstraction is not collinear with the  $O \cdots H \cdots C$  angle of 141.1°. The  $O \cdots H$  and  $H \cdots C$  distance are 1.3 and 1.2 Å respectively. This non-collinear H abstraction phenomenon is in agreement with previous electronic structure studies [12, 262]. IRC calculations show that the molecule goes through a complex (P1-c) before separating into the two product fragments H<sub>2</sub>O and ketyl radical (HCCO), which requires small dissociation energy of 1.9 kcal mol<sup>-1</sup>.

Calculated from the electronic structures mentioned above, the rate constant  $k_1$  for H abstraction product channel  $\text{CH}_2\text{CO} + \text{OH} \longrightarrow \text{HCCO} + \text{H}_2\text{O}$  (R3-1) is highly temperature-dependent, as shown in Figure 3-3a. The increase is as large as 5 orders of magnitude, from  $6.6 \times 10^{-17}$  cm<sup>3</sup>molecule<sup>-1</sup>s<sup>-1</sup> at 200 K to  $1.05 \times 10^{-11}$  cm<sup>3</sup>molecule<sup>-1</sup>s<sup>-1</sup> at 3000 K, meaning that this channel is only favorable at high temperatures. This is expected behavior due to the high energetic barrier associated with TS1. A change of pressure does not appear to have an effect on rate coefficients, as the reactive complex can not be collisionally stabilized. Shown in Figure 3-3a, the calculated values were compared with that of the analogous reaction propene + OH  $\longrightarrow$  propen-1-yl + H<sub>2</sub>O which were calculated theoretically by Zdor *et al.* [11].  $k_{\text{propene+OH}}$  is found to be higher than  $k_1$  by about a factor of 5 at 3000 K and factor of 10 at 300 K. This could be due to that the barrier heights of abstraction for ketene + OH (6.5 kcal mol<sup>-1</sup>) is slightly higher than that for propene + OH which is around 4.5 kcal mol<sup>-1</sup> (averaged between cis- and trans-isomers of propen-1-yl) [11].  $k_1$  was also compared with the rate parameters  $k_{\text{mech}}^{1a}$ – $k_{\text{mech}}^{1c}$  used in kinetic mechanisms.  $k_{\text{mech}}^{1a}$  and  $k_{\text{mech}}^{1b}$  are significantly higher than  $k_1$ ,

especially at low temperatures. The discrepancies are still considerable between 1000 and 3000 K, which is the temperature range of interest for combustion, with over one magnitude of difference at 1000 K. Unlike  $k_{\text{mech}}^{1a}$  and  $k_{\text{mech}}^{1b}$ ,  $k_1$  exhibits curvature on the Arrhenius plot, due to the quantum tunneling effect which contributes to increasing the rate coefficients especially at low temperature and with a tight transition state (such as TS1). It is worth noting that better treatment can result in a higher  $k_1$  at low temperatures. For instance, 1D tunneling treatments with more accurate representations of the barrier (e.g., Harmonic or Quartic barrier) with respect to the Eckart barrier (used in the present work) result in higher  $k_1$ , which is demonstrated in Appendix A. In addition, multidimensional tunneling, e.g., Small Curvature Tunneling (SCT) method and Semiclassical Instanton Theory, can result in even higher values of  $k_1$ . The corner cutting effect introduced by these methods reduces the barrier width and thus increases significantly the tunneling transmission coefficient. We expect the tunneling effect to be even more significant at very low temperatures ( $< 200$  K) which we did not investigate. We recommend applying corrections using these methods if a proper value for  $k_1$  is needed at very low temperatures. The bending curve indicates that a non-zero temperature exponent  $n$  is needed for interpreting  $k_1$  in modified Arrhenius expressions. Therefore the  $k_{\text{mech}}^{1c}$  used in the mechanism by Gimenez-Lopez *et al.* [293], having  $n = 2$ , captures this temperature dependency sufficiently.

### 3.4.2 Pathway 2: OH Addition on the Olefinic Carbon Atom

Because the electron density is higher around the two carbon atoms than that of the hydrogen atoms, it can be predicted that the addition of hydroxyl radical on carbon atoms should be easier and have lower barriers than H abstraction. Calculation results agree with this prediction by giving a much lower barrier height ( $0.7 \text{ kcal mol}^{-1}$ ) for the OH addition on olefinic carbon. The transition-state for this process (TS2) is found to be early and loose, since its structure is close to RC and has a low imaginary frequency of  $169 \text{ cm}^{-1}$ . It can also be seen from the  $O \cdots C$  distance on the critical translational degree of freedom which is as long as  $2.1 \text{ \AA}$  and the little deviation of ketene molecule from its original structure. Although higher than RC, the energy of TS2 lies lower than the reactants by  $0.4 \text{ kcal mol}^{-1}$ . Thus the reaction may have similar characteristics as barrierless processes because of the submerged TS. The OH addition on  $C_\alpha$  forms adduct  $\text{CH}_2(\text{OH})\text{CO}$  (INT1), whose well depth is  $32.6 \text{ kcal mol}^{-1}$ . This energy reduction by addition is found higher than that of analogous systems such as OH addition on alkenes, which are reported to be  $26.2 \text{ kcal mol}^{-1}$  for ethylene + OH [297], and  $27.2 \text{ kcal mol}^{-1}$  (terminal addition) or  $28.2 \text{ kcal mol}^{-1}$  (central addition) for propene + OH [11]. This could be explained by the structural difference between ketene and alkenes, i.e., the nature of the carbon atom in ketene on the opposite site to the addition (i.e., the  $C_\beta$ ) is not olefinic but carbonyl ( $\text{C}=\text{O}$ ). The different electron density caused can lead to the difference in the energy reduced. In addition, part of the difference results from the different levels of theory used for electronic structure calculations. Despite of the presence of the deep well, the intermediate  $\text{CH}_2(\text{OH})\text{CO}$  (INT1) is unlikely to be stabilized because of the excess energy of the molecule after crossing the barrier and the relatively lower barrier of the

dissociation (TS3, 11.1 kcal mol<sup>-1</sup>) into bimolecular products CH<sub>2</sub>OH + CO by breaking the C–C bond.

Besides the most favorable pathway leading to CH<sub>2</sub>OH + CO, we found several possible transformations for CH<sub>2</sub>(OH)CO (details provided in Appendix A): (i) H atom migration from C<sub>α</sub> to C<sub>β</sub> (TS4), (ii) H atom migration from hydroxy group to C<sub>β</sub> (TS5) and (iii) H atom elimination (TS9). But the barrier heights of these pathways (37.1, 46.6 and 52.9 kcal mol<sup>-1</sup> in the same order) are higher than that of the C–C bond scission (11.1 kcal mol<sup>-1</sup>). It indicates that these channels are slow and unlikely to have dominant impacts on the overall reaction kinetics except at exceptionally high temperatures, which is confirmed by RRKM/ME calculations. The migration of H atom from C<sub>α</sub> to C<sub>β</sub> forms CH(OH)CHO (P6). This structure is considered to be a product molecule, because the barrier for it to be thermally disassociated into CHO and hydroxymethylene (HCOH) is very high (around 90 kcal mol<sup>-1</sup>). However, this step is still possible at very high temperatures. The HCOH molecule generated has two unpaired electrons and thus is short-lived to form formaldehyde rapidly. [298] Even so, it is still possible for HCOH to react with hydroxyl radical to produce CO<sub>2</sub>, H<sub>2</sub> and H radical. [299] Hou *et al.* [12] recorded a transition state for H atom migration onto the hydroxy group to eliminate a H<sub>2</sub>O molecule and ketyenyl radical, which is the product of Pathway 1. We did not include it in this work because that (i) it could not be reproduced by B2PLYP-D3/cc-PVTZ and that (ii) its barrier [12] (65.3 kcal mol<sup>-1</sup>) is too high to influence the kinetics of the reactions even at combustion temperatures.

The migration of H atom of the hydroxy group onto C<sub>β</sub> results in the isomerization to CH<sub>2</sub>(O)CHO (INT2). The barrier for this transformation is quite high (46.6 kcal mol<sup>-1</sup>) and the resulted CH<sub>2</sub>(O)CHO is not stable. It is easy to disassociate into HCO radical and CH<sub>2</sub>O by C-C bond scission requiring only 8.14 kcal mol<sup>-1</sup> (TS6). Two less favorable channels for CH<sub>2</sub>(O)CHO transformation exist: (i) H atom elimination producing H + (CHO)<sub>2</sub> (TS7, 23.9 kcal mol<sup>-1</sup>) and (ii) H atom migration to O atom forming CH(OH)CHO with a hydroxy group (TS8, 36.6 kcal mol<sup>-1</sup>). Despite the fast rate of C-C bond scission, the fate of the CHO + CH<sub>2</sub>O product channel depends on the isomerization from CH<sub>2</sub>(OH)CO (INT1) to CH<sub>2</sub>(O)CHO (INT2), which is the highest barrier (TS5) along its pathway. Giving the slow rate of TS5, the CHO + CH<sub>2</sub>O product channel is unlikely to be a dominant pathway as previously assumed.

The rate coefficients and branching ratios calculated are consistent with the estimation above. The pathway is dominated by the product channel CH<sub>2</sub>CO + OH → CH<sub>2</sub>OH + CO (R3-2), while other channels are too slow to contribute to the overall kinetics. The rate constant  $k_2$ , as shown in Figure 3-3b, is found to have opposite temperature dependencies between low- and high-temperature regimes. It decreases from 2.2 to  $1.4 \times 10^{-12}$  cm<sup>3</sup>molecule<sup>-1</sup>s<sup>-1</sup> as temperature increases from 200 to 400 K. Then it rises when the temperature gets higher than 400 K, to as fast as  $1.24 \times 10^{-11}$  cm<sup>3</sup>molecule<sup>-1</sup>s<sup>-1</sup> at 3000 K. The minimum point, where temperature dependency shows a regime switch, occurs at around 400–500 K. The negative temperature dependence at low temperatures is in accord with the measurements by Brown *et al.* [6]. This could be explained by the relative situation of the capture and re-dissociation of the reactive complex (RC) versus the subsequent crossing of the submerged barrier (TS2). [300] At low temperatures, the averaged energy of TS2 is lower than that of the reactants, which results

in negative apparent activation energy. At higher temperature, the increase of vibrational energy makes the averaged energy of TS2 higher than that of the reactants, which leads to positive apparent activation energy. [301]  $k_2$  is found independent of pressure, which is different to the high pressure dependency of the ethylene + OH and propene + OH addition reactions [11, 297]. This could result from the submerged nature and the low barrier height of TS3 which, as mentioned previously, makes  $\text{CH}_2(\text{OH})\text{CO}$  unlikely to be stabilized. As it can be seen in Figure 3-3b, the commonly used rate parameters  $k_{\text{mech}}^{2a}$  and  $k_{\text{mech}}^{2b}$  are about one magnitude higher than the calculated results and do not capture the shift in temperature dependency. By tracing the source, they are found to be obtained by fitting the experimental results of Brown *et al.* [6] and then extrapolating them to high temperatures. They are not expected to be accurate enough because the original data were measured (i) for the total rate constant ( $\text{CH}_2\text{CO} + \text{OH} \longrightarrow \text{products}$ ) and (ii) at low temperatures between 193 and 423 K. Clearly, the rate parameters in current kinetic mechanisms should be updated to better describe the temperature dependency of  $k_2$ .

### 3.4.3 Pathway 3: OH Addition on the Carbonyl Carbon Atom

For OH radical to attack the carbonyl carbon ( $C_\beta$ ) of ketene, small and submerged barrier (TS10) was also found due to the high electron density around the carbon atom. The barrier is slightly higher than the addition on olefinic carbon (TS2) by only  $0.1 \text{ kcal mol}^{-1}$ , and lying under the reactants ( $-0.3 \text{ kcal mol}^{-1}$ ). This transition state is also an early and loose one, with a low imaginary frequency of  $260 \text{ cm}^{-1}$  and a  $O \cdots C$  distance of  $2.2 \text{ \AA}$  which is close to the reactive complex. The addition leads to the intermediate carboxymethyl radical  $\text{CH}_2\text{COOH}$  (INT3), which is a very deep well, since the energy to climb up both sides are high (barrier over TS10 is  $46.6 \text{ kcal mol}^{-1}$  and barrier over TS11 is  $36.0 \text{ kcal mol}^{-1}$ ). In a system with intense collisional energy transfer or with low kinetic energy, molecules can be stabilized into  $\text{CH}_2\text{COOH}$  and trapped in this well. If not stabilized, the molecules can easily overcome TS11 where the hydrogen atom on the hydroxy group of  $\text{CH}_2\text{COOH}$  migrates to the carbon atom to form  $\text{CH}_3\text{CO}_2$  (INT4). The  $\text{CH}_3\text{CO}_2$  produced are usually with excess energy which can overcome the low barrier of TS12 and dissociate into bimolecular products  $\text{CH}_3 + \text{CO}_2$ . If the excess energy is sufficiently high,  $\text{CH}_3\text{CO}_2$  is isomerized into  $\text{CH}_3\text{OCO}$  (INT5) which can further dissociate into  $\text{CO} + \text{CH}_3\text{O}$  or  $\text{CO}_2 + \text{CH}_3$  (details provided in Appendix A).

As mentioned in the section 3.3.2, Pathway 3 is dominated by the  $\text{CH}_3 + \text{CO}_2$  product channel (R3-3a) and the collisional stabilization of  $\text{CH}_2\text{COOH}$  (R3-3b). As shown in Figure 3-3c,  $k_{3a}$  depends positively on temperature but negatively on pressure. It increases with temperature and flattens at around 3000 K, while higher pressure reduces  $k_{3a}$  dramatically especially at low temperatures. The effect of pressure is weakened as temperature rises until it can be neglected at 3000 K. At very low pressures,  $k_{3a}$  reaches its collisionless limit at around  $1 \times 10^{-12} \text{ cm}^3 \text{ molecule}^{-1} \text{ s}^{-1}$ . Gimenez-Lopez *et al.* [293] used a rate parameter  $k_{\text{mech}}^{3a}$  which is estimated from  $k_{\text{mech}}^{2a}$  using the branching ratio obtained by Grussdorf *et al.* [261]. Thus it is normal that it has a temperature dependency opposite to our results

$k_{3a}$ . As shown in Figure 3-3d, higher pressures promote stabilization of  $\text{CH}_2\text{COOH}$  greatly, especially at typical combustion temperatures (1000 - 3000 K) and  $k_{3b}$  exhibits negative temperature dependency especially at high temperatures. At its high-pressure limit, however, the temperature dependence of  $k_{3b}$  switches to positive, similar to that of  $k_2$ . This is because at the high-pressure limit collision process is so fast that it is not rate-determining and the capture of bimolecular reactants through the submerged barrier TS10 becomes the rate-limiting step. In addition, the dissociation of stabilized  $\text{CH}_2\text{COOH}$  is possible but found to have considerable rates only at high temperatures and most probably into bimolecular product  $\text{CH}_3 + \text{CO}_2$  (R3-4a). At temperature over 1000 K, it is possible to dissociate back to the bimolecular reactants  $\text{CH}_2\text{CO} + \text{OH}$  (R3-4b). The rate parameters for R3-3a–R3-4b and the species  $\text{CH}_2\text{COOH}$  are not included in many kinetic mechanisms. Thus it is necessary to include them, since reaction R3-3b dominates at low temperatures and high pressures which are relevant conditions for new Internal Combustion Engine (ICE) technologies.

The overall rate coefficients of this pathway  $k_3$  are obtained and depicted in Figure 3-5. As temperature increases,  $k_3$  first decreases ( $< 500$  K), then increases (500–1000 K) and decreases again at high temperature ( $> 1000$  K). This temperature dependence is the composite effect that originated from that of  $k_{3a}$  and  $k_{3b}$ . Moderate pressure effect is spotted at 500–3000 K where higher pressures accelerate the reactions. These variations are results of cancellation effects between  $k_{3a}$  and  $k_{3b}$  since they are both highly temperature- and pressure-dependent but exhibiting opposite trends. The dissociation to bimolecular product  $\text{CH}_2\text{CO} + \text{OH} \longrightarrow \text{CH}_3 + \text{CO}_2$  (R3-3a) is the most favorable at low pressures and high temperatures, whereas the collisional stabilization of  $\text{CH}_2\text{CO} + \text{OH} \longrightarrow \text{CH}_2\text{COOH}$  (R3-3b) dominates at high pressures and low temperatures. It is worth noting that the collisionless limit of  $k_3$  is the same as  $k_{3a}$  and the high-pressure limit is the same as  $k_{3b}$ . The high-pressure limit of  $k_3$  is also compared with  $k_2$ , as they both affect the kinetics of the entrance channels of OH addition. They present similar trends in temperature dependency but  $k_3$  is slightly lower than  $k_2$  due to the fact that TS10 is higher than TS2 by only 0.1 kcal mol<sup>-1</sup>.

### 3.4.4 Overall Rate Constant

As shown in Figure 3-2, experimental values of the overall rate constant  $k_{\text{overall}}$  are scarce and mostly measured at low temperature (200–500 K). Among available data of  $k_{\text{overall}}$  at around standard condition (298 K and 1 atm), Oehlers *et al.* [9] reported  $1.2 \times 10^{-11}$  cm<sup>3</sup>molecule<sup>-1</sup>s<sup>-1</sup>, Hatakeyama *et al.* [8] reported  $1.8 \times 10^{-11}$  cm<sup>3</sup>molecule<sup>-1</sup>s<sup>-1</sup>, and Brown *et al.* [6] reported  $3.3 \times 10^{-11}$  cm<sup>3</sup>molecule<sup>-1</sup>s<sup>-1</sup>. The rate constants vary between each other within a factor of 3. In addition, Faubel *et al.* [7] provided a lower limit of  $1.7 \times 10^{-12}$  cm<sup>3</sup>molecule<sup>-1</sup>s<sup>-1</sup>. Our calculated value under the same condition ( $2.6 \times 10^{-12}$  cm<sup>3</sup>molecule<sup>-1</sup>s<sup>-1</sup>) is slightly higher than the lower limit but significantly lower than other measured values by about a factor of 5. The reason for this discrepancy could be multi-fold and from the uncertainty in different steps of the calculations. It could partly originate in the uncertainty in the calculated total electronic energy, especially for that of TS2 and TS10, the inner transition states for Pathway 2 and 3 respectively, which may affect  $k_{\text{overall}}$  at low temperature. They are assessed through sensitivity analysis

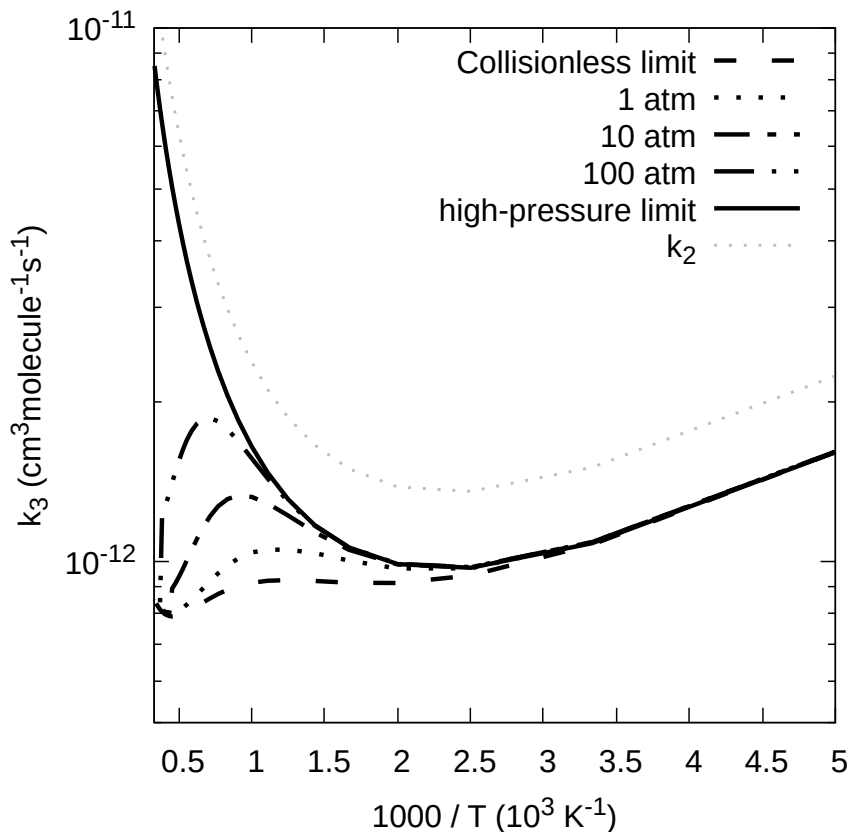


Figure 3-5: Overall rate coefficients for Pathway 3 (OH addition on the carbonyl carbon atom) at different temperatures.

later in section 3.4.7 and the resulting uncertainties are significant especially at low temperatures. Different treatments on quantum tunneling effects also introduce uncertainties, especially for the H abstraction reaction at low temperature, as mentioned in section 3.4.1. It is expected that by applying multidimensional tunneling models instead of the 1D models currently used in this work,  $k_1$  may increase significantly at low temperatures. The 1D hindered rotor approximation may introduce some uncertainty in the partition functions and thus the rate coefficients. Thus more accurate modeling of anharmonicity might improve the accuracy. In our electronic structure calculations, multireference behavior is possible for TS15 ( $T_1=0.043$ ) (geometry can be found in Appendix A). Although TS15 is less possible to affect the overall kinetics because of its high barrier, a multireference treatment on related channels would provide some more accuracy. Possible roaming channels that are not studied in the present work might also alter rate coefficients.

A negative temperature dependency was observed at low temperatures ( $< 400\text{ K}$ ), which is in accord with the experimental results from Brown *et al.* [6]. But at higher temperatures ( $> 400\text{ K}$ ), the temperature dependency shifts to positive. This behavior is the same as R3-2 and can be easily explained by the fact that R3-2 always composes the major share in  $k_{\text{overall}}$  with  $BR_2$  remain as high as 50%–70% over the entire temperature range studied (see in section 3.4.5). Slight positive pressure dependency of  $k_{\text{overall}}$  was found at typical combustion

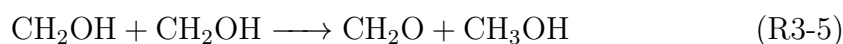
temperatures (500–3000 K) while it is negligible at low temperatures ( $< 500$  K). Since  $k_1$  and  $k_2$  are pressure independent, the slight pressure dependence comes from  $k_3$ . Similarly, the collisionless and high-pressure limits are defined by that of  $k_3$ .

### 3.4.5 Branching Ratios

It can be seen from Figure 3-4 that the most dominant channel is always the production of  $\text{CH}_2\text{OH} + \text{CO}$  (R3-2), whose fraction  $BR_2$  varies between 50% and 70% over all conditions. As temperature increases,  $BR_2$  rises from  $\sim 60\%$  to maximum  $\sim 70\%$ , before it falls and reaches  $\sim 50\%$  at 3000 K. The H abstraction channel (R3-1) is highly temperature dependent because of its relatively high barrier (with respect to R3-2–R3-3b).  $BR_1$  rises rapidly from almost zero (0.2%) at 500 K to almost half (44%) at 3000 K. Although  $BR_1$  is still lower than  $BR_2$  at 3000 K, it is expected to surpass  $BR_2$  at a higher temperature if we assume the same trends. This result is different than the RRKM calculations by Hou *et al.* [12], which indicate that  $BR_2$  always decreases with temperature and the overtake by  $BR_1$  happens quite early given that  $BR_1 \approx 65\%$  and  $BR_2 \approx 30\%$  at 3000 K. Opposite to  $BR_1$ , the total share of Pathway 3 decreases with temperature from  $\sim 40\%$  at 300 K to  $\sim 5\%$  at 3000 K. The intercept where  $BR_1$  overtake  $RR_3$  is around 1500–2000 K depending on pressure. Since  $k_1$  and  $k_2$  are pressure independent, the total pressure dependency comes from Pathway 3, whose fraction rises with higher pressures. Within Pathway 3, the production of  $\text{CH}_3 + \text{CO}_2$  (R3-3a) and  $\text{CH}_2\text{COOH}$  (R3-3b) are in competition, for that the  $\text{CH}_2\text{COOH}$ , usually with excess energy when produced, either be stabilized or undergo isomerization forming  $\text{CH}_3 + \text{CO}_2$  eventually. Its positive pressure effect is because the promotion of  $k_{3b}$  by pressure exceeded the reduction of  $k_{3a}$ . Same as the conclusion in section 3.4.3, the stabilization to  $\text{CH}_2\text{COOH}$  depends greatly on and is favored at low temperatures or high pressures.

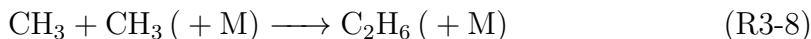
### 3.4.6 Product Formation

With the branching ratios concluded in the section 3.4.5, it is clear that the main products for  $\text{CH}_2\text{CO} + \text{OH}$  reaction are (i)  $\text{HCCO} + \text{H}_2\text{O}$  by H abstraction, (ii)  $\text{CH}_2\text{OH} + \text{CO}$  by OH addition on olefinic carbon, (iii)  $\text{CO}_2 + \text{CH}_3$  by OH addition on carbonyl carbon and (iv) collisionally stabilized  $\text{CH}_2\text{COOH}$  radical. This conclusion is in accord with Hou *et al.* [12]. The ketylenyl radical ( $\text{HCCO}$ ) generated is an important combustion intermediate and highly reactive. In combustion atmosphere, it can not only decompose into CO or  $\text{CO}_2$  by H, O, OH and  $\text{O}_2$ , [10, 302–305] but can also produce larger hydrocarbons by reacting with CH,  $\text{C}_2\text{H}_2$  and etc. [306–308] The  $\text{CH}_2\text{OH}$  radicals produced are of great excess energy, which make them likely to go through recombination reactions (R3-5) [309] or rapidly react with  $\text{O}_2$  (R3-6) [310, 311], producing formaldehyde ( $\text{CH}_2\text{O}$ ).

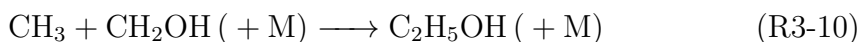
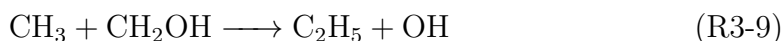




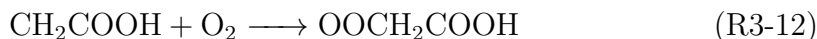
R3-5 and R3-6, instead of the channel  $\text{CH}_2\text{CO} + \text{OH} \longrightarrow \text{CHO} + \text{CH}_2\text{O}$ , are the main source of formaldehyde detected in experiments. [261] Similarly, the methyl radicals generated are most likely to recombine to form  $\text{C}_2\text{H}_5 + \text{H}$  (R3-7) or ethane through a third body reaction R3-8 [312,313].



The methyl radical may also recombine with  $\text{CH}_2\text{OH}$  to produce  $\text{C}_2\text{H}_5 + \text{OH}$  (R3-9), or  $\text{C}_2\text{H}_5\text{OH}$  (R3-10) if a collisional third body is present.



The collisionally stabilized  $\text{CH}_2\text{COOH}$  is also an important intermediate in the acetic acid ( $\text{CH}_3\text{COOH}$ ) oxidation mechanism [314]. It may react with H radical to form acetic acid by R3-11 and with  $\text{O}_2$  to form  $\text{OOCH}_2\text{COOH}$  by R3-12. [315]

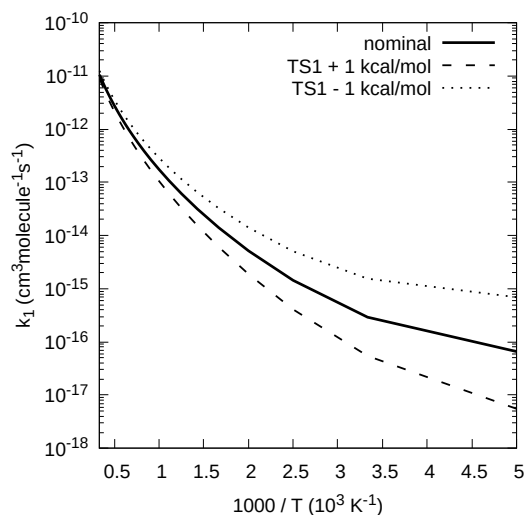


### 3.4.7 Sensitivity Analysis for TS1, TS2 and TS10

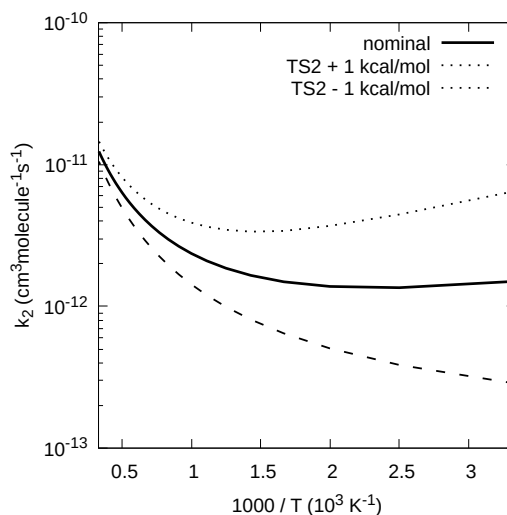
As mentioned in section 3.4.4, the uncertainty of the resulted rate coefficients could be partly attributed to the uncertainty in the electronic energy calculated. Concerning the PES of this reaction system, we expect that the entrance barriers affect significantly the rate coefficients of their corresponding pathways and the overall kinetics. In order to assess their impacts, we changed their energy artificially by  $\pm 1 \text{ kcal mol}^{-1}$ , the same as the uncertainty in our electronic energy calculations. The impacts on their corresponding pathways are presented in Figure 3-6 and the impacts on  $k_{\text{overall}}$  are presented in Figure 3-7.

Concerning the H abstraction pathway, tweaking the TS1 energy ( $\Delta E_{\text{TS1}}$ ) affects  $k_1$  significantly at low temperature (the relative change  $\Delta k/k_0 \approx 10$  at 200 K), as shown in Figure 3-6a. At high temperature, the impact is less significant with  $\Delta k/k_0 \approx 0.2$  at 3000 K. The more pronounced effect of lowering the barrier at low temperature can be explained by the fact that the probability of finding the reactant molecules with energy lower than the barrier, is higher at low temperatures. But this effect can not be projected onto  $k_{\text{overall}}$  because of the low branching ratio of  $k_1$  at low temperature (shown in Figure 3-7a). On the contrary, the effect of tweaking TS1 energy on  $k_{\text{overall}}$  becomes more marked at high temperatures because of the increasing branching ratio of  $k_1$ .

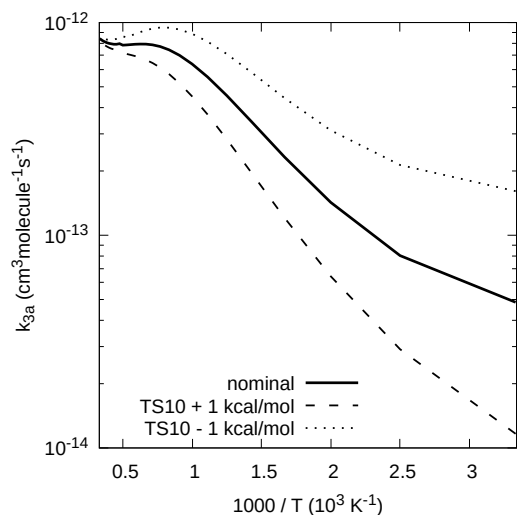
Concerning OH addition pathways (pathways 2 and 3), TS2 and TS10 are slightly submerged under the reactants ( $\Delta E_{\text{TS2}} = -0.4 \text{ kcal mol}^{-1}$  and  $\Delta E_{\text{TS10}} = -0.3 \text{ kcal mol}^{-1}$ ). They are very close to each other with only  $0.1 \text{ kcal mol}^{-1}$  of difference according to our calculations ( $0.07 \text{ kcal mol}^{-1}$  reported by Hou *et al.* [12]). If we consider the uncertainty of the method we use in Section 3.2.1 ( $\pm 1 \text{ kcal mol}^{-1}$ ), there is no way to be certain (i) whether TS2 and TS10 are actually



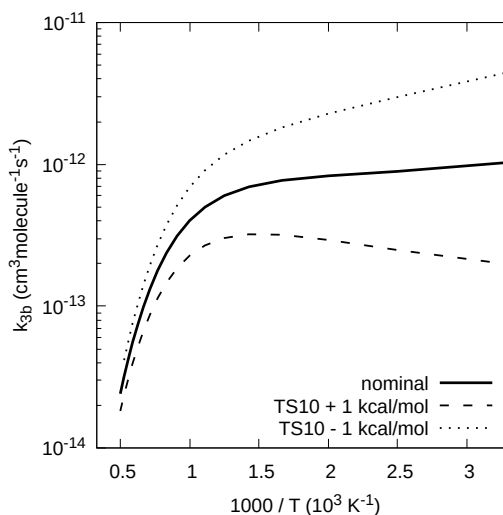
(a) Effect of TS1 energy on  $k_1$



(b) Effect of TS2 energy on  $k_2$



(c) Effect of TS10 energy on  $k_{3a}$



(d) Effect of TS10 energy on  $k_{3b}$

Figure 3-6: Effect of the uncertainty in TS1, TS2 and TS10 energies on the rate coefficients of their corresponding pathways at 1 atm. Effects at other pressures are qualitatively the same.

submerged and (ii) what the relative position of the two barriers are. Therefore we study not only their individual impacts but also their combined impact by tweaking them simultaneously in the same or opposite directions.

As shown in Figure 3-6b–3-6d, the effect of tweaking TS2 energy on  $k_2$ , and the effect of TS10 energy on  $k_{3a}$  and  $k_{3b}$ , are more significant at low temperature than at high temperatures, which is a trend already noticed above for the H abstraction pathway. In addition, it is worth noting that tweaking the barrier height changes the slope of their Arrhenius curves (i.e., the temperature dependence of the rate coefficients) especially at low temperatures. As shown in Figure 3-6b, reducing TS2 energy by 1 kcal mol<sup>-1</sup> resulted in a greater negative temperature dependency of  $k_2$  which is closer to the one measured for  $k_{\text{overall}}$  by Brown *et al.* [6]. Increasing TS2 by 1 kcal mol<sup>-1</sup>, which changed the submerged nature of TS2, also changed

the temperature dependency of  $k_2$  into a positive one. Similar changes are found on  $k_{3b}$  when tweaking TS10 energy (Figure 3-6d). Therefore, the question whether TS2 and TS10 are submerged, is crucial for the temperature dependence of the rate coefficients of their corresponding channels.

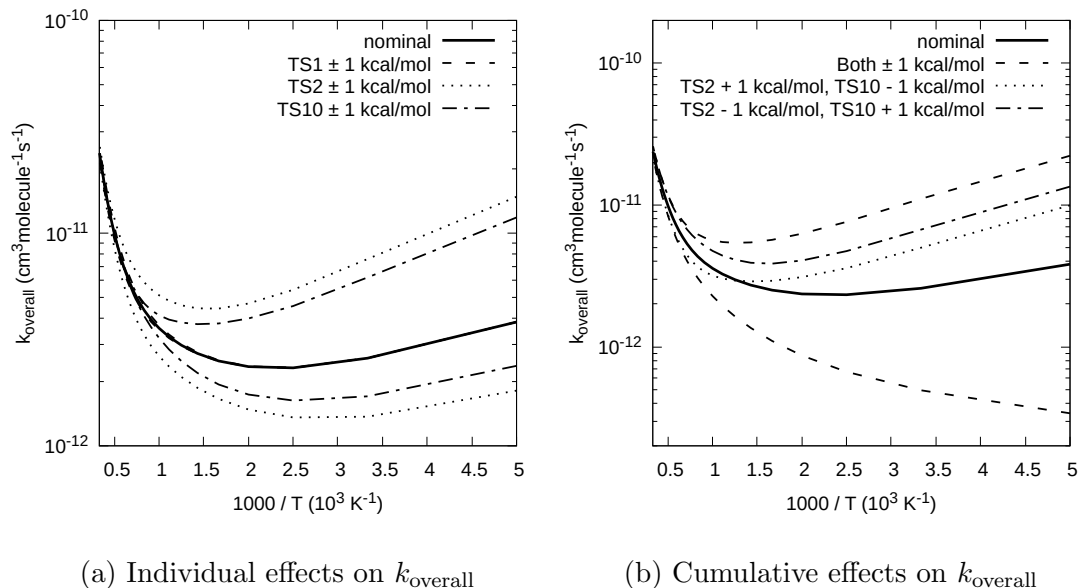


Figure 3-7: Effect of the uncertainty in TS1, TS2 and TS10 energies on  $k_{\text{overall}}$  at 1 atm. Effects at other pressures are qualitatively the same. If not specified, lines above the nominal case are for reduced energies whereas lines below are for increased energies. (a) Individual effects of TS1, TS2 and TS10 energies. Tweaking TS1 energy results in minor changes, as their curves mostly overlap with the nominal one. (b) Cumulative effects of tweaking TS2 and TS10 energy simultaneously in the same or opposite direction.

Because of the large branching ratios of the two OH addition pathways, the effect of tweaking TS2 and TS10 is projected onto  $k_{\text{overall}}$ , especially at low temperature. As shown in Figure 3-7a, tweaking TS2 seems to have greater impact on  $k_{\text{overall}}$  than tweaking TS10, for that TS2 energy is  $0.1 \text{ kcal mol}^{-1}$  lower than S10 and  $k_2$  is the most dominant at all conditions investigated. When tweaking TS2 and TS10 both in the same direction, the overall effect results simply from the summation of their individual effects, for there is no connection between the two pathways. When tweaking TS2 and TS10 in the opposite directions, their relative heights and the submerged nature of one TS change. For the case TS2  $-1 \text{ kcal mol}^{-1}$  and TS10  $+1 \text{ kcal mol}^{-1}$ , TS2 is still lower than TS10 but TS10 energy becomes higher than the reactants. Part of the effect on  $k_{\text{overall}}$  of lowering TS2 is canceled out by the increase of TS10 because of the lower branching ratio of pathway 3. For the case TS2  $+1 \text{ kcal mol}^{-1}$  and TS10  $-1 \text{ kcal mol}^{-1}$ , TS2 becomes higher than both TS10 and the reactants. As shown in Figure 3-7b, as  $k_2$  decreases significantly,  $k_{\text{overall}}$  becomes lower than its nominal value at high temperature (around  $T > 800 \text{ K}$ ). This is because of the low branching ratio of pathway 3 at high temperature, therefore the increase of  $k_{\text{overall}}$  by lowering TS10 is comparable to its reduction by increasing TS2. Therefore, the uncertainty in TS2 and TS10 energy have significant impacts on  $k_{\text{overall}}$  especially at low temperature

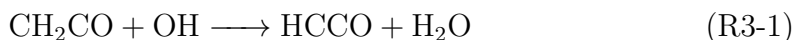
whereas the effect of TS1 energy on  $k_{\text{overall}}$  is negligible.

### 3.5 Conclusions

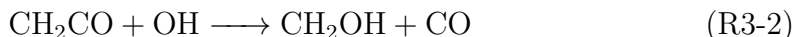
In this paper, we refine and enrich the potential energy surface (PES) of the  $\text{CH}_2\text{CO} + \text{OH}$  reaction using B2PLYP-D3/cc-pVTZ and CCSD(T)-F12/cc-pVTZ-F12 method. From this PES, temperature- and pressure-dependent rate coefficients and branching ratios at 200–3000 K and 0.01–100 atm for the multi-channel reaction are calculated using RRKM-TST/ME method.

Based on the PES and RRKM/ME results, the reaction proceeds via 3 pathways whose scheme can be simplified to only 6 reactions:

*Pathway 1: H abstraction by OH radical*



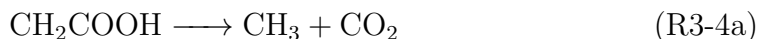
*Pathway 2: OH addition on olefinic carbon atom of ketene*



*Pathway 3: OH addition on carbonyl carbon atom of ketene*



*Dissociation of  $\text{CH}_2\text{COOH}$*



We found that channel  $\text{CH}_2\text{CO} + \text{OH} \longrightarrow \text{CH}_2\text{OH} + \text{CO}$  (R3-2) for OH addition on olefinic carbon (Pathway 2), is the fastest ( $10^{-12}$ – $10^{-11}$   $\text{cm}^3\text{molecule}^{-1}\text{s}^{-1}$ ) and the most dominant (50%–70%) over the entire range of temperature and pressure we investigated. Its rate constant  $k_2$  exhibits opposite temperature dependencies at low- and high-temperature regimes, negative at low temperature and positive at high pressure. The turning point where the temperature dependency switches is at around 400 K. The rest channels have to compete for the second dominant place. H abstraction channel  $\text{CH}_2\text{CO} + \text{OH} \longrightarrow \text{HCCO} + \text{H}_2\text{O}$  (R3-1) is favored mostly at high temperature whereas OH addition on carbonyl carbon (Pathway 3) is promoted mostly at low temperature. R3-1 is highly temperature dependent and its rate constant  $k_1$  increases dramatically with temperature. The crossover temperature where it becomes more dominant than Pathway 3 lies in the range 1500–2000 K. Both R3-1 and R3-2 are independent of pressure whereas channels in Pathway 3 are highly pressure-dependent. Inside Pathway 3, channel  $\text{CH}_2\text{CO} + \text{OH} \longrightarrow \text{CH}_3 + \text{CO}_2$  (R3-3a) and  $\text{CH}_2\text{CO} + \text{OH} \longrightarrow \text{CH}_2\text{COOH}$  (R3-3b) are also in competition. The collisional stabilization of  $\text{CH}_2\text{COOH}$  (R3-3b) is favored at high pressures whereas R3-3a is favored at low pressures. The stabilized  $\text{CH}_2\text{COOH}$  is most likely to be dissociated into product  $\text{CH}_3 + \text{CO}_2$  (R3-4a) or back into the reactants (R3-4b) at high temperatures. The rate constant  $k_{\text{overall}}$  for the overall reaction is found to have the same temperature dependency as R3-2,

while its slight positive pressure dependency at  $T > 500$  K is inherited from R3-3a and R3-3b. The uncertainty in the energy of TS2 and TS10 (the transition states at the entrances of the two OH addition pathways) are found to have significant impacts on the kinetics of the reaction, especially at low temperatures.

The rate parameters used in current kinetic mechanisms are found outdated, thus the rate coefficients obtained in this work are fitted into modified Arrhenius expressions in order to assist combustion modeling. The update of these parameters is expected to impact the combustion of hydrocarbon fuels such as acetylene, acetone, propyne, allene, and gasoline, which is necessary to be investigated through further studies.

# Chapter 4

## Identification of Key Thermokinetic Parameters for Mechanism Development

### 4.1 Introduction

This chapter aims to identify key thermokinetic parameters, including important reactions and thermodynamic parameters, to the laminar flame speed of gasoline surrogates at highly diluted conditions. The investigation is conducted through the sensitivity analysis of laminar flame speeds using a starting mechanism. A three-step approach, as shown in Figure 4-1, is applied to fulfill these tasks:

- selection of the surrogate, conditions, and the starting mechanism;
- sensitivity analysis of  $S_L$  at various conditions;
- analysis of the sensitivity results to identify key parameters.

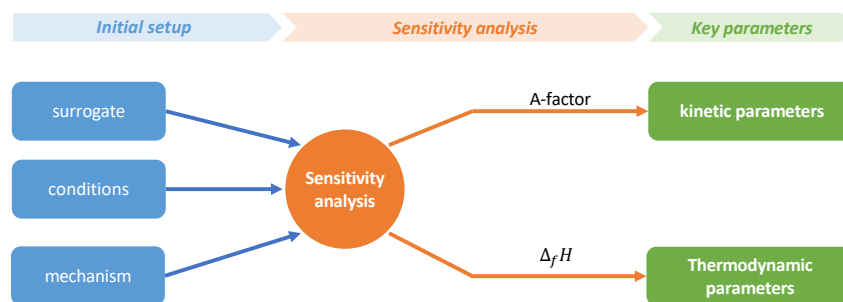


Figure 4-1: Schematic diagram of the approach used in Chapter 4.

### 4.2 Setup of the Initial Model

#### 4.2.1 Surrogate Composition

The accurate chemical modeling unquestionably requires a correct representation of the fuel of interest. To reproduce the engine combustion conditions to be studied, a fuel surrogate that best represents the properties of the real gasoline

fuel should be used. In the case of gasoline fuels, the most important and standard properties are the Research Octane Number (RON) and Motor Octane Number (MON), which show the anti-knock ability of a fuel. RON is tested in a test engine at 600 rpm, whereas MON is tested with premixed fuel/oxidizer mixtures at 900 rpm, close to road conditions. So MON is usually 8 to 12 lower than RON. The difference between MON and RON also called octane sensitivity (OS) is found to depend on the composition of the fuel, such as the fraction of aromatics. The gasoline, used in present work and the experiments by our partners in the MACDIL project, has a RON of 96.6 and a MON of 86.2.

Table 4.1: List of some surrogates candidates.

Surrogate	Composition (liquid vol%)	RON/MON	Ref.
Stanford A	63% isooctane, 17% n-heptane, 20% toluene	88/85	[316]
LLNL	57% isooctane, 16% n-heptane, 23% toluene, 4% 2-pentene	89/85	[25]
IFPEN	36% isooctane, 12% n-heptane, 37% toluene, 15% ethanol	100/92	[57]
TRF 95-1	79% isooctane, 6% n-heptane, 5% toluene, 10% ethanol	97/95	[74]
TRF 95-4	41% isooctane, 13% n-heptane, 36% toluene, 10% ethanol	98/91	[74]
Surrogate for TAE 10000	40% isooctane, 15% n-heptane, 35% toluene, 10% ethanol	96/88	
Surrogate for TAE 7500	44% isooctane, 15% n-heptane, 36% toluene, 5% ethanol	95/88	

A list of surrogates used by scholars is shown in Table 4.1, with their RON, MON, and compositions. It can be seen that these surrogates mostly contain isooctane ( $i\text{-C}_8\text{H}_{18}$ ), n-heptane ( $n\text{-heptane}$ ), toluene ( $\text{C}_6\text{H}_5\text{CH}_3$ ) and ethanol ( $\text{C}_2\text{H}_5\text{OH}$ ). Isooctane, the standard 100 points on the octane rating scale, is a major component of gasoline and often exists in gasoline fuel with large proportions to increase resistance to knocking. N-heptane is another standard compound, set to be the zero point of octane rating. Mixtures of n-heptane and isooctane are the Primary Reference fuels (PRFs) for octane ratings and are commonly used as convenient surrogates for fuels with variable octane ratings. [48, 56, 65] However, practical fuels are very different from PRFs in compositions and behave quite differently than PRFs in engines as design and operating conditions change. [218] Pitz et al. [48] suggested that any gasoline surrogate should not only contain n-heptane, isooctane, but also toluene, as a result of the fact that toluene is typically the most abundant aromatic in gasoline. Toluene Reference Fuel (TRF), mixtures of n-heptane, isooctane, and toluene, becomes the new standard, as studies [54, 56, 218, 316] have shown that the characteristics of a real gasoline at engine operating conditions can be satisfactorily predicted and successfully repeated using a TRF with the same octane rating. As a result of the increased concern of fossil fuel availability and environment issues arising from the release of  $\text{CO}_2$  and pollutants, ethanol has gained interest as an alternative fuel to increase octane sensitivity (OS) in the recent decades. [56] The advantages of having a high Octane Number (RON = 109 and MON = 90) [317] and being easily blended with hydrocarbon fuels make ethanol very attractive in practical combustion applications. [56] Some studies

have suggested that the addition of ethanol in gasoline leads to an increase in fuel efficiency and engine performance [318,319] as a result of the presence of the oxygenated compound. Thus, TRFs with ethanol addition (TRFEs) is becoming popular as a surrogate to better reproduce modern commercial gasolines.

Table 4.2: Comparison on the properties and composition of the gasoline and its TRFE surrogate. Reproduced from Ref. [24]

Gasoline (B71 1188 ESSH EUROS + 20)		TRFE surrogate (for TAE 7500 gasoline)	
<i>properties:</i>			
RON	96.6	RON	95
C/H/O (mass%)	85.1/13.1/1.8	C/H/O (mass%)	84.79/13.34/1.87
$\rho$ (kg/m <sup>3</sup> )	753.0	$\rho$ (kg/m <sup>3</sup> )	750.5
<i>composition (liq.vol.%):</i>			
ethanol	5.0	ethanol	5.0
n-heptane	3.6	n-heptane	15.0
isooctane	50.0	isooctane	44.0
aromatics (benzene)	33.7 (0.1)	toluene	36.0
olefin	6.2		
methyl-cyclohexane	1.5		

A surrogate blend for the TOTAL TAE 7500 gasoline was optimized, using the Surrogate Blend Optimizer (SBO) module in CHEMKIN Pro, to emulate the properties of the gasoline of interest (B71 1188 ESSH EUROS + 20) [24] due to their similar properties. Comparison between the gasoline and the TRFE surrogate are shown in Table 4.2 which is adapted from Ref. [24]. The obtained surrogate composition is similar to that of TRF 95-4 used by KAUST to represent the FACE fuel F with 5% ethanol addition, which is 44% isooctane, 15% n-heptane, 36% toluene and 5% ethanol. This surrogate composition, having the Octane number as desired (RON=95 and MON=88), is used for the investigation. Unless specified, the word “TRFE” in the following sections refers to the TRFE surrogate with this composition.

## 4.2.2 Mixture Composition

TRFE/air/EGR mixtures are studied in the present work. The TRFE composition in liquid volume fraction is as described in Section 4.2.1, and the same composition in mole fraction is shown in Table 4.3. The composition of the synthetic air is 79.1% N<sub>2</sub> and 20.9% O<sub>2</sub>. The EGR composition (74.16% N<sub>2</sub>, 13.62% CO<sub>2</sub> and 12.22% H<sub>2</sub>O) used in the present work, is the same as the PRISME experiments [24] in the MACDIL project, where it is synthesized according to the measured composition of the burnt gases for the stoichiometric TRFE/air flame. For convenience, the word “EGR” refers to this synthetic EGR, when used alone without adjectives in the following text of the present work. Since the mixtures used in SI engines are usually equal or near stoichiometric, the equivalence ratio is set to 1.1, where  $S_L$  is around its maximum. The above information is consistent with the PRISME experiments.



Table 4.3: Composition and mole fraction of the fuel, air and EGR used in the present work.

Name	Composition	Mole Fraction ( $X_i$ )
TRFE	isooctane/n-heptane/toluene/ethanol	0.3363/0.1284/0.4273/0.1080
air	O <sub>2</sub> /N <sub>2</sub>	0.21/0.79
synthetic EGR	CO <sub>2</sub> /H <sub>2</sub> O/N <sub>2</sub>	0.1362 / 0.1222 / 0.7416

The EGR ratio is defined as the ratio of recirculated exhaust gas over the whole mixture.

$$\text{EGR ratio} = \frac{X_{\text{EGR}}}{X_{\text{fuel}} + X_{\text{air}} + X_{\text{EGR}}} \quad (4.1)$$

$$\text{where } X_{\text{fuel}} + X_{\text{air}} + X_{\text{EGR}} = 1 \quad (4.2)$$

When  $X_{\text{EGR}}$  and  $\phi$  (equivalence ratio) are known,

$$X_{\text{fuel}} = (1 - X_{\text{EGR}}) / \left(1 + \frac{\nu_{\text{fuel}}}{\phi r_{\text{O}_2/\text{air}}}\right) \quad (4.3)$$

$$X_{\text{air}} = \frac{\nu_{\text{fuel}}}{\phi r_{\text{O}_2/\text{air}}} X_{\text{fuel}} \quad (4.4)$$

where  $r_{\text{O}_2/\text{air}} = 0.21$  is the ratio of O<sub>2</sub> in air, and  $\nu_{\text{fuel}} = 9.78585$  is the overall stoichiometric coefficient for the TRFE surrogate.  $\nu_{\text{fuel}}$  is calculated as,

$$\nu_{\text{fuel}} = \sum X_i \nu_i \quad (4.5)$$

$$\nu_i = N_i^{\text{C}} + 0.25N_i^{\text{H}} - 0.5N_i^{\text{O}} \quad (4.6)$$

where  $X_i$  is the mole fraction of component  $i$  (such as isooctane) in the fuel,  $\nu_i$  is its stoichiometric coefficient, and  $N_i^{\text{C}}$  is the number of carbon atom in the molecule of component  $i$ . It is worth mentioning that the equivalence ratio is defined as the ratio of the actual fuel/air ratio to the stoichiometric fuel/air ratio.

$$\phi = \left(\frac{X_{\text{fuel}}}{r_{\text{O}_2/\text{air}} X_{\text{air}}}\right) / \left(\frac{1}{\nu_{\text{fuel}}}\right) = \frac{\nu_{\text{fuel}} X_{\text{fuel}}}{r_{\text{O}_2/\text{air}} X_{\text{air}}} \quad (4.7)$$

### 4.2.3 Investigated Conditions

The investigated conditions for the flame speed calculations and sensitivity analysis are selected to simulate three types of conditions:

**practical conditions** which are within the condition range in real engines.

They have low EGR ratios (0% and 20%) and are consistent with the PRISME experiments.

**target conditions** which are difficult to obtain either practically or experimentally. They have very high EGR ratios (50% and 70%) and are estimations for the study and development of high EGR regimes. Such regimes require high initial temperature to ensure the presence of the flame. Higher pressure is also predicted at such conditions.

**dedicated conditions** have the same dilution ratios as target conditions, but with dedicated EGR composed of equimolar CO<sub>2</sub> and H<sub>2</sub>O. They are used

to emphasize on the dilution effects of CO<sub>2</sub> and H<sub>2</sub>O. Details of these conditions are shown in Table 4.4.

Table 4.4: Conditions investigated in the present chapter for the identification of key thermokinetic parameters to laminar flame speed.

Category	No.	EGR composition	EGR ratio	$T_u$ (K)	P (bar)	$\phi$
practical	C1	synthetic EGR	0%	473	5	1.1
	C2	synthetic EGR	20%	473	5	1.1
target	C3	synthetic EGR	50%	1200	10	1.1
	C4	synthetic EGR	70%	1500	20	1.1
dedicated	C5	CO <sub>2</sub> /H <sub>2</sub> O (50%/50%)	50%	1200	10	1.1
	C6	CO <sub>2</sub> /H <sub>2</sub> O (50%/50%)	70%	1500	10	1.1

#### 4.2.4 Starting Mechanism

To locate important reactions and thermodynamic properties regarding the laminar flame speed, it is necessary to use mechanisms that have good performance in fitting experimental data. In addition to that, the mechanism should be a comprehensive one with a large number of species and reactions so that the possibility of missing potentially important reactions is reduced. Following these principles, the present work adopts the detailed mechanism (LLNL 2011) for multi-component gasoline surrogate fuels, developed by Mehl *et al.* [25], as the starting mechanism. It is widely used in the combustion community and validated based on various types of experiments, such as ignition delay times (IDT) from rapid compression machines (RCM) and shock tubes (ST), laminar flame speeds ( $S_L$ ) from spherical bombs, and speciation from jet stirred reactors (JSR).

Table 4.5: List of candidate mechanisms.

Ref.	Mechanism	Species	Genealogy	Base fuel
[132]	LLNL 2011	1550	LLNL [124, 130]	Multi-component
[320]	Hasse 2000	29	Pitsch 1996 [321]	isooctane
[55]	Jerzembeck 2009	99	LLNL	PRF
[322]	Luong 2013	171	LLNL 2011	PRF
[323]	Niemeyer 2015	213	LLNL 2011	TRF
[219]	Pitsch 2015	339	LLNL 2011	TRFE
[324]	Reitz 2015	109	LLNL 2011 + Aramco Mech 1.3 [325]	TRFE
p.w.	E-Reitz 2016	158	Reitz 2015	TRFE
p.w.	MACDIL 2016	564	LLNL 2011	TRFE

p.w. = present work

The performance of the starting mechanisms (LLNL 2011) on  $S_L$  is compared with other candidates, which are listed in Table 4.5. Among the candidates, MACDIL 2016 and E-Reitz 2016 are reduced and skeletal mechanisms respectively, developed in the present work. MACDIL 2016 mechanism is obtained by reducing LLNL 2011, with 10% tolerance to  $S_L$ , at highly diluted conditions (12% CO<sub>2</sub> +

12% H<sub>2</sub>O,  $T_u = 650$  K,  $P = 10$  atm,  $\phi = 1.1$ , fuel = TAE 10000). The E-Reitz 2016 mechanism is developed from Reitz 2015 [324] with the addition of the ethanol subset from the Aramco 1.3 mechanism [325].

Figure 4-2 shows the comparison based on the experimental data by Endouard *et al.* [13] for isooctane/air/ flames with CO<sub>2</sub> dilution. It is found that the Hasse 2000 mechanism overestimates the flame speed while other mechanisms underestimate it. The results obtained by LLNL 2011 and the reduced mechanism (MACDIL 2016) are identical. The E-Reitz 2016 is found to yield slightly better results, especially at low dilution ratios, than Reitz 2015 whose results are similar to that of LLNL 2011. It implies that the comprehensive ethanol subset added may be important to the  $S_L$  of larger hydrocarbons such as isooctane. To summarize, the performance of the starting mechanism LLNL 2011 in predicting the  $S_L$  of isooctane/air/CO<sub>2</sub> flames is among the best within the candidate mechanism.

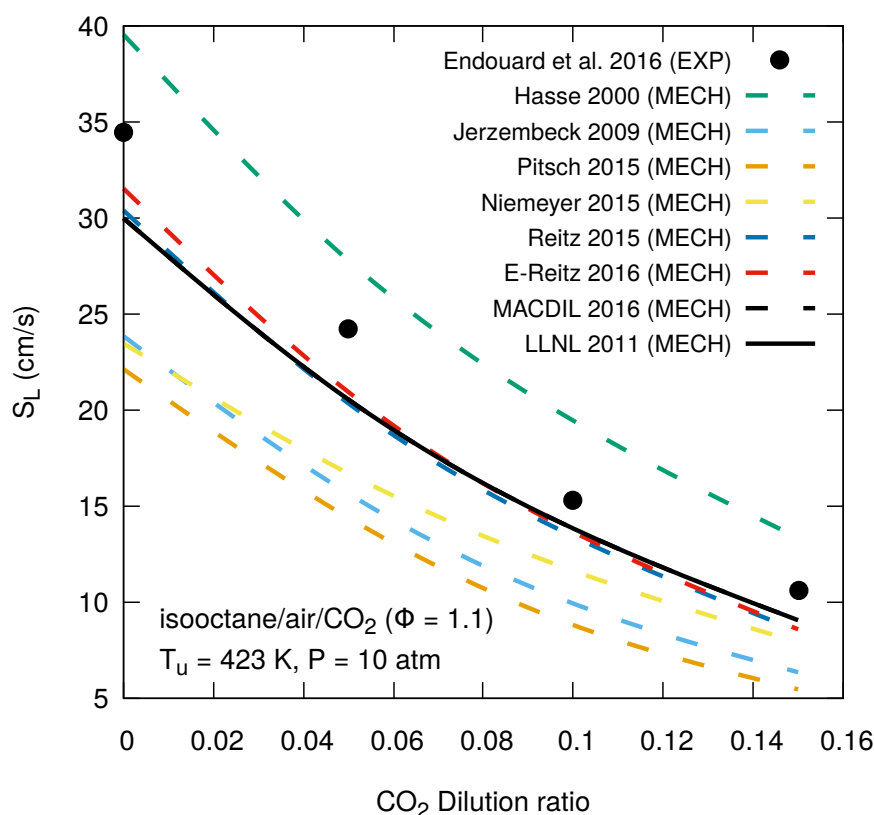


Figure 4-2: Comparison of the  $S_L$  calculated with the candidate mechanisms. Experimental data are from Endouard *et al.* [13], for the isooctane/air/CO<sub>2</sub> mixture,  $\phi = 1.1$ ,  $T_u = 423$  K,  $P = 10$  atm.

The effect of increasing EGR ratio on the laminar flame speed of TRF/air/EGR was simulated with MACDIL 2016 and E-Reitz, shown in Figure 4-3a. It is found that MACDIL 2016 produces  $S_L$  results closer to the experiments under high EGR ratios. For the interests in the study of ethanol addition to PRF (ERF, according to the naming in Ref. [15]), the two mechanisms were compared for ERFs with different fractions of ethanol, shown in Figure 4-3b. Both mechanisms overestimate the flame speeds. E-reitz has better results in the overall performance, which is

not surprising because it includes a very comprehensive ethanol subset. However, on the difference of  $S_L$  between surrogates with 5% and 15% ethanol addition, the two mechanisms exhibit similar performance, which indicates that the reduced ethanol subset in MACDIL 2016 is sufficient to have equivalent performance than the comprehensive ethanol subset in E-Reitz. Further improvement for ERF needs to be done for both mechanisms.

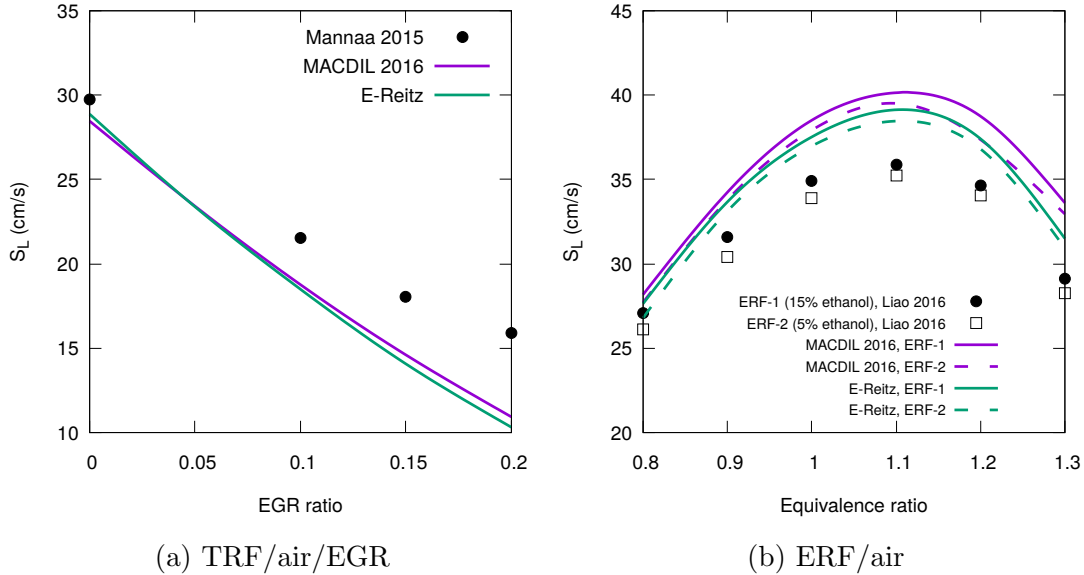


Figure 4-3: Comparison on the calculated  $S_L$  by MACDIL 2016 and E-Reitz with experiments. (a) TRFE/air/EGR flames, experimental data from Manna *et al.* [14]. fuel composition (vol.%): 18% n-heptane, 77% isooctane, 5% toluene; EGR composition: 14% H<sub>2</sub>O, 10% CO<sub>2</sub>, 76% N<sub>2</sub>;  $\phi = 1.1$ ,  $T_u = 358$  K,  $P = 6$  bar. (b) ERF/air flames with different ethanol concentration, experimental data from Liao *et al.* [15]. ERF-1 composition (vol.%): 10% n-heptane, 75% isooctane, 15% ethanol; ERF-2 composition: 10% n-heptane, 85% isooctane, 5% ethanol;  $T_u = 298.15$  K,  $P = 1$  atm.

Based on the above evaluation, the LLNL 2011 mechanism is chosen to be the starting mechanism. MACDIL 2016 and E-Reitz are also considered to make some sensitivity calculations when using the full mechanism is computationally expensive.

### 4.3 Important Reactions

The thousands of reactions occurring inside the flame front are controlling the propagation of flame from the chemical aspect and their rates have influences on the laminar flame speeds. Each of these reactions affects the flame speed differently, thus a change in the rate constant of a reaction may affect the flame speed dramatically or negligibly, depending on their sensitivity. This section aims to identify those sensitive reactions, kinetics parameters of which need to be refined to get more accurate  $S_L$  under highly-diluted conditions.

Since the reactions occurring during combustion are numerous, so far it is not possible for a mechanism to include all of them. The mechanisms used today

usually are designed for specific fuels and conditions. For example, the LLNL 2011 mechanism is designed for gasoline surrogates under engine conditions. For the engine conditions with high EGR ratios under high pressure and temperature, which is the main concern of the present work, some reactions important under these conditions might not be included in the LLNL 2011 mechanism. Among these excluded reactions, reactions between radicals and dilution content, such as CO<sub>2</sub>, CO and H<sub>2</sub>O are expected to have impacts on flame speeds and thus should be taken into concern when establishing the refined mechanism for combustion under highly-diluted conditions. Therefore, the important reactions that we aim to identify consist of two parts: (i) reactions already in the mechanisms, and (ii) reactions between radicals and dilution content.

For reactions that are already included in the mechanisms, those that affect  $S_L$  the most should be identified to further refine their kinetic parameters.  $S_L$  sensitivity of exponential factor ( $A$ ) in the rate constant expression was evaluated to identify the reactions most sensible to flame speeds. Bibliography review is performed for the obtained reactions to find those not fully investigated and 6 reactions of interest are targeted.

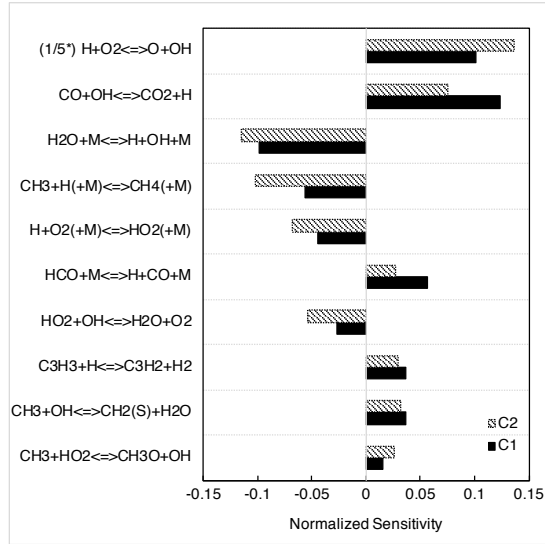
### 4.3.1 Conventional Sensitivity Analysis Based on $S_L$

Figure 4-4 compared the top 10 sensitivity results at practical conditions at different equivalence ratios. There are 4 reactions that are sensitive at all conditions.

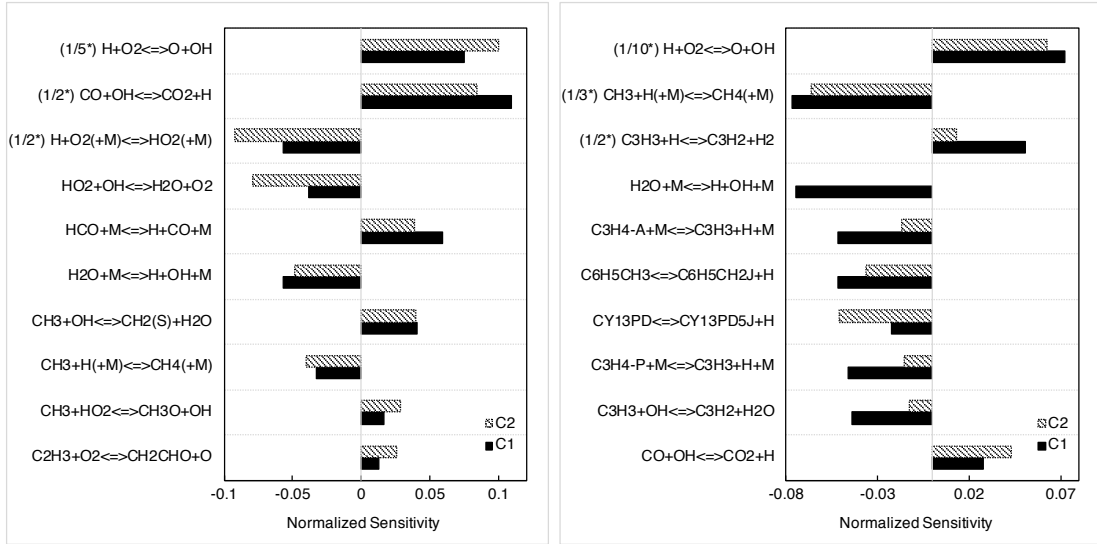


R 4.1 is the major chain branching reaction and therefore is the most sensitive at all conditions. R 4.2 is the major heat release step in hydrocarbon combustion and is found to be the second most sensitive at lean and near stoichiometric conditions as shown in Figure 4-4b and 4-4a. However, it is exceeded by other reactions and drop the 10th place at rich conditions. R 4.3 is the thermal dissociation of combustion product H<sub>2</sub>O, and therefore inhibits  $S_L$  and has negative sensitivity. R 4.4 is a chain-terminating step as it consumes H radicals, and also has negative sensitivity. It is also found that sensitive reactions are similar for lean and near stoichiometric conditions, but different at the rich condition. The former involves mainly light radicals, such as H, OH, HO<sub>2</sub>, methyl (CH<sub>3</sub>), formyl (HCO) and vinyl (C<sub>2</sub>H<sub>3</sub>) radicals, while the latter involves mainly larger fuel radicals, i.e., benzyl (C<sub>6</sub>H<sub>5</sub>CH<sub>2</sub>), and intermediates, i.e., allene (C<sub>3</sub>H<sub>4</sub>-A), propyne (C<sub>3</sub>H<sub>4</sub>-P), propargyl (C<sub>3</sub>H<sub>3</sub>) radicals, and cyclopentadiene (C<sub>5</sub>H<sub>6</sub>).

For lean and near stoichiometric conditions, important reactions involve mainly



(a)  $\phi = 1.1$

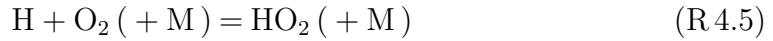


(b)  $\phi = 0.8$

(c)  $\phi = 1.4$

Figure 4-4: Sensitive reactions at practical conditions (C1 and C2) at different equivalence ratios. (a)  $\phi = 1.1$ . (b)  $\phi = 0.8$ . (c)  $\phi = 1.4$ .

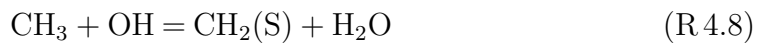
light radicals, such as the H, OH, HO<sub>2</sub> radicals in the hydrogen sub-mechanism,



formyl (HCO) radical in the H<sub>2</sub>/CO sub-mechanism,

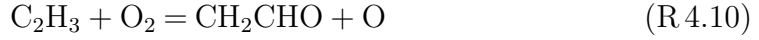


methyl (CH<sub>3</sub>) radical in the CH<sub>4</sub> sub-mechanism,



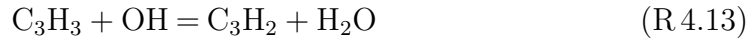
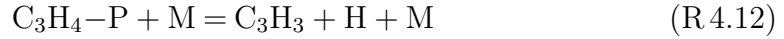
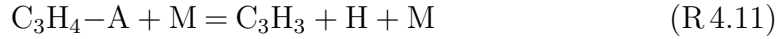


and vinyl ( $\text{C}_2\text{H}_3$ ) radical in the  $\text{C}_2$  sub-mechanism.



Among them, in the hydrogen subset, R 4.5 is a chain terminating reaction which compete with R 4.1 for H radicals, and therefore is important at diluted or high pressure conditions. As consequence, the higher production of  $\text{HO}_2$  radicals at diluted conditions, could enhance the subsequent reactions consuming  $\text{HO}_2$  radicals, such as R 4.6. In the  $\text{H}_2/\text{CO}$  subset, R 4.7 is chain branching as the H radical produced is more reactive than HCO and therefore have positive effect on  $S_L$ .

For rich conditions, important reactions involve mainly the propargyl ( $\text{C}_3\text{H}_3$ ) radical in the  $\text{C}_3$  subset,



larger intermediate cyclopentadiene ( $\text{C}_5\text{H}_6$ , "CY13PD" in the mechanism),

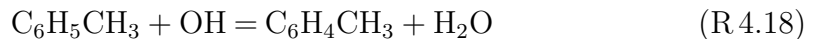


and fuel or fuel radical such as toluene ( $\text{C}_6\text{H}_5\text{CH}_3$ ) or benzyl ( $\text{C}_6\text{H}_5\text{CH}_2$ , "C6H5CH2J" in the mechanism) radical.



In addition, the effect of EGR on the change in sensitivity values are also different and even opposite at rich conditions. It implies that the mechanism of EGR effect is different at rich conditions and should be studied separately.

Figure 4-5 compares the top 25 sensitive reactions at practical and target conditions C1–C4 with near stoichiometric mixtures. By comparing results from Figure 4-5a and 4-5b, sensitive reactions under the effect of synthetic EGR are analyzed. In addition to the reactions summarized in the last paragraph, 4 reactions in the toluene oxidation sub-mechanism are also found common through C1–C4.



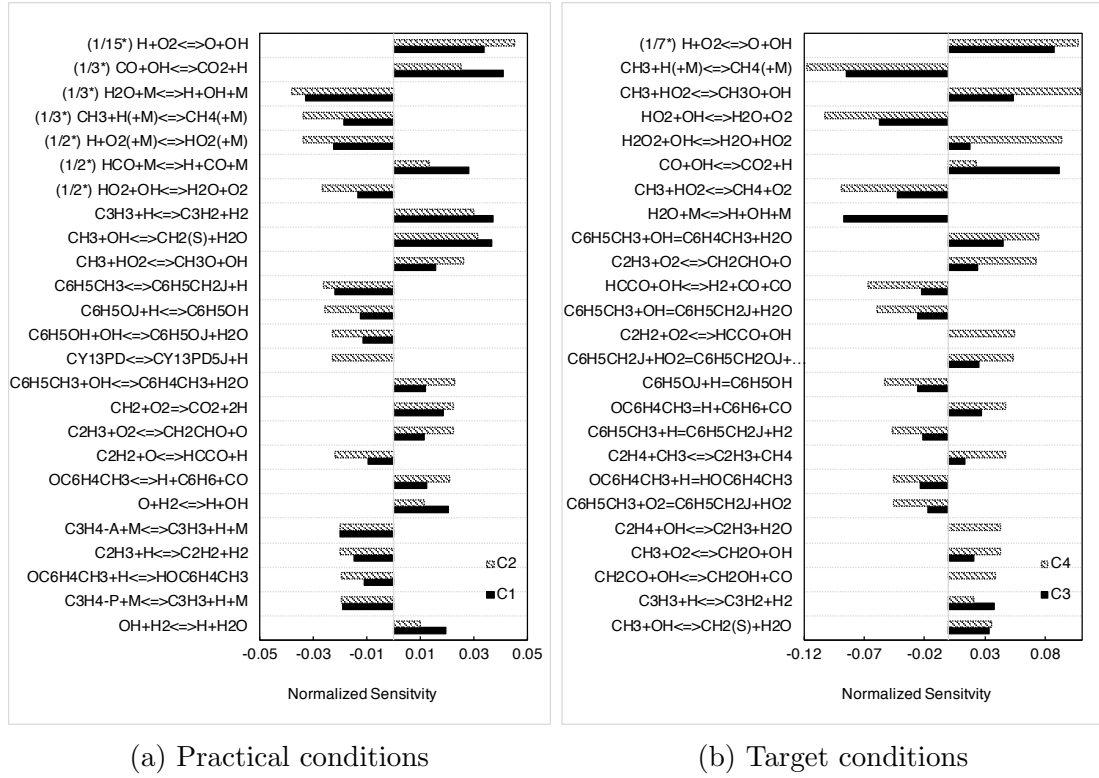
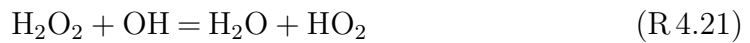


Figure 4-5: Sensitive reactions for practical and target conditions (C1–C4) at  $\phi = 1.1$ .



Figure 4-6 shows the evolution of sensitivity with the variation of conditions from C1 to C4, where EGR ratio is increased from 0% to 70%. The relative sensitivity of a reaction at a certain condition, is defined by the relative difference of its normalized sensitivity at that condition with respect to its normalized sensitivity at the reference condition (C1). Noted that initial temperature and pressure also change with the variation from C1 to C4, therefore Figure 4-6 only provides a rough estimation of evolution of sensitivity with EGR ratio. It is found that the sensitivity of R 4.6, R 4.9–R 4.10 and R 4.17–R 4.20 increase by more than a factor of 4 as dilution get higher. In the contrary, the sensitivity of R 4.1–R 4.4, R 4.8 and R 4.14 either increase only slightly or decrease with EGR ratio.

Figure 4-7 shows the top 25 reactions at dedicated conditions C5–C6, where EGR composition is 50%CO<sub>2</sub>/50%H<sub>2</sub>O. In addition to these common reactions found above, more reactions are identified at highly diluted conditions C3–C6 (Figure 4-5b and 4-7). They can be separated into the same categories as that of the common reactions, for example reactions involving HO<sub>2</sub> radical in the H<sub>2</sub> subset,



reactions of methyl radical in the CH<sub>4</sub> subset,





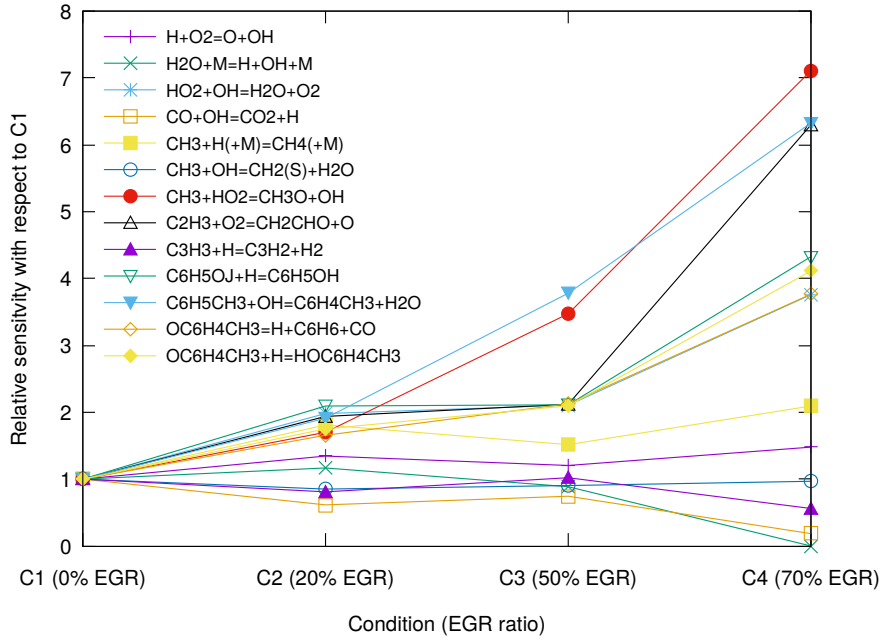


Figure 4-6: Evolution of sensitivity with EGR ratio, for the common reactions at conditions C1–C4. The relative sensitivity of a reaction at a certain condition is calculated as  $s_i^{rel}(C_j) = \frac{s_i(C_j) - s_i(C_1)}{s_i(C_1)}$ , where  $s_i(C_j)$  is the normalized sensitivity of the  $i$ th reaction at the  $j$ th condition.

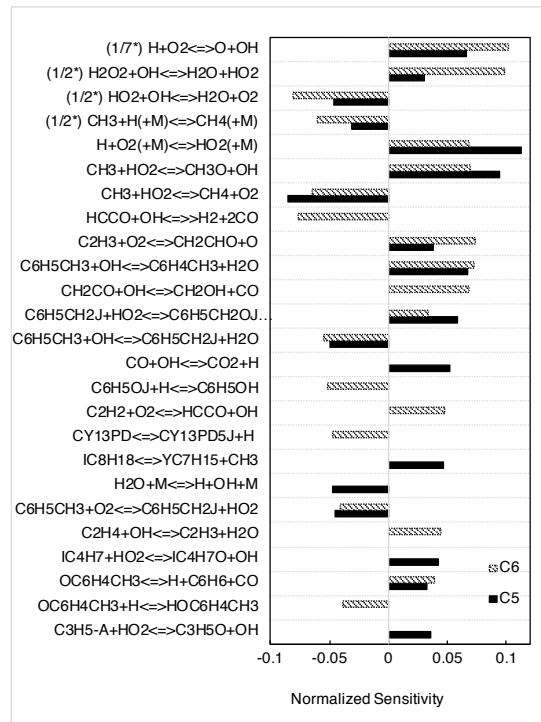
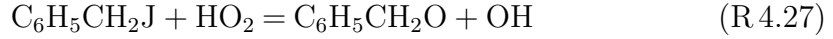
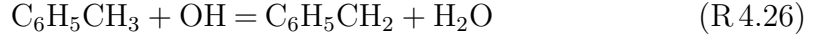
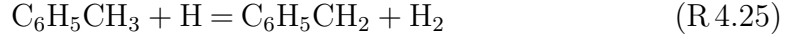
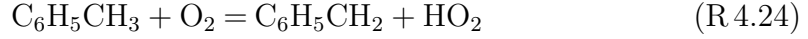


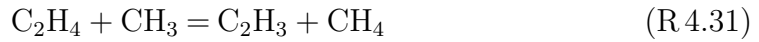
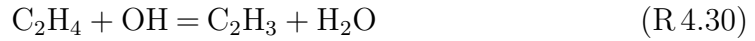
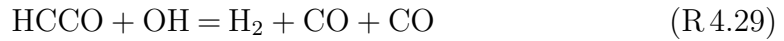
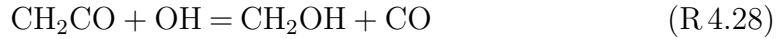
Figure 4-7: Sensitive reactions for dedicated conditions (C5–C6) at  $\phi = 1.1$ .



and reactions of toluene or benzyl radical in the toluene subset.



However, reactions in the C<sub>2</sub> subset are also identified to be sensitive at highly diluted conditions. They involve ketene (CH<sub>2</sub>CO) and ketyl (HCCO) radical, ethylene (C<sub>2</sub>H<sub>4</sub>), and acetylene (C<sub>2</sub>H<sub>2</sub>).



The results for target (C3 and C4) and dedicated (C5 and C6) conditions are similar, which indicate that these reactions are important at both nitrogen-dominant and CO<sub>2</sub>/H<sub>2</sub>O dilution environment.

### 4.3.2 Sensitivity Analysis Based on Composite Functions of $S_L$

Local variations of parameters, i.e., EGR ratio, initial temperature and pressure, are investigated based on condition C2 ( $\phi = 1.1$ ), using sensitivity analysis on composite functions as introduced in Section 2.6.2. Sensitivity on both absolute and relative changes is calculated. With respect to the reference case C2 ( $\phi = 1.1$ ), three new calculations are performed by varying locally, (i) the EGR ratio from 20% to 25%, (ii) initial temperature from 473 to 523 K, and (iii) pressure from 5 to 6 bar, respectively. The normalized sensitivity on the absolute and relative changes of  $S_L$  is calculated according to the method introduced in Section 2.6.2.

As shown in Figure 4-8, more reactions are found sensitive to the local variation of EGR ratio,



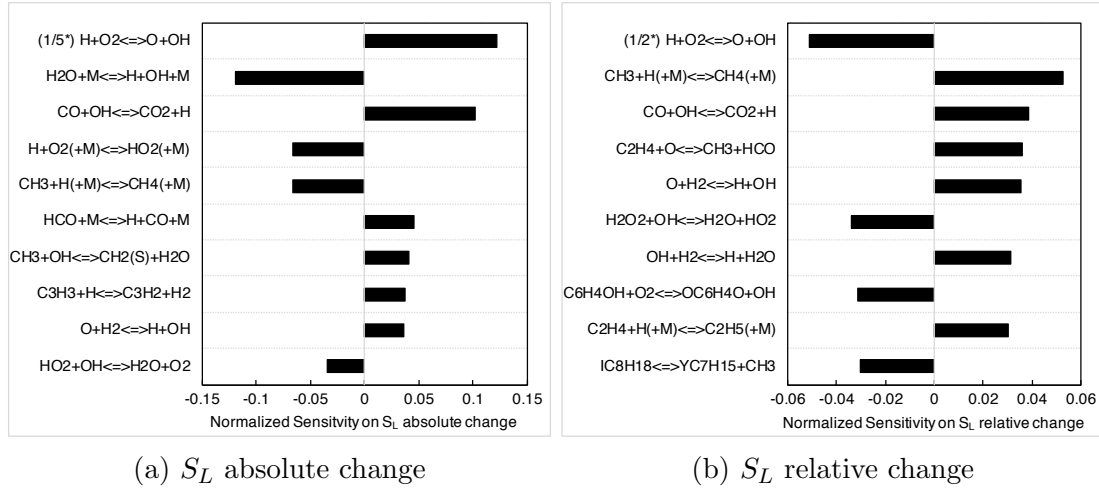
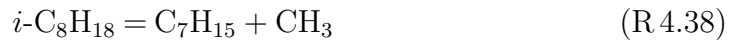
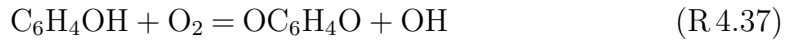
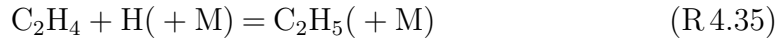


Figure 4-8: Reactions sensitive to the (a) absolute and (b) relative changes in  $S_L$  caused by the local variation of EGR ratio. Reference case is condition C2 at  $\phi = 1.1$ , based on which EGR ratio in the new calculation is varied locally from 20% to 25%. Methods to derive normalized sensitivity on composite functions, such as the absolute and relative change in  $S_L$ , are described in Section 2.6.2.

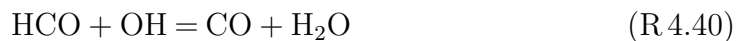


where R 4.33 is one of the important chain branching reactions in hydrocarbon combustion, R 4.34 may accelerate the flame as it produce H radicals and could be affected by  $\text{H}_2\text{O}$  concentration in the mixture, and R 4.38 is related to the initial cracking of the fuel component, isooctane ( $i\text{-C}_8\text{H}_{18}$ ).

Figure 4-9 identifies sensitive reactions when the initial temperature is changed. It is found that reactions involving cyclopentadiene ( $\text{C}_5\text{H}_6$ , “CY13PD” in the mechanism) and cyclopentadienyl ( $\text{C}_5\text{H}_5$ , “CY13PD5J” in the mechanism) radical, such as R 4.15 and



are quite sensitive to initial temperature. As shown in Figure 4-11, 3 more reactions are found responsive to pressure variation.



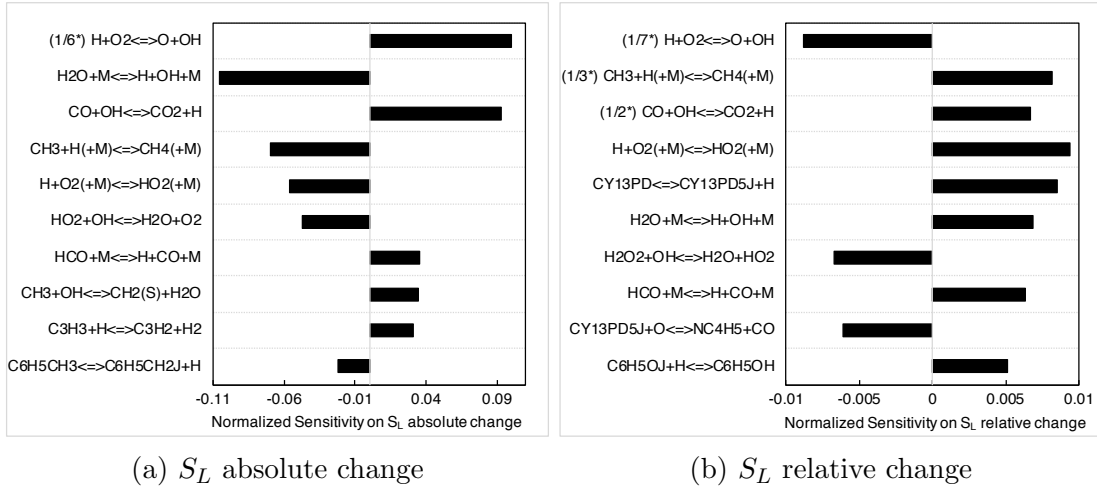


Figure 4-9: Reactions sensitive to the (a) absolute and (b) relative changes in  $S_L$  caused by the local variation of initial temperature. Reference case is condition C2 at  $\phi = 1.1$ , based on which the  $T_u$  in the new calculation is varied locally from 473 to 523 K. Methods to derive normalized sensitivity on composite functions, such as the absolute and relative change in  $S_L$ , are described in Section 2.6.2.

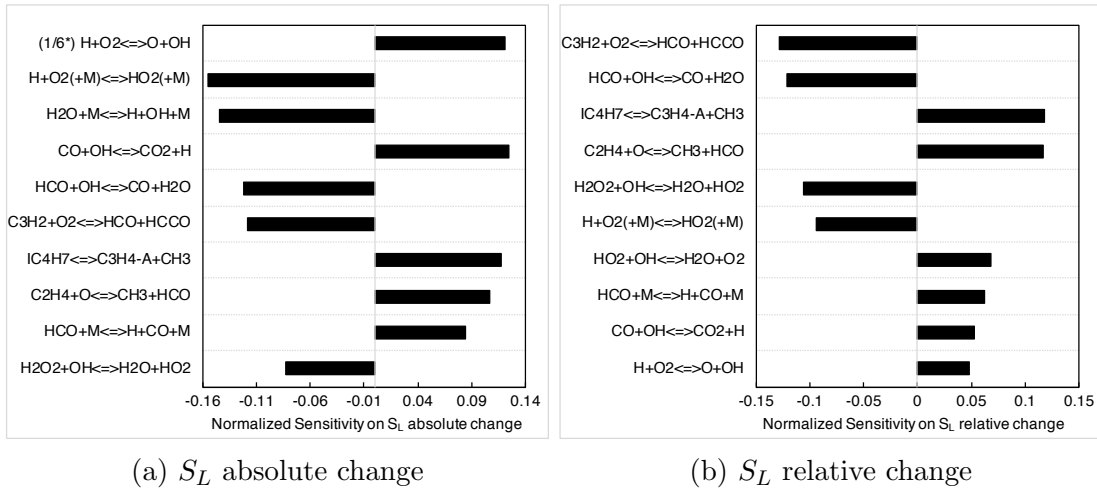
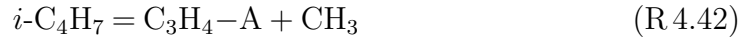


Figure 4-10: Sensitive reactions for the changes in  $S_L$  caused by varying pressure. Reference case is condition C2 at  $\phi = 1.1$ , and then change is made on pressure from 5 to 6 bar.

Figure 4-11: Reactions sensitive to the (a) absolute and (b) relative changes in  $S_L$  caused by the local variation of pressure. Reference case is condition C2 at  $\phi = 1.1$ , based on which the pressure in the new calculation is varied locally from 5 to 6 bar. Methods to derive normalized sensitivity on composite functions, such as the absolute and relative change in  $S_L$ , are described in Section 2.6.2.

### 4.3.3 Important In-mechanism Reactions

The important reactions identified in the above sections, using sensitivity analysis with the starting mechanism (LLNL 2011 [25]), are listed in Table 4.6.

Table 4.6: Important in-mechanism reactions identified in the present work.

<u><i>H<sub>2</sub> sub-mechanism</i></u>	<u><i>H<sub>2</sub>/CO sub-mechanism</i></u>
H + O <sub>2</sub> = O + OH	CO + OH = CO <sub>2</sub> + H
O + H <sub>2</sub> = H + OH	HCO + M = H + CO + M
H + O <sub>2</sub> (+ M) = HO <sub>2</sub> (+ M)	HCO + OH = CO + H <sub>2</sub> O
H <sub>2</sub> O + M = H + OH + M	
HO <sub>2</sub> + OH = H <sub>2</sub> O + O <sub>2</sub>	<u><i>CH<sub>4</sub> sub-mechanism</i></u>
H <sub>2</sub> O <sub>2</sub> + OH = H <sub>2</sub> O + HO <sub>2</sub>	CH <sub>3</sub> + H (+ M) = CH <sub>4</sub> (+ M)
OH + H <sub>2</sub> = H + H <sub>2</sub> O	CH <sub>3</sub> + OH = CH <sub>2</sub> (S) + H <sub>2</sub> O
	CH <sub>3</sub> + HO <sub>2</sub> = CH <sub>3</sub> O + OH
<u><i>C<sub>2</sub>-C<sub>3</sub> sub-mechanism</i></u>	CH <sub>3</sub> + HO <sub>2</sub> = CH <sub>4</sub> + O <sub>2</sub>
C <sub>2</sub> H <sub>3</sub> + O <sub>2</sub> = CH <sub>2</sub> CHO + O	CH <sub>3</sub> + O <sub>2</sub> = CH <sub>2</sub> O + OH
C <sub>3</sub> H <sub>4</sub> -A + M = C <sub>3</sub> H <sub>3</sub> + H + M	
C <sub>3</sub> H <sub>4</sub> -P + M = C <sub>3</sub> H <sub>3</sub> + H + M	<u><i>C<sub>5</sub>H<sub>6</sub> sub-mechanism</i></u>
C <sub>3</sub> H <sub>3</sub> + OH = C <sub>3</sub> H <sub>2</sub> + H <sub>2</sub> O	C <sub>5</sub> H <sub>6</sub> = C <sub>5</sub> H <sub>5</sub> + H
C <sub>3</sub> H <sub>3</sub> + H = C <sub>3</sub> H <sub>2</sub> + H <sub>2</sub>	C <sub>5</sub> H <sub>5</sub> + O = <i>n</i> -C <sub>4</sub> H <sub>5</sub> + CO
CH <sub>2</sub> CO + OH = CH <sub>2</sub> OH + CO	
HCCO + OH = H <sub>2</sub> + CO + CO	<u><i>C<sub>6</sub>H<sub>5</sub>CH<sub>3</sub> sub-mechanism</i></u>
C <sub>2</sub> H <sub>4</sub> + OH = C <sub>2</sub> H <sub>3</sub> + H <sub>2</sub> O	C <sub>6</sub> H <sub>5</sub> CH <sub>3</sub> = C <sub>6</sub> H <sub>5</sub> CH <sub>2</sub> + H
C <sub>2</sub> H <sub>4</sub> + CH <sub>3</sub> = C <sub>2</sub> H <sub>3</sub> + CH <sub>4</sub>	C <sub>6</sub> H <sub>5</sub> O + H = C <sub>6</sub> H <sub>5</sub> OH
C <sub>2</sub> H <sub>2</sub> + O <sub>2</sub> = HCCO + OH	C <sub>6</sub> H <sub>5</sub> CH <sub>3</sub> + OH = C <sub>6</sub> H <sub>4</sub> CH <sub>3</sub> + H <sub>2</sub> O
C <sub>2</sub> H <sub>4</sub> + H (+ M) = C <sub>2</sub> H <sub>5</sub> (+ M)	OC <sub>6</sub> H <sub>4</sub> CH <sub>3</sub> = H + C <sub>6</sub> H <sub>6</sub> + CO
C <sub>2</sub> H <sub>4</sub> + O = CH <sub>3</sub> + HCO	OC <sub>6</sub> H <sub>4</sub> CH <sub>3</sub> + H = HOC <sub>6</sub> H <sub>4</sub> CH <sub>3</sub>
C <sub>3</sub> H <sub>2</sub> + O <sub>2</sub> = HCO + HCCO	C <sub>6</sub> H <sub>5</sub> CH <sub>3</sub> + O <sub>2</sub> = C <sub>6</sub> H <sub>5</sub> CH <sub>2</sub> + HO <sub>2</sub>
	C <sub>6</sub> H <sub>5</sub> CH <sub>3</sub> + H = C <sub>6</sub> H <sub>5</sub> CH <sub>2</sub> + H <sub>2</sub>
<u><i>i-C<sub>8</sub>H<sub>18</sub> sub-mechanism</i></u>	C <sub>6</sub> H <sub>5</sub> CH <sub>3</sub> + OH = C <sub>6</sub> H <sub>5</sub> CH <sub>2</sub> + H <sub>2</sub> O
<i>i</i> -C <sub>8</sub> H <sub>18</sub> = C <sub>7</sub> H <sub>15</sub> + CH <sub>3</sub>	C <sub>6</sub> H <sub>5</sub> CH <sub>2</sub> J + HO <sub>2</sub> = C <sub>6</sub> H <sub>5</sub> CH <sub>2</sub> O + OH
<i>i</i> -C <sub>4</sub> H <sub>7</sub> = C <sub>3</sub> H <sub>4</sub> -A + CH <sub>3</sub>	C <sub>6</sub> H <sub>4</sub> OH + O <sub>2</sub> = OC <sub>6</sub> H <sub>4</sub> O + OH

It can be summarized that reactions having major impacts on  $S_L$  mostly fall into 4 categories:

**Fundamental reactions in the H<sub>2</sub>, H<sub>2</sub>/CO, CH<sub>4</sub> sub-mechanisms.** These reactions are expected to be present and of the highest values in the sensitivity results, since they are the most fundamental reactions for every combustion problems. They are extensively investigated by the combustion community with various experimental measurements and theoretical calculations on the rate constants. However, further studies are still necessary to improve the uncertainties, considering the high sensitivity of these reactions.

**Reactions involving C<sub>2</sub>-C<sub>3</sub> hydrocarbons.** The C<sub>2</sub>-C<sub>3</sub> hydrocarbons, such as vinyl (C<sub>2</sub>H<sub>3</sub>), propargyl (C<sub>3</sub>H<sub>3</sub>), allene and propene, are proved to be important intermediates during combustion. [110, 111] They link not only to smaller molecules as they are intermediate steps before conversion to CO, but also to the larger molecules, such as the formation of aromatics through

the propargyl  $C_3H_3$  radicals. Due to their significance, it is necessary to study the kinetics of these reactions comprehensively.

**Reactions involving aromatic radicals.** Aromatic radicals, are key components in mechanisms for polycyclic aromatic hydrocarbon (PAH) growth and soot formation [326], and have received considerable attention [202, 327, 328] They are particularly important in TRF, which are the main surrogates of our concern, as they are produced in the early stage of the oxidation of toluene. An accurate understanding of their oxidation kinetics is a crucial aspect of combustion modeling [142, 327]. These reactions should be reviewed comprehensively, to improve the performance of the mechanisms.

**Alkane fuels decomposition reactions.** Fuel decomposition reactions are important to flame speeds, since they produce fuel derived radicals, such as isooctyl ( $i-C_8H_{17}$ ) radicals, at the early stage of the cracking process of large fuel molecules. The different reactions of the resulting alkyl radicals are also proved to be kinetic controlling reactions under various regimes from low to high temperatures and pressures. [29]

These above conclusions are also consistent with the important reactions found for ignition delay time [85].

#### 4.3.4 Radical + Diluent Molecule Reactions

Under highly diluted conditions,  $CO_2$ ,  $H_2O$  and  $CO$  are abundant in the mixture. The high concentration of  $CO_2$  may affect the flame through a direct chemical reaction of  $CO_2$  within the fuel oxidation process. Studies on the effect of  $CO_2$  on the laminar flame speed for hydrogen and small hydrocarbons [329–334] have identified both radiative [332, 333] and chemical effects [329] as important. It has been pointed out in several studies that  $CO_2$  is not inert but participates in chemical reactions primarily through  $CO_2 + H = CO + OH$ . [329, 335–337] It is due to the fact that thermal dissociation of  $CO_2$  is strongly endothermic and occurs only at high temperatures, while reactions of  $CO_2$  with free radicals may proceed at lower temperatures and is comparatively fast even at medium temperatures. [329] In the combustion of hydrocarbons, it is conceivable that radicals with two or more carbon atoms may also participate in reducing  $CO_2$ . [338] Reactions of large hydrocarbon and aromatic radicals might be promoted under high dilution, high temperature and pressure, considering not only the high  $CO_2$  concentration but also that they can be easily generated during the combustion of TRF and are important for further reactions. As a consequence, it is necessary to investigate the interactions between  $CO_2$  and radicals.

Table 4.7 provides an overview of the known reactions between these radicals and diluent molecules. It is found that the reactions of radicals with dilution components are very little studied, especially for those with  $CO_2$ , which means it is a great area that needs to be explored. The radicals of interest for reactions with diluent molecules are as follows:

- Benzyl Radical ( $C_6H_5CH_2$ )
- Phenoxy Radical ( $C_6H_5O$ )
- Isooctyl Radical ( $iC_8H_{17}$ )
- Vinyl Radical ( $C_2H_3$ )
- Methylene Radicals ( $CH_2$ )
- Methyldiyne Radical ( $CH$ )

Table 4.7: Known reactions between radicals and diluent molecules ( $\text{CO}_2$ ,  $\text{H}_2\text{O}$ ,  $\text{CO}$ ).

Radicals	$\text{CO}_2$ <sup>1,2</sup>	$\text{CO}$	$\text{H}_2\text{O}$
$\text{C}_6\text{H}_5$ (phenyl)		×	×
$\text{C}_6\text{H}_5\text{CH}_2$ (benzyl)		×	
$\text{C}_6\text{H}_5\text{O}$ (phenoxy)			
<i>i</i> - $\text{C}_8\text{H}_{17}$ (isooctyl)			
$\text{C}_5\text{H}_5$ (cyclopentadienyl)			
HCCO (ketenyl)			
$\text{C}_3\text{H}_3$ (propargyl)			
$\text{C}_3\text{H}_5$ -A (allyl)		×	
$\text{C}_2\text{H}_3$ (vinyl)		×	×
CH (methylidyne)	×	×	×
$\text{CH}_2$ (triplet/singlet) (methylene)	×	×	×
$\text{CH}_3$ (methyl)	×	×	×

<sup>1</sup> The × symbol indicates that the reaction is known or reported, but not necessarily studied comprehensively.

<sup>2</sup> Blank indicates that the reaction is not known or not studied.

### 4.3.5 Reactions of Interests for Further Theoretical Studies

The reactions identified in the above sections are briefly reviewed on the studies in the literature, which is included in Table B.1 in Appendix B. 6 reactions of interests, as listed in Table 4.8, are identified for further theoretical investigations. Among them, the  $\text{CH}_2\text{CO} + \text{OH}$  reaction is studied in this work and presented in Chapter 3, while the other 5 reactions are planned for future work. Significance and brief literature reviews of these reactions are presented below.

Table 4.8: Reactions of interests for further theoretical investigations.

Main species	Reaction	Label
ketene	$\text{CH}_2\text{CO} + \text{OH} \longrightarrow \text{products}$	R <i>int.1</i>
propargyl radical	$\text{C}_3\text{H}_3 + \text{OH} \longrightarrow \text{products}$	R <i>int.2</i>
	$\text{C}_3\text{H}_3 + \text{HO}_2 \longrightarrow \text{products}$	R <i>int.3</i>
aromatic radicals	$\text{C}_6\text{H}_5\text{O} + \text{HO}_2 \longrightarrow \text{products}$	R <i>int.4</i>
	$\text{C}_6\text{H}_5\text{O} + \text{H} = \text{C}_6\text{H}_5\text{OH}$	R <i>int.5</i>
	$\text{OC}_6\text{H}_4\text{CH}_3 + \text{H} = \text{HOC}_6\text{H}_4\text{CH}_3$	R <i>int.6</i>

R *int.i* denotes the *i*th reaction of interest.

#### The Ketene + hydroxyl reaction (R int.1)

Significance and literature review of this reaction is explained and its rate coefficients are calculated in Chapter 3.

#### Propargyl + radical reactions (R int.2, R int.3)

Propargyl ( $\text{C}_3\text{H}_3$ ) radical is a critical species of the gas-phase chemistry producing the “first aromatic ring” [339–345], for example, phenyl and benzene,

which then can react further to form polycyclic aromatic hydrocarbons (PAHs) and ultimately soot [326]. The reaction of a propargyl radical with another propargyl is the dominant path to benzene/phenyl formation in many fuel-rich flames. [340, 344, 345] Therefore, reactions involving  $C_3H_3$  are of significance in understanding the mechanism of combustion and flames. The reactions between Propargyl and OH (R *int.1*) is of great research interests, due to the fact that OH is the primary oxidizing agent for propargyl in rich and stoichiometric flames, since the oxidation by molecular oxygen is slow. [345, 346] As stated by Hansen *et al.* [344], detailed analysis of the potential energy surface (PES), performed by Miller in his unpublished results, indicates clearly that the only significant products resulted from the addition of OH to  $C_3H_3$  are  $C_2H_4 + CO$  and  $C_2H_3 + HCO$ , which are both formed as a consequence of OH adding to the CH end of propargyl, followed by a 1,3-hydrogen transfer. Although this molecular study is present, accurate rate coefficients are still absent. For the reactions between Propargyl and  $HO_2$  (R *int.2*), there is no direct experimental kinetic data available so far. Wang [347] estimated the rate constant to be  $3 \times 10^{11} \text{ cm}^3\text{mol}^{-1}\text{s}^{-1}$ , equal for both product channels leading to propene (p- $C_3H_4$ ) and allene (a- $C_3H_4$ ) with  $O_2$ , based on the rate constants of the analogous reactions  $C_2H_4 + O_2 \longrightarrow C_2H_3 + HO_2$  and  $C_2H_5 + HO_2 \longrightarrow C_2H_6 + O_2$ . These rates should be considered as upper limits because the propargyl radical is expected to be less reactive than  $C_2H_5$  and  $C_2H_3$ . Thus detailed molecular and kinetics study on this reaction is necessary.

#### Phenoxy/Methylphenoxy + radical reactions (R *int.4*–R *int.6*)

The phenoxy radical ( $C_6H_5O$ ) is an important reactive intermediate in the oxidation of small aromatic hydrocarbons, key additives to unleaded gasoline. [348, 349] It is a free radical derived from phenol ( $C_6H_5OH$ ). Due to hyperconjugation of the oxyl radical moiety with the aromatic ring [350], the phenoxy radical and its substituted derivatives are relatively stable, and they often persist at low to moderate temperatures [351]. These persistent free radicals (PFRs) are believed to be important in the formation of dioxins [352] and particulate matter [353] in post-combustion and atmospheric environments. The resonance structures are present for phenoxy radical as shown in Figure 4-12, due to the delocalization of the unpaired electron to the ortho- and para- positions of the benzene ring. [16]

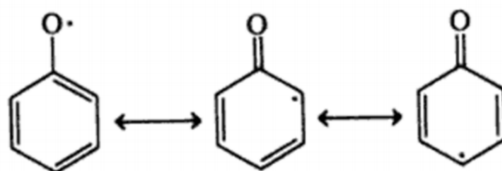


Figure 4-12: Resonance structures of the phenoxy radical. Graphic taken from Ref. [16].

On account of the relatively high stability of the  $C_6H_5O$  radical in comparison with those of alkoxy radicals, it may undergo extensive bimolecular reactions with reactive combustion species such as the H, O and  $HO_2$  radicals, in addition to its well known unimolecular fragmentation process. [348, 354–356] The bimolecular  $C_6H_5O +$  radical association reaction is not only very exothermic but also is



expected to be fast because it is a radical-radical association process. On account of the presence of resonance structures in  $C_6H_5O$ , these reactions may take place via several pathways [357].

The phenoxy reaction with O atom was well studied by Lin and Mebel [357], providing calculated rate constant over a wide temperature range. For phenoxy reactions with H radical (R *int.5*), Buth *et al.* [358] conducted experiments at room temperature and obtained a simple rate coefficient without Arrhenius expressions. Davis *et al.* [359] studied the benzene/air and toluene/air flames and found the rate coefficients are pressure dependent. The fall-off of the rate constant was then examined using the RRKM and variational transition-state theories (VTST) by extrapolating the reverse high-pressure limit rate constants in another mechanism. The resulting rate constant is valid among the temperature range of 1000–1200 K. The absence of accurate rate coefficients over the full temperature range of combustion problems indicates that experimental and theoretical evaluations are necessary. For phenoxy reactions with HO<sub>2</sub> radical (R *int.4*), Skokov *et al.* [360] presented a detailed quantum chemical study using the modified Perdew-Wang (MPW1K) density functional method. However, for some reason, they did not publish any results on the rate constants. Therefore studies on the rate coefficients of the reaction are still needed.

## 4.4 Important Thermodynamic Parameters

The laminar flame speed mostly depends not only on reaction rates but also on thermal diffusivities. Thus, the accuracy of the thermochemical parameters of the species inside a mechanism is vital in order to get accurate flame speeds. Among the thermochemical parameters, Standard Enthalpy of Formation ( $\Delta_f^{298}H$ ) is one of the most important, which is defined as the change in enthalpy when one mole of a substance is formed from its elements under the standard conditions. Its accuracy affects the heat release in the reactions and thus affects the result of energy conservation when calculating the flame speed. Therefore great improvement of the flame speed could be achieved if more accurate values can be updated for these data. Although most of the known important ones are already sufficiently accurate, it is still crucial to get an understanding of the important species affecting the flame speed.

The sensitivities of the heat of formation ( $\Delta_f^{298}H$ ) of the species to laminar flame speed were evaluated under the dedicated conditions C5 and C6, shown in Figure 4-13 and 4-14 respectively. The  $\Delta_f^{298}H$  of some species are found to be commonly sensitive to  $S_L$  at both conditions. These species mostly involve in into three combustion sub-mechanism: (i) the combustion of toluene, e.g., toluene ( $C_6H_5CH_3$ ) and benzyl ( $C_6H_5CH_2$ ) radical, phenyl ( $C_6H_5$ ) radical, cyclopentadiene ( $C_5H_6$ ) and cyclopentadienyl ( $C_5H_5$ ) radical; (ii) intermediate  $C_2$ – $C_3$  species, e.g., acetylene ( $C_2H_2$ ), vinyl ( $C_2H_3$ ) radical, and propargyl  $C_3H_3$  radical; (iii) final conversion to combustion products, i.e., H radical, carbon monoxide (CO), and water ( $H_2O$ ).

Figure 4-15 compares the sensitivity at three different dilution ratio, and present the evolution of sensitivity with dilution ratio. It is found that species, whose sensitivities increase with increasing dilution ratio, are similar to the com-

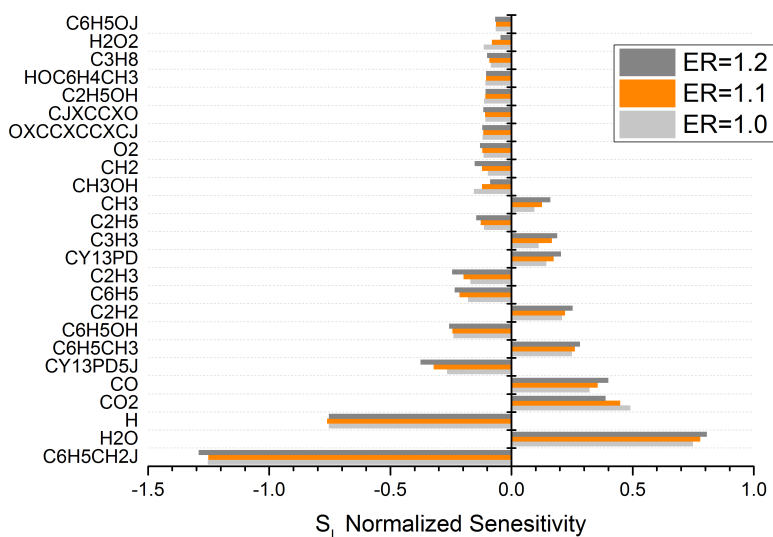


Figure 4-13:  $\Delta_f^{298}H$  sensitivity of  $S_L$  at condition C5 with various equivalence ratios ( $\phi = 1.0, 1.1, 1.2$ ). Results are obtained using the MACDIL 2016 mechanism.

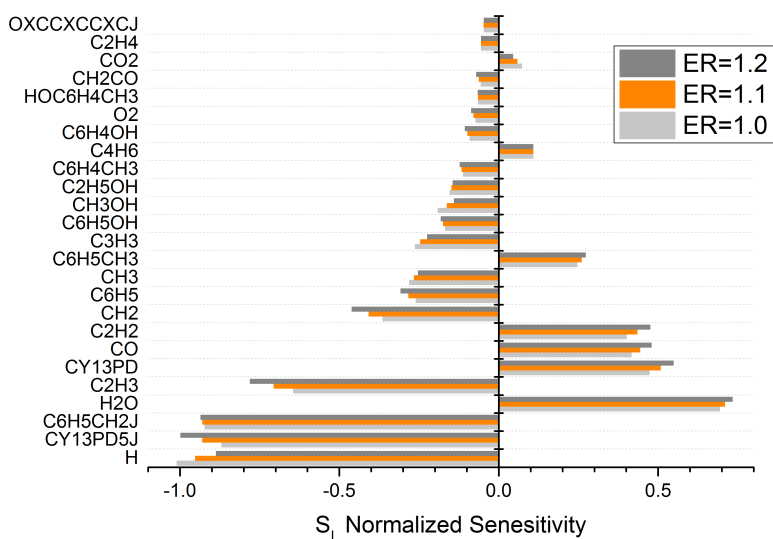


Figure 4-14:  $\Delta_f^{298}H$  sensitivity of  $S_L$  at condition C6 with various equivalence ratios ( $\phi = 1.0, 1.1, 1.2$ ). Results are obtained using the MACDIL 2016 mechanism.

mon sensitive species identified above. They are (i) species involved in the combustion of toluene, e.g.,  $C_6H_5CH_3$ ,  $C_6H_5CH_2$ ,  $C_6H_5OH$ , and  $C_5H_5$ , and (i) intermediate  $C_2$  species, such as  $C_2H_2$  and  $C_2H_3$ . It is worth noting that although  $H_2O_2$  is not quite sensitive at 30% and 50% dilution ratio, its sensitivity becomes significant at 70% of dilution. The change of sign in its sensitivity value indicates that changes in reaction regimes involving  $H_2O_2$  may be possible between 50% and 70% of dilution.

In summary, the above results indicate that the thermodynamic properties of

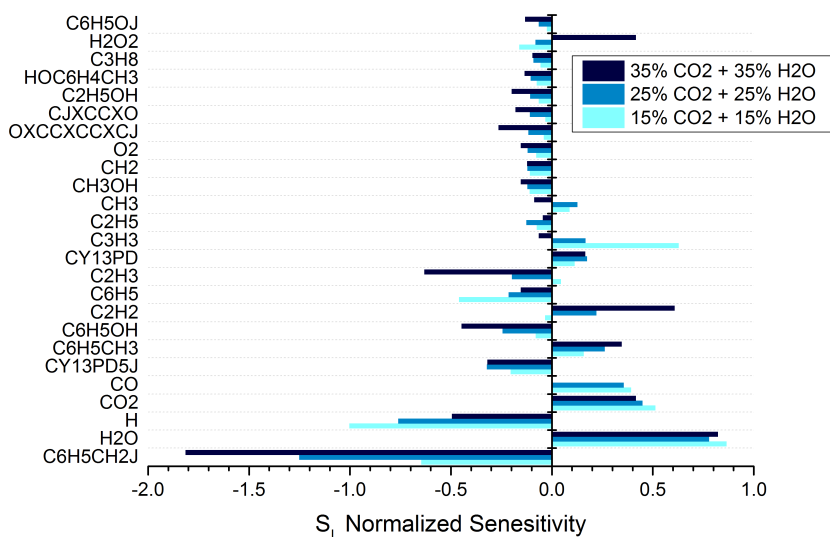


Figure 4-15: Comparison of  $\Delta_f^{298}H$  sensitivity of  $S_L$  at various dilution ratios (30%, 50% and 70%). The rest condition, i.e., initial temperature, pressure, equivalence ratio, are the same as condition C5: 1200 K, 10 bar,  $\phi = 1.1$ . Results are obtained using the MACDIL 2016 mechanism.

toluene related species and  $C_2$  species are important to the laminar flame speed of TRFE/air/ $CO_2$ / $H_2O$  flames.

## 4.5 Conclusions

This chapter aims to identify the key thermokinetic parameters to the laminar flame speed of TRFE flame at diluted conditions. First, the setup of the initial model to simulate the laminar flame speed is introduced, including the composition of the surrogate fuel and synthetic EGR, the conditions at which calculations are performed, and the starting mechanisms, used in the present work. Based on this setup, two types of sensitivity analysis, the conventional sensitivity analysis and sensitivity analysis on composite functions, are performed to identify the important reactions in the starting mechanism. Results show that sensitive reactions mostly fall into four categories: (i) fundamental reactions in the hydrogen and methane sub-mechanisms, (ii) reactions involving intermediate  $C_2$ – $C_3$  molecules, (iii) reactions involving aromatic radicals, and (iv) alkane fuels decomposition reactions. In addition, radical + diluent molecule reactions are also considered. Species with important thermodynamic property, i.e., heat of formation ( $\Delta_f^{298}H$ ), are identified using sensitivity analysis. Results show that important species are mostly toluene related species and  $C_2$  molecules. A brief literature review was conducted to identify reactions of interest for future theoretical studies. Among them, The  $CH_2CO + OH$  reaction is studied theoretically in Chapter 3, while the other 5 reactions are planned for future works.

# Chapter 5

## Kinetic Study on the Chemical Effects of H<sub>2</sub>O and CO<sub>2</sub> Dilution on Laminar Flame Speeds

### 5.1 Introduction

In this chapter, the dilution effects of H<sub>2</sub>O and CO<sub>2</sub> on laminar flame speeds are investigated, using mainly the false-species method and the novel sensitivity analysis on composite functions as described in Chapter 2. The dilution ratio is defined as the fraction of the diluent molecule, such as H<sub>2</sub>O and CO<sub>2</sub>, in the whole mixture, unless specified. The investigations focus mainly on the chemical effects of H<sub>2</sub>O and CO<sub>2</sub> on small molecule fuels, i.e., hydrogen (H<sub>2</sub>), syngas (H<sub>2</sub>/CO), and methane (CH<sub>4</sub>). This is consistent with the first of the four categories of important reactions identified in Chapter 4. Reactions in these sub-mechanisms are at the final stage of combustion events and tightly linked to the concentration of the radical pool and the formation of final products (i.e., H<sub>2</sub>O and CO<sub>2</sub>). Therefore they are highly sensitive to flame speeds and their mechanisms might be affected directly by the dilution of H<sub>2</sub>O and CO<sub>2</sub>. The present work focus on the small species as they are the most sensitive for flame speed evaluation. Further studies is necessary to explore the impact of heavier molecules.

### 5.2 Diluted Flames of Hydrogen (H<sub>2</sub>)

#### 5.2.1 Laminar Flame Speeds

The performance of three mechanisms, the starting mechanism LLNL 2011 [25], Kéromnès 2013 [17] and Konnov 2019 [98], are compared based on laminar flame speed with experiments at both standard condition and H<sub>2</sub>O diluted conditions.

#### Computational Details

Laminar flame speeds are calculated using the PREMIX code implemented in CHEMKIN PRO. By using continuations, the length of the domain was extended to 120 cm, and final grids with over 1000 points were obtained with the restriction GRAD=0.01 and CURV=0.01, to ensure freely-propagating and grid-insensitive

flames. Multi-component transport and thermal diffusion (the Soret effect) are considered.

## H<sub>2</sub>/air flame

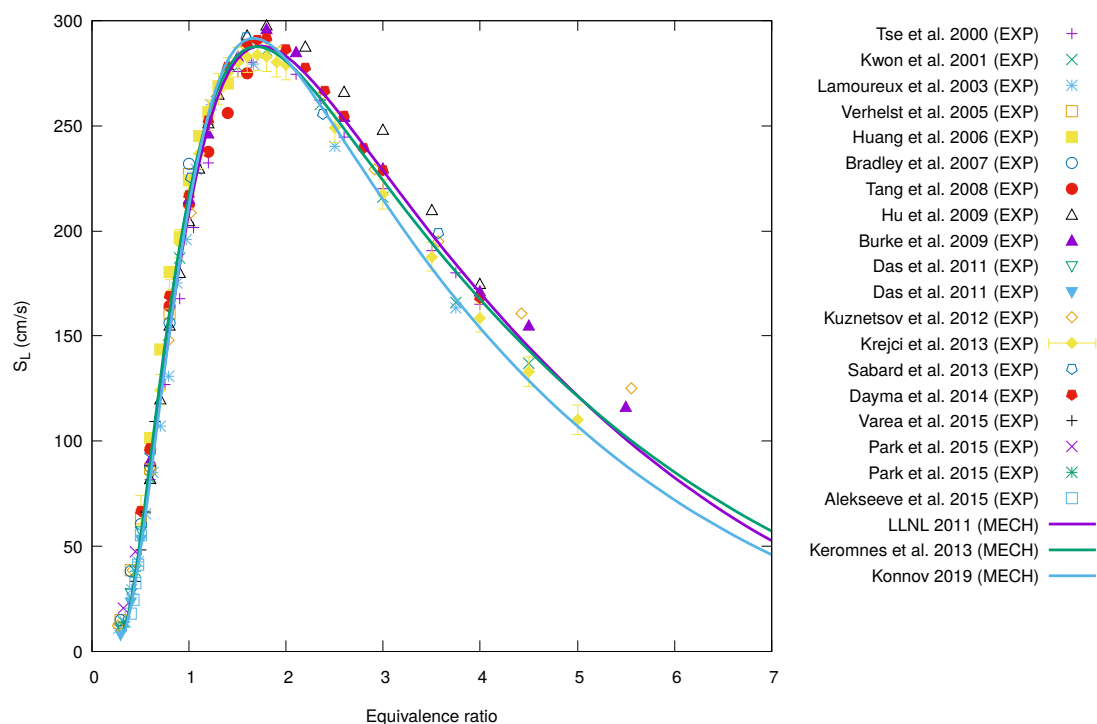


Figure 5-1: Fundamental  $S_L$  of H<sub>2</sub>/air mixture at 298 K and 1 atm.

Laminar flame speeds of hydrogen/air flame at standard conditions (298 K, 1 atm) are reported in Figure 5-1. The experimental data are obtained using various methods, such as spherical flame method, heat flux method and stagnation flame method, and are all after the year 2000. They are quite close in terms of values with the largest discrepancy of less than 30 cm/s (or 10% relatively) for mixtures with  $\phi \leq 3$ . The predictions of the three mechanisms for such mixtures are similar and show good agreement with experiments, located in the center of the data range. For very rich mixtures ( $\phi > 3$ ), the discrepancy of experiments becomes larger up to about 20% relatively. The predictions for such mixtures are also different between the mechanisms, with Konnov 2019 located at the lower bound while the other two at the upper bound of the experimental band. All the mechanisms show good performance since they are comprehensively validated on such conditions at the time of development.

## H<sub>2</sub>/air flame diluted by H<sub>2</sub>O

Figure 5-2a–5-2c shows the comparison on H<sub>2</sub>O diluted hydrogen /air flames. It is obvious that H<sub>2</sub>O dilution decreases flame speeds significantly. As shown in Figure 5-2a, the predictions of the mechanisms are all significantly lower than the measurements. It may be due to the fact that the values are measured at an initial temperature of 373 K (or 100 °C), which is the condensation temperature of water

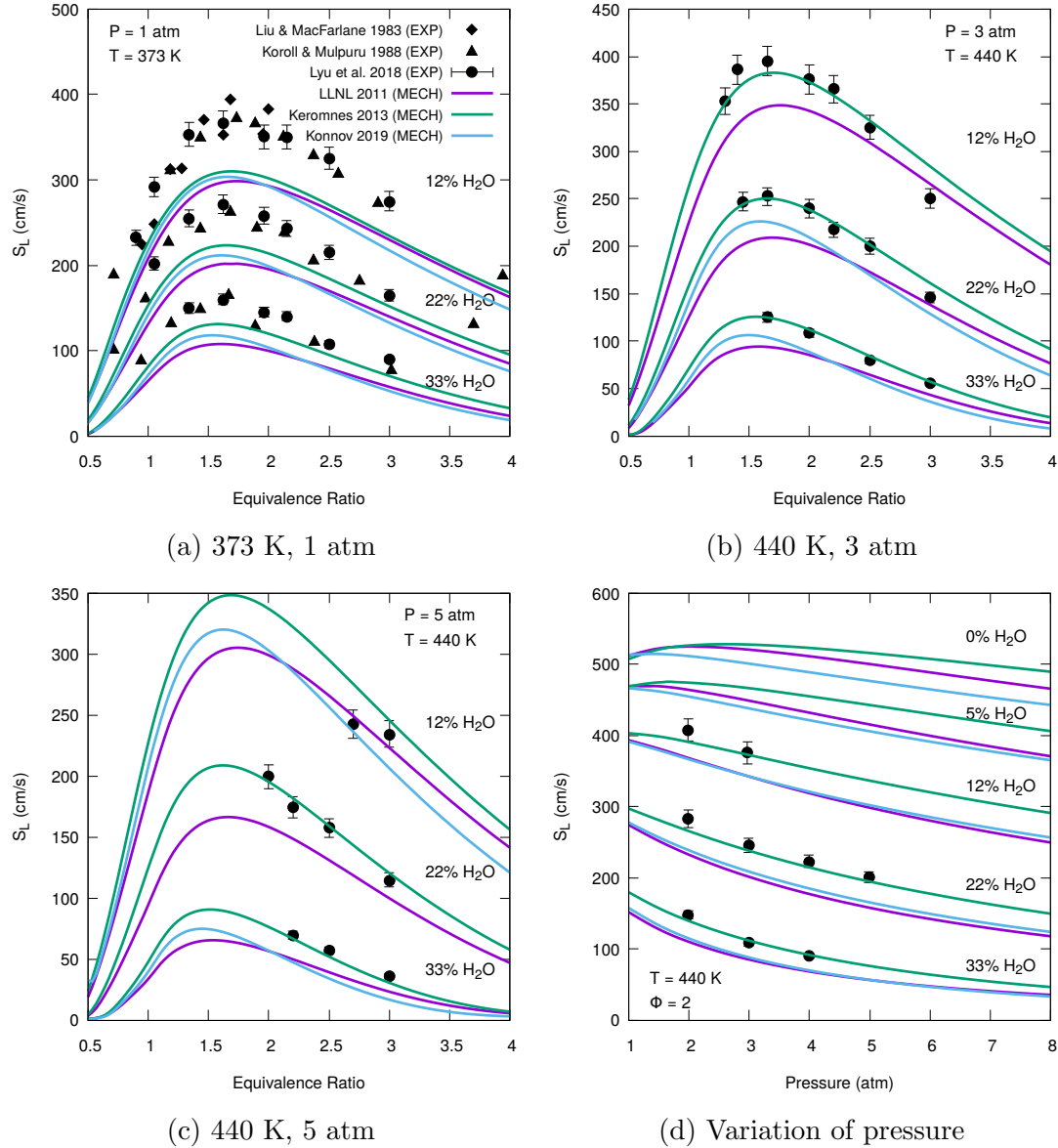


Figure 5-2: Laminar flame speed of  $H_2$ /air/ $H_2O$  mixture with different  $H_2O$  dilution ratios. Figures 5-2a–5-2c show evolution of  $S_L$  with equivalence ratio, and Figure 5-2d shows evolution with pressure.

vapor. Some part of the  $H_2O$  dilution may be condensed to liquid and therefore the actual  $H_2O$  dilution ratio is lower than designated which lead to higher flame speed measured. This possibility is supported by the fact that the mechanisms predict closer values with measurements at higher temperature (440 K) as shown in Figure 5-2b and 5-2c. Therefore, the uncertainty of the measurements in Figure 5-2a is questioned and not considered in the following validation.

For the 440 K case, measurements in Figure 5-2b is for pressure of 3 atm and 5-2c for 5 atm. The relative positions between the mechanism predicted values are similar for the two pressures. The K eromn es 2013 mechanism exhibits excellent agreement with experimental data at all the different  $H_2O$  dilution ratios, with its predicted values lying within the uncertainty range of the measurements for most points. Although it includes recently measured rate coefficients and updated

third-body collisional efficiencies for H<sub>2</sub>O molecules, the Konnov 2019 mechanism predicts values lower than the experiments and that of K eromn es 2013. The difference is by about 20 cm/s at pressure of 3 atm and 30 cm/s at 5 atm, for near stoichiometric and rich mixtures ( $\phi \geq 1.5$ ), however, the trend (or slope) of the curves are similar to that of K eromn es 2013. The starting mechanism, LLNL 2011, also generates predictions lower than measurements, by degrees similar to Konnov 2019. It predicts the evolution of  $S_L$  with equivalence ratio more moderate than the experiments, K eromn es 2013 and Konnov 2019, lower than Konnov 2019 for lean and near stoichiometric conditions and higher for rich conditions, with the interception at equivalence ratio of about 2–2.5.

Figure 5-2d shows the comparison based on the variation of pressure from 1 to 8 atm, for H<sub>2</sub>O dilution ratio from 0% to 33% and equivalence ratio of 2. For high dilution ratios (i.e., 22% and 33%), all three mechanisms predict a reasonable pressure evolution. The increase in pressure reduces  $S_L$  significantly but becomes less effective when reaching higher pressures. However, at lower dilution ratios (i.e., 0%, 5%, and 12%), a different trend is predicted by the mechanisms, where  $S_L$  increase slightly before it is reduced at higher pressure. This non-monotonic pressure dependence is consistent with the existing findings [361–364], and is associated with the change of reaction regimes where chain terminating reaction  $H + O_2 (+ M) = HO_2 (+ M)$  becomes dominant after the inflection pressure. The disappearing of the initial increase in  $S_L$  at higher H<sub>2</sub>O dilution is explained by that the chain branching reaction  $H_2 + OH = H_2O + H$  is suppressed by the high H<sub>2</sub>O concentration. Besides the values, the difference in the predictions of the mechanisms is that K eromn es 2013 predicts a strong non-monotonic pressure dependence which is still not yet suppressed by H<sub>2</sub>O at 12% dilution, while the other two mechanisms predict weaker trends. This may be due to the difference between the mechanisms in rate coefficients for the two mentioned reactions.

Based on the comparison with the above measurements, especially at H<sub>2</sub>O diluted conditions, it can be concluded that the K eromn es 2013 mechanism has the best overall performance and therefore is used for the following investigation on H<sub>2</sub>O dilution effects on hydrogen/air flames.

## 5.2.2 Effects of H<sub>2</sub>O Dilution on H<sub>2</sub>/air flames

In this section, H<sub>2</sub>O dilution effects on the  $S_L$ , flame temperatures and radical concentrations are quantified, and sensitive reactions for  $S_L$  are identified using sensitivity analysis. The investigated condition is the stoichiometric H<sub>2</sub>/air diluted by H<sub>2</sub>O with initial temperature of 440 K and pressure of 5 atm. It is the same as Figure 5-2c where mechanism predictions agree with the experiments by Lyu *et al.* [364] very well.

### Laminar Flame Speeds

Figure 5-3a shows the evolution of  $S_L$  with dilution ratio when diluted using different false species. It is obvious that H<sub>2</sub>O dilution reduces the  $S_L$  significantly and almost linearly at low dilution ratios. If constant effectiveness is assumed, the  $S_L$  would be reduced to zero at about 30% of dilution. However, at higher dilution ratios, the reduction effect becomes weaker, as the curve is bent and no

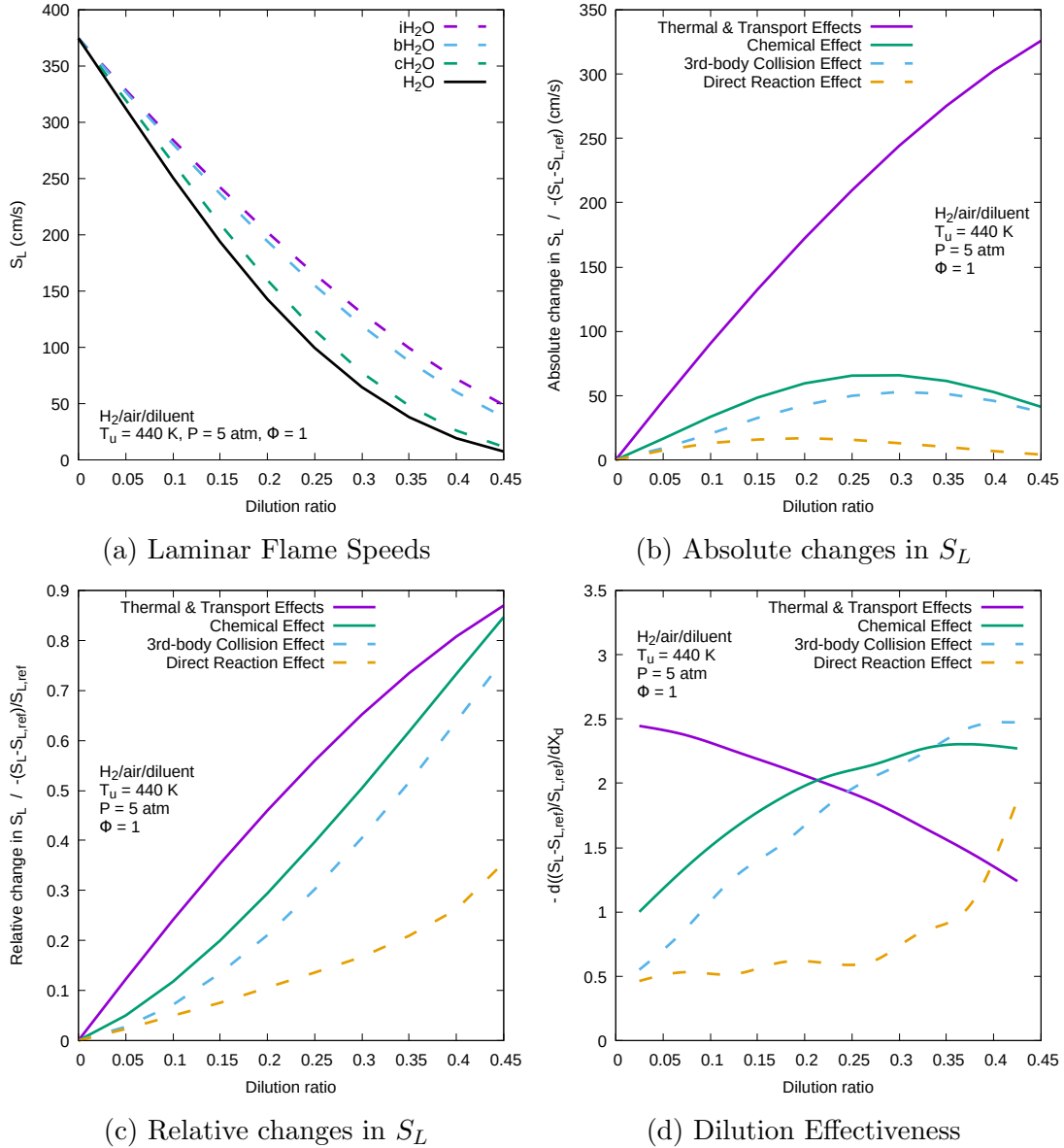


Figure 5-3: Quantification of H<sub>2</sub>O dilution effects on the  $S_L$  of stoichiometric H<sub>2</sub>/air mixtures at initial temperature of 440 K and pressure of 5 atm. Simulations are done using the Kéromnès 2013 mechanism [17]. The original negative values in Figure 5-3b–5-3d are adjusted to positive for visual convenience.

longer linear. As a consequence, the range of possible flame existence is broadened and simulations estimate that the  $S_L$  is reduced to nearly zero at around 55%. The reduction of  $S_L$  is mostly due to the thermal and transport effects, and further reduced by chemical effects. If only thermal and transports effects are considered (i.e., the iH<sub>2</sub>O curve in Figure 5-3a), the curvature is small and close to linear. The introduction of chemical effects increases curvature, as shown by the black bent curve of the real H<sub>2</sub>O molecule in Figure 5-3a). Therefore, it can be concluded that (i) H<sub>2</sub>O dilution reduces  $S_L$  non-linearly, (ii) the non-linearity is enhanced by chemical effects, and (iii) the reduction effect is weakened as dilution gets higher.

The thermal and transport effects are mainly contributed by the thermal effect. It is due to the fact that H<sub>2</sub>O is less diffusive comparing to other molecules in the



mixture (e.g., the binary diffusion coefficient of H<sub>2</sub>O is about only 14% of that of H at the same temperature and pressure), and its transport effects should not be significant. As mentioned in Section 2.5.1, within the thermal effects, concentration changes reduce  $S_L$  while heat capacity changes may contribute to the reduction either positively or negatively. In the present case, the specific heat capacity of the diluent (H<sub>2</sub>O, a 3-atom molecule) is higher than that of the product at normal conditions (mostly N<sub>2</sub>, a 2-atom molecule). Therefore it contributes positively to the reduction of flame temperature, which leads to reduced flame speeds.

Figure 5-3b depicts the absolute changes in  $S_L$  due to the different effects, while Figure 5-3c depicts the relative changes. It is implied by the figures clearly that 3rd-body collision effect is significantly greater than the direct reaction effect, and is the main contributor to chemical effects. In addition, the collision effect of H<sub>2</sub>O is larger than normal bath gas (i.e., the bH<sub>2</sub>O curve in Figure 5-3a). As shown in Figure 5-3b, the absolute changes caused by 3rd-body collision, direct reaction, and the total chemical effects, increase initially to a maximum and then decrease as  $X_d$  gets higher. In fact, the decrease at later stages is due to the limitation of the low  $S_L$  at reference cases. By considering the relative changes, we get rid of this limitation and found that the dilution effects all increase monotonically with  $X_d$ .

To further study the relative strength of the dilution effects, the dilution effectiveness (i.e., derivative of the relative changes) is studied, as shown in Figure 5-3d. It is found that the thermal and transport effects become weaker with increase dilution, while the chemical effects show the opposite trend and grow stronger. The interception occurs at about 20% dilution. Therefore, it is estimated, based on Figure 5-3c, that the chemical effects could surpass the thermal and transport effects at  $X_d > 0.45$ . Another interesting observation is that the effectiveness of direct reaction remains constant (or increase only slightly) at low dilution ( $X_d < 0.2$ ) but increases rapidly at higher dilution ( $X_d > 0.2$ ).

## Flame Temperature

Figure 5-4 shows the evolution of the flame temperature ( $T_f$ ) with increasing dilution. As shown in Figure 5-4a, H<sub>2</sub>O dilution reduces  $T_f$  linearly with a large gradient (211.8 K for every 10% dilution). The overlap of the curves using different false species in Figure 5-4b indicates that flame temperature is not affected by H<sub>2</sub>O dilution chemically. The linear correlation between  $T_f$  and  $X_d$ , caused by the thermal effect, is explained in section 2.5.1.

## Radical concentrations

Figure 5-5 shows the variation of the max mole fraction of radicals against dilution ratio. In the reaction zone, radicals are produced, accumulated, and then consumed. Therefore, the evolution of their maximum mole fractions reflects the variation of system reactivity. The max mole fraction of highly reactive radicals, H, OH and O, decrease monotonically with increasing  $X_d$ . Whereas the less reactive radicals, HO<sub>2</sub> and H<sub>2</sub>O<sub>2</sub>, first increase at low dilution and then decrease as  $X_d$  gets higher. The reduction of  $[H]_{\max}$  is much faster than that of  $[OH]_{\max}$ . As a consequence, the domination of H radical is overruled by OH as dilution gets

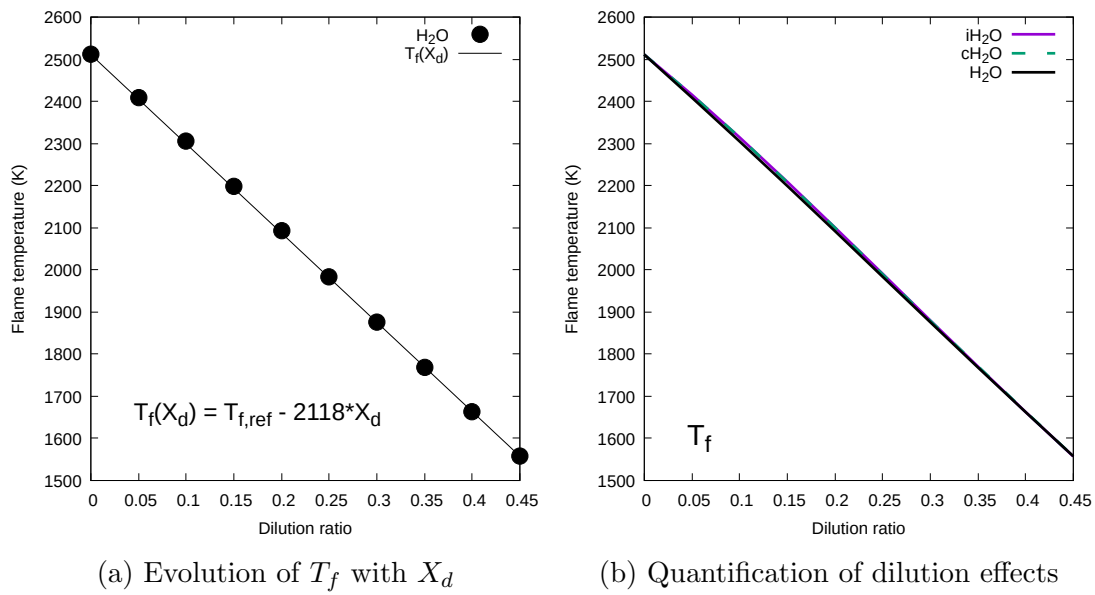


Figure 5-4: Effects of  $\text{H}_2\text{O}$  dilution on the flame temperature.

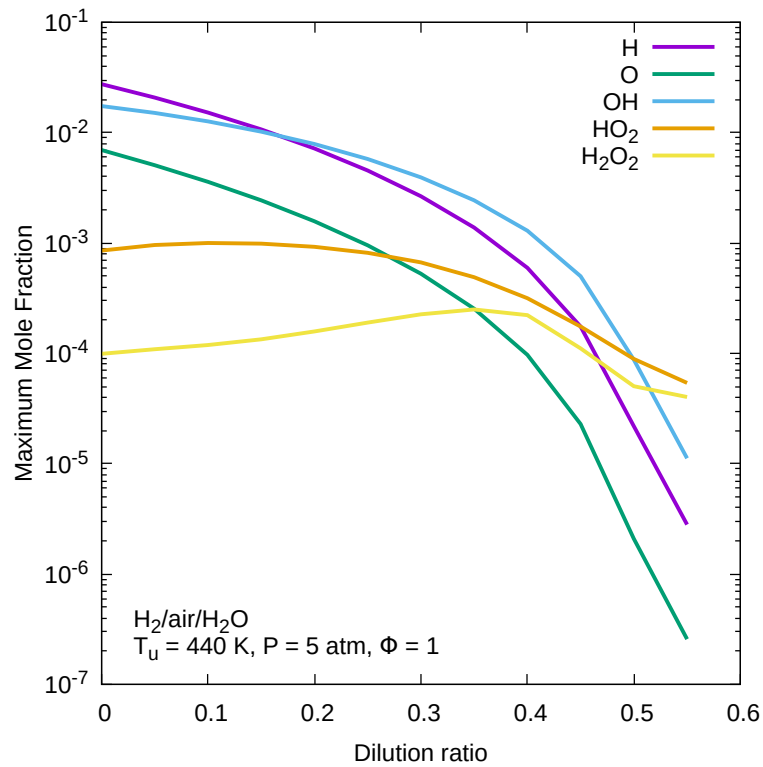
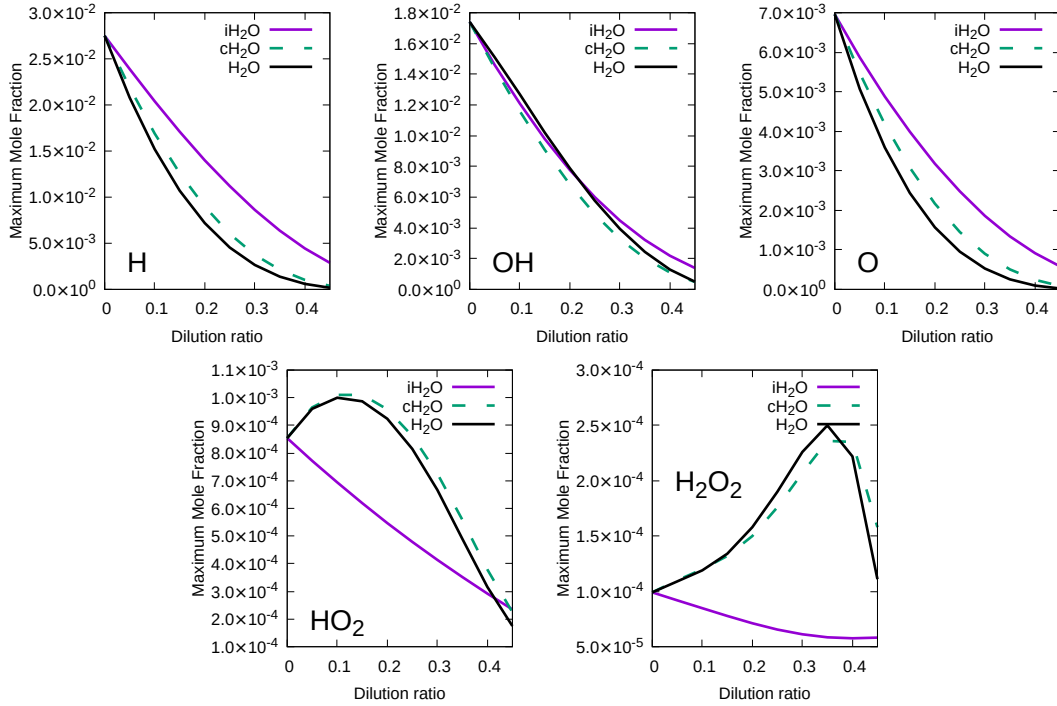
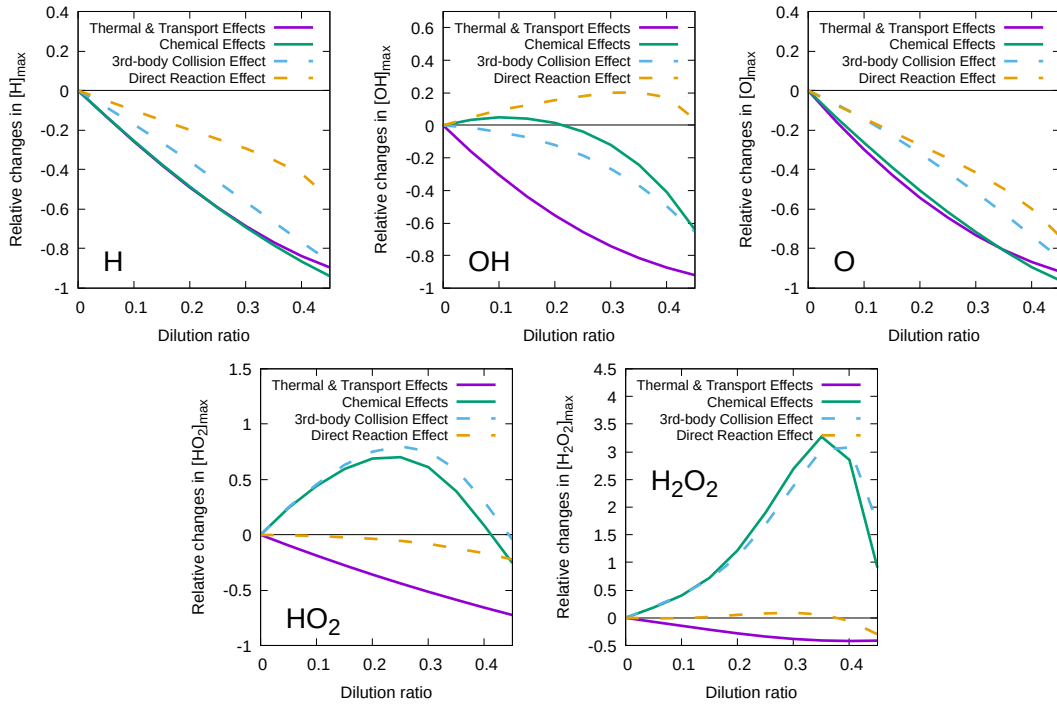


Figure 5-5: Evolution of maximum mole fraction of H, OH, O,  $\text{HO}_2$ , and  $\text{H}_2\text{O}_2$  radicals with dilution ratio.

higher than 20%. Figure 5-6a shows more clearly the non-monotonic evolution of  $[\text{HO}_2]_{\text{max}}$  and  $[\text{H}_2\text{O}_2]_{\text{max}}$ . Although they exhibit similar trends,  $[\text{HO}_2]_{\text{max}}$  starts to drop at low dilution ( $X_d \approx 0.1$ ) while  $[\text{H}_2\text{O}_2]_{\text{max}}$  drops at a much later stage ( $X_d \approx 0.35$ ). Their reduction is not as significant as H, OH, O radicals, and remain at the scale of  $10^{-4}$ – $10^{-3}$ . As dilution gets more intense ( $X_d > 0.5$ ), they surpass  $[\text{H}]_{\text{max}}$  and  $[\text{OH}]_{\text{max}}$  and become the most dominant radicals.



(a) Evolution of maximum mole fraction with dilution ratio.



(b) Quantification of various dilution effects.

Figure 5-6: Dilution effects of  $iH_2O$ ,  $cH_2O$  and  $H_2O$  on the maximum mole fraction of the H, OH, O,  $HO_2$ , and  $H_2O_2$  radicals. (a) Evolution of maximum mole fraction with dilution ratio. (b) Quantification of various dilution effects. The quantification, for example, of the direct reaction effect is calculated as the relative difference of the maximum mole fraction (e.g.,  $[H]_{max}$ ) at a certain dilution ratio of  $H_2O$  with respect to the reference case, i.e., the maximum mole fraction at the same dilution ratio of  $cH_2O$ .

The dilution effects on maximum mole fraction are separated (5-6a) and quantified (Figure 5-6b). It is obvious that thermal and transport effects reduce the mole fraction of all the radicals, while chemical effects have different influence depending on radicals. Concerning H radicals, chemical effects reduce  $[H]_{\max}$  with similar effectiveness as thermal and transport effects. It is mainly contributed by 3rd-body collision, the effectiveness of which is about twice of direct reaction effects. The reduction is mainly through the three-body reaction  $H + O_2 (+ M) = HO_2 (+ M)$ , where  $H_2O$  molecules are efficient collision partners. Other three-body reactions, such as  $H + H (+ M) = H_2 (+ M)$ , may also play a role. Concerning OH radicals, total chemical effect is positive at low dilution ( $X_d < 0.2$ ) but become negative at higher dilution ( $X_d > 0.2$ ). This results from the opposite effects of direct reaction and 3rd-body collision on  $[OH]_{\max}$ . 3rd-body collision reduces  $[OH]_{\max}$  and becomes more effective at dilution gets more intense. It affects mainly through the reactions  $OH + OH (+ M) = H_2O_2 (+ M)$  and  $H + OH (+ M) = H_2O (+ M)$ . Direct reactions increases  $[OH]_{\max}$  but its effect decreases at high dilution ( $X_d > 0.3$ ), e.g., almost negligible at  $X_d = 0.45$ . Concerning the  $HO_2$  radicals, its mole fraction would decrease with  $X_d$  if only thermal and transport effects are considered, which implies that chemistry plays an important role. 3rd-body collisions increase  $[HO_2]_{\max}$  significantly while direct reactions reduce it slightly. The overall chemical effect is therefore positive and dominated by 3rd-body collisions. The non-monotonic trend of  $[HO_2]_{\max}$  is originated from the same trend of the 3rd-body effect, which is weakened at high dilutions ( $X_d > 0.25$ ). The initial rise is mainly due to  $H + O_2 (+ M) = HO_2 (+ M)$ , which is an important chain terminating reaction in competition against  $H + O_2 = O + OH$  for H radicals and produce the less reactive  $HO_2$  radicals. The drop at higher dilution ratio could be due to (i) the lower concentration of H radicals which reduces the rate of  $H + O_2 (+ M) = HO_2 (+ M)$ , and (ii) the consumption of  $HO_2$  through  $HO_2 + HO_2 = H_2O_2 + O_2$  when  $[HO_2]$  gets higher.  $[HO_2]_{\max}$  exhibits the similar trend but also some difference: (i) the drop occurs much later, and (ii) effectiveness of chemistry increases with  $X_d$  before the drop occurs. This is possibly the accumulative results of two reactions: (i) the three-body reaction  $OH + OH (+ M) = H_2O_2 (+ M)$ , and (ii) the recombination of  $HO_2$  radicals to produce  $H_2O_2$  after  $HO_2$  is accumulated to higher concentration. The effect of direct reactions on  $[HO_2]_{\max}$  is not significant, slightly positive at low dilution and slightly negative at high dilution ( $X_d > 0.4$ ). The affecting mechanisms of direct reactions are studied in the next section using sensitivity analysis.

## Sensitivity Analysis

Key reactions, to which  $S_L$  is sensitive, are identified using sensitivity analysis. Figure 5-7 shows the evolution of these sensitivities with dilution ratio, with the left bar showing the values at the non-diluted condition. For the top 10 reactions shown, their sensitivities all increase with  $X_d$ , which is possibly due to the low reference value of  $S_L$  at higher dilution. Therefore, the relative position of these reactions and their response to  $X_d$  are more useful. As the most important chain-branching reaction,  $H + O_2 = O + OH$  remains as the most sensitive at all conditions. On one hand, the most responsive to  $X_d$  is reaction  $H + O_2 (+ M) = HO_2 (+ M)$ , which is not important at normal condition but becomes the second

most sensitive at  $X_d = 0.4$ . In addition, sensitivity to  $\text{HO}_2 + \text{H} = \text{OH} + \text{OH}$  and  $\text{HO}_2 + \text{OH} = \text{H}_2\text{O} + \text{O}_2$  also respond positively to  $X_d$ . Therefore, it is reasonable to suggest that  $\text{H}_2\text{O}$  dilution enhances chaining termination through  $\text{H} + \text{O}_2 (+ \text{M}) = \text{HO}_2 (+ \text{M})$  and leads to reduced  $S_L$ . As a consequence, the higher concentration of  $\text{HO}_2$  radicals promotes its own consumption through  $\text{HO}_2 + \text{H} = \text{OH} + \text{OH}$  and  $\text{HO}_2 + \text{OH} = \text{H}_2\text{O} + \text{O}_2$ . The  $\text{HO}_2 + \text{H} = \text{OH} + \text{OH}$  reaction, producing OH radicals, is chain branching and increases  $S_L$ . While the  $\text{HO}_2 + \text{OH} = \text{H}_2\text{O} + \text{O}_2$  reaction is chain-terminating and decreases  $S_L$ . On the other hand, some reactions important at normal condition, such as  $\text{OH} + \text{H}_2 = \text{H} + \text{H}_2\text{O}$  and  $\text{H} + \text{OH} + \text{M} = \text{H}_2\text{O} + \text{M}$ , are suppressed at diluted conditions.

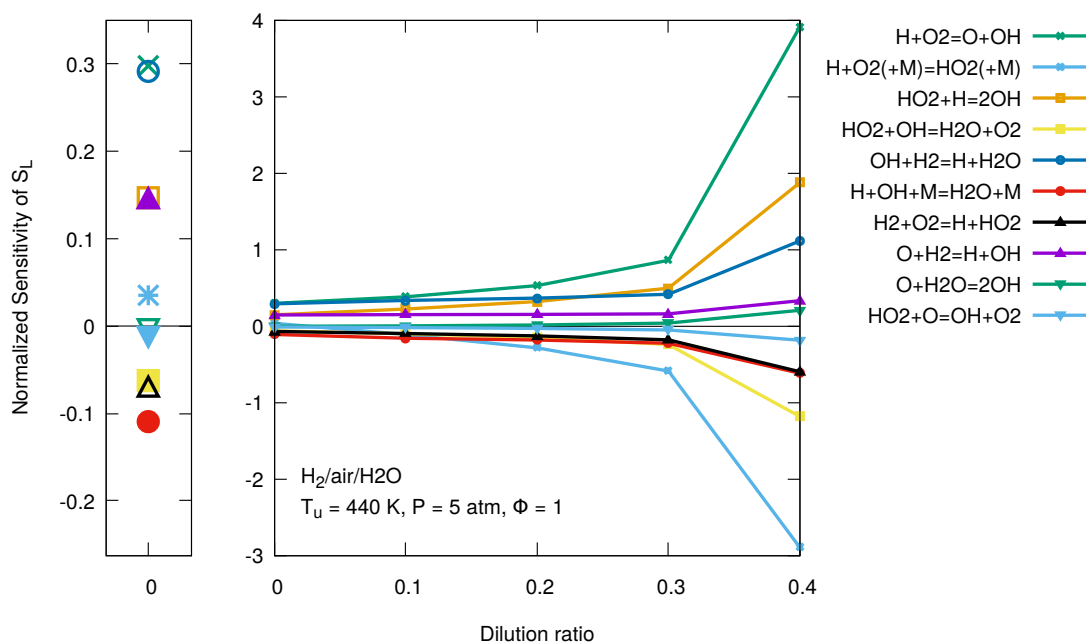
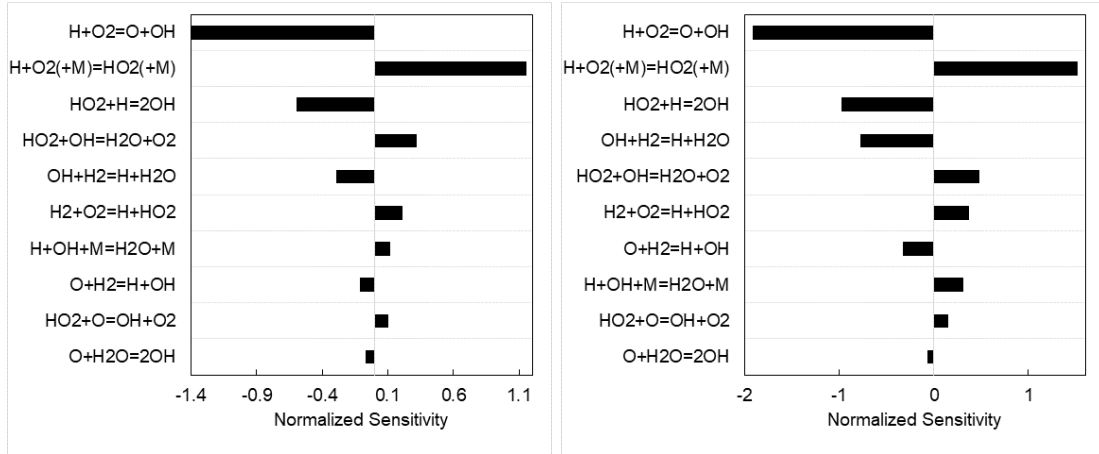
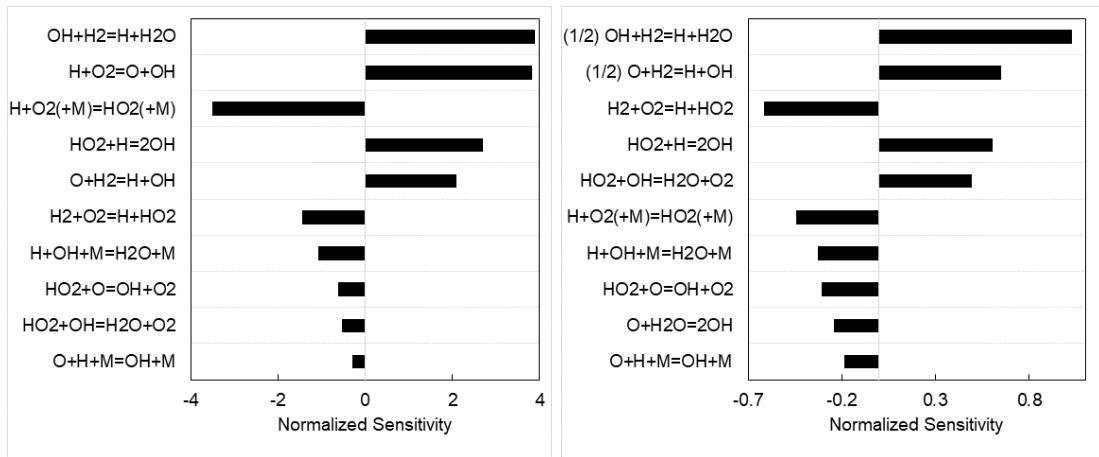


Figure 5-7: Evolution of  $S_L$  normalized sensitivity with  $\text{H}_2\text{O}$  dilution ratio. Investigated conditions:  $\text{H}_2/\text{air}/\text{H}_2\text{O}$  flame,  $\phi = 1$ ,  $T_u = 440$  K,  $P = 5$  atm.

Reactions important to the chemical effects are also studied and shown in Figure 5-8, using the sensitivity analysis of composite functions as introduced in section 2.6.2. The evolution of  $S_L$  relative changes with  $X_d$  are shown in Figure 5-9. Concerning 3rd-body collision effect, sensitivity on absolute and relative changes (Figure 5-8a and 5-8b respectively) give similar results. They confirmed that 3rd-body collision effect is mainly contributed by  $\text{H} + \text{O}_2 (+ \text{M}) = \text{HO}_2 (+ \text{M})$  while  $\text{H} + \text{OH} + \text{M} = \text{H}_2\text{O} + \text{M}$  is much less significant. The presence of reactions without a 3rd-body in the results is because the resulted change in radical concentration could enhance or inhibit other reactions involving these radicals. It is also suggested that successive  $\text{HO}_2$  consuming reactions play important roles, with the  $\text{HO}_2 + \text{OH} = \text{H}_2\text{O} + \text{O}_2$  reaction enhancing the 3rd-body collision effect (or reduce  $S_L$ ) and the  $\text{HO}_2 + \text{H} = \text{OH} + \text{OH}$  reaction inhibiting it (or increase  $S_L$ ). Normally, it is expected that the sensitivity of these sensitive reactions should increase with increasing  $X_d$ . However, Figure 5-9a shows that they exhibit a different and non-monotonic trend: increase ( $X_d < 0.1$ ) then decrease ( $0.1 < X_d < 0.3$ ) and increase again ( $X_d > 0.3$ ). More in-depth investigations are needed to explore the reason behind this behavior.



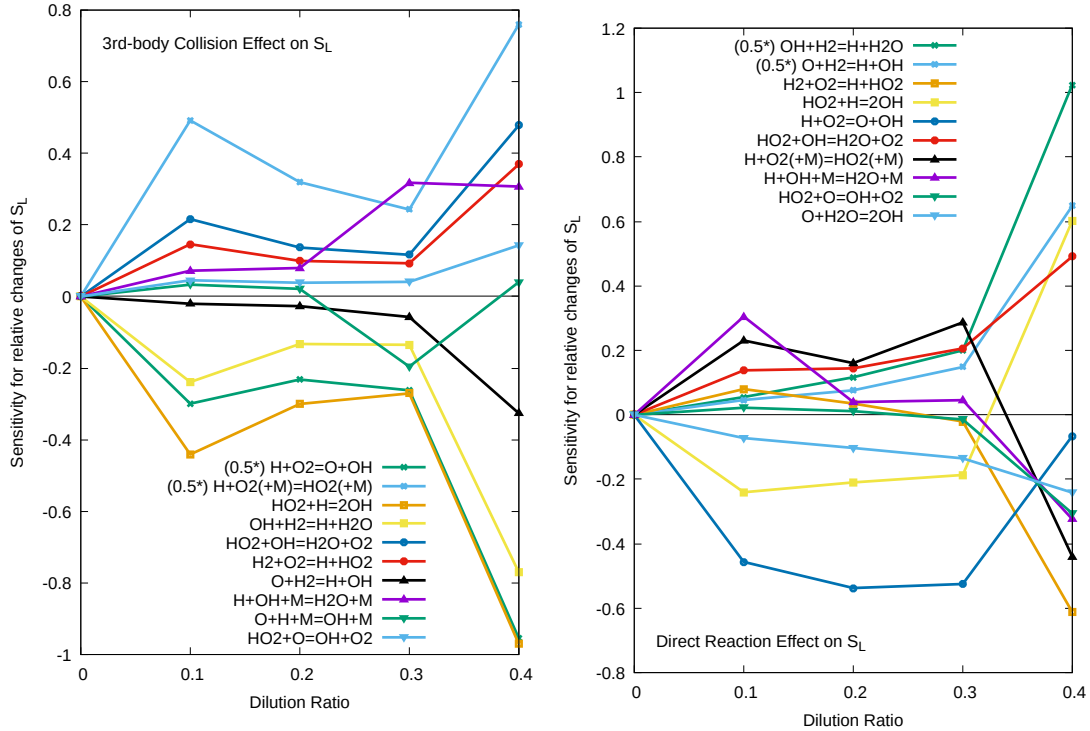
(a)  $S_L$  absolute changes by 3rd-body collision (b)  $S_L$  relative changes by 3rd-body collision



(c)  $S_L$  absolute changes by direct reactions (d)  $S_L$  relative changes by direct reactions

Figure 5-8: Sensitivity of  $S_L$  changes caused by chemical effects of  $H_2O$  dilution. Investigated conditions:  $H_2$ /air/ $H_2O$  flame,  $\phi = 1$ ,  $X_d = 0.4$ ,  $T_u = 440$  K,  $P = 5$  atm.

Concerning the direct reaction effect, sensitivity on absolute and relative changes (Figure 5-8c and 5-8d respectively) are quite different. Bared in mind that Figure 5-8c reflects the combined sensitivity (original values and magnified changes) while Figure 5-8d reflects only the changes in sensitivity. It is found that the most sensitive and responsive reaction is  $OH + H_2 = H + H_2O$ , converting fuel to product and OH to H radical. As it can be seen in Figure 5-9b, the sensitivity of this reaction is small at low dilution but increases rapidly with  $X_d$ . Unlike its inhibiting behavior on the 3rd-body collision effect, it is found to enhance the direct reaction effect.  $H_2O$  dilution could shift the chemical balance of  $OH + H_2 = H + H_2O$  to the reverse direction, leading to less H radical and slower fuel consumption speed and eventually lower  $S_L$ . The second important chain-branching reaction in combustion,  $O + H_2 = H + OH$  is also found to contribute significantly to the direct reaction effect.



(a)  $S_L$  relative changes by 3rd-body collision (b)  $S_L$  relative changes by direct reactions

Figure 5-9: Evolution, with  $H_2O$  dilution ratio, of the sensitivity of  $S_L$  relative changes caused by chemical effects. Investigated conditions:  $H_2/air/H_2O$  flame,  $\phi = 1$ ,  $T_u = 440$  K,  $P = 5$  atm.

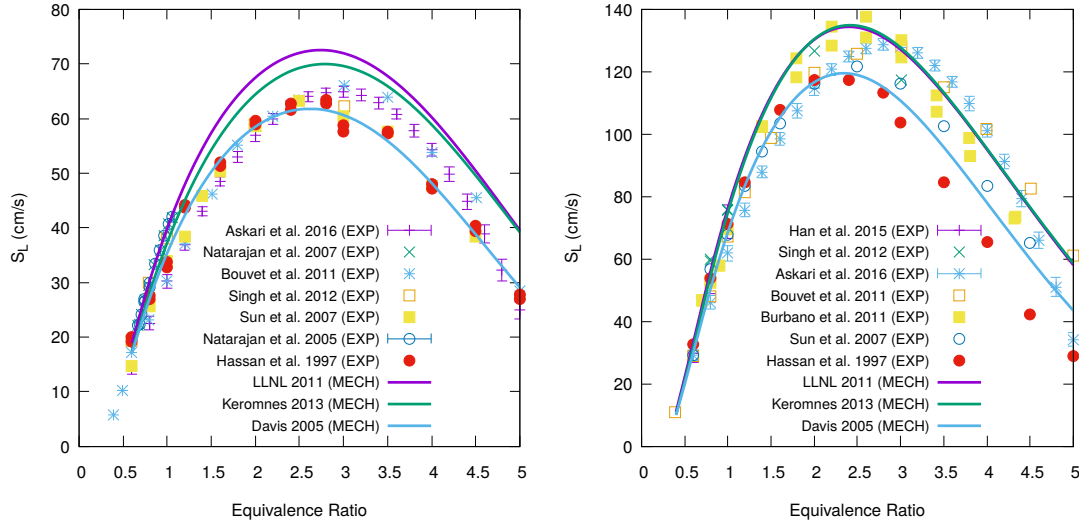
## 5.3 Diluted Flames of Syngas ( $H_2/CO$ )

### 5.3.1 Laminar Flame Speeds

The laminar flame speeds of syngas ( $H_2/CO$ ) mixture are calculated using three mechanisms and compared with measurements. The three mechanisms used are the starting mechanism LLNL 2011, K eromn es 2013, and Davis 2005 [102]. As mentioned in Chapter 1, previous evaluation [92] stated that the K eromn es 2013 mechanism has the overall best performance on various types of experimental data among the popular syngas mechanisms at the time. Davis 2005 is a widely used optimized mechanism for syngas and is included only for comparison purposes. More recent optimized mechanisms, such as the ELTE 2016 mechanism [365], are not adopted. The computation details are the same as those for hydrogen/air flames in the previous section.

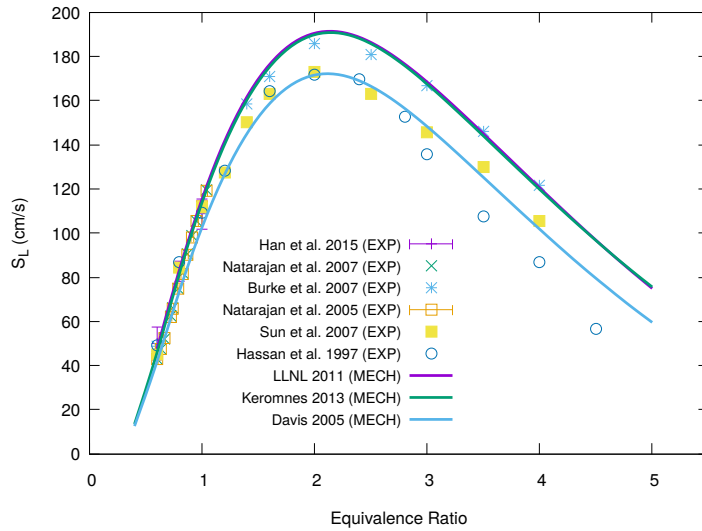
#### $H_2/CO/air$ flames

The laminar flame speeds at standard conditions (298 K, 1 atm) for syngas mixtures with various  $H_2/CO$  ratios are shown in Figure 5-10. For syngas mixtures with 5%  $H_2$  (as shown in Figure 5-10a), the discrepancies between experimental data are less than 10 cm/s (or 15% relatively) while the discrepancies between mechanism predictions are as large as 15–20 cm/s in maximum flame speed. The LLNL 2011 and K eromn es 2013 mechanism overestimate  $S_L$  with predic-



(a)  $H_2/CO = 0.05/0.95$

(b)  $H_2/CO = 0.25/0.75$



(c)  $H_2/CO = 0.5/0.5$

Figure 5-10: Comparison between mechanism predictions and measurements on the  $S_L$  of  $H_2/CO$ /air mixture at standard conditions (298 K, 1 atm).

tions higher than experimental data by about 5 and 10 cm/s in maximum  $S_L$ , respectively. The Davis 2005 mechanism, however, has good agreement with measurements and marks the lower bound of the data range. Since Davis 2005 is an optimized mechanism, it implies that comprehensive syngas mechanisms could be further improved to better predict the  $S_L$  of syngas mixture with very low hydrogen fraction. For syngas mixtures with 5%  $H_2$  (as shown in Figure 5-10b), the discrepancies between experimental data are larger, about 30 cm/s (or 20% relatively) for maximum  $S_L$  values and also fuel-rich conditions. The predictions by all the mechanisms all lie within the experimental data range, with the almost identical values from LLNL 2011 and K eromn es 2013 marking the upper bound while the predictions by Davis 2005 marking the lower bound of the experimental data. Similar situation are also found for equimolar syngas mixtures (as shown in Figure 5-10c). The large difference between the predictions could be associated



with the radical pool concentration calculated by the mechanism, especially the most H radical. It can be concluded that all three mechanisms have good agreements for syngas mixtures with 25% and 50% hydrogen, as their predictions are all within the uncertainty of measurements.

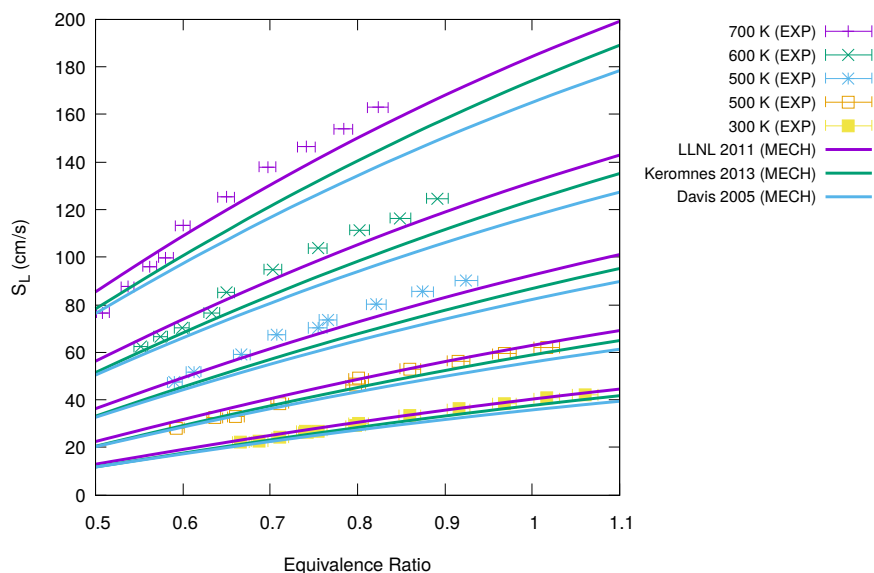


Figure 5-11: Effect of temperature on the  $S_L$  of  $H_2/CO/air$  mixture ( $H_2/CO = 0.05/0.95$ ) at 1 atm. Experimental data are from Ref. [18].

Figure 5-11 shows the effect of initial temperature on flame speed. Increasing  $T_u$  leads to higher  $S_L$  and the increase is more effective at higher temperatures. Predictions of the mechanisms are compared with experiments by Natarajan *et al.* [18]. It is found that all the models predict  $S_L$  sufficiently close to the measurements. For all the temperatures (300–700 K), results from LLNL 2011 go through the experimental data set, while the other near the lower bound. Between Kéromnès 2013 and Davis 2005, Kéromnès 2013 predicts values slightly higher than Davis 2005, but the evolution with equivalence ratio is consistent with that of LLNL 2011. Figure 5-12 shows the effect of pressure. Large discrepancies, as large as 10 cm/s, are found between the predicted  $S_L$  by the three mechanisms. The predicted pressure dependence are similar to each other, but more significant compared to the moderate reduction in  $S_L$  of the experimental data. It implies that the pressure dependence of these mechanisms could be further improved.

### $H_2/CO/air$ flames diluted by $CO_2$

Figure B-1 shows the  $S_L$  at various  $CO_2$  dilution ratio (in fuel) for the equimolar syngas mixture. It is seen that increasing dilution of  $CO_2$  reduces  $S_L$ . Although with quite large differences (up to 30 cm/s), all the three mechanisms predict values sufficiently close to experiments, considering the fact that the uncertainty of measurement is also large and about the same scale. Similar to previous validations, Kéromnès 2013 marks the upper bound, Davis 2005 marks the lower bound, and LLNL 2011 goes through the experimental data range. In addition, the disagreement between LLNL 2011 and Kéromnès 2013 is mostly located at the range where  $\phi \leq 2.5$ , while the predictions from the two mechanisms become closer as

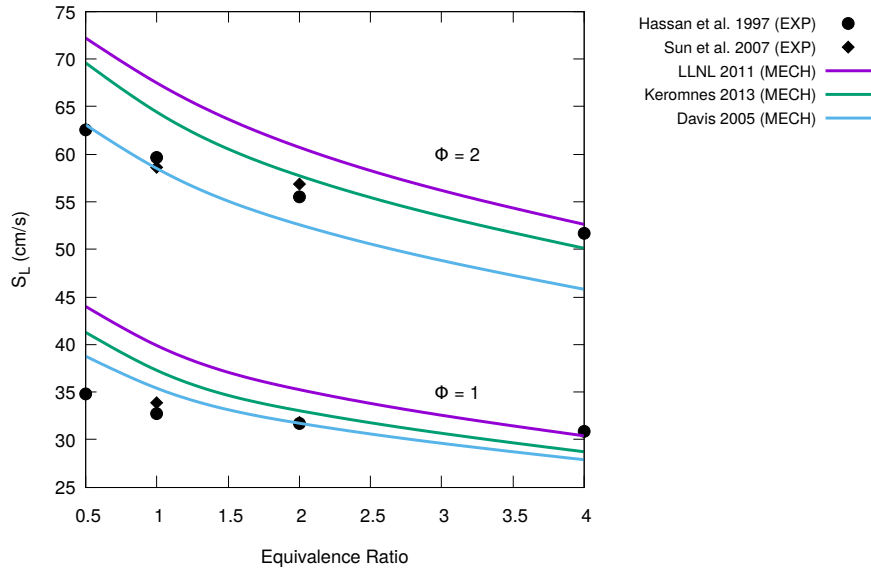


Figure 5-12: Effect of pressure on the  $S_L$  of  $H_2/CO/air$  mixture ( $H_2/CO = 0.05/0.95$ ) at 298 K. Experimental data are from Ref. [19,20].

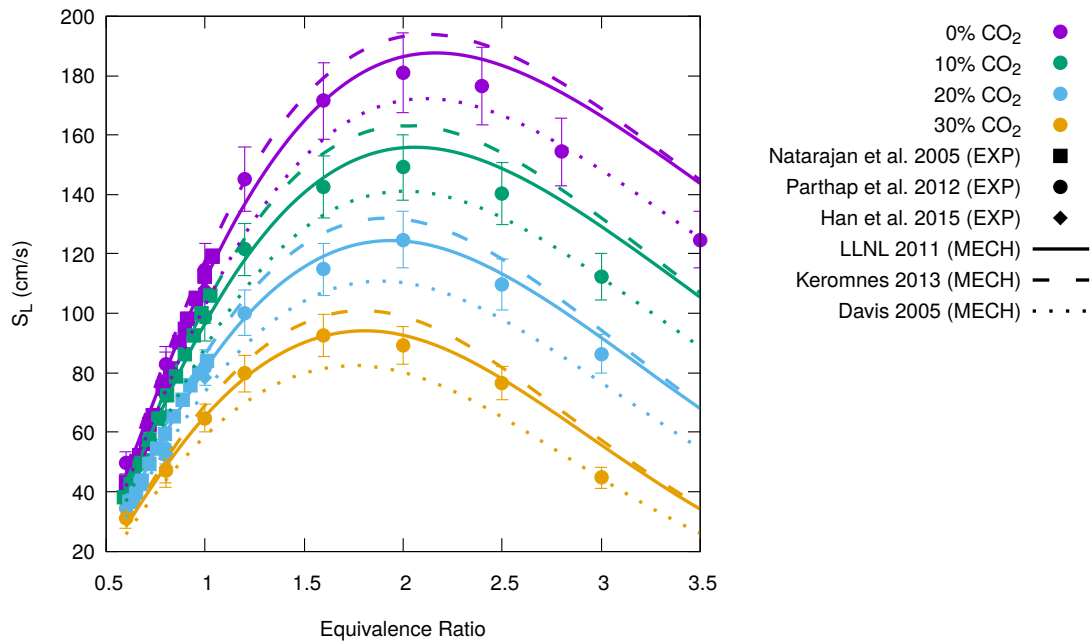


Figure 5-13: Effect of  $CO_2$  dilution in fuel on the laminar flame speed of equimolar syngas ( $H_2/CO = 1/1$ ) at standard conditions (298 K, 1 atm). Experimental data are from Natarajan *et al.* [18], Prathap *et al.* [21], and Han *et al.* [22].

the mixture gets richer. From Figure 5-14a and 5-14b, it can be seen that  $CO_2$  dilution reduces  $S_L$  almost linearly at the range of 0–40% ratio in fuel. Increase of hydrogen concentration in fuel (as shown in Figure 5-14a) and initial temperature (Figure 5-14b) both lead to higher flame speeds. All the mechanisms show good agreement, considering the uncertainty of experiments.

These validations show that the three mechanisms can predict with sufficient accuracy on the evolution of flame speed with equivalence ratio, temperature,

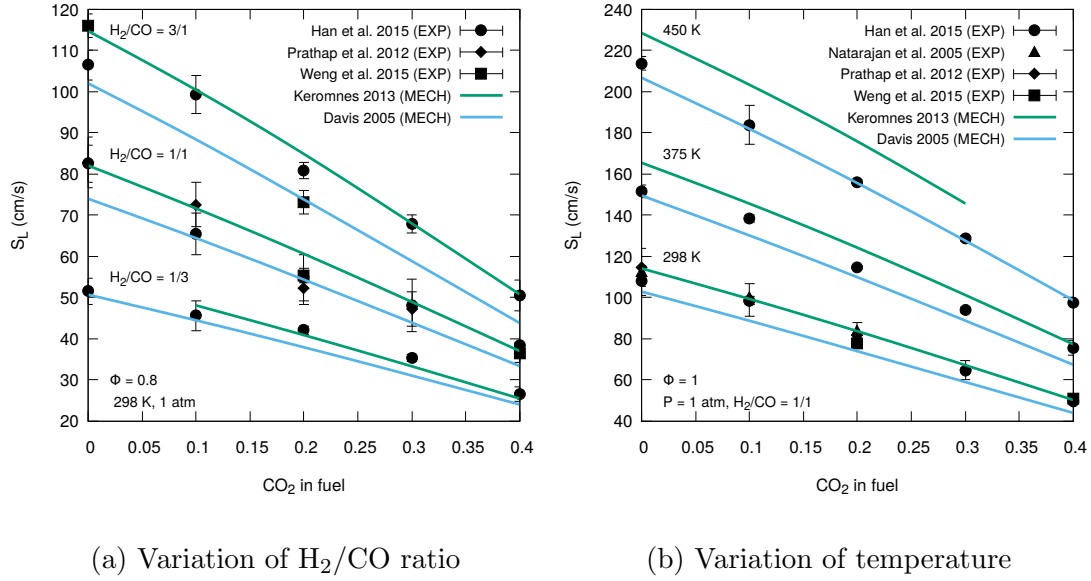


Figure 5-14: Effect of  $CO_2$  dilution in fuel on  $S_L$ , with variation of (a)  $H_2/CO$  ratio and (b) initial temperature. Experimental data are Ref [18,21,22] and Wang *et al.* [23].

pressure, and  $CO_2$  dilution. For further study on the dilution effect of  $CO_2$ , the K eromn es 2013 mechanism is used for its inclusion of more state-of-the-art rate parameters.

### 5.3.2 Effect of $CO_2$ Dilution on $H_2/CO/air$ flames

#### Effect on Laminar Flame Speed

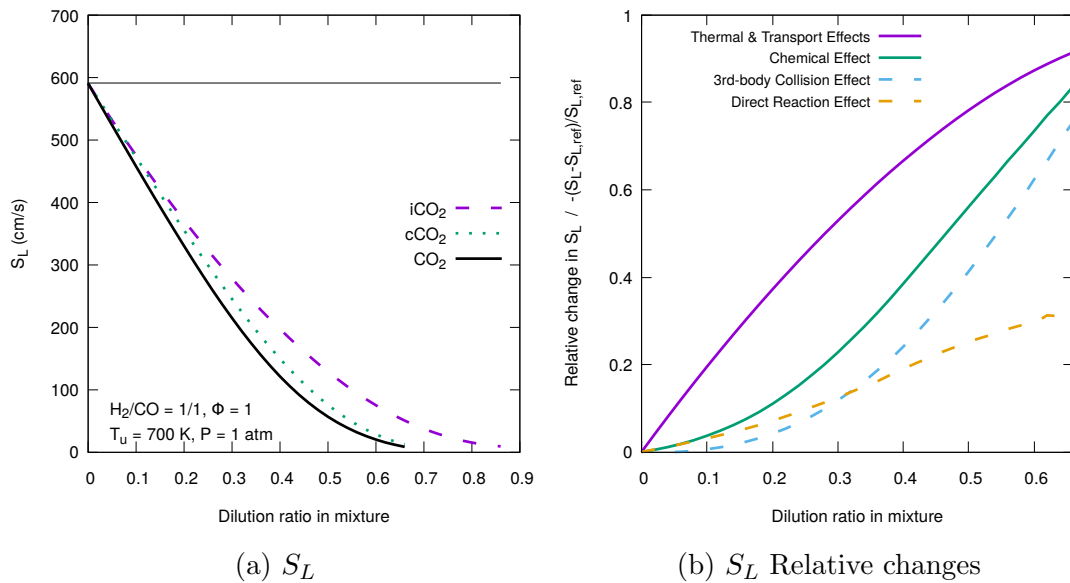


Figure 5-15: False-species analysis on the different effects of  $CO_2$  on the  $S_L$  of syngas/air flames.

Figure 5-15 shows the effects of  $CO_2$  dilution on laminar flame speeds. In the

previous section, the dilution ratio is defined as the mole fraction of  $\text{CO}_2$  in the fuel mixture, which is convenient for experimental setups but not consistent with the definition used in the present work. Therefore, the following investigations abandon this definition and define the dilution ratio as the fraction of  $\text{CO}_2$  in the whole mixture, which is consistent with other parts of this thesis. As shown in Figure 5-15a, the reducing effects are similar to the  $\text{H}_2\text{O}$  dilution effect on hydrogen/air flame (Figure 5-3a). The reduction is mainly due to the thermal effect, and chemical effects further reduce  $S_L$  and bring more curvature to the curve. As shown in Figure 5-3a, for hydrogen/air flame diluted by  $\text{H}_2\text{O}$ , chemical effect is dominated by third-body collision effect, at all dilution ratios. However, for syngas/air flames diluted by  $\text{CO}_2$  as shown in Figure 5-15b, direct reaction effect is the main contributor to the total chemical effect at low dilution, especially at lower than 10% dilution. Third-body collision effect is negligible at low dilution, but increases as dilution get higher. It surpasses the direct reaction effect at 30% dilution and takes over the dominant role. Eventually, at very high dilution (about 60%), the third-body collision effect is about twice of direct reaction effect. This may be due to the presence of CO sub-mechanism which allows direct participation of  $\text{CO}_2$  in these reactions. While the influence of  $\text{CO}_2$  concentration through the many three-body reactions in the  $\text{H}_2$  sub-mechanism increase slowly, since  $\text{CO}_2$  is not an effective collision partner comparing to  $\text{H}_2\text{O}$ .

## Sensitivity Analysis

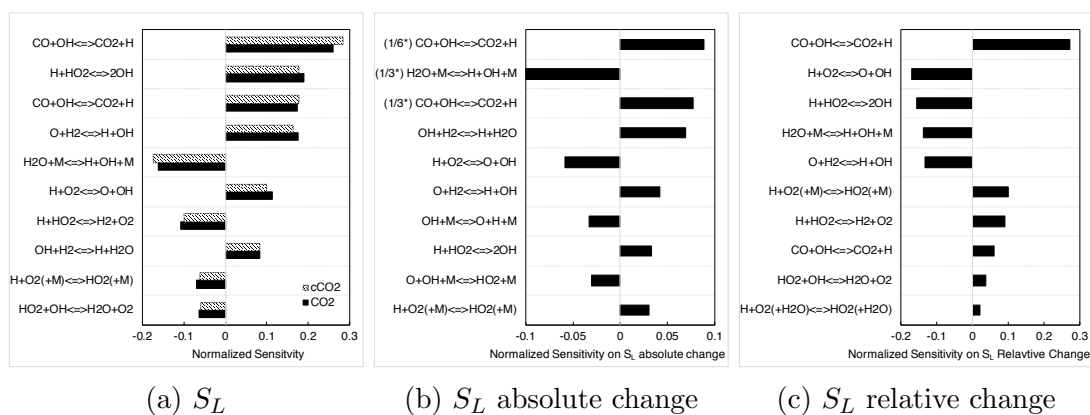


Figure 5-16: Sensitivity of important reactions in the  $\text{CO}_2$  diluted  $\text{H}_2/\text{CO}/\text{air}$  flame, performed based on its (a)  $S_L$ , (b) absolute and (c) relative changes in  $S_L$  caused by direct reaction effect (difference between  $\text{CO}_2$  and  $\text{cCO}_2$  dilution). The reference condition is: stoichiometric equimolar  $\text{H}_2/\text{CO}$  mixture with 40%  $\text{CO}_2$  dilution in fuel at standard conditions (298 K, 1 atm).

Both conventional sensitivity analysis and sensitivity analysis on composite functions are used to identify key reactions that are sensitive to the chemical effects of  $\text{CO}_2$  dilution, with their results shown in Figure 5-16. The investigation is based on stoichiometric, equimolar syngas mixture at 40% dilution in fuel by  $\text{CO}_2$  and  $\text{cCO}_2$  respectively, the difference between which is related to the direct reaction effect of  $\text{CO}_2$ . Figure 5-16a shows the sensitive reactions to  $S_L$ , while Figure 5-16b and 5-16c shows reactions sensitive to the absolute and relative difference in  $S_L$ ,

respectively. Results for relative change shows reactions whose sensitivity changes significantly with the change of condition, while results for absolute change also include reactions that are most sensitive at both conditions.

In these results, the most significant change in the sensitivity is for the major heat release step,  $\text{CO} + \text{OH} = \text{CO}_2 + \text{H}$ , which is inhibited by the high concentration of  $\text{CO}_2$ . This thermal dissociation of  $\text{CO}_2$  consumes H radical and produces CO and the less reactive OH radicals, which has the effect of reducing the flame speed. It is found that several other H radical consuming reactions are enhance, such as  $\text{H} + \text{HO}_2 = \text{H}_2 + \text{O}_2$ ,  $\text{H} + \text{O}_2 (+ \text{M}) = \text{HO}_2 (+ \text{M})$  which also have negative effect on  $S_L$ , but also reactions such as  $\text{H} + \text{HO}_2 = \text{OH} + \text{OH}$  and  $\text{H} + \text{O}_2 = \text{O} + \text{OH}$  which could increase system reactivity. In these reactions, less reactive radicals, such as O, OH, and  $\text{HO}_2$  are produced. It is worth noting that the thermal dissociation of  $\text{H}_2\text{O}$ ,  $\text{H}_2\text{O} + \text{M} = \text{H} + \text{OH} + \text{M}$ , is inhibited, possibly due to the abundant presence of OH radicals. This increases the formation of the final product ( $\text{H}_2\text{O}$ ) and may have a positive effect on  $S_L$ . The higher concentration of  $\text{H}_2\text{O}$  is also supported by the fact that chain terminating reaction  $\text{H} + \text{O}_2 (+ \text{H}_2\text{O}) = \text{HO}_2 (+ \text{H}_2\text{O})$ , having  $\text{H}_2\text{O}$  as collision partners, is enhanced and have negative effects on  $S_L$ . The enhance of the same reaction but collision partners with other molecules,  $\text{H} + \text{O}_2 (+ \text{M}) = \text{HO}_2 (+ \text{M})$ , could be associated with the increased concentration of CO, which has collisional efficiency of higher than other bath gas molecules. In summary, the direct reaction effect of  $\text{CO}_2$  is mainly due to the promotion of thermal dissociation of  $\text{CO}_2$ , and the chain-terminating  $\text{H} + \text{O}_2 (+ \text{M}) = \text{HO}_2 (+ \text{M})$  reaction, which both compete H radicals with the chain branching  $\text{H} + \text{O}_2 = \text{O} + \text{OH}$  reaction.

## 5.4 Diluted Flames of Methane ( $\text{CH}_4$ )

### 5.4.1 Laminar Flame Speeds

In this section, predictions using two mechanisms, GRI Mech 3.0 [108] and Aramco Mech 3.0 [113], are compared with experiments on the laminar flame speed of methane, for both non-diluted and diluted conditions. GRI Mech 3.0 is a widely used comprehensive mechanism for natural gas combustion, but it has not been updated in the recent decade. Aramco Mech 3.0 is a widely used core mechanism, including sub-mechanism for many  $\text{C}_1 - \text{C}_4$  species, which has been constantly updated and is one of the state-of-the-art core mechanisms in the combustion community. They are both validated comprehensively on various types of experimental data of methane, including laminar flame speeds.

### Computational Detail

By using continuations, the length of the domain was extended to 20 cm, and final grids with about 400 points were obtained with the restriction  $\text{GRAD}=0.04$  and  $\text{CURV}=0.04$ , to ensure freely-propagating and grid-insensitive flames. Multi-component transport and thermal diffusion (the Soret effect) are considered.

## CH<sub>4</sub>/air flames

For the laminar flame speed of CH<sub>4</sub>/air mixtures at standard conditions (298 K, 1 atm), numerous measurements are available. However, it is reported that measurements before the year 1990 didn't consider flame stretch correctly and resulted in higher  $S_L$ . [84], such as the measurement by Egolfopoulos *et al.* [366] shown in Figure 5-17. Therefore, only experimental data obtained after the year 1990 are used in this work to validate mechanism predictions. Figure 5-17a shows the comparison of two mechanism with measurements. Although abundant data are available, the discrepancy between different sources is more than 5 cm/s (around 15% of relative difference). The large variation could be caused by multiple reasons, such as the different apparatus, flame contour processing methods, stretch extrapolation methods, and etc.. Both mechanisms predict reasonable values lying within the experimental range, with GRI Mech 3.0 near the upper bound while Aramco Mech 3.0 near the lower bound. Their difference is mainly located at lean and near stoichiometric conditions, but not significant (about 2 cm/s at largest deviation) considering the larger experimental uncertainty. Recent measurements have effectively reduced uncertainty, due to the advancing in experimental methods, such as the flat flame methods which do not require extrapolation to zero stretch and thus are expected to be more accurate. It can be seen from Figure 5-17b, where the same comparison is presented but with only experimental data obtained after the year 2010.

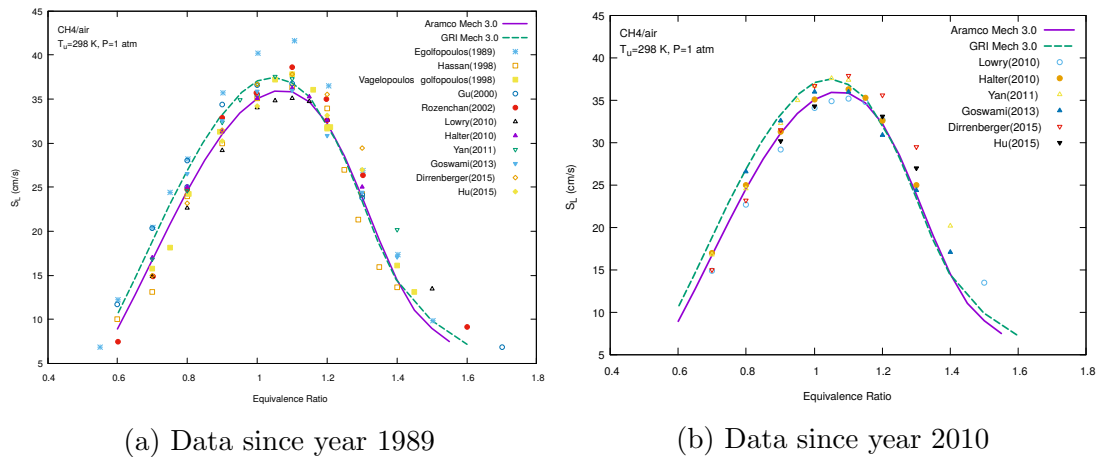


Figure 5-17: Laminar flame speed of CH<sub>4</sub>/air mixtures at standard conditions (298 K, 1 atm).

Figure 5-18 shows comparison of  $S_L$  at higher temperature (up to 600 K) and pressure (up to 10 bar). As shown in Figure 5-18a, both mechanisms have good agreement with measurements at lean and stoichiometric conditions. However, for rich mixtures, both mechanisms underestimate, but results from Aramco Mech 3.0 is closer to measurements. The pressure dependence is more clearly shown in Figure 5-18b, where excellent agreement with experiments is found for Aramco Mech 3.0. The effect of temperature on  $S_L$  is also well reproduced.

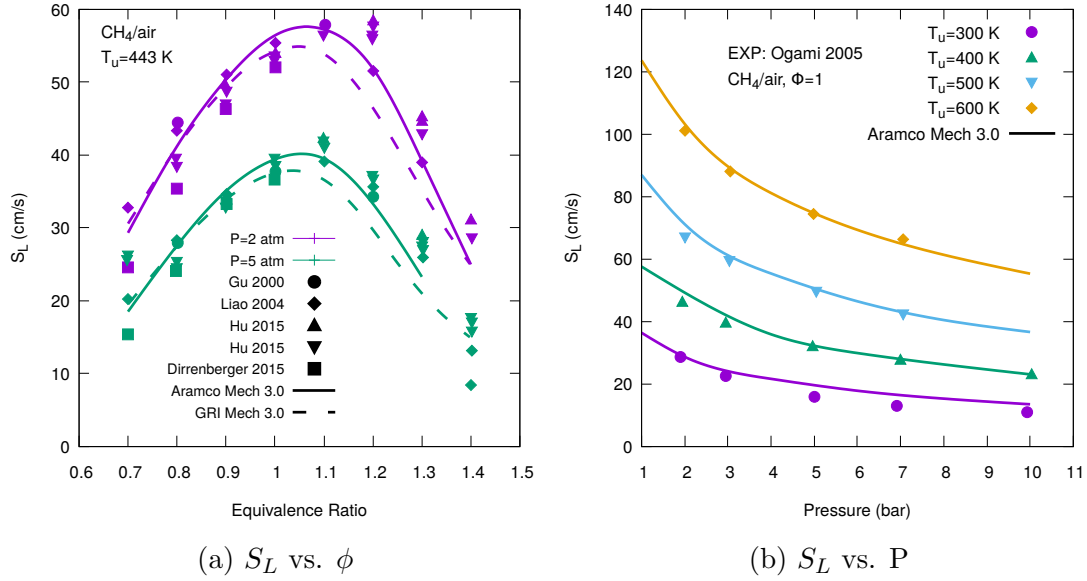


Figure 5-18: Laminar flame speed of CH<sub>4</sub>/air flames at higher temperature and pressure.

### CH<sub>4</sub>/air Flames Diluted by CO<sub>2</sub>

The CO<sub>2</sub> dilution effect on  $S_L$  is presented in Figure 5-19. In Figure 5-19a, methane/air flames are diluted up to 15%. Considering the discrepancies between experimental data, predictions from the two mechanisms are in overall good agreement. At  $\phi = 0.8$  and  $\phi = 1$ , Aramco Mech 3.0 predicts lower values than GRI Mech 3.0, while it is the opposite at  $\phi = 1.2$ . It is found that both mechanisms agree with measurements at low dilution ratios (less than 5%), but underestimate at higher dilution. Therefore, the effectiveness of CO<sub>2</sub> dilution they predicted is slightly stronger than observed from experiments. In Figure 5-19b, Aramco Mech 3.0 shows excellent agreements with experiments from Hu *et al.* [367] for non-diluted and 10% CO<sub>2</sub> diluted cases. False-species analysis is also conducted, and it is found that the third-body collisional effect is negligible based on the fact that curves for iCO<sub>2</sub> and cCO<sub>2</sub> overlap with each other. It implies that the chemical effect of CO<sub>2</sub> is mainly contributed by direct reactions at this condition.

In summary, both mechanisms show good agreement with experiments, but the pressure dependence for rich mixtures and the effectiveness of CO<sub>2</sub> dilution could be further improved. In the present work, Aramco Mech 3.0 is used for the investigation of the chemical effects of CO<sub>2</sub> on methane flames.

## 5.4.2 Effect of CO<sub>2</sub> Dilution

### Effect on Laminar Flame Speed

False-species analysis is used to study and quantify the various type of CO<sub>2</sub> dilution effects. Using false inert species (iCO<sub>2</sub>), collider species (cCO<sub>2</sub>), and real CO<sub>2</sub> as diluent respectively, the laminar flame speed is calculated using Aramco Mech 3.0 at initial temperature of 600 K, and pressure of 1 atm. The difference between iCO<sub>2</sub> and non-diluted cases is related to the thermal and transport effect, while that between real CO<sub>2</sub> and iCO<sub>2</sub> denotes the chemical effects. The chemical effect

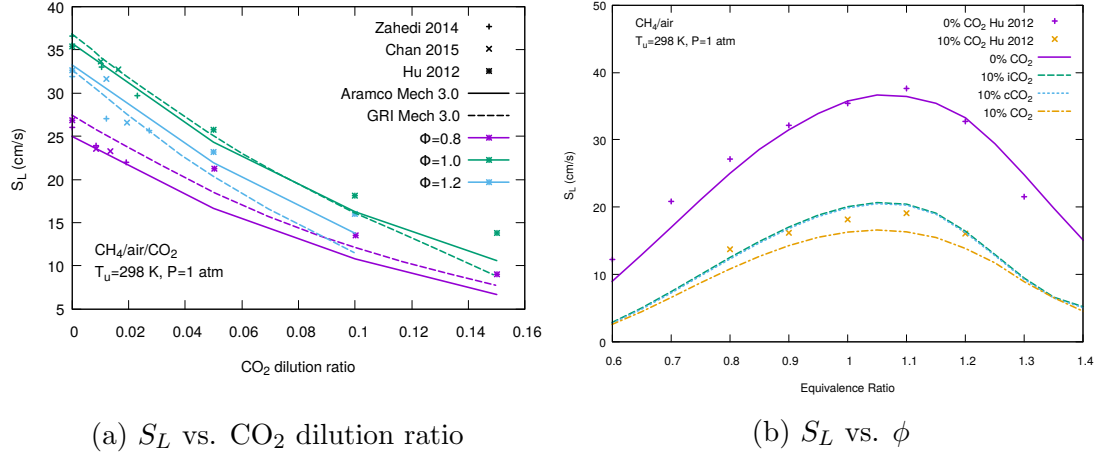


Figure 5-19: Effect of  $\text{CO}_2$  dilution on the  $S_L$  of  $\text{CH}_4/\text{air}$  flames. (a) comparison of  $S_L$  with respect to  $\text{CO}_2$  dilution ratio at various equivalence ratios. (b) comparison of  $S_L$  with respect to equivalence ratio, with false-species analysis to locate the composite effects of  $\text{CO}_2$ .

can be divided into third-body collision effect (between  $c\text{CO}_2$  and  $i\text{CO}_2$ ) and direct reaction effect (between  $\text{CO}_2$  and  $c\text{CO}_2$ ). As shown in Figure 5-20a, flame speed is reduced effectively by the introduction of  $\text{CO}_2$  dilution. The reduction is almost linear at low dilution ratios, while it becomes moderate as dilution increases. It can be concluded that the reduction effect of  $\text{CO}_2$  dilution on  $S_L$  is not linear. The reduction is mainly contributed by the thermal and transport effects (seen from the  $i\text{CO}_2$  curves in Figure 5-20a), which is also not linear but less bent than the curve for real  $\text{CO}_2$ . The fact that the  $i\text{CO}_2$  and  $c\text{CO}_2$  curves are so close to each other that almost overlap, indicates that the third-body collision effect of  $\text{CO}_2$  is subtle for methane flames. The Considerable amount of reduction in  $S_L$  is contributed by the direct reaction effects, which can be recognized from the separation between  $\text{CO}_2$  and  $c\text{CO}_2$  curves. The separation increases as dilution increases, reaches a maximum at around 15% dilution, and then decreases as dilution ratio further increases. It can be concluded that the presence of the direct reaction effect brings more curvature to the evolution of  $S_L$  with  $\text{CO}_2$  dilution, and is one of the contributors to the non-linearity.

The different types of dilution effects are quantified by the relative changes caused in  $S_L$ , and compared in Figure 5-20b. It is found that the thermal effect is about twice of chemical effect, and both of them depend positively on the dilution ratio but the increase becomes less rapid at higher dilution. The direct reaction effect is the main contributor to the total chemical effect, which is also shown in Figure 5-21a. This situation is completely opposite to the  $\text{H}_2\text{O}$  dilution effect, where third-body collision is dominant. It is mainly due to two reasons. On one hand,  $\text{H}_2\text{O}$  is a much more efficient collision partner than  $\text{CO}_2$ , because its collision efficiency is more than 3–6 times of  $\text{CO}_2$ . On the other hand, the chemical effect of  $\text{CO}_2$  dilution is mainly through reversing the reaction  $\text{CO} + \text{OH} = \text{CO}_2 + \text{H}$  whose rate is not affected by the concentration of collision partners. But  $\text{H}_2\text{O}$  dilution effect is mainly through the three-body reaction  $\text{H} + \text{O}_2 (+ \text{M}) = \text{HO}_2 (+ \text{M})$ , where  $\text{H}_2\text{O}$  is a very strong collider. It is worth noting in Figure 5-20b that, although third-body collision effect is negligible at low dilution ( $< 20\%$ ), it is



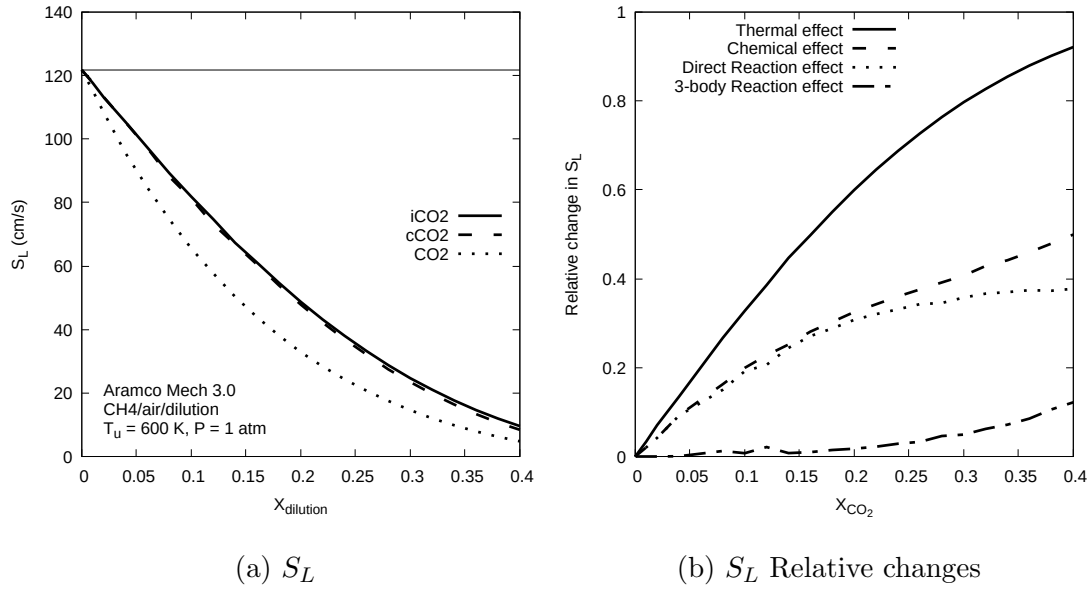


Figure 5-20: False-species analysis on the different effects of  $\text{CO}_2$  on the  $S_L$  of  $\text{CH}_4/\text{air}$  flames.

enhanced rapidly as dilution gets higher. The reason might be similar to that for syngas flames, where the abundant OH radicals inhibit the back dissociation of  $\text{H}_2\text{O}$ , the higher concentration of which could then enhance many three-body reactions. The reason why the effects are not observed at low dilution, may be due to that their rates are only comparable with reactions such as the reverse of  $\text{CO} + \text{OH} = \text{CO}_2 + \text{H}$  when  $\text{H}_2\text{O}$  concentration gets higher at higher dilution.

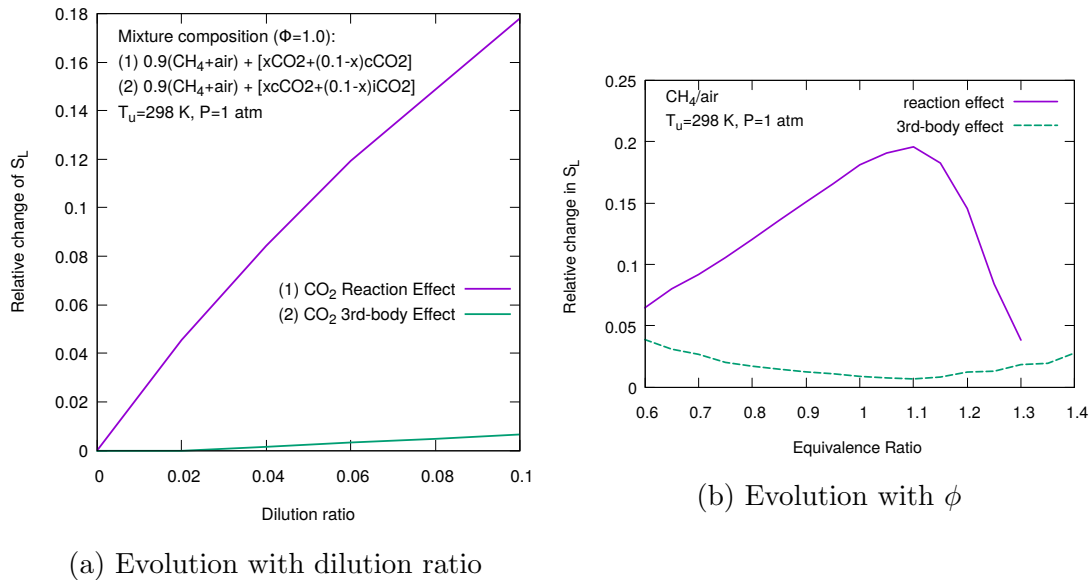


Figure 5-21: Evolution of the chemical effects of  $\text{CO}_2$  dilution with (a) dilution ratio and (b) equivalence ratio.

Figure 5-21b shows the evolution of with equivalence ratio for direct reaction effect and third-body collision effect respectively. It is found that the direct reaction effect is higher for near stoichiometric mixtures, but lower for lean and rich

mixtures. This is because the excess fuel (or oxidizer) for rich (or lean) mixtures reduce the reactant concentrations that could actually participate in reactions in a direct manner. On the contrary, the third-body collision effect shows the opposite trend, more effective for lean and rich mixtures and less for stoichiometric mixtures. The reason for this phenomenon needs further investigation.

### Effect on Temperature Profile

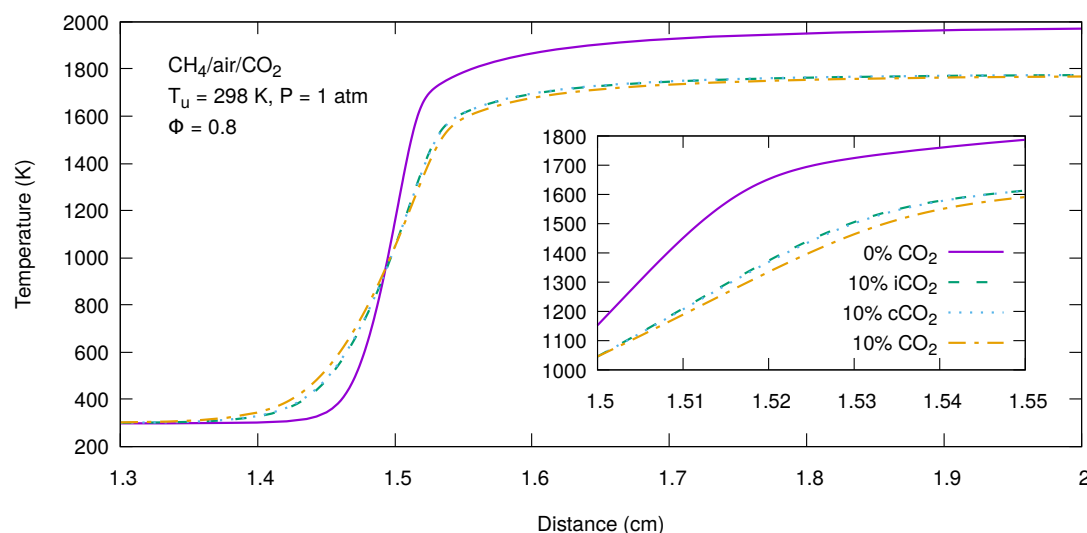


Figure 5-22: Temperature profile of methane/air flames at non-diluted condition and diluted conditions by  $\text{CO}_2$ ,  $i\text{CO}_2$ , and  $c\text{CO}_2$ .

Figure 5-22 depicts the various types of  $\text{CO}_2$  dilution effects on the temperature evolution with distance, using false-species analysis. It is found that the introduction of  $\text{CO}_2$  reduces significantly not only the flame temperature but also the temperature gradient in the reaction zone, which leads to larger flame thickness. Based on the difference between curves for  $i\text{CO}_2$ ,  $c\text{CO}_2$ , and  $\text{CO}_2$ , it can be concluded that the reduction in flame temperature and temperature gradient is mainly contributed by the thermal effect. The rest contribution is from direct reaction effect, while the third-body collision effect is negligible. It is because that the major heat release step,  $\text{CO} + \text{OH} = \text{CO}_2 + \text{H}$ , is influenced by direct reactions, and not affected by third-body collisions. The above phenomena are consistent with that for flame speed.

### Effect on Speciation Profile

Figure 5-23–5-25 show the direct reaction effect on the species concentrations, for lean, stoichiometric and rich conditions. Mole fractions of H, OH, O and  $\text{CH}_3$  radicals and important intermediate formaldehyde ( $\text{CH}_2\text{O}$ ) and ethane ( $\text{C}_2\text{H}_6$ ) are compared. It is found that the concentration of all the four radicals are reduced by direct reactions, except for rich mixtures. H radicals are consumed by the thermal dissociation of  $\text{CO}_2$ . It also compete H radicals with the major chain branching reaction  $\text{H} + \text{O}_2 = \text{O} + \text{OH}$ , which lead to lower formation of O and OH radicals. Since methyl ( $\text{CH}_3$ ) radicals are mostly produced by the attacking of methane

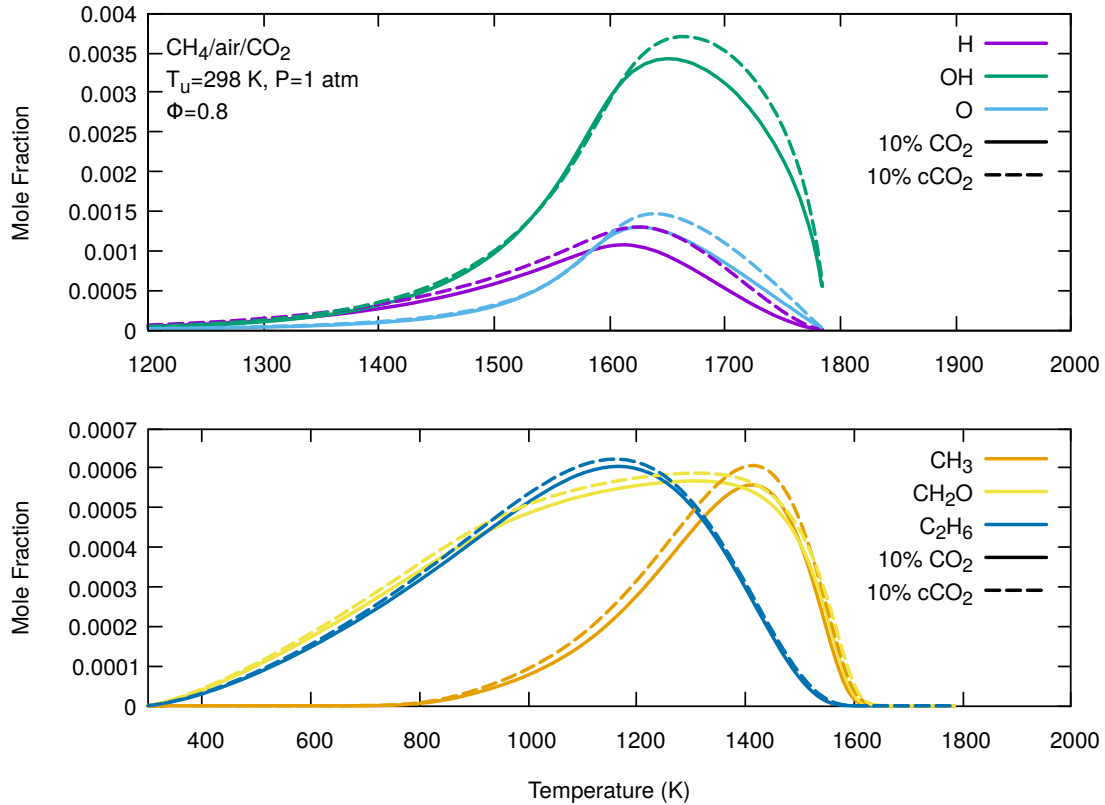


Figure 5-23: Direct reaction effect of CO<sub>2</sub> dilution on the speciation profiles of the important radicals (H, OH, O, and CH<sub>3</sub>) and intermediate species (CH<sub>2</sub>O and C<sub>2</sub>H<sub>6</sub>) in lean CH<sub>4</sub>/air/CO<sub>2</sub> flames ( $\phi = 0.8$ ).

by H, OH, O radicals, its concentration is also lowered. For rich mixtures, the concentration of O and OH radicals are increased, opposite to the trend for lean and stoichiometric mixtures. The concentration of intermediate CH<sub>2</sub>O and C<sub>2</sub>H<sub>6</sub> are also found to be reduced by direct reactions. It is because they are both formed via reactions of methyl radical, whose concentration is reduced. It can be concluded that the direct reaction effect systematically reduces the concentration of important radicals and intermediate species, resulting in degenerated reactivity and reduced flame speed.

### Sensitivity Analysis

As concluded in the above sections, the direct reactions dominate the chemical effect of CO<sub>2</sub>. Therefore, reactions sensitive to the direct reaction effect are investigated, using sensitivity analysis on composite functions, i.e., absolute and relative changes in  $S_L$  respectively. On one hand, Figure 5-26 shows reactions with high sensitivity at both conditions and also whose sensitivity change largely under the direct reaction effect. On the other hand, Figure 5-27 shows only those whose sensitivity are changed significantly.

Results for mixtures at all richness have four common sensitive reactions.



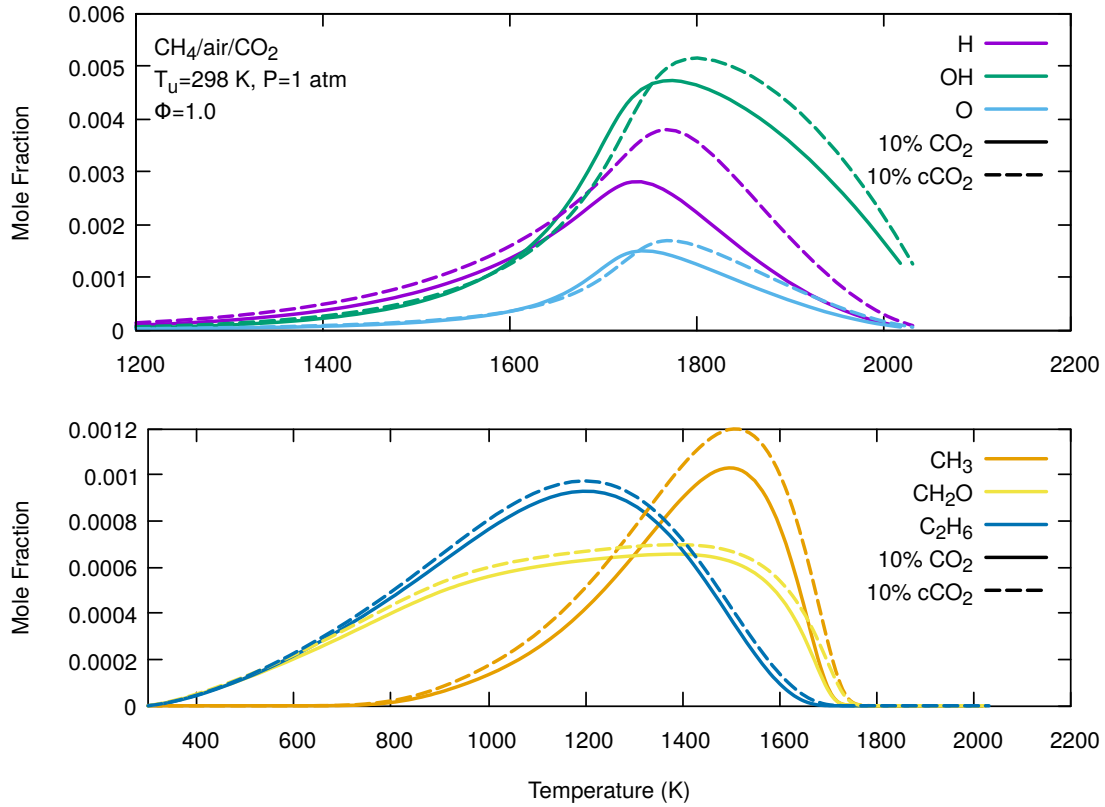
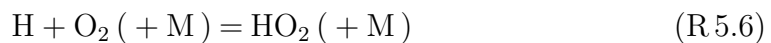


Figure 5-24: Direct reaction effect of CO<sub>2</sub> dilution on the speciation profiles of the important radicals (H, OH, O, and CH<sub>3</sub>) and intermediate species (CH<sub>2</sub>O and C<sub>2</sub>H<sub>6</sub>) in stoichiometric CH<sub>4</sub>/air/CO<sub>2</sub> flames ( $\phi = 1.0$ ).



They are all important steps for methane oxidation at both normal and diluted conditions. R 5.1 is the major chain branching step producing radicals. The reverse of R 5.2 is the thermal dissociation of methane and is one of the main sources of CH<sub>3</sub> radicals. R 5.3 is a chain terminating step which produces final product H<sub>2</sub>O. R 5.4, the dissociation of HCO, is an important step producing CO, which eventually is converted to final product CO<sub>2</sub> and releases large amount of heat.

For lean and stoichiometric mixtures, two fundamental reactions are also found highly sensitive,



as they are major heat release and chain terminating steps respectively. Other

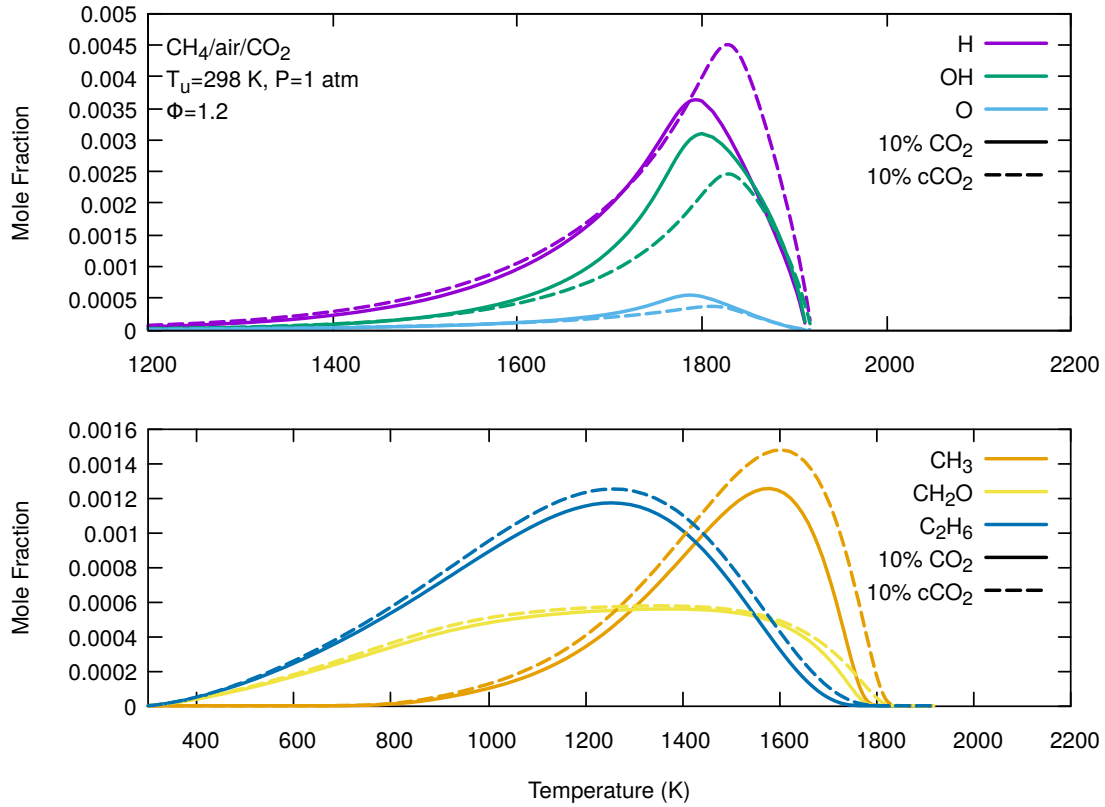


Figure 5-25: Direct reaction effect of  $\text{CO}_2$  dilution on the speciation profiles of the important radicals (H, OH, O, and  $\text{CH}_3$ ) and intermediate species ( $\text{CH}_2\text{O}$  and  $\text{C}_2\text{H}_6$ ) in rich  $\text{CH}_4/\text{air}/\text{CO}_2$  flames ( $\phi = 1.2$ ).

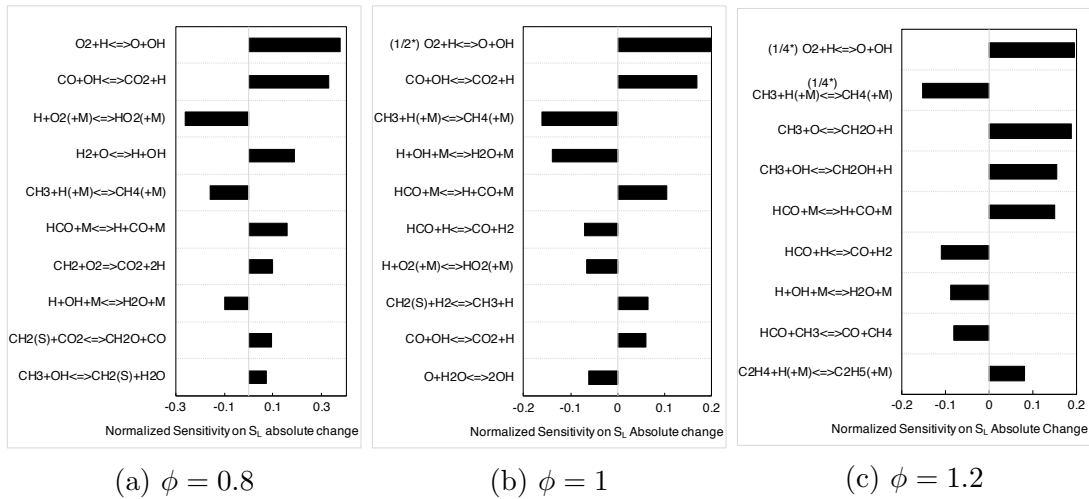


Figure 5-26: Composite sensitivity analysis based on absolute changes in  $S_L$  caused by the direct reaction effect of  $\text{CO}_2$ .  $S_L$  absolute changes is calculated based on 10%  $\text{CO}_2$  and 10%  $\text{cCO}_2$  diluted cases.

sensitive reactions for stoichiometric mixtures include mainly: (i) production and consumption of hydroxyl (OH) radicals, such as the  $\text{O} + \text{H} + \text{M} = \text{OH} + \text{M}$  and  $\text{O} + \text{H}_2\text{O} = \text{OH} + \text{OH}$  reactions, (ii) conversion of formyl (HCO) radical into CO, such as the  $\text{HCO} + \text{H} = \text{CO} + \text{H}_2$  and  $\text{HCO} + \text{O}_2 = \text{CO} + \text{HO}_2$  reactions, and (iii)

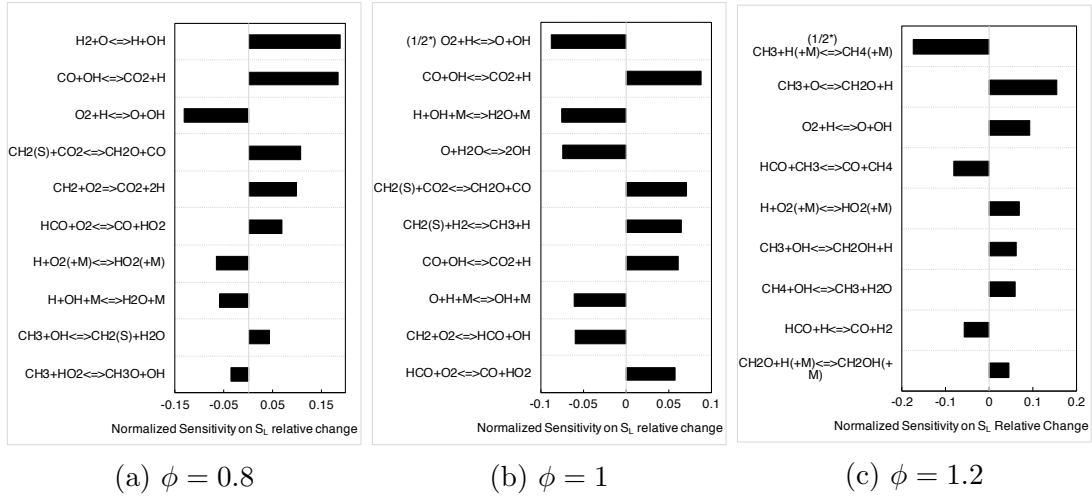
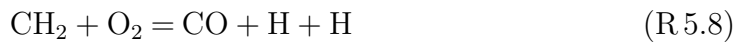


Figure 5-27: Composite sensitivity analysis based on relative changes in  $S_L$  caused by the direct reaction effect of  $\text{CO}_2$ .  $S_L$  relative changes is calculated based on 10%  $\text{CO}_2$  and 10%  $\text{cCO}_2$  diluted cases.

the formation of singlet methylene  $\text{CH}_2(\tilde{a}^1A_1)$  radical (abbreviated as  $\text{CH}_2(\text{S})$  in the following text), such as  $\text{CH}_3 + \text{H} = \text{CH}_2(\text{S}) + \text{H}_2$  reaction, enhancing another channel to the formation of final products,  $\text{CH}_3 \longrightarrow \text{CH}_2(\text{S}) \longrightarrow \text{CO} \longrightarrow \text{CO}_2$ . It is implied that  $\text{CO}_2$  dilution shift the chemical balance of R 5.4, leading to more CO and OH radicals, whose degenerating effect can propagate in the reverse direction of the main  $\text{CH}_3$  consumption channel, i.e.,  $\text{CO}_2 \longrightarrow \text{CO} \longrightarrow \text{HCO} \longrightarrow \text{CH}_2\text{O} \longrightarrow \text{CH}_3$ . Due to the higher concentration of  $\text{CH}_3$  radical resulted, the consumption channels through triplet  $\text{CH}_2(\tilde{a}^1A_1)$  and singlet ( $\text{CH}_2(\text{S})$ ) methylene radicals are enhanced. This is more obvious in the result for lean mixtures, where  $\text{CH}_2(\text{S})$  is formed through the  $\text{CH}_3 + \text{OH} = \text{CH}_2(\text{S}) + \text{H}_2\text{O}$  reaction and consumed by reacting with  $\text{CO}_2$ .



The CO and  $\text{CH}_2\text{O}$  formed in R 5.7 may again take part in the degeneration of the main reaction channel. Reaction channel through  $\text{CH}_2$  are also enhanced, especially for the removal of  $\text{CH}_2$  through the reaction



which is a chain branching step generating two H radicals and increases the flame speeds. In summary,  $\text{CO}_2$  dilution degenerates of the main channel, reducing system reactivity and flame speed, however, the reduction is partly compensated by the enhancement of  $\text{CH}_2$  and  $\text{CH}_2(\text{S})$  channels.

For rich mixtures, the increased  $\text{CH}_3$  concentration caused by  $\text{CO}_2$  dilution seems to affect on other reaction channels based on the sensitivity results. It degenerates the consumption of fuel, through the  $\text{CH}_3 + \text{H} (^+M) = \text{CH}_4 (^+M)$ . Although it leads to methane removal by OH radicals,  $\text{CH}_4 + \text{OH} = \text{CH}_3 + \text{H}_2\text{O}$ , this reaction further reduces system reactivity as it consumes radicals. However, it is partly compensated by the enhance of  $\text{CH}_3 \longrightarrow \text{CH}_2\text{O}$  channels though reactions with O and OH radicals which are abundant in rich mixtures.  $\text{CH}_3$  radicals can

be converted into  $\text{CH}_2\text{O}$  directly through reaction with O radical, i.e.,  $\text{CH}_3 + \text{O} = \text{CH}_2\text{O} + \text{H}$ , or indirectly through the  $\text{CH}_3 \longrightarrow \text{CH}_2\text{OH} \longrightarrow \text{CH}_2\text{O}$  channel, i.e., sequence through  $\text{CH}_3 + \text{OH} = \text{CH}_2\text{OH} + \text{H}$  and  $\text{CH}_2\text{OH} (+ \text{M}) = \text{CH}_2\text{O} + \text{H} (+ \text{M})$  reactions. These reactions produce H radical and increase the system reactivity. The reaction channel through  $\text{CH}_3$  recombination into ethane ( $\text{C}_2\text{H}_6$ ), usually enhanced at rich conditions, is not much affected by the direct reaction effect of  $\text{CO}_2$ . It is possibly due to that the enhancement depends mainly on the collision with third bodies, which is excluded in this investigation. Therefore, it can be concluded that in rich mixtures, the direct reaction effect of  $\text{CO}_2$  dilution reduces reactivity by degenerating the main channel and fuel conversion to  $\text{CH}_3$ , but the reduction is partly compensated by enhancing the  $\text{CH}_3 \longrightarrow \text{CH}_2\text{O}$  channels which produce H radicals.

## 5.5 Conclusions

In this chapter, we studied the dilution effects of  $\text{H}_2\text{O}$  and  $\text{CO}_2$  on laminar flame speed, by investigating the  $S_L$  of three mixtures, namely the  $\text{H}_2/\text{air}/\text{H}_2\text{O}$ ,  $\text{H}_2/\text{CO}/\text{air}/\text{CO}_2$ , and  $\text{CH}_4/\text{air}/\text{CO}_2$  mixtures.

Using false species analysis, the dilution effect of  $\text{H}_2\text{O}$  and  $\text{CO}_2$  is quantified into thermal and transport effect and chemical effect, which can be separated into the third-body collision effect and the direct reaction effect. It is found that the reduction of  $S_L$  with increasing dilution ratio is not linear, and becomes weaker at high dilutions. The reduction is mainly contributed by the thermal effect, while the chemical effect further reduces  $S_L$  and increase the non-linearity. Concerning the chemical effect of  $\text{H}_2\text{O}$  on  $\text{H}_2/\text{air}$  flames, it is mainly contributed by the third-body collision effect, whose relative effectiveness is about twice of that for direct reaction effect. Concerning the chemical effect of  $\text{CO}_2$  on  $\text{H}_2/\text{CO}/\text{air}$  flames, direct reaction effect dominates at low dilution ( $< 30\%$ ), while third-body collision effect is dominant at higher dilution ( $> 30\%$ ). Concerning the chemical effect of  $\text{CO}_2$  on  $\text{CH}_4/\text{CO}/\text{air}$  flames, it is dominated by direct reaction effect in the entire range of dilution ratio investigated (0–40%).

Sensitivity analysis on composite functions is used to study the mechanism of the chemical effects. In  $\text{H}_2/\text{air}/\text{H}_2\text{O}$  mixtures, third-body collision effect of  $\text{H}_2\text{O}$  is found to reduce  $S_L$  mainly through the efficient participation of  $\text{H}_2\text{O}$  in the chain terminating reaction  $\text{H} + \text{O}_2 (+ \text{M}) = \text{HO}_2 (+ \text{M})$ , and it enhances subsequent  $\text{HO}_2$  consuming reactions  $\text{HO}_2 + \text{H} = \text{OH} + \text{OH}$  and  $\text{HO}_2 + \text{OH} = \text{H}_2\text{O} + \text{O}_2$  which affect  $S_L$  in opposite ways, i.e., increases and reduces  $S_L$  respectively. The direct reaction effect of  $\text{H}_2\text{O}$  is found to be mainly contributed by the reaction  $\text{OH} + \text{H}_2 = \text{H} + \text{H}_2\text{O}$ , where high  $\text{H}_2\text{O}$  concentration push the reaction in its reverse direction, leading to less H radical and therefore reduces  $S_L$ . In  $\text{H}_2/\text{CO}/\text{air}/\text{CO}_2$  mixtures, the direct reaction effect of  $\text{CO}_2$  is studied. It is mainly contributed by the major heat release step  $\text{CO} + \text{OH} = \text{CO}_2 + \text{H}$ , where the high  $\text{CO}_2$  concentration shifts the reaction reversibly, i.e., the thermal dissociation of  $\text{CO}_2$ , competing for H radicals with the major chain branching reactions  $\text{H} + \text{O}_2 = \text{O} + \text{OH}$ . The resulting reduced H radical concentration leads to reduced  $S_L$ , and the increase OH concentration may lead to higher  $\text{H}_2\text{O}$  concentration which further reduce  $S_L$  through third-body collision in the  $\text{H} + \text{O}_2 (+ \text{H}_2\text{O}) = \text{HO}_2 (+ \text{H}_2\text{O})$  reaction.

In CH<sub>4</sub>/air/CO<sub>2</sub> mixtures, the thermal dissociation of CO<sub>2</sub> degenerates the main CH<sub>3</sub> consumption channel, i.e., CO<sub>2</sub> → CO → HCO → CH<sub>2</sub>O → CH<sub>3</sub>, leading to higher CH<sub>3</sub> concentration. For lean and stoichiometric mixtures, it is partly compensated by the enhancement of CH<sub>2</sub> and CH<sub>2</sub>(S) channels which affects  $S_L$  positively through reaction CH<sub>2</sub> + O<sub>2</sub> = CO + H + H and CH<sub>2</sub>(S) + CO<sub>2</sub> = CH<sub>2</sub>O + CO respectively. For rich mixtures, it is partly compensated by enhancing the CH<sub>3</sub> → CH<sub>2</sub>O channels which produce H radicals.

This part of the investigation could be further improved using comprehensive reaction pathway analyses. Future investigations are needed to explore the chemical effects of H<sub>2</sub>O and CO<sub>2</sub> on the flames of larger molecule fuels.



THIS PAGE INTENTIONALLY LEFT BLANK

# Chapter 6

## Detailed and Semi-Detailed Mechanisms for One Gasoline Surrogate (TRFE): Mechanisms, Validation on $S_L$ and Insights to Correlations of $S_L$

In this chapter, two kinetic mechanisms, a detailed one and a semi-detailed one, designated for the combustion of one gasoline surrogate, Toluene Reference Fuel with Ethanol Addition (TRFE), is developed. The detailed mechanism, namely MACDIL-DTL, has 2339 species and 9440 reactions. The semi-detailed mechanism, namely MACDIL-RDC, is reduced from MACDIL-DTL for the purpose of 1-D flame speed calculations, and contains 1032 species and 5420 reactions. The kinetic details of the two mechanisms are presented in Section 6.1 and 6.2, respectively. Both mechanisms, including the kinetic model, thermodynamic and transport data, are provided in supplementary files. In Section 6.3, the predictive performance of the MACDIL-RDC mechanism is validated based on experimentally measured laminar flame speeds of TRFE/air/EGR mixtures. Based on the effect of EGR predicted by the mechanism, insights to the development of correlations for laminar flame speed at diluted conditions are provided, and a new dilution term is proposed in Section 6.4.

### 6.1 Detailed Mechanism: MACDIL-DTL

A detailed kinetic mechanism (MACDIL-DTL), consisting of 2339 species and 9440 reactions, is established for the combustion of the TRFE fuel. The mechanism is designated for the calculation of the laminar flame speeds of gasoline surrogates at highly-diluted conditions. It is also capable to perform 0-D homogeneous calculations to obtain ignition delay times (IDT) in wide condition ranges, since it includes both low-temperature and high-temperature reactions. The kinetic details of the mechanism are presented hereafter.

### 6.1.1 Formulation of the Mechanism

The development of MACDIL-DTL is based on the starting mechanism, LLNL 2011 [25], where key reactions and their corresponding sub-mechanisms at diluted conditions are identified in Chapter 4. The MACDIL-DTL mechanism is formulated by compiling state-of-the-art mechanisms from literature for small molecules and the fuel components, which replace the corresponding sub-mechanisms in LLNL 2011. Table 6.1 summarizes its basic composition, where its core (C<sub>0</sub>–C<sub>4</sub>) sub-mechanism is from Aramco Mech 3.0 [113], a state-of-art mechanism for the oxidation of small hydrocarbons. For the oxidation of the four components in the TRFE fuel, their sub-mechanisms are also based on state-of-art mechanisms. Then the rate coefficients of some key reactions identified in Chapter 4 are reviewed and preferred values from literature are used. Details about the sub-mechanism adopted are introduced in this section and rate coefficients for some key reactions are discussed in Section 6.1.2 (the next section).

Table 6.1: Sources of the sub-mechanisms in the MACDIL-DTL mechanism.

Sub-mechanisms	Source	Ref.
<b>starting mechanism (C<sub>0</sub>–C<sub>14</sub>)</b>	LLNL 2011	[25]
<b>core (C<sub>0</sub>–C<sub>4</sub>)</b>	Aramco Mech 3.0	[113]
C <sub>0</sub> –C <sub>1</sub> (H <sub>2</sub> /CO)	Kéromnès <i>et al.</i> 2013	[17]
C <sub>1</sub> (methane/DME)	Burke <i>et al.</i> 2015	[368]
C <sub>1</sub> (methanol)	Burke <i>et al.</i> 2016	[369]
C <sub>1</sub> –C <sub>2</sub>	Metcalfe <i>et al.</i> 2013	[109]
C <sub>3</sub> (propene/allene/propyne)	Burke <i>et al.</i> 2015	[110, 111]
C <sub>4</sub> (isobutene)	Zhou <i>et al.</i> 2016	[112]
C <sub>4</sub> (1-butene/2-butene)	Li <i>et al.</i> 2017	[370, 371]
C <sub>4</sub> (1,3-butadiene)	Zhou <i>et al.</i> 2017	[113]
<b>fuel component</b>		
ethanol (C <sub>2</sub> H <sub>5</sub> OH)	Zhang <i>et al.</i> 2018	[156]
n-heptane ( <i>n</i> -heptane)	Zhang <i>et al.</i> 2016	[128]
isooctane (i-C <sub>8</sub> H <sub>18</sub> )	Atef <i>et al.</i> 2017	[136]
toluene (C <sub>6</sub> H <sub>5</sub> CH <sub>3</sub> )	Yuan <i>et al.</i> 2015	[202, 203]

#### The Core (C<sub>0</sub>–C<sub>4</sub>) Sub-Mechanism

The MACDIL-DTL mechanism adopts the Aramco Mech 3.0 [113] as the core sub-mechanism for C<sub>0</sub>–C<sub>4</sub> species. Aramco Mech 3.0 is a comprehensive core mechanism which is constantly updated and commonly used as the base elements when developing mechanisms for larger molecules. The mechanism has been validated on a vast amount of experimental data, such as ignition delay time, speciation profiles and laminar flame speed. And it contains sub-mechanisms for the oxidation of various small molecule fuels, such as hydrogen (H<sub>2</sub>) and syngas (H<sub>2</sub>/CO), small alkanes such as methane (CH<sub>4</sub>), ethane (C<sub>2</sub>H<sub>6</sub>), and propane (C<sub>3</sub>H<sub>8</sub>), olefines such as ethene (C<sub>2</sub>H<sub>4</sub>), propene (C<sub>3</sub>H<sub>6</sub>), alkynes such as acetylene (C<sub>2</sub>H<sub>2</sub>) and propyne (C<sub>3</sub>H<sub>4</sub>), aldehydes such as formaldehyde (CH<sub>2</sub>O) and acetaldehyde (CH<sub>3</sub>CHO), alcohols such as methanol (CH<sub>3</sub>OH) and ethanol (C<sub>2</sub>H<sub>5</sub>OH), and dimethyl ether (CH<sub>3</sub>OCH<sub>3</sub>) (DME). The C<sub>0</sub>–C<sub>4</sub> mechanisms netted under Aramco Mech 3.0 in

Table 6.1 are all components of Aramco Mech 3.0. For instance, the hydrogen and syngas sub-mechanism is based on K eromn es 2013 [17] which is found to have good overall performance and used in the evaluations of dilution effects in Chapter 5 of the present work.

### ***n*-heptane Sub-Mechanism**

The sub-mechanism for *n*-heptane in MACDIL-DTL is from the model developed by Zhang *et al.* [128]. The main features of this mechanism is that reaction rate rules consistent with that developed for pentane isomers [114, 115] and *n*-hexane [372] are adopted and new reaction classes in low-temperature chemistry are accordingly added. For high-temperature chemistry, rate coefficients of important reactions, such as the decomposition of fuel, H abstraction by radicals, and decomposition of fuel derived radicals, are evaluated based on experimental measurements and theoretical calculations. For low-temperature chemistry, rate coefficients for many reaction classes are estimated by analogy to that for *n*-hexane and modified within uncertainty for optimized performance. The performance of the Zhang 2016 [128] mechanism is comprehensively validated based on experiments data for ignition delays, speciation profiles, and laminar flame speeds over a wide range of conditions. Excellent agreement on experimentally measured laminar flame speeds shows that the mechanism has a good predictive performance to capture the evolution of  $S_L$  with equivalence ratio, initial temperature, and pressure. The Zhang 2016 [128] mechanism also contains sub-mechanisms for pentane isomers and *n*-hexane, which are also integrated in MACDIL-RDC.

### **Isooctane Sub-Mechanism**

MACDIL-DTL adopts the kinetic model developed by Atef *et al.* [136] for the isooctane sub-mechanism. The Atef 2017 [136] mechanism is commonly accepted to be state-of-the-art for the oxidation kinetics of isooctane. It is comprehensively validated against ignition delay data measured in rapid compression machines (RCM) and shock tubes (ST), speciation data measured in jet-stirred reactors (JSR), and laminar flame speeds, for conditions with pressure up to 40 atm, and temperature up to 1060 K. Its major improvements, with respect to the LLNL 2011 mechanism [25], are (i) the re-evaluated thermodynamic data based on updated group values suggested by Burke *et al.* [129], Simmie and Somers [373], and Sabbe *et al.* [374], and (ii) the addition of nine reaction classes, especially the alternative isomerisation pathways of peroxy-alkyl hydroperoxide (OOQOOH), such as concerted elimination of HO<sub>2</sub> radicals, hydrogen-exchange and third O<sub>2</sub> additions. [136] In addition, the rate coefficients for these reactions are estimated by analogy, while that for the other reactions are evaluated based on either experimental measured or theoretical calculated values. When integrated in the MACDIL-DTL, only the isooctane sub-mechanism in Atef 2017 is adopted, i.e., without the common reactions with the *n*-heptane sub-mechanism and reactions for C<sub>0</sub>–C<sub>4</sub> species.

## Toluene Sub-Mechanism

The toluene sub-mechanism in MACDIL-DTL adopts the mechanisms developed by Yuan *et al.* [202,203], which is comprehensively validated for toluene oxidation and pyrolysis based on a large amount of experimental data from ST, RCM, JSR, flow reactor (FR), and laminar flame speeds. It is developed based on the mechanism developed by the same team [179,195], by updating the rate coefficients of some key reactions, such as important pressure-dependent and chemically activated reactions, based on theoretical studies in the literature. Validations based on laminar flame speeds of toluene/air mixtures show that the Yuan 2015 mechanism could sufficiently capture the evolution of  $S_L$  with equivalence ratio and initial temperature. The Yuan 2015 mechanism also contains sub-mechanism for the oxidation of 1,3-cyclopentadiene (C<sub>5</sub>H<sub>6</sub>), benzene (C<sub>6</sub>H<sub>6</sub>), and polycyclic aromatic hydrocarbons (PAH) which are also integrated in MACDIL-DTL.

## Ethanol Sub-Mechanism

The ethanol sub-mechanism in MACDIL-DTL adopts the recently developed mechanism by Zhang *et al.* [156]. The mechanism is updated based on Aramco Mech 1.3 [325] with evaluation of the important reactions identified using sensitivity analysis, e.g., H atom abstraction by HO<sub>2</sub> and OH radicals, decomposition of  $\alpha$ -hydroxyethyl (CH<sub>3</sub>CHOH) and ethoxy (C<sub>2</sub>H<sub>5</sub>O) radicals, and O<sub>2</sub> addition on  $\alpha$ -hydroxyethyl (CH<sub>2</sub>CH<sub>2</sub>OH) radicals. The mechanism is validated against experimental data of ignition delay times and speciation profiles from JSR and flow reactors over a wide range of conditions. When integrated into MACDIL-DTL, common reactions with the core mechanism, such as reactions in the C<sub>0</sub>–C<sub>1</sub> sub-mechanisms, are excluded (or not updated).

## Nomenclature, Thermodynamic and Transport Data

The nomenclature of the species names follows the same rules as Aramco Mech 3.0, with which the starting mechanism LLNL 2011 [25], Zhang 2016 [128] for *n*-heptane and Atef 2017 [136] for isooctane are consistent, except for aromatic species which follows the nomenclature by Yuan 2015 [202].

The thermodynamic data used in MACDIL-DTL is consistent with those in the sub-mechanisms [113,128,136,202], which are mostly from the database by Goldsmith *et al.* [375], Burke *et al.* [129], Simmie and Somers [373], and Sabbe *et al.* [374], and calculations using Benson's group additive method [376]. Transport data used in MACDIL-DTL is also the same as the sub-mechanisms. Noted that theoretically calculated transport data for small molecules by Jasper [100] are tested but not used in the present work.

For the CH<sub>2</sub>COOH radical ( $\dot{\text{C}}\text{H}_2\text{C}(\text{OH})=\text{O}$ ), involved in the CH<sub>2</sub>CO + OH reaction studied in Chapter 3, thermal dynamic data is from the database of Reaction Mechanism Generator (RMG) [377], where the thermochemistry is calculated theoretically using DFT/QCI method and the transport property is estimated using group additivity.

## 6.1.2 Preferred Rate Coefficients for Some Key Reactions

The rate coefficients in the MACDIL-DTL mechanism are evaluated for some key reactions, which are in the first category of the identified reactions in Chapter 4, i.e., the fundamental reactions in the hydrogen and syngas sub-mechanisms. They are briefly described in this section. Evaluation of the reactions in the remaining three categories is planned for future works.

### Reactions in H<sub>2</sub> Sub-Mechanism

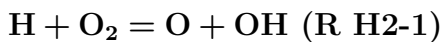
As reactions in the H<sub>2</sub> sub-mechanism are fundamental to combustion and not numerous, they are all evaluated. Details of their rate coefficients are shown in table 6.2. Some kinetically important reactions with preferred rate coefficients are discussed.

Table 6.2: Rate coefficients for reactions in the hydrogen sub-mechanism of MACDIL-DTL.

No.	Reaction	$A$ <sup>1</sup>	$n$	$E_a$ <sup>2</sup>	Ref.
H2-1	H + O <sub>2</sub> = O + OH	1.04E+14	0.00	1.529E+04	[378, 379]
H2-2	H <sub>2</sub> + O = H + OH	5.08E+04	2.67	6.292E+03	[10, 380]
		3.15E+46	-12.97	1.146E+04	
H2-3	H <sub>2</sub> + OH = H <sub>2</sub> O + H	2.14E+08	1.52	3.450E+03	[10]
H2-4	OH + OH = H <sub>2</sub> O + O	2.67E+06	1.82	-1.647E+03	[381, 382]
H2-5	H <sub>2</sub> + M = H + H + M	4.58E+19	-1.40	1.044E+05	[383]
	$\epsilon_{H_2} = 2.5, \epsilon_{H_2O} = 12.0, \epsilon_{CO} = 1.9, \epsilon_{CO_2} = 3.8, \epsilon_{HE} = 0.83$				
H2-6	O + O + M = O <sub>2</sub> + M	6.17E+15	-0.50	0.00	[383]
	$\epsilon_{H_2} = 2.5, \epsilon_{H_2O} = 12.0, \epsilon_{CO} = 1.9, \epsilon_{CO_2} = 3.8, \epsilon_{HE} = 0.83$				
H2-7	O + H + M = OH + M	4.71E+18	-1.00	0.00	[383]
	$\epsilon_{H_2} = 2.5, \epsilon_{H_2O} = 12.0, \epsilon_{CO} = 1.5, \epsilon_{CO_2} = 2.0, \epsilon_{HE} = 0.75$				
H2-8a	H <sub>2</sub> O + M = H + OH + M	6.06E+27	-3.31	1.208E+05	[384]
	$\epsilon_{H_2O} = 0, \epsilon_{H_2} = 3.0, \epsilon_{N_2} = 2.0, \epsilon_{O_2} = 1.5, \epsilon_{HE} = 1.1$				
H2-8b	H <sub>2</sub> O + H <sub>2</sub> O = H + OH + H <sub>2</sub> O	1.00E+26	-2.44	1.202E+05	[384]
H2-9a	H + O <sub>2</sub> (+ M) = HO <sub>2</sub> (+ M)	4.66E+12	0.44	0.00	[385-388]
	$F_{cent} = 0.5, \text{Low-pressure limit:}$	2.25E+21	-1.95	0.00	
	$\epsilon_{AR} = 0.0, \epsilon_{CO_2} = 0.0, \epsilon_{H_2O} = 0.0, \epsilon_{O_2} = 1.0, \epsilon_{H_2} = 1.5, \epsilon_{HE} = 0.57$				
H2-9b	H + O <sub>2</sub> (+ AR) = HO <sub>2</sub> (+ AR)	4.66E+12	0.44	0.00	[385, 386]
	$F_{cent} = 0.5, \text{Low-pressure limit:}$	2.66E+19	-1.36	0.00	
H2-9c	H + O <sub>2</sub> (+ CO <sub>2</sub> ) = HO <sub>2</sub> (+ CO <sub>2</sub> )	4.66E+12	0.44	0.00	[385, 386]
	$F_{cent} = 0.5, \text{Low-pressure limit:}$	2.23E+18	-0.79	0.00	
H2-9d	H + O <sub>2</sub> (+ H <sub>2</sub> O) = HO <sub>2</sub> (+ H <sub>2</sub> O)	4.66E+12	0.44	0.00	[389]
	$F_{cent} = 0.5, \text{Low-pressure limit:}$	2.04E+20	-1.20	0.00	
H2-10	HO <sub>2</sub> + H = OH + OH	7.08E+13	0.00	2.950E+02	[390]
H2-11	HO <sub>2</sub> + H = H <sub>2</sub> + O <sub>2</sub>	1.14E+10	1.08	5.538E+02	[391]
H2-12	H <sub>2</sub> O + O = H + HO <sub>2</sub>	2.20E+08	2.00	6.160E+04	[392]
H2-13	HO <sub>2</sub> + O = OH + O <sub>2</sub>	2.85E+10	1.00	-7.239E+02	[393]
H2-14	HO <sub>2</sub> + OH = H <sub>2</sub> O + O <sub>2</sub>	3.08E+12	0.07	-1.151E+03	[394]
		8.00E+12	0.32	6.896E+03	
H2-15	HO <sub>2</sub> + HO <sub>2</sub> = H <sub>2</sub> O <sub>2</sub> + O <sub>2</sub>	1.03E+14	0.00	1.104E+04	[395]
		1.94E+11	0.00	-1.409E+03	
H2-16a	H <sub>2</sub> O <sub>2</sub> (+ M) = OH + OH (+ M)	2.00E+12	0.90	4.875E+04	[87, 396]
	$F_{cent} = 0.43, \text{Low-pressure limit:}$	2.49E+24	-2.30	4.875E+04	
	$\epsilon_{H_2O} = 0.00, \epsilon_{CO_2} = 1.6, \epsilon_{N_2} = 1.5, \epsilon_{O_2} = 1.2, \epsilon_{HE} = 0.65, \epsilon_{H_2O_2} = 7.7, \epsilon_{H_2} = 3.7, \epsilon_{CO} = 2.8$				
H2-16b	H <sub>2</sub> O <sub>2</sub> (+ H <sub>2</sub> O) = OH + OH (+ H <sub>2</sub> O)	2.00E+12	0.90	4.875E+04	[396]
	$F_{cent} = 0.51, \text{Low-pressure limit:}$	1.87E+25	-2.30	4.875E+04	
H2-17	H <sub>2</sub> O <sub>2</sub> + H = H <sub>2</sub> O + OH	2.03E+07	2.02	2.620E+03	[397]
H2-18	H <sub>2</sub> O <sub>2</sub> + H = HO <sub>2</sub> + H <sub>2</sub>	5.02E+06	2.07	4.300E+03	[397]
H2-19	H <sub>2</sub> O <sub>2</sub> + O = OH + HO <sub>2</sub>	9.55E+06	2.00	3.970E+03	[383]
H2-20	H <sub>2</sub> O <sub>2</sub> + OH = H <sub>2</sub> O + HO <sub>2</sub>	1.74E+12	0.00	3.180E+02	[398]
		7.59E+13	0.00	7.269E+03	
	<i>rate constants not included:</i>				
H2-2	H <sub>2</sub> + O = H + OH	8.84E+05	2.34	7.058E+03	p.w.
H2-21	H + O <sub>2</sub> + H = H <sub>2</sub> + O <sub>2</sub>	8.80E+22	-1.84	8.000E+02	[95]
H2-22	H + O <sub>2</sub> + H = OH + OH	4.00E+22	-1.84	8.000E+02	[95]
H2-23	H + O <sub>2</sub> + O = OH + O <sub>2</sub>	7.35E+22	-1.84	8.000E+02	[95]
H2-24	H + O <sub>2</sub> + OH = H <sub>2</sub> O + O <sub>2</sub>	2.56E+22	-1.84	8.000E+02	[95]

<sup>1</sup> The units for the pre-exponential factor are  $s^{-1}$  for unimolecular reactions,  $cm^3 mol^{-1} s^{-1}$  for bimolecular reactions, and  $cm^6 mol^{-2} s^{-1}$  for termolecular reactions.

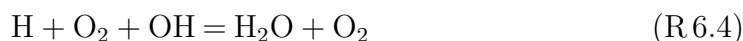
<sup>2</sup> The unit for apparent activation energy  $E_a$  is  $cal mol^{-1}$ .



Reaction  $\text{H} + \text{O}_2 = \text{O} + \text{OH}$  is commonly accepted as the most important chain-branching reaction of hydrogen or hydrocarbon oxidation, and often shown in sensitivity analysis as the most sensitive reaction. The rate coefficient most widely used for this reaction is generated from the shock tube measurement by Hong *et al.* [378], with its valid temperature range extended to 1100–3370 K because of its excellent agreement with the previous experimental measurements by Masten *et al.* [399]. Recent measurement was conducted by Wang *et al.* [379] over 1428–1520 K and the obtained rate coefficients agree with the measurement by Hong *et al.* [378] remarkably well. However, if extrapolated into higher temperatures, the fitted Arrhenius expression shows considerable deviation with respect to the one proposed by Hong *et al.* [378], the valid temperature range of which is wider. Consequently, the present work accepts the suggestion by Konnov [98] and keeps the expression by Hong *et al.* [378] unchanged.

**$\text{H} + \text{O}_2 + \text{X} \longrightarrow \text{products}$  (R H2-21–24) and  $\text{O} + \text{H}_2 = \text{H} + \text{OH}$  (R H2-2)**

As introduced in Chapter 1.4, chemical termolecular reactions is found to play a significant role in combustion kinetics. [95–97] Recently, Burke and Klippenstein [95] studied the  $\text{H} + \text{O}_2 + \text{X} \longrightarrow \text{products}$  reactions (R H2-21–R H2-24) where X could be H, O, OH or other radicals,



and derived their rate coefficients which are found to decrease the predicted  $S_L$  significantly for hydrogen/air flames when integrated in kinetic mechanisms. The reduced  $S_L$  makes the existing hydrogen mechanisms less predictive, which implies that some other parts in the mechanism must also be modified to obtain sufficient agreement with experiments. [98] Konnov [98] demonstrated that it can be compensated by the use of the theoretically calculated transport properties by Jasper *et al.* [99, 100] which increase  $S_L$ . However, this approach only affects the laminar flame speeds results, and could not compensate characteristics obtained from 0-D calculations, e.g., ignition delay times and speciation profiles, where the modified mechanism is reported to be less predictive than the original mechanism at some conditions [98].

The present work proposes another compensating approach, which affects ignition delay time and speciation profiles as well. It is done through the alteration of the rate constant of the  $\text{O} + \text{H}_2 = \text{H} + \text{OH}$  reaction within its uncertainty range. Reaction  $\text{O} + \text{H}_2 = \text{H} + \text{OH}$  is the another chain-branching step besides R H2-1. Nguyen and Stanton [380] computed its rate coefficients using the SCTST theory based on an accurate PES. As shown in Figure 6-1, their calculated values agree with the available measurements very well, except for these reported by Dubinsky

and McKenney and Marshall and Fontijn, which exhibit trends differ from other experiments. However, the commonly used expression recommended by Baulch *et al.* [10] is fitted based on all the experiments including them. Thus it causes the difference between the suggestion by Baulch *et al.* [10] and the calculation by Nguyen and Stanton [380], especially at the temperature range of 500–1600 K which is important for combustion. However, at higher temperatures (over 2000 K) the computed values are lower than experiments, which may be due to, as the authors suggested, the reaction between excited  $H_2$  molecules with oxygen atoms. By reviewing the above literature, the present work adopts the rate coefficients by Nguyen and Stanton [380] for 200–1600 K and the values by Baulch *et al.* [10] for 1700–3600 K, by fitting them into double Arrhenius expressions.

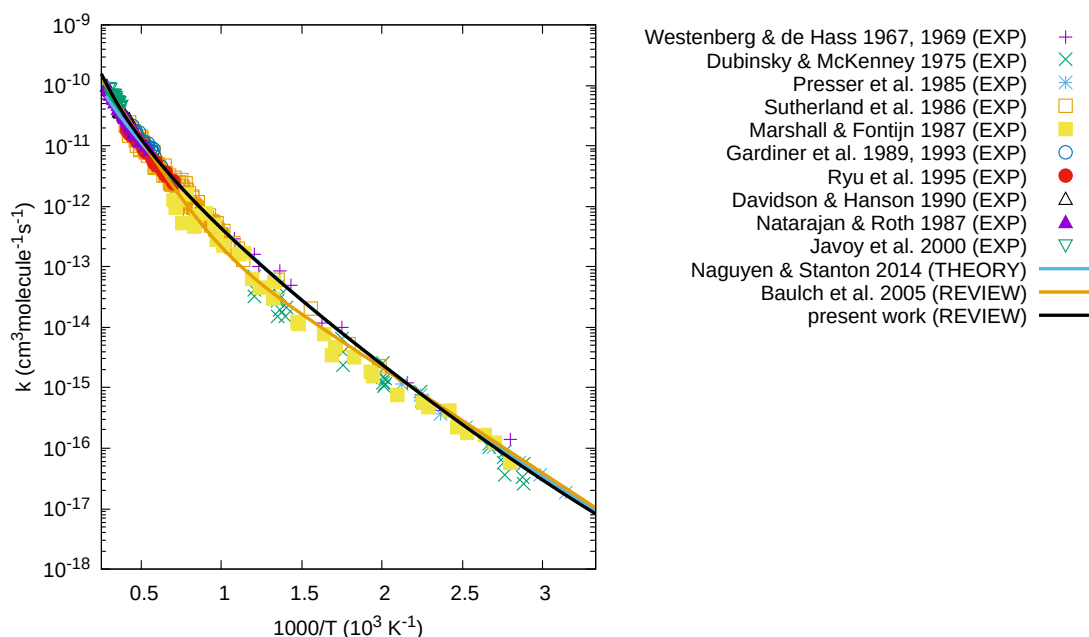


Figure 6-1: Rate coefficients of the  $O + H_2 = H + OH$  reaction.

Adoption of this expression is estimated to increase the predicted values for flame speeds, and therefore compensate for the reduction caused by R H2-21–24. It is found that the compensating effect is less significant than the approach by Konnov [98], but the resulted  $S_L$  of hydrogen/air flames at standard condition still agree with experimental measurements. Due to the fact that this approach is not comprehensively validated, especially on ignition delay times and species concentration profiles, both the  $H + O_2 + X$  reactions (R H2-21–24) and the proposed rate constants for  $O + H_2 = H + OH$  (R H2-2) are not included in the current versions of the mechanism. For the rate constant of  $O + H_2 = H + OH$  (R H2-2), the current version of mechanism keeps the commonly used expression by Baulch *et al.* [10].

### $H_2 + OH = H + H_2O$

The latest measurements on the reaction  $H_2 + OH = H + H_2O$  were performed by Lam *et al.* [400], and the obtained rate constant is in excellent agreement with historical value, as shown in Figure 6-2. However, the rate expression proposed by the same team, which is adopted in the mechanism of Kromns *et al.* [17], is lower



than most experiments at high temperature (2000–2500 K). Recent theoretical studies are abundant [401–406], but their discrepancies are larger than that of the experimental data, as reviewed by Alekseev and Konnov [93, 98]. Therefore, the present work adopts the expression recommended by Baulch *et al.* [10], which is commonly used in kinetic mechanisms.

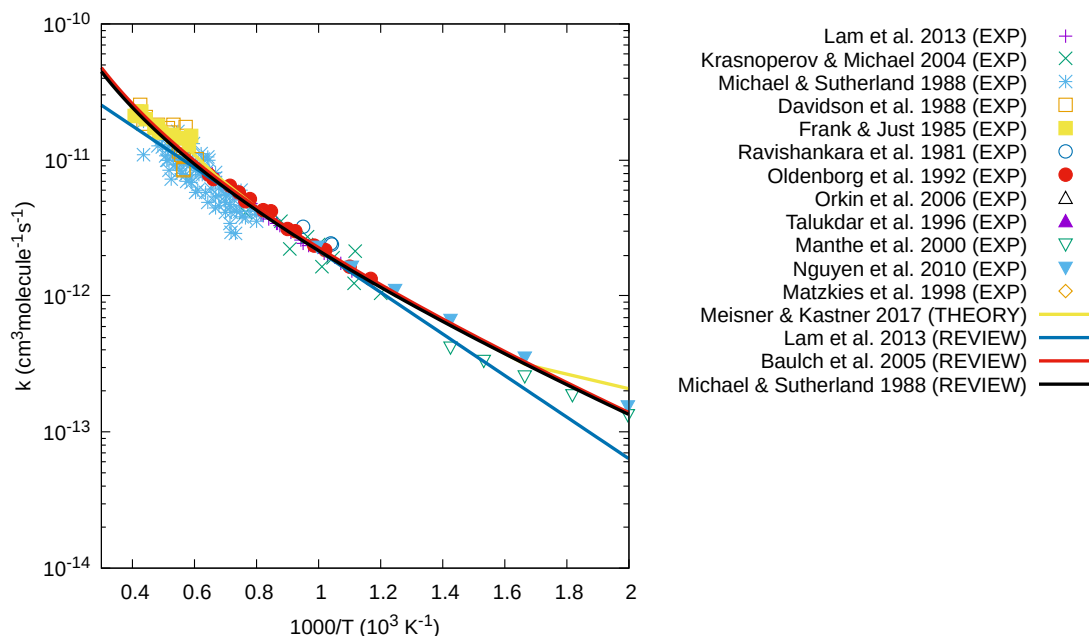


Figure 6-2: Rate coefficients of the  $\text{H}_2 + \text{OH} = \text{H} + \text{H}_2\text{O}$  reaction.

### $\text{OH} + \text{OH} = \text{H}_2\text{O} + \text{O}$

The experimental data for the rate coefficients of the reaction  $\text{OH} + \text{OH} = \text{H}_2\text{O} + \text{O}$  is quite scattered, as shown in Figure 6-3. Nguyen and Stanton [382] calculated the thermal rate constants using SCTST, which lies well within the experimental data band while the recommendation by Baulch *et al.* [10] is at the upper bound. Later measurement at low temperature by Altinay and Macdonald [381] show excellent agreement with this calculation results. Therefore, the present work accepts the expression suggested by Konnov [98] which is fitted from the theoretical rate coefficients by Nguyen and Stanton [382].

### $\text{H} + \text{O}_2 (+ \text{M}) = \text{HO}_2 (+ \text{M})$

As for the chain-branching reaction R H2-1, reaction  $\text{H} + \text{O}_2 (+ \text{M}) = \text{HO}_2 (+ \text{M})$  is important in hydrocarbon combustion because it is a major chain-termination channel. The competition between the two reactions affects greatly various combustion phenomena, e.g., the 3rd explosion limit of  $\text{H}_2/\text{O}_2$  mixtures, the ignition, extinction, and propagation of hydrocarbon flames. Recent assessment on the kinetics uncertainty of R H2-9 by Tao *et al.* [407] indicates that more accurate rate coefficients with lower uncertainty are critical to the progress of combustion modeling. Following this imperative need, experimental measurements have been carried out recently. Shao *et al.* [389] measured, using shock tubes, the low-pressure limit rate coefficients in bath gas Ar,  $\text{N}_2$ ,  $\text{CO}_2$ , and  $\text{H}_2\text{O}$ , with an estimated uncertainty of 12–24% depending on the collider. Arrhenius expressions, valid for the temperature range of 1000–1430 K, were derived with a temperature dependence suggested

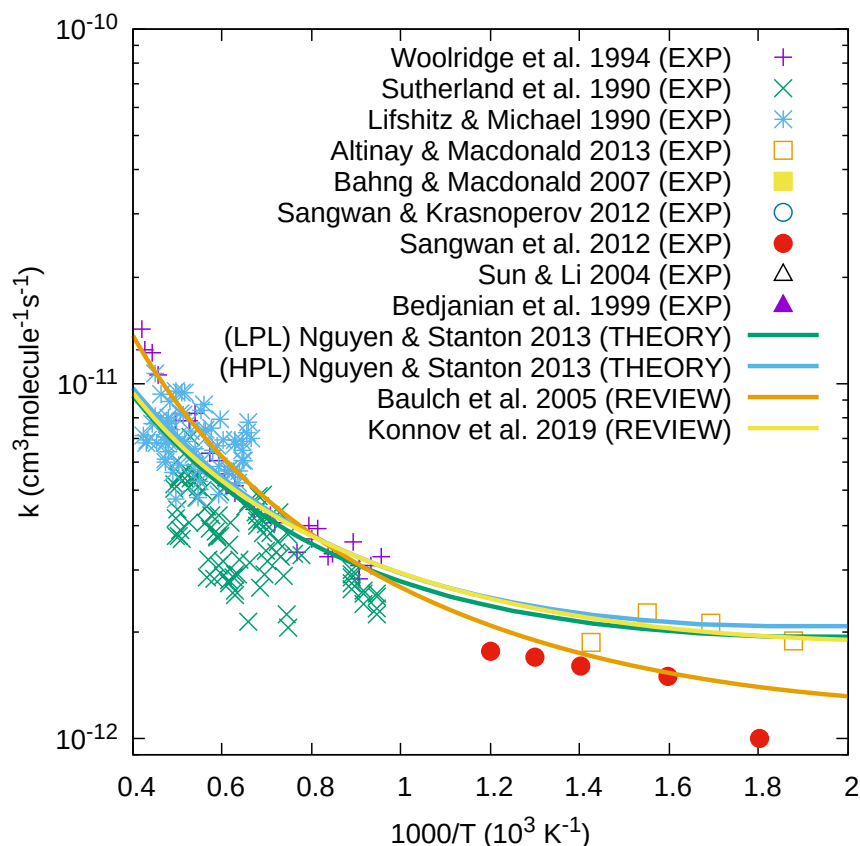


Figure 6-3: Rate coefficients of the  $\text{OH} + \text{OH} = \text{H}_2\text{O} + \text{O}$  reaction.

by Troe [385]. Choudhary *et al.* [386] performed measurements at higher temperature (1450–2000 K), with estimated uncertainty of 9–28%. Good agreement was found with the extrapolation of the data from Shao *et al.* [389]. By combining the existing experimental values, they proposed new expressions that have an extended temperature range of 1000–2000 K. The present work adopts the low-pressure limiting rate coefficients from Choudhary *et al.* [386] for Ar, N<sub>2</sub>, and CO<sub>2</sub> as colliders, and that from Shao *et al.* [389] for H<sub>2</sub>O. They are combined with the value at the high-pressure limit obtained by Troe [385]. The 3rd-body collisional efficiency for other collider species, such as He, O<sub>2</sub>, H<sub>2</sub>, CO, CH<sub>4</sub>, and C<sub>2</sub>H<sub>6</sub> are from the works by Michael *et al.* [387] and Kromns *et al.* [17].

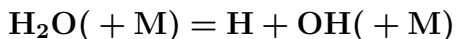
### Thermal Dissociation of H<sub>2</sub> and O<sub>2</sub>

The thermal dissociation of H<sub>2</sub> (R H2-5) and of O<sub>2</sub> (reverse of R H2-6), have high barriers and are initiation steps at high temperatures. The reverse reactions, destroying two H or O radicals, however, could proceed at lower temperatures and are important chain termination steps. As they are extensively studied in the past and no recent studies exist, the present work accepts the recommendation by Tsang and Hampson [408].

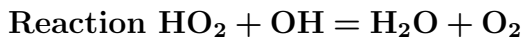
### Thermal Dissociation of OH

The thermal dissociation of OH radical (reverse of R H2-7) was measured, for the first time, by Naudet *et al.* [409] with Ar as bath gas. The measured rate coefficients show good agreement with the estimation by Tsang and Hampson

[408]. Therefore, the present work adopts the expression proposed by Tsang and Hampson [408].



The recombination of H atoms with OH radicals (the reverse reaction) is important for flame propagation, because of its radical-destroying nature. The rate coefficients for the dissociation of water were measured by Srinivasan and Michael [384] using shock tubes, with a claimed accuracy of  $\pm 18\%$ . However, this rate constant is reported to be lower than the recommendation by Tsang and Hampson [408] and direct implementation leads to an overestimation of flame speeds. [17] The uncertainty of this reaction is evaluated to be about a factor of 2. [89] The present work adopts the rate coefficients suggested by Konnov [98] which is modified based on the measurement by Srinivasan and Michael [384].

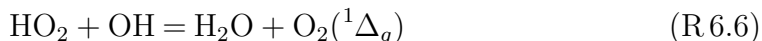


The H atom abstraction reaction by OH radical from HO<sub>2</sub>,



, is a chain-termination channel in hydrocarbon combustion and proceeds on a barrierless potential energy surface. Combining various measurements at different temperatures [410–412], the rate coefficient exhibit negative temperature dependency at low temperature but positive dependency at high temperature. Theoretical calculations [394,413] confirmed this trend, which is due to the submerged transition state along the reaction coordinate. This nature is also reflected in the rate expression suggested by Hong *et al.* [411] which is used in the mechanism by Konnov [98]. Recent ab initio post-CCSD(T) calculations at the W3X-L//CCSD(FC)/cc-pVTZ level by Monge-Palacios and Sarathy [394], obtained new expressions of the rate coefficients, which is lower than that of Hong *et al.* [411] by about a factor of 2. The later revisit by Liu *et al.* [414] using the Quasi-Classical trajectory (QCT) approach shows excellent agreement with this new expression. Therefore, the present work updated this reaction using the expression by Monge-Palacios and Sarathy [394].

It is worth noting that the recombination of OH and HO<sub>2</sub> radicals can also produce singlet oxygen O<sub>2</sub>(<sup>1</sup>Δ<sub>g</sub>),



, which proceed through a different PES. Although the branching ratio is reported to be insignificant (lower than 0.5% below 1000 K) [394], it may play a role when combustion events are seeded with ozone (O<sub>3</sub>). [94] The current version of the mechanism does not include this reaction and the only excited species included in the mechanism is OH(<sup>2</sup>Σ<sup>+</sup>). Integration of reactions involving excited species, such as O<sub>2</sub>(<sup>1</sup>Δ<sub>g</sub>) and O<sub>2</sub>(a<sup>1</sup>Δ<sub>g</sub>), is planned for future works.

## Reactions in H<sub>2</sub>/CO Sub-Mechanism

The rate coefficients of the reactions in the CO sub-mechanism are evaluated, as shown in Table 6.3, and some of the reactions are described.

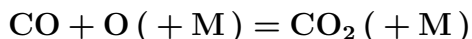


Table 6.3: Rate coefficients for reactions in the CO sub-mechanism of MACDIL-DTL.

No.	Reaction	P <sup>1</sup>	A <sup>2</sup>	n	E <sub>a</sub> <sup>3</sup>	Ref.				
CO-1	CO + O(+M) = CO <sub>2</sub> (+M) <i>F<sub>cent</sub></i> = 0.5, low pressure limit:		1.06E+13	-3.08E-01	6.94E+03	[415-417]				
			1.17E+24	-2.79E+00	4.19E+03					
	$\epsilon_{\text{H}_2} = 2.5, \epsilon_{\text{H}_2\text{O}} = 12.0, \epsilon_{\text{CO}} = 1.75, \epsilon_{\text{CO}_2} = 3.6, \epsilon_{\text{HE}} = 0.7, \epsilon_{\text{AR}} = 0.87$									
CO-2	CO + O <sub>2</sub> = CO <sub>2</sub> + O		5.06E+13	0.00E+00	6.32E+04	[418]				
CO-3	CO + OH = CO <sub>2</sub> + H		7.02E+04	2.05E+00	-3.56E+02	[419]				
			5.76E+12	-6.64E-01	3.32E+02					
CO-4	HOCO = CO + OH		6.30E+32	-5.96E+00	3.25E+04	[105]				
			0.001	1.55E-08	2.93E+00		8.77E+03			
			0.003	1.77E+03	3.40E-01		1.81E+04			
			0.0296	2.02E+13	-1.87E+00		2.28E+04			
			0.0987	1.68E+18	-3.05E+00		2.43E+04			
			0.2961	2.50E+24	-4.63E+00		2.71E+04			
			0.9869	4.54E+26	-5.12E+00		2.76E+04			
			2.9607	7.12E+28	-5.60E+00		2.85E+04			
			9.869	5.48E+29	-5.70E+00		2.89E+04			
			29.607	9.89E+31	-6.19E+00		3.05E+04			
			98.69	5.74E+33	-6.53E+00		3.21E+04			
			296.07	2.61E+33	-6.29E+00		3.22E+04			
			986.9	6.30E+32	-5.96E+00		3.25E+04			
			CO-5	HOCO = CO <sub>2</sub> + H			1.90E+38	-8.05E+00	3.42E+04	[105]
							0.001	4.76E+18	-3.82E+00	
0.003	2.23E+20	-4.15E+00				1.90E+04				
0.0099	7.56E+21	-4.43E+00				2.03E+04				
0.0296	9.11E+24	-5.19E+00				2.24E+04				
0.0987	3.14E+29	-6.38E+00				2.52E+04				
0.2961	1.15E+32	-7.04E+00				2.67E+04				
0.9869	1.07E+36	-8.11E+00				2.91E+04				
2.9607	2.44E+36	-8.15E+00				2.93E+04				
9.869	6.66E+35	-7.92E+00				2.92E+04				
29.607	1.72E+38	-8.51E+00				3.13E+04				
98.69	3.01E+41	-9.29E+00				3.40E+04				
296.07	6.77E+36	-7.83E+00				3.16E+04				
986.9	1.90E+38	-8.05E+00				3.42E+04				
CO-6	CO + HO <sub>2</sub> = CO <sub>2</sub> + OH					1.57E+05	2.18E+00	1.79E+04	[420]	
CO-7	HCO + M = H + CO + M		4.75E+11	6.60E-01	1.49E+04	[103, 421]				
	$\epsilon_{\text{AR}} = 0.87, \epsilon_{\text{N}_2} = 1.0, \epsilon_{\text{H}_2} = 2.5, \epsilon_{\text{H}_2\text{O}} = 12.0, \epsilon_{\text{CO}} = 1.9, \epsilon_{\text{CO}_2} = 3.8$									
CO-8	HCO + O <sub>2</sub> = CO + HO <sub>2</sub>		6.92E+06	1.90E+00	-1.37E+03	[422]				
CO-9	HCO + H = CO + H <sub>2</sub>		1.20E+14	0.00E+00	0.00E+00	[423]				
CO-10	HCO + O = CO + OH		3.02E+13	0.00E+00	0.00E+00	[383]				
CO-11	HCO + O = CO <sub>2</sub> + H		3.00E+13	0.00E+00	0.00E+00	[383]				
CO-12	HCO + OH = CO + H <sub>2</sub> O		1.19E+15	-1.15E+00	4.12E+03	[424, 425]				
			1.98E+14	-6.61E-01	4.09E+02					
CO-13	HCO + HO <sub>2</sub> = CO <sub>2</sub> + H + OH		3.00E+13	0.00E+00	0.00E+00	[383]				
CO-14	HCO + HO <sub>2</sub> = CO + H <sub>2</sub> O <sub>2</sub>		3.00E+12	0.00E+00	0.00E+00	[383]				
CO-15	HCO + HCO = H <sub>2</sub> + CO + CO		3.00E+12	0.00E+00	0.00E+00	[383, 426, 427]				
CO-16	HOCO + H = H <sub>2</sub> + CO <sub>2</sub>		4.07E+17	-1.38E+00	5.97E+02	[428]				
CO-17	HOCO + H = H <sub>2</sub> O + CO		1.96E+14	-6.00E-02	1.63E+03	[428]				
CO-18	HOCO + O = OH + CO <sub>2</sub>		2.95E+12	1.70E-01	-6.99E+01	[428]				
CO-19	HOCO + OH = H <sub>2</sub> O + CO <sub>2</sub>		4.56E+12	0.00E+00	-8.90E+01	[428]				
			9.54E+06	2.00E+00	-8.90E+01					
CO-20	HOCO + OH = H <sub>2</sub> O <sub>2</sub> + CO		3.90E+05	2.09E+00	5.44E+03	[428]				
CO-21	HOCO + O <sub>2</sub> = HO <sub>2</sub> + CO <sub>2</sub>		1.38E+10	8.42E-01	1.60E+02	[428]				
CO-22	HOCO + HO <sub>2</sub> = H <sub>2</sub> O <sub>2</sub> + CO <sub>2</sub>		3.00E+13	0.00E+00	0.00E+00	[428]				

<sup>1</sup> The unit for pressure is atm and The pressure dependent rate coefficients are in PLOG format.

<sup>2</sup> The units for the pre-exponential factor are  $s^{-1}$  for unimolecular reactions,  $cm^3 mol^{-1} s^{-1}$  for bimolecular reactions, and  $cm^6 mol^{-2} s^{-1}$  for termolecular reactions.

<sup>3</sup> The unit for apparent activation energy  $E_a$  is  $cal mol^{-1}$ .

The 3rd-body recombination reaction of CO and the O radical, are found to be highly pressure-dependent and have non-Arrhenius rate coefficients. [429] Studies on its reaction kinetics are limited in number and contradictory in the proposed values. For example, as mentioned by Nilsson and Konnov [428], the rate constants at the low-pressure limit obtained by Westmoreland *et al.* [416] using QRRK analysis is about one magnitude higher than that by Troe [429]. Recent molecular dynamics studies by Jasper and Dawes [430] led to a value (with an estimated uncertainty of  $\pm 40\%$ ) at the high-pressure limit at 1000–5000 K, which is also about 7–35 times larger than that obtained by Troe [429]. Later Jasper [415] found that the main source of error is from the multidimensional effect which is not typically included in statistical treatments of spin-forbidden kinetics. By using a

novel MD method taking into account this effect, a new expression  $k_{\infty}(T) = 3.04 \times 10^{-12}(T/300 \text{ K})^{-0.308} \exp(-3494 \text{ K}/T) \text{ cm}^3 \text{ molecule}^{-1} \text{ s}^{-1}$  was proposed for the high-pressure limit for  $T = 300\text{--}5000 \text{ K}$  and is estimated to be more accurate than previous ones. [415] Most syngas mechanisms [17, 102, 103, 431, 432] accept the suggestion by Allen *et al.* [417] to combine the low-pressure rate constant by Westmoreland *et al.* [416] and the high-pressure rate constant by Troe [429], but implement them with modification considering the uncertainty. In the mechanism by Nilsson and Konnov [428], the high-pressure rate constant by Jasper and Dawes [430] is used combining with the low-pressure limiting value recommended by Tsang and Hampson [383] The present work adopts the latest expression for the high-pressure limit obtained by Jasper [415] and the low-pressure limit used by Kromns *et al.* [17] which multiply the values of Westmoreland *et al.* [416] by a factor of 0.87. Values for 3rd-body collisional efficiencies are also adopted from K eromn es *et al.* [17].

### CO + OH = CO<sub>2</sub> + H

The CO + OH = CO<sub>2</sub> + H reaction is one of the major heat release step in hydrocarbon combustion, and therefore is highly sensitive to flame speed. The mechanism of the reaction is found to proceed via the formation of the HOCO complex [419], the presence of which is confirmed by time-resolved direct frequency comb spectroscopy (TRFCS) experiments [433]. The chemically activated HOCO could undergo dissociation into bimolecular products CO<sub>2</sub> + H, or stabilization by collisions. The electronic structure and reaction kinetics of this reaction has been extensively studied both experimentally and theoretically in the recent decades. [105, 106, 379, 419, 434–450] Recent studies have also found that its reaction kinetics are affected by a third CO<sub>2</sub> [106] or H<sub>2</sub>O [107] molecule. Concerning the rate coefficients for this reaction, the present work adopts the expression fitted from the theoretically calculated values by Joshi and Wang [419], since it agrees with experimental data very well. The rate coefficients for reactions involving the HOCO complex is adopted from the theoretical work by Weston *et al.* [105].

### The CH<sub>2</sub>CO + OH reaction

The temperature and pressure rate coefficients for the CH<sub>2</sub>CO + OH reaction, calculated theoretically in Chapter 3, are also included in the MACDIL-DTL mechanism.

## 6.2 Semi-Detailed Mechanism: MACDIL-RDC

To evaluate the performance of the developed mechanism, validation based on laminar flame speeds is necessary, by comparing the values obtained by experimental measurements and mechanism predictions. The many low-temperature reactions in MACDIL-DTL, such as those reactions that are specifically sensitive to ignition delay, are not necessarily important for laminar flame speeds which depend largely on the high-temperature chemistry. As a result, although it is possible, using MACDIL-DTL for 1-D flame speed calculations is neither reasonable nor efficient computationally. Therefore, a reduced mechanism is wishable in order to calculate  $S_L$  with sufficient accuracy but less computational resources. Aiming to

validate the mechanism over a wide range of conditions, the present work reduces the MACDIL-DTL mechanism in a moderate way. A semi-detailed mechanism (MACDIL-RDC), about half the size of the original one (1032 species and 5420 reactions), is therefore generated.

Table 6.4: Conditions used in the reduction of MACDIL-DTL to generate MACDIL-RDC mechanism.

No.	Mixture	$T_u$ (K)	P (bar)	EGR%	$\phi$
1	TRFE/air/EGR	700	5	20%	0.8
2					1.1
3					1.3
4	TRFE/air/EGR	1000	20	50%	0.8
5					1.1
6					1.3

Similarly, the reduction of MACDIL-DTL based on 1-D flame speed calculations is challenging. In addition, extraction of high-temperature reactions using species structural information is not considered, because it could lead to the loss of some low-temperature reactions that are sensitive in the flames at high fresh-gas temperatures. Therefore, the present work proposes an alternative way to reduce MACDIL-DTL, which is reduction based on 0-D ignition delay calculations at conditions (as shown in Table 6.4) that are carefully selected to keep reactions sensitive to laminar flame speeds. The most important feature is the selected initial temperatures (700 and 1000 K). The condition at  $T_u = 1000$  K makes sure that the temperature in the homogeneous reactor is greater than 1000 K at any given time, where high-temperature reactions are sensitive and kept in the reduced mechanism. The condition at  $T_u = 700$  K is selected because it is inside and near the low-temperature end of the negative temperature coefficient (NTC) range for the TRFE fuel investigated (as shown in Figure 6-4). This makes sure that the temperature in the homogeneous reactor is greater than 700 K and the temperature rise could cover the NTC temperature range and the transition to high temperatures. As a result, the reactions responsible for the NTC behavior are kept in the mechanism, since they might be important for flames at high initial temperatures. Concerning other reduction parameters, target properties are ignition delay time (IDT), maximum mole fractions of the H and OH radicals, with restriction to a maximum 4% error tolerance. The TRFE/air/EGR mixture is used, the same as that of the experiments for validation. In addition, high EGR ratio and pressure are selected, since they are conditions of interest for both scientific and application purposes.

Figure 6-4 shows the comparison of the predictions by MACDIL-RDC and MACDIL-DTL based on ignition delay time. The overlapping curves indicate the sufficient predictive performance of MACDIL-RDC. The predictive performance of MACDIL-RDC in laminar flame speeds is discussed in Section 6.3 (the next section).

It is worth mentioning that, calculations of laminar flame speeds and reduction based on laminar flame speeds, using the MACDIL-DTL mechanism is still planned for future works. Comparison between the laminar flame speeds predicted by MACDIL-DTL and MACDIL-RDC is also subject to future works.

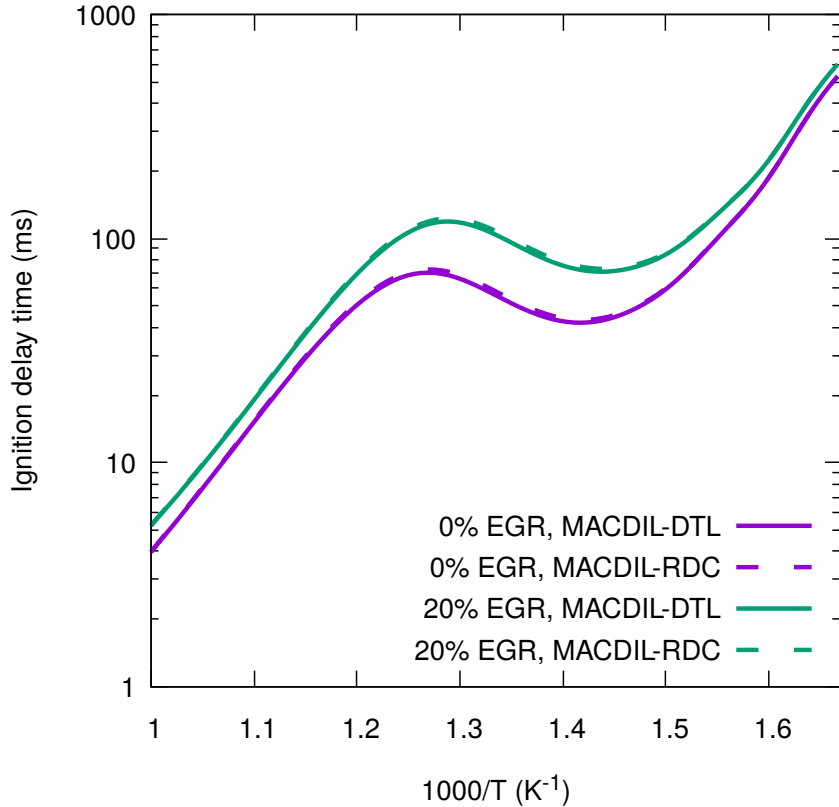


Figure 6-4: Comparison of the predictive ability of MACDIL-RDC with respect to MACDIL-DTL, based on the ignition delay time of TRFE/air/mixtures at initial temperature of 600–1000 K and pressure of 10 bar.

## 6.3 Validation of MACDIL-RDC on the Laminar Flame Speeds of TRFE/air/EGR Mixtures

### 6.3.1 Introduction

In this section, the semi-detailed mechanism, MACDIL-RDC is validated on the laminar flame speed of the TRFE fuel at EGR diluted conditions, based on the experiments conducted by our partner, the PRISME lab.

Concerning the detail of flame speed computation, the domain is extended gradually to 20 cm to make the flame freely-propagating, and grid control parameters are refined to  $\text{GRAD}=0.1$  and  $\text{CURV}=0.1$  by using continuations as shown in Table 6.5 to ensure grid-independent results. Thermal diffusion (Soret effect) is considered and the mixture average transport is used.

### 6.3.2 Laminar Flame Speed of TRFE/air/EGR Mixtures

The MACDIL-RDC mechanism is validated based on the  $S_L$  of TRFE surrogate measured using the spherical flame method by the PRISME lab [24]. Description

Table 6.5: Continuations used in 1-D  $S_L$  calculations of TRFE/air/EGR flames.

Parameter	Continuations							
	0	1	2	3	4	5	6	7
starting axial position (cm)	0	0	-1	-2	-5	-5	-5	-5
ending axial position (cm)	0.5	2	3	5	10	15	15	15
adaptive grid control based on solution gradient	1.0	0.5	0.5	0.4	0.3	0.2	0.2	0.1
adaptive grid control based on solution curvature	1.0	0.9	0.5	0.4	0.3	0.2	0.2	0.1
thermal diffusion (Soret effect)							×	×

Table 6.6: List of conditions in the PRISME experiments [24].

EGR Ratio		$T_u$ (K)		P (bar)		$\phi$
0%	×	373,423,473	×	1,2,3,5	×	0.8–1.4
10%	×	373,423,473	×	1,2,3,5	×	0.8–1.4
20%	×	373,423,473	×	1,2,3,5	×	0.8–1.4

about the experimental apparatus can be found in Ref. [24]. The results are stretch-corrected using the non-linear extrapolation method developed by Kelly and Law [234] (method No.3 in Table 2.1 of Section 2.4.2). The conditions of the available data points are shown in Table 6.6. The compositions (in mole fractions) of the TRFE fuel, the synthetic air, and the synthetic EGR are the same as described in Table ?? of Section 4.2.2. The definition of EGR ratio is defined as the mole fraction of the synthetic EGR in the whole TRFE/air/EGR mixture, which is described in Equation 4.1. The definition and derivation of equivalence ratio is explained in Equations 4.1–4.7 of Section 4.2.2. In addition, the compositions of the mixtures used in the experiments at different equivalence ratios and EGR ratios are provided in Table B.2 in Appendix B. Simulations using the LLNL 2011 and MACDIL-RDC mechanisms are performed on the same measured equivalence ratios as the experiments.

In the present work, the laminar flame speeds predicted with the MACDIL-RDC mechanism is compared with the experimental measurements at  $T_u = 473$  K, as shown in in Figure 6-5. The data for laminar flame speeds at  $T_u = 473$  K measured by experiments and predicted with the two mechanisms are provided in Table B.3 of Appendix B. Comparison with data points at  $T_u = 373$  K and  $T_u = 423$  K are subject to future works. The laminar flame speed predicted by the MACDIL-RDC mechanism is found to have a good overall agreement with the measurements from PRISME, with a mean absolute percentage error (MAPE) of 10.1% for all data points at 473 K. For instance, at the equivalence ratio of 1.1 where flame speed is at local maximum, MACDIL-RDC over-estimates by 1–5 cm/s (less than 10% relatively). It is acceptable considering experimental uncertainties. It is worth noting that the error bars of experimental values presented in the figures are the standard deviation of at least three repeated measurements. However, actual experimental uncertainty could be larger, since experimental and post-processing uncertainties, such as uncertainties in mixture composition (equivalence ratio) and flame contour averaging processes, are not accounted for. In addition, some inconsistency in the measurements is observed on the equivalence ratio where maximum  $S_L$  is located. As shown in Figure 6-5, the local maximum



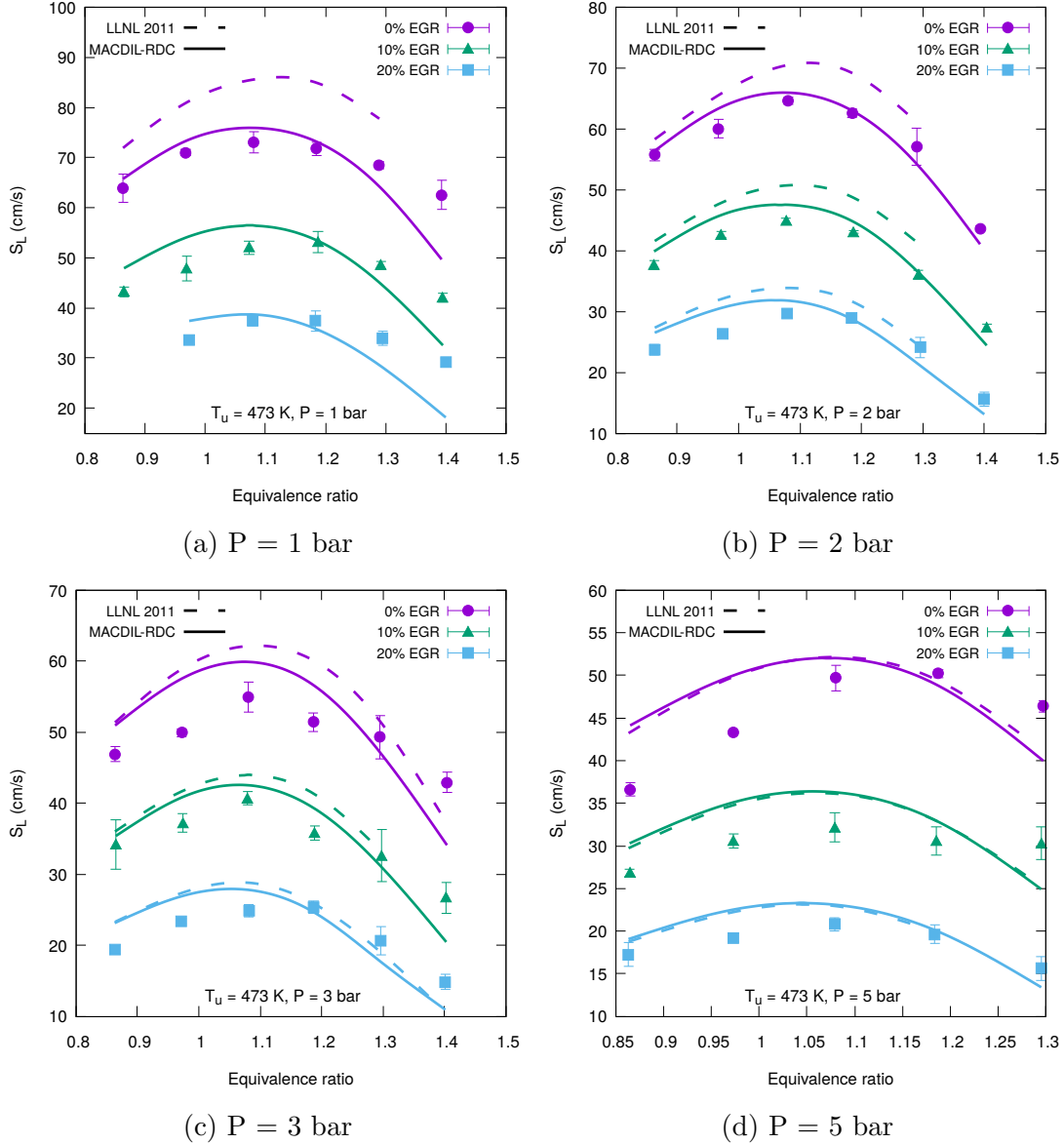


Figure 6-5: Validation of the MACDIL-RDC mechanism on the  $S_L$  of TR-FE/air/EGR flames at 473 K with various pressures and EGR ratio. Experiments are from Ref. [24]. Predictions by the starting mechanism (LLNL 2011 [25]) is also compared. In Figure (a), there is only one curve predicted LLNL 2011 at the 0% EGR condition due to convergence problem using the computational detail described in Section 6.3.1. At the 10% EGR condition, these is one point  $\phi \approx 1.1$  converged. At the 10% EGR condition, non of the points converged. For details about the data, please refer to Table B.3 in Appendix B.

of most curves is located at about  $\phi \approx 1.1$ . Differently, the maximum is found at  $\phi \approx 1.2$  for some curves, i.e., the 10% EGR curve in Figure 6-5a, 20 % EGR curve in Figure 6-5c, and the 0% EGR curve in Figure 6-5d. However, MACDIL-RDC predicts a constant value of  $\phi \approx 1.1$  at all conditions. The inconsistency is not due to the effect of EGR, due to that (i) it is also found at non-diluted cases and (ii) it is reported that EGR does not affect this value for TRF [75] and ethanol [72] flames and maximum  $S_L$  is always located at  $\phi \approx 1.1$ . Therefore, the

inconsistency could be associated with uncertainties in either the measured equivalence ratio, flame speed or both. For leaner mixtures ( $\phi < 1.2$ ), slightly higher  $S_L$  (by about 1–5 cm/s) is predicted, except for the 0% EGR cases at 3 and 5 bar (Figure 6-5c and 6-5d), whereas for richer mixtures ( $\phi > 1.2$ ), MACDIL-RDC predicts values slightly lower than experiments. The discrepancy grows larger as the mixture becomes richer, with the largest deviation found to be about 10 cm/s at  $\phi \approx 1.4$ . It implies that the predictability of MACDIL-RDC could be improved for rich mixtures.

With respect to the starting mechanism, the MACDIL-RDC mechanism predicts overall lower flame speeds and shows considerable improvement especially at lower pressure and lower EGR ratio conditions. For instance, for slightly rich mixtures ( $\phi \approx 1.1$ ) at pressure of 2 bar (as shown in Figure 6-5a), the predicted  $S_L$  by MACDIL-RDC is lower than LLNL 2011 by about 5 cm/s at 0% EGR, 3 cm/s at 10% EGR, and 2 cm/s at 20% EGR. With these lower values compared with that of LLNL 2011, calculated flame speeds from MACDIL-RDC are closer to the measurements, as the curves go through the experimental data. By comparing all the curves at different pressures for the same EGR ratio, it can be seen that the discrepancy between the two mechanisms becomes smaller as pressure increases. This might be due to the fact that the starting mechanism is designated for high pressure and its validation conditions in the original paper are at pressures higher than 3 atm [25]. Considering curves at various EGR ratio for the same pressure, it is found that although the absolute difference between the two mechanisms decrease as dilution gets higher, the relative difference stays constant. For example, in Figure 6-5b, the discrepancies are about 7% at  $\phi = 1.1$ , 10% at  $\phi = 1.2$ , and 13% at  $\phi = 1.1$ , for all the three EGR ratios. It may suggest that the improvement is consistent at different dilution ratios and the seemingly lower difference at high EGR is due to the decrease of the absolute values of the reference flame speed. In addition, for some conditions, such as the 10% and 20% EGR cases in Figure 6-5a, calculations using the starting mechanism failed to converge using the computational details described in Section 6.3.1 but calculations using MACDIL-RDC converge at the same conditions, which may imply that MACDIL-RDC is comparatively more robust (or less stiff).

The predictions from two correlation formulas, proposed by Gülder *et al.* [26] and Yahyaoui *et al.* [27] respectively, are compared with the laminar flame speed at 473 K and 5 bar, as shown in Figure 6-6. The two correlations are used extensively in our partner institutions (IFPEN and Renault) for alternative SI engine development. The Gülder’s correlation [26], developed in 1984, is obtained by fitting directly on experimental data by Metghalchi and Keck [62, 451] for various fuels at high temperature (750 K), pressure (40 bar) and EGR ratio (20%). The corresponding curves for the Gülder’s correlation [26] shown in Figure 6-6 are generated for isoctane with the addition of 5% ethanol in liquid volume fraction (i.e.,  $v = 0.05$ , the same as the TRFE fuel used in the present work) diluted by  $\text{CO}_2/\text{N}_2$  (15%/85%), using the following formulas,

$$S_{L,0}(\phi) = Z \cdot W \cdot \phi^\eta \cdot \exp[-\xi(\phi - 1.075)^2] \quad (6.1)$$

$$S_L(\phi, T, P, x_d) = S_{L,0}(\phi) \left(\frac{T}{T_0}\right)^\alpha \left(\frac{P}{P_0}\right)^\beta (1 - f \cdot x_d) \quad (6.2)$$

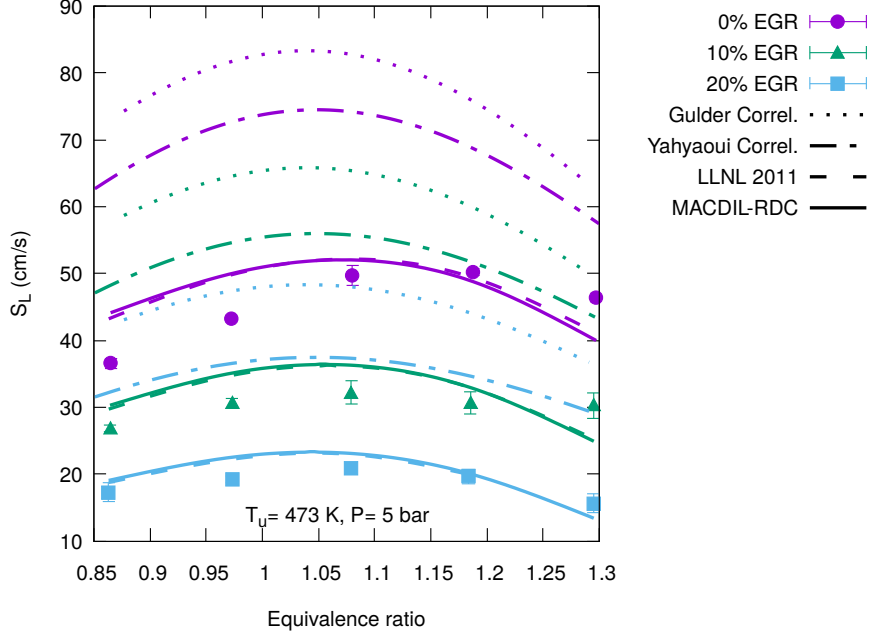


Figure 6-6: Additional comparison with predictions by correlations at the 473 K, 5 bar condition (Figure 6-5d). The experimental data are the same as in Figure 6-5d. The Gülder *et al.* [26] correlation is designated for isooctane/ethanol blend diluted by  $N_2/CO_2$  and the Yahyaoui *et al.* [27].

where  $x_d$  is dilution ratio (or the mole fraction of dilution in the whole mixture) and  $f = 2.3$  is the effectiveness of dilution, and the values for the remaining parameters are,  $Z = 1 + 0.07v^{0.35}$ ,  $W = 46.58$  cm/s,  $\eta = -0.326$ ,  $\xi = 4.48$ ,  $\alpha = 1.56 + 0.23v^{0.46}$ , and  $\beta = -0.22$ . The Yahyaoui's correlation [27], developed in 2009, is obtained based on the predictions by an auto-generated kinetic mechanism that is validated on measurements on gasoline and surrogates, from Zhao *et al.* [54] at low pressure and Jerzembeck *et al.* [55] at high pressure (up to 25 bar). The corresponding curves for the Yahyaoui's correlation [27] are generated for gasoline and TRF surrogates (42.9% isooctane, 13.7% n-heptane, and 43.4% toluene) with addition of 10.8% of ethanol in mole fraction (i.e.,  $X_{\text{ethanol}} = 0.1080$ , the same as the TRFE fuel used in the present work) diluted by  $N_2$ , using the following formulas,

$$S_{L,0}(\phi) = Z \cdot W \cdot \phi^\eta \cdot \exp[-\xi(\phi - 0.68157)^2] \quad (6.3)$$

$$S_L(\phi, T, P, x_d) = S_{L,0}(\phi) \left( \frac{T}{400K} \right)^\alpha \left( \frac{P}{1atm} \right)^\beta f(x_d) \quad (6.4)$$

$$f(x_d) = 1 - 2.4832x_d - 0.0020312x_d^2 - 0,0041743x_d^3 \quad (6.5)$$

where  $f(x_d)$  is the dilution term,  $Z = 1 + 0.14892X_{\text{ethanol}}^{2.4698}$ ,  $W = 90.31$  cm/s,  $\eta = 2.4269$ ,  $\xi = 3.154$ ,  $\alpha = 2.236 - 0.19877X_{\text{ethanol}}^{6.7936E-15}$ , and  $\beta = -0.28327$ . It is found that both correlations over-predict systematically the laminar flame speed for all the three conditions (0%, 10%, and 20% EGR ratios). For example, the flame speeds at  $\phi \approx 1.1$  predicted by the Gülder correlation are higher than measurements by about 30 cm/s. The Yahyaoui correlation is comparatively closer to experiments, with overestimation about 20 cm/s at the same condition. The

difference between Gülder and Yahyaoui correlations could be associated with that flame stretch corrections are not considered in the early experimental data based on which the Gülder’s formula is generated. The difference between correlations with the measured flame speeds of TRFE, could be due to that their validation is mostly based on the different compositions of fuels and EGR than the TRFE used in the present work. Besides the absolute value, the reduction effect of EGR on flame speed predicted by the two correlations are found to be stronger. For  $\phi \approx 1.1$ , flame speed is reduced by about 30 cm/s from 0% to 20% of EGR as shown by the experiments and mechanism predictions, while this reduction is about 40 cm/s as predicted by the two correlations. It can be concluded that a correlation for TRFE surrogates at diluted conditions may be needed, as Gülder and Yahyaoui correlations are not accurate enough for predicting either  $S_L$  absolute values or the effect of EGR.

### 6.3.3 Effect of EGR on Laminar Flame Speed

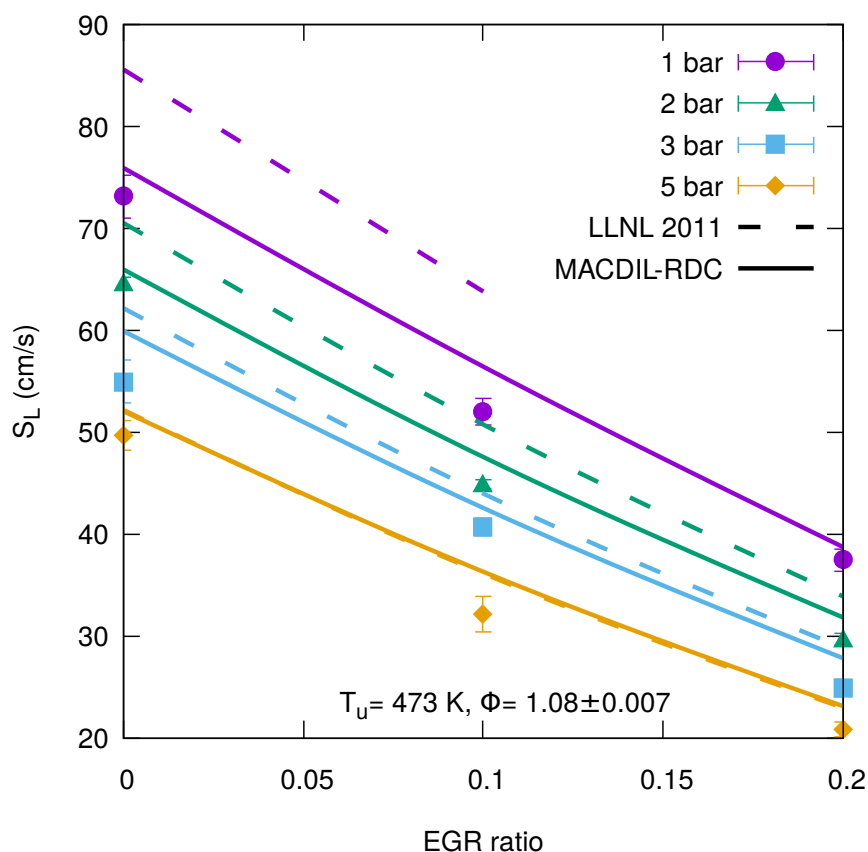


Figure 6-7: Evolution of  $S_L$  with EGR ratio for TRFE/air/EGR mixtures with  $\phi \approx 1.1$  at  $T_u = 473$  K at various. The data shown are the same as that in 6-5. The predicted line at  $P = 1$  bar using LLNL 2011 (the purple dashed line) stops at 10% of EGR ratio, as only calculations at 0% and 10% EGR converged.

The decreasing evolution of the laminar flame speeds of TRFE/air flames with EGR dilution ratio is shown in Figure 6-7 and 6-8, with a comparison with the predictions by MACDIL-RDC and LLNL 2011. It is found that flame speeds

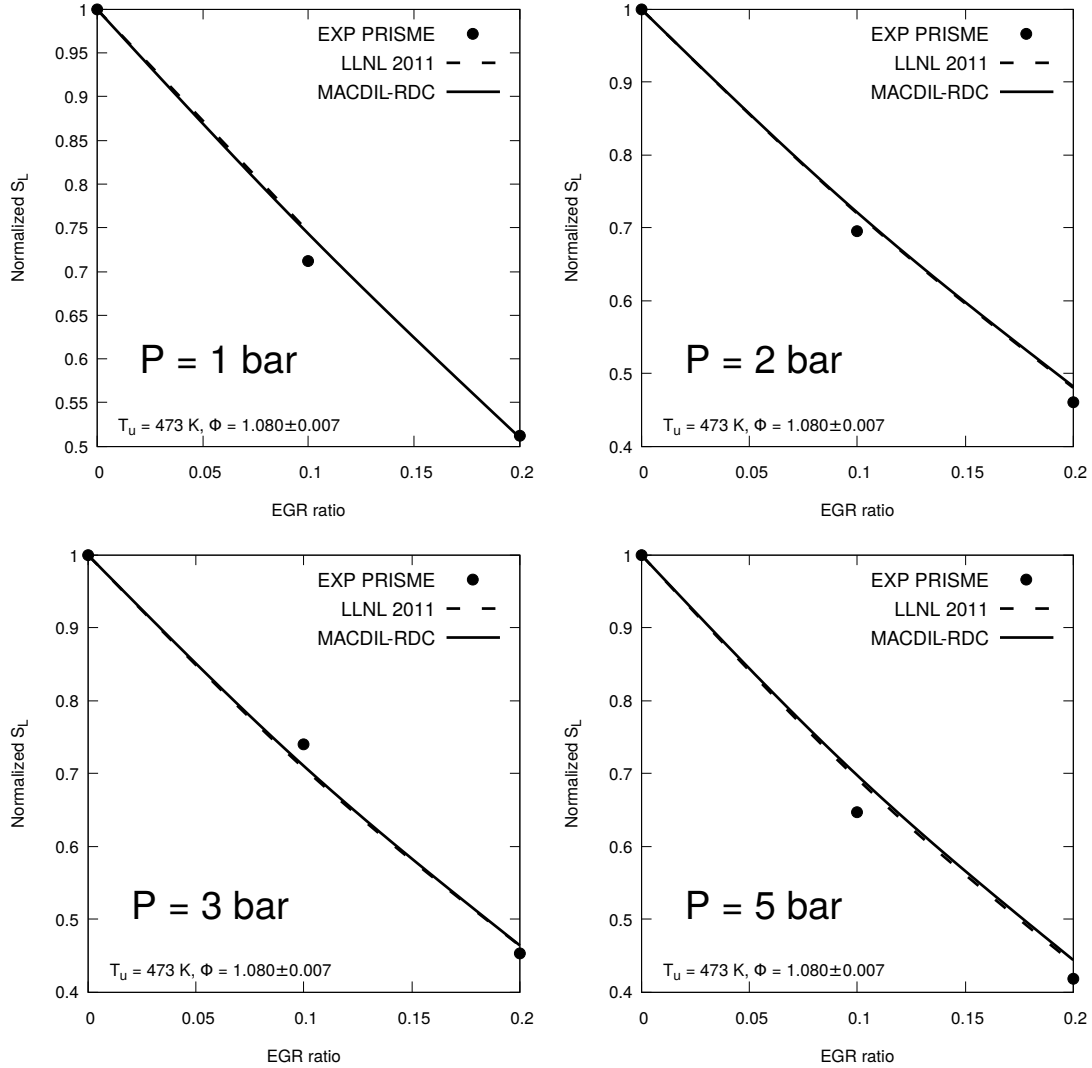


Figure 6-8: Evolution of normalized  $S_L$  with EGR ratio for TRFE/air/EGR mixtures with  $\phi \approx 1.1$  at  $T_u = 473$  K and various pressures. The data shown in these figures are reproduced from those in Figure 6-7 and Figure 6-5. Normalized  $S_L$  at a certain EGR ratio is defined as the ratio between its  $S_L$  over the  $S_L$  at the reference case, i.e., the 0% EGR case. In the  $P = 1$  bar figure, the predicted (dashed) line for LLNL 2011 stops at 10% of EGR ratio, as only calculations at 0% and 10% EGR converged.

decrease significantly with EGR ratio and the reduction seems linear with only minor curvature. Although slightly over-predicting as shown in Figure 6-7, both MACDIL-RDC and LLNL 2011 predicted curves show good agreement with experiments on the gradient with EGR ratio, as shown in Figure 6-8. Additional comparison is made based on isoctane/air flames as shown in Figure 6-9. Dilution effect of pure  $\text{CO}_2$  and  $\text{H}_2\text{O}$ , as well as EGR (same composition as present work) are compared with the experiments by Endouard *et al.* [13]. It is found that the reducing effect on  $S_L$  is the strongest for  $\text{CO}_2$ , weaker for  $\text{H}_2\text{O}$ , and weakest for synthesis EGR which has  $\text{N}_2$  as a major component. The MACDIL-RDC mechanism shows excellent agreement with experiments for all the three diluent. Therefore It can be concluded that both mechanisms are sufficient to capture the

EGR effects on flame speed.

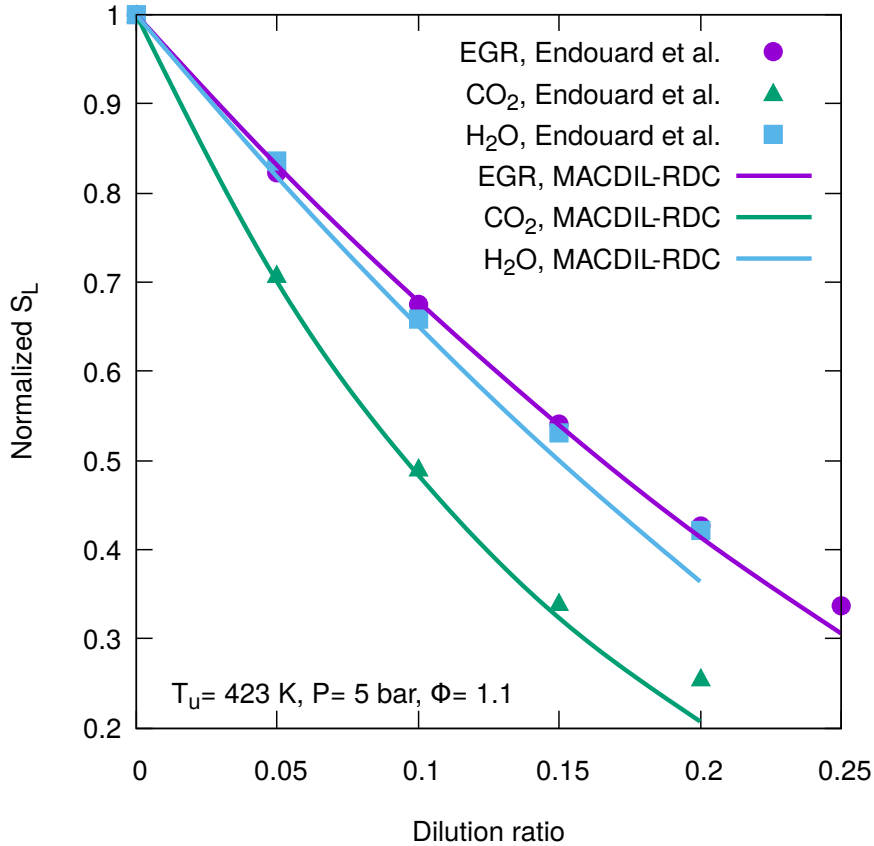


Figure 6-9: Effect of CO<sub>2</sub>, H<sub>2</sub>O, N<sub>2</sub> dilution on the  $S_L$  of isooctane/air flames at  $T_u = 423$  K,  $P = 5$  bar, and  $\phi = 1.1$ . The EGR composition is 12.4% CO<sub>2</sub>, 14% H<sub>2</sub>O, and 73.6% N<sub>2</sub>. Experimental data are from Endouard *et al.* [13].

Figure 6-10 shows the normalized  $S_L$  with respect to the flame speed at non-diluted case, i.e., normalized  $S_L = S_{L,diluted}/S_{L,non-diluted}$ , at 10% and 20% EGR dilution, respectively, and their evolution with equivalence ratio. It is found that 10% EGR reduces flame speed by about 30% and 20% EGR reduces  $S_L$  by about 60%. In Figure 6-10a, experimental data at the pressure of 1 bar shows that EGR effect is stronger at lean and rich conditions, while slightly weaker at near stoichiometric conditions. The variation is less than 10% for both EGR ratios. However, experimental data at 5 bar in Figure 6-10b show a different trend that EGR effect becomes stronger as equivalence ratio increases. The increase of EGR effect is more than 10% for both EGR ratios. The predictions by both mechanisms agree with the former trend at both 1 and 5 bar pressures. The difference in EGR effect of different equivalence ratios could be associated with the different heat release and temperature profiles in these mixtures where both the thermal effect and the chemically influencing mechanism of EGR could be different. The disagreement between experiments and mechanisms at 5 bar, may suggest that either the experimental trend is contaminated by uncertainties or different kinetics happens at this condition that is not captured by the mechanisms. To better explore this discrepancies or phenomena, further comparison and investigations are required. In addition, the horizontal lines predicted by Gülder and Yahyaoui

correlations (as shown in Figure 6-10b) is simply due to the fact that equivalence ratio dependence of dilution effect is not accounted in the formulas. It suggests the necessity to consider the dilution term in correlation formulas as a function of equivalence ratio.

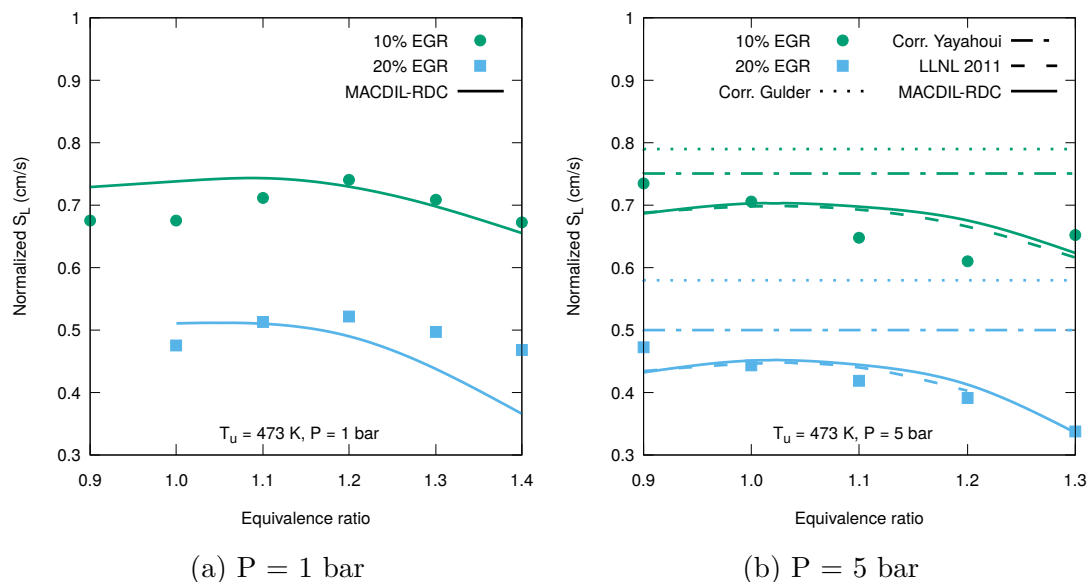


Figure 6-10: Equivalence ratio dependence of the EGR effect on the  $S_L$  of TRFE/air flames at  $T_u = 473$  K and pressure of (a) 1 bar and (b) 5 bar. The data shown in the two figures are reproduced from those in Figure 6-5. Normalized  $S_L$  at a certain EGR ratio is defined as the ratio between its  $S_L$  over the  $S_L$  at the reference case, i.e., the 0% EGR case. In Figure 6-10b predictions from correlations are also compared. For the formulas of the two correlations, please refer to the text.

Similarly, the pressure dependence of EGR effect is also studied, as shown in Figure 6-11. Different to equivalence ratio dependence, the experimental data do not show any clear pattern on pressure dependence. The predictions of both mechanisms predict a slightly stronger trend of EGR effect, with, however, only minor variations. This slight increase of EGR effect is due to that dilution affects  $S_L$  partly by participating in three-body reactions as collision partners whose concentration is increased by elevated pressure. In addition, it is expected that a significant difference could show at higher pressure, as the pressure of 5 bar is not sufficiently high. Further comparison at higher pressure is required to investigate the pressure dependence.

### 6.3.4 Summary

The performance of the semi-detailed mechanism (MACDIL-RDC) is validated on the laminar flame speed of the TRFE/air/EGR mixture. With an overall good agreement with experimental data, the mechanism shows predictions with sufficient accuracy in terms of both absolute values of laminar flame speed and the reduction in  $S_L$  caused by EGR dilution. Considerable improvement with respect to the starting mechanism, LLNL 2011, are also observed, especially at

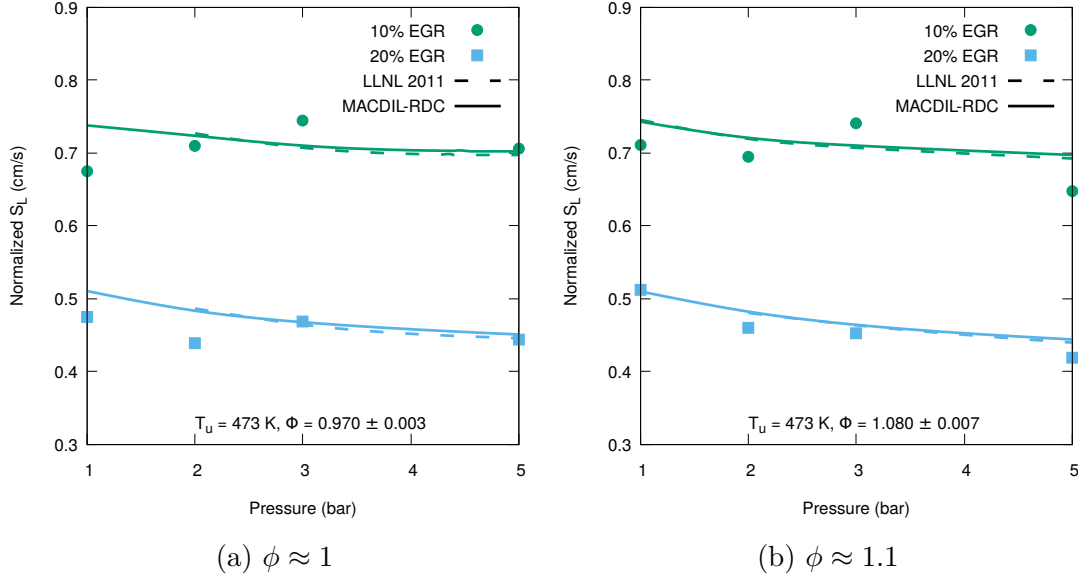


Figure 6-11: Pressure dependence of the EGR effect on the  $S_L$  of TRFE/air flames at  $T_u = 473$  K and equivalence ratios of (a)  $\phi \approx 1$  and (b)  $\phi \approx 1.1$ . The data shown in the two figures are reproduced from those in Figure 6-5. Normalized  $S_L$  at a certain EGR ratio is defined as the ratio between its  $S_L$  over the  $S_L$  at the reference case, i.e., the 0% EGR case.

lower pressure and probably at lower EGR dilution conditions. The effect of EGR is found to depend on equivalence ratio and pressure. Although having good agreement with TRFE data, it is necessary to further validate the mechanism comprehensively based on the laminar flame speed of other fuels, and other types of experimental data, such as ignition delay and speciation profiles, only after which a generally good performance can be claimed.

## 6.4 Insights to the Development of Correlations for Laminar Flame speed at Diluted Conditions

Considering the effect of dilution on  $S_L$ , Figure 6-12 show the prediction by the MACDIL-RDC mechanism up to 50%. It is clear that dilution effect is not linear, and becomes less effective as dilution ratio gets higher. Therefore, the dilution term  $f(x_d)$  in an appropriate correlation formula

$$S_L = S_{L,x_d=0} f(x_d) \quad (6.6)$$

where  $x_d$  is the dilution ratio (defined as the mole fraction of the diluent in the whole mixture), should satisfies the following requirements:

1. when  $x_d = 0$ ,  $f(x_d) = f(0) = 1$ ;
2. when  $x_d = 1$ ,  $f(x_d) = f(1) = 0$  or  $\lim_{x_d \rightarrow 1} f(x_d) = 0$ ;
3. for all  $x_d$  in  $0 \leq x_d < 1$ , the first derivative  $f'(x_d) \leq 0$ ;



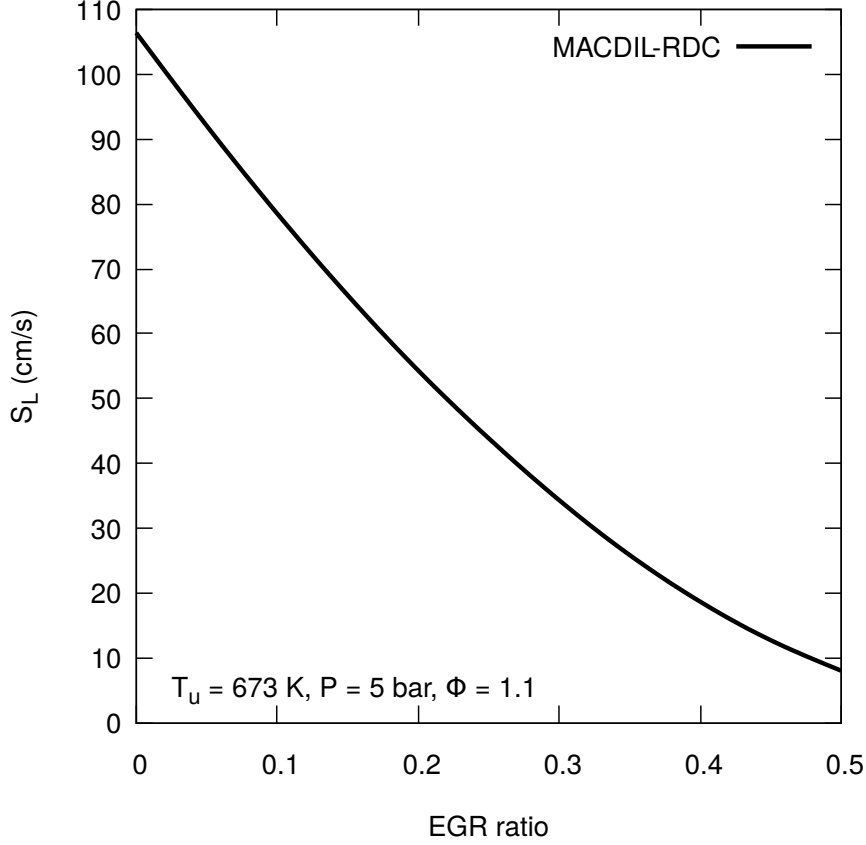


Figure 6-12: Effect of EGR on the laminar flame speeds of TRFE/air/EGR mixtures, at 673 K, 5 bar and  $\phi = 1.1$ , predicted by the MACDIL-RDC mechanism.

4. when  $x_d = 1$ , the first derivative  $f'(x_d) = f'(1) = 0$  or  $\lim_{x_d \rightarrow 1} f'(x_d) = 0$ .

Although the dilution terms in the literature as summarized in Section 1.3.3 all satisfy requirement 1, they could not assure requirement 2, because if dilution ratio gets higher, the flame speed may become negative instead of approaching to zero. Therefore, to better represent the behavior of dilution effect, a new and simpler formula for the dilution term, which satisfies all the four requirements, is proposed in the present work,

$$f(x_d) = \exp\left(-\frac{\mu x_d}{1-x_d}\right), \quad 0 \leq x_d < 1 \quad (6.7)$$

where  $\mu > 0$  is a fitting parameter and could also be a function of equivalence ratio and the fractions of each EGR components, i.e.,  $\mu = \mu(\phi, X_{\text{CO}_2}, X_{\text{H}_2\text{O}}, X_{\text{N}_2}, \dots)$ . As shown in Figure 6-13a, The  $f(x_d)$  obtained using Equation 6.7 equals to unity at the non-diluted case, decreases non-linearly with  $x_d$ , and approaches to zero as  $x_d$  get to 1. The parameter  $\mu$  controls the effectiveness, and greater  $\mu$  leads to faster reduction in  $S_L$ . The first derivative of Equation 6.7 has the form

$$f'(x_d) = -\frac{\mu}{(1-x_d)^2} \exp\left(-\frac{\mu x_d}{1-x_d}\right), \quad 0 \leq x_d < 1 \quad (6.8)$$

and is visualized in Figure 6-13b. It can be seen clearly from the figure that it

satisfies requirements 3 and 4, because  $\mu$  is positive. In addition, when  $x_d = 0$ , the slope of the reduction  $f'(0) = -\mu$ , which also implies the control of parameter  $\mu$  over the dilution effectiveness.

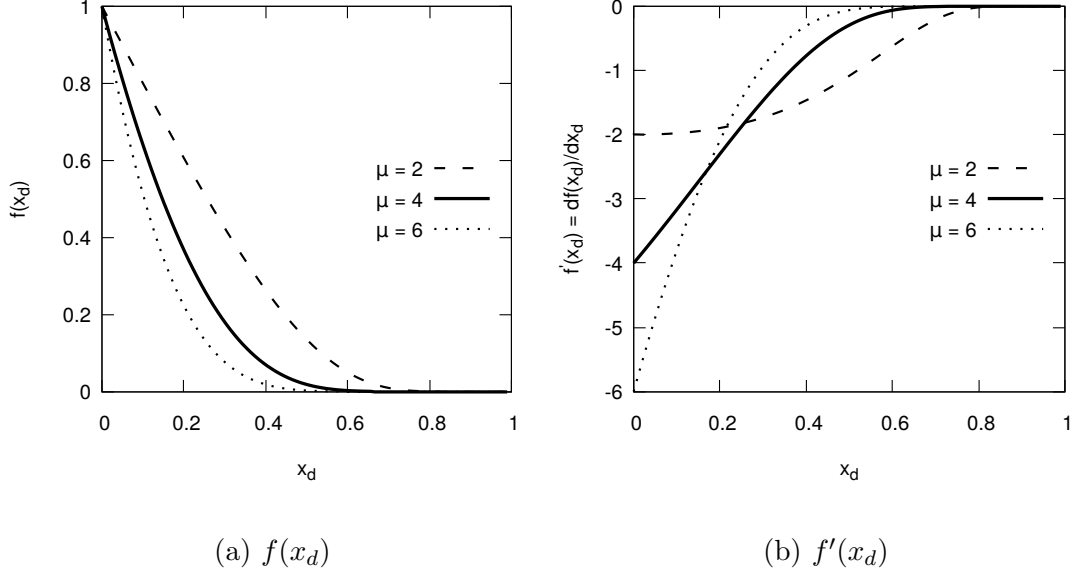


Figure 6-13: The dilution term used in the present work and its derivative.

Furthermore, if a single expression term, like Equation 6.7, could not give sufficient fit, one could try the double expression term

$$f(x_d) = A_1 \exp\left(-\frac{\mu_1 x_d}{1-x_d}\right) + A_2 \exp\left(-\frac{\mu_2 x_d}{1-x_d}\right) \quad (6.9)$$

where  $A_1 + A_2 = 1$ ,  $\mu_1, \mu_2 > 0$ ,  $0 \leq x_d < 1$

or the multi-expression term

$$f(x_d) = \sum_{i=1}^N A_i \exp\left(-\frac{\mu_i x_d}{1-x_d}\right) \quad (6.10)$$

where  $\sum_{i=1}^N A_i = 1$ ,  $\mu_1, \mu_2, \dots > 0$ ,  $0 \leq x_d < 1$

As shown in Figure 6-12, the dilution effect also depend on the equivalence ratio. To best accommodate this dependency, the parameter  $\mu_i$  in Equation 6.10 can be expressed as a function of  $\phi$

$$\mu_i(\phi) = \mu_{i,0} + \mu_{i,1}(\phi - \phi_m) + \mu_{i,2}(\phi - \phi_m)^2 \quad (6.11)$$

where  $\phi_m$  is the equivalence ratio where  $S_L$  is maximum at the reference condition. The  $\phi$  containing terms in Equation 6.11 could be less or more depending on the required fitting accuracy. Since the effectiveness of different diluent molecules in reducing  $S_L$  differs, the  $\mu$  function should also account for the mole fractions of the components when dealing having a mixture as diluent. It can be accommodated

easily and Equation 6.11 becomes

$$\mu_i(\phi, X_j) = \sum_j X_j [\mu_{i,j,0} + \mu_{i,j,1}(\phi - \phi_m) + \mu_{i,j,2}(\phi - \phi_m)^2] \quad (6.12)$$

where  $\sum_j X_j = 1$  are the mole fractions of each component in the diluent mixture.

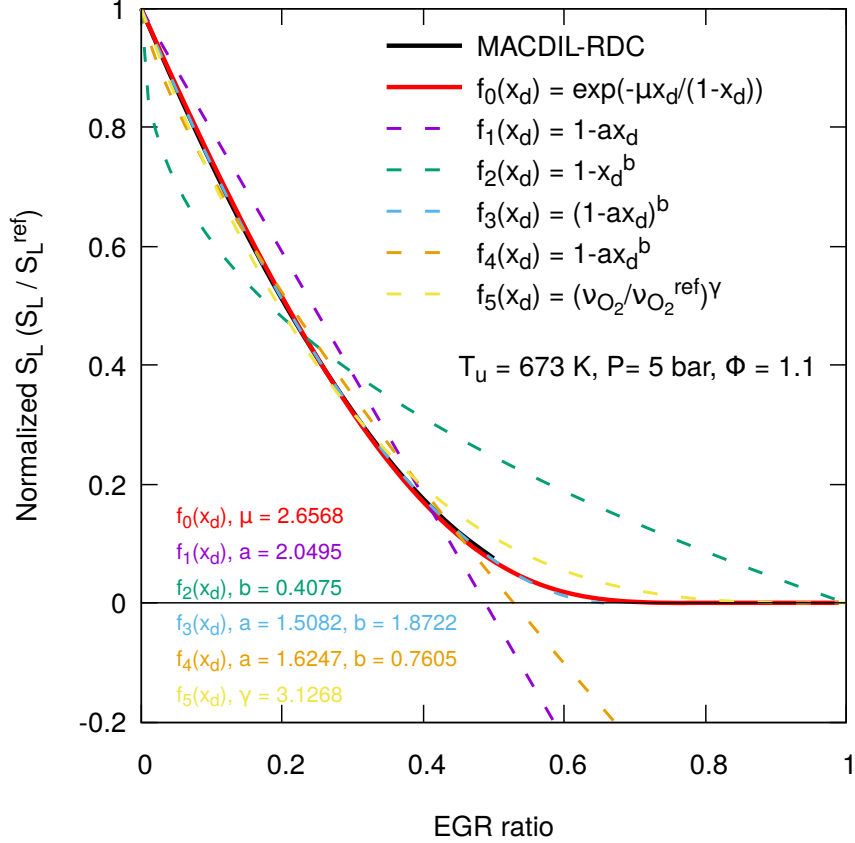


Figure 6-14: Comparison on the performance of the proposed dilution term (Equation 6.7) and other dilution terms in the literature in fitting the EGR effects on the laminar flame speeds predicted by MACDIL-RDC as shown in Figure 6-12.

Figure 6-14 shows that the proposed single-expression  $f(x_d)$  fits the non-linear curve of dilution effect very well, with only one variation parameter. The other correlation formulas do not fit as well and have various drawbacks. For example, expression  $f_1(x_d)$  and  $f_4(x_d)$  generate negative values at high dilution, which violate requirement 2. Expression  $f_2(x_d)$  satisfies requirement 2, but the slope at  $x_d = 0$  is negative infinity and thus could not fit the data well. Expression  $f_3(x_d)$  fits the data very well, but the validity is limited up to around 65% of dilution where  $1 - ax_d = 0$  and the flame speed is also equal to zero. A limitation of highest dilution ratio is appreciable but this limitation in expression  $f_3(x_d)$  is not necessarily the actual limit where the flame quenches. The mixture should become unable to be ignited before the flame speed reaches zero. Therefore a validity over the full range of dilution ratios ( $0 \leq x_d < 1$ ) coupled with measured flammable limits would be desirable. Expression  $f_5(x_d)$  satisfies all the four requirements, but could not generate a fitted curve sufficiently close to the data. With respect

to these formulas, Equation 6.7 proposed in the present work provides the closest fit and therefore is the most appropriate for dilution effects. It can be concluded that fitting using the dilution term proposed in the present work can achieve more accurate fitting results with fewer parameters. In addition, the equivalence ratio dependence of dilution effect can also be well accommodated in the proposed dilution terms.

## 6.5 Conclusions

In this chapter, a detailed mechanism (MACDIL-DTL) and a semi-detailed mechanism (MACDIL-RDC) is established for the combustion of the TRFE fuel. Validations of the MACDIL-RDC mechanism based on the laminar flame speed of TRFE/air/EGR flames, show that the mechanism has a good predictive performance on both the absolute values of  $S_L$  and the reducing effect of EGR on  $S_L$ . Based on the non-linear effect of EGR as predicted by the MACDIL-RDC mechanism, a new dilution term with the form

$$f(x_d) = \exp\left(-\frac{\mu(\phi)x_d}{1-x_d}\right), \quad 0 \leq x_d < 1$$

is proposed to describe with the evolution of  $S_L$  with dilution ratio, whose fitting performance, with respect to existing dilution terms, is found to be more accurate with less parameters.

Further comprehensive validations over a wide range of fuels and conditions are required before using the mechanisms for predictions. The kinetic parameters in the mechanisms could be more comprehensively assessed and their predictive performance could be further improved especially for fuel-rich mixtures. Future works also include the development of a new correlation formula for the laminar flame speed of TRFE.air/EGR mixtures, with the proposed dilution terms integrated.

THIS PAGE INTENTIONALLY LEFT BLANK

# Chapter 7

## Conclusions and Future Works

### 7.1 Conclusions

The present work aims to (i) explore the effects of dilution by mostly  $\text{CO}_2$  and  $\text{H}_2\text{O}$  on the combustion chemistry in flames, (ii) establish kinetic mechanisms to simulate the laminar flame speed of gasoline and gasoline surrogates at more diluted conditions than air, and (iii) provide insights to fluid dynamic research for the development of engines functioning at high EGR ratios. A multi-scale approach is adopted for the present kinetic modeling study: from the investigation of ab initio electronic structure and reaction kinetic studies (“micro scale”), to the development of kinetic mechanisms and simulation of laminar flame speeds (“macro scale”). Based on the results of the modeling work presented in the above chapters, the main conclusions of the present work are as follows.

At the “micro scale”, the  $\text{CH}_2\text{CO} + \text{OH}$  reaction, identified as one of the potential important reactions for combustion at highly-diluted conditions, is studied theoretically in Chapter 3. The potential energy surface (PES) of the reaction, consisting of 35 stationary points, is obtained using B2PLYP-D3/cc-pVTZ for geometries and a composite method containing CCSD(T)-F12/cc-pVTZ-F12 for energies with chemical accuracy. Based on the PES, temperature- and pressure-dependent rate coefficients and branching ratios at 200–3000 K and 0.01–100 atm for the multi-channel reaction are calculated using RRKM-TST/ME method. The results show that the reaction proceeds via 3 pathways: (i) H abstraction from ketene by OH radical, whose dominant reaction is  $\text{CH}_2\text{CO} + \text{OH} \longrightarrow \text{HCCO} + \text{H}_2\text{O}$ ; (ii) OH addition on the olefinic carbon atom of ketene, whose dominant reaction is  $\text{CH}_2\text{CO} + \text{OH} \longrightarrow \text{CH}_2\text{OH} + \text{CO}$ ; (iii) OH addition on the carbonyl carbon atom of ketene, whose dominant reactions are  $\text{CH}_2\text{CO} + \text{OH} \longrightarrow \text{CH}_3 + \text{CO}_2$  and  $\text{CH}_2\text{CO} + \text{OH} \longrightarrow \text{CH}_2\text{COOH}$ . The olefinic addition pathway dominates the reaction (50%–70%) over the entire range of temperature and pressure investigated. Its rate constant exhibits non-monotonic temperature dependence, due to the submerged nature of its initial transition state. The rest pathways compete for the second dominant place. The carbonyl addition pathway is favored at low temperatures, while the abstraction pathway becomes more dominant at high temperature ( $> 1500$  K). The rate coefficients for the abstraction and olefinic addition pathways are independent of pressure, while that for the carbonyl addition pathway is highly pressure-dependent. The carbonyl addition pathway leads to bimolecular products  $\text{CH}_3 + \text{CO}_2$  at low pressure, but collisionally stabilized  $\text{CH}_2\text{COOH}$  at

high pressure. The  $\text{CH}_2\text{COOH}$  is most likely to be dissociated to products  $\text{CH}_3 + \text{CO}_2$  or back to the reactants at high temperatures. Uncertainty analysis shows that the accuracy in the energy of the initial transition states of the two addition pathways is crucial for the reaction kinetics, especially at low temperatures. The obtained updated rate coefficients are fitted into modified Arrhenius expressions and implemented in the kinetic mechanisms developed in the present work.

At the “macro scale”, important reactions to the laminar flame speed of the TRFE fuel at highly-diluted conditions are firstly identified, using sensitivity analysis with a chosen starting mechanism, in Chapter 4. Results show that sensitive reactions mostly fall into four categories: (i) fundamental reactions in the hydrogen, syngas and methane sub-mechanisms, (ii) reactions involving intermediate  $\text{C}_2$ – $\text{C}_3$  molecules, (iii) reactions involving aromatic radicals, and (iv) alkane fuel decomposition reactions. In addition, radical + diluent molecule (e.g.,  $\text{CO}_2$  and  $\text{H}_2\text{O}$ ) reactions are also considered.

Sub-mechanisms corresponding to the first category investigated in Chapter 5, by studying the dilution effects of  $\text{CO}_2$  and  $\text{H}_2\text{O}$  on the laminar flame speed of hydrogen ( $\text{H}_2$ ), syngas ( $\text{H}_2/\text{CO}$ ) and methane  $\text{CH}_4$ , using mainly false-species methods and sensitivity analysis. The dilution effect is quantified into the thermal and transport effect and the chemical effect, which can be separated into effects of third-body collisions and direct reactions. Results show that the total dilution effect in reducing  $S_L$  is not linear, and becomes weaker at high dilutions. It is mainly contributed by the thermal effect, while the chemical effect further reduces  $S_L$  and increase the non-linearity. The relative dominance within the chemical effect is found to be different depending on both the diluent molecule and the fuel. The chemical effect of  $\text{H}_2\text{O}$  is mainly contributed by third-body collisions while that of  $\text{CO}_2$  is mainly dominated by direct reactions. The chemical effects of  $\text{H}_2\text{O}$  dilution on hydrogen flames are studied. Third-body collision effect of  $\text{H}_2\text{O}$  is found to reduce  $S_L$  mainly through the efficient participation of  $\text{H}_2\text{O}$  in the chain terminating reaction  $\text{H} + \text{O}_2 (+ \text{M}) = \text{HO}_2 (+ \text{M})$ , and it enhances subsequent  $\text{HO}_2$  consuming reactions  $\text{HO}_2 + \text{H} = \text{OH} + \text{OH}$  and  $\text{HO}_2 + \text{OH} = \text{H}_2\text{O} + \text{O}_2$  which affect  $S_L$  in opposite ways, i.e., increases and reduces  $S_L$  respectively. The direct reaction effect of  $\text{H}_2\text{O}$  is found to be mainly contributed by the reaction  $\text{OH} + \text{H}_2 = \text{H} + \text{H}_2\text{O}$ , where high  $\text{H}_2\text{O}$  concentration push the reaction in its reverse direction, leading to less H radical and therefore reduces  $S_L$ . The chemical effects of  $\text{CO}_2$  dilution on syngas and methane flames are studied. The direct reaction effect is found to reduce  $S_L$  mainly through the thermal dissociation of  $\text{CO}_2$ , i.e., the reverse of the major heat release step  $\text{CO} + \text{OH} = \text{CO}_2 + \text{H}$ , which competes for H radicals with the major chain branching reactions  $\text{H} + \text{O}_2 = \text{O} + \text{OH}$ . In syngas flames, flame speed is further reduced by the resulted higher  $\text{H}_2\text{O}$  concentration through thrid-body collision in the  $\text{H} + \text{O}_2 (+ \text{H}_2\text{O}) = \text{HO}_2 (+ \text{H}_2\text{O})$  reaction. In methane flames, the main  $\text{CH}_3$  consumption channel,  $\text{CH}_3 \longrightarrow \text{CH}_2\text{O} \longrightarrow \text{HCO} \longrightarrow \text{CO} \longrightarrow \text{CO}_2$  is degenerated by high  $\text{CO}_2$  concentration. It is partly compensated in lean and stoichiometric mixtures by the enhancement of the  $\text{CH}_2$  and  $\text{CH}_2(\text{S})$  channels which affects  $S_L$  positively through reactions  $\text{CH}_2 + \text{O}_2 = \text{CO} + \text{H} + \text{H}$  and  $\text{CH}_2(\text{S}) + \text{CO}_2 = \text{CH}_2\text{O} + \text{CO}$ , respectively, and in rich mixtures by the enhancement of the alternative  $\text{CH}_3 \longrightarrow \text{CH}_2\text{O}$  channel through  $\text{CH}_2\text{OH}$  where H radicals are produced.

Based on the above-identified key reactions and sub-mechanism, as well as the

chemical effect of H<sub>2</sub>O and CO<sub>2</sub> dilution studied, a detailed mechanism (MACDIL-DTL) and a semi-detailed mechanism (MACDIL-RDC) is established for the combustion of the TRFE fuel at highly-diluted conditions. The MACDIL-RDC mechanism is validated based on the laminar flame speed of TRFE/air/EGR flames, and results show that the mechanism has a good predictive performance on both the absolute values of  $S_L$  and the reducing effect of EGR on  $S_L$ . Considerable improvement in terms of predicted flame speed is observed with respect to the starting mechanism. Insights to the development of correlations for laminar flame speed at highly-diluted conditions are provided based on the non-linear effect of EGR as predicted by the MACDIL-RDC mechanism. A new dilution term with the form

$$f(x_d) = \exp\left(-\frac{\mu(\phi)x_d}{1-x_d}\right), \quad 0 \leq x_d < 1$$

is proposed to describe with the evolution of  $S_L$  with dilution ratio, which fits the predicted trends better with less parameters with respect to the existing dilution terms.

In summary, the present multi-scale modeling work studied theoretically the rate coefficients of the CH<sub>2</sub>CO + OH reaction, identified key reactions to the laminar flame speed of the TRFE fuel at diluted conditions, investigated the effect of CO<sub>2</sub> and H<sub>2</sub>O dilution on laminar flame speeds, developed detailed and semi-detailed kinetic mechanisms validated on the laminar flame speed of the TRFE fuel, and proposed a new dilution term for correlations used for larger-scale flame studies such as CFD simulations. These works fulfill the initial objectives introduced at the beginning, but further studies are still necessary to improve and enrich understanding of the combustion chemistry at diluted conditions.

## 7.2 Future Works

Future works are required and planned for both the general understanding of diluted combustion chemistry and the tasks of the MACDIL project.

At the “micro scale”, the uncertainty of the rate coefficients of the CH<sub>2</sub>CO + OH could be further reduced, by using more advanced methods in the electronic structure and reaction kinetics to treat the very sensitive initial transition states and the remaining the complexity in this reaction, e.g., possible roaming and multireference behaviors. The reaction kinetics of other important reactions at diluted conditions could be studied theoretically. 5 reactions of interest within the topic and scope of the present project, as listed in Chapter 4, are planned for future works. In addition, unknown radical + diluent molecule reactions could be studied theoretically to examine the possibility of the presence of these reactions in combustion events.

At the “macro scale”, the chemical effects of CO<sub>2</sub> and H<sub>2</sub>O dilution is an ambitious research direction. The present work has only studied the effect on the combustion of small molecules. The chemical effects on the sub-mechanisms of larger molecules, such as the other three categories of important reactions identified, should be studied in future works as they are also sensitive to the laminar flame speed, especially at diluted conditions. Other methods besides false-species



methods and sensitivity analysis, such as reaction pathway analysis, could be used in the investigations. More advanced technologies, such as machine learning and neural networks, could be used to assist the post-processing and understanding of the obtained data.

Similar for the mechanism development, the current version of the detailed and semi-detailed mechanisms contains manually reviewed rate coefficients for only the small molecules, while the other sub-mechanisms are adopted from state-of-the-art mechanisms in the literature. The mechanisms could be still improved, by reviewing the rate coefficients of important reactions in these sub-mechanisms. In addition, it is still necessary to validate the current version of the mechanisms comprehensively over wide ranges of experimental data, so that it can be used in predictions safely. The proposed dilution terms could be used in correlation formulas, and a correlation for the laminar flame speed of TRFE/air/EGR mixture is planned for future works.

During the simulations for the TRFE fuel, we observed a possible interesting phenomena of the laminar flame speed that at high initial temperatures and pressures (near the negative temperature coefficient (NTC) range, such as 873 K and 10 bar) the  $S_L$  of rich mixtures may be accelerated by the possible low-temperature chemistry happening in the preheating zone (as shown in Figure 7-1a). Although no experimental measurement is available, both the starting mechanism (LLNL 2011) and our mechanism (MACDIL-RDC) predict this behavior (as shown in Figure 7-1b). Investigations into this possible phenomenon are also planned for future works.

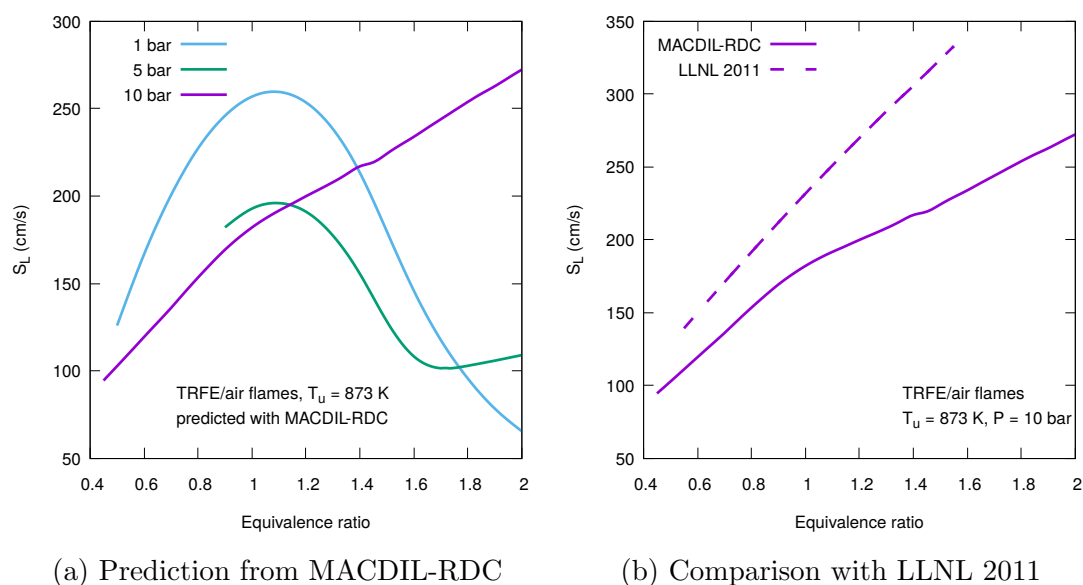


Figure 7-1: Laminar flame speeds of TRFE/air mixtures at initial conditions the near negative temperature (NTC) region. Elevated  $S_L$  of rich mixtures are observed at initial temperature of 873 K and pressure of 10 bar and 5 bar. (a) the  $S_L$  at different pressures predicted with MACDIL-RDC. (b) comparison of the predictions between MACDIL-RDC and LLNL 2011 on the  $S_L$  of TRFE/air mixtures at  $T_u = 873$  K and P = 10 bar.

# Appendix A

## Supporting Information for Chapter 3

### A.1 Electronic Structure

#### A.1.1 Potential Energy Surface

In the paper that this document supports, only the potential energy surface of the dominant pathways are presented. In addition to that, the full  $\text{CH}_2\text{CO} + \text{OH}$  potential energy surface (including insignificant pathways) is presented here in Figure A-1.

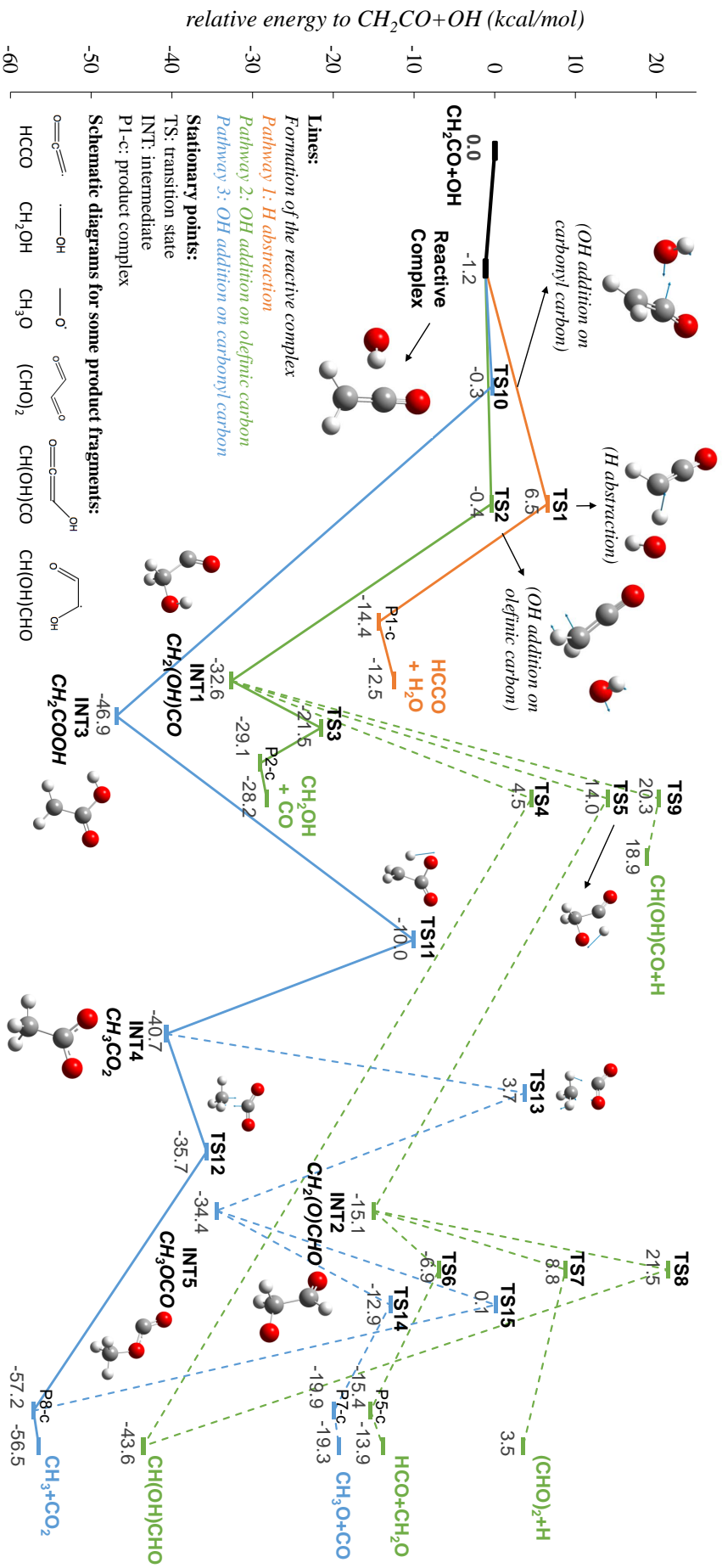
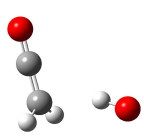


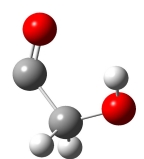
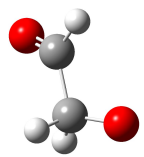
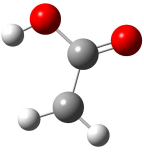
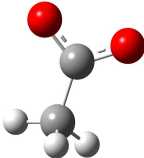
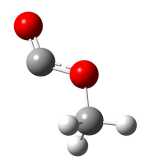
Figure A-1: The  $\text{CH}_2\text{CO}+\text{OH}$  potential energy surface (including ZPE). Total relative electronic energy for all and geometry for some stationary points are demonstrated. Black lines: barrierless formation of the reactive complex (RC); Orange lines: Pathway 1; Green lines: Pathway 2; Blue lines: Pathway 3. Solid lines: most probable product channels; Dashed lines: less probable product channels. Geometries were obtained at B2PLYP-D3/cc-pVTZ level and energies were obtained using CCSD(T)-F12/cc-pVTZ-F12 with extrapolation to basis set limit (See Equation 3.1).

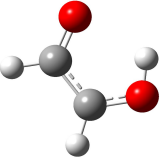
## A.1.2 Optimized Geometries

### Reactive Complex

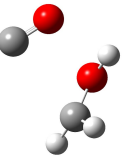
RC		O	-0.139652	-0.352221	1.602905
		C	-0.355822	-0.720100	-0.838676
		H	-1.344882	-0.782615	-1.259500
		O	0.743623	1.443799	-0.901201
		H	-0.103531	1.898648	-1.014425
		H	0.519379	-0.917754	-1.430060

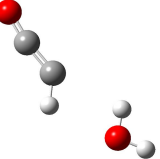
### Unimolecular Wells

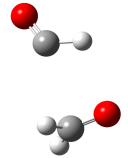
INT1		C	0.005732	-0.026310	-0.012243
		H	-0.012952	0.000340	1.074722
		H	1.051034	0.076896	-0.325571
		C	-0.689437	1.222537	-0.528327
		O	-1.513573	1.268460	-1.377429
		H	-0.579412	-1.234162	-0.432160
INT2		C	-0.006134	0.750933	0.016857
		C	-0.142265	-0.769603	-0.025258
		O	-0.776251	1.492582	-0.533527
		O	1.047285	-1.415937	0.068101
		H	0.862767	1.107283	0.598653
		H	-0.773025	-1.088261	-0.862776
INT3		C	-0.085776	0.121754	-0.031099
		C	-0.404375	0.013925	1.382519
		O	1.188245	-0.193222	-0.400935
		O	-0.886244	0.470415	-0.866163
		H	-1.406516	0.259611	1.688169
		H	0.315587	-0.298242	2.123445
INT4		C	0.028740	-0.004155	-0.037104
		C	-0.139865	-0.007286	1.440735
		O	1.117370	0.224901	-0.625607
		O	-0.903347	-0.210935	-0.857083
		H	-0.393712	0.999970	1.767948
		H	-0.947163	-0.679054	1.720685
INT5		C	-1.570090	-0.846185	0.000000
		C	0.280040	0.596487	0.000000
		O	-0.138122	-0.669073	0.000000
		O	1.400612	0.980330	0.000000
		H	-1.727617	-1.917971	0.000000
		H	-2.005096	-0.403217	0.891113
		H	-2.005096	-0.403217	-0.891113

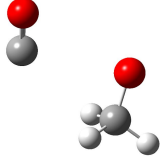
<b>P6</b>		C	-0.549785	0.715819	-0.115843
		C	-0.627144	-0.701822	-0.108456
		O	0.500758	-1.374268	0.075397
		O	0.549128	1.266306	0.046819
		H	-1.472692	1.286178	-0.266564
		H	-1.518851	-1.291780	-0.238489
		H	1.183122	-0.676526	0.171531

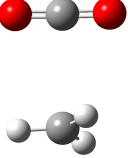
### Product Complexes

<b>P1-c</b>		C	-0.756274	-1.238321	0.829413
		O	-1.300213	-2.167006	1.306215
		C	-0.165141	-0.142799	0.495851
		H	0.246606	0.326482	-0.378984
		O	1.092067	1.407354	-1.995154
		H	0.550176	1.600147	-2.763936
		H	1.438818	2.259601	-1.720134

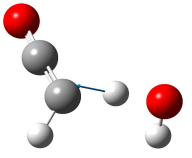
<b>P2-c</b>		C	-1.931900	0.006431	-0.218218
		O	-1.354081	0.128565	1.011716
		O	1.592156	0.176525	-0.115823
		C	2.548525	0.119495	-0.719727
		H	-1.366218	0.303064	-1.088972
		H	-3.005287	0.081270	-0.201822
		H	-0.399830	0.146557	0.904310

<b>P5-c</b>		C	-0.416430	1.657618	0.193735
		C	0.024604	-1.725673	-0.075099
		O	-0.537749	2.828355	0.276179
		O	1.037737	-1.154226	-0.396624
		H	0.506384	1.122285	-0.136651
		H	-0.048614	-2.824522	-0.089473
		H	-0.873086	-1.174949	0.247383

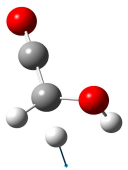
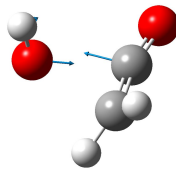
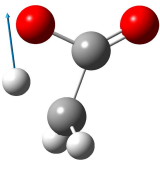
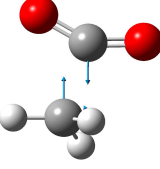
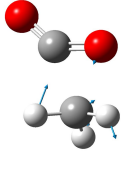
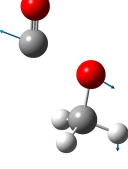
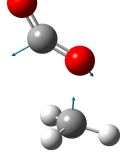
<b>P7-c</b>		C	-1.836683	-1.027716	0.131596
		C	0.735432	1.205494	-0.578798
		O	-0.665683	-1.164378	0.824837
		O	1.794600	1.166301	-0.183260
		H	-1.773766	-1.763855	-0.687721
		H	-2.716357	-1.294702	0.725245
		H	-1.944122	-0.044978	-0.336298

<b>P8-c</b>		C	-0.197338	0.014965	-2.297175
		C	0.095582	-0.022357	0.992670
		O	1.240868	0.165853	0.899432
		O	-1.048374	-0.211901	1.098694
		H	0.810804	-0.360835	-2.311998
		H	-1.023523	-0.658667	-2.150782
		H	-0.381883	1.062041	-2.462748

### Transition States

<b>TS1</b>		C	0.061337	-0.015252	-0.011606
		O	0.146312	-0.077760	1.143531
		C	0.074021	0.013424	-1.328375
		H	-0.775311	-0.273556	-1.923390
		O	1.113421	2.075912	-1.837098
		H	0.271258	2.478812	-2.092117
		H	0.865955	0.795246	-1.783837

TS2		C	-0.285403	0.890986	0.031685
		H	-0.647456	1.306045	-0.892641
		H	-0.567468	1.344845	0.966532
		C	0.837112	0.181241	-0.005800
		O	1.764927	-0.512176	-0.032064
		O	-1.808921	-0.566776	-0.141665
		H	-1.608835	-1.042901	0.676216
TS3		C	-0.918334	0.641380	0.096448
		O	-1.374474	-0.616114	-0.152267
		O	1.611674	-0.458116	-0.002357
		C	1.207377	0.615791	-0.097932
		H	-0.953869	0.999304	1.119151
		H	-1.190790	1.337303	-0.681039
		H	-1.139602	-1.194941	0.579136
TS4		C	-0.777238	0.486718	-0.085619
		C	0.618984	0.566133	-0.071152
		O	1.443222	-0.497905	0.030498
		O	-1.547556	-0.455808	-0.012210
		H	-0.274910	1.117381	0.950138
		H	1.116839	1.504067	-0.251503
		H	0.898003	-1.296858	0.033881
TS5		C	-1.198178	1.697537	0.000000
		C	-1.294132	0.226329	0.000000
		O	-1.842415	2.689854	0.000000
		O	0.152720	0.136979	0.000000
		H	0.082675	1.553962	0.000000
		H	-1.756456	-0.191671	-0.895586
		H	-1.756456	-0.191671	0.895586
TS6		C	-1.074836	1.946651	-0.000505
		C	-1.116828	-0.095370	0.008564
		O	-1.813839	2.614898	-0.618357
		O	0.078226	-0.411814	0.027871
		H	-0.171550	2.235120	0.566936
		H	-1.715032	-0.148484	-0.914968
		H	-1.721225	-0.089069	0.934797
TS7		C	0.025335	0.738128	0.036646
		C	-0.056019	-0.748521	0.387306
		O	-0.931990	1.462915	0.134591
		O	0.948455	-1.395708	0.600452
		H	1.033826	1.084040	-0.244936
		H	-0.426373	-0.989481	-1.378235
		H	-1.072089	-1.106162	0.627166
TS8		C	-1.235962	1.934741	-0.009303
		C	-1.145407	0.459336	0.033075
		O	-2.025873	2.369303	0.851719
		O	-0.119508	-0.231912	0.000567
		H	-0.713353	2.608363	-0.686050
		H	-2.060931	0.952751	1.228912
		H	-2.158193	0.037555	-0.171096

TS9		C	-2.455379	2.026789	-0.007308
		C	-2.415683	0.697092	0.023100
		O	-2.552975	3.184379	-0.023296
		O	-1.966757	0.005168	-1.093886
		H	-4.434295	0.289051	-0.296621
		H	-2.443677	0.218207	0.990636
		H	-2.735474	-0.415992	-1.494604
TS10		C	-0.180684	-0.348976	0.370354
		O	-0.141048	-0.144687	1.506681
		C	-0.370537	-0.756526	-0.888929
		H	-1.381946	-0.922146	-1.221952
		O	0.733925	1.287642	-0.741508
		H	-0.039464	1.854713	-0.870812
		H	0.471554	-0.921093	-1.533239
TS11		C	0.039759	0.000000	0.016584
		C	0.088289	0.000000	1.507357
		O	1.387529	0.000000	-0.143863
		O	-0.800930	0.000000	-0.830991
		H	-0.131557	0.925671	2.022722
		H	-0.131557	-0.925671	2.022722
		H	1.385789	0.000000	1.145606
TS12		C	-0.078509	0.002291	0.026636
		C	0.151334	-0.014335	1.644602
		O	1.103044	-0.582223	2.103894
		O	-0.843637	0.649076	2.036174
		H	0.834155	0.463619	-0.336068
		H	-0.130373	-1.054316	-0.214658
		H	-0.959437	0.535890	-0.300428
TS13		C	-0.007412	0.006992	-0.082919
		C	-0.032227	0.066211	1.946929
		O	1.096978	0.220637	1.355849
		O	-0.479881	0.031768	3.040977
		H	-0.720677	0.812403	-0.171781
		H	-0.446506	-0.978612	-0.116222
		H	0.846677	0.117388	-0.739030
TS14		C	-2.478528	-0.371561	0.000000
		C	-0.379964	1.459542	0.000000
		O	-1.084239	-0.353582	0.000000
		O	0.746428	1.615118	0.000000
		H	-2.737266	-1.436509	0.000000
		H	-2.908314	0.077946	0.896174
		H	-2.908314	0.077946	-0.896174
TS15		C	-2.250432	-0.224717	0.026742
		C	0.141237	0.841519	-0.137082
		O	-0.464960	0.007027	0.518021
		O	1.171464	1.411799	-0.328339
		H	-2.626397	0.771642	0.196291
		H	-2.128243	-0.529910	-1.000272
		H	-2.563037	-0.985967	0.724637

### A.1.3 Electronic Energies and T1 diagnostics

The total electronic energy (relative to the reactants CH<sub>2</sub>CO + OH), as well as its composition of each stationary points on the potential energy surface are listed in Table A.1 for local minima and in Table A.2 for transition states. T1 diagnostics are performed for all the stationary points using CCSD(T)-F12/cc-PVTZ-F12 calculations. We found the value for TS15 is high (> 0.04) which implies existence of multireference behaviour. However, it can be neglected because TS15 is unlikely to impact significantly on the overall kinetics. The imaginary frequency of transition states are also included in Table A.2.

#	Species	T1 <sup>a</sup>	Energy relative to CH <sub>2</sub> CO + OH (kcal mol <sup>-1</sup> )				
			Total	CCSD(T)-F12/cc-PVTZ-F12	M2-F12/cc-PVQZ-F12	M2-F12/cc-PVTZ-F12	ZPE <sup>b</sup>
r	CH <sub>2</sub> CO + OH	0.017 0.010	<b>0.0</b>	0.0	0.0	0.0	0.0
rc	CH <sub>2</sub> CO ~ OH	0.023	<b>-1.2</b>	-2.9	-1.1	-1.2	1.7
INT1	CH <sub>2</sub> (OH)CO	0.018	<b>-32.6</b>	-38.1	-41.1	-41.2	5.5
INT2	CH <sub>2</sub> (O)CHO	0.023	<b>-15.1</b>	-19.2	-15.3	-15.4	4.2
INT3	CH <sub>2</sub> COOH	0.021	<b>-46.9</b>	-51.8	-52.0	-52.0	4.9
INT4	CH <sub>3</sub> CO <sub>2</sub>	0.023	<b>-40.9</b>	-45.5	-45.3	-45.4	4.5
INT5	CH <sub>3</sub> OCO	0.020	<b>-34.4</b>	-40.1	-42.9	-42.9	5.6
P1-c	H <sub>2</sub> O ~ HCCO	0.020	<b>-14.4</b>	-15.8	-17.0	-16.9	1.5
P2-c	CO ~ CH <sub>2</sub> OH	0.017	<b>-29.1</b>	-31.1	-31.8	-31.8	2.0
P5-c	HCO ~ CH <sub>2</sub> O	0.019	<b>-15.4</b>	-16.3	-18.5	-18.5	0.9
P7-c	CO ~ CH <sub>3</sub> O	0.019	<b>-19.9</b>	-21.6	-16.8	-16.9	1.6
P8-c	CO <sub>2</sub> ~ CH <sub>3</sub>	0.016	<b>-57.2</b>	-58.5	-64.2	-64.2	1.3
P1	H <sub>2</sub> O + HCCO	0.010 0.024	<b>-12.5</b>	-12.6	-13.8	-13.8	0.1
P2	CO + CH <sub>2</sub> OH	0.018 0.016	<b>-28.2</b>	-29.7	-30.6	-30.6	1.5
P3	H + CH(OH)CO	0.016	<b>18.9</b>	20.6	13.4	13.4	-1.7
P4	H + (HCO) <sub>2</sub>	0.016	<b>3.5</b>	5.4	-0.5	-0.5	-2.0
P5	HCO + CH <sub>2</sub> O	0.021 0.016	<b>-13.9</b>	-13.6	-15.8	-15.8	-0.3
P6	CH(OH)CHO	0.028	<b>-43.6</b>	-49.7	-46.3	-46.3	6.2
P7	CO + CH <sub>3</sub> O	0.018 0.018	<b>-19.3</b>	-20.4	-15.6	-15.7	1.0
P8	CO <sub>2</sub> + CH <sub>3</sub>	0.018 0.009	<b>-56.5</b>	-57.4	-63.2	-63.2	0.9

<sup>a</sup>obtained using CCSD(T)-F12/cc-PVTZ-F12 calculations.

<sup>b</sup>obtained using B2PLYPD3/cc-pVTZ calculations.

Table A.1: Total relative energy of the local minima on the CH<sub>2</sub>CO + OH potential energy surface and their composition in energy. + : the two fragments are at infinite separation; ~ : the two fragments form a Van der Waals complex.

### A.1.4 Vibrational Frequencies

Table A.3 presents the vibrational frequencies for the stationary points, which are obtained at B2PLYPD3/cc-pVTZ level. The underlined frequencies were replaced by corresponding hindered rotor potential profiles in the RRKM/ME calculations. The values in bold and italic complex numbers (e.g., ***1561.9i***) are the imaginary frequencies for transition states.



#	Reaction	$v_i$ (cm <sup>-1</sup> ) <sup>a</sup>	T1 <sup>a</sup>	Energy relative to ketene + OH (kcal mol <sup>-1</sup> )				
				Total	CCSD(T)-F12/cc-PVTZ-F12	M2-F12/cc-PVQZ-F12	M2-F12/cc-PVTZ-F12	ZPE <sup>b</sup>
TS1	RC → P1-c	1,561.9	0.031	<b>6.5</b>	7.0	10.0	10.0	-0.5
TS2	RC → INT1	169.2	0.029	<b>-0.4</b>	-2.6	1.6	1.6	2.2
TS3	INT1 → P2-c	327.2	0.020	<b>-21.5</b>	-24.9	-24.5	-24.5	3.3
TS4	INT1 → P6	1,398.5	0.023	<b>4.5</b>	1.5	-0.6	-0.6	3.0
TS5	INT1 → INT2	2,020.8	0.033	<b>14.0</b>	11.9	19.0	18.9	2.0
TS6	INT2 → P5-c	314.1	0.032	<b>-6.9</b>	-9.0	-2.7	-2.5	2.2
TS7	INT2 → P4	913.0	0.034	<b>8.8</b>	9.7	16.0	15.9	-1.0
TS8	INT2 → P6	1,584.1	0.033	<b>21.5</b>	21.5	24.8	24.7	-0.1
TS9	INT1 → P3	241.7	0.019	<b>20.3</b>	21.1	16.1	16.1	-0.7
TS10	RC → INT3	259.8	0.030	<b>-0.3</b>	-2.3	1.6	1.5	2.0
TS11	INT3 → INT4	2,044.4	0.025	<b>-10.0</b>	-12.0	-10.0	-10.0	1.9
TS12	INT4 → P8-c	641.1	0.035	<b>-35.7</b>	-39.5	-34.0	-34.1	3.8
TS13	INT4 → INT5	1,070.8	0.032	<b>3.7</b>	0.2	2.8	2.8	3.5
TS14	INT5 → P7-c	386.8	0.023	<b>-12.9</b>	-16.1	-9.8	-9.8	3.1
TS15	INT5 → P8-c	2,304.3	0.043	<b>0.1</b>	-2.6	-2.1	-2.1	2.7

<sup>a</sup>obtained using CCSD(T)-F12/cc-PVTZ-F12 calculations.

<sup>b</sup>obtained using B2PLTYP-D3/cc-PVTZ calculations.

Table A.2: Total relative energy of the transition states on the CH<sub>2</sub>CO + OH potential energy surface and their composition in energy. + : the two fragments are at infinite separation; ~ : the two fragments form a Van der Waals complex.

Molecule	Frequencies (1/cm)														
RC	72.6	145.2	164.2	269.3	438.3	517.0	542.3	608.3	999.3	1151.6	1416.3	2197.0	3210.0	3315.8	3775.1
INT1	<u>187.5</u>	217.6	284.0	688.6	808.6	896.4	1073.1	1229.3	1326.4	1406.1	1482.8	1890.6	3018.4	3128.2	3822.2
INT2	<u>111.3</u>	341.0	510.3	662.4	955.7	1008.1	1110.7	1132.8	1255.1	1368.8	1400.4	1798.0	2896.4	2945.1	3029.1
INT3	<u>219.2</u>	443.6	<u>445.2</u>	603.0	604.9	751.9	903.2	993.5	1210.6	1328.7	1485.2	1770.9	3179.9	3305.3	3831.9
INT4	<u>35.1</u>	411.8	571.7	665.6	909.2	1004.9	1263.6	1400.2	1469.8	1482.8	1596.1	3072.0	3147.8	3165.8	14969.7
INT5	<u>57.0</u>	<u>216.8</u>	319.8	620.1	999.0	1127.5	1183.5	1230.5	1485.0	1510.3	1516.3	1856.8	3080.2	3164.2	3192.2
P1-c	<u>29.2</u>	53.2	132.0	135.9	193.0	319.5	535.4	556.7	642.3	1252.3	1648.2	2104.8	3279.0	3824.6	3931.7
P2-c	26.5	33.1	61.5	101.6	<u>121.1</u>	<u>469.8</u>	593.6	1074.2	1215.2	1386.3	1500.3	2152.4	3152.2	3295.4	3858.6
P5-c	52.7	78.6	105.3	141.0	153.6	203.9	1127.6	1215.6	1278.4	1542.0	1782.9	1891.4	2747.2	2938.4	3010.5
P6	278.5	423.9	<u>653.7</u>	810.4	820.4	949.3	1021.6	1212.2	1348.1	1418.2	1544.8	1617.1	3040.5	3257.4	3535.4
P7-c	<u>34.4</u>	57.6	58.2	89.3	119.9	803.3	965.3	1115.5	1386.5	1393.5	1526.4	2161.8	2937.6	3019.2	3068.3
P8-c	<u>7.5</u>	57.6	58.2	89.3	119.9	803.3	965.3	1115.5	1386.5	1393.5	1526.4	2161.8	2937.6	3019.2	3068.3
TS1	<i>1561.9i</i>	98.1	<u>177.0</u>	334.5	477.5	507.7	561.0	818.3	960.2	1151.6	1316.5	1622.8	2170.5	3268.4	3782.6
TS2	<i>169.2i</i>	96.4	<u>170.7</u>	427.2	459.4	489.7	711.8	760.4	1007.3	1132.3	1408.5	2190.2	3205.0	3303.0	3773.6
TS3	<i>327.2i</i>	<u>85.5</u>	146.5	<u>362.9</u>	388.1	628.2	974.4	1096.8	1192.6	1386.8	1504.7	1984.3	3115.8	3257.9	3830.1
TS4	<i>1398.5i</i>	200.2	<u>513.5</u>	596.6	721.0	797.0	1028.4	1209.3	1214.7	1332.9	1464.0	1748.8	1892.0	3260.4	3758.2
TS5	<i>2020.8i</i>	165.4	489.3	638.4	684.6	975.9	1008.2	1079.8	1134.2	1296.4	1489.5	1907.9	2005.8	3046.6	3098.0
TS6	<i>314.1i</i>	<u>30.9</u>	233.1	331.2	594.1	757.0	1108.1	1136.9	1241.2	1472.2	1623.8	1899.2	2886.0	2905.0	2961.0
TS7	<i>913.0i</i>	<u>151.3</u>	287.8	335.7	435.4	556.5	875.2	1055.8	1076.1	1336.5	1380.5	1748.2	1782.6	2955.5	2974.1
TS8	<i>1584.1i</i>	208.7	356.0	553.0	666.9	807.3	898.6	1046.8	1183.6	1302.5	1342.7	1578.5	1670.5	2822.3	3140.3
TS9	<i>241.7i</i>	215.6	234.8	343.1	360.0	529.8	647.9	698.5	1036.1	1174.2	1292.2	1417.8	2175.3	3202.1	3775.0
TS10	<i>259.8i</i>	<u>203.4</u>	260.1	318.3	436.5	486.1	603.0	676.6	997.9	1124.6	1416.3	2167.4	3206.9	3325.4	3776.6
TS11	<i>2044.4i</i>	406.1	513.6	543.8	634.9	931.4	993.5	1042.2	1108.2	1153.0	1408.6	1800.2	2007.9	3140.4	3251.1
TS12	<i>641.1i</i>	<u>115.8</u>	389.4	557.8	611.2	957.6	977.1	1067.5	1327.9	1438.3	1486.6	1810.6	3087.5	3201.1	3225.7
TS13	<i>1070.8i</i>	<u>42.1</u>	389.4	557.8	611.2	957.6	977.1	1067.5	1327.9	1438.3	1486.6	1810.6	3087.5	3201.1	3225.7
TS14	<i>386.8i</i>	<u>95.4</u>	<u>166.2</u>	207.5	321.7	1003.9	1135.7	1168.6	1431.4	1440.7	1527.5	2097.5	3004.2	3070.1	3100.4
TS15	<i>2304.3i</i>	<u>34.0</u>	241.6	369.6	649.9	772.6	805.6	919.1	1131.7	1445.1	1450.9	1989.9	3111.2	3283.5	3286.4

\* Underlined: replaced by 1D hindered rotor potentials. Bold and italic complex numbers: imaginary frequencies.

Table A.3: List of Frequencies for the stationary points.

## A.1.5 Hindered Rotor Potentials

In the present paper, the torsional modes were treated as 1D hindered rotors, whose potential profiles were scanned by increments of 30°. These values are obtained at B2PLYPD3/cc-pVTZ level and presented in Table A.4.

Molecule	Frequency replaced (1/cm)	Hindered rotor potentials (kcal/mol)											
INT1	187.5	0.0000	0.4906	1.8862	2.9685	2.9978	2.9196	3.0777	2.4460	0.9860	0.0709	0.1011	0.1823
INT2	111.3	0.0000	0.1246	0.0140	1.3107	4.5967	4.4104	3.0327	2.2203	3.0985	5.2352	4.4942	1.2136
INT3	219.2	0.0013	1.4165	4.7173	6.1684	3.5620	0.9526	0.0000	0.9561	3.5623	6.1649	4.7218	1.4146
	445.2	5.8466	7.0809	9.8812	11.0522	7.8856	2.5559	0.0000	2.5620	7.8863	11.0554	9.8762	7.0782
INT4	35.1	0.0082	0.0214	0.0000	0.0301	0.0120	0.0286	0.0030	0.0286	0.0115	0.0167	0.0073	0.0221
INT5	57.0	0.0000	0.0904	0.1659	0.1030	0.0005	0.0903	0.1646	0.0934	0.0010	0.0846	0.1627	0.0913
	216.8	0.4208	2.2699	6.3239	8.5932	6.5263	2.2057	0.0000	2.2074	6.5294	8.5956	6.3253	2.2698
P1-c	29.2	0.0084	0.0382	0.0650	0.0426	0.0087	0.0153	0.0681	0.1419	0.1635	0.1018	0.0314	0.0011
P2-c	121.1	0.0000	0.1766	0.3705	0.4526	0.4578	0.4158	0.3988	0.4348	0.4866	0.4591	0.3676	0.1479
	469.8	0.0000	1.0357	3.3023	3.4718	1.0261	0.0002	0.2214	0.1696	1.9667	4.0990	2.3381	0.3989
P6	653.7	0.0000	2.8140	8.6264	12.6622	11.6227	8.6691	7.3533	8.6687	11.6238	12.6554	8.6240	2.8124
P7-c	34.4	0.0000	0.1009	0.1932	0.2009	0.0980	0.0029	0.0037	0.0938	0.1967	0.2176	0.1187	0.0159
P8-c	7.5	0.0000	0.0063	0.0004	0.0035	0.0021	0.0038	0.0010	0.0049	0.0001	0.0051	0.0008	0.0038
TS1	177.0	0.0877	0.0030	0.2195	0.6962	1.4797	2.3579	0.0000	0.0835	0.5342	1.3532	2.1723	0.5227
TS2	170.7	0.3818	1.4182	2.4219	3.0240	3.1653	2.9472	2.2750	1.2397	0.2444	0.0411	0.1294	0.0048
TS3	85.5	0.0000	0.7301	1.4028	0.9521	0.5068	0.3154	0.3170	0.4913	0.7964	1.1774	1.3685	0.6917
	362.9	0.0102	1.1590	3.4607	5.4306	5.6708	4.0018	1.6290	0.1145	0.4522	2.3076	2.6531	0.7994
TS4	513.5	0.0000	1.8852	6.1357	8.9981	8.5102	5.9991	4.2233	4.9457	7.4216	8.4218	6.0563	2.1172
TS6	30.9	0.0441	0.0043	0.0072	0.1204	0.6617	1.9511	2.5246	2.2476	2.3697	2.4515	1.3494	0.3301
TS7	151.3	0.0000	1.7499	5.0721	6.8152	5.4755	4.2727	4.6214	5.7061	6.3336	5.6551	3.4393	0.8384
TS10	203.4	0.0000	0.5381	2.0827	3.9787	2.9839	1.2333	0.1306	0.1236	0.2146	0.1989	0.1965	0.2256
TS12	115.8	0.0067	0.3415	0.6915	0.4034	0.0018	0.3340	0.6956	0.3931	0.0000	0.2938	0.7009	0.3609
TS13	42.1	0.0000	0.4499	1.2693	0.2755	0.0090	0.6056	1.1894	0.1663	0.0360	0.6792	1.2575	0.3602
TS14	95.4	0.0000	0.6529	2.2002	3.7227	4.7071	5.2460	5.4109	5.2444	4.7032	3.7227	2.1930	0.6489
	166.2	0.0000	0.6677	1.4489	0.6536	0.0022	0.7660	1.4485	0.7684	0.0015	0.6516	1.4461	0.6732
TS15	34.0	0.0000	0.0250	0.0395	0.0245	0.0011	0.0260	0.0404	0.0266	0.0025	0.0272	0.0423	0.0274

Table A.4: 1D hindered rotor potential profiles scanned by increments of 30° at B2PLYPD3/cc-pVTZ level for the stationary points.

## A.1.6 ROHF Treatment

The spin contamination for TS6 and TS7 was found abnormal (0.15 and 0.20 respectively, which should normally lower than 0.1) for single point calculations with unrestricted Hartree Fock (UHF) reference wave functions for both CCSD(T)-F12 and MP2-F12. To eliminate the spin contamination, restricted open shell (ROHF) orbitals was thus adopted as base for the calculations on the two transition state structures and also on the wells they connect to eliminate errors. For MP2 calculations, ROHF was used for self-consistent field (SCF) calculations and the resulted orbitals were adopted in MP2 calculations directly. For coupled cluster CCSD(T) calculations, difficulty increased due to the limitation that ROHF orbitals were not integrated in CCSD(T) in the ORCA software. Alternatively, ROHF orbitals were transformed into unrestricted spin orbitals (UHF) which is compatible with CCSD(T), for molecules with unpaired electrons. While restricted spin orbitals (RHF) was used for molecules with no unpaired electron. For H atom which is produced from the dissociation of CH<sub>2</sub>(O)CHO via TS7, the Post Hartree Fock energies were taken from Computational Chemistry Comparison and Benchmark DataBase (CCCBDB) [452]. The corresponding method/basis are CCSD(T)/cc-pVTZ, MP2/cc-PVQZ and MP2/cc-pVTZ, respectively. The energy obtained

were integrated in the potential energy surface by equation A.1 with CH<sub>2</sub>(O)CHO (INT2) chosen as reference.

$$\Delta E = \Delta E_{\text{UHF,CH}_2(\text{O})\text{CHO}} + (\Delta E_{\text{ROHF}} - \Delta E_{\text{ROHF,CH}_2(\text{O})\text{CHO}}) \quad (\text{A.1})$$

The obtained energies relative to CH<sub>2</sub>(O)CHO (INT02) and the barrier heights corresponding to TS06 and TS07 were shown in Table A.5, and compared with the values obtained with UHF reference wave functions on the PES in Figure A-2. The calculations with ROHF reference predicted slightly lower values for forward barriers and slightly higher values for reverse barriers. The differences are less than 0.7 kcal mol<sup>-1</sup> in the relative energies and less than 0.4 kcal mol<sup>-1</sup> in barrier heights. Even though the difference in energy is negligible, the implementation of ROHF is still necessary to assure reasonable electronic structures.

		Total (UHF)	Total (ROHF)	$\Delta E_{\text{ROHF-UHF}}$	ROHF-CCSD(T) /cc-PVTZ	ROHF-MP2 /cc-PVQZ	ROHF-MP2 /cc-PVTZ	ZPE <sup>a</sup>
<i>Species</i>								
INT2	CH <sub>2</sub> (O)CHO	<b>0.00</b>	<b>0.00</b>	<b>0.00</b>	0.00	0.00	0.00	0.00
TS6	H <sub>2</sub> (O)C-CHO	<b>8.17</b>	<b>7.81</b>	<b>-0.36</b>	10.53	2.49	3.28	-1.92
TS7	H-CHOCHO	<b>23.84</b>	<b>23.74</b>	<b>-0.10</b>	29.36	21.60	22.11	-5.11
P4	H <sup>b</sup> + (HCO) <sub>2</sub> <sup>c</sup>	<b>18.56</b>	<b>18.33</b>	<b>-0.23</b>	24.47	15.37	15.41	-6.11
P5-c	CH <sub>2</sub> O <sup>c</sup> ~ CHO	<b>-0.34</b>	<b>-0.97</b>	<b>-0.63</b>	2.10	-3.90	-4.06	-3.23
P5	CH <sub>2</sub> O <sup>c</sup> + CHO	<b>1.19</b>	<b>0.60</b>	<b>-0.59</b>	5.16	-1.04	-0.89	-4.41
<i>Barriers</i>								
	INT2 → TS6	<b>8.17</b>	<b>7.81</b>	<b>-0.36</b>	10.53	2.49	3.28	-1.92
	P5-c → TS6	<b>8.51</b>	<b>8.77</b>	<b>0.26</b>	8.42	6.39	7.34	1.30
	INT2 → TS7	<b>23.84</b>	<b>23.74</b>	<b>-0.10</b>	29.36	21.60	22.11	-5.11
	P4 → TS7	<b>5.28</b>	<b>5.41</b>	<b>0.13</b>	4.89	6.23	6.70	1.00

<sup>a</sup> Zero-point energies (ZPE) were obtained by B2PLYP-D3/cc-PVTZ.

<sup>b</sup> Post Hartree Fock energies for H atom were taken from Computational Chemistry Comparison and Benchmark DataBase (CCCBDB). Corresponding method/basis are CCSD(T)/cc-PVTZ, MP2/cc-PVQZ and MP2/cc-PVTZ, respectively.

<sup>c</sup> Post Hartree Fock energies for molecules with no unpaired electron was obtained by RHF reference wavefunction. The corresponding method/basis are RHF-CCSD(T)/cc-PVTZ, RHF-MP2/cc-PVQZ and RHF-MP2/cc-PVTZ, respectively.

Table A.5: Energies relative to CH<sub>2</sub>(O)CHO (INT02) and barrier heights (kcal mol<sup>-1</sup>) obtained by calculations with restricted open shell (ROHF) reference wave functions for channel CH<sub>2</sub>(O)CHO → CH<sub>2</sub>O + CHO and CH<sub>2</sub>(O)CHO → H + (HCO)<sub>2</sub>, compared with values obtained with unrestricted (UHF) reference wave functions. (+ : means the two fragments are at infinite separation; ~ : means the two fragments form a Van der Waals complex.)

## A.2 RRKM/ME

### A.2.1 Long-range TST Treatments

In the present work, barrierless steps (i.e., the capture of the bimolecular reactants and the dissociation into bimolecular products in this system) were treated according to long-range transition state theory [282] (long-range TST). The long-range interaction between the two fragments are mostly treated as dipole-dipole interaction, since the dispersion interaction were comparatively small and can be neglected. The exception is the interaction between CH<sub>3</sub> and CO<sub>2</sub>, the dipole moments of which are both zero, as they are treated as dispersion interaction. The

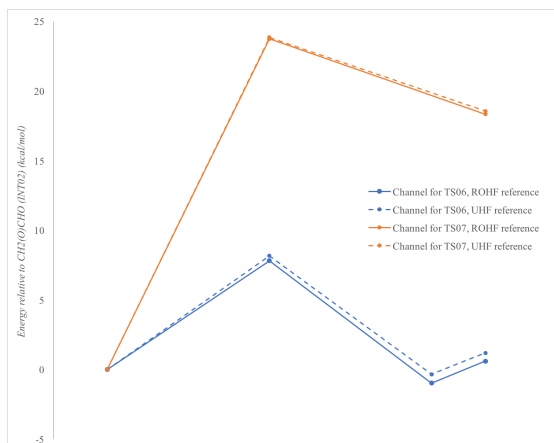


Figure A-2: Comparison between restricted open shell (ROHF) and unrestricted (UHF) reference wave functions on the potential energy surface of the channel  $\text{CH}_2(\text{O})\text{CHO} \longrightarrow \text{CH}_2\text{O} + \text{CHO}$  and  $\text{CH}_2(\text{O})\text{CHO} \longrightarrow \text{H} + (\text{HCO})_2$ .

long-range TST approximates the interaction potential with a power-law dependence on the distance between the fragments,

$$V(R) = -\frac{V_0}{R^n} \quad (\text{A.2})$$

where  $R$  is the distance,,  $V_0$  is the strength of interaction or the potential pre-factor, and  $n$  is the potential power exponent. For dipole-dipole interactions,  $n = 3$  and  $V_0 = d_1 d_2$ , where  $d_i$  are the dipole moments of the fragments. For dispersion interactions,  $n = 6$  and  $V_0$  could be replaced by the dispersion coefficient  $C_6$  which is approximated as  $1.5\alpha_1\alpha_2E_1E_2/(E_1 + E_2)$ , where  $\alpha_i$  are the polarizabilities and  $E_i$  are the ionization energies of the fragments. Then the rate constants could be calculated as

$$k = C_1\mu^{-1/2}V_0^{2/n}T^{1/2-2/n} \quad (\text{A.3})$$

where  $\mu$  is the reduced mass of the system and  $C_1$  is a the dimensionless proportionality constant at  $\mu J$ -VTST level which depends only on the type of interaction and the total degrees of freedom of the system. The values of the parameters  $C_1$ ,  $n$  and  $V_0$  for different bimolecular systems are presented in Table A.6.

Table A.6: Parameters used in long-range TST calculations.

fragments	interaction type	shape <sup>1</sup>	$C_1$	$n$	$V_0$ (a.u.)
$\text{CH}_2\text{CO} + \text{OH}$	dipole-dipole	$N$ - $L$	5.36	3	0.42
$\text{HCCO} + \text{H}_2\text{O}$	dipole-dipole	$N$ - $N$	5.42	3	0.54
$\text{CH}_2\text{OH} + \text{CO}$	dipole-dipole	$N$ - $L$	5.36	3	0.01
$\text{CH}_2\text{O} + \text{HCO}$	dipole-dipole	$N$ - $N$	5.42	3	0.72
$\text{CH}_3\text{O} + \text{CO}$	dipole-dipole	$N$ - $L$	5.36	3	0.02
$\text{CH}_3 + \text{CO}_2$	dispersion	$N$ - $L$	8.55	6	86.81

<sup>1</sup>  $L$  refers to “linear” and  $N$  refers to “non-linear”.

## A.2.2 Entrance Channels

In the present work, the entrance channels are expected to have significant effects on the overall kinetics, especially at low temperature. All the three pathways proceed via the reactive complex which is a very shallow well. This barrierless step was treated using long-range TST and can be considered as the outer TS of this system. The inner TS for H abstraction lies higher than the reactants while those for OH addition pathways are submerged. They were all treated using conventional TST. Master equation was used to link all the microscopic reactions and collisional energy transfers with a matrix and to derive phenomenological rate coefficients by solving its eigenvalues. Thus the outer and inner TS are considered as separate transition states whose number of states are calculated individually and associated by the Master Equation without approximation such as the Two-Transition State method (2TS method).

However, we did tested 2TS method and compared the resulted rate coefficients. In this method, the effective number of states ( $N_{\text{eff}}$ ) can be calculated either statistically

$$\text{Statistical} \quad 1/N_{\text{eff}} = 1/N_{\text{outer}} + 1/N_{\text{inner}} \quad (\text{A.4})$$

or dynamically

$$\text{Dynamical} \quad N_{\text{eff}} = \min(N_{\text{outer}}, N_{\text{inner}}) \quad (\text{A.5})$$

The rate constants calculated with and without using 2TS method are presented in the Figure A-3 for Pathway 2 (OH addition on olefinic carbon). Results showed that the calculated rate constants are identical at 1 atm and there are slight difference at low temperature (200–300 K) under 100 atm. Both the two 2TS methods get results slightly lower than without 2TS methods. This could probably due to the possibility of collisional stabilization of reactive complex at low temperature and high pressure, which could break the collision-free assumption in 2TS method. The same type of comparison were also done for pathway 1 (H abstraction) and pathway 3 (OH addition on carbonyl carbon) under the pressure of 0.01, 1 and 100 atm. Besides the same slight difference at low temperature under 100 atm found for pathway 3 (OH addition on olefinic carbon), all the other results are identical. Thus, under the investigated temperature and pressure range, the differences between 2TS method and direct ME calculations on the calculated rate coefficients of this reacting system can be considered as negligible.

## A.2.3 Quantum Tunneling Treatment

It is expected that quantum tunneling effect could be significant for the H abstraction pathway (pathway 1) especially at low temperatures. In the present work, quantum tunneling correction on the distinct barriers were all treated using one-dimensional (1D) tunneling model with Eckart barriers. Here we tested the other 1D tunneling models with Harmonic and Quartic barriers and compared with the results of Eckart barriers. Figure A-4a shows that better presentations of the barrier with respect to the Eckart model (i.e., the Harmonic and Quartic models) resulted in increased rate coefficients of pathway 1, especially at low temperatures (< 500 K). At temperature of 200 K, by applying the Harmonic model,

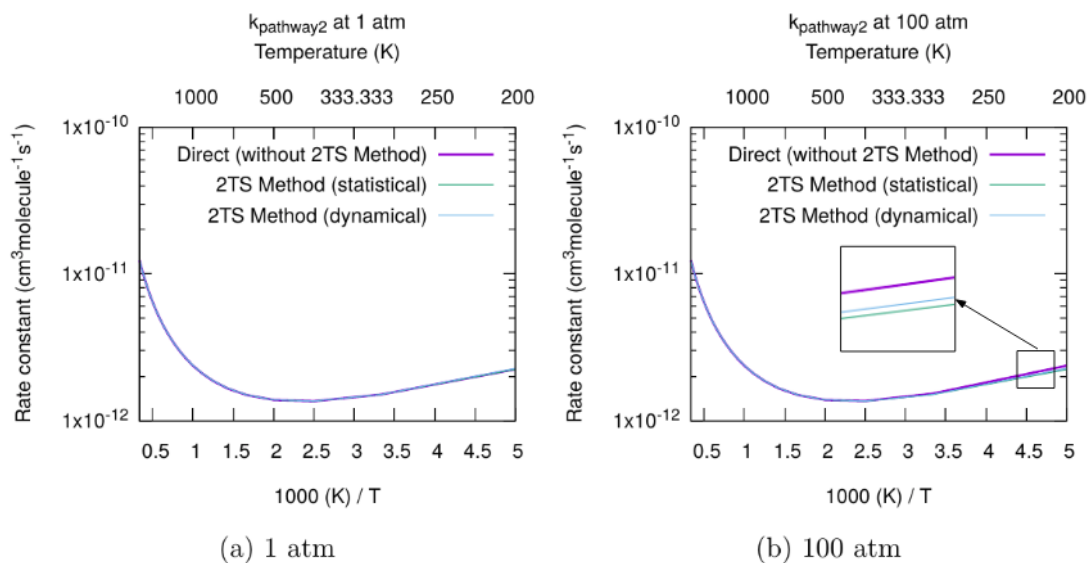


Figure A-3: Comparison on the overall rate constant of Pathway 2 with and without using the 2TS method.

$k_{\text{pathway1}}$  is elevated by around one order of magnitude with respect to that of the Eckart model, from  $6.8 \times 10^{-17}$  to  $6.1 \times 10^{-16} \text{ cm}^3 \text{ molecule}^{-1} \text{ s}^{-1}$ . However, it is still not significant enough comparing to the other two pathways, which are at the scale of  $10^{-12}$  and about 4 orders of magnitudes higher. Same comparison were also performed on the other two pathways but the effect is negligible due to the shallow well of the reactive complex and the loose nature of their transition states. Therefore, the impact of applying different 1D tunneling models on the overall rate coefficients is negligible (shown in Figure A-4b).

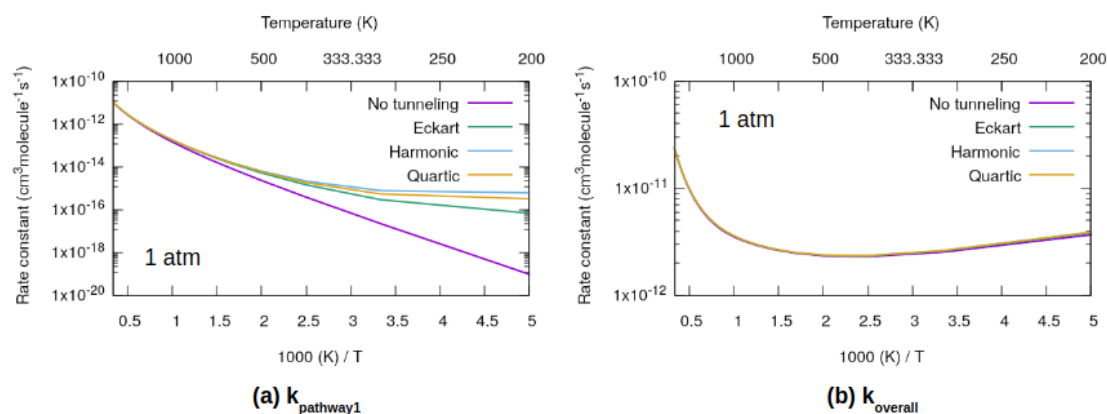


Figure A-4: Comparison of different 1D tunneling models on the calculated rate coefficients.

It is also expected that the increase of the rate coefficients especially at low temperatures could be more significant if a multidimensional tunneling model (such as the SCT method) is applied. The corner-cutting effect of the multidimensional methods could reduce the barrier width and thus resulted in higher tunneling transmission coefficients. We do not expect that, within the temperature range we investigated, the  $k_{\text{pathway1}}$  could be increased to a scale comparable

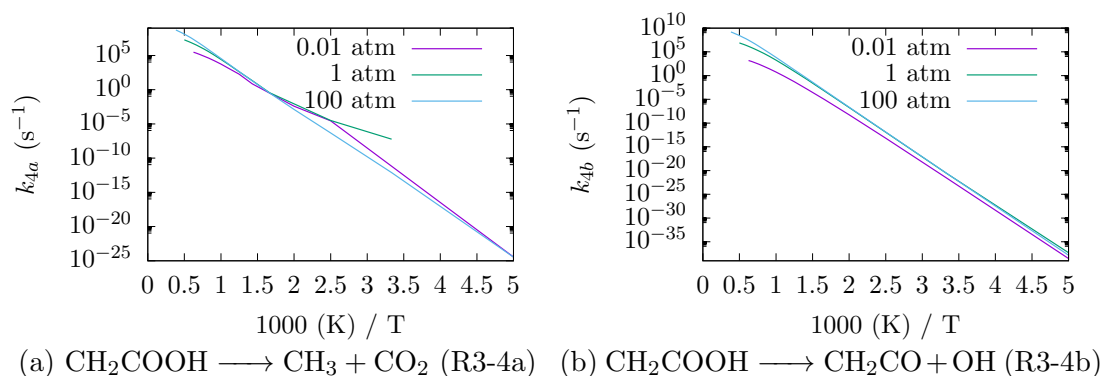


Figure A-5: Arrhenius plot for  $\text{CH}_2\text{COOH}$  dissociation channel R3-4a and R3-4b.

with that of the other two pathways (e.g., around  $10^{-12} \text{ cm}^3\text{molecule}^{-1}\text{s}^{-1}$  at 200 K). However, we still encourage the readers to apply multidimensional tunneling models especially if they intend to use the rate coefficients of this reaction at very low temperatures which could be interesting for atmospheric chemistry and astrochemistry.

## A.2.4 Rate Coefficients for R3-4a and R3-4b

Rate coefficients for R3-4a and R3-4b are presented in Figure A-5. For rate coefficients of other insignificant channels, we refer the readers to the file `CH2CO+OH_out.txt`.

## A.2.5 Simplified Scheme

A simplified scheme of the system could be obtained by keeping only the significant channels (R3-1–R3-3b) and the significant secondary channels (R3-4a and R3-4b).

## A.2.6 Fitted Arrhenius Expressions

The fitted modified Arrhenius expressions with PLOG formalism are provided in the file `CH2CO+OH_arrfit.txt`, in both single and double Arrhenius expressions. They were obtained using the auxiliary code in the MESS software. We recommend readers to use the result in double Arrhenius expressions, when implementing these rate coefficients in their mechanisms.

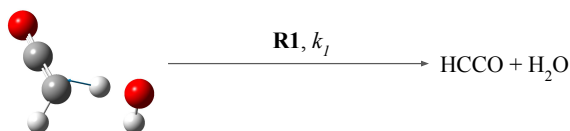
Specially, the fitted expressions for the simplified scheme (R3-1–R3-4b) are presented here in double Arrhenius expressions in Listing A.1, in order to be easily implemented in CHEMKIN input chemistry files. We found that the species  $\text{CH}_2\text{COOH}$  is not included in most mechanisms for hydrocarbon combustion. Therefore, in order to use our provided rate constants in combustion modeling, the thermodynamic and transport parameters of  $\text{CH}_2\text{COOH}$  should also be included in the mechanism.

```

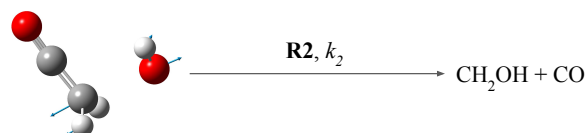
1 !----- CHEM -----!
2 !
3 !   CH2CO+OH Reactions, by Boyang XU, 2018
4 !   RRKM/ME rate constants fit to double Arrhenius expressions
5 !   Using code MESS_TPfit written by Franklin Goldsmith
6 !

```

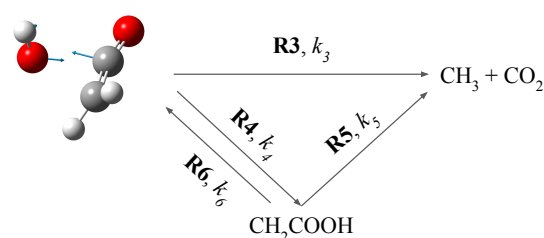
**Pathway 1: H abstraction**



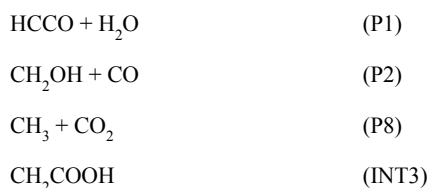
**Pathway 2: OH addition on olefinic carbon**



**Pathway 3: OH addition on carbonyl carbon**



**Products:**



**Reactions:**

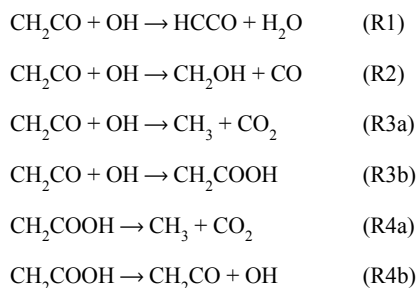


Figure A-6: Simplified Scheme of the  $\text{CH}_2\text{CO} + \text{OH}$  reaction. It includes 6 significant reaction channels and 4 major products.

```
7 !-----!
8
9 ! \rket{1} (pressure-independent)
10 ! fit btw. 300 and 3000 K with MAE of 0.4%, 1.1%
11 CH2CO+OH=>HCCO+H2O 3.93E+04 2.45 4524.0
12 DUPLICATE
13 CH2CO+OH=>HCCO+H2O 2.60E+02 2.70 1279.0
14 DUPLICATE
15
16 ! \rket{2} (pressure-independent)
17 ! fit btw. 300 and 3000 K with MAE of 0.0%, 0.2%
18 CH2CO+OH=>CH2OH+CO 3.50E+07 1.41 -1249.0
19 DUPLICATE
20 CH2CO+OH=>CH2OH+CO 4.09E+06 1.76 2088.0
21 DUPLICATE
22
23 ! \rket{3a}
24 CH2CO+OH=>CH3+CO2 4.57E-02 3.80 1933.0
25 PLOG/1.000E-04 1.17E+12 -0.11 36.7/
26 PLOG/1.000E-04 3.61E-15 -15.54 -90580.0/ ! fit btw. 300 and 3000 K with MAE of 2.4%, 6.3%
27 PLOG/1.000E-03 1.17E+12 -0.11 36.4/
28 PLOG/1.000E-03 2.81E-07 -0.80 -26580.0/ ! fit btw. 300 and 3000 K with MAE of 2.4%, 6.3%
29 PLOG/1.000E-02 1.54E+12 -0.15 133.4/
30 PLOG/1.000E-02 1.34E-08 -0.62 -27880.0/ ! fit btw. 300 and 3000 K with MAE of 2.5%, 6.6%
31 PLOG/1.000E+00 2.70E+25 -3.95 9988.0/
32 PLOG/1.000E+00 3.06E+08 0.91 374.8/ ! fit btw. 300 and 3000 K with MAE of 0.5%, 1.8%
33 PLOG/1.000E+01 4.64E+23 -3.26 12900.0/
34 PLOG/1.000E+01 3.92E+05 1.68 431.6/ ! fit btw. 300 and 3000 K with MAE of 1.7%, 4.7%
35 PLOG/2.000E+01 4.58E+22 -2.93 13610.0/
36 PLOG/2.000E+01 4.22E+04 1.93 348.5/ ! fit btw. 300 and 3000 K with MAE of 2.3%, 6.8%
37 PLOG/5.000E+01 1.70E+22 -2.76 15250.0/
38 PLOG/5.000E+01 9.90E+02 2.38 196.4/ ! fit btw. 300 and 3000 K with MAE of 3.1%, 9.7%
39 PLOG/1.000E+02 9.59E+21 -2.66 16670.0/
40 PLOG/1.000E+02 2.67E+01 2.83 3.0/ ! fit btw. 300 and 3000 K with MAE of 3.8%, 10.6%
41 PLOG/1.000E+03 1.18E-14 7.58 -3470.0/
42 PLOG/1.000E+03 -9.20E+00 3.80 20850.0/ ! fit btw. 400 and 3000 K with MAE of 2.7%, 6.0%
43
44 ! \rket{3b}
45 CH2CO+OH=>CH2COOH 4.22E+11 0.17 474.4
46 PLOG/1.000E-04 4.32E-12 -4.31 -52150.0/
47 PLOG/1.000E-04 1.55E+39 -10.42 15460.0/ ! fit btw. 400 and 1300 K with MAE of 10.3%, 29.9%
48 PLOG/1.000E-03 2.17E+30 -7.46 6325.0/
49 PLOG/1.000E-03 1.10E+26 -6.52 2253.0/ ! fit btw. 300 and 1400 K with MAE of 1.4%, 3.2%
50 PLOG/1.000E-02 3.60E+40 -9.90 9611.0/
51 PLOG/1.000E-02 3.69E+33 -8.17 3450.0/ ! fit btw. 300 and 1600 K with MAE of 1.0%, 2.1%
52 PLOG/1.000E+00 7.99E+39 -8.61 12690.0/
53 PLOG/1.000E+00 7.01E+27 -5.50 3350.0/ ! fit btw. 300 and 2000 K with MAE of 1.2%, 3.2%
54 PLOG/1.000E+01 4.40E+37 -7.57 14670.0/
55 PLOG/1.000E+01 1.34E+22 -3.48 2325.0/ ! fit btw. 300 and 2200 K with MAE of 2.3%, 7.4%
56 PLOG/2.000E+01 4.54E+36 -7.19 15140.0/
57 PLOG/2.000E+01 3.63E+20 -2.94 2011.0/ ! fit btw. 300 and 2300 K with MAE of 2.6%, 8.5%
58 PLOG/5.000E+01 1.64E+35 -6.66 15720.0/
59 PLOG/5.000E+01 6.51E+18 -2.34 1657.0/ ! fit btw. 300 and 2500 K with MAE of 3.0%, 9.8%
```



```

60 PLOG/1.000E+02 6.97E+33 -6.19 15970.0/
61 PLOG/1.000E+02 2.20E+17 -1.85 1331.0/ ! fit btw. 300 and 2600 K with MAE of 3.3%, 9.9%
62 PLOG/1.000E+03 1.57E+22 -2.71 10170.0/
63 PLOG/1.000E+03 9.78E+15 -1.42 918.5/ ! fit btw. 300 and 3000 K with MAE of 4.2%, 10.3%
64
65 ! \rket{4a}
66 CH2COOH=>CH3+C02 2.66E+10 0.43 32660.0
67 PLOG/1.000E-04 1.67E+29 -6.49 33280.0/
68 PLOG/1.000E-04 1.03E-23 4.43 -13970.0/ ! fit btw. 400 and 1300 K with MAE of 8.3%, 30.9%
69 PLOG/1.000E-03 4.40E+12 -1.39 25740.0/
70 PLOG/1.000E-03 2.48E+12 -1.53 23050.0/ ! fit btw. 500 and 1400 K with MAE of 16.7%, 39.4%
71 PLOG/1.000E-02 -8.86E+14 -9.06 -23460.0/
72 PLOG/1.000E-02 1.45E+03 1.60 20450.0/ ! fit btw. 400 and 1600 K with MAE of
4727376701.8%, 56728376057.3%
73 PLOG/1.000E+00 2.32E-03 3.86 21910.0/
74 PLOG/1.000E+00 2.21E-31 -1.24 -36360.0/ ! fit btw. 300 and 2000 K with MAE of 56.5%,
252.1%
75 PLOG/1.000E+01 1.47E-65 20.37 -9836.0/
76 PLOG/1.000E+01 4.20E+23 -3.49 39350.0/ ! fit btw. 300 and 2200 K with MAE of 11.4%, 29.6%
77 PLOG/2.000E+01 1.47E+33 -6.10 47410.0/
78 PLOG/2.000E+01 5.22E+15 -1.57 32890.0/ ! fit btw. 300 and 2300 K with MAE of 3.1%, 10.4%
79 PLOG/5.000E+01 1.36E+32 -5.74 47740.0/
80 PLOG/5.000E+01 2.77E+14 -1.13 32620.0/ ! fit btw. 300 and 2500 K with MAE of 2.8%, 8.9%
81 PLOG/1.000E+02 2.37E+30 -5.20 47150.0/
82 PLOG/1.000E+02 6.78E+13 -0.93 32480.0/ ! fit btw. 300 and 2600 K with MAE of 2.8%, 6.6%
83 PLOG/1.000E+03 3.02E+23 -3.15 43840.0/
84 PLOG/1.000E+03 1.60E+12 -0.39 32050.0/ ! fit btw. 300 and 3000 K with MAE of 2.9%, 6.8%
85
86 ! \rket{4b}
87 CH2COOH=>CH2CO+OH 9.09E+20 -2.03 50340.0
88 PLOG/1.000E-04 1.41E-04 -5.95 -2914.0/
89 PLOG/1.000E-04 7.47E+46 -12.08 64910.0/ ! fit btw. 400 and 1300 K with MAE of 10.7%, 30.0%
90 PLOG/1.000E-03 1.02E+37 -8.84 54820.0/
91 PLOG/1.000E-03 1.62E+30 -7.25 50040.0/ ! fit btw. 300 and 1400 K with MAE of 1.3%, 2.4%
92 PLOG/1.000E-02 1.32E+53 -13.12 60790.0/
93 PLOG/1.000E-02 5.96E+35 -8.05 51360.0/ ! fit btw. 300 and 1600 K with MAE of 1.0%, 2.6%
94 PLOG/1.000E+00 2.89E+51 -11.47 63640.0/
95 PLOG/1.000E+00 2.65E+31 -5.84 51560.0/ ! fit btw. 300 and 2000 K with MAE of 1.6%, 3.4%
96 PLOG/1.000E+01 6.20E+45 -9.43 63540.0/
97 PLOG/1.000E+01 6.53E+28 -4.89 51200.0/ ! fit btw. 300 and 2200 K with MAE of 2.3%, 6.5%
98 PLOG/2.000E+01 2.08E+44 -8.92 63590.0/
99 PLOG/2.000E+01 4.71E+27 -4.49 50980.0/ ! fit btw. 300 and 2300 K with MAE of 2.5%, 8.0%
100 PLOG/5.000E+01 1.36E+42 -8.18 63470.0/
101 PLOG/5.000E+01 1.34E+26 -3.95 50680.0/ ! fit btw. 300 and 2500 K with MAE of 2.7%, 9.1%
102 PLOG/1.000E+02 1.77E+40 -7.57 63170.0/
103 PLOG/1.000E+02 1.25E+25 -3.60 50460.0/ ! fit btw. 300 and 2600 K with MAE of 2.8%, 10.0%
104 PLOG/1.000E+03 7.57E+32 -5.30 60820.0/
105 PLOG/1.000E+03 7.01E+21 -2.50 49730.0/ ! fit btw. 300 and 3000 K with MAE of 3.0%, 10.1%

```

Listing A.1: Fitted double Arrhenius expressions with PLOG formalism for R3-1–R3-4b.

## A.2.7 Effect of the Updated Rate Coefficients on the Laminar Flame Speed of Acetone

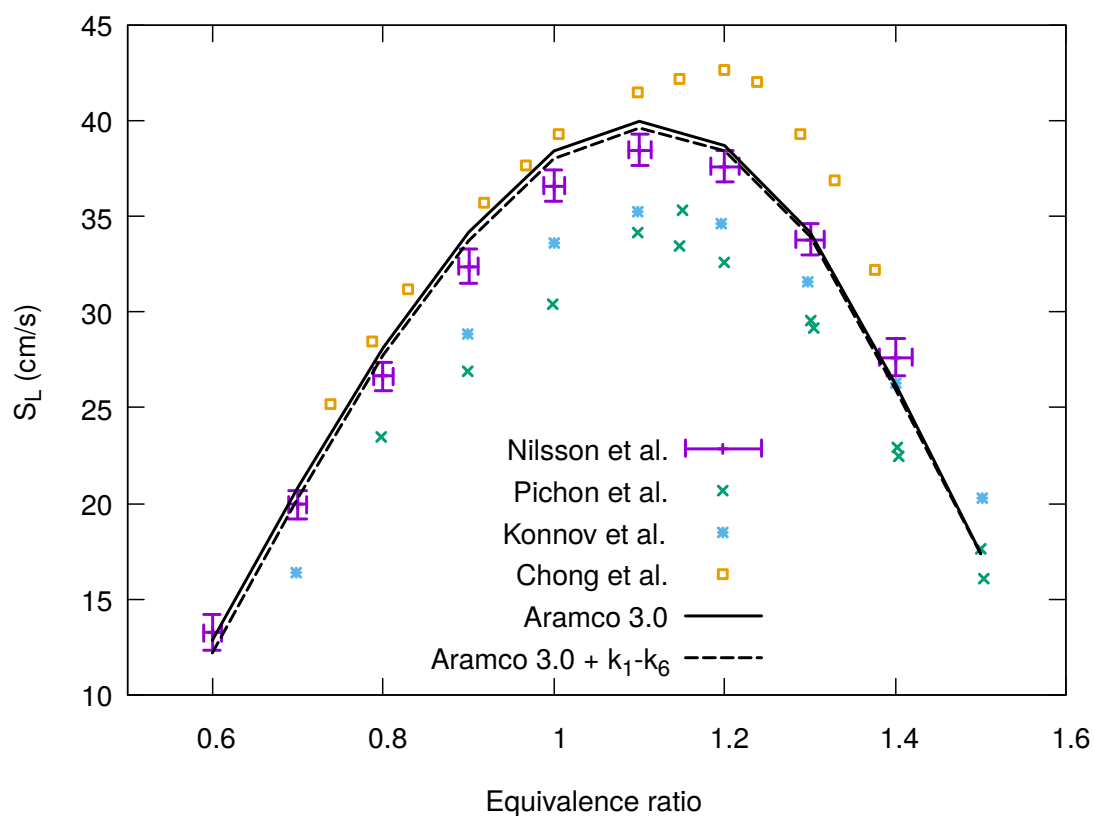


Figure A-7: Effect of the updated rate coefficients on the laminar flame speeds of acetone/air mixture at standard conditions (298 K, 1 atm). Aramco Mech 3.0 is used as the reference mechanism in simulations.

THIS PAGE INTENTIONALLY LEFT BLANK

# Appendix B

## Supporting Information for Chapter 4, 5 and 6

### B.1 Supporting Information for Chapter 4

Table B.1: List of important species and reactions, with evaluation of investigation interests for the present work.

Category	Species	Reactions	D+	P+	T+	D,T+	M?	K?	T? (K)	Interesting?	Ref	
Vinyl	C2H2	C2H2+O2=HCCO+OH c2h2+h(+M)=c2h3(+M)	↗	--	↗	↗		✓		x	Marinov 1998	
	C2H3	C2H3+O2=CH2CHO+O	↗	↗	↗	↗		✓		x	Multiple records Marinov 1998	
	C2H4	C2H4+OH=C2H3+H2O c2h4+oh=ch2o+ch3	↗	--	↗	↗	✓	✓	250 - 3000	x	Multiple records Huynh 2008	
	C3H3	c3h3+oh=hco+c2h3 c3h3+ho2=c3h4+o2				↗				✓	Hansen 2009 Wang 2001	
Allene/Propene	C3H3	c3h3+o2=ch2co+hco c3h5+h(+M)=c3h6(+M)				--	✓	✓	250 - 2000	x	Hahn 2001	
	C3H5	c3h5+ho2=oh+c2h3+ch2o C3H5-A+HO2=C3H5O+OH	↗	↗	--	--	✓	✓	900 - 3000	x	Blanquart 2009	
	C3H6	c3h6+oh=c3h5+h2o				↘	✓	✓	400 - 2000	x	Goldsmith 2011	
C4+ Olefinc	iC4H7	IC4H7+HO2=IC4H7O+OH	↗	↗	--	--	✓	✓	400 - 2000	x	Goldsmith 2011	
	C5H6	CY13PD=CY13PD5J+H	--	↘	↘	↗	✓	✓	300 - 1500	x	Chen 2000	
Ketenyl	HCCO	HCCO+OH=>H2+2CO hcco+o2=>co2+co+h	--	↘	↗	↗	✓	✓	500 - 2500	x	Robinson 2011 Mai 2014	
	CH2CO	CH2CO+OH=CH2OH+CO C6H5OJ+H=C6H5OH C6H5OJ+HO2=RODC6JDO+OH	↗	--	↘	↗	✓	✓	300 - 2000	x	Klippenstein 2002	
	C6H5OJ	CH2CO+OH=CH2OH+CO C6H5OJ+H=C6H5OH C6H5OJ+HO2=RODC6JDO+OH	↗	--	↘	↗	✓	✓	1000 - 1200	✓	Hou 2000 Davis 1996 Skokov 2005	
Aromatic	C6H5OJ	c6h5o+o=oc6h4o+h c6h5o=c5h5+co				↗	✓	✓	300 - 3000	x	Lin 1995	
	C6H5CH3	C6H5CH3+O2=C6H5CH2J+HO2 C6H5CH3+H=C6H5CH2J+H2	↗	↗	--	--	✓	✓	300 - 1600	x	Carstensen 2012	
		C6H5CH3	C6H5CH3+OH=C6H5CH2J+H2O C6H5CH3+OH=C6H4CH3+H2O	↗	↗	↗	--	✓	✓		x	Oehlschlaeger 2006 (1) Oehlschlaeger 2006 (2)
		C6H5CH2J	C6H5CH2J+H2O C6H5CH2J+OH=C6H5CH2OJ+OH	↗	↗	↗	--	✓	✓		x	Seta 2006 Seta 2006
	OC6H4CH3	c7h8+ho2=c6h5ch2+h2o2 OC6H4CH3=H+C6H6+CO	↗	↗	--	↘	✓	✓	300 - 1400	x	Altaravneh 2011	
	Isooctane	IC8H18	IC8H18=YC7H15+CH3 ic8h18=tc4h9+ic4h9	↗	↗	--	↘	✓	✓	300 - 1600	x	da Silva 2009 Carstensen 2012

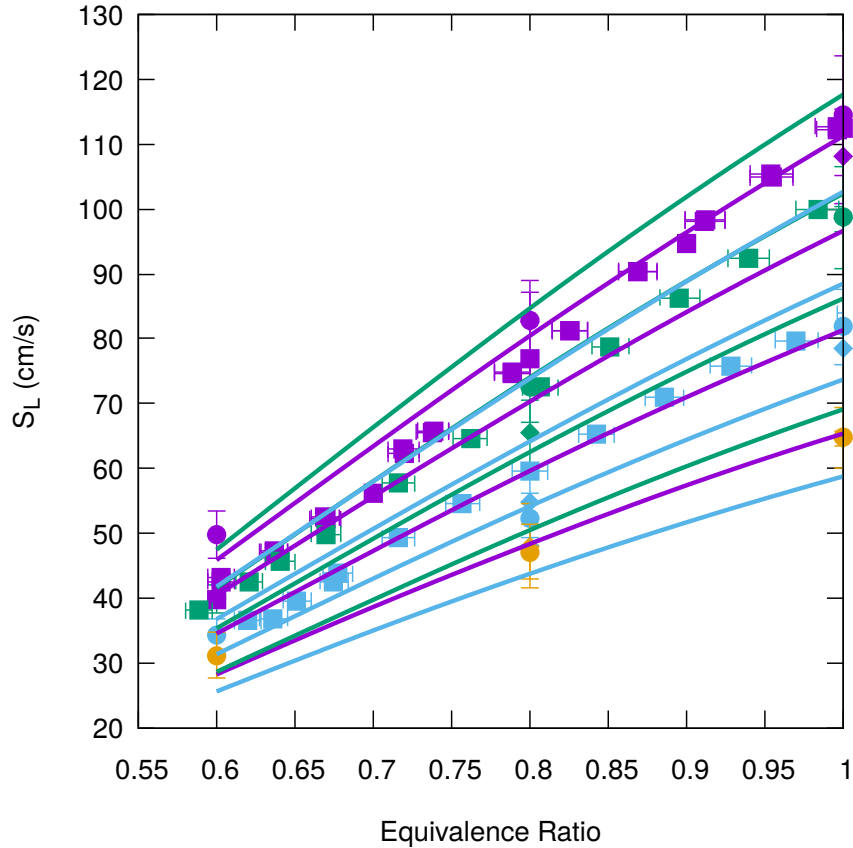


Figure B-1: Effect of  $\text{CO}_2$  dilution in fuel on the laminar flame speed of lean equimolar syngas ( $\text{H}_2/\text{CO} = 1/1$ ) at standard conditions (298 K, 1 atm). Experimental data are from Natarajan *et al.* [18], Prathap *et al.* [21], and Han *et al.* [22].

## B.2 Supporting Information for Chapter 5

### B.2.1 Diluted Flames of Syngas ( $\text{H}_2/\text{CO}$ )

### B.2.2 Diluted Flames of Methane ( $\text{CH}_4$ )

## B.3 Supporting Information for Chapter 6

### B.3.1 The Detailed and Semi-Detailed Mechanisms

The files for the detailed and semi-detailed mechanism, MACDIL-DTL and MACDIL-RDC, are enclosed in the supplementary materials.

### B.3.2 Validation of MACDIL-RDC on Laminar Flame Speeds of TRFE/air/EGR Mixtures

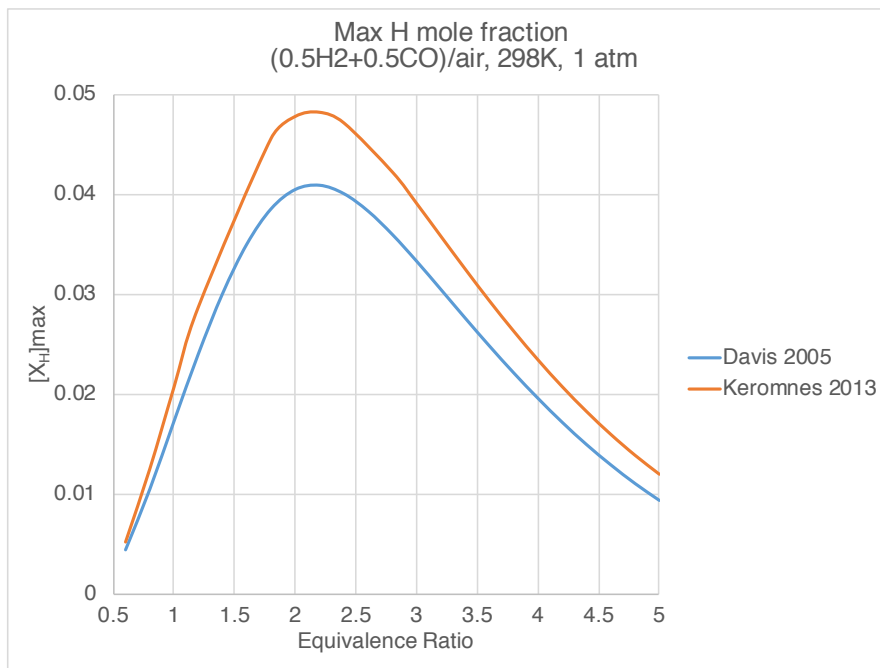


Figure B-2: Comparison of maximum mole fraction of H radicals predicted by the LLNL 2011 and K eromn es 2013 mechanisms.

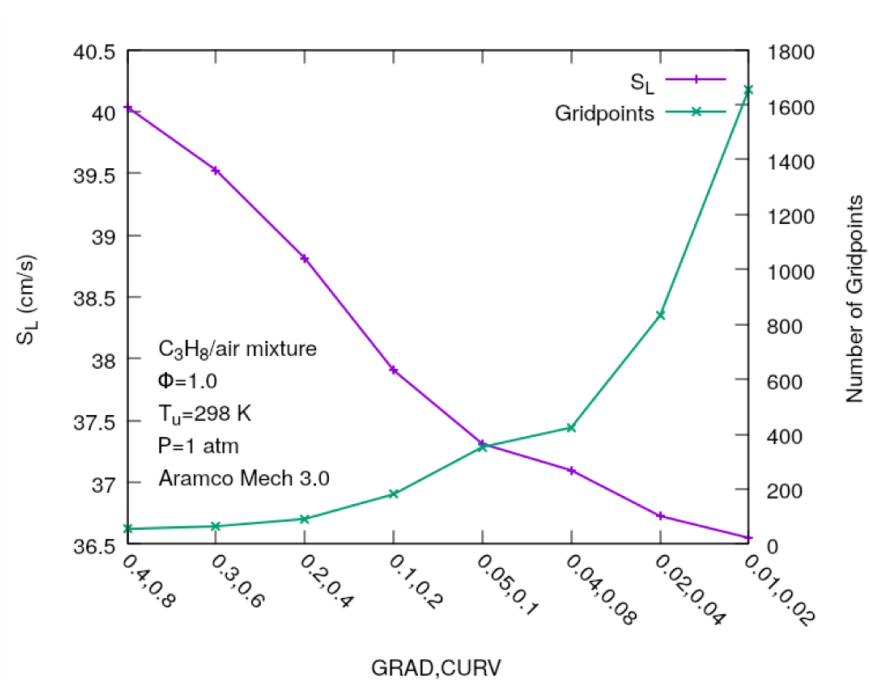
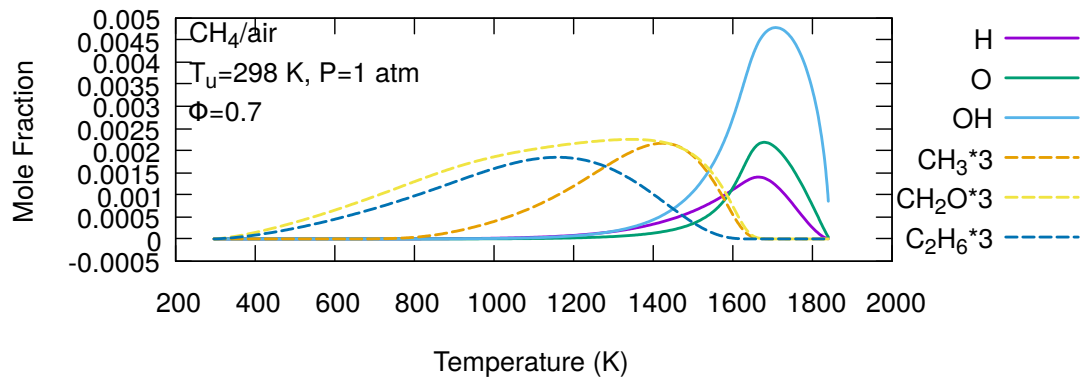
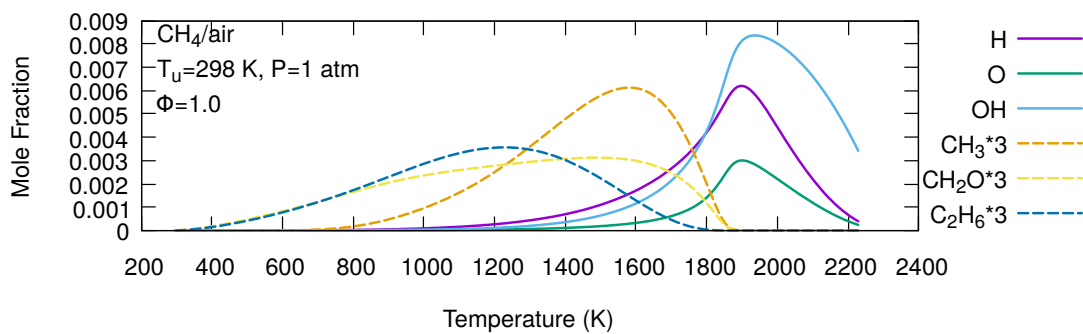


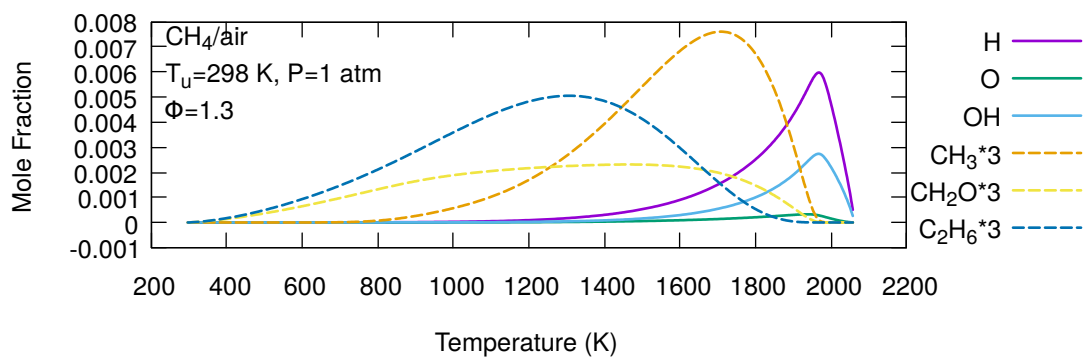
Figure B-3: Evolution of  $S_L$  and the number of grid points with adaptive grid control parameters, for the calculation of laminar flame speeds of CH<sub>4</sub>/air/ flames.



(a)  $\phi = 0.7$



(b)  $\phi = 1.0$



(c)  $\phi = 1.3$

Figure B-4: Evolution of species mole fraction against temperature at standard conditions (298 K, 1 atm).

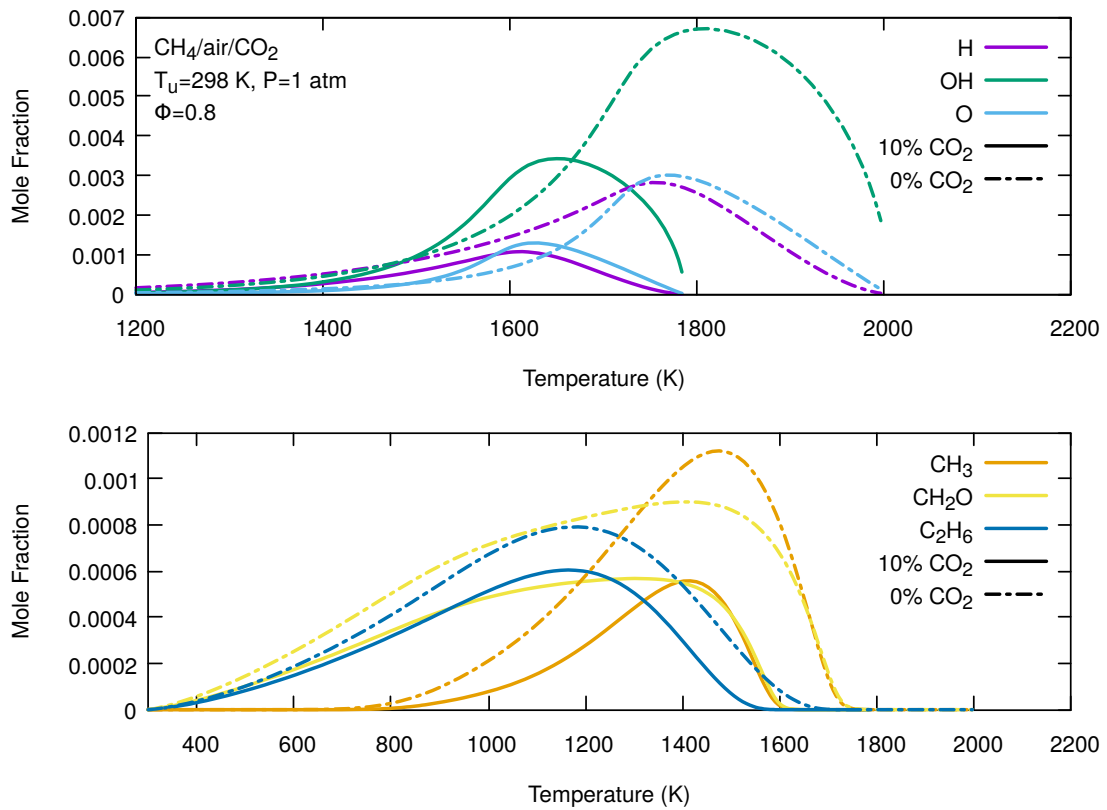


Figure B-5: Effect of CO<sub>2</sub> dilution on the speciation profiles of the important radicals (H, OH, O, and CH<sub>3</sub>) and intermediate species (CH<sub>2</sub>O and C<sub>2</sub>H<sub>6</sub>) in lean CH<sub>4</sub>/air/CO<sub>2</sub> flames ( $\phi = 0.8$ ).



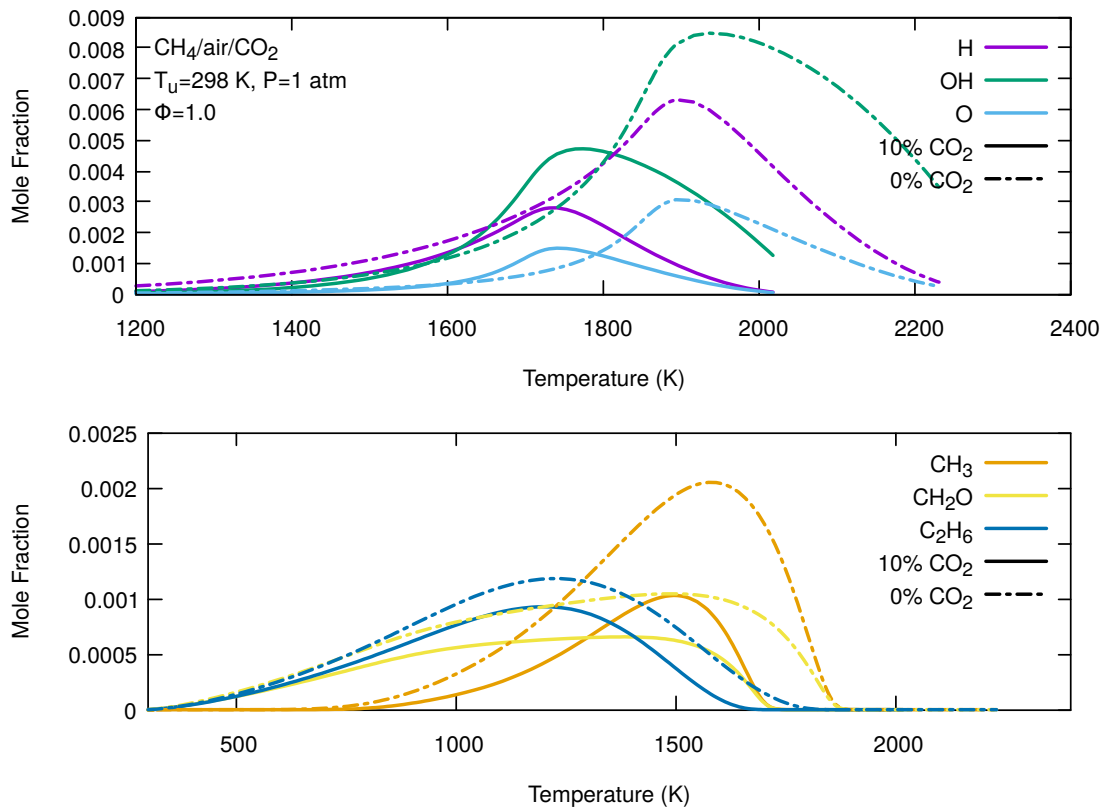


Figure B-6: Effect of CO<sub>2</sub> dilution on the speciation profiles of the important radicals (H, OH, O, and CH<sub>3</sub>) and intermediate species (CH<sub>2</sub>O and C<sub>2</sub>H<sub>6</sub>) in stoichiometric CH<sub>4</sub>/air/CO<sub>2</sub> flames ( $\phi = 1.0$ ).

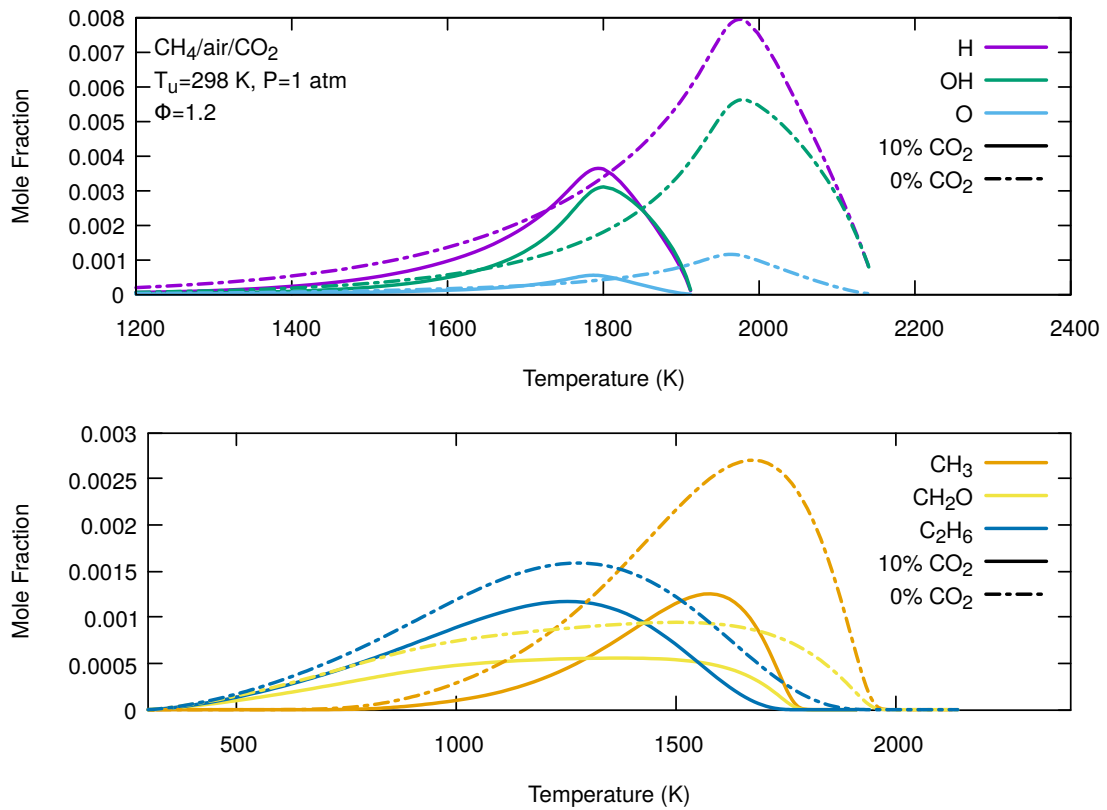


Figure B-7: Effect of CO<sub>2</sub> dilution on the speciation profiles of the important radicals (H, OH, O, and CH<sub>3</sub>) and intermediate species (CH<sub>2</sub>O and C<sub>2</sub>H<sub>6</sub>) in rich CH<sub>4</sub>/air/CO<sub>2</sub> flames ( $\phi = 1.2$ ).

Table B.2: Compositions in mole fractions of the mixtures used in the experiments at different equivalence ratios and EGR ratios. The measured equivalence ratios are from Ref. [24].

EGR ratio	$\phi$	fuel/air/EGR			detailed composition (mole fraction)									
		$X_{fuel}$	$X_{air}$	$X_{EGR}$	isooctane	n-heptane	toluene	ethanol	O <sub>2</sub>	CO <sub>2</sub>	H <sub>2</sub> O	N <sub>2</sub>	N <sub>2</sub> in air	N <sub>2</sub> in EGR
0%	0.8633	0.018189	0.981811	0.000000	0.006117	0.002336	0.007772	0.001964	0.206180	0.000000	0.000000	0.775630	0.775630	0.000000
0%	0.8635	0.018192	0.981808	0.000000	0.006118	0.002336	0.007774	0.001965	0.206180	0.000000	0.000000	0.775628	0.775628	0.000000
0%	0.8650	0.018224	0.981776	0.000000	0.006129	0.002340	0.007787	0.001968	0.206173	0.000000	0.000000	0.775603	0.775603	0.000000
0%	0.9674	0.020338	0.979662	0.000000	0.006840	0.002611	0.008691	0.002197	0.205729	0.000000	0.000000	0.773933	0.773933	0.000000
0%	0.9720	0.020433	0.979567	0.000000	0.006872	0.002624	0.008731	0.002207	0.205709	0.000000	0.000000	0.773858	0.773858	0.000000
0%	0.9727	0.020446	0.979554	0.000000	0.006876	0.002625	0.008737	0.002208	0.205706	0.000000	0.000000	0.773847	0.773847	0.000000
0%	1.0803	0.022657	0.977343	0.000000	0.007620	0.002909	0.009681	0.002447	0.205242	0.000000	0.000000	0.772101	0.772101	0.000000
0%	1.0807	0.022665	0.977335	0.000000	0.007622	0.002910	0.009685	0.002448	0.205240	0.000000	0.000000	0.772095	0.772095	0.000000
0%	1.1850	0.024799	0.975201	0.000000	0.008340	0.003184	0.010596	0.002678	0.204792	0.000000	0.000000	0.770409	0.770409	0.000000
0%	1.1864	0.024828	0.975172	0.000000	0.008350	0.003188	0.010609	0.002681	0.204786	0.000000	0.000000	0.770386	0.770386	0.000000
0%	1.1878	0.024856	0.975144	0.000000	0.008359	0.003191	0.010621	0.002684	0.204780	0.000000	0.000000	0.770364	0.770364	0.000000
0%	1.2895	0.026927	0.973073	0.000000	0.009055	0.003457	0.011506	0.002908	0.204345	0.000000	0.000000	0.768728	0.768728	0.000000
0%	1.2951	0.027040	0.972960	0.000000	0.009093	0.003472	0.011554	0.002920	0.204322	0.000000	0.000000	0.768639	0.768639	0.000000
0%	1.2974	0.027088	0.972912	0.000000	0.009110	0.003478	0.011575	0.002926	0.204311	0.000000	0.000000	0.768600	0.768600	0.000000
0%	1.3930	0.029026	0.970974	0.000000	0.009761	0.003727	0.012403	0.003135	0.203905	0.000000	0.000000	0.767069	0.767069	0.000000
0%	1.4039	0.029246	0.970754	0.000000	0.009835	0.003755	0.012497	0.003159	0.203858	0.000000	0.000000	0.766896	0.766896	0.000000
0%	1.4050	0.029268	0.970732	0.000000	0.009843	0.003758	0.012506	0.003161	0.203854	0.000000	0.000000	0.766878	0.766878	0.000000
10%	0.8621	0.016348	0.883652	0.100000	0.005498	0.002099	0.006986	0.001766	0.185567	0.013620	0.012220	0.772245	0.698085	0.074160
10%	0.8644	0.016391	0.883609	0.100000	0.005512	0.002105	0.007004	0.001770	0.185558	0.013620	0.012220	0.772211	0.698051	0.074160
10%	0.8647	0.016397	0.883603	0.100000	0.005514	0.002105	0.007006	0.001771	0.185557	0.013620	0.012220	0.772206	0.698046	0.074160
10%	0.8649	0.016400	0.883600	0.100000	0.005515	0.002106	0.007008	0.001771	0.185556	0.013620	0.012220	0.772204	0.698044	0.074160
10%	0.9690	0.018334	0.881666	0.100000	0.006166	0.002354	0.007834	0.001980	0.185150	0.013620	0.012220	0.770676	0.696516	0.074160
10%	0.9718	0.018386	0.881614	0.100000	0.006183	0.002361	0.007856	0.001986	0.185139	0.013620	0.012220	0.770635	0.696475	0.074160
10%	0.9733	0.018413	0.881587	0.100000	0.006192	0.002364	0.007868	0.001989	0.185133	0.013620	0.012220	0.770613	0.696453	0.074160
10%	1.0730	0.020256	0.879744	0.100000	0.006812	0.002601	0.008655	0.002188	0.184746	0.013620	0.012220	0.769158	0.694998	0.074160
10%	1.0771	0.020333	0.879668	0.100000	0.006838	0.002611	0.008688	0.002196	0.184730	0.013620	0.012220	0.769097	0.694937	0.074160
10%	1.0792	0.020372	0.879628	0.100000	0.006851	0.002616	0.008705	0.002200	0.184722	0.013620	0.012220	0.769066	0.694906	0.074160
10%	1.1854	0.022327	0.877673	0.100000	0.007508	0.002867	0.009540	0.002411	0.184311	0.013620	0.012220	0.767522	0.693362	0.074160
10%	1.1874	0.022364	0.877636	0.100000	0.007521	0.002872	0.009556	0.002415	0.184304	0.013620	0.012220	0.767492	0.693332	0.074160
10%	1.1875	0.022364	0.877636	0.100000	0.007521	0.002872	0.009556	0.002415	0.184304	0.013620	0.012220	0.767492	0.693332	0.074160
10%	1.1884	0.022381	0.877619	0.100000	0.007527	0.002874	0.009563	0.002417	0.184300	0.013620	0.012220	0.767479	0.693319	0.074160
10%	1.2919	0.024278	0.875722	0.100000	0.008165	0.003117	0.010374	0.002622	0.183902	0.013620	0.012220	0.765981	0.691821	0.074160
10%	1.2926	0.024290	0.875710	0.100000	0.008169	0.003119	0.010379	0.002623	0.183899	0.013620	0.012220	0.765971	0.691811	0.074160
10%	1.2953	0.024340	0.875660	0.100000	0.008186	0.003125	0.010401	0.002629	0.183889	0.013620	0.012220	0.765931	0.691771	0.074160
10%	1.2976	0.024382	0.875618	0.100000	0.008200	0.003131	0.010418	0.002633	0.183880	0.013620	0.012220	0.765898	0.691738	0.074160
10%	1.3951	0.026161	0.873839	0.100000	0.008798	0.003359	0.011179	0.002825	0.183506	0.013620	0.012220	0.764492	0.690332	0.074160
10%	1.4028	0.026301	0.873699	0.100000	0.008845	0.003377	0.011238	0.002840	0.183477	0.013620	0.012220	0.764382	0.690222	0.074160
10%	1.4029	0.026304	0.873696	0.100000	0.008846	0.003377	0.011240	0.002841	0.183476	0.013620	0.012220	0.764380	0.690220	0.074160
10%	1.4039	0.026322	0.873678	0.100000	0.008852	0.003380	0.011247	0.002843	0.183472	0.013620	0.012220	0.764366	0.690206	0.074160
20%	0.8628	0.014543	0.785457	0.200000	0.004891	0.001867	0.006214	0.001571	0.164946	0.027240	0.024440	0.768831	0.620511	0.148320
20%	0.8632	0.014550	0.785450	0.200000	0.004893	0.001868	0.006217	0.001571	0.164945	0.027240	0.024440	0.768826	0.620506	0.148320
20%	0.9718	0.016343	0.783657	0.200000	0.005496	0.002098	0.006983	0.001765	0.164568	0.027240	0.024440	0.767409	0.619089	0.148320
20%	0.9733	0.016368	0.783632	0.200000	0.005505	0.002102	0.006994	0.001768	0.164563	0.027240	0.024440	0.767389	0.619069	0.148320
20%	1.0789	0.018102	0.781898	0.200000	0.006088	0.002324	0.007735	0.001955	0.164199	0.027240	0.024440	0.766019	0.617699	0.148320
20%	1.0812	0.018141	0.781859	0.200000	0.006101	0.002329	0.007752	0.001959	0.164190	0.027240	0.024440	0.765989	0.617669	0.148320
20%	1.1837	0.019819	0.780181	0.200000	0.006665	0.002545	0.008468	0.002140	0.163838	0.027240	0.024440	0.764663	0.616343	0.148320
20%	1.1867	0.019867	0.780133	0.200000	0.006681	0.002551	0.008489	0.002146	0.163828	0.027240	0.024440	0.764625	0.616305	0.148320
20%	1.2953	0.021636	0.778364	0.200000	0.007276	0.002778	0.009245	0.002337	0.163457	0.027240	0.024440	0.763228	0.614908	0.148320
20%	1.2963	0.021653	0.778347	0.200000	0.007282	0.002780	0.009252	0.002338	0.163453	0.027240	0.024440	0.763214	0.614894	0.148320
20%	1.3999	0.023332	0.776668	0.200000	0.007847	0.002996	0.009970	0.002520	0.163100	0.027240	0.024440	0.761887	0.613567	0.148320
20%	1.4012	0.023354	0.776646	0.200000	0.007854	0.002999	0.009979	0.002522	0.163096	0.027240	0.024440	0.761871	0.613551	0.148320

Table B.3: Laminar flame speeds of TRFE/air/EGR mixtures. Experimental measurements from Ref. [24] and predictions using the LLNL 2011 [25] and the MACDIL-RDC mechanisms are compared.

EGR ratio	P (bar)	experiments		LLNL 2011		MACDIL-RDC	
		$\phi$ <sup>1</sup>	$S_L$ (cm/s) <sup>2</sup>	$\phi$	$S_L$ (cm/s) <sup>3</sup>	$\phi$	$S_L$ (cm/s)
0%	1	0.8633	63.94 ± 2.81	0.8633	71.92	0.8633	65.75
		0.9674	70.96 ± 0.60	0.9674	80.88	0.9674	73.30
		1.0807	73.11 ± 2.10	1.0807	85.58	1.0807	75.93
		1.1850	71.74 ± 1.30	1.1850	84.94	1.1850	73.18
		1.2895	68.47 ± 0.63	1.2895	77.76	1.2895	64.22
		1.3930	62.52 ± 2.87	1.3930	---	1.3930	49.69
	2	0.8633	55.73 ± 0.98	0.8633	58.31	0.8633	56.41
		0.9674	60.02 ± 1.51	0.9674	65.56	0.9674	63.37
		1.0807	64.58 ± 0.56	1.0807	70.52	1.0807	65.96
		1.1850	62.56 ± 0.75	1.1850	69.18	1.1850	62.99
		1.2895	57.08 ± 3.05	1.2895	61.14	1.2895	54.29
		1.3930	43.64 ± 0.38	1.3930	---	1.3930	41.07
	3	0.8635	46.94 ± 1.01	0.8633	51.38	0.8635	50.96
		0.9720	49.96 ± 0.55	0.9674	58.65	0.9720	57.55
		1.0807	54.96 ± 2.06	1.0807	62.16	1.0807	59.91
		1.1864	51.44 ± 1.30	1.1850	60.19	1.1864	56.65
		1.2951	49.30 ± 3.01	1.2895	52.15	1.2951	46.99
		1.4039	42.92 ± 1.42	1.3930	38.71	1.4039	34.11
	5	0.8650	36.59 ± 0.77	0.8633	43.23	0.8650	44.14
		0.9727	43.33 ± 0.21	0.9674	49.58	0.9727	49.99
		1.0803	49.70 ± 1.50	1.0807	52.16	1.0803	52.04
		1.1878	50.22 ± 0.45	1.1850	49.53	1.1878	48.79
		1.2974	46.39 ± 0.70	1.2895	41.80	1.2974	39.99
10%	1	0.8649	43.21 ± 0.95	0.8633	---	0.8649	47.92
		0.9690	47.88 ± 2.43	0.9674	---	0.9690	54.09
		1.0730	52.03 ± 1.30	1.0807	63.79	1.0730	56.42
		1.1875	53.09 ± 2.09	1.1850	---	1.1875	53.38
		1.2919	48.48 ± 0.79	1.2895	---	1.2919	44.82
		1.3951	42.00 ± 0.88	1.3930	---	1.3951	32.55
	2	0.8621	37.64 ± 0.72	0.8633	41.59	0.8621	39.88
		0.9718	42.63 ± 0.46	0.9674	47.66	0.9718	45.86
		1.0771	44.88 ± 0.47	1.0807	50.74	1.0771	47.55
		1.1874	43.05 ± 0.19	1.1850	48.80	1.1874	44.72
		1.2926	36.05 ± 0.72	1.2895	41.45	1.2926	36.43
		1.4039	27.30 ± 0.64	1.3930	---	1.4039	24.43
	3	0.8647	34.18 ± 3.49	0.8633	36.02	0.8647	35.40
		0.9733	37.20 ± 1.32	0.9674	41.49	0.9733	40.87
		1.0792	40.70 ± 0.89	1.0807	43.96	1.0792	42.55
		1.1884	35.81 ± 1.00	1.1850	41.45	1.1884	39.25
		1.2976	32.62 ± 3.68	1.2895	33.89	1.2976	31.00
		1.4028	26.68 ± 2.12	1.3930	---	1.4028	20.47
	5	0.8644	26.86 ± 0.44	0.8633	29.73	0.8644	30.30
		0.9733	30.58 ± 0.78	0.9674	34.59	0.9733	35.12
		1.0792	32.16 ± 1.73	1.0807	36.12	1.0792	36.29
		1.1854	30.60 ± 1.63	1.1850	32.96	1.1854	32.95
		1.2953	30.27 ± 1.91	1.2895	25.74	1.2953	24.92
20%	1	0.9733	33.65 ± 0.74	0.9674	---	0.9733	37.41
		1.0789	37.43 ± 1.06	1.0807	---	1.0789	38.71
		1.1837	37.44 ± 2.03	1.1850	---	1.1837	35.83
		1.2953	34.01 ± 1.41	1.2895	---	1.2953	28.10
		1.3999	29.22 ± 0.60	1.3999	---	1.3999	18.16
	2	0.8632	23.66 ± 0.87	0.8633	27.34	0.8632	26.52
		0.9733	26.35 ± 0.28	0.9674	31.90	0.9733	30.63
		1.0789	29.71 ± 0.56	1.0807	33.87	1.0789	31.80
		1.1837	28.95 ± 0.71	1.1850	31.64	1.1837	28.78
		1.2953	24.09 ± 1.67	1.2895	24.73	1.2953	21.14
		1.3999	15.63 ± 1.13	1.3999	---	1.3999	13.12
	3	0.8628	19.44 ± 0.41	0.8633	23.29	0.8628	23.14
		0.9718	23.39 ± 0.36	0.9674	27.23	0.9718	26.91
		1.0812	24.86 ± 0.84	1.0807	28.81	1.0812	27.80
		1.1867	25.39 ± 0.87	1.1850	25.96	1.1867	24.68
		1.2963	20.61 ± 1.97	1.2895	---	1.2963	17.66
		1.4012	14.84 ± 1.10	1.3930	11.28	1.4012	10.93
	5	0.8632	17.26 ± 1.41	0.8633	18.76	0.8632	19.06
		0.9733	19.21 ± 0.44	0.9674	22.10	0.9733	22.53
		1.0789	20.81 ± 0.78	1.0807	22.93	1.0789	23.10
		1.1837	19.64 ± 1.08	1.1850	19.93	1.1837	20.12
		1.2953	15.61 ± 1.41	1.2953	---	1.2953	13.41

<sup>1</sup> Each laminar flame speed presented is the average value of at least three measurements.

<sup>2</sup> The uncertainty is defined as the standard deviation of at least three measurements.

<sup>3</sup> "----" means the calculation failed to converge using the grid control parameters (GRAD = 0.1 and CURV = 0.1 as described in Section 6.3.1) and the conditions as describe in Table 6.5 of Section 6.3.2.

THIS PAGE INTENTIONALLY LEFT BLANK

# Bibliography

- [1] International Energy Agency. *World Energy Outlook 2018*, 2018. <https://www.iea.org/weo2018/>.
- [2] D.A. McQuarrie, J.D. Simon, H.A. Cox, and J. Choi. *Physical Chemistry: A Molecular Approach*. Physical Chemistry: A Molecular Approach. University Science Books, 1997.
- [3] Thierry Poinsot and Denis Veynante. *Theoretical and numerical combustion*. RT Edwards, Inc., 2005.
- [4] Alexander A Konnov, Akram Mohammad, Velamati Ratna Kishore, Nam Il Kim, Chockalingam Prathap, and Sudarshan Kumar. A comprehensive review of measurements and data analysis of laminar burning velocities for various fuel+ air mixtures. *Progress in Energy and Combustion Science*, 68:197–267, 2018.
- [5] Vladimir Alekseev. *Laminar burning velocity of hydrogen and flame structure of related fuels for detailed kinetic model validation*. PhD thesis, Lund University, 2015.
- [6] Anne C Brown, Carlos E Canosa-Mas, A Douglas Parr, and Richard P Wayne. Temperature dependence of the rate of the reaction between the oh radical and ketene. *Chem. Phys. Lett.*, 161(6):491–496, 1989.
- [7] C Faubel, H Gg Wagner, and W Hack. Reaktionen von kohlenstoffdioxid, teil ii die reaktion von hydroxylradikalen mit kohlenstoffdioxid und mit keten. *Ber. Bunsenges. Phys. Chem.*, 81(7):689–692, 1977.
- [8] Shiro Hatakeyama, Shigeo Honda, Nobuaki Washida, and Hajime Akimoto. Rate constants and mechanism for reactions of ketenes with oh radicals in air at 299±2k. *Bull. Chem. Soc. Jpn.*, 58(8):2157–2162, 1985.
- [9] C Oehlers, F Temps, H Gg Wagner, and M Wolf. Kinetics of the reaction of oh radicals with CH<sub>2</sub>CO. *Ber. Bunsenges. Phys. Chem.*, 96(2):171–175, 1992.
- [10] DL Baulch, Craig T Bowman, CJ Cobos, RA Cox, Th Just, JA Kerr, MJ Pilling, D Stocker, J Troe, and W Tsang. Evaluated kinetic data for combustion modeling: supplement ii. *J. Phys. Chem. Ref. Data*, 34(3):757–1397, 2005.
- [11] Judit Zádor, Ahren W Jasper, and James A Miller. The reaction between propene and hydroxyl. *Phys. Chem. Chem. Phys.*, 11(46):11040–11053, 2009.

- [12] Hua Hou, Baoshan Wang, and Yueshu Gu. Mechanism of the OH + CH<sub>2</sub>CO reaction. *Phys. Chem. Chem. Phys.*, 2(10):2329–2334, 2000.
- [13] C Endouard, F Halter, C Chauveau, and Fabrice Foucher. Effects of co<sub>2</sub>, h<sub>2</sub>o, and exhaust gas recirculation dilution on laminar burning velocities and markstein lengths of iso-octane/air mixtures. *Combustion Science and Technology*, 188(4-5):516–528, 2016.
- [14] Ossama Manna, Morkous S Mansour, William L Roberts, and Suk H Chung. Laminar burning velocities at elevated pressures for gasoline and gasoline surrogates associated with ron. *Combustion and Flame*, 162(6):2311–2321, 2015.
- [15] Y-H Liao and William L Roberts. Laminar flame speeds of gasoline surrogates measured with the flat flame method. *Energy & Fuels*, 30(2):1317–1324, 2016.
- [16] Derek Charles Nonhebel, Derek Charles Nonhebel, JC Walton, and John Christopher Walton. *Free-radical chemistry: structure and mechanism*. CUP Archive, 1974.
- [17] Alan Kéromnès, Wayne K Metcalfe, Karl A Heufer, Nicola Donohoe, Apurba K Das, Chih-Jen Sung, Jürgen Herzler, Clemens Naumann, Peter Griebel, Olivier Mathieu, et al. An experimental and detailed chemical kinetic modeling study of hydrogen and syngas mixture oxidation at elevated pressures. *Combustion and Flame*, 160(6):995–1011, 2013.
- [18] J Natarajan, S Nandula, T Lieuwen, and J Seitzman. Laminar Flame Speeds of Synthetic Gas Fuel Mixtures. *ASME Turbo Expo 2005: Power for Land, Sea, and Air*, page 677 686, 2005.
- [19] G. M. Faeth M. I. Hassan, K. T. Aung. Properties of Laminar Premixed CO/H<sub>2</sub>/Air Flames at Various Pressures. *Journal of Propulsion and Power*, 13:239–245, 1997.
- [20] Hongyan Sun, S I Yang, G Jomaas, and C K Law. High-pressure laminar flame speeds and kinetic modeling of carbon monoxide/hydrogen combustion. *Proceedings of the Combustion Institute*, 31:439 446, 2007.
- [21] C. Prathap, Anjan Ray, and M.R. Ravi. Effects of dilution with carbon dioxide on the laminar burning velocity and flame stability of H<sub>2</sub>CO mixtures at atmospheric condition. *Combustion and Flame*, 159:482–492, 2012.
- [22] Minchao Han, Yuhua Ai, Zheng Chen, and Wenjun Kong. Laminar flame speeds of H<sub>2</sub>/CO with CO<sub>2</sub> dilution at normal and elevated pressures and temperatures. *Fuel*, 148:32–38, 2015.
- [23] Z.H. Wang, W.B. Weng, Y. He, Z.S. Li, and K.F. Cen. Effect of H<sub>2</sub>/CO ratio and N<sub>2</sub>/CO<sub>2</sub> dilution rate on laminar burning velocity of syngas investigated by direct measurement and simulation. *Fuel*, 141:285–292, 2015.

- [24] Marco Di Lorenzo, Pierre Brequigny, Fabrice Foucher, and Christine Mounaïm-Rousselle. Validation of trf-e as gasoline surrogate through an experimental laminar burning speed investigation. *Fuel*, 253:1578–1588, 2019.
- [25] Marco Mehl, William J Pitz, Charles K Westbrook, and Henry J Curran. Kinetic modeling of gasoline surrogate components and mixtures under engine conditions. *Proc. Combust. Inst.*, 33(1):193–200, 2011.
- [26] Ömer L Gülder. Correlations of laminar combustion data for alternative si engine fuels. Technical report, SAE Technical Paper, 1984.
- [27] Roda Bounaceur, Oliver Herbinet, Rene Fournet, Pierre-Alexandre Glaude, Frederique Battin-Leclerc, Antonio Pires da Cruz, Mohammed Yahyaoui, Karine Truffin, and Gladys Moreac. Modeling the laminar flame speed of natural gas and gasoline surrogates. Technical report, SAE Technical Paper, 2010.
- [28] Charles K. Westbrook and Henry J. Curran. Chapter 7 Detailed kinetics of fossil and renewable fuel combustion. *Computer Aided Chemical Engineering*, 45:363–443, 2019.
- [29] Antonio Cavaliere and Mara de Joannon. Mild combustion. *Progress in Energy and Combustion science*, 30(4):329–366, 2004.
- [30] Hyun Kyu Suh. Investigations of multiple injection strategies for the improvement of combustion and exhaust emissions characteristics in a low compression ratio (cr) engine. *Applied Energy*, 88(12):5013–5019, 2011.
- [31] G Najafi, B Ghobadian, T Tavakoli, DR Buttsworth, TF Yusaf, and M Faizollahnejad. Performance and exhaust emissions of a gasoline engine with ethanol blended gasoline fuels using artificial neural network. *Applied Energy*, 86(5):630–639, 2009.
- [32] Dae Hee Lee, Jun Sik Lee, and Jae Suk Park. Effects of secondary combustion on efficiencies and emission reduction in the diesel engine exhaust heat recovery system. *Applied energy*, 87(5):1716–1721, 2010.
- [33] Haiqiao Wei, Tianyu Zhu, Gequn Shu, Linlin Tan, and Yuesen Wang. Gasoline engine exhaust gas recirculation—a review. *Applied energy*, 99:534–544, 2012.
- [34] Galloni Fontana and E Galloni. Experimental analysis of a spark-ignition engine using exhaust gas recycle at wot operation. *Applied Energy*, 87(7):2187–2193, 2010.
- [35] Michele Kaiser, Uwe Krueger, Roderick Harris, and Luke Cruff. doing more with less—the fuel economy benefits of cooled egr on a direct injected spark ignited boosted engine. Technical report, SAE Technical Paper, 2010.
- [36] Gamal Hassan Abd-Alla. Using exhaust gas recirculation in internal combustion engines: a review. *Energy Conversion and Management*, 43(8):1027–1042, 2002.



- [37] Fatih Sarikoc, Maurice Kettner, Amin Velji, Ulrich Spicher, Alina Krause, and Alfred Elsaesser. Potential of reducing the nox emissions in a spray guided di gasoline engine by stratified exhaust gas recirculation (egr). Technical report, SAE Technical Paper, 2006.
- [38] G Fontana and E Galloni. Variable valve timing for fuel economy improvement in a small spark-ignition engine. *Applied Energy*, 86(1):96–105, 2009.
- [39] Yun-long Bai, Zhi Wang, and Jian-xin Wang. Part-load characteristics of direct injection spark ignition engine using exhaust gas trap. *Applied Energy*, 87(8):2640–2646, 2010.
- [40] Zulfukar Ali Ahmed and Dinesh Kumar Sharma. A modelling and analysis of exhaust gas recirculation system to lower the nox emission from internal combustion engine: a review on advanced and novel concepts. *International Journal of Renewable Energy Technology*, 9(1-2):118–135, 2018.
- [41] Deepak Agarwal, Shrawan Kumar Singh, and Avinash Kumar Agarwal. Effect of exhaust gas recirculation (egr) on performance, emissions, deposits and durability of a constant speed compression ignition engine. *Applied energy*, 88(8):2900–2907, 2011.
- [42] Rowland S Benson and Norman Dan Whitehouse. *Internal combustion engines: a detailed introduction to the thermodynamics of spark and compression ignition engines, their design and development*, volume 1. Elsevier, 2013.
- [43] George A Lavoie, John B Heywood, and James C Keck. Experimental and theoretical study of nitric oxide formation in internal combustion engines. *Combustion science and technology*, 1(4):313–326, 1970.
- [44] Yiannis A Leventis, Iraklis Pavlatos, and Richard F Abrams. Control of diesel soot, hydrocarbon and nox emissions with a particulate trap and egr. Technical report, SAE Technical Paper, 1994.
- [45] Börje Grandin, Hans-Erik Ångström, Per Stålhammar, and Eric Olofsson. Knock suppression in a turbocharged si engine by using cooled egr. Technical report, SAE Technical Paper, 1998.
- [46] Börje Grandin and Hans-Erik Ångström. Replacing fuel enrichment in a turbo charged si engine: lean burn or cooled egr. Technical report, SAE Technical Paper, 1999.
- [47] Sebastien Potteau, Philippe Lutz, Samuel Leroux, Stephanie Moroz, and Eva Tomas. Cooled egr for a turbo si engine to reduce knocking and fuel consumption. Technical report, SAE Technical Paper, 2007.
- [48] William J Pitz, Nicholas P Cernansky, Frederick L Dryer, FN Egolfopoulos, JT Farrell, Daniel G Friend, and H Pitsch. Development of an experimental database and chemical kinetic models for surrogate gasoline fuels. Technical report, SAE Technical Paper, 2007.

- [49] JT Farrell, NP Cernansky, FL Dryer, CK Law, DG Friend, CA Hergart, RM McDavid, AK Patel, Charles J Mueller, and H Pitsch. Development of an experimental database and kinetic models for surrogate diesel fuels. Technical report, SAE Technical Paper, 2007.
- [50] William J Pitz and Charles J Mueller. Recent progress in the development of diesel surrogate fuels. *Progress in Energy and Combustion Science*, 37(3):330–350, 2011.
- [51] D Bradley, RA Hicks, M Lawes, CGW Sheppard, and R Woolley. The measurement of laminar burning velocities and markstein numbers for iso-octane–air and iso-octane–n-heptane–air mixtures at elevated temperatures and pressures in an explosion bomb. *Combustion and flame*, 115(1-2):126–144, 1998.
- [52] Y Huang, CJ Sung, and JA Eng. Laminar flame speeds of primary reference fuels and reformer gas mixtures. *Combustion and Flame*, 139(3):239–251, 2004.
- [53] JPJ Van Lipzig, EJK Nilsson, LPH De Goey, and A Alexander Konnov. Laminar burning velocities of n-heptane, iso-octane, ethanol and their binary and tertiary mixtures. *Fuel*, 90(8):2773–2781, 2011.
- [54] Zhenwei Zhao, Jordan P Conley, Andrei Kazakov, and Frederick L Dryer. Burning velocities of real gasoline fuel at 353 k and 500 k. *SAE transactions*, pages 2624–2629, 2003.
- [55] S Jerzembeck, N Peters, Pitsch Pepiot-Desjardins, and H Pitsch. Laminar burning velocities at high pressure for primary reference fuels and gasoline: Experimental and numerical investigation. *Combustion and Flame*, 156(2):292–301, 2009.
- [56] Louis Sileghem, VA Alekseev, Jeroen Vancoillie, KM Van Geem, EJK Nilsson, Sebastian Verhelst, and AA Konnov. Laminar burning velocity of gasoline and the gasoline surrogate components iso-octane, n-heptane and toluene. *Fuel*, 112:355–365, 2013.
- [57] Patricia Dirrenberger, Pierre-Alexandre Glaude, Roda Bounaceur, Hervé Le Gall, A Pires da Cruz, AA Konnov, and F Battin-Leclerc. Laminar burning velocity of gasolines with addition of ethanol. *Fuel*, 115:162–169, 2014.
- [58] Ossama A Manna, Morkous S Mansour, William L Roberts, and Suk Ho Chung. Laminar burning velocities of fuels for advanced combustion engines (face) gasoline and gasoline surrogates with and without ethanol blending associated with octane rating. *Combustion Science and Technology*, 188(4-5):692–706, 2016.
- [59] Charles K Westbrook, Marco Mehl, William J Pitz, and Magnus Sjöberg. Chemical kinetics of octane sensitivity in a spark-ignition engine. *Combustion and Flame*, 175:2–15, 2017.

- [60] S Mani Sarathy, Aamir Farooq, and Gautam T Kalghatgi. Recent progress in gasoline surrogate fuels. *Progress in Energy and Combustion Science*, 65:67–108, 2018.
- [61] Thomas W. Ryan and Samuel S. Lestz. The laminar burning velocity of isooctane, n-heptane, methanol, methane, and propane at elevated temperature and pressures in the presence of a diluent. In *SAE Technical Paper*. SAE International, 02 1980.
- [62] Mohamad Metghalchi and James C Keck. Burning velocities of mixtures of air with methanol, isooctane, and indolene at high pressure and temperature. *Combustion and flame*, 48:191–210, 1982.
- [63] mer L. Glder. Correlations of laminar combustion data for alternative s.i. engine fuels. In *SAE Technical Paper*. SAE International, 08 1984.
- [64] David B. Rhodes and James C. Keck. Laminar burning speed measurements of indolene-air-diluent mixtures at high pressures and temperatures. In *SAE Technical Paper*. SAE International, 02 1985.
- [65] Kamal Kumar, JE Freeh, CJ Sung, and Y Huang. Laminar flame speeds of preheated iso-octane/o<sub>2</sub>/n<sub>2</sub> and n-heptane/o<sub>2</sub>/n<sub>2</sub> mixtures. *Journal of propulsion and power*, 23(2):428–436, 2007.
- [66] Fabien Halter, Fabrice Foucher, Ludovic Landry, and Christine Mounaïm-Rousselle. Effect of dilution by nitrogen and/or carbon dioxide on methane and iso-octane air flames. *Combustion Science and Technology*, 181(6):813–827, 2009.
- [67] AJ Smallbone, W Liu, CK Law, XQ You, and H Wang. Experimental and modeling study of laminar flame speed and non-premixed counterflow ignition of n-heptane. *Proceedings of the Combustion Institute*, 32(1):1245–1252, 2009.
- [68] Toni Tahtouh, Fabien Halter, and Christine Mounaïm-Rousselle. Laminar premixed flame characteristics of hydrogen blended iso-octane–air–nitrogen mixtures. *International Journal of Hydrogen Energy*, 36(1):985–991, 2011.
- [69] SP Marshall, S Taylor, CR Stone, TJ Davies, and RF Cracknell. Laminar burning velocity measurements of liquid fuels at elevated pressures and temperatures with combustion residuals. *Combustion and Flame*, 158(10):1920–1932, 2011.
- [70] JX Zhou, Mathieu Cordier, Christine Mounaïm-Rousselle, and Fabrice Foucher. Experimental estimate of the laminar burning velocity of iso-octane in oxygen-enriched and co<sub>2</sub>-diluted air. *Combustion and Flame*, 158(12):2375–2383, 2011.
- [71] Bénédicte Galmiche, Fabien Halter, and Fabrice Foucher. Effects of high pressure, high temperature and dilution on laminar burning velocities and markstein lengths of iso-octane/air mixtures. *Combustion and Flame*, 159(11):3286–3299, 2012.

- [72] Tobias Knorsch, Andreas Zackel, Dmitrii Mamaikin, Lars Zigan, and Michael Wensing. Comparison of different gasoline alternative fuels in terms of laminar burning velocity at increased gas temperatures and exhaust gas recirculation rates. *Energy & Fuels*, 28(2):1446–1452, 2014.
- [73] Atmadeep Bhattacharya, Deb Kumar Banerjee, Dmitrii Mamaikin, Amitava Datta, and Michael Wensing. Effects of exhaust gas dilution on the laminar burning velocity of real-world gasoline fuel flame in air. *Energy & Fuels*, 29(10):6768–6779, 2015.
- [74] O Manna, MS Mansour, WL Roberts, and SH Chung. Effects of residual combustion gases at elevated pressures on laminar burning velocities for gasoline and gasoline surrogate. In *European Combustion Meeting*, pages 2–7, 2015.
- [75] Ossama A Manna, Morkous S Mansour, William L Roberts, and Suk Ho Chung. Influence of ethanol and exhaust gas recirculation on laminar burning behaviors of fuels for advanced combustion engines (face-c) gasoline and its surrogate. *Energy & fuels*, 31(12):14104–14115, 2017.
- [76] Berk Can Duva, Lauren Chance, and Elisa Toulson. Laminar flame speeds of premixed iso-octane/air flames at high temperatures with co2 dilution. In *WCX SAE World Congress Experience*. SAE International, apr 2019.
- [77] Ömer L Gülder. Laminar burning velocities of methanol, ethanol and iso-octane-air mixtures. In *Symposium (international) on combustion*, volume 19, pages 275–281. Elsevier, 1982.
- [78] C Hasse, M Bollig, N Peters, and HA Dwyer. Quenching of laminar iso-octane flames at cold walls. *Combustion and flame*, 122(1-2):117–129, 2000.
- [79] Marcos Chaos, Andrei Kazakov, Zhenwei Zhao, and Frederick L Dryer. A high-temperature chemical kinetic model for primary reference fuels. *International Journal of Chemical Kinetics*, 39(7):399–414, 2007.
- [80] John B Heywood. *Internal combustion engine fundamentals*. Mcgraw-hill, 1988.
- [81] Iltesham Z Syed, Yeliana, Abhijit Mukherjee, Jeffrey D Naber, and Donna Michalek. Numerical investigation of laminar flame speed of gasoline-ethanol/air mixtures with varying pressure, temperature and dilution. *SAE International Journal of Engines*, 3(1):517–528, 2010.
- [82] Johan CG Andrae and RA Head. Hcci experiments with gasoline surrogate fuels modeled by a semidetailed chemical kinetic model. *Combustion and flame*, 156(4):842–851, 2009.
- [83] Jianqin Fu, Banglin Deng, Yi Wang, Jing Yang, Daming Zhang, Zhengxin Xu, and Jingping Liu. Numerical study and correlation development on laminar burning velocities of n-butanol, iso-octane and their blends: focusing on diluent and blend ratio effects. *Fuel*, 124:102–112, 2014.

- [84] E Ranzi, A Frassoldati, R Grana, A Cuoci, T Faravelli, AP Kelley, and CK Law. Hierarchical and comparative kinetic modeling of laminar flame speeds of hydrocarbon and oxygenated fuels. *Progress in Energy and Combustion Science*, 38(4):468–501, 2012.
- [85] Henry J Curran. Developing detailed chemical kinetic mechanisms for fuel combustion. *Proceedings of the Combustion Institute*, 37(1):57–81, 2019.
- [86] Stephen Dooley, Sang Hee Won, Joshua Heyne, Tanvir I. Farouk, Yiguang Ju, Frederick L. Dryer, Kamal Kumar, Xin Hui, Chih-Jen Sung, Haowei Wang, Matthew A. Oehlschlaeger, Venkatesh Iyer, Suresh Iyer, Thomas A. Litzinger, Robert J. Santoro, Tomasz Malewicki, and Kenneth Brezinsky. The experimental evaluation of a methodology for surrogate fuel formulation to emulate gas phase combustion kinetic phenomena. *Combustion and Flame*, 159:1444–1466, 2012.
- [87] Juan Li, Zhenwei Zhao, Andrei Kazakov, and Frederick L. Dryer. An updated comprehensive kinetic model of hydrogen combustion. *International Journal of Chemical Kinetics*, 36:566–575, 2004.
- [88] Marcus Conaire, Henry J Curran, John M Simmie, William J Pitz, and Charles K Westbrook. A comprehensive modeling study of hydrogen oxidation. *International Journal of Chemical Kinetics*, 36:603–622, 2004.
- [89] Alexander A Konnov. Remaining uncertainties in the kinetic mechanism of hydrogen combustion. *Combustion and Flame*, 152:507–528, 2008.
- [90] Zekai Hong, David F Davidson, and Ronald K Hanson. An improved H<sub>2</sub>/O<sub>2</sub> mechanism based on recent shock tube/laser absorption measurements. *Combustion and Flame*, 158:633–644, 2011.
- [91] Michael P Burke, Marcos Chaos, Yiguang Ju, Frederick L Dryer, and Stephen J Klippenstein. Comprehensive H<sub>2</sub>/O<sub>2</sub> kinetic model for high-pressure combustion. *International Journal of Chemical Kinetics*, 44:444–474, 2011.
- [92] Carsten Olm, István Gy Zsély, Róbert Pálvölgyi, Tamás Varga, Tibor Nagy, Henry J Curran, and Tamás Turányi. Comparison of the performance of several recent hydrogen combustion mechanisms. *Combustion and Flame*, 161(9):2219–2234, 2014.
- [93] Vladimir A. Alekseev and Alexander A. Konnov. Data consistency of the burning velocity measurements using the heat flux method: Hydrogen flames. *Combustion and Flame*, 194(Ann. Phys. Chem. 207 6 1867):28–36, 8 2018.
- [94] Alexander A. Konnov. On the role of excited species in hydrogen combustion. *Combustion and Flame*, 162:3755–3772, 2015.
- [95] Michael P. Burke and Stephen J. Klippenstein. Ephemeral collision complexes mediate chemically termolecular transformations that affect system chemistry. *Nature Chemistry*, 9:1078, 2017.

- [96] Rex T. Skodje. Gas-phase chemical kinetics: Three is the magic number. *Nature Chemistry*, 9:1038–1039, 2017.
- [97] Mark C. Barbet, Kevin McCullough, and Michael P. Burke. A framework for automatic discovery of chemically termolecular reactions. *Proceedings of the Combustion Institute*, 2018.
- [98] Alexander A. Konnov. Yet another kinetic mechanism for hydrogen combustion. *Combustion and Flame*, 203:14–22, 2019.
- [99] Ahren W Jasper, Eugene Kamarchik, James A Miller, and Stephen J Klippenstein. First-principles binary diffusion coefficients for h, h<sub>2</sub>, and four normal alkanes+ n<sub>2</sub>. *The Journal of chemical physics*, 141(12):124313, 2014.
- [100] Ahren W Jasper and James A Miller. Lennard–jones parameters for combustion and chemical kinetics modeling from full-dimensional intermolecular potentials. *Combustion and Flame*, 161(1):101–110, 2014.
- [101] D Healy, DM Kalitan, CJ Aul, EL Petersen, G Bourque, and HJ Curran. Oxidation of c1- c5 alkane quinary natural gas mixtures at high pressures. *Energy & Fuels*, 24(3):1521–1528, 2010.
- [102] Scott G. Davis, Ameya V. Joshi, Hai Wang, and Fokion Egolfopoulos. An optimized kinetic model of H<sub>2</sub>/CO combustion. *Proceedings of the Combustion Institute*, 30:1283–1292, 2005.
- [103] Juan Li, Zhenwei Zhao, Andrei Kazakov, Marcos Chaos, Frederick L. Dryer, and James J. Scire. A comprehensive kinetic mechanism for CO, CH<sub>2</sub>O, and CH<sub>3</sub>OH combustion. *International Journal of Chemical Kinetics*, 39:109–136, 2007.
- [104] Hai Wang, Xiaoqing You, Ameya V Joshi, Scott G Davis, Alexander Laskin, Fokion Egolfopoulos, and Chung K Law. *USC Mech version II. High-temperature combustion reaction model of H<sub>2</sub>/CO/C<sub>1</sub>–C<sub>4</sub> compounds*, 2007.
- [105] Ralph E Weston, Thanh Lam Nguyen, John F Stanton, and John R Barker. HO + CO Reaction Rates and H/D Kinetic Isotope Effects: Master Equation Models with ab Initio SCTST Rate Constants. *The Journal of Physical Chemistry A*, 117:821–835, 2013.
- [106] Artem E Masunov, Elizabeth Wait, and Subith S Vasu. Chemical reaction CO + OH → CO<sub>2</sub> + H autocatalyzed by carbon dioxide: quantum chemical study of the potential energy surfaces. *The Journal of Physical Chemistry A*, 120(30):6023–6028, 2016.
- [107] Linyao Zhang, Li Yang, Yijun Zhao, Jiayu Zhang, Dongdong Feng, and Shaozeng Sun. Effects of Water Molecule on CO Oxidation by OH: Reaction Pathways, Kinetic Barriers and Rate Constants. *The Journal of Physical Chemistry A*, 121:4868–4880, 2017.

- [108] Gregory P Smith, David M Golden, Michael Frenklach, Nigel W Morarty, Boris Eiteneer, Mikhail Goldenberg, C Thomas Bowman, Ronald K Hanson, Soonho Song, WC Gardiner Jr, et al. Gri-mech 3.0. URL [http://www.me.berkeley.edu/gri\\_mech](http://www.me.berkeley.edu/gri_mech), 1999.
- [109] Wayne K Metcalfe, Sinéad M Burke, Syed S Ahmed, and Henry J Curran. A hierarchical and comparative kinetic modeling study of c1- c2 hydrocarbon and oxygenated fuels. *International Journal of Chemical Kinetics*, 45(10):638–675, 2013.
- [110] Sinéad M Burke, Wayne Metcalfe, Olivier Herbinet, Frédérique Battin-Leclerc, Francis M Haas, Jeffrey Santner, Frederick L Dryer, and Henry J Curran. An experimental and modeling study of propene oxidation. part 1: Speciation measurements in jet-stirred and flow reactors. *Combustion and Flame*, 161(11):2765–2784, 2014.
- [111] Sinéad M Burke, Ultan Burke, Reuben Mc Donagh, Olivier Mathieu, Irmis Osorio, Charles Keesee, Anibal Morones, Eric L Petersen, Weijing Wang, Trent A DeVerter, et al. An experimental and modeling study of propene oxidation. part 2: Ignition delay time and flame speed measurements. *Combustion and Flame*, 162(2):296–314, 2015.
- [112] Chong-Wen Zhou, Yang Li, Eoin O’Connor, Kieran P Somers, Sébastien Thion, Charles Keesee, Olivier Mathieu, Eric L Petersen, Trent A DeVerter, Matthew A Oehlschlaeger, et al. A comprehensive experimental and modeling study of isobutene oxidation. *Combustion and Flame*, 167:353–379, 2016.
- [113] Chong-Wen Zhou, Yang Li, Ultan Burke, Colin Banyon, Kieran P Somers, Shuiting Ding, Saadat Khan, Joshua W Hargis, Travis Sikes, Olivier Mathieu, et al. An experimental and chemical kinetic modeling study of 1,3-butadiene combustion: Ignition delay time and laminar flame speed measurements. *Combustion and Flame*, 197:423–438, 2018.
- [114] John Bugler, Kieran P Somers, Emma J Silke, and Henry J Curran. Revisiting the kinetics and thermodynamics of the low-temperature oxidation pathways of alkanes: a case study of the three pentane isomers. *The Journal of Physical Chemistry A*, 119(28):7510–7527, 2015.
- [115] John Bugler, Brandon Marks, Olivier Mathieu, Rachel Archuleta, Alejandro Camou, Claire Grégoire, Karl A Heufer, Eric L Petersen, and Henry J Curran. An ignition delay time and chemical kinetic modeling study of the pentane isomers. *Combustion and Flame*, 163:138–156, 2016.
- [116] John M Simmie. Detailed chemical kinetic models for the combustion of hydrocarbon fuels. *Progress in energy and combustion science*, 29(6):599–634, 2003.
- [117] S Mani Sarathy, Charles K Westbrook, Marco Mehl, William J Pitz, Casimir Togbe, Philippe Dagaut, Hai Wang, Matthew A Oehlschlaeger, Ulrich Niemann, Kalyanasundaram Seshadri, et al. Comprehensive chemical kinetic

- modeling of the oxidation of 2-methylalkanes from c7 to c20. *Combustion and flame*, 158(12):2338–2357, 2011.
- [118] Charles K Westbrook, William J Pitz, Olivier Herbinet, Henry J Curran, and Emma J Silke. A comprehensive detailed chemical kinetic reaction mechanism for combustion of n-alkane hydrocarbons from n-octane to n-hexadecane. *Combustion and flame*, 156(1):181–199, 2009.
- [119] Chunsheng Ji, Enoch Dames, Yang L Wang, Hai Wang, and Fokion N Egolopoulos. Propagation and extinction of premixed c5–c12n-alkane flames. *Combustion and Flame*, 157(2):277–287, 2010.
- [120] Charles K Westbrook, Jürgen Warnatz, and William J Pitz. A detailed chemical kinetic reaction mechanism for the oxidation of iso-octane and n-heptane over an extended temperature range and its application to analysis of engine knock. In *Symposium (International) on Combustion*, volume 22(1), pages 893–901. Elsevier, 1989.
- [121] Eliseo Ranzi, Paolo Gaffuri, Tiziano Faravelli, and Philippe Dagaut. A wide-range modeling study of n-heptane oxidation. *Combustion and Flame*, 103(1-2):91–106, 1995.
- [122] C Chevalier, WJ Pitz, J Warnatz, CK Westbrook, and H Melenk. Hydrocarbon ignition: automatic generation of reaction mechanisms and applications to modeling of engine knock. In *Symposium (International) on Combustion*, volume 24(1), pages 93–101. Elsevier, 1992.
- [123] GM Côme, V Warth, PA Glaude, R Fournet, F Battin-Leclerc, and G Scacchi. Computer-aided design of gas-phase oxidation mechanisms application to the modeling of n-heptane and iso-octane oxidation. In *Symposium (International) on Combustion*, volume 26(1), pages 755–762. Elsevier, 1996.
- [124] Henry J Curran, Paolo Gaffuri, William J Pitz, and Charles K Westbrook. A comprehensive modeling study of n-heptane oxidation. *Combustion and flame*, 114(1-2):149–177, 1998.
- [125] Olivier Herbinet, Benoit Husson, Zeynep Serinyel, Maximilien Cord, Valérie Warth, René Fournet, Pierre-Alexandre Glaude, Baptiste Sirjean, Frédérique Battin-Leclerc, Zhandong Wang, et al. Experimental and modeling investigation of the low-temperature oxidation of n-heptane. *Combustion and flame*, 159(12):3455–3471, 2012.
- [126] Matteo Pelucchi, Mattia Bissoli, Carlo Cavallotti, Alberto Cuoci, Tiziano Faravelli, Alessio Frassoldati, Eliseo Ranzi, and Alessandro Stagni. Improved kinetic model of the low-temperature oxidation of n-heptane. *Energy & Fuels*, 28(11):7178–7193, 2014.
- [127] Lars Seidel, Kai Moshhammer, Xiaoxiao Wang, Thomas Zeuch, Katharina Kohse-Höinghaus, and Fabian Mauss. Comprehensive kinetic modeling and experimental study of a fuel-rich, premixed n-heptane flame. *Combustion and Flame*, 162(5):2045–2058, 2015.



- [128] Kuiwen Zhang, Colin Banyon, John Bugler, Henry J Curran, Anne Rodriguez, Olivier Herbinet, Frédérique Battin-Leclerc, Christine B'Chir, and Karl Alexander Heufer. An updated experimental and kinetic modeling study of n-heptane oxidation. *Combustion and Flame*, 172:116–135, 2016.
- [129] SM Burke, JM Simmie, and HJ Curran. Critical evaluation of thermochemical properties of c1–c4 species: updated group-contributions to estimate thermochemical properties. *Journal of Physical and Chemical Reference Data*, 44(1):013101, 2015.
- [130] Henry J Curran, Paolo Gaffuri, William J Pitz, and Charles K Westbrook. A comprehensive modeling study of iso-octane oxidation. *Combustion and flame*, 129(3):253–280, 2002.
- [131] M Hartmann, I Gushterova, M Fikri, C Schulz, R Schießl, and U Maas. Auto-ignition of toluene-doped n-heptane and iso-octane/air mixtures: High-pressure shock-tube experiments and kinetics modeling. *Combustion and Flame*, 158(1):172–178, 2011.
- [132] M Mehl, WJ Pitz, M Sjöberg, and John E Dec. Detailed kinetic modeling of low-temperature heat release for prf fuels in an hcci engine. Technical report, SAE Technical Paper, 2009.
- [133] S Mani Sarathy, Goutham Kukkadapu, Marco Mehl, Weijing Wang, Tamour Javed, Sungwoo Park, Matthew A Oehlschlaeger, Aamir Farooq, William J Pitz, and Chih-Jen Sung. Ignition of alkane-rich face gasoline fuels and their surrogate mixtures. *Proceedings of the Combustion Institute*, 35(1):249–257, 2015.
- [134] David Vuilleumier, Hatem Selim, Robert Dibble, and Mani Sarathy. Exploration of heat release in a homogeneous charge compression ignition engine with primary reference fuels. Technical report, SAE Technical Paper, 2013.
- [135] Wontae Hwang, John Dec, and Magnus Sjöberg. Spectroscopic and chemical-kinetic analysis of the phases of hcci autoignition and combustion for single- and two-stage ignition fuels. *Combustion and Flame*, 154(3):387–409, 2008.
- [136] Nour Atef, Goutham Kukkadapu, Samah Y Mohamed, Mariam Al Rashidi, Colin Banyon, Marco Mehl, Karl Alexander Heufer, Ehson F Nasir, Adamu Alfazazi, Apurba K Das, et al. A comprehensive iso-octane combustion model with improved thermochemistry and chemical kinetics. *Combustion and Flame*, 178:111–134, 2017.
- [137] Suarwee Snitsiriwat and Joseph W Bozzelli. Thermochemical properties for isooctane and carbon radicals: computational study. *The Journal of Physical Chemistry A*, 117(2):421–429, 2013.
- [138] Itsaso Auzmendi-Murua and Joseph W Bozzelli. Thermochemistry, reaction paths, and kinetics on the secondary isooctane radical reaction with 3o2. *International Journal of Chemical Kinetics*, 46(2):71–103, 2014.

- [139] Suarwee Snitsiriwat and Joseph W Bozzelli. Thermochemistry, reaction paths, and kinetics on the tert-isooctane radical reaction with  $\text{o}_2$ . *The Journal of Physical Chemistry A*, 118(26):4631–4646, 2014.
- [140] HongBo Ning, ChunMing Gong, ZeRong Li, and XiangYuan Li. Pressure-dependent kinetics of initial reactions in iso-octane pyrolysis. *The Journal of Physical Chemistry A*, 119(18):4093–4107, 2015.
- [141] Zhandong Wang and S Mani Sarathy. Third  $\text{o}_2$  addition reactions promote the low-temperature auto-ignition of n-alkanes. *Combustion and Flame*, 165:364–372, 2016.
- [142] Judit Zádor, Craig A Taatjes, and Ravi X Fernandes. Kinetics of elementary reactions in low-temperature autoignition chemistry. *Progress in energy and combustion science*, 37(4):371–421, 2011.
- [143] S Mani Sarathy, Sungwoo Park, Bryan W Weber, Weijing Wang, Peter S Veloo, Alexander C Davis, Casimir Togbe, Charles K Westbrook, Okjoo Park, Guillaume Dayma, et al. A comprehensive experimental and modeling study of iso-pentanol combustion. *Combustion and flame*, 160(12):2712–2728, 2013.
- [144] Judit Zádor, Ravi X Fernandes, Yuri Georgievskii, Giovanni Meloni, Craig A Taatjes, and James A Miller. The reaction of hydroxyethyl radicals with  $\text{o}_2$ : A theoretical analysis and experimental product study. *Proceedings of the Combustion Institute*, 32(1):271–277, 2009.
- [145] Gabriel da Silva, Joseph W Bozzelli, Long Liang, and John T Farrell. Ethanol oxidation: Kinetics of the  $\alpha$ -hydroxyethyl radical+  $\text{o}_2$  reaction. *The Journal of Physical Chemistry A*, 113(31):8923–8933, 2009.
- [146] K Alexander Heufer, S Mani Sarathy, Henry J Curran, Alexander C Davis, Charles K Westbrook, and William J Pitz. Detailed kinetic modeling study of n-pentanol oxidation. *Energy & Fuels*, 26(11):6678–6685, 2012.
- [147] Casimir Togbe, Philippe Dagaut, A Mz -Ahmed, P Di vart, Fabien Halter, and Fabrice Foucher. Experimental and detailed kinetic modeling study of 1-hexanol oxidation in a pressurized jet-stirred reactor and a combustion bomb. *Energy & Fuels*, 24(11):5859–5875, 2010.
- [148] Liming Cai, Yasar Uygun, Casimir Togb , Heinz Pitsch, Herbert Olivier, Philippe Dagaut, and S Mani Sarathy. An experimental and modeling study of n-octanol combustion. *Proceedings of the Combustion Institute*, 35(1):419–427, 2015.
- [149] Fokion N Egolfopoulos, DX Du, and Chung King Law. A study on ethanol oxidation kinetics in laminar premixed flames, flow reactors, and shock tubes. In *Symposium (international) on combustion*, volume 24(1), pages 833–841. Elsevier, 1992.
- [150] Nick M Marinov. A detailed chemical kinetic model for high temperature ethanol oxidation. *International Journal of Chemical Kinetics*, 31(3):183–220, 1999.

- [151] Juan Li, Andrei Kazakov, and Frederick L Dryer. Experimental and numerical studies of ethanol decomposition reactions. *The Journal of Physical Chemistry A*, 108(38):7671–7680, 2004.
- [152] Priyank Saxena and Forman A Williams. Numerical and experimental studies of ethanol flames. *Proceedings of the Combustion Institute*, 31(1):1149–1156, 2007.
- [153] LR Cancino, M Fikri, AAM Oliveira, and C Schulz. Measurement and chemical kinetics modeling of shock-induced ignition of ethanol- air mixtures. *Energy & Fuels*, 24(5):2830–2840, 2010.
- [154] Nicolas Leplat, P Dagaut, C Togbé, and Jacques Vandooren. Numerical and experimental study of ethanol combustion and oxidation in laminar premixed flames and in jet-stirred reactor. *Combustion and Flame*, 158(4):705–725, 2011.
- [155] Changyoul Lee, Stijn Vranckx, Karl A Heufer, Sergey V Khomik, Yasar Uygun, Herbert Olivier, and Ravi X Fernandez. On the chemical kinetics of ethanol oxidation: shock tube, rapid compression machine and detailed modeling study. *Zeitschrift für Physikalische Chemie*, 226(1):1–28, 2012.
- [156] Yingjia Zhang, Hilal El-Merhubi, Benoîte Lefort, Luis Le Moyne, Henry J Curran, and Alan Kéromnès. Probing the low-temperature chemistry of ethanol via the addition of dimethyl ether. *Combustion and Flame*, 190:74–86, 2018.
- [157] Gaurav Mittal, Sinéad M Burke, Varun A Davies, Bikash Parajuli, Wayne K Metcalfe, and Henry J Curran. Autoignition of ethanol in a rapid compression machine. *Combustion and Flame*, 161(5):1164–1171, 2014.
- [158] Roda Bounaceur, Isabelle Da Costa, René Fournet, Francis Billaud, and Frédérique Battin-Leclerc. Experimental and modeling study of the oxidation of toluene. *International journal of chemical kinetics*, 37(1):25–49, 2005.
- [159] Alexander Burcat, Christopher Snyder, and Theodore Brabbs. Ignition delay times of benzene and toluene with oxygen in argon mixtures. *NASA Technical Memorandum 87312*, 1985.
- [160] DF Davidson, BM Gauthier, and RK Hanson. Shock tube ignition measurements of iso-octane/air and toluene/air at high pressures. *Proceedings of the Combustion Institute*, 30(1):1175–1182, 2005.
- [161] V Vasudevan, DF Davidson, and RK Hanson. Shock tube measurements of toluene ignition times and oh concentration time histories. *Proceedings of the Combustion Institute*, 30(1):1155–1163, 2005.
- [162] Gaurav Mittal and Chih-Jen Sung. Autoignition of toluene and benzene at elevated pressures in a rapid compression machine. *Combustion and Flame*, 150(4):355–368, 2007.

- [163] Hsi-Ping S Shen, Jeremy Vanderover, and Matthew A Oehlschlaeger. A shock tube study of the auto-ignition of toluene/air mixtures at high pressures. *Proceedings of the Combustion Institute*, 32(1):165–172, 2009.
- [164] Subith S Vasu, David F Davidson, and Ronald K Hanson. Shock-tube experiments and kinetic modeling of toluene ignition. *Journal of propulsion and power*, 26(4):776–783, 2010.
- [165] SG Davis and Chung King Law. Determination of and fuel structure effects on laminar flame speeds of c1 to c8 hydrocarbons. *Combustion Science and Technology*, 140(1-6):427–449, 1998.
- [166] T Hirasawa, CJ Sung, A Joshi, Z Yang, H Wang, and Chung King Law. Determination of laminar flame speeds using digital particle image velocimetry: binary fuel blends of ethylene, n-butane, and toluene. *Proceedings of the Combustion Institute*, 29(2):1427–1434, 2002.
- [167] Xin Hui, Apurba K Das, Kamal Kumar, Chih-Jen Sung, Stephen Dooley, and Frederick L Dryer. Laminar flame speeds and extinction stretch rates of selected aromatic hydrocarbons. *Fuel*, 97:695–702, 2012.
- [168] Chunsheng Ji, Enoch Dames, Hai Wang, and Fokion N Egolfopoulos. Propagation and extinction of benzene and alkylated benzene flames. *Combustion and Flame*, 159(3):1070–1081, 2012.
- [169] RJ Johnston and JT Farrell. Laminar burning velocities and markstein lengths of aromatics at elevated temperature and pressure. *Proceedings of the combustion institute*, 30(1):217–224, 2005.
- [170] K Brezinsky, TA Litzinger, and Int Glassman. The high temperature oxidation of the methyl side chain of toluene. *International journal of chemical kinetics*, 16(9):1053–1074, 1984.
- [171] K Brezinsky, AB Lovell, and I Glassman. The oxidation of toluene perturbed by no2. *Combustion science and technology*, 70(1-3):33–46, 1990.
- [172] JL Emdee, Ka Brezinsky, and I Glassman. A kinetic model for the oxidation of toluene near 1200 k. *The Journal of Physical Chemistry*, 96(5):2151–2161, 1992.
- [173] Stephen D Klotz, Kenneth Brezinsky, and Irvin Glassman. Modeling the combustion of toluene-butane blends. In *Symposium (International) on Combustion*, volume 27(1), pages 337–344. Elsevier, 1998.
- [174] P Dagaut, G Pengloan, and A Ristori. Oxidation, ignition and combustion of toluene: Experimental and detailed chemical kinetic modeling. *Physical Chemistry Chemical Physics*, 4(10):1846–1854, 2002.
- [175] I Da Costa, R Fournet, F Billaud, and F Battin-Leclerc. Experimental and modeling study of the oxidation of benzene. *International journal of chemical kinetics*, 35(10):503–524, 2003.

- [176] R Sivaramakrishnan, RS Tranter, and K Brezinsky. High-pressure, high-temperature oxidation of toluene. *Combustion and flame*, 139(4):340–350, 2004.
- [177] R Sivaramakrishnan, RS Tranter, and K Brezinsky. A high pressure model for the oxidation of toluene. *Proceedings of the combustion institute*, 30(1):1165–1173, 2005.
- [178] WK Metcalfe, S Dooley, and FL Dryer. Comprehensive detailed chemical kinetic modeling study of toluene oxidation. *Energy & Fuels*, 25(11):4915–4936, 2011.
- [179] Yuyang Li, Jianghuai Cai, Lidong Zhang, Tao Yuan, Kuiwen Zhang, and Fei Qi. Investigation on chemical structures of premixed toluene flames at low pressure. *Proceedings of the Combustion Institute*, 33(1):593–600, 2011.
- [180] A Hamins and K Seshadri. The structure of diffusion flames burning pure, binary, and ternary solutions of methanol, heptane, and toluene. *Combustion and flame*, 68(3):295–307, 1987.
- [181] Valéry Detilleux and Jacques Vandooren. Experimental and kinetic modeling evidences of a c7h6 pathway in a rich toluene flame. *The Journal of Physical Chemistry A*, 113(41):10913–10922, 2009.
- [182] Yuyang Li, Lidong Zhang, Zhenyu Tian, Tao Yuan, Jing Wang, Bin Yang, and Fei Qi. Experimental study of a fuel-rich premixed toluene flame at low pressure. *Energy & Fuels*, 23(3):1473–1485, 2009.
- [183] Valéry Detilleux and Jacques Vandooren. Experimental and kinetic modeling investigation of toluene combustion in premixed, one-dimensional and laminar toluene-oxygen-argon flames. *Proceedings of the Combustion Institute*, 33(1):217–224, 2011.
- [184] Akira Matsugi and Akira Miyoshi. Modeling of two-and three-ring aromatics formation in the pyrolysis of toluene. *Proceedings of the Combustion Institute*, 34(1):269–277, 2013.
- [185] Richard D Smith. A direct mass spectrometric study of the mechanism of toluene pyrolysis at high temperatures. *Journal of Physical Chemistry*, 83(12):1553–1563, 1979.
- [186] KM Pamidimukkala, RD Kern, MR Patel, HC Wei, and JH Kiefer. High-temperature pyrolysis of toluene. *Journal of Physical Chemistry*, 91(8):2148–2154, 1987.
- [187] MB Colket and DJ Seery. Reaction mechanisms for toluene pyrolysis. In *Symposium (International) on combustion*, volume 25(1), pages 883–891. Elsevier, 1994.
- [188] Ronald A Eng, Andreas Gebert, Elke Goos, Horst Hippler, and Chatuna Kachiani. Incubation times, fall-off and branching ratios in the thermal decomposition of toluene: Experiments and theory. *Physical Chemistry Chemical Physics*, 4(16):3989–3996, 2002.

- [189] R Sivaramakrishnan, Robert S Tranter, and K Brezinsky. High pressure pyrolysis of toluene. 1. experiments and modeling of toluene decomposition. *The Journal of Physical Chemistry A*, 110(30):9388–9399, 2006.
- [190] R Sivaramakrishnan, Robert S Tranter, and K Brezinsky. High pressure pyrolysis of toluene. 2. modeling benzyl decomposition and formation of soot precursors. *The Journal of Physical Chemistry A*, 110(30):9400–9404, 2006.
- [191] Matthew A Oehlschlaeger, David F Davidson, and Ronald K Hanson. Thermal decomposition of toluene: Overall rate and branching ratio. *Proceedings of the Combustion Institute*, 31(1):211–219, 2007.
- [192] Taichang Zhang, Lidong Zhang, Xin Hong, Kuiwen Zhang, Fei Qi, Chung K Law, Taohong Ye, Pinghui Zhao, and Yiliang Chen. An experimental and theoretical study of toluene pyrolysis with tunable synchrotron vuv photoionization and molecular-beam mass spectrometry. *Combustion and Flame*, 156(11):2071–2083, 2009.
- [193] Frédéric Lannuzel, Roda Bounaceur, Raymond Michels, Gérard Scacchi, and Paul-Marie Marquaire. An extended mechanism including high pressure conditions (700 bar) for toluene pyrolysis. *Journal of Analytical and Applied Pyrolysis*, 87(2):236–247, 2010.
- [194] Bikau Shukla, Akio Susa, Akira Miyoshi, and Mitsuo Koshi. In situ direct sampling mass spectrometric study on formation of polycyclic aromatic hydrocarbons in toluene pyrolysis. *The Journal of Physical Chemistry A*, 111(34):8308–8324, 2007.
- [195] Lidong Zhang, Jianghuai Cai, Taichang Zhang, and Fei Qi. Kinetic modeling study of toluene pyrolysis at low pressure. *Combustion and Flame*, 157(9):1686–1697, 2010.
- [196] RP Lindstedt and LQ Maurice. Detailed kinetic modelling of toluene combustion. *Combustion science and technology*, 120(1-6):119–167, 1996.
- [197] WJ Pitz, R Seiser, JW Bozzelli, I Da Costa, R Fournet, F Billaud, F Battin-Leclerc, K Seshadri, and CK Westbrook. Chemical kinetic characterization of combustion toluene. Technical report, Lawrence Livermore National Lab., CA (US), 2001.
- [198] Johan CG Andrae, P Björnbohm, RF Cracknell, and GT Kalghatgi. Autoignition of toluene reference fuels at high pressures modeled with detailed chemical kinetics. *Combustion and Flame*, 149(1-2):2–24, 2007.
- [199] Yasuyuki Sakai, Hiroaki Ozawa, Teppei Ogura, Akira Miyoshi, Mitsuo Koshi, and William J. Pitz. Effects of toluene addition to primary reference fuel at high temperature. In *Powertrain & Fluid Systems Conference and Exhibition*. SAE International, oct 2007.
- [200] K Narayanaswamy, G Blanquart, and H Pitsch. A consistent chemical mechanism for oxidation of substituted aromatic species. *Combustion and Flame*, 157(10):1879–1898, 2010.

- [201] Zhenyu Tian, William J Pitz, René Fournet, Pierre-Alexander Glaude, and Frédérique Battin-Leclerc. A detailed kinetic modeling study of toluene oxidation in a premixed laminar flame. *Proceedings of the Combustion Institute*, 33(1):233–241, 2011.
- [202] Wenhao Yuan, Yuyang Li, Philippe Dagaut, Jiuzhong Yang, and Fei Qi. Investigation on the pyrolysis and oxidation of toluene over a wide range conditions. i. flow reactor pyrolysis and jet stirred reactor oxidation. *Combustion and Flame*, 162(1):3–21, 2015.
- [203] Wenhao Yuan, Yuyang Li, Philippe Dagaut, Jiuzhong Yang, and Fei Qi. Investigation on the pyrolysis and oxidation of toluene over a wide range conditions. ii. a comprehensive kinetic modeling study. *Combustion and Flame*, 162(1):22–40, 2015.
- [204] Takamasa Seta, Masakazu Nakajima, and Akira Miyoshi. High-temperature reactions of oh radicals with benzene and toluene. *The Journal of Physical Chemistry A*, 110(15):5081–5090, 2006.
- [205] Stephen J Klippenstein, Lawrence B Harding, and Yuri Georgievskii. On the formation and decomposition of c7h8. *Proceedings of the combustion institute*, 31(1):221–229, 2007.
- [206] Gabriel da Silva and Joseph W Bozzelli. The c7h5 fulvenallenyl radical as a combustion intermediate: Potential new pathways to two-and three-ring pahn. *The Journal of Physical Chemistry A*, 113(44):12045–12048, 2009.
- [207] Gabriel da Silva and Joseph W Bozzelli. Kinetic modeling of the benzyl+ho2 reaction. *Proceedings of the Combustion Institute*, 32(1):287–294, 2009.
- [208] Gabriel da Silva, John A Cole, and Joseph W Bozzelli. Thermal decomposition of the benzyl radical to fulvenallene (c7h6)+ h. *The Journal of Physical Chemistry A*, 113(21):6111–6120, 2009.
- [209] Gabriel da Silva, John A Cole, and Joseph W Bozzelli. Kinetics of the cyclopentadienyl+ acetylene, fulvenallene+ h, and 1-ethynylcyclopentadiene+ h reactions. *The Journal of Physical Chemistry A*, 114(6):2275–2283, 2010.
- [210] Gabriel da Silva and Adam J Trevitt. Chemically activated reactions on the c 7 h 5 energy surface: propargyl+ diacetylene, i-c 5 h 3+ acetylene, and n-c 5 h 3+ acetylene. *Physical Chemistry Chemical Physics*, 13(19):8940–8952, 2011.
- [211] Gabriel da Silva, Adam J Trevitt, Michael Steinbauer, and Patrick Hemberger. Pyrolysis of fulvenallene (c7h6) and fulvenallenyl (c7h5): Theoretical kinetics and experimental product detection. *Chemical Physics Letters*, 517(4-6):144–148, 2011.
- [212] Marco Derudi, Daniela Polino, and Carlo Cavallotti. Toluene and benzyl decomposition mechanisms: elementary reactions and kinetic simulations. *Physical Chemistry Chemical Physics*, 13(48):21308–21318, 2011.

- [213] Benoite Lefort and Wing Tsang. High temperature stability of larger aromatic compounds. *Combustion and Flame*, 158(4):657–665, 2011.
- [214] Daniela Polino and Carlo Cavallotti. Fulvenallene decomposition kinetics. *The Journal of Physical Chemistry A*, 115(37):10281–10289, 2011.
- [215] Daniela Polino, Antonino Famulari, and Carlo Cavallotti. Analysis of the reactivity on the c7h6 potential energy surface. *The Journal of Physical Chemistry A*, 115(27):7928–7936, 2011.
- [216] Carlo Cavallotti, Daniela Polino, Alessio Frassoldati, and Eliseo Ranzi. Analysis of some reaction pathways active during cyclopentadiene pyrolysis. *The Journal of Physical Chemistry A*, 116(13):3313–3324, 2012.
- [217] Karthik V Puduppakkam, Chitralkumar V Naik, Cheng Wang, and Ellen Meeks. Validation studies of a detailed kinetics mechanism for diesel and gasoline surrogate fuels. Technical report, SAE Technical Paper, 2010.
- [218] Johan CG Andrae. Development of a detailed kinetic model for gasoline surrogate fuels. *Fuel*, 87(10-11):2013–2022, 2008.
- [219] Liming Cai and Heinz Pitsch. Optimized chemical mechanism for combustion of gasoline surrogate fuels. *Combustion and flame*, 162(5):1623–1637, 2015.
- [220] Liming Cai and Heinz Pitsch. Mechanism optimization based on reaction rate rules. *Combustion and Flame*, 161(2):405–415, 2014.
- [221] Xudong Zhen, Yang Wang, and Daming Liu. An overview of the chemical reaction mechanisms for gasoline surrogate fuels. *Applied thermal engineering*, 124:1257–1268, 2017.
- [222] I.N. Levine. *Quantum Chemistry*. Pearson Education, 2013.
- [223] Stefan Grimme. Semiempirical hybrid density functional with perturbative second-order correlation. *The Journal of Chemical Physics*, 124:034108, 2006.
- [224] Jinhua Wang, Zhilong Wei, Senbin Yu, Wu Jin, Yongliang Xie, Meng Zhang, and Zuohua Huang. Effects of stretch and preferential diffusion on tip opening of laminar premixed bunsen flames of syngas/air mixtures. *Fuel*, 148:1–8, 2015.
- [225] Laurent Selle, Thierry Poinso, and Bernard Ferret. Experimental and numerical study of the accuracy of flame-speed measurements for methane/air combustion in a slot burner. *Combustion and Flame*, 158(1):146–154, 2011.
- [226] Simon Crispin Taylor. *Burning velocity and the influence of flame stretch*. PhD thesis, University of Leeds, 1991.
- [227] Xiaotian Li, Erjiang Hu, Xin Meng, Cheng Peng, Xin Lu, and Zuohua Huang. Effect of lewis number on nonlinear extrapolation methods from expanding spherical flames. *Combustion Science and Technology*, 189(9):1510–1526, 2017.



- [228] Christodoulos Xiouris, Tailai Ye, Jagannath Jayachandran, and Fokion N Egolfopoulos. Laminar flame speeds under engine-relevant conditions: uncertainty quantification and minimization in spherically expanding flame experiments. *Combustion and Flame*, 163:270–283, 2016.
- [229] Paul Clavin. Dynamic behavior of premixed flame fronts in laminar and turbulent flows. *Progress in energy and combustion science*, 11(1):1–59, 1985.
- [230] CK Wu and Chung King Law. On the determination of laminar flame speeds from stretched flames. In *Symposium (International) on Combustion*, volume 20(1), pages 1941–1949. Elsevier, 1985.
- [231] Chung King Law. Dynamics of stretched flames. In *Symposium (international) on combustion*, volume 22(1), pages 1381–1402. Elsevier, 1989.
- [232] Chung King Law and CJ Sung. Structure, aerodynamics, and geometry of premixed flamelets. *Progress in energy and combustion science*, 26(4-6):459–505, 2000.
- [233] Zheng Chen. On the extraction of laminar flame speed and markstein length from outwardly propagating spherical flames. *Combustion and Flame*, 158(2):291–300, 2011.
- [234] Andrew P Kelley and Chung King Law. Nonlinear effects in the extraction of laminar flame speeds from expanding spherical flames. *Combustion and Flame*, 156(9):1844–1851, 2009.
- [235] Andrew P Kelley, John K Bechtold, and Chung K Law. Premixed flame propagation in a confining vessel with weak pressure rise. *Journal of Fluid Mechanics*, 691:26–51, 2012.
- [236] Fujia Wu, Wenkai Liang, Zheng Chen, Yiguang Ju, and Chung K Law. Uncertainty in stretch extrapolation of laminar flame speed from expanding spherical flames. *Proceedings of the Combustion Institute*, 35(1):663–670, 2015.
- [237] Wenkai Liang, Fujia Wu, and Chung K Law. Extrapolation of laminar flame speeds from stretched flames: Role of finite flame thickness. *Proceedings of the Combustion Institute*, 36(1):1137–1143, 2017.
- [238] LPH De Goey, A Van Maaren, and RM Quax. Stabilization of adiabatic premixed laminar flames on a flat flame burner. *Combustion science and technology*, 92(1-3):201–207, 1993.
- [239] Roy Theodorus Elisabeth Hermanns, JA Kortendijk, RJM Bastiaans, and LPH De Goey. Laminar burning velocities of methane-hydrogen-air mixtures. *Praca doktorska, Technische Universitat Eindhoven*, 2007.
- [240] M Goswami, JGH Van Griensven, RJM Bastiaans, A Alexander Konnov, and LPH De Goey. Experimental and modeling study of the effect of elevated pressure on lean high-hydrogen syngas flames. *Proceedings of the Combustion Institute*, 35(1):655–662, 2015.

- [241] Fokion N Egolfopoulos, Nils Hansen, Yiguang Ju, Katharina Kohse-Höinghaus, Chung King Law, and Fei Qi. Advances and challenges in laminar flame experiments and implications for combustion chemistry. *Progress in Energy and Combustion Science*, 43:36–67, 2014.
- [242] MJE Frisch, GW Trucks, H Bernhard Schlegel, Gustavo E Scuseria, Michael A Robb, James R Cheeseman, Giovanni Scalmani, Vincenzo Barone, Benedetta Mennucci, GAe Petersson, et al. *Gaussian 09, Revision A.02*. Gaussian Inc.: Wallingford, CT, 2009.
- [243] Frank Neese. The orca program system. *Wiley Interdiscip. Rev.: Comput. Mol. Sci.*, 2(1):73–78, 2012.
- [244] Marcus D Hanwell, Donald E Curtis, David C Lonie, Tim Vandermeersch, Eva Zurek, and Geoffrey R Hutchison. Avogadro: an advanced semantic chemical editor, visualization, and analysis platform. *J. Cheminf.*, 4(1):17, 2012.
- [245] Y Georgievskii and SJ Klippenstein. Mess. 2016.3.23, 2017.
- [246] Yuri Georgievskii, James A Miller, Michael P Burke, and Stephen J Klippenstein. Reformulation and solution of the master equation for multiple-well chemical reactions. *J. Phys. Chem. A*, 117(46):12146–12154, 2013.
- [247] Robert J Kee, Joseph F Grcar, Mitchell D Smooke, James A Miller, and Ellen Meeks. Premix: a fortran program for modeling steady laminar one-dimensional premixed flames. *Sandia National Laboratories Report*, (SAND85-8249), 1985.
- [248] RJ Kee, FM Rupley, JA Miller, ME Coltrin, JF Grcar, E Meeks, HK Moffat, AE Lutz, G Dixon-Lewis, MD Smooke, et al. Chemkin-pro 15131. *Reaction Design, San Diego, CA*, 2013.
- [249] Boyang Xu, Julian Garrec, André Nicolle, Mickaël Matrat, and Laurent Catoire. Temperature and pressure dependent rate coefficients for the reaction of ketene with hydroxyl radical. *The Journal of Physical Chemistry A*, 123(13):2483–2496, 2019.
- [250] Hermann Staudinger. Ketene, eine neue körperklasse. *Ber. Dtsch. Chem. Ges.*, 38(2):1735–1739, 1905.
- [251] JV Michael, DF Nava, WA Payne, and LJ Stief. Absolute rate constants for the reaction of atomic hydrogen with ketene from 298 to 500 k. *J. Chem. Phys.*, 70(11):5222–5227, 1979.
- [252] Hironobu Umemoto, Shigeru Tsunashima, Shin Sato, Nobuaki Washida, and Shiro Hatakeyama. The reactions of hydrogen and deuterium atoms with four ketenes. *Bull. Chem. Soc. Jpn.*, 57(9):2578–2580, 1984.
- [253] J. Hranisavljevic, S.S. Kumaran, and J.V. Michael.  $\text{H} + \text{CH}_2\text{CO} \rightarrow \text{CH}_3 + \text{CO}$  at high temperature: A high pressure chemical activation reaction with positive barrier. *Symp. (Int.) Combust.*, 27(1):159–166, 1998.

- [254] RW Carr Jr, ID Gay, GP Glass, and H Niki. Reaction of ketene with atomic hydrogen and oxygen. *J. Chem. Phys.*, 49(2):846–852, 1968.
- [255] Nobuaki Washida, Shiro Hatakeyama, Hiroo Takagi, Takeshi Kyogoku, and Shin Sato. Reaction of ketenes with atomic oxygen. *J. Chem. Phys.*, 78(7):4533–4540, 1983.
- [256] P Frank, KA Bhaskaran, and Th Just. High-temperature reactions of triplet methylene and ketene with radicals. *J. Phys. Chem.*, 90(10):2226–2231, 1986.
- [257] Graham Hancock and Mathew R Heal. Rate constant for reaction of  $\text{CH}(\text{X}^2\Pi)$  with ketene. *J. Chem. Soc., Faraday Trans.*, 88(15):2121–2123, 1992.
- [258] Anna S Savchenkova, Alexander S Semenikhin, Ivan V Chechet, Sergey G Matveev, Alexander A Konnov, and Alexander M Mebel. Mechanism and rate constants of the  $\text{ch}_2+\text{ch}_2\text{co}$  reactions in triplet and singlet states: A theoretical study. *J. Comput. Chem.*, 2018.
- [259] AS Semenikhin, EG Shubina, AS Savchenkova, IV Chechet, SG Matveev, AA Konnov, and AM Mebel. Mechanism and rate constants of the  $\text{CH}_3 + \text{CH}_2\text{CO}$  reaction: A theoretical study. *Int. J. Chem. Kinet.*, 50(4):273–284, 2018.
- [260] J Ebrecht, W Hack, and H Gg. Wagner. Elementary reactions of ketene with fluorine and chlorine atoms in the gas phase. *Ber. Bunsenges. Phys. Chem.*, 94(5):587–593, 1990.
- [261] J Grussdorf, J Nolte, F Temps, and H Gg. Wagner. Primary products of the elementary reactions of  $\text{CH}_2\text{CO}$  with f, cl, and oh in the gas phase. *Ber. Bunsenges. Phys. Chem.*, 98(4):546–553, 1994.
- [262] Kuangsen Sung and Thomas T Tidwell. Theoretical study of the reactivity of ketene with free radicals. *J. Org. Chem.*, 63(26):9690–9697, 1998.
- [263] Michael A Edwards and John F Hershberger. Kinetics of the  $\text{CN} + \text{CH}_2\text{CO}$  and  $\text{NCO} + \text{CH}_2\text{CO}$  reactions. *Chem. Phys.*, 234(1-3):231–237, 1998.
- [264] Yoshiaki Hidaka, Kenichi Kimura, and Hiroyuki Kawano. High-temperature pyrolysis of ketene in shock waves. *Combust. Flame*, 99(1):18–28, 1994.
- [265] Yoshiaki Hidaka, Kenichi Kimura, Kenji Hattori, and Tatsuya Okuno. Shock tube and modeling study of ketene oxidation. *Combust. Flame*, 106(1):155–167, 1996.
- [266] J. Vandooren and P.J. Van Tiggelen. Reaction mechanisms of combustion in low pressure acetylene-oxygen flames. *Symp. (Int.) Combust.*, 16(1):1133–1144, 1977.
- [267] JA Barnard and TW Honeyman. The gaseous oxidation of acetone. i. the high-temperature reaction. *Proc. R. Soc. Lond. A*, 279(1377):236–247, 1964.

- [268] JA Barnard and TW Honeyman. The gaseous oxidation of acetone. ii. the low-temperature reaction. *Proc. R. Soc. Lond. A*, 279(1377):248–259, 1964.
- [269] S. Pichon, G. Black, N. Chaumeix, M. Yahyaoui, J.M. Simmie, H.J. Curran, and R. Donohue. The combustion chemistry of a fuel tracer: Measured flame speeds and ignition delays and a detailed chemical kinetic model for the oxidation of acetone. *Combustion and Flame*, 156(2):494 – 504, 2009.
- [270] A.A. Burluka, M. Harker, H. Osman, C.G.W. Sheppard, and A.A. Konnov. Laminar burning velocities of three C<sub>3</sub>H<sub>6</sub>O isomers at atmospheric pressure. *Fuel*, 89(10):2864–2872, 2010.
- [271] Vronique Dias, Jacques Vandooren, and Herv Jeanmart. An experimental and modeling study of the addition of acetone to H<sub>2</sub>/O<sub>2</sub>/ar flames at low pressure. *Proc. Combust. Inst.*, 35(1):647–653, 2015.
- [272] Cheng Tung Chong and Simone Hochgreb. Measurements of laminar flame speeds of acetone/methane/air mixtures. *Combust. Flame*, 158(3):490–500, 2011.
- [273] E.J.K. Nilsson, L.P.H. de Goey, and A.A. Konnov. Laminar burning velocities of acetone in air at room and elevated temperatures. *Fuel*, 105:496 – 502, 2013.
- [274] Yi Wu, Vincent Modica, Bjorn Rossow, and Frédéric Grisch. Effects of pressure and preheating temperature on the laminar flame speed of methane/air and acetone/air mixtures. *Fuel*, 185:577–588, 2016.
- [275] T Faravelli, A Goldaniga, L Zappella, E Ranzi, P Dagaut, and M Cathonnet. An experimental and kinetic modeling study of propyne and allene oxidation. *Proc. Combust. Inst.*, 28(2):2601–2608, 2000.
- [276] Moah Christensen and Alexander A Konnov. Laminar burning velocity of diacetyl+air flames. further assessment of combustion chemistry of ketene. *Combust. Flame*, 178:97–110, 2017.
- [277] SM Sarathy, MJ Thomson, WJ Pitz, and T Lu. An experimental and kinetic modeling study of methyl decanoate combustion. *Proc. Combust. Inst.*, 33(1):399–405, 2011.
- [278] Thomas T Tidwell. Ketene chemistry after 100 years: ready for a new century. *Eur. J. Org. Chem.*, 2006(3):563–576, 2006.
- [279] Stefan Grimme, Jens Antony, Stephan Ehrlich, and Helge Krieg. A consistent and accurate ab initio parametrization of density functional dispersion correction (dft-d) for the 94 elements h-pu. *J. Chem. Phys.*, 132(15):154104, 2010.
- [280] Trygve Helgaker, Wim Klopper, Henrik Koch, and Jozef Noga. Basis-set convergence of correlated calculations on water. *J. Chem. Phys.*, 106(23):9639–9646, 1997.

- [281] Stephen J Klippenstein. Ab initio theoretical chemical kinetics, lecture notes in 2010 princeton-combustion institute summer school on combustion, July 2010.
- [282] Yuri Georgievskii and Stephen J Klippenstein. Long-range transition state theory. *J. Chem. Phys.*, 122(19):194103, 2005.
- [283] C Franklin Goldsmith, Lawrence B Harding, Yuri Georgievskii, James A Miller, and Stephen J Klippenstein. Temperature and pressure-dependent rate coefficients for the reaction of vinyl radical with molecular oxygen. *J. Phys. Chem. A*, 119(28):7766–7779, 2015.
- [284] Robert J Kee, Graham Dixon-Lewis, Jürgen Warnatz, Michael E Coltrin, and James A Miller. A fortran computer code package for the evaluation of gas-phase multicomponent transport properties. *Sandia Natl. Lab. [Tech. Rep.] SAND86-8246*, 13:80401–1887, 1986.
- [285] C Franklin Goldsmith, William H Green, and Stephen J Klippenstein. Role of  $O_2 + QOOH$  in low-temperature ignition of propane. 1. temperature and pressure dependent rate coefficients. *J. Phys. Chem. A*, 116(13):3325–3346, 2012.
- [286] Robert J Kee, Joseph F Grcar, Mitchell D Smooke, James A Miller, and E Meeks. Premix: A fortran program for modeling steady laminar one-dimensional premixed flames. *Sandia Natl. Lab. [Tech. Rep.] SAND85-8249*, (SAND85-8249), 1985.
- [287] Xiaolong Gou, James A Miller, Wenting Sun, and Yiguang Ju. Implementation of plog function in chemkin ii and iii. 2011.
- [288] Lawrence Livermore National Laboratory. *LLNL 2011 Mechanism: A detailed chemical kinetic mechanism for the simulation of gasoline surrogate mixtures.*, 2011.
- [289] Chong Wen Zhou, Yang Li, Ultan Burke, Colin Banyon, Kieran P. Somers, Shuiting Ding, Saadat Khan, Joshua W. Hargis, Travis Sikes, Olivier Mathieu, Eric L. Petersen, Mohammed AlAbbad, Aamir Farooq, Youshun Pan, Yingjia Zhang, Zuohua Huang, Joseph Lopez, Zachary Loparo, Subith S. Vasu, and Henry J. Curran. An experimental and chemical kinetic modeling study of 1,3-butadiene combustion: Ignition delay time and laminar flame speed measurements. *Combust. Flame*, 197:423–438, 2018.
- [290] Combustion Chemistry Center, NUI Galway. *Aramco Mech 3.0*, 2018.
- [291] Gregory P Smith, David M Golden, Michael Frenklach, Nigel W Moriarty, Boris Eiteneer, Mikhail Goldenberg, C Thomas Bowman, Ronald K Hanson, Soonho Song, and WC Gardiner Jr. *GRI-Mech 3.0*, 1999.
- [292] H Wang, E Dames, B Sirjean, DA Sheen, R Tangko, A Violi, JYW Lai, FN Egolfopoulos, DF Davidson, and RK Hanson. *JetSurF version 2.0: A high-temperature chemical kinetic model of n-alkane (up to n-dodecane), cyclohexane, and methyl-, ethyl-, n-propyl and n-butyl-cyclohexane oxidation at high temperatures*, 2010.

- [293] Jorge Gimenez-Lopez, Christian Tihic Rasmussen, Hamid Hashemi, Maria U Alzueta, Yide Gao, Paul Marshall, C Franklin Goldsmith, and Peter Glarborg. Experimental and kinetic modeling study of  $C_2H_2$  oxidation at high pressure. *Int. J. Chem. Kinet.*, 48(11):724–738, 2016.
- [294] Mechanical and Aerospace Engineering (Combustion Research), University of California at San Diego. *San Diego Mech, version 2016-12-14*, 2016.
- [295] Juan C Prince and Forman A Williams. Short chemical-kinetic mechanisms for low-temperature ignition of propane and ethane. *Combust. Flame*, 159(7):2336–2344, 2012.
- [296] Thanh Lam Nguyen, Luc Vereecken, and Jozef Peeters. Quantum chemical and theoretical kinetics study of the  $O(^3P) + C_2H_2$  reaction: A multistate process. *J. Phys. Chem. A*, 110(21):6696–6706, 2006.
- [297] Juan P Senosiain, Stephen J Klippenstein, and James A Miller. Reaction of ethylene with hydroxyl radicals: A theoretical study. *J. Phys. Chem. A*, 110(21):6960–6970, 2006.
- [298] Peter R Schreiner, Hans Peter Reisenauer, Frank C Pickard Iv, Andrew C Simmonett, Wesley D Allen, Edit Mátyus, and Attila G Császár. Capture of hydroxymethylene and its fast disappearance through tunnelling. *Nature*, 453(7197):906, 2008.
- [299] Robert Humpfer, Harry Oser, and Horst-Henning Grotheer. Formation of  $HCOH + H_2$  through the reaction  $CH_3 + OH$ . experimental evidence for a hitherto undetected product channel. *Int. J. Chem. Kinet.*, 27(6):577–595, 1995.
- [300] Ian R Sims. Low-temperature reactions: Tunnelling in space. *Nat. Chem.*, 5(9):734, 2013.
- [301] Michael Mozurkewich and Sidney W Benson. Negative activation energies and curved arrhenius plots. 1. theory of reactions over potential wells. *J. Phys. Chem.*, 88(25):6429–6435, 1984.
- [302] GP Glass, SS Kumaran, and JV Michael. Photolysis of ketene at 193 nm and the rate constant for  $H + HCCO$  at 297 k. *J. Phys. Chem. A*, 104(36):8360–8367, 2000.
- [303] Jozef Peeters, Werner Boullart, and Katia Devriendt.  $CH(a^4\Sigma^-$  and/or  $X^2\Pi)$  formation in the reaction between ketyl radicals and oxygen atoms. determination of the ch yield between 405 and 960 k. *J. Phys. Chem.*, 99(11):3583–3591, 1995.
- [304] David L Osborn. The reaction of  $HCCO + O_2$ : Experimental evidence of prompt  $CO_2$  by time-resolved fourier transform spectroscopy. *J. Phys. Chem. A*, 107(19):3728–3732, 2003.
- [305] Peng Zou and David L Osborn. On the mechanism of the  $HCCO + O_2$  reaction: Probing multiple pathways to a single product channel. *Phys. Chem. Chem. Phys.*, 6(8):1697–1705, 2004.

- [306] PJ Liu, YF Chang, H Sun, ZM Su, and RS Wang. Dynamics of biradical micro-reaction between hcco and ch. *Chem. Res. Chin. Univ.*, 26(4):723–726, 2005.
- [307] F Temps, H Gg Wagner, and M Wolf. Some experiments concerning the reactions of hcco with C<sub>2</sub>H<sub>2</sub>, O<sub>2</sub>, no, and NO<sub>2</sub>. *Z. Phys. Chem.*, 176(1):27–39, 1992.
- [308] KK Murray, KG Unfried, GP Glass, and RF Curl. Acetylene combustion reactions. rate constant measurements of hcco with O<sub>2</sub> and C<sub>2</sub>H<sub>2</sub>. *Chem. Phys. Lett.*, 192(5-6):512–516, 1992.
- [309] U Meier, HH Grotheer, G Riekert, and Th Just. Study of hydroxyl reactions with methanol and ethanol by laser-induced fluorescence. *Ber. Bunsenges. Phys. Chem.*, 89(3):325–327, 1985.
- [310] Alexander Schocker, Masanori Uetake, Nozomu Kanno, Mitsuo Koshi, and Kenichi Tonokura. Kinetics and rate constants of the reaction CH<sub>2</sub>OH + O<sub>2</sub> → CH<sub>2</sub>O + HO<sub>2</sub> in the temperature range of 236–600 k. *J. Phys. Chem. A*, 111(29):6622–6627, 2007.
- [311] Theodore S Dibble. Mechanism and dynamics of the CH<sub>2</sub>OH + O<sub>2</sub> reaction. *Chem. Phys. Lett.*, 355(1-2):193–200, 2002.
- [312] Baoshan Wang, Hua Hou, Laurie M Yoder, James T Muckerman, and Christopher Fockenberg. Experimental and theoretical investigations on the methyl-methyl recombination reaction. *J. Phys. Chem. A*, 107(51):11414–11426, 2003.
- [313] Stephen J Klippenstein, Yuri Georgievskii, and Lawrence B Harding. Predictive theory for the combination kinetics of two alkyl radicals. *Phys. Chem. Chem. Phys.*, 8(10):1133–1147, 2006.
- [314] Carlo Cavallotti, Matteo Pelucchi, and Alessio Frassoldati. Analysis of acetic acid gas phase reactivity: Rate constant estimation and kinetic simulations. *Proc. Combust. Inst.*, 37(1):539–546, 2019.
- [315] Claudette M Rosado-Reyes and Joseph S Francisco. Atmospheric oxidation pathways of acetic acid. *J. Phys. Chem. A*, 110(13):4419–4433, 2006.
- [316] R K Hanson B M Gauthier, D F Davidson. Shock tube determination of ignition delay times in full-blend and surrogate fuel mixtures. *Combustion and Flame*, 139:300–311, 2004.
- [317] James E Anderson, Thomas G Leone, Michael H Shelby, Timothy J Wallington, Jeffrey J Bizub, Michael Foster, Michael G Lynskey, and Dusan Polovina. Octane Numbers of Ethanol-Gasoline Blends: Measurements and Novel Estimation Method from Molar Composition. In *SAE 2012 World Congress & Exhibition*, volume 1, pages 2012–01–1274, 2012.
- [318] M Al-Hasan. Effect of ethanolunleaded gasoline blends on engine performance and exhaust emission. *Energy Conversion and Management*, 44:1547–1561, 2003.

- [319] FH Palmer. Vehicle performance of gasoline containing oxygenates. In *INTERNATIONAL CONFERENCE ON PETROLEUM BASED FUELS AND AUTOMOTIVE APPLICATIONS. IMECHE CONFERENCE PUBLICATIONS 1986-11. PAPER NO C319/86*, 1986.
- [320] C. Hasse, M. Bollig, N. Peters, and H.A. Dwyer. Quenching of laminar iso-octane flames at cold walls. *Combustion and Flame*, 122(1):117 – 129, 2000.
- [321] H. Pitsch, N. Peters, and K. Seshadri. Numerical and asymptotic studies of the structure of premixed iso-octane flames. *Symposium (International) on Combustion*, 26(1):763 – 771, 1996.
- [322] Minh Bau Luong, Zhaoyu Luo, Tianfeng Lu, Suk Ho Chung, and Chun Sang Yoo. Direct numerical simulations of the ignition of lean primary reference fuel/air mixtures with temperature inhomogeneities. *Combustion and Flame*, 160(10):2038–2047, 2013.
- [323] Kyle E Niemeyer and Chih-Jen Sung. Reduced chemistry for a gasoline surrogate valid at engine-relevant conditions. *Energy & Fuels*, 29(2):1172–1185, 2015.
- [324] Hu Wang, Mingfa Yao, Zongyu Yue, Ming Jia, and Rolf D Reitz. A reduced toluene reference fuel chemical kinetic mechanism for combustion and polycyclic-aromatic hydrocarbon predictions. *Combustion and Flame*, 162(6):2390–2404, 2015.
- [325] Wayne K. Metcalfe, Sinad M. Burke, Syed S. Ahmed, and Henry J. Curran. A hierarchical and comparative kinetic modeling study of c1–c2 hydrocarbon and oxygenated fuels. *International Journal of Chemical Kinetics*, 45(10):638–675, 2013.
- [326] H Richter and J B Howard. Formation of polycyclic aromatic hydrocarbons and their growth to soota review of chemical reaction pathways. *Progress in Energy and Combustion Science*, 26:565 608, 2000.
- [327] Frédérique Battin-Leclerc. Detailed chemical kinetic models for the low-temperature combustion of hydrocarbons with application to gasoline and diesel fuel surrogates. *Progress in Energy and Combustion Science*, 34(4):440–498, 2008.
- [328] Chiara Saggese, Alessio Frassoldati, Alberto Cuoci, Tiziano Faravelli, and Eliseo Ranzi. A wide range kinetic modeling study of pyrolysis and oxidation of benzene. *Combustion and Flame*, 160:1168–1190, 2013.
- [329] Fengsham Liu, Hongsheng Guo, and Gregory J. Smallwood. The chemical effect of CO<sub>2</sub> replacement of N<sub>2</sub> in air on the burning velocity of CH<sub>4</sub> and H<sub>2</sub> premixed flames. *Combustion and Flame*, 133:495–497, 2003.
- [330] A A Konnov and I V Dyakov. Measurement of propagation speeds in adiabatic flat and cellular premixed flames of C<sub>2</sub>H<sub>6</sub>+O<sub>2</sub>+CO<sub>2</sub>. *Combustion and Flame*, 136:371 376, 2004.



- [331] N Lamoureux, N Djebali-Chaumeix, and C E Paillard. Laminar flame velocity determination for H<sub>2</sub>/air/He/CO<sub>2</sub> mixtures using the spherical bomb method. *Experimental Thermal and Fluid Science*, 27:385–393, 2003.
- [332] Jiongming Ruan, Hideaki Kobayashi, Takashi Niioka, and Yiguang Ju. Combined effects of nongray radiation and pressure on premixed CH<sub>4</sub>/O<sub>2</sub>/CO<sub>2</sub> flames. *Combustion and Flame*, 124:225–230, 2001.
- [333] Yiguang Ju, Goro Masuya, and Paul D Ronney. Effects of radiative emission and absorption on the propagation and extinction of premixed gas flames. *Symposium (International) on Combustion*, 27:2619–2626, 1998.
- [334] D L Zhu, F N Egolfopoulos, and C K Law. Experimental and numerical determination of laminar flame speeds of methane/(Ar, N<sub>2</sub>, CO<sub>2</sub>)-air mixtures as function of stoichiometry, pressure, and flame temperature. *Symposium (International) on Combustion*, 22:1537–1545, 1989.
- [335] Fengshan Liu, Hongsheng Guo, Gregory J Smallwood, and mer L Glder. The chemical effects of carbon dioxide as an additive in an ethylene diffusion flame: implications for soot and NO<sub>x</sub> formation. *Combustion and Flame*, 125:778–787, 2001.
- [336] C Zhang, A Atreya, and K Lee. Sooting structure of methane counterflow diffusion flames with preheated reactants and dilution by products of combustion. *Symposium (International) on Combustion*, 24:1049–1057, 1992.
- [337] A R Masri, R W Dibble, and R S Barlow. Chemical kinetic effects in nonpremixed flames of H<sub>2</sub>/CO<sub>2</sub> fuel. *Combustion and Flame*, 91:285–309, 1992.
- [338] Peter Glarborg and Line L B Bentzen. Chemical Effects of a High CO<sub>2</sub> Concentration in Oxy-Fuel Combustion of Methane. *Energy & Fuels*, 22:291–296, 2008.
- [339] S Scherer, Th Just, and P Frank. High-temperature investigations on pyrolytic reactions of propargyl radicals. *Proceedings of the Combustion Institute*, 28:1511–1518, 2000.
- [340] Charles S McEnally, Lisa D Pfefferle, Burak Atakan, and Katharina Kohse-Hinghaus. Studies of aromatic hydrocarbon formation mechanisms in flames: Progress towards closing the fuel gap. *Progress in Energy and Combustion Science*, 32:247–294, 2006.
- [341] James A Miller and Stephen J Klippenstein. The Recombination of Propargyl Radicals and Other Reactions on a C<sub>6</sub>H<sub>6</sub>Potential. *Journal of Physical Chemistry A*, 107:7783–7799, 2003.
- [342] Michael Kamphus, Marina Braun-Unkhoff, and Katharina Kohse-Hinghaus. Formation of small PAHs in laminar premixed low-pressure propene and cyclopentene flames: Experiment and modeling. *Combustion and Flame*, 152:28–59, 2008.

- [343] James A Miller and Carl F Melius. Kinetic and thermodynamic issues in the formation of aromatic compounds in flames of aliphatic fuels. *Combustion and Flame*, 91:21–39, 1992.
- [344] Nils Hansen, James A. Miller, Phillip R. Westmoreland, Tina Kasper, Katharina Kohse-Hinghaus, Juan Wang, and Terrill A. Cool. Isomer-specific combustion chemistry in allene and propyne flames. *Combustion and Flame*, 156:2153–2164, 2009.
- [345] James A. Miller, Michael J. Pilling, and Jrgen Troe. Unravelling combustion mechanisms through a quantitative understanding of elementary reactions. *Proceedings of the Combustion Institute*, 30:43–88, 2005.
- [346] David K. Hahn, Stephen J. Klippenstein, and James A. Miller. A theoretical analysis of the reaction between propargyl and molecular oxygen. *Faraday Discussions*, 119:79–100, 2001.
- [347] Hai Wang. A new mechanism for initiation of free-radical chain reactions during high-temperature, homogeneous oxidation of unsaturated hydrocarbons: Ethylene, propyne, and allene. *International Journal of Chemical Kinetics*, 33:698–706, 2001.
- [348] Kenneth Brezinsky. The high-temperature oxidation of aromatic hydrocarbons. *Progress in Energy and Combustion Science*, 12:1–24, 1986.
- [349] Irvin Glassman, Richard A Yetter, and Nick G Glumac. *Combustion*. Academic press, 2014.
- [350] Gabriel da Silva, Chiung-Chu Chen, and Joseph W Bozzelli. Bond dissociation energy of the phenol OH bond from ab initio calculations. *Chemical Physics Letters*, 424:42–45, 2006.
- [351] Gabriel da Silva and Joseph W Bozzelli. Variational Analysis of the Phenyl + O<sub>2</sub> and Phenoxy + O Reactions. *Journal of Physical Chemistry A*, 112:3566–3575, 2008.
- [352] Mohammednoor Altarawneh, Bogdan Z Dlugogorski, Eric M Kennedy, and John C Mackie. Quantum Chemical Investigation of Formation of Polychlorodibenzo- p-Dioxins and Dibenzofurans from Oxidation and Pyrolysis of 2-Chlorophenol. *Journal of Physical Chemistry A*, 111:2563–2573, 2007.
- [353] Barry Dellinger, Slawomir Lomnicki, Lavrent Khachatryan, Zofia Maskos, Randall W Hall, Julien Adoukpe, Cheri McFerrin, and Hieu Truong. Formation and stabilization of persistent free radicals. *Proceedings of the Combustion Institute*, 31:521–528, 2007.
- [354] Anne Marie Schmoltner, Deon S Anex, and Yuan T Lee. Infrared multiphoton dissociation of anisole: production and dissociation of phenoxy radical. *The Journal of Physical Chemistry*, 96:1236–1240, 1992.

- [355] Chin-Yu Lin and M C Lin. Thermal decomposition of methyl phenyl ether in shock waves: the kinetics of phenoxy radical reactions. *The Journal of Physical Chemistry*, 90:425–431, 1986.
- [356] A J Colussi, F Zabel, and S W Benson. The very low-pressure pyrolysis of phenyl ethyl ether, phenyl allyl ether, and benzyl methyl ether and the enthalpy of formation of the phenoxy radical. *International Journal of Chemical Kinetics*, 9:161–178, 1977.
- [357] M C Lin and A M Mebel. Ab initio molecular orbital study of the O + C<sub>6</sub>H<sub>5</sub>O reaction. *Journal of Physical Organic Chemistry*, 8:407–420, 1995.
- [358] Rainer Buth, Karlheinz Hoyermann, and Johann Seeba. Reactions of phenoxy radicals in the gas phase. *Symposium (International) on Combustion*, 25:841–849, 1994.
- [359] S G DAVIS, H Wang, K Breinsky, and C K Law. Laminar flame speeds and oxidation kinetics of benzene-air and toluene-air flames. *Symposium (International) on Combustion*, 26:1025–1033, 1996.
- [360] S Skokov, A Kazakov, and F L Dryer. A theoretical study of oxidation of phenoxy and benzyl radicals by HO<sub>2</sub>. In *The 4th Joint Meeting of the US Sections of the Combustion Institute*, page 1–6, 2005.
- [361] Michael P Burke, Marcos Chaos, Frederick L Dryer, and Yiguang Ju. Negative pressure dependence of mass burning rates of H<sub>2</sub>/CO/O<sub>2</sub>/diluent flames at low flame temperatures. *Combustion and Flame*, 157(4):618–631, 2010.
- [362] SD Tse, DL Zhu, and Chung King Law. Morphology and burning rates of expanding spherical flames in H<sub>2</sub>/O<sub>2</sub>/inert mixtures up to 60 atmospheres. *Proceedings of the Combustion Institute*, 28(2):1793–1800, 2000.
- [363] M Kuznetsov, R Redlinger, W Breitung, J Grune, A Friedrich, and N Ichikawa. Laminar burning velocities of hydrogen-oxygen-steam mixtures at elevated temperatures and pressures. *Proceedings of the Combustion Institute*, 33(1):895–903, 2011.
- [364] Yajin Lyu, Penghua Qiu, Li Liu, Chenchen Yang, and Shaozeng Sun. Effects of steam dilution on laminar flame speeds of H<sub>2</sub>/air/H<sub>2</sub>O mixtures at atmospheric and elevated pressures. *International Journal of Hydrogen Energy*, 2018.
- [365] Tamás Varga, Carsten Olm, Tibor Nagy, István Gy Zsély, Éva Valkó, Róbert Pálvölgyi, Henry J Curran, and Tamás Turányi. Development of a joint hydrogen and syngas combustion mechanism based on an optimization approach. *International journal of chemical kinetics*, 48(8):407–422, 2016.
- [366] Fokion N Egolfopoulos, Peck Cho, and Chung King Law. Laminar flame speeds of methane-air mixtures under reduced and elevated pressures. *Combustion and flame*, 76(3-4):375–391, 1989.

- [367] Erjiang Hu, Xue Jiang, Zuohua Huang, and Norimasa Iida. Numerical Study on the Effects of Diluents on the Laminar Burning Velocity of Methane/Air Mixtures. *Energy & Fuels*, 26:4242–4252, 2012.
- [368] Ultan Burke, Kieran P Somers, Peter OToole, Chis M Zinner, Nicolas Marquet, Gilles Bourque, Eric L Petersen, Wayne K Metcalfe, Zeynep Serinyel, and Henry J Curran. An ignition delay and kinetic modeling study of methane, dimethyl ether, and their mixtures at high pressures. *Combustion and flame*, 162(2):315–330, 2015.
- [369] Ultan Burke, Wayne K Metcalfe, Sinead M Burke, K Alexander Heufer, Philippe Dagaut, and Henry J Curran. A detailed chemical kinetic modeling, ignition delay time and jet-stirred reactor study of methanol oxidation. *Combustion and Flame*, 165:125–136, 2016.
- [370] Yang Li, Chong-Wen Zhou, and Henry J. Curran. An extensive experimental and modeling study of 1-butene oxidation. *Combustion and Flame*, 181:198–213, 2017.
- [371] Yang Li, Chong-Wen Zhou, Kieran P. Somers, Kuiwen Zhang, and Henry J. Curran. The oxidation of 2-butene: A high pressure ignition delay, kinetic modeling study and reactivity comparison with isobutene and 1-butene. *Proceedings of the Combustion Institute*, 36:403–411, 2017.
- [372] Kuiwen Zhang, Colin Banyon, Casimir Togbé, Philippe Dagaut, John Bugler, and Henry J Curran. An experimental and kinetic modeling study of n-hexane oxidation. *Combustion and Flame*, 162(11):4194–4207, 2015.
- [373] John M Simmie and Kieran P Somers. Benchmarking compound methods (cbs-qb3, cbs-apno, g3, g4, w1bd) against the active thermochemical tables: A litmus test for cost-effective molecular formation enthalpies. *The Journal of Physical Chemistry A*, 119(28):7235–7246, 2015.
- [374] Maarten K Sabbe, Mark Saeys, Marie-Françoise Reyniers, Guy B Marin, Veronique Van Speybroeck, and Michel Waroquier. Group additive values for the gas phase standard enthalpy of formation of hydrocarbons and hydrocarbon radicals. *The Journal of Physical Chemistry A*, 109(33):7466–7480, 2005.
- [375] C Franklin Goldsmith, Gregory R Magoon, and William H Green. Database of small molecule thermochemistry for combustion. *The Journal of Physical Chemistry A*, 116(36):9033–9057, 2012.
- [376] SW Benson. Thermodynamic kinetics, 1976.
- [377] Connie W. Gao, Joshua W. Allen, William H. Green, and Richard H. West. Reaction mechanism generator: Automatic construction of chemical kinetic mechanisms. *Comput. Phys. Commun.*, 203:212–225, 2016.
- [378] Z. Hong, D.F. Davidson, E.A. Barbour, and R.K. Hanson. A new shock tube study of the  $\text{H} + \text{O}_2 \longrightarrow \text{OH} + \text{O}$  reaction rate using tunable diode laser absorption of  $\text{H}_2\text{O}$  near  $2.5 \mu\text{m}$ . *Proceedings of the Combustion Institute*, 33:309–316, 2011.

- [379] Shengkai Wang, David F Davidson, and Ronald K Hanson. A Shock Tube and Laser Absorption Study of CH<sub>2</sub>O Oxidation via Simultaneous Measurements of OH and CO. *The Journal of Physical Chemistry A*, 121:8561–8568, 2017.
- [380] Thanh Lam Nguyen and John F Stanton. Accurate ab initio thermal rate constants for reaction of O(<sup>3</sup>P) with H<sub>2</sub> and isotopic analogues. *The journal of physical chemistry. A*, 118:4918–28, 2014.
- [381] Gokhan Altinay and R Glen Macdonald. Determination of the rate constant for the  $\text{oh}(\text{x}2\pi) + \text{oh}(\text{x}2\pi) \rightarrow \text{h}_2\text{o} + \text{o}(\text{3p})$  reaction over the temperature range 295 to 701 k. *The Journal of Physical Chemistry A*, 118(1):38–54, 2013.
- [382] Thanh Lam Nguyen and John F Stanton. Ab initio thermal rate calculations of HO + HO = O(<sup>3</sup>P) + H<sub>2</sub>O reaction and isotopologues. *The journal of physical chemistry. A*, 117:2678–86, 2013.
- [383] W Tsang and RF Hampson. Chemical kinetic data base for combustion chemistry. part i. methane and related compounds. *Journal of physical and chemical reference data*, 15(3):1087–1279, 1986.
- [384] NK Srinivasan and JV Michael. The thermal decomposition of water. *International journal of chemical kinetics*, 38(3):211–219, 2006.
- [385] Jürgen Troe. Detailed modeling of the temperature and pressure dependence of the reaction  $\text{h} + \text{o}_2 (+ \text{m}) \rightarrow \text{ho}_2 (+ \text{m})$ . *Proceedings of the combustion institute*, 28(2):1463–1469, 2000.
- [386] Rishav Choudhary, Julian J Girard, Yuzhe Peng, Jiankun Shao, David F Davidson, and Ronald K Hanson. Measurement of the reaction rate of  $\text{h} + \text{o}_2 + \text{m} \rightarrow \text{ho}_2 + \text{m}$ , for  $\text{m} = \text{ar}, \text{n}_2, \text{co}_2$ , at high temperature with a sensitive oh absorption diagnostic. *Combustion and Flame*, 203:265–278, 2019.
- [387] J V Michael, M C Su, J W Sutherland, J J Carroll, and A F Wagner. Rate Constants For  $\text{H} + \text{O}_2 + \text{M} \rightarrow \text{HO}_2 + \text{M}$  in Seven Bath Gases. *The Journal of Physical Chemistry A*, 106:5297–5313, 2002.
- [388] R. X. Fernandes, K. Luther, J. Troe, and V. G. Ushakov. Experimental and modelling study of the recombination reaction  $\text{H} + \text{O}_2 (+\text{M}) \rightarrow \text{HO}_2 (+\text{M})$  between 300 and 900 K, 1.5 and 950 bar, and in the bath gases  $\text{M} = \text{He}, \text{Ar},$  and  $\text{N}_2$ . *Physical Chemistry Chemical Physics*, 10:4313–4321, 2008.
- [389] Jiankun Shao, Rishav Choudhary, Adam Susa, David F Davidson, and Ronald K Hanson. Shock tube study of the rate constants for  $\text{h} + \text{o}_2 + \text{m} \rightarrow \text{ho}_2 + \text{m}$  ( $\text{m} = \text{ar}, \text{h}_2\text{o}, \text{co}_2, \text{n}_2$ ) at elevated pressures. *Proceedings of the Combustion Institute*, 37(1):145–152, 2019.
- [390] M. A. Mueller, R. A. Yetter, and F. L. Dryer. Flow reactor studies and kinetic modeling of the  $\text{h}_2/\text{o}_2/\text{nox}$  and  $\text{co}/\text{h}_2\text{o}/\text{o}_2/\text{nox}$  reactions. *International Journal of Chemical Kinetics*, 31(10):705–724, 1999.

- [391] J.V. Michael, J.W. Sutherland, L.B. Harding, and A.F. Wagner. Initiation in H<sub>2</sub>/O<sub>2</sub>: Rate constants for H<sub>2</sub>+O<sub>2</sub>H+HO<sub>2</sub> at high temperature. *Proceedings of the Combustion Institute*, 28:1471–1478, 2000.
- [392] Patrick F Conforti, Matthew Braunstein, Bastiaan J Braams, and Joel M Bowman. Global potential energy surfaces for O(P3)+H<sub>2</sub>O(A11) collisions. *The Journal of Chemical Physics*, 133:164312, 2010.
- [393] A. Fernandez-Ramos and A. J. C. Varandas. A vtst study of the h + o<sub>3</sub> and o + ho<sub>2</sub> reactions using a six-dimensional dmbe potential energy surface for ground state ho<sub>3</sub>. *The Journal of Physical Chemistry A*, 106(16):4077–4083, 2002.
- [394] Manuel Monge-Palacios and S Mani Sarathy. Ab initio and transition state theory study of the oh+ ho<sub>2</sub> → h<sub>2</sub>o+ o<sub>2</sub> (3 σ g-)/o<sub>2</sub> (1 δ g) reactions: yield and role of o<sub>2</sub> (1 δ g) in h<sub>2</sub>o<sub>2</sub> decomposition and in combustion of h<sub>2</sub>. *Physical Chemistry Chemical Physics*, 20(6):4478–4489, 2018.
- [395] Ch. Kappel, K. Luther, and J. Troe. Shock wave study of the unimolecular dissociation of H<sub>2</sub>O<sub>2</sub> in its falloff range and of its secondary reactions. *Physical Chemistry Chemical Physics*, 4:4392–4398, 2002.
- [396] J. Troe. The thermal dissociation/recombination reaction of hydrogen peroxide H<sub>2</sub>O<sub>2</sub>(+M)2OH(+M) III. Analysis and representation of the temperature and pressure dependence over wide ranges. *Combustion and Flame*, 158:594–601, 2011.
- [397] Benjamin A Ellingson, Daniel P Theis, Oksana Tishchenko, Jingjing Zheng, and Donald G Truhlar. Reactions of Hydrogen Atom with Hydrogen Peroxide. *The Journal of Physical Chemistry A*, 111:13554–13566, 2007.
- [398] Zekai Hong, Robert D Cook, David F Davidson, and Ronald K Hanson. A shock tube study of OH + H(2)O(2) → H(2)O + HO(2) and H(2)O(2) + M → 2OH + M using laser absorption of H(2)O and OH. *The journal of physical chemistry. A*, 114:5718–27, 2010.
- [399] David A Masten, Ronald K Hanson, and Craig T Bowman. Shock tube study of the reaction hydrogen atom + oxygen .fwdarw. hydroxyl + oxygen atom using hydroxyl laser absorption. *The Journal of Physical Chemistry*, 94:7119–7128, 1990.
- [400] Kinga Yiu Lam, David F. Davidson, and Ronald K. Hanson. A Shock Tube Study of H<sub>2</sub> + OH → H<sub>2</sub>O + H Using OH Laser Absorption. *International Journal of Chemical Kinetics*, 45:363–373, 2013.
- [401] Jan Meisner and Johannes Kästner. Reaction rates and kinetic isotope effects of H<sub>2</sub> + OH → H<sub>2</sub>O + H. *The Journal of Chemical Physics*, 144:174303, 2016.
- [402] Jan Meisner and Johannes Kästner. Erratum: reaction rates and kinetic isotope effects of H<sub>2</sub> + OH → H<sub>2</sub>O + H [j. chem. phys. 144, 174303 (2016)]. *The Journal of Chemical Physics*, 147:049903, 2017.

- [403] Peng Sun, Zhaojun Zhang, Jun Chen, Shu Liu, and Dong H Zhang. Well converged quantum rate constants for the  $\text{H}_2 + \text{OH} \longrightarrow \text{H}_2\text{O} + \text{H}$  reaction via transition state wave packet. *The Journal of Chemical Physics*, 149:064303, 2018.
- [404] Ralph Welsch. Low Temperature Thermal Rate Constants for the Water Formation Reaction  $\text{H}_2 + \text{OH}$  from Rigorous Quantum Dynamics Calculations. *Angewandte Chemie*, 130:13334–13337, 2018.
- [405] Ralph Welsch. Rigorous close-coupling quantum dynamics calculation of thermal rate constants for the water formation reaction of  $\text{H}_2 + \text{OH}$  on a high-level PES. *The Journal of Chemical Physics*, 148:204304, 2018.
- [406] Ralph Welsch. Kinetic isotope effects in the water forming reaction  $\text{H}_2/\text{D}_2 + \text{OH}$  from rigorous close-coupling quantum dynamics simulations. *Physical Chemistry Chemical Physics*, 2019.
- [407] Yujie Tao, Gregory P Smith, and Hai Wang. Critical kinetic uncertainties in modeling hydrogen/carbon monoxide, methane, methanol, formaldehyde, and ethylene combustion. *Combustion and Flame*, 195, 2018.
- [408] W Tsang and R F Hampson. Chemical Kinetic Data Base for Combustion Chemistry. Part I. Methane and Related Compounds. *Journal of Physical and Chemical Reference Data*, 15:1087–1279, 1986.
- [409] Valerie Naudet, Sandra Javoy, and Claude-Etienne Paillard. A high temperature chemical kinetics study of the reaction:  $\text{OH} + \text{ar} = \text{h} + \text{o} + \text{ar}$  by atomic resonance absorption spectrophotometry. *Combustion science and technology*, 164(1):113–128, 2001.
- [410] Leon F Keyser. Kinetics of the reaction hydroxyl + hydroperoxo  $\rightarrow$  water + oxygen from 254 to 382 K. *The Journal of Physical Chemistry*, 92:1193–1200, 1988.
- [411] Zekai Hong, King-Yiu Lam, Ritobrata Sur, Shengkai Wang, David F. Davidson, and Ronald K. Hanson. On the rate constants of  $\text{OH} + \text{HO}_2$  and  $\text{HO}_2 + \text{HO}_2$ : A comprehensive study of  $\text{H}_2\text{O}_2$  thermal decomposition using multi-species laser absorption. *Proceedings of the Combustion Institute*, 34:565–571, 2013.
- [412] Emmanuel Assaf and Christa Fittschen. Cross Section of OH Radical Overtone Transition near  $7028 \text{ cm}^{-1}$  and Measurement of the Rate Constant of the Reaction of OH with  $\text{HO}_2$  Radicals. *The journal of physical chemistry. A*, 120:7051–9, 2016.
- [413] Michael P. Burke, Stephen J. Klippenstein, and Lawrence B. Harding. A quantitative explanation for the apparent anomalous temperature dependence of  $\text{OH} + \text{HO}_2 = \text{H}_2\text{O} + \text{O}_2$  through multi-scale modeling. *Proceedings of the Combustion Institute*, 34:547–555, 2013.

- [414] Yang Liu, Mengna Bai, Hongwei Song, Daiqian Xie, and Jun Li. Anomalous kinetics of the reaction between OH and HO<sub>2</sub> on an accurate triplet state potential energy surface. *Physical Chemistry Chemical Physics*, 21:12667–12675, 2019.
- [415] Ahren W Jasper. Multidimensional effects in nonadiabatic statistical theories of spin-forbidden kinetics: A case study of 3o+ co→ co<sub>2</sub>. *The Journal of Physical Chemistry A*, 119(28):7339–7351, 2015.
- [416] P. R. Westmoreland, J. B. Howard, J. P. Longwell, and A. M. Dean. Prediction of rate constants for combustion and pyrolysis reactions by bimolecular QRRK. *AIChE Journal*, 32:1971–1979, 1986.
- [417] Mark T. Allen, Richard A. Yetter, and Frederick L. Dryer. High pressure studies of moist carbon monoxide / nitrous oxide kinetics. *Combustion and Flame*, 109:449–470, 1997.
- [418] Alexander Sharipov and Alexander Starik. Theoretical study of the reaction of carbon monoxide with oxygen molecules in the ground triplet and singlet delta states. *The Journal of Physical Chemistry A*, 115(10):1795–1803, 2011.
- [419] Ameya V. Joshi and Hai Wang. Master equation modeling of wide range temperature and pressure dependence of CO + OH products. *International Journal of Chemical Kinetics*, 38:57–73, 2006.
- [420] Xiaoqing You, Hai Wang, Elke Goos, Chih-Jen Sung, and Stephen J Klippenstein. Reaction Kinetics of CO + HO<sub>2</sub> Products: Ab Initio Transition State Theory Study with Master Equation Modeling. *The Journal of Physical Chemistry A*, 111:4031–4042, 2007.
- [421] SiOk Ryu, Kuan Soo Shin, and Soon Muk Hwang. Determination of the Rate Coefficients of the CH<sub>4</sub>+O<sub>2</sub>HO<sub>2</sub>+CH<sub>3</sub> and HCO+O<sub>2</sub>HO<sub>2</sub>+CO Reactions at High Temperatures. *Bulletin of the Korean Chemical Society*, 38:228–236, 2017.
- [422] Nancy Faheber, Gernot Friedrichs, Paul Marshall, and Peter Glarborg. Glyoxal Oxidation Mechanism: Implications for the Reactions HCO + O<sub>2</sub> and OCHCHO + HO<sub>2</sub>. *The journal of physical chemistry. A*, 119:7305–15, 2015.
- [423] Jrgen Troe and Vladimir Ushakov. Classical Trajectory Study of the Reaction between H and HCO. *The Journal of Physical Chemistry A*, 111:6610–6614, 2007.
- [424] Malte Dntgen and Kai Leonhard. Reactions of Chemically Activated Formic Acid Formed via HO + H. *The journal of physical chemistry. A*, 120:1819–24, 2016.
- [425] Malte Dntgen and Kai Leonhard. Addition to Reactions of Chemically Activated Formic Acid Formed via HO + H. *The Journal of Physical Chemistry A*, 122:7775, 2018.



- [426] L.N. Krasnoperov, E.N. Chesnokov, H. Stark, and A.R. Ravishankara. Elementary reactions of formyl (HCO) radical studied by laser photolysis-transient absorption spectroscopy. *Proceedings of the Combustion Institute*, 30:935–943, 2005.
- [427] Abraham Horowitz and Jack G. Calvert. The quantum efficiency of the primary processes in formaldehyde photolysis at 3130 and 25c. *International Journal of Chemical Kinetics*, 10(7):713–732, 1978.
- [428] E. J. K. Nilsson and A. A. Konnov. Role of hoco chemistry in syngas combustion. *Energy & Fuels*, 30(3):2443–2457, 3 2016.
- [429] J Troe. Predictive possibilities of unimolecular rate theory. *The Journal of Physical Chemistry*, 83:114–126, 1979.
- [430] Ahren W Jasper and Richard Dawes. Non-born–oppenheimer molecular dynamics of the spin-forbidden reaction  $O(^3P) + CO(X^1\Sigma^+) \rightarrow CO_2(\tilde{X}^1\sigma_g^+)$ . *The Journal of chemical physics*, 139(15):154313, 2013.
- [431] Christian Lund Rasmussen, Jørn Hansen, Paul Marshall, and Peter Glarborg. Experimental measurements and kinetic modeling of co/h2/o2/nox conversion at high pressure. *International Journal of Chemical Kinetics*, 40(8):454–480, 2008.
- [432] M. Goswami, R.J.M. Bastiaans, A.A. Konnov, and L.P.H. de Goey. Laminar burning velocity of lean H2/CO mixtures at elevated pressure using the heat flux method. *International Journal of Hydrogen Energy*, 39:1485–1498, 2014.
- [433] Bryce J Bjork, Think Q Bui, Oliver H Heckl, P Bryan Changala, Ben Spaun, Paula Heu, David Follman, Christoph Deutsch, Garrett D Cole, Markus Aspelmeyer, et al. Direct frequency comb measurement of od+ co doco kinetics. *Science*, 354(6311):444–448, 2016.
- [434] Xinli Song, Jicun Li, Hua Hou, and Baoshan Wang. Ab initio study of the potential energy surface for the OH+COH+CO2 reaction. *The Journal of Chemical Physics*, 125:094301, 2006.
- [435] Adriana Caracciolo, Dandan Lu, Nadia Balucani, Gianmarco Vanuzzo, Domenico Stranges, Xingan Wang, Jun Li, Hua Guo, and Piergiorgio Casavecchia. A Combined Experimental-Theoretical Study of the OH + CO H + CO2 Reaction Dynamics. *The Journal of Physical Chemistry Letters*, 9:1229 1236, 2018.
- [436] Sergey V Panteleev, Artm E Masunov, and Subith S Vasu. Molecular Dynamics Study of Combustion Reactions in a Supercritical Environment. Part 2: Boxed MD Study of CO + OH CO2 + H Reaction Kinetics. *The Journal of Physical Chemistry A*, 122:897 908, 2018.
- [437] Linyao Zhang, Li Yang, Yijun Zhao, Jiayu Zhang, Dongdong Feng, and Shaozeng Sun. Effects of Water Molecule on CO Oxidation by OH: Reaction Pathways, Kinetic Barriers and Rate Constants. *The Journal of Physical Chemistry A*, 121:4868–4880, 2017.

- [438] Ehsan F Nasir and Aamir Farooq. A Shock-Tube Study of the CO + OH Reaction Near the Low-Pressure Limit. *The Journal of Physical Chemistry A*, 120:3924–3928, 2016.
- [439] Joseph T Brice, Tao Liang, Paul L Raston, Anne B McCoy, and Gary E Douberly. Infrared Stark and Zeeman spectroscopy of OHCO: The entrance channel complex along the OH + CO trans-HOCO reaction pathway. *The Journal of Chemical Physics*, 145:124310, 2016.
- [440] Jun Li, Jun Chen, Dong H Zhang, and Hua Guo. Quantum and quasi-classical dynamics of the OH + CO H + CO<sub>2</sub> reaction on a new permutationally invariant neural network potential energy surface. *The Journal of chemical physics*, 140:044327, 2014.
- [441] Christopher J Johnson, Rico Otto, and Robert E Continetti. Spectroscopy and dynamics of the HOCO radical: insights into the OH + CO H + CO<sub>2</sub> reaction. *Physical Chemistry Chemical Physics*, 16:19091–19105, 2014.
- [442] Jun Li, Yimin Wang, Bin Jiang, Jianyi Ma, Richard Dawes, Daiqian Xie, Joel M Bowman, and Hua Guo. Communication: A chemically accurate global potential energy surface for the HO + CO H + CO<sub>2</sub> reaction. *The Journal of Chemical Physics*, 136:041103, 2012.
- [443] Jianyi Ma, Jun Li, and Hua Guo. Quantum Dynamics of the HO + CO H + CO<sub>2</sub> Reaction on an Accurate Potential Energy Surface. *The journal of physical chemistry letters*, 3:2482–6, 2012.
- [444] Jun Li, Changjian Xie, Jianyi Ma, Yimin Wang, Richard Dawes, Daiqian Xie, Joel M Bowman, and Hua Guo. Quasi-Classical Trajectory Study of the HO + CO H + CO<sub>2</sub> Reaction on a New ab Initio Based Potential Energy Surface. *The Journal of Physical Chemistry A*, 116:5057–5067, 2012.
- [445] Nanase Kohno, Mari Izumi, Hiroshi Kohguchi, and Katsuyoshi Yamasaki. Acceleration of the Reaction OH + CO H + CO<sub>2</sub> by Vibrational Excitation of OH. *The Journal of Physical Chemistry A*, 115:4867–4873, 2011.
- [446] Hua-Gen Yu, James T Muckerman, and Joseph S Francisco. Quantum force molecular dynamics study of the reaction of O atoms with HOCO. *The Journal of Chemical Physics*, 127:094302, 2007.
- [447] Wei-Chen Chen and R A Marcus. On the theory of the reaction rate of vibrationally excited CO molecules with OH radicals. *The Journal of Chemical Physics*, 124:024306, 2006.
- [448] Juan P. Senosiain, Stephen J. Klippenstein, and James A. Miller. A complete statistical analysis of the reaction between OH and CO. *Proceedings of the Combustion Institute*, 30:945–953, 2005.
- [449] Wei-Chen Chen and R A Marcus. On the theory of the CO+OH reaction, including H and C kinetic isotope effects. *The Journal of Chemical Physics*, 123:094307, 2005.

- [450] R S Zhu, E G W Diau, M C Lin, and A M Mebel. A Computational Study of the OH(OD) + CO Reactions: Effects of Pressure, Temperature, and Quantum-Mechanical Tunneling on Product Formation. *Journal of Physical Chemistry A*, 105:11249–11259, 2001.
- [451] MAKJ Metghalchi and James C Keck. Laminar burning velocity of propane-air mixtures at high temperature and pressure. *Combustion and flame*, 38:143–154, 1980.
- [452] Nist computational chemistry comparison and benchmark database, nist standard reference database number 101, release 19, april 2018, editor: Russell d. johnson iii.



**Titre :** Compréhension et Modélisation de Flamme d'Essence à Fortes Charges et Fortes Dilutions

**Mots clés :** combustion, essence, EGR, modélisation, chimie physique, cinétique

**Résumé :** La réduction des émissions de CO<sub>2</sub> et de polluants est un des enjeux essentiels pour faire face aux problèmes liés au changement climatique. Dans le secteur des transports, la technologie de recirculation des gaz d'échappement (EGR) est souvent utilisée dans les moteurs turbo-compressés à allumage commandé pour réduire la consommation de carburant, inhiber les risques de cliquetis et réduire les émissions de NOx. Cependant, des taux d'EGR élevés restent difficiles à atteindre car ils réduisent le dégagement de chaleur et la stabilité du moteur. L'augmentation du niveau de turbulence et la mise en oeuvre de systèmes à allumage commandé avancés n'apportant pas d'améliorations suffisantes dans des conditions aussi extrêmes, la chimie de la combustion pour les très hautes dilutions suscite un intérêt croissant. Le présent travail vise à comprendre la chimie de combustion des flammes prémélangées essence/air très diluées et à établir un mécanisme cinétique détaillé par modélisation multi-échelle afin de prévoir les caractéristiques de combustion avec une précision suffisante dans des conditions de forte dilution.

Ce travail adopte une approche de modélisation multi-échelle et cible la vitesse de flamme laminaire ( $S_L$ ) d'un substitut d'essence, appelé TRFE et qui est constitué d'isooctane, de n-heptane, de toluène et d'éthanol. Pour la modélisation à l'échelle microscopique, la réaction entre

le cétène et le radical hydroxyle, qui pourrait être importante pour la  $S_L$  dans des conditions très diluées, est étudiée théoriquement à l'aide de méthodes de structure électronique *ab initio* pour la surface d'énergie potentielle (PES) et Rice – Ramsperger – Kassel – Marcus Theory couplé à l'équation maîtresse (RRKM / ME) pour les coefficients de vitesse. Des PES détaillées sont obtenues, les voies dominantes sont identifiées et leurs coefficients de vitesse phénoménologiques sont dérivés pour être utilisés dans la modélisation de la combustion. Pour la modélisation à l'échelle macroscopique, les paramètres cinétiques, thermodynamiques et de transport importants pour la vitesse de la flamme laminaire dans des conditions très diluées sont d'abord identifiés à l'aide d'une analyse de sensibilité réalisée sur une version initiale du mécanisme TRFE de départ. Les réactions sensibles impliquent principalement HO<sub>2</sub>, les espèces C<sub>2</sub> – C<sub>3</sub> et des radicaux issus du carburant. Le mécanisme initial, via un travail spécifique à chacun des sous-mécanismes, est mis à jour à l'aide des paramètres cinétiques les plus récents issus de la littérature. Enfin, un mécanisme détaillé adapté aux calculs de vitesse de flamme laminaire dans des conditions de forte dilution est validé. Un terme mathématique de dilution pour les corrélations  $S_L$  dans des conditions de forte dilution est proposé pour une utilisation dans les simulations de calcul dynamique du fluide (CFD).

**Title :** Multi-Scale Kinetic Modeling of Highly-Diluted Gasoline Premixed Flames

**Keywords :** combustion, gasoline, EGR, modeling, physical chemistry, kinetics

**Abstract :** Reducing CO<sub>2</sub> and pollutant emission is the essential challenge when dealing with climate change problems. In the transport sector, exhaust gas recirculation (EGR) technology is often used in turbocharged gasoline spark ignition (SI) engines to increase fuel economy, inhibit knock tendency, and reduce NOx emissions. However, high EGR ratios are still difficult to achieve, as they result in reduced heat release and engine stability. As increasing turbulence level and advance spark ignition systems could not bring sufficient improvements at such extreme conditions, growing interest is cast onto the combustion chemistry under high dilution. The present work aims to understand the combustion chemistry of highly-diluted gasoline premixed flames and to establish a detailed kinetic mechanism by multi-scale modeling to predict combustion characteristics with sufficient accuracy at highly-diluted conditions.

This work adopts a multi-scale modeling approach, and targets on the laminar flame speed ( $S_L$ ) of a gasoline surrogate, which is named toluene reference fuel with ethanol addition (TRFE) and consist of isooctane, n-heptane, toluene, and ethanol. For micro-scale modeling, the reaction between ketene and hydroxyl radical, which might be important to the  $S_L$  at highly-diluted conditions, is studied theoretically

using *ab initio* electronic structure methods for the potential energy surface (PES) and Rice–Ramsperger–Kassel–Marcus Theory coupled with Master Equation (RRKM/ME) for the rate coefficients. Detailed PES is obtained, dominant pathways are identified, and their phenomenological rate coefficients are derived to be utilized in combustion modeling. For macro-scale modeling, firstly, important kinetic, thermodynamic, and transport parameters to the laminar flame speed ( $S_L$ ) at highly-diluted conditions, are firstly identified using sensitivity analysis based on a starting mechanism. Sensitive reactions are found to mostly involve HO<sub>2</sub>, C<sub>2</sub>–C<sub>3</sub> species and fuel radicals. Secondly, in the sub-mechanisms where these reactions lies, diluted flames of the corresponding fuels are studied and chemical detail of the dilution effects are explored. The starting mechanism is updated by state-of-the-art kinetics parameters found in the literature for each sub-mechanisms. Finally, a detailed mechanism suitable for laminar flame speed calculations at highly-diluted conditions is established after validation. A mathematical dilution term for  $S_L$  correlations at highly-diluted conditions is proposed for the use in computational fluid dynamic (CFD) simulations.